MECHANOBIOLOGICAL ANALYSIS OF THE DEVELOPING ATRIOVENTRICULAR VALVE

A Dissertation

Presented to the Faculty of the Graduate School

of Cornell University

In Partial Fulfillment of the Requirements for the Degree of

Doctor of Philosophy

by

Russell A. Gould

January, 2014

MECHANOBIOLOGICAL ANALYSIS OF THE DEVELOPING ATRIOVENTRICULAR VALVE

Russell A. Gould, Ph. D.

Cornell University 2014

Valvular structural and functional defects account for millions of defects in human births, and their effects can be immediately life threatening or cause more subtle cell and/or matrix changes that can lead to functional defects later in life. Nearly all study of mechanical action on cellular function focuses on the “normal and pathological” adult age. This neglects key stages in the functional life cycle of tissues where remodeling is most active yet, controlled, early development. Until the basic interactions between cells and their microenvironment are understood in this context, our ability to understand congenital malformation and manipulate these phenomena remains limited. The objective of this thesis was to understand the role of mechanics combined with biology during the developmental process of valvulogenesis. This thesis demonstrates that valve interstitial cells respond to mechanical strain and directionality by regulating cellular proliferation, differentiation, and matrix remodeling. Using a novel bioreactor and in-vivo perturbation studies, we found that mechanical stretch directly inhibits myofibroblastic activation in mitral valve progenitor cells through a RhoA dependent mechanism. Consequently, Rac1 expression is promoted matrix condensation, as typically seen in mature quiescent leaflets. In post-natal valve maturation, we determined that tissue stretch correlates with tissue

biomechanics and underlying cellular deformation. However, in pathological conditions such as Marfan Syndrome, tissue stretch becomes decoupled with cellular deformation by an unknown mechanism. Lastly, we modeled the molecular mechanisms of early cushion development applying systems biology model of ordinary differential equations. In addition to predicting and confirming a new heterogeneous phenotype, we concluded with 3 other possible hypotheses, which are included in the discussion. The biological and computer models developed in this thesis can be used in future experiments to explore the combined biological and mechanical regulation of multi-scale valve formation. My hope is that the results presented in this thesis will eventually be useful for developing efficient strategies to control tissue adaptation and remodeling as well as accelerate the construction of cardiovascular tissue replacements.

BIOGRAPHICAL SKETCH

Russell A. Gould graduated with magna summa cum laude honors in 2007 from the Rensselaer Polytechnic University with a B.S. in Biomedical Engineering. During his undergraduate studies, Russell received the Irving Shapiro Scholarship 34' Scholars Award for his academic honors and was a member of the Tau Beta Pi Engineering Society. Russell also obtained the National Collegiate Inventors and Innovators Alliance (NCIIA) Design award. This was one of ten national stipends in the 2007 Biomedical Engineering Idea competition for his senior design project, the Real-Time Intra-Operative Cerebrospinal Fluid Leak Detector. Russell studied as a Ph.D. candidate in Biomedical Engineering at Cornell University where he received a 2 year NSF STEM (Science, Technology, Engineering, and Math) GK-12 fellowship to design and teach science curriculum in the classroom. Above all, his goal was to inspire and motivate high school students to become interested in science and technology. His research focuses on understanding the mechanobiological pathways which govern valvulogenesis.

Dedicated to my family

ACKNOWLEDGMENTS

Above all, I would like to acknowledge both my mother and father. They are two people full of wisdom, integrity, and character. There are times in everyone's life when decisions are made, and you hope they turn out positive. As I reflect, I know I did not fully have the knowledge or discipline to make many of those decisions, and without the guidance of my parents, I would not be where I am today. I am humbled to call them as my parents. I would also like to thank my grandfather. He is passed away now, but as a medical doctor, he inspired me to become interested in math, engineering, and medicine. We had many wonderful conservations and I truly appreciate his guidance.

I would like to express my gratitude to Professor Jonathan Butcher. I gravitated towards his inspiring and ambitious personality. He always believed in me and would never settle for any underachieving. More importantly, I cannot thank the patience he had with me. Whether it was directly related to my research, or outside influences, he was always understanding of the big picture.

I would also like to express my thanks to Professor Jeffery Varner. Jeff gave me the opportunity to work in his systems biology lab which helped me to develop a tool set that has made me a better-rounded researcher. He led by example, and through his mentorship I am a more confident and truly believe that anything is possible with hard work. We shared some great conversations, and I will miss our chats about the latest video games.

Lastly, I would thank all of those that have helped me in my research here at

Cornell. Thanks to my lab mates Philip Buskohl, Gretchen Mahler, Cagatay Huseyin Yalcin, Anirikh Chakrabarti, Jen Richards, Emily Howell, Laura Hockaday, Stephanie Lindsey, and Chelsea Gregg. I would also like to thank Adam Neuman with his help in collecting and generating the data used in Figure 9.3.

Beyond research there has also been Katrina Shum. She has stood by me in every way.

Finally, I would like to acknowledge Cornell and the many sources of funding for my research: NSF (National Science Foundation), AHA (American Heart Association), and NIH (National Institute of Health).

Portions of the material presented in this Thesis have been previously published in scientific journals. Portions of Chapter 3 was published in the May 2012 issue of the *Acta Biomaterialia*, Chapter 5 was published in the September 2012 issue of *PLoS One*, and Chapter 6 was published in the March *2013 WIRES Systems Biology and Medicine*. I have received permission from the publishers to reprint this information in this document.

TABLE OF CONTENTS

LIST OF FIGURES

LIST OF TABLES

LIST OF ABBREVIATIONS

EMT- Endothelial to Mesenchymal Transition

VIC- Valvular Interstitial Cell

AVC- Atrioventricular Canal

ABS- Anisotropic Bioreactor System

BAV- Bicuspid Aortic Valve

HLHS- Hypoplastic Left Heart Syndrome

OFT- Outflow Tract

FEA- Finite Element Analysis

CHAPTER 1

INTRODUCTION TO VALVULOGENESIS

1.1: Valvular Morphogenesis

Initiation of Valvular Morphogenesis - Valvulogenesis is a complex process involving the formation and morphogenesis of both the atrioventricular and semilunar valves. The early embryonic heart is a single myocardial tube lined with endocardial cells. During the looping process, simultaneous valve formation initiates by deposition of hyaluronan-rich gelatinous matrix, called cardiac jelly, forming swellings, which project into the lumen. At the onset of Hamburger and Hamilton ($HH14^{-}$, E9.0 in mouse), a process called EMT (epithelial-mesenchymal transition) takes place in which endocardial cells lining the cushions rapidly differentiate towards a mesenchymal phenotype. This process is associated with downregulation of cell-cell contacts, such as E-cadherin and PECAM1, the acquisition of cell-matrix adhesions, and cytoskeleton rearrangement [1]. Loss of tight junctions in EMT is concomitant with the acquisition of a spindle shaped morphology and migratory/invasive phenotype. The invasiveness of the mesenchymal phenotype is critical, as these cells dive into the hyaluronan-rich cardiac jelly, degrade the underlying matrix, and deposit newly synthesized collagen I, II, III, versican, and other proteoglycans [2]. These newly populated mesenchymal swellings are called “cushions” due to their soft visual appearance while stitched to the myocardial wall. These cushions are formed in pairs that oppose each other during the cardiac cycle to act as primitive valves by maintaining unidirectional blood flow [3]. One pair of cushions develops in the atrioventricular (AV) canal, while the set (proximal and distal) develops in the outflow tract (OFT). The processes by which the AV and outflow cushions remodel into thin fibrous leaflets are discussed below.

Atrioventricular Valve Remodeling - By HH26 (E12.5 in mouse), the AV cushions fuse together at the midline along a superior/inferior axis, dividing the canal into the right and left conduits. Even before fusing, the expansion of the cushions creates a “dog-bone” shape of the ventricular inlet that begins to divert blood flow around the cushions, potentially contributing to their eventual fusion [4]. From the left and right lateral aspects of this fused central cushion mass evolves the septal leaflets of the left and right AV valves. At about the same time as central cushion fusion, new cushions begin to form from the left and right lateral walls, which will eventually form the mural AV leaflets. The process by which the AV leaflets form is thought to involve a process of proliferation, extension, condensation, and delamination [5] (Figure 1.1). Briefly, a subendocardial portion of the AV cushion expands and extends along the myocardial substrate, which is mediated in part by a fibroblast growth factor 4 (FGF4) section by the endocardium [6]. These cells form a progressive-like zone and begin to differentiate further towards a fibroblastic phenotype [7]. This zone of differentiated cells condenses the cushion matrix into a thinner and more fibrous tissue consisting of a subendocardial surface, which is largely positive for laminin, while the ventricular side is predominately collagen III. Furthermore, fenestrations between the myocardial wall and valve tissue begin to form, possibly due to expansion of the ventricular cavities or changes in hemodynamic loading [8]. Upon further delamination, residual contacts between the valve tissue and myocardium form the site of newly developing papillary muscles. This creates mesenchymal tissue strands that develop into the tendinous chords of the AV valves. By HH36 full delamination from the myocardial wall occurs and the distinct tri-layer structure (atrialis/spongiosa, fibrosa, and ventricularis) with a largely organized lamellar network of elastin and newly formed collagen (I,II,III,V,VI) [9].

Semilunar Valve Morphogenesis - Similar to AV valves in terms of mesenchymal transformation and formation of the tri-layered valve structure, semilunar valves become excavated from the aortic side inward. Between HH17 and HH26 (E10–E12), the conal and truncal cushion pairs of

the outflow tract become invaded and populated by activated endocardially derived cells. The aorticopulmonary (AP) septum spirals through the out flow tract lumen with a counterclockwise rotation so that the right portion of the semilunar ring is derived from the original left side of the primitive outflow tract [10, 11]. The splitting of the parietal and septal distal truncal cushions by the AP septum, combined with the intercalated cushions of the distal outflow tract creates the six cushions required for the formation of the semilunar valves which is completed by HH34 (E14.5). The tissue on the arterial side becomes a more condensed, fibrous matrix as the small depression continues to deepen, sculpting the leaflet cusps. By HH39–40, the leaflets begin to appear trilaminar in nature, with an elastin–collagen lamellar structure forming at the ventricular surface. By HH45, fibrous tissue is seen radiating from the attachment of the valve cusps into the aortic wall from the base to the level of the commissures, creating an anchoring ring of fibro-cartilaginous tissue around the sinuses [12].

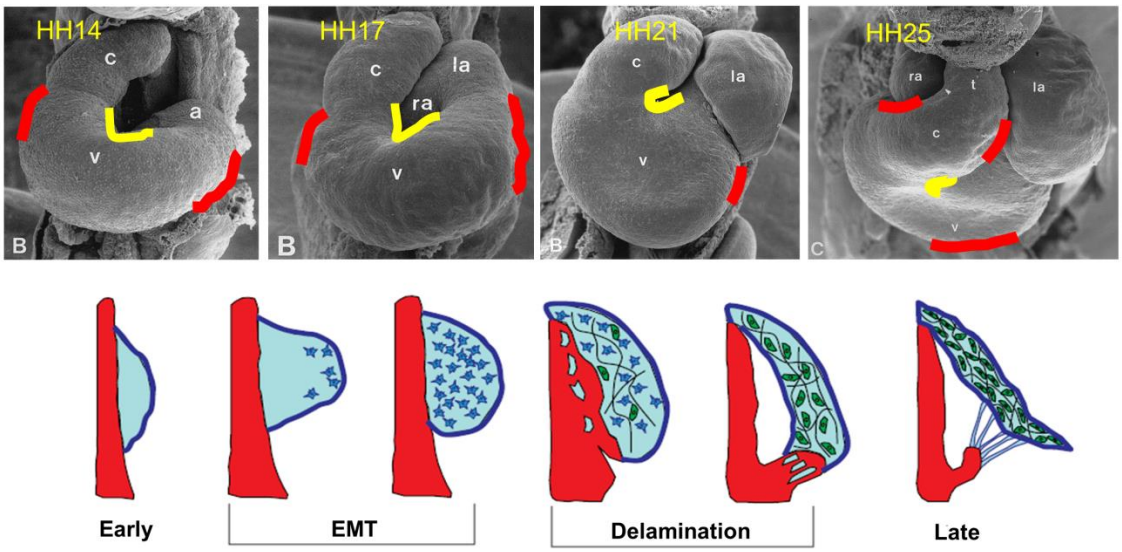

Human		Mouse [E]	Chick (HH)
days	weeks	E	HH
22	3	7.5-8.5	7.0-10.0
24	4	8.0-8.5	9.0-12.0
26	3.5+	9.0-11.0	11.0-12.0
28	4	10.0-11.0	13.0-22.0
29	4	11.0-13.5	15.0-23.0
31	5	12	24.0-28.0
33	4.5+	12.0-13.0	25.0-28.0
35	5	13.0-15.0	26.0-31.0
37-43	5+ to 6	15.0+	27.0-34.0

Figure 1.1 – Summary diagram illustrating heart and valve morphogenesis with respect to embryonic chick, mouse, and human staging.

1.2: Model Systems to Study Valve Development

Generating suitable quantitative data is essential for developing a model with predictive capability. *In vivo* experimental and/or genetic perturbations of animal models, coupled with well-controlled in vitro analyses, have been vital to understanding mechanisms of cell and tissue level morphogenesis. Technology capable of generating large amounts of data across multiple experimental scales is relatively straightforward to apply; however, the technology that can be applied is dependent on the animal model. As a result, investigators often combine data from multiple animal models when performing computational studies [13]. A discussion of different

animal models as well as appropriate corresponding experimental assays essential for connecting molecular and morphogenetic aspects of cardiac development proceeds below.

Zebrafish - Employed in research since the 1970's, the zebrafish (*Danio rerio*) is small, can be cultured inexpensively, and can produce up to 200 eggs per week as an adult. The zebrafish embryo is transparent, develops rapidly, and grows externally from the mother, which allows for ease in experimental manipulation and observation [14] Zebrafish have a unique ability to develop in the absence of a functioning heart for at least 5 days post fertilization, since sufficient oxygen is obtained by diffusion [15]. Its genome has been fully sequenced, and zebrafish eggs have been found to tolerate microinjection and DNA delivery very well. Genetic manipulation via morpholinos and transgenics is among the simplest to perform of all vertebrate models [16, 17]. Furthermore, whole genome genetics and phenotype screens from mutagenesis agents can be filtered using a high throughput format [18, 19]. While the genetic and molecular process of myocardial formation of the zebrafish broadly parallels that of the human, the zebrafish only possesses a two-chambered, essentially right-sided heart. In addition, zebrafish valves do not develop through endocardial-mesenchymal transition (EMT) as in larger, higher order models [20]. Instead, the valves fold inward to create a thin, bilayerd tissue without mesenchyme until much later [21]. Likewise, there are also differences in outflow tract/aortic arch morphogenesis compared to human morphogenesis [22]. The embryonic zebrafish heart is only a few hundred microns in length when fully grown, which limits non-genetic experimental inquiry and/or tissue isolation.

Amphibian - Amphibians, such as the African clawed frog (*Xenopus laevis*) and the eastern newt (*Notophthalmus viridescens*), have a three-chambered heart containing two atria, a single shared ventricle, and a shared outflow tract with a spiral shaped valve that helps partition relatively unmixed flow to the lungs and the rest of the body [23]. Amphibian eggs can be

cultured very easily, but mesodermal cells are pigmented, limiting in vivo optical analysis during heart development stages. Morpholinos can also be developed and employed in frog embryogenesis similar to zebrafish hearts [24]. Frog embryos were used to show that cardiac laterality extends to the cellular level, with heterotaxic chambers and valves populated by cells from both sides [25]. Fewer studies have been conducted with the newt model, but recent findings show adult newt ventricular regeneration is similar to that of zebrafish suggesting it will become a more common model choice for heart development as its genome is clarified [26].

Avian - Avian models such as the chick (*gallus gallus*) and quail (*Coturnix*) are well characterized and long applied in experimental embryogenesis ranging from cell isolation to *in-vivo* perturbation models. Within two to three days, chick embryos gastrulate, neurulate, and fold into three-dimensional (3-D) animals with beating hearts, somites, and complex nervous systems. Complete cardiac morphogenesis in the avian model occurs from approximately 2.5-10 days, which is slower compared to other small animal models and enables investigation of highly time sensitive transient features of morphogenesis such as septation and outflow tract morphogenesis [5]. Such rapid development is an advantage for experimental design and timely data collection. The anatomy of the chick heart closely parallels that of the human heart. In particular, the left ventricle, atrioventricular valves, and outflow tract valves are similar in shape, matrix composition, and cellularity. The principle differences between chick and human are that the right AV valve develops into a muscular flap valve in the right AV junction and the aorta arises from the right fourth aortic arch instead of the left [27]. Chick embryos can be cultured *in ovo* or removed from the eggshell [28] making them semi-transparent and of sufficient size to enable microscope guided experimentation [29, 30]. These experiments include microsurgery, tissue ablation, transplantation chimeras, local gene delivery, and biochemical delivery via soaked materials [31, 32]. Experiments using the avian model have generated significant insight into the contributions of local cell populations to tissue morphogenesis and physical

function. Although genetic manipulation is more technically challenging and time consuming in the avian embryo, some transgenics are available for study [33].

Drosophila - The fly (Drosophila melanogaster) is one of the most intensively studied organisms in biology and has served as a model system for the investigation of cardiac development. The *Drosophila* heart (also called the dorsal vessel) is an organ for hemolymph circulation that resembles the vertebrate heart at its transient linear tube stage. Dorsal vessel morphogenesis shares several similarities with early events of vertebrate heart development. In particular, cardiac progenitors are derived from laterally positioned mesoderm, being specified through the use of conserved cellular induction pathways and downstream transcriptional effectors [34]. At these early stages of heart development, the drosophila has been an attractive system for the study of cardiogenesis due to its relatively simple structure and the productive use of *Drosophila* genetic approaches [35]. Genetic analyses have identified and/or confirmed hundreds of important intracellular transducers, which provide large gene regulatory networks essential for mapping the underlying cardiac specification [36]. Currently, projects such as the Berkeley Drosophila Genome are in the middle of a sustained effort to define the expression patterns of all predicted genes in the genome [37]. This information will be critical in identifying what genes contribute to the cardiac phenotype.

Rat -The rat (*Rattus norvegicus*) has been used extensively in cardiac research, although studies focusing on embryonic development have been limited. This is largely due to the abundance of genetic models available in mice and the overall economic cost. The majority of investigations focus on later stage pathogenesis of cardiovascular disease and/or the effects of drug intervention [38]. In general, the rat embryo, fetus, and postnatal morphologies correlate with both mouse and human development, and nearly all the features (external and internal) of the embryonic chick [39]. This provides an excellent morphological and chronological model for

all stages of cardiac development. A major advantage of the rat is the relative ease with which surgical techniques can be performed when necessary for some disease or treatment models [40]. In many cases, measurement of relevant circulatory, biochemical, and hemodynamics parameters have been largely optimized for understanding cardiac function.

Mouse - Mice (*Mus musculus*) are the mammalian animal model of choice for cardiac developmental genetics. The mouse has a relatively fast gestation cycle, many pups per litter, and relatively short post-natal development compared to other mammals. Nearly every genetic tool developed has reagents available for the mouse. Mice tolerate oocyte injections very well, and their embryonic stem cells receive DNA easily. Unlike the other animal models, mice have a placental circulation and a fully four chambered heart with correct laterality, similar to humans [41]. However, the chordae of the murine AV valves are far less prominent than the pronounced tendinous chords of the human heart valves and heart beat frequency during development is 6-8 fold higher [27]. The cellularity and matrix striation of mouse valves are significantly less prominent than in humans or avians, in part because of their small size. Mouse embryos are difficult to culture outside of the mother, precluding experimentation except during the earliest stages of cardiogenesis [42]. Quantifying mouse heart physiology has also been challenging because of its size and speed with investigators normally relying on approximations from the dorsal aorta.

The largest integrated database of genetic, genomic, and phenotypic data has been generated for the laboratory mouse and compiled by the Mouse Genome Database (MGD) [43]. Reporter genes, such as *lacZ* or GFP, provide a sensitive method of detecting and following gene expression trends during morphogenesis. Mutant mouse transgenesis, either to overexpress or knock out specific genes, is an indispensable component of current research [44, 45]. Tissue-specific promoter targeting constructs, especially when combined with conditional expression

systems such as Cre/Lox, has permitted spatial and temporal mapping of gene mapping and perturbation through manipulation [46-48].

Overall, each animal system has advantages and limitations to studying cardiogenesis, and no one model yet captures all components. A key challenge with a multi-scale approach is merging and analyzing data acquired from multiple animal models, especially in situations where the morphogenetic processes are known to be different (Table 1.1).

Model organism	Defined cardiac morphogenesis staging	Anatomical similarity to human heart	Ease of genetic manipulation	Ease of experimental manipulation	Ease of in vivo observation
Zebrafish	+	+	+++	+	+++
Amphibian	+	++	++	++	++
Avian	+++	+++	+	+++	+++
Mouse	++	+++	+++	-	+

Table 1.1 - Summary of advantages and disadvantages of using animal models to study embryonic valve development.

In-Vitro Experimentation - In vitro culture systems enable well-controlled investigation of fundamental molecular, cellular, and tissue level responses in isolation from other tissues. These experiments require the ability to isolate pure tissue segments that can either be explanted directly or digested to obtain cells. Genetic manipulation of cells and tissues, including overexpression and knockdown, is achieved through a variety of methods including electroporation, viral delivery, or lipid carriers [49-51]. The vast majority of genetic manipulation studies have used isolated cells cultured on artificial plastic substrates. The physical properties of the cellular microenvironment (*e.g.* stiffness) can have profound effects on cell phenotype [52]. Tunable soft culture substrates have been developed to overcome these limitations, most notably polyacrylamide and polydimethylsulfone (PDMS) gels [53]. These materials can be further functionalized via microfabrication and selective polymerization techniques to exhibit

gradients in stiffness, adhesion ligands, growth factors, and even gene plasmid concentration [54]. While microfabrication and selective polymerization approaches enable high throughput screening of the effects of the different gradient paramters on cell phenotype, these model systems remain inherently two dimensional (2D). Three dimensional (3D) culture models can be created using tissue engineering techniques, mainly with aqueous hydrogels created from natural extracellular components, which include collagen, fibrin, alginate, and hyaluronic acid [55]. The addition of hybridizing biopolymers and synthetic polymers can enhance the range of possible material properties [56]. One of the first examples of a tissue engineering approach used a collagen hydrogel to study embryonic heart valve formation. Runyan and Markwald *et al.* isolated avian AV canals (chick HH14- or mouse embryos E8.5) and then explanted onto the surface of a collagen gel surface [57]. It has since become a staple assay to study 3D matrix interactions in developmental biology.

Genomics and epigenomics - The emerging epigenomic changes and the interactions between *cis*-acting elements and protein factors may play a central role in gene regulation [58]. To understand the crosstalk between DNA and protein on a genome-wide scale, techniques like ChIP-seq take the appraoch of combining chromatin immunoprecipitation with microarray technology [59, 60]. This high throughput strategy helps screen the targets of critical transcription factors and profile the genome-wide distribution of histone modifications, which will enable the feasibility of conducting large-scale studies, such as the Human Epigenome Project [61]. Many variations of the CHIP technology have been implemented such as the presence of DNA methylation (MeDIPchip) or DNA methylation based on the hypersensitivity to DNaseI cleavage (DNase-chip) [62, 63]. Other applications include the analysis of sequence variations by genotyping microarrays, copy number variations (Array-CGH), or RNA profiling (mRNA, microRNA). A custom-made, cardiovascular-based cDNA microarray, termed the CardioChip, was created to characterize gene expression in end-stage cardiomyopathies relative to gene

expression associated with heart function [64]. Even more recent, NGS technology (Next Generation Sequencing) has revolutionized the genomic and transcriptomic approaches to biology reducing the sequencing cost and significantly increasing the throughput [65]. It is expected that NGS will become more important in the study of inherited and complex cardiovascular diseases (CVDs) [66]. However, the NGS approach to the genetics of CVDs represents a territory, which has not been widely investigated.

These approaches have been useful for characterizing expression profiles in developmental, normal, and diseased conditions [67]. For example Chen *et al.* and colleagues found that *Csx/Nkx2-5*-deficient hearts were hypertrabeculated and noncompacted at birth. At adulthood, the mice exhibited progressive heart failure characterized by chamber dilatation with extensive trabecular formation [68, 69] (It is important to note though that mice lacking this supposedly essential identifier of cardiac phenotype still produced a functioning heart, emphasizing the fact that perfect "markers" aren't necessarily functionally essential). Upon microarray analysis, aberrant expression was revealed in a number of genes including the potential downstream targets, such as bone morphogenic protein-10 (BMP-10). A similar approach was used to understand the existence of regulatory pathways active in developing AV valves and bone progenitor cells. Overall, MC3T3 cells (pre-osteoblasts) were significantly more similar to late stage valves (E17.5), supporting the hypothesis that valve maturation involves the expression of many genes also expressed in osteoblast differentiation [70].

1.3: Embryonic Valve Biology

Initiation of EMT - Efforts to investigate the mechanisms of epithelial to mesenchymal transition and cushion formation have been greatly facilitated by the use of a three-dimensional collagen gel explants. In this system, AV canals (chick or mouse embryos) are isolated and then explanted onto the collagen gel surface. The endocardium of the AV canal adheres to the

surface, from which a subset of these cells undergoes the mesenchymal transformation and invades the underlying matrix. Interestingly, EMT does not take place if the myocardium is removed directly after the endocardium has been attached to the collagen gel surface (HH14- or E9.0). This suggests that the AV myocardium has a unique capacity to secrete specific signals for EMT [71]. After these landmark observational studies, the focus shifted to understand the makeup of the myocardial inductive signal for EMT in AV canal endocardial cells. Through segmental patterning, it was found that myocardial cells express BMP2 in a manner consistent with the segmental pattern of cushion formation. Using these AV explants in mice, Sugi et al. showed that BMP2 was sufficient to induce EMT in mouse AV canal cultures in the absence of AV myocardium [72]. Furthermore, treatment of AV cultures with Noggin, a BMP inhibitor, prevented mesenchymal cell formation in untreated cultures, and also prevented BMP2 induced EMT in AV cultures with intact AV myocardium (Figure 1.2).

Interestingly, BMP2 treatments of AV explants resulted in increased TGFβ2 protein levels [72]. This is particularly important because antagonists to TGFβ2 and TGFβ3 show that they play distinct but complementary roles in regulating the initial transformation events in chick. Endocardial TGFβ2 expression is required for cell separation and hypertrophy, while TGFβ3 signaling is required for mesenchymal transformation and migration [73]. TGFβ3 induces expression of MMP-2 and MT-MMP, which digest the collagen IV endocardial matrix, permitting invasion [74]. At the onset of EMT in chick cardiogenesis, TGFβ3 is expressed in transforming endothelial and invading mesenchymal cells, while BMP2 is expressed in the subjacent myocardium. To restrict this entire process to the cushion forming region in the lumen, endocardial Notch1 signals repress myocardial BMP2 through the Hey1 transcription factor [75]. Furthermore, chick AV explants experiments have investigated the combinatory role of both TGFβ3 and BMP2. In summary, it was found that (1) myocardial derived inductive signals upregulate the expression of AV endothelial TGFβ3 at the onset of EMT, (2) TGFβ3 needs to be

expressed by these endothelial cells to trigger the initial phenotypic changes of EMT, and (3) myocardial BMP2 acts synergistically with TGFβ3 in the initiation of EMT [76].

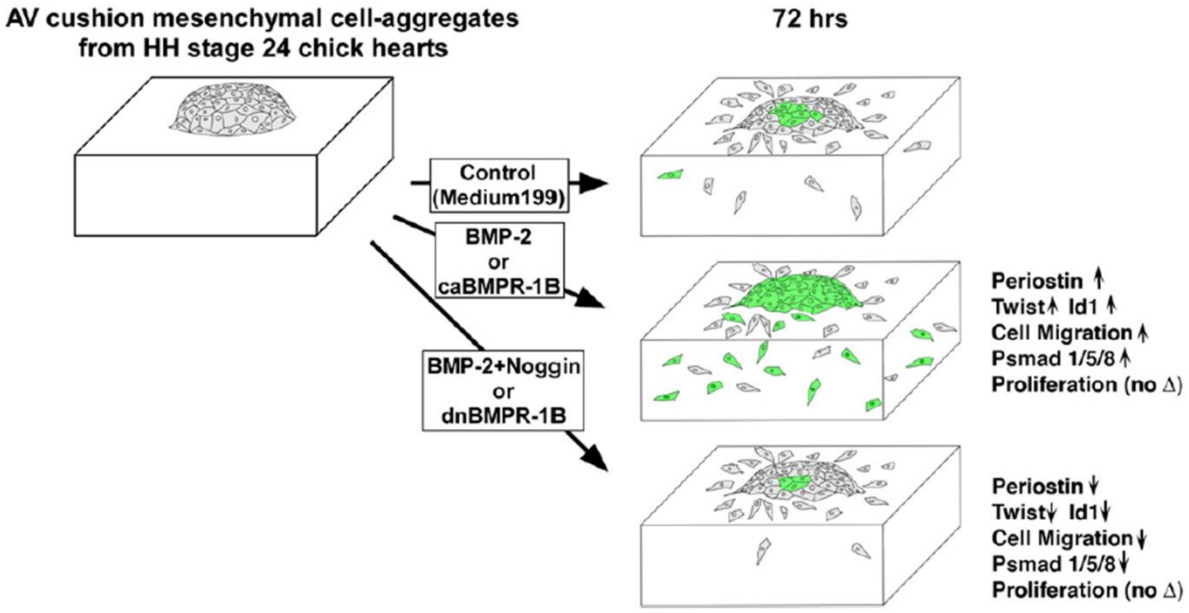

Figure 1.2 – Summary diagram illustrating the results from bioassays to assess the role of BMP2 and BMP signaling using AV cushion mesenchymal cell aggregates cultured on 3D-collagen gels. Exogenous BMP2 or caBMPR1B treatments induced mesenchymal cell migration and expression of periostin, Twist and Id1, while a BMP antagonist, Noggin, or dnBMPR1B treatment inhibited BMP2 promoted cell migration and expression of periostin, Twist and Id1. Phospho-Smad 1/5/8 expression was induced by BMP2 or caBMPR1B treatments but reduced by Noggin or dnBMPR1B treatments. Inai, K., et al., *BMP-2 induces cell migration and periostin expression during atrioventricular valvulogenesis.* Dev Biol, 2008. **315**(2): p. 383-96.

Cushion Maturation - In the chick, the early EMT phase occurs between Hamburger and Hamilton (HH) stage 14 through 25, while the later phase of valvular maturation occurs from HH25 onward (even after birth). During this remodeling, the cushion mesenchyme transitions from an activated myofibroblast (a-smooth muscle actin, MMP-2 positive, highly proliferative) to a more quiescent fibroblast (a-SMA, MMP-2 negative, sparsely mitotic) [77]. The molecular and cellular regulation of this process is far less understood than EMT, but mutant mouse models and in-vitro experimentation have determined important roles for a number of signaling

pathways [78-80]. Disruption of these pathways leads to either hypoplastic (thinned, rigid, sparsely populated) or hyperplastic (swollen, weak, densely populated) valves that lead to late embryonic and/or postnatal lethality through valvular stenosis or insufficiency.

VEGFA: In vivo and in vitro experiments suggest that low level endocardial expression of vascular endothelial growth factor alpha (VEGFA) is required to permit EMT [81], but higher doses (~3 fold) inhibits this process [82]. VEGFA action through its receptor Flk-1 and transcription factor NFATc1 is required for cushion extension and condensation into leaflets, as well as for proliferation of valvular endothelial cells that line the cushions [79, 83]. Thus, persistent low levels of VEGFA result in hyperplastic valves while premature elevation of VEGFA results in hypoplastic valves. **TGFβ:** Transforming growth factor beta (TGFβ) stimulates proliferation and migration through its receptor (TBRII/III) complexing with Alk1 or Alk2 (which also interact with BMP receptors) and activating the smad1/5 transduction pathway, but inhibits of proliferation and migration through receptor complexing with Alk5 and activation of smad2/3 [84, 85]. Both TGFβ2 and TGFβ3 are strong inducers of migration, compaction, and differentiation towards a fibroblastic phenotype through positive expression of alpha-SMA and vimentin in mice and avian models, respectively [86]. **BMP:** Bone morphogenetic protein (BMP) activates transcription of AV mesenchymal genes through its receptor (TBRI/II) and phosphorylation of smad 1/5/8 [87]. Type I BMP receptors, BMPR1A (Alk3), BMPR1B (Alk6), and Alk2 have all been localized in AV cushion mesenchyme in stage-24 chick embryos. AV explant experiments applying exogenous BMP2 or caBMPR1B (Alk6) treatments significantly promoted expression of an extracellular matrix (ECM) proteins [88]. Similar to cartilage development, BMP2 is sufficient to induce SOX9 and aggrecan expression through pSMAD 1/5, which has been confirmed in a number of assays using prefused endocardial cushions [80, 89]. **FGF:** Fibroblastic growth factor **(**FGF2) signals to the nucleus by binding to the FGFR and activating multiple signaling pathways, namely phosphorylated MAPK (dpERK). FGF2 has also

been localized throughout the leaflet (and chorade), and increases during maturation. Similar to limb and tendon development, FGF is sufficient to drive scleraxis (SCX) and tenomodulin (TNMD) expression through dpERK, which has also been confirmed in a number of assays using avian cushions [90, 91]. **RhoA:** Ras homolog gene family, member A (RhoA) is a small GTPase protein known to regulate the actin cytoskeleton and the formation of stress fibers. It is activated when bound to the GTP-bound form of Rho GTPase and phosphorylates a LIM kinase, which in turn inhibits actin-depolymerizing activity. RhoA can also directly signal to the transcription factor serum response factor (SRF) which drives myofibroblastic activation and alpha smooth muscle actin production. Studies have shown that the RhoA pathway is necessary for endocardial cell transformation, proliferation, and migration during cushion formation [92, 93].

1.4: Transcriptional Regulation of Valve Formation

The role of growth factors directing the differentiation of mesenchymal valve progenitor cells and maturation into elongated heart valves with highly organized ECM remains widely unknown. Recent work by Chakraborty et al. conducted gene expression profiling analysis of murine E12.5 AV endocardial cushions compared with E17.5. They hypothesized that existence of shared regulatory pathways active in developing AV valves and bone progenitor cells. Overall, MC3T3 cells (pre-osteoblasts) were significantly more similar to E17.5 valves than to E12.5 cushions, supporting the hypothesis that valve maturation involves the expression of many genes also expressed in osteoblasts. Several transcription factors characteristic of mesenchymal and osteoblast precursor cells, including Twist1, Sox9, Tbx20, and Msx1/Msx2, are predominant in E12.5 cushion [70]. Interestingly, the roles of growth and key transcription factors identified within these microarrays have been widely studied in developing valves.

Sox9 - Sox9 is thought to be a master regulator required for endocardial cushion cell lineage expansion, as well as differentiation associated with cartilage progenitor cells [94, 95]. In both chick and mouse, Sox9 is expressed within the endocardial cushions and remodeling leaflets. BMP2 activates expression of Sox9 and the cartilage differentiation marker Col2a1, which has been observed in cultured avian endocardial cushion cells [96]. Upon gene knockout of Sox9 in mice, embryonic lethality occurs between E11.5 and E12.5 with hypoplastic endocardial cushions. It is thought that loss of Sox9 inhibits EMT after delamination and initial migration, but before definitive mesenchymal transformation [97]. Upon targeted loss of Sox9 with Col2a1Cre in the remodeling valve, decreased expression of cartilage-associated proteins Col2a1 occurs. In adult mice, heterozygous loss of Sox9 in Col2a1Cre results in thickened valve leaflets and calcification characteristic of valve disease [95]. This suggests that that a relationship between BMP and Sox9 has a critical role in endocardial cushion formation and valve remodeling.

Msx1/Msx2 - Expression of the Msx1 and Msx2 homeobox genes have been shown to be co-coordinately regulated with the BMP2 and BMP4 ligands in a variety of developing tissues. It known that that both Msx1 and Msx2 are crucial downstream effectors of BMP signaling in endocardial cushion. Upon mouse knockout, Msx1 and Msx2 single homozygous mutant mice exhibited normal valve formation, while hypoplastic AV cushions and malformed AV valves were evident in the double Msx1 and Msx2 homozygous mutant mouse. These results support redundant functions for Msx1 and Msx2 during AV valve morphogenesis. In the Msx1/2 mutant embryos, endocardial expression of Notch1, BMP2/ 4, and NFATc1 is reduced, and patterning of the AVC myocardium also is abnormal, leading to compromised EMT [98]. In addition, loss of both Msx1 and Msx2 were also found to affect secondary heart field and neural crest anomalies related to defects in cell proliferation and migration [99]. Taken together, combined Msx1 and Msx2 mutations lead to a spectrum of cardiac malformations including double outlet right

ventricle (DORV), pulmonary stenosis, atrial and ventricular septal defects, and hypoplastic ventricle [100].

Twist1 - Endocardial cushion expression of Twist1 is induced by BMP2 in both chicken and mouse embryos. During valve morphogenesis, Twist1 is expressed throughout the endocardial cushions of the AVC and OFT, and expression is down-regulated in the remodeling valves [80]. Shelton et al. performed gain and loss of function studies in avian endocardial cushion cell cultures to demonstrate that Twist1 promotes cell proliferation and migration, while increasing the expression of periostin and MMP-2 [101]. Twist1 activity was examined in transgenic mice with persistent expression in the developing valves. Persistent Twist1 expression leads to increased valve cell proliferation, increased expression of Tbx20, and increased ECM gene expression, characteristic of early valve progenitors. Among the ECM genes predominant in the endocardial cushions, Col2a1 was identified as a direct transcriptional target of Twist1. Increased Twist1 expression also leads to dysregulation of fibrillar collagen and periostin expression, as well as enlarged hypercellular valve leaflets prior to birth [102].

Tbx20 - Tbx20 is thought to maintain BMP2 expression localized to the AVC region. Tbx20 is strongly expressed in the myocardium of the AVC in both mouse and chick [103, 104]. Mice lacking Tbx20 in the AVC myocardium fail to form the AVC constriction, and EMT is severely perturbed. Furthermore, downstream genes, such as Twist1, Sox9, and Msx1, involved in the EMT initiation were found nearly absent. Upon re-expression of BMP2 in the AVC myocardium, BMP2 substantially rescues the EMT defects resulting from the lack of Tbx20, suggesting BMP2 is one of the key downstream targets of Tbx20 in AVC development [105]. Furthermore, Tbx20 gain and loss of function studies performed in chicken AVC explants were found to increase cell proliferation and migration while repressing ECM maturation. Tbx20 promotes expression of the ECM remodeling enzymes, MMP9 and MMP13, while repressing expression of the chondroitin

sulfate proteoglycans, aggrecan, and versican [106]. Overall, Tbx20 has essential roles in regulating AVC development that coordinate early cushion formation.

1.5: Biomechanics and Mechanobiology Atrioventricular Valvulogenesis

Virtually unexplored is how mechanical signals regulate valvulogenesis. The primitive heart is formed within 48 hours of development and resembles a single tube surrounded by myocardium. At these early stages, the tube acts as a suction pump to regulate blood flow [107]. During diastolic loading, expansion of the tube pulls fluid into the tube and throughout the embryo. The heart then undergoes a complex folding to form a four chambered organ in response to the increased hemodynamic demands. This folding is critical to sustain the total energy needed through systolic loading and pulsatile fluid flow [108]. During cardiac morphogenesis, cardiac jelly swellings appear in the AV canal and OT and are critical for maintaining unidirectional blood flow during pulsatile contractions. Both theoretical and biological tissue models, suggest the duration of valve growth and function is dependent upon blood hemodynamics. Hemodynamic metrics of the embryonic heart (e.g. cardiac output, systolic blood pressure, and heart rate) [109-113] increase monotonically with developmental stage.

	HR, bpm (mean)	Ventricular Systolic Pressure (mmHg)	Ventricular Diastolic Pressure (mmHg)	Transvalvular Pressure (mmgHg)
Human				
14	162	31	8.45	22.55
16	160	35.4	9.65	25.75
18	155	39.9	10.8	29.1
20	150	44.2	12.1	32.1
22	147	48.7	13.2	35.5
24	144	51.1	14.5	36.6
26	142	57.7	15.7	42
Chick : Stage (HH)				
16	110	1.15	0.25	0.9
18	147.5	1.31	0.33	0.98
21	145	1.61	0.34	1.27
24	155	1.96	0.4	1.56
27	155	2.35	0.56	1.79
29	194	3.45	0.82	2.63
Mouse: Emb Day				
10.5	124.7	3.44	0.52	2.92
11.5	135.6	5.01	0.5	4.51
12.5	147.3	6.43	0.9	5.53
13.5	173.6	9	0.86	8.14
14.5	194.3	11.2	0.88	10.32

Table 1.2 – Summary of pressures within the developing heart and across the valve regions shown for human, chick, and mouse models. Adapted from [109, 114, 115].

Developing valves are unique in that they are always under significant mechanical force during the cardiac cyclic. During systolic loading, the valve opens and the surface facing the passing blood is exposed to significant wall shear stress (WSS), while the opposing side experiences disturbed blood flow and eddy formation. During diastole, the valve is closed and blood pressure imposes a force normal on the leaflet preventing retro-grade blood flow with distinct orthogonal mechanical tissue response, and highly anisotropic ECM. At stages HH14-HH25, the magnitude of wall shear stress is greatest in the inner curvatures and sites of lumen constrictions, corresponding to the site of cushion and OFT formation [4]. Recent studies have even found that high unidirectional shear stress promote cushion extension in the direction of flow in contrast to recirculating flows, which encourages the pre-valvular sculpting process

[116]. One could speculate that shear induced mechanisms are important factors for remodeling of the developing AV valves based upon the correlation of WSS and valve formation. A number of studies have supported shear sensitivity to directly regulate valve mechanobiology. Balachandran et al. found in-vitro that shear strain is critical for driving the epithelial-mesenchymal transition process through direct regulation of the TGFβ1 morphogen, and was both magnitude and directional dependent [117]. Other studies in-vivo have found that the mechanosensitive gene kruppel-like factor-2 (KFL2) will result in AV valve dysgenesis in zebrafish knockouts [118]. In avian models, venous clipping induced an increased in shear stress resulted in augmented KLF2 levels and abnormal valve development [119].

During later stages of formation (HH36, HH42), the AV valve condenses and elongate to thin leaflet like structures capable of withstanding remarkable hemodynamic loads [5]. During diastolic loading, resident valve cells are thought to be exposed by cyclic deformation [120] and studies have shown that embryonic cushions alter their structural composition in strengthening to maintain unidirectional flow amidst increasing hemodynamic loading [3, 107, 109, 113, 121]. However, the role of mechanical strain on embryonic valvular mesenchymal cells is almost completely unknown. Rhia et al. found that murine embryonic mesenchymal progenitor cell differentiated towards fibroblasts like-phenotype through positive expression of smooth muscle α-actin at both the protein and gene expression level in response to cyclic strain. As a positive control, TGFβ was added and found to have synergistic effects with cyclic strain on alpha-SMA mRNA expression [122]. Several studies have shown that adult valvular interstitial cells (VIC) regulate their phenotype based on the mechanical strain [123, 124]. VIC are normally fibroblastic-like cells (vimentin positive, α-smooth muscle actin negative, MMP-2 negative) but become activated (α-SMA, MMP-2 positive) in various disease [125] and remodeling conditions [126, 127]. This has been associated with elevated TGFβ and BMP signaling [128, 129].

1.6: Relevance and Significance: Congenital Defects, Stem Cells, and Tissue Engineering.

Congenital heart defects (CHD) affect 1-2% of all Americans and are significant contributor to heart valve disease [130]. Valvular structural and functional defects account for 20-30% of all defects in live human births, and their effects can be immediately life threatening or cause more subtle cell and/or matrix changes that can lead to functional defects later in life [131]. The embryonic heart grows and develops to adapt to ventricular geometry and function to optimize efficiency. The valves are critical for maintaining unidirectional blood flow and pressure within the developing heart chambers. It would be unsurprising that many of the defects within the heart and valves arise from alterations of the normal hemodynamic environment. It has been suggested by Goerttlet et al. that deviations from normal heart development, is a result of displaced blood-streams [132]. However, distinctions between gene and hemodynamic related abnormalities are not that well defined. Genetics allow do not provide the full picture, as roughly only 10-15 percent of the left ventricular outflow malformations are linked to chromosomal abnormalities. While genetic mutations explain a significant portion of congenital heart defects, mutating a single gene rarely copies a human cardiac phenotype [133]. Alternatively, an alternative hypothesis is that mechanical perturbation through blood flow is a key regulator of normal and abnormal phenotypes may be likely.

Bicuspid aortic valve disease is the most frequent congenital anomaly of the heart. It is commonly associated with aortic valve stenosis and regurgitation, though symptoms largely exacerbate later in life, despite the abnormal valve formation. In BAV, patients possess a valve of limited mobility, as the free edge is rounded and of unequal size. Excessive length of one leaflet results in abnormal contact which in turn leads to abnormal function. Later in life, the valve will become thickened, diffuse, and calcified [134]. Recent analysis involving families with BAV found that overrepresentation of NOTCH1 missense variants among patients with

bicuspid aortic valves and thoracic aortic aneurysms [135]. This suggests that mutations of the gene directly effects valve formation and dysfunctional morphogenesis. While this provides an important explanation, large calcific deposits are unusual before the age of thirty, and very prevelant thereafter. Interestingly, BAV patients without signficant stenosis or regurgitation were found to have larger annulus, aortic sinus, and proximal ascending aorta when compared to normal valves [136]. The peak aortic velocity and systolic wall velocity were also found higher in these BAV patients, implying these regions are subjected to increased stress levels [137].

Perturbations in ECM expression (elastin, collagen, and proteoglycans) can also lead to cardiac defects. For example, mutations in FBN1 (an extracellular glycoprotein of the ECM that acts to maintain tissue elasticity of the valve leaflets and aortic wall by linking smooth muscle cells to adjacent elastin fibrils) have been observed in patients with Marfan syndrome (MFS) [138]. Targeted deletion of Fbn1 in mice phenocopies the defects observed in Marfan syndrome indicative of a causal relationship between FBN1mutations and valve malformation [139]. These mice have upregulated TGF-β signaling, mitral valve prolapse and die shortly after birth due to aortic dissection caused by weakening of the aortic wall [140]. In humans, mutations in the TGF-β receptors, TGFBR1 and TGFBR have been associated with both Marfan and Loeys-Dietz syndromes. Interestingly, reduced expression of FBN1in the aorta of patients with BAVs was also reported [141].

Hypoplastic left heart syndrome (HLHS) is marked by severe underdevelopment of the left ventricle and patients born with HLHS continue to have some of the highest mortality rates within the first year among all infants with congenital heart defects [142]. To date, no single mutation or chromosomal abnormalities has been identified as the culprit. Cardiac defects associated with HLHS also include valve hypoplascia, hypoplastic aorta, and coarctation of the

aorta. The underdeveloped tissues are thought to be the result of underdeveloped blood flow from the left ventricle and outflow tract during development [143]. In HLHS, almost 50 percent of patients have malformed valves, suggesting that alterations in the site of the primordial mitral valve may induce HLHS [144]. Harh et al. was one of the first to investigate this hypothesis by placing a nylon device in the left AV canal to reduce blood flow and hemodynamic loading. It was found that this greatly reduced the left ventricle size and the developing AV valve resulted in a thickened hypoplastic valve. Others have also mechanically induced HLHS through ligation techniques, which have been shown to display altered ventricular filling patterns, epicardial strain patterns, and reduced AV inflow velocity [145]. The increasing amount of information regarding HLHS adds credence to the paradigm that altered hemodynamic loading in development results in both altered heart formation and dysfunctional valves.

HVD is particularly devastating for children, as the current therapy of prosthetic valve replacement necessitates multiple open heart surgeries to accommodate growth and requires debilitating anti-coagulant therapy [146]. Living heart valve replacements created through tissue engineering have the potential to alleviate these concerns with the potential for growth and an anticoagulant endothelial surface, but efforts to date have had limited success due to persistent transvalvular pressure gradients and cell-mediated leaflet thickening and contraction [147]. Because native valvular cells are not accessible as a source for these devices, other autologous cell sources are necessary. A study by Sutherland et al. used bone marrow derived mesenchymal stem cells (MSC) to populate polymeric valve-like scaffolds, and showed that this population could recapitulate both endothelial and fibroblastic like cells, which in turn secreted and organized a fibrillar matrix somewhat similar to native valves (though the valves were still mechanically insufficient) [148]. A separate study by Visconti et al injected clonal populations of MSC into lethally irradiated mice and found that a subset of these cells were recruited to heart valve leaflets, and were phenotypically indistinct from the native cells [149]. These studies

suggest that bone marrow derived stem cells can differentiate into valvular specific phenotypes if exposed to valvular specific mechanical stimulation regimens.

Embryonic cushion mesenchyme is also pluripotent, capable of differentiating into bone, cartilage, and even cardiac muscle, yet normally forms fibroblastic cells [150]. The mechanism that directs this fibroblastic regulation is not known, but by association may be the normal stage specific valvular mechanical stimulation regimen. Indeed, altered tissue stress distributions and hemodynamic loading are implicated in a variety of adult valvular diseases, which also present osteochondral cell phenotypes. Therefore, determining the relationships between stage specific valvular mechanical environments and valvulogenic molecular regulation may not only help to delineate causes of CHD and motivate mechanically based repair schemes, but begin to establish a developmentally based "road map" to direct the differentiation of precursor/stem cells into valvular specific phenotypes, a critical unmet need.

1.7: Objective of this Research

The control of planar connective tissue assembly and remodeling is important target for bioengineering. Tissue biomechanical function is driven by local cellular responses to environmental stimuli. These may include mechanical cues, including secreting and/or degrading extracellular matrix proteins, releasing soluble growth factors, and reorganizing cell-cell/cell-matrix adhesive interactions. Nearly all study of mechanical action on cellular function focuses on the "normal and pathological" adult age. This neglects key stages in the functional life cycle of tissues where remodeling is most active yet, controlled: "embryonic development". Until the basic interactions between cells and their microenvironment are understood in this context, our ability to manipulate these phenomena remains limited. The overall goal of my thesis therefore, is to identify key mechanosensitive signaling networks, which underlie heart valve maturation and remodeling across the development continuum. My guiding hypothesis is

that mechanical loading and subsequent strain fields play a large role in directing resident mesenchymal differentiation. By using a developmentally focused approach, I hope my research will inform efficient strategies for control tissue adaptation and remodeling as well as accelerate the construction of cardiovascular tissue replacements. To achieve this, several research goals were set, and the results of each are presented and discussed in separate chapter. They are summarized as follows:

Goal 1: Optimize the Isolation and Culture of Pure Populations of Avian Progenitor Mitral Valve Cells. Native embryonic mitral valve cells are not easily obtained and cannot be obtained commercially. Therefore, techniques and methods to isolate and culture these cells within an avian animal model were tested and optimized. Typical results in both 2-D and 3-D are presented, and a discussion regarding limitations and assumptions are presented in Chapter 2.

Goal 2: Develop and Implement a Bioreactor for Understanding the Role of Strain Magnitude and Directionality in Valve Development. Valves are subjected to a constant barrage of mechanical forces while maintaining unidirectional blood flow. Mechanical stretch has been identified as one of the central regulators of interstitial cell development and homeostasis. However, understanding the mechano-biological response of VIC to both strain magnitude and directionality is technically challenging. We therefore developed a strain bioreactor and applied physiological anisotropic stretch profiles to adult VIC. Cell proliferation, matrix remodeling, and differentiation markers were assessed and discussed in Chapter 3.

Goal 3: Determine the role of Mechanical Stretch and Hemodynamic Loading on Embryonic Valve Differentiation and Morphogenesis. The mechanisms by which sustained cyclic loading directs the cellular response to coordinate embryonic valve morphogenesis and function are not known, but central to leaflet maturation. We explored how mechanosensitive small GTPases

RhoA and Rac1 participate in atrioventricular valve morphogenesis and remodeling. Using a combination of in-vitro and in-vivo methods, we found that cyclic loading regulates a switch from RhoA to Rac1 which drives cell quiescence while simultaneously condensing the ECM. The results and discussion are presented in Chapter 4.

Goal 4: Determine the Relationship between Post-natal Biomechanics and Cellular Deformation in Normal and Genetic Mutant Murine Mitral Valve Leaflets. Changes in local cell-matrix deformation relationships may be an important metric for determining mechanisms of normal and pathological tissue remodeling in valves, as in aging or genetic mutation. Therefore, a novel testing device was constructed to quantify global biomechanical and local cell-matrix relationships in FBN1 mutant murine mitral valves. We found that local cell and matrix kinematics are decoupled to different degrees correlating with magnitude of global valve tissue stretch which are presented and discussed in Chapter 5.

Goal 5: Generate and Analyze Mechanistic Model to Predict Signaling "BottleNecks" During Valve Development. It is well appreciated that a systems level approach may be an essential resource to accelerate information generation concerning the functional relationships across multiple length scales and structural development. Computer simulations modeling valve development is a great opportunity as the underlying cell signaling and morphogenesis is extremely controlled and consistent. Hence, we generated a model to understand the differentiation states during the epithelial to mesenchymal transformation found in early cushion development. The effectives and feasibility of our model was tested in adult epithelial cells and the results are presented and discussed in Chapter 7.

Goal 6: Develop Multidisciplinary Inquiry Based Learning Activities Using Engineering Frameworks used in Secondary Education. Embryonic development offers a unique

perspective on the function of many biological processes and their heightened sensitivity to environmental factors. I developed a hands-on lesson to investigate the effects of prostaglandin E1 (PGE1) on the morphogenesis of chick neo-vasculature. PGE1 is applied to shell-less (ex-ovo) cultured chick embryos, which are highly accessible and intrinsically spawn inquiry. The student activities mirror the scientific research process and the results are presented and discussed in Chapter 8.

The significance and consequences of these studies are presented in Chapter 9, followed by a concluding summary in Chapter 10.

REFERENCES

1. Nakajima, Y., et al., *Expression of smooth muscle alpha-actin in mesenchymal cells during formation of avian endocardial cushion tissue: a role for transforming growth factor beta3.* Dev Dyn, 1997. **209**(3): p. 296-309.
2. Person, A.D., S.E. Klewer, and R.B. Runyan, *Cell biology of cardiac cushion development.* Int Rev Cytol, 2005. **243**: p. 287-335.
3. Moorman, A.F. and V.M. Christoffels, *Cardiac chamber formation: development, genes, and evolution.* Physiol Rev, 2003. **83**(4): p. 1223-67.
4. Yalcin, H.C., et al., *Hemodynamic patterning of the avian atrioventricular valve.* Dev Dyn, 2011. **240**(1): p. 23-35.
5. Butcher, J.T. and R.R. Markwald, *Valvulogenesis: the moving target.* Philos Trans R Soc Lond B Biol Sci, 2007. **362**(1484): p. 1489-503.
6. Sugi, Y., et al., *Fibroblast growth factor (FGF)-4 can induce proliferation of cardiac cushion mesenchymal cells during early valve leaflet formation.* Dev Biol, 2003. **258**(2): p. 252-63.
7. Zhao, B., et al., *BMP and FGF regulatory pathways in semilunar valve precursor cells.* Dev Dyn, 2007. **236**(4): p. 971-80.
8. Combs, M.D. and K.E. Yutzey, *Heart valve development: regulatory networks in development and disease.* Circ Res, 2009. **105**(5): p. 408-21.
9. Hurle, J.M., et al., *Elastic extracellular matrix of the embryonic chick heart: an immunohistological study using laser confocal microscopy.* Dev Dyn, 1994. **200**(4): p. 321-32.
10. Bajolle, F., et al., *Rotation of the myocardial wall of the outflow tract is implicated in the normal positioning of the great arteries.* Circ Res, 2006. **98**(3): p. 421-8.
11. Thompson, R.P., V. Abercrombie, and M. Wong, *Morphogenesis of the truncus arteriosus of the chick embryo heart: movements of autoradiographic tattoos during septation.* Anat Rec, 1987. **218**(4): p. 434-40, 394-5.
12. Garcia-Martinez, V., D. Sanchez-Quintana, and J.M. Hurle, *Histochemical and ultrastructural changes in the extracellular matrix of the developing chick semilunar heart valves.* Acta Anat (Basel), 1991. **142**(1): p. 87-96.
13. Yutzey, K.E. and J. Robbins, *Principles of genetic murine models for cardiac disease.* Circulation, 2007. **115**(6): p. 792-9.
14. Williams, R., *Thanks be to zebrafish.* Circ Res, 2010. **107**(5): p. 570-2.
15. Sehnert, A.J., et al., *Cardiac troponin T is essential in sarcomere assembly and cardiac contractility.* Nat Genet, 2002. **31**(1): p. 106-10.
16. Fishman, M.C., *Genomics. Zebrafish--the canonical vertebrate.* Science, 2001. **294**(5545): p. 1290-1.
17. Talbot, W.S. and N. Hopkins, *Zebrafish mutations and functional analysis of the vertebrate genome.* Genes Dev, 2000. **14**(7): p. 755-62.
18. Wienholds, E., et al., *Efficient target-selected mutagenesis in zebrafish.* Genome Res, 2003. **13**(12): p. 2700-7.
19. Love, D.R., et al., *Technology for high-throughput screens: the present and future using zebrafish.* Curr Opin Biotechnol, 2004. **15**(6): p. 564-71.
20. Beis, D., et al., *Genetic and cellular analyses of zebrafish atrioventricular cushion and valve development.* Development, 2005. **132**(18): p. 4193-204.
21. Scherz, P.J., et al., *High-speed imaging of developing heart valves reveals interplay of morphogenesis and function.* Development, 2008. **135**(6): p. 1179-87.

22. Schroeder, J.A., et al., *Form and function of developing heart valves: coordination by extracellular matrix and growth factor signaling.* J Mol Med (Berl), 2003. **81**(7): p. 392-403.
23. Vandevelde, S., et al., *The development of the therapeutic community in correctional establishments: a comparative retrospective account of the 'democratic' Maxwell Jones TC and the hierarchical concept-based TC in prison.* Int J Soc Psychiatry, 2004. **50**(1): p. 66-79.
24. Heasman, J., *Morpholino oligos: making sense of antisense?* Dev Biol, 2002. **243**(2): p. 209-14.
25. Chin, A.J., *Analysis of two aspects of left-right patterning of the vertebrate heart. Heart tube position and heart tube chirality.* Methods Mol Biol, 2000. **136**: p. 261-70.
26. Singh, B.N., et al., *Heart of newt: a recipe for regeneration.* J Cardiovasc Transl Res, 2010. **3**(4): p. 397-409.
27. Wessels, A. and D. Sedmera, *Developmental anatomy of the heart: a tale of mice and man.* Physiol Genomics, 2003. **15**(3): p. 165-76.
28. Yalcin, H.C., et al., *An ex-ovo chicken embryo culture system suitable for imaging and microsurgery applications.* J Vis Exp, 2010(44).
29. Stern, C.D., *The chick; a great model system becomes even greater.* Dev Cell, 2005. **8**(1): p. 9-17.
30. Gilbert, S.F. and S. Sarkar, *Embracing complexity: organicism for the 21st century.* Dev Dyn, 2000. **219**(1): p. 1-9.
31. Alsan, B.H. and T.M. Schultheiss, *Regulation of avian cardiogenesis by Fgf8 signaling.* Development, 2002. **129**(8): p. 1935-43.
32. Yalcin, H.C., et al., *Two-photon microscopy-guided femtosecond-laser photoablation of avian cardiogenesis: noninvasive creation of localized heart defects.* Am J Physiol Heart Circ Physiol, 2010. **299**(5): p. H1728-35.
33. Voiculescu, O., C. Papanayotou, and C.D. Stern, *Spatially and temporally controlled electroporation of early chick embryos.* Nat Protoc, 2008. **3**(3): p. 419-26.
34. Tao, Y. and R.A. Schulz, *Heart development in Drosophila.* Semin Cell Dev Biol, 2007. **18**(1): p. 3-15.
35. Ocorr, K., et al., *Genetic control of heart function and aging in Drosophila.* Trends Cardiovasc Med, 2007. **17**(5): p. 177-82.
36. Piazza, N. and R.J. Wessells, *Drosophila models of cardiac disease.* Prog Mol Biol Transl Sci, 2011. **100**: p. 155-210.
37. Hoskins, R.A., et al., *Genome-wide analysis of promoter architecture in Drosophila melanogaster.* Genome Res, 2011. **21**(2): p. 182-92.
38. Bader, M., *Rat models of cardiovascular diseases.* Methods Mol Biol, 2010. **597**: p. 403-14.
39. Marcela, S.G., et al., *Chronological and morphological study of heart development in the rat.* Anat Rec (Hoboken), 2012. **295**(8): p. 1267-90.
40. Patten, R.D. and M.R. Hall-Porter, *Small animal models of heart failure: development of novel therapies, past and present.* Circ Heart Fail, 2009. **2**(2): p. 138-44.
41. Horsthuis, T., et al., *Can recent insights into cardiac development improve our understanding of congenitally malformed hearts?* Clin Anat, 2009. **22**(1): p. 4-20.
42. Piliszek, A., G.S. Kwon, and A.K. Hadjantonakis, *Ex utero culture and live imaging of mouse embryos.* Methods Mol Biol, 2011. **770**: p. 243-57.
43. Bult, C.J., et al., *The Mouse Genome Database (MGD): mouse biology and model systems.* Nucleic Acids Res, 2008. **36**(Database issue): p. D724-8.
44. van der Weyden, L., D.J. Adams, and A. Bradley, *Tools for targeted manipulation of the mouse genome.* Physiol Genomics, 2002. **11**(3): p. 133-64.

45. Guan, C., et al., *A review of current large-scale mouse knockout efforts.* Genesis, 2010. **48**(2): p. 73-85.
46. Chien, K.R., *To Cre or not to Cre: the next generation of mouse models of human cardiac diseases.* Circ Res, 2001. **88**(6): p. 546-9.
47. Utomo, A.R., A.Y. Nikitin, and W.H. Lee, *Temporal, spatial, and cell type-specific control of Cre-mediated DNA recombination in transgenic mice.* Nat Biotechnol, 1999. **17**(11): p. 1091-6.
48. Van Vliet, P., et al., *Early cardiac development: a view from stem cells to embryos.* Cardiovasc Res, 2012. **96**(3): p. 352-62.
49. Nakamura, H., et al., *Gain- and loss-of-function in chick embryos by electroporation.* Mech Dev, 2004. **121**(9): p. 1137-43.
50. Chesnutt, C. and L. Niswander, *Plasmid-based short-hairpin RNA interference in the chicken embryo.* Genesis, 2004. **39**(2): p. 73-8.
51. Xia, H., et al., *siRNA-mediated gene silencing in vitro and in vivo.* Nat Biotechnol, 2002. **20**(10): p. 1006-10.
52. Yeung, T., et al., *Effects of substrate stiffness on cell morphology, cytoskeletal structure, and adhesion.* Cell Motil Cytoskeleton, 2005. **60**(1): p. 24-34.
53. Khanafer, K., et al., *Effects of strain rate, mixing ratio, and stress-strain definition on the mechanical behavior of the polydimethylsiloxane (PDMS) material as related to its biological applications.* Biomed Microdevices, 2009. **11**(2): p. 503-8.
54. Kim, D.H., et al., *Microengineered platforms for cell mechanobiology.* Annu Rev Biomed Eng, 2009. **11**: p. 203-33.
55. Gould, R.A., et al., *Cyclic strain anisotropy regulates valvular interstitial cell phenotype and tissue remodeling in three-dimensional culture.* Acta Biomater, 2012. **8**(5): p. 1710-9.
56. Lutolf, M.P. and J.A. Hubbell, *Synthetic biomaterials as instructive extracellular microenvironments for morphogenesis in tissue engineering.* Nat Biotechnol, 2005. **23**(1): p. 47-55.
57. Lencinas, A., et al., *Collagen gel analysis of epithelial-mesenchymal transition in the embryo heart: an in vitro model system for the analysis of tissue interaction, signal transduction, and environmental effects.* Birth Defects Res C Embryo Today, 2011. **93**(4): p. 298-311.
58. Hawkins, R.D., G.C. Hon, and B. Ren, *Next-generation genomics: an integrative approach.* Nat Rev Genet, 2010. **11**(7): p. 476-86.
59. Blow, M.J., et al., *ChIP-Seq identification of weakly conserved heart enhancers.* Nat Genet, 2010. **42**(9): p. 806-10.
60. Park, P.J., *ChIP-seq: advantages and challenges of a maturing technology.* Nat Rev Genet, 2009. **10**(10): p. 669-80.
61. Wu, J., et al., *ChIP-chip comes of age for genome-wide functional analysis.* Cancer Res, 2006. **66**(14): p. 6899-902.
62. Shibata, Y. and G.E. Crawford, *Mapping regulatory elements by DNaseI hypersensitivity chip (DNase-Chip).* Methods Mol Biol, 2009. **556**: p. 177-90.
63. Palmke, N., D. Santacruz, and J. Walter, *Comprehensive analysis of DNA-methylation in mammalian tissues using MeDIP-chip.* Methods, 2011. **53**(2): p. 175-84.
64. Barrans, J.D., et al., *Global gene expression profiling of end-stage dilated cardiomyopathy using a human cardiovascular-based cDNA microarray.* Am J Pathol, 2002. **160**(6): p. 2035-43.
65. Davey, J.W., et al., *Genome-wide genetic marker discovery and genotyping using next-generation sequencing.* Nat Rev Genet, 2011. **12**(7): p. 499-510.
66. Faita, F., et al., *Next generation sequencing in cardiovascular diseases.* World J Cardiol, 2012. **4**(10): p. 288-95.

67. Gal-Yam, E.N., et al., *Cancer epigenetics: modifications, screening, and therapy.* Annu Rev Med, 2008. **59**: p. 267-80.
68. Akazawa, H. and I. Komuro, *Cardiac transcription factor Csx/Nkx2-5: Its role in cardiac development and diseases.* Pharmacol Ther, 2005. **107**(2): p. 252-68.
69. Chen, H., et al., *BMP10 is essential for maintaining cardiac growth during murine cardiogenesis.* Development, 2004. **131**(9): p. 2219-31.
70. Chakraborty, S., et al., *Shared gene expression profiles in developing heart valves and osteoblast progenitor cells.* Physiol Genomics, 2008. **35**(1): p. 75-85.
71. Krug, E.L., C.H. Mjaatvedt, and R.R. Markwald, *Extracellular matrix from embryonic myocardium elicits an early morphogenetic event in cardiac endothelial differentiation.* Dev Biol, 1987. **120**(2): p. 348-55.
72. Sugi, Y., et al., *Bone morphogenetic protein-2 can mediate myocardial regulation of atrioventricular cushion mesenchymal cell formation in mice.* Dev Biol, 2004. **269**(2): p. 505-18.
73. Boyer, A.S., et al., *TGFbeta2 and TGFbeta3 have separate and sequential activities during epithelial-mesenchymal cell transformation in the embryonic heart.* Dev Biol, 1999. **208**(2): p. 530-45.
74. Song, W., K. Jackson, and P.G. McGuire, *Degradation of type IV collagen by matrix metalloproteinases is an important step in the epithelial-mesenchymal transformation of the endocardial cushions.* Dev Biol, 2000. **227**(2): p. 606-17.
75. Delot, E.C., *Control of endocardial cushion and cardiac valve maturation by BMP signaling pathways.* Mol Genet Metab, 2003. **80**(1-2): p. 27-35.
76. Nakajima, Y., et al., *Mechanisms involved in valvuloseptal endocardial cushion formation in early cardiogenesis: roles of transforming growth factor (TGF)-beta and bone morphogenetic protein (BMP).* Anat Rec, 2000. **258**(2): p. 119-27.
77. Aikawa, E., et al., *Human semilunar cardiac valve remodeling by activated cells from fetus to adult: implications for postnatal adaptation, pathology, and tissue engineering.* Circulation, 2006. **113**(10): p. 1344-52.
78. Sanford, L.P., et al., *TGFbeta2 knockout mice have multiple developmental defects that are non-overlapping with other TGFbeta knockout phenotypes.* Development, 1997. **124**(13): p. 2659-70.
79. Chang, C.P., et al., *A field of myocardial-endocardial NFAT signaling underlies heart valve morphogenesis.* Cell, 2004. **118**(5): p. 649-63.
80. Ma, L., et al., *Bmp2 is essential for cardiac cushion epithelial-mesenchymal transition and myocardial patterning.* Development, 2005. **132**(24): p. 5601-11.
81. Dor, Y., et al., *A novel role for VEGF in endocardial cushion formation and its potential contribution to congenital heart defects.* Development, 2001. **128**(9): p. 1531-8.
82. Miquerol, L., B.L. Langille, and A. Nagy, *Embryonic development is disrupted by modest increases in vascular endothelial growth factor gene expression.* Development, 2000. **127**(18): p. 3941-6.
83. Johnson, E.N., et al., *NFATc1 mediates vascular endothelial growth factor-induced proliferation of human pulmonary valve endothelial cells.* J Biol Chem, 2003. **278**(3): p. 1686-92.
84. Blobe, G.C., et al., *A novel mechanism for regulating transforming growth factor beta (TGF-beta) signaling. Functional modulation of type III TGF-beta receptor expression through interaction with the PDZ domain protein, GIPC.* J Biol Chem, 2001. **276**(43): p. 39608-17.
85. Chen, Y.G. and J. Massague, *Smad1 recognition and activation by the ALK1 group of transforming growth factor-beta family receptors.* J Biol Chem, 1999. **274**(6): p. 3672-7.
86. Chiu, Y.N., et al., *Transforming growth factor beta, bone morphogenetic protein, and vascular endothelial growth factor mediate phenotype maturation and tissue remodeling*

by embryonic valve progenitor cells: relevance for heart valve tissue engineering. Tissue Eng Part A, 2010. **16**(11): p. 3375-83.
87. Hata, A., et al., *Smad6 inhibits BMP/Smad1 signaling by specifically competing with the Smad4 tumor suppressor.* Genes Dev, 1998. **12**(2): p. 186-97.
88. Inai, K., et al., *BMP-2 induces cell migration and periostin expression during atrioventricular valvulogenesis.* Dev Biol, 2008. **315**(2): p. 383-96.
89. Massague, J. and D. Wotton, *Transcriptional control by the TGF-beta/Smad signaling system.* EMBO J, 2000. **19**(8): p. 1745-54.
90. Zhang, J., et al., *The FGF-BMP signaling axis regulates outflow tract valve primordium formation by promoting cushion neural crest cell differentiation.* Circ Res, 2010. **107**(10): p. 1209-19.
91. Han, L. and A.I. Gotlieb, *Fibroblast growth factor-2 promotes in vitro mitral valve interstitial cell repair through transforming growth factor-beta/Smad signaling.* Am J Pathol, 2011. **178**(1): p. 119-27.
92. Butcher, J.T., et al., *Periostin promotes atrioventricular mesenchyme matrix invasion and remodeling mediated by integrin signaling through Rho/PI 3-kinase.* Dev Biol, 2007. **302**(1): p. 256-66.
93. Tavares, A.L., et al., *TGF beta-mediated RhoA expression is necessary for epithelial-mesenchymal transition in the embryonic chick heart.* Dev Dyn, 2006. **235**(6): p. 1589-98.
94. Wehrli, B.M., et al., *Sox9, a master regulator of chondrogenesis, distinguishes mesenchymal chondrosarcoma from other small blue round cell tumors.* Hum Pathol, 2003. **34**(3): p. 263-9.
95. Lincoln, J., et al., *Sox9 is required for precursor cell expansion and extracellular matrix organization during mouse heart valve development.* Dev Biol, 2007. **305**(1): p. 120-32.
96. Lincoln, J., C.M. Alfieri, and K.E. Yutzey, *BMP and FGF regulatory pathways control cell lineage diversification of heart valve precursor cells.* Dev Biol, 2006. **292**(2): p. 292-302.
97. Akiyama, H., et al., *Essential role of Sox9 in the pathway that controls formation of cardiac valves and septa.* Proc Natl Acad Sci U S A, 2004. **101**(17): p. 6502-7.
98. Chen, Y.H., et al., *Msx1 and Msx2 are required for endothelial-mesenchymal transformation of the atrioventricular cushions and patterning of the atrioventricular myocardium.* BMC Dev Biol, 2008. **8**: p. 75.
99. Chen, Y.H., et al., *Msx1 and Msx2 regulate survival of secondary heart field precursors and post-migratory proliferation of cardiac neural crest in the outflow tract.* Dev Biol, 2007. **308**(2): p. 421-37.
100. Chakraborty, S., M.D. Combs, and K.E. Yutzey, *Transcriptional regulation of heart valve progenitor cells.* Pediatr Cardiol, 2010. **31**(3): p. 414-21.
101. Shelton, E.L. and K.E. Yutzey, *Twist1 function in endocardial cushion cell proliferation, migration, and differentiation during heart valve development.* Dev Biol, 2008. **317**(1): p. 282-95.
102. Chakraborty, S., et al., *Twist1 promotes heart valve cell proliferation and extracellular matrix gene expression during development in vivo and is expressed in human diseased aortic valves.* Dev Biol, 2010. **347**(1): p. 167-79.
103. Stennard, F.A., et al., *Cardiac T-box factor Tbx20 directly interacts with Nkx2-5, GATA4, and GATA5 in regulation of gene expression in the developing heart.* Dev Biol, 2003. **262**(2): p. 206-24.
104. Plageman, T.F., Jr. and K.E. Yutzey, *T-box genes and heart development: putting the "T" in heart.* Dev Dyn, 2005. **232**(1): p. 11-20.
105. Cai, X., et al., *Myocardial Tbx20 regulates early atrioventricular canal formation and endocardial epithelial-mesenchymal transition via Bmp2.* Dev Biol, 2011. **360**(2): p. 381-90.

106. Shelton, E.L. and K.E. Yutzey, *Tbx20 regulation of endocardial cushion cell proliferation and extracellular matrix gene expression.* Dev Biol, 2007. **302**(2): p. 376-88.
107. Forouhar, A.S., et al., *The embryonic vertebrate heart tube is a dynamic suction pump.* Science, 2006. **312**(5774): p. 751-3.
108. Manning, A. and J.C. McLachlan, *Looping of chick embryo hearts in vitro.* J Anat, 1990. **168**: p. 257-63.
109. Hu, N., et al., *Diastolic filling characteristics in the stage 12 to 27 chick embryo ventricle.* Pediatr Res, 1991. **29**(4 Pt 1): p. 334-7.
110. Phoon, C.K., *Circulatory physiology in the developing embryo.* Curr Opin Pediatr, 2001. **13**(5): p. 456-64.
111. Keller, B.B., et al., *In vivo assessment of embryonic cardiovascular dimensions and function in day-10.5 to -14.5 mouse embryos.* Circ Res, 1996. **79**(2): p. 247-55.
112. Hu, N. and E.B. Clark, *Hemodynamics of the stage 12 to stage 29 chick embryo.* Circ Res, 1989. **65**(6): p. 1665-70.
113. Butcher, J.T., et al., *Transitions in early embryonic atrioventricular valvular function correspond with changes in cushion biomechanics that are predictable by tissue composition.* Circ Res, 2007. **100**(10): p. 1503-11.
114. Ishiwata, T., et al., *Developmental changes in ventricular diastolic function correlate with changes in ventricular myoarchitecture in normal mouse embryos.* Circ Res, 2003. **93**(9): p. 857-65.
115. Johnson, P., et al., *Intracardiac pressures in the human fetus.* Heart, 2000. **84**(1): p. 59-63.
116. Tan, H., et al., *Fluid flow forces and rhoA regulate fibrous development of the atrioventricular valves.* Dev Biol, 2013. **374**(2): p. 345-56.
117. Balachandran, K., et al., *Cyclic strain induces dual-mode endothelial-mesenchymal transformation of the cardiac valve.* Proc Natl Acad Sci U S A, 2011. **108**(50): p. 19943-8.
118. Bartman, T., et al., *Early myocardial function affects endocardial cushion development in zebrafish.* PLoS Biol, 2004. **2**(5): p. E129.
119. Vermot, J., et al., *Reversing blood flows act through klf2a to ensure normal valvulogenesis in the developing heart.* PLoS Biol, 2009. **7**(11): p. e1000246.
120. Sacks, M.S., W. David Merryman, and D.E. Schmidt, *On the biomechanics of heart valve function.* J Biomech, 2009. **42**(12): p. 1804-24.
121. Patten, B., T. Kramer, and A. Barry, *Valvular action in the embryonic chick heart by localized apposition of endocardial masses.* Anat Rec, 1948. **102**: p. 299-311.
122. Riha, G.M., et al., *Cyclic strain induces vascular smooth muscle cell differentiation from murine embryonic mesenchymal progenitor cells.* Surgery, 2007. **141**(3): p. 394-402.
123. Taylor, P.M., S.P. Allen, and M.H. Yacoub, *Phenotypic and functional characterization of interstitial cells from human heart valves, pericardium and skin.* J Heart Valve Dis, 2000. **9**(1): p. 150-8.
124. Taylor, P.M., et al., *The cardiac valve interstitial cell.* Int J Biochem Cell Biol, 2003. **35**(2): p. 113-8.
125. Jian, B., et al., *Progression of aortic valve stenosis: TGF-beta1 is present in calcified aortic valve cusps and promotes aortic valve interstitial cell calcification via apoptosis.* Ann Thorac Surg, 2003. **75**(2): p. 457-65; discussion 465-6.
126. Rabkin, E., et al., *Evolution of cell phenotype and extracellular matrix in tissue-engineered heart valves during in-vitro maturation and in-vivo remodeling.* J Heart Valve Dis, 2002. **11**(3): p. 308-14; discussion 314.
127. Rabkin-Aikawa, E., et al., *Dynamic and reversible changes of interstitial cell phenotype during remodeling of cardiac valves.* J Heart Valve Dis, 2004. **13**(5): p. 841-7.

128. Merryman, W.D., et al., *Synergistic effects of cyclic tension and transforming growth factor-beta1 on the aortic valve myofibroblast.* Cardiovasc Pathol, 2007. **16**(5): p. 268-76.
129. Balachandran, K., et al., *Elevated cyclic stretch induces aortic valve calcification in a bone morphogenic protein-dependent manner.* Am J Pathol, 2010. **177**(1): p. 49-57.
130. Roger, V.L., et al., *Heart disease and stroke statistics--2011 update: a report from the American Heart Association.* Circulation, 2011. **123**(4): p. e18-e209.
131. Hoffman, J.I. and S. Kaplan, *The incidence of congenital heart disease.* J Am Coll Cardiol, 2002. **39**(12): p. 1890-900.
132. Goerttlet, *Normale aud pathologische Entwicklung des menschlichen Herzens.* 1958.
133. McBride, K.L., et al., *Linkage analysis of left ventricular outflow tract malformations (aortic valve stenosis, coarctation of the aorta, and hypoplastic left heart syndrome).* Eur J Hum Genet, 2009. **17**(6): p. 811-9.
134. Yener, N., et al., *Bicuspid aortic valve.* Ann Thorac Cardiovasc Surg, 2002. **8**(5): p. 264-7.
135. McKellar, S.H., et al., *Novel NOTCH1 mutations in patients with bicuspid aortic valve disease and thoracic aortic aneurysms.* J Thorac Cardiovasc Surg, 2007. **134**(2): p. 290-6.
136. Garg, V., et al., *Mutations in NOTCH1 cause aortic valve disease.* Nature, 2005. **437**(7056): p. 270-4.
137. Warner, P.J., et al., *Augmentation index and aortic stiffness in bicuspid aortic valve patients with non-dilated proximal aortas.* BMC Cardiovasc Disord, 2013. **13**: p. 19.
138. Pyeritz, R.E., *The Marfan syndrome.* Annu Rev Med, 2000. **51**: p. 481-510.
139. Pereira, L., et al., *Targetting of the gene encoding fibrillin-1 recapitulates the vascular aspect of Marfan syndrome.* Nat Genet, 1997. **17**(2): p. 218-22.
140. Ng, C.M., et al., *TGF-beta-dependent pathogenesis of mitral valve prolapse in a mouse model of Marfan syndrome.* J Clin Invest, 2004. **114**(11): p. 1586-92.
141. Dietz, H.C., et al., *Recent progress towards a molecular understanding of Marfan syndrome.* Am J Med Genet C Semin Med Genet, 2005. **139C**(1): p. 4-9.
142. Rasiah, S.V., et al., *Antenatal perspective of hypoplastic left heart syndrome: 5 years on.* Arch Dis Child Fetal Neonatal Ed, 2008. **93**(3): p. F192-7.
143. Harh, J.Y., et al., *Experimental production of hypoplastic left heart syndrome in the chick embryo.* Am J Cardiol, 1973. **31**(1): p. 51-6.
144. Uva, M.S., et al., *Surgery for congenital mitral valve disease in the first year of life.* J Thorac Cardiovasc Surg, 1995. **109**(1): p. 164-74; discussion 174-6.
145. Sedmera, D., et al., *Remodeling of chick embryonic ventricular myoarchitecture under experimentally changed loading conditions.* Anat Rec, 1999. **254**(2): p. 238-52.
146. Pai, R.G., *Degenerative valve disease.* J Am Coll Cardiol, 2006. **48**(12): p. 2601; author reply 2602.
147. Hoerstrup, S.P., et al., *Functional living trileaflet heart valves grown in vitro.* Circulation, 2000. **102**(19): p. 44-49.
148. Sutherland, F.W., et al., *From stem cells to viable autologous semilunar heart valve.* Circulation, 2005. **111**(21): p. 2783-91.
149. Visconti, R.P., et al., *An in vivo analysis of hematopoietic stem cell potential: hematopoietic origin of cardiac valve interstitial cells.* Circ Res, 2006. **98**(5): p. 690-6.
150. Lincoln, J., C.M. Alfieri, and K.E. Yutzey, *Development of heart valve leaflets and supporting apparatus in chicken and mouse embryos.* Dev Dyn, 2004. **230**(2): p. 239-50.

Chapter 2

Isolation and Culture of Embryonic Valve Progenitor Cells

2.1: Introduction

Proper formation and function of embryonic heart valves is critical for developmental progression. The early embryonic heart is a U-shaped tube of endocardium surrounded by myocardium. The myocardium secretes cardiac jelly, a hyaluronan-rich gelatinous matrix, into the atrioventricular (AV) junction and outflow tract (OFT) lumen. At stage HH14 valvulogenesis begins when a subset of endocardial cells receive signals from the myocardium, undergo endocardial to mesenchymal transformation (EMT), and invade the cardiac jelly. At stage HH25 the valvular cushions are fully mesenchymalized, and it is this mesenchyme that eventually forms the valvular and septal apparatus of the heart. Understanding the mechanisms that initiate and modulate the process of EMT and cell differentiation are important because of their connection to serious congenital heart defects. In this study we present methods to isolate pre-EMT endocardial and post-EMT mesenchymal cells, which are the two different cell phenotypes of the prevalvular cushion. Pre-EMT endocardial cells can be cultured with or without the myocardium. Post-EMT AV cushion mesenchymal cells can be cultured inside mechanically constrained or stress-free collagen gels. These 3D *in vitro* models mimic key valvular morphogenic events and are useful for deconstructing the mechanisms of early and late stage valvulogenesis.

2.2: Protocol Preparation

1.) Preparation

1.1) Incubate fertile quail or chicken eggs to stage 14^{-} (about 2 days) or 25 (about 4.5 days) at 60% humidity and 37^{o}C.

1.2) Prepare sterile Earl's Balanced Salt Solution (EBSS)

1.2.1) Add 100 mL 10X EBSS to 600 mL 18 MΩ water

1.2.2.) Add 2.2 g sodium bicarbonate

1.2.3.) Adjust the pH of the solution to 7.2

1.2.4.) Bring the solution up to 1000 mL

1.2.5.) Sterilize the solution by passing through a 0.2 µm filter

1.3) Prepare sterile M199 culture medium.

1.3.1.) Add 1 package of M199 powder to 700 mL 18 MΩ water.

1.3.2.) Add 2.2 g sodium bicarbonate

1.3.3.) Adjust the pH of the solution to 7.2.

1.3.4.) Add 10 mL (1%) Penicillin-Streptomycin

1.3.5.) Bring the solution up to 1000 mL

1.3.6) Sterilize the solution by passing through a 0.2 µm filter

1.3.7.) Add 1 mL sterile 100X Insulin-Transferrin-Selenium-G supplement

1.3.8) Add 10 mL (1%) sterile chicken serum

1.4) Prepare three dimensional collagen gels at a collagen concentration of 1.5 mg/mL. Previous work in our lab has shown that a collagen concentration of more than 1.5 mg/mL provides a matrix that is too biomechanically stiff for the cells to move through. Collagen gel concentrations lower than 1.5 mg/mL have so few collagen fibers that the cell clump can shred the fibers locally, producing an island of cells.

1.4.1) Add the following ice-cold reagents to a sterile 15 mL centrifuge tube in order

- 3X M199: Volume = total volume necessary / 3

- Sterile 18 MΩ water: Volume = total volume necessary – (M199 volume + chicken serum volume + 0.1 M NaOH volume + collagen volume)
- Sterile chicken serum: Volume = total volume necessary * 0.01
- Rat tail collagen I: Volume = (collagen gel concentration * total volume necessary) / collagen stock concentration
- Sterile 0.1 M NaOH: Volume = collagen volume * 0.2

Note: The amount of water, 0.1 M NaOH, and collagen added will vary depending on the concentration of the collagen stock solution.

1.4.2.) Mix the collagen solution well with a sterile pipette.

1.4.3.) Immediately transfer 0.3 mL of the collagen solution into 1.9 cm^2 growth area wells. This is enough collagen solution to completely cover the well and to provide a gel that is approximately 3 mm thick. A gel thickness of at least 250 □m is necessary for cell invasion studies.

1.4.4.) Allow the collagen solution to gel for at least 1 hour at 37^oC, 5% CO_2, and 100% humidity.

2.3: Pre-EMT endocardial cell isolation and culture

2.) Pre-EMT cell isolation and culture

2.1.) Embryo isolation

2.1.1.) Place one inch long piece of laboratory tape over the larger end of the egg. This is where the air cell is located. The tape stabilizes the fragile quail egg shell.

2.1.2.) Gently puncture the taped area of the egg in the air cell with the tip of sterilized curved scissors.

2.1.3.) Cut a hole in the taped portion of the egg that is large enough to allow the yolk to pass through. Start the hole at the puncture and cut outward in a spiral shape. Make sure to cut through the outer membrane, but avoid piercing the yolk.

2.1.4.) When the hole in the shell is complete, visualize the quail embryo. The embryo is normally located on the top side of the yolk.

2.1.5.) Begin to pour the yolk through the hole cut in the egg with one hand. Hold a #55 tweezer in the other hand. As the embryo exits the egg on the top side of the yolk, gently slide the #55 tweezers under the embryo and remove it from the yolk.

Note: For chicken eggs, the embryo isolation involves cracking the chicken egg on a sharp, clean surface and breaking the egg into a 100 mm petri dish. The embryo should be located on the top side of the yolk. Gently slide #55 tweezers under the embryo and remove it from the yolk.

2.1.6.) Place the embryo into a 100 mm petri dish containing sterile, ice-cold EBSS.

2.2.) Stage the embryos according to the criteria of Hamburger and Hamilton[1]. Embryos at stage 14^- are past stage 13, but not yet at stage 14, with 20-21 somites and a tail bud. A key characteristic of stage 14^- embryos is the head angle, which is slightly greater than 90º to the body.

2.3.) Remove the hearts from quail embryos at stage 14^- with #55 tweezers by cutting transversely where the AV canal and OFT make contact with the thoracic wall. Place the hearts together on one side of the petri dish.

2.4.) Collect the isolated hearts with a sterile transfer pipette and place them into a new 100 mm petri dish filled with sterile, ice-cold EBSS.

2.5.) Cut the OFTs and AV canals transversely from the ventricles with #55 tweezers.

2.6.) Section the remaining AV canals and/or outflow tracts (OFTs) longitudinally.

2.7.) Set a pipette to a volume of 20 uL. Use this pipette to aspirate six longitudinally-cut AV canals and OFTs.

2.8.) Expel the AV canals and OFTs onto the collagen gel. Aspirate any excess EBSS from the surface of the gel.

2.9.) Use #55 tweezers to orient the explants so they are flat and so the lumen side faces the collagen gel. Try not to puncture the collagen gel with the tweezers.

2.10.) After 2 hours at 37^{o}C and 5% CO_2, remove the myocardium from the explants with #55 tweezers. The endocardial cells should be left behind on the surface of the collagen gel. Alternatively, the myocardium can be left on the explant. With the myocardium removed, the endocardial cells with not undergo EMT without intervention. With the myocardium present a subset of endocardial cells will transform into mesenchyme, but the degree of transformation can be modulated with external factors.
Note: Even if the myocardium will be left on, the explant must be allowed at least 2 hours to attach to the gel before medium is added.

2.11.) Add 0.4 mL M199 medium to each well containing explants.

2.12.) Culture the cells at 37^{o}C, 5% CO_2, and 100% humidity.

2.4: Post-EMT AV cushion mesenchymal cell isolation and culture

3.) Post-EMT cell isolation and culture

3.1.) Crack the chicken egg on a sharp, clean surface and break the egg into a 100 mm petri dish. The embryo should be located on the top side of the yolk. Pick up the embryo with #5 tweezers by grabbing the membranes surrounding the embryo and place the embryo into a 100 mm petri dish filled with sterile, ice-cold EBSS.

3.2.) Stage the embryos according to the criteria of Hamburger and Hamilton[1]. Features of a stage 25 embryo include distinct elbow and knee joints and slight eye pigmentation.

3.3.) Isolate the hearts from all HH25 embryos and place the hearts together on one side of the petri dish.

3.4.) Collect the isolated hearts with a sterile transfer pipette and place them into a new 100 mm petri dish filled with sterile, ice-cold EBSS.

3.5.) Isolate the AV region from all hearts at once. Place the AVs together on one side of the petri dish. Gently agitate the AV region to remove all blood, which can affect cell viability.

3.6.) Collect the isolated AVs with a sterile transfer pipette and place them into a new 100 mm petri dish filled with sterile, ice-cold EBSS.

3.7.) Sequentially isolate the cushions from the AV. Make sure there is no myocardium present on the AV cushions.

3.8.) Collect the isolated cushions with a sterile transfer pipette and place them into a sterile 15 mL centrifuge tube.

3.9.) Spin the cushions to the bottom of the centrifuge tube at 15 x g for 3 minutes.

3.10.) Use a sterile 1000 mL tip to remove as much of the EBSS supernatant as possible without disturbing the cushions.

3.11.) Add 1 mL of 0.25% Trypsin-EDTA that has been pre-warmed to 37^{o}C. Allow the cushions to incubate in trypsin until they are completely dissolved, which is normally about 3-5 minutes.

3.12.) Add 100 µL of chicken serum to the centrifuge tube to quench the trypsin.

3.13.) Pellet the cells at 160 x g for 5 minutes. Remove the supernatant with a sterile, 1000 µL tip.

3.14.) Resuspend the cells in 2 mL of M199 medium and mix by pipetting. Take 10 µL of the cell suspension to count on a hemocytometer and determine the total number of cells that have been isolated.

3.15.) Determine how many collagen gels will be made based on the number of cells isolated. Cells need to be plated at a density of 2×10^5 cells/mL with a 250 µL gel volume.

3.16.) Pellet the cells at 160 x g for 5 minutes. Remove the supernatant with a sterile, 1000 µL tip.

3.17.) Using the protocol listed above, add 3X M199, water, chicken serum, collagen, and 0.1 M NaOH, in that order, to the cell pellet. Mix by gentle pipetting.

3.18.) Add 250 uL to each 1.9 cm^2 growth area well.

3.19.) Allow the collagen solution to gel for at least 1 hour at 37^oC, 5% CO_2, and 100% humidity.

3.20.) Add 0.4 mL of culture media and incubate overnight.

3.21.) To continue culturing the gels in stress-free conditions, liberate the gels from the sides of the culture well using a sterile 200 ul pipet tip. Mechanically constrained cultures are gels that remain attached to the sides of the culture well.

2.5: Representative Results

4. Results

4.1.) An HH14$^-$ quail embryo (Figure 2.1 left) and an HH25 chicken embryo (Figure 2.1 right) are shown here. A key characteristic of stage 14$^-$ embryos is the head angle. At

stage 14$^-$ the head is at slightly greater than 90º angle to the body. Features of a stage 25 embryo include distinct elbow and knee joints and slight eye pigmentation.

Figure 2.1 – Representative images of avian embryo at stage 14- (left) and HH25 (right).

4.2.) The HH14$^-$ valve endocardial explants are shown after 2 hours of culture with the myocardium present (Figure 2.2 left) or removed (Figure 2.2 right).

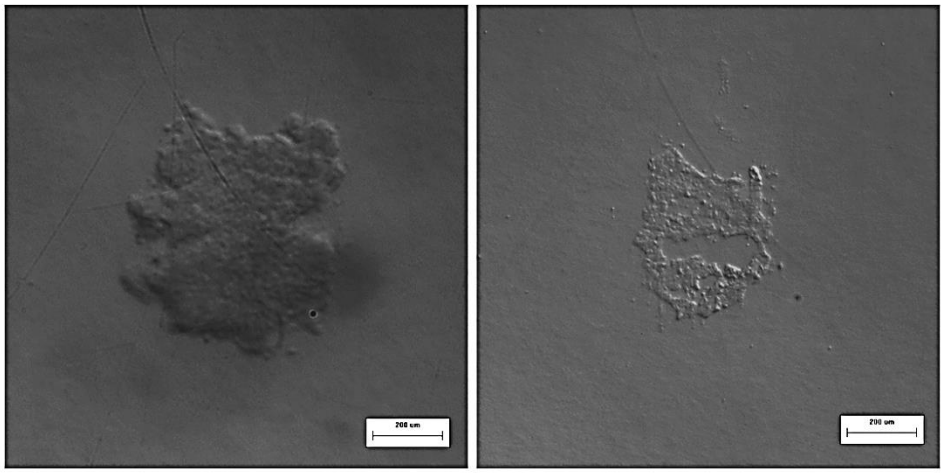

Figure 2.2 – Representative images of endocardial explants at stage 14- with myocardium (left) and without myocardium (right).

4.3.) In HH14$^-$ valve endocardial explants with the myocardium present many of the cells undergo endocardial to mesenchymal transformation and have a spindle-shaped, mesenchymal phenotype after 48 hours of culture (Figure 2.3 left). When the myocardium is removed all of the cells maintain a cobblestone-shaped, endocardial phenotype after 48 hours in culture (Figure 2.3 right).

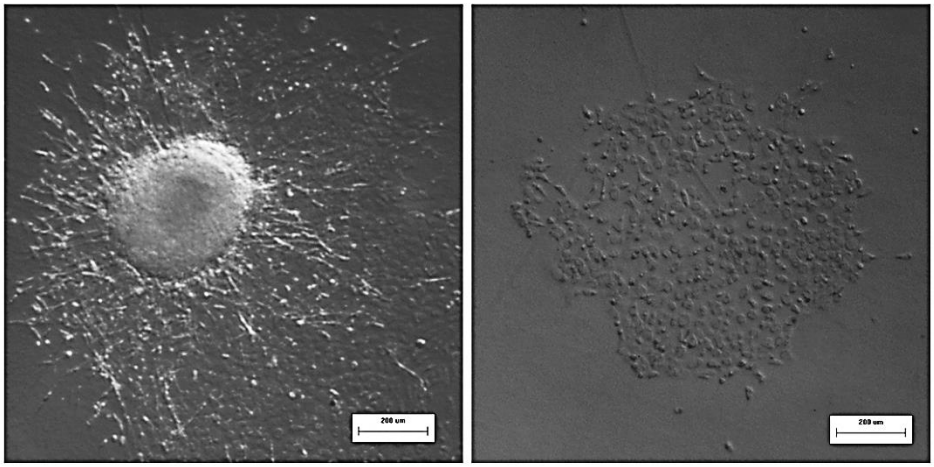

Figure 2.3 – Representative images of endocardial explants at stage HH14- after 48 hours with myocardium (left) and without myocardium (right).

4.4) HH25 valve mesenchymal cells in a collagen gel are rounded immediately after seeding (Figure 2.4). After 48 hours of culture in a constrained collagen gel the HH25 mesenchymal cells are beginning to spread (Figure 2.4 left). HH25 cells in a stress-free collagen gel 7 days after seeding and 6 days after liberation have compacted the gel to approximately 50% of the original area (Figure 2.4 right).

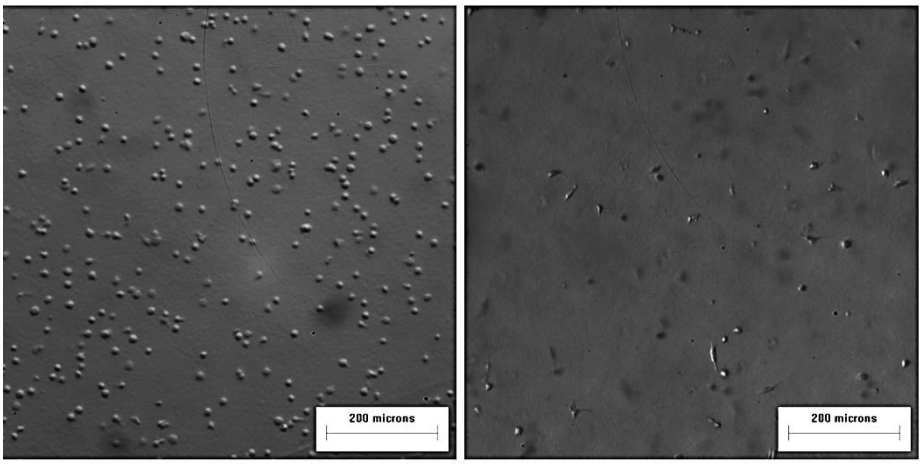

Figure 2.4 – Representative images endocardial cells at HH25 within a collagen hydrogel immediately after seeding (left) and after 48 hours in culture (right).

2.6: Discussion

The method for isolating endocardial cells from stage HH14^{-} hearts originally developed by Runyan and Markwald provides a controlled, *in vitro* environment to study the factors that initiate and modulate embryonic EMT [1]. HH14^{-} endocardial explants cultured without myocardium will not undergo EMT without biomechanical or biochemical intervention. If the myocardium is left on the explant it will signal a subset of endocardial cells to undergo mesenchymal transformation, but external factors may regulate this process. Isolating embryonic progenitor mesenchymal cells from HH25 AV valve cushion using the method described by Butcher et al. provides an opportunity to determine what signals drive differentiation toward mature valvular interstitial cells [2]. Culturing the cells in mechanically stressed or stress-free conditions allows the researcher to probe biomechanical stimuli, and factors added to the culture medium can provide biochemical signals. *In vitro* models that help to decipher mechanisms affecting EMT, cell differentiation, and structural remodeling can be used to better understand the causes of congenital heart defects and could help determine ways to drive stem cells toward mature valve cell phenotypes for tissue engineering applications [3].

Table 2. 1- Specific reagents and equipment:

Name of the reagent	Company	Catalogue number	Comments
Extra fine Bonn scissors, curved	Fine Science Tools	14085-08	
Dumont tweezers #55	World Precision Instruments, Inc.	14099	Purchasing tweezers from fine science has also been done.
Dumont tweezers #5	World Precision Instruments, Inc.	14098	
Sterile transfer pipettes	Samco Scientific	2041S	
4-well culture plates	Nunc	176740	
Sterile disposable filter units, PES 0.2um pore membrane	Nalgene	566-0020	
Sterile 15 mL centrifuge tubes	Corning	430828	
Sterile petri dishes, 100 mm x 15 mm	VWR International	25384-342	
Laboratory tape	VWR International	89097-920	
Rat-tail collagen I	BD Biosciences	354236	Stock concentration should be at least 4mg/ml.
10X Earl's Balanced Salt Solution	Quality Biological, Inc.	119-064-131	We have the protocol to now make the solution in the lab.
M199 powder	Invitrogen	31100-035	Gibco can also be used.
Penicillin-Streptomycin	Invitrogen	15140-122	
Insulin-Transferrin-Selenium-G	Invitrogen	41400-045	Use 1ml per 1Liter. Each bottle makes 10

supplement (100X)			Liters (.1%).
Chicken serum	Invitrogen	16110-082	Use 5% chick serum for HH25 cells.
0.25% Trypsin-EDTA	Invitrogen	25200-056	
Sodium bicarbonate	Sigma-Aldrich	S5761	
Sodium hydroxide solution, 1.0 N	Sigma-Aldrich	S2770	
Fertile quail eggs (*Coturnix coturnix*)	Lake Cumberland Game Bird Farm		
Fertile chicken eggs (*Gallus gallus*)	Cornell University Poultry Farm		

REFERENCES

1. Runyan, R.B. and R.R. Markwald, *Invasion of mesenchyme into three-dimensional collagen gels: a regional and temporal analysis of interaction in embryonic heart tissue.* Dev Biol, 1983. **95**(1): p. 108-14.
2. Chiu, Y.N., et al., *Transforming growth factor beta, bone morphogenetic protein, and vascular endothelial growth factor mediate phenotype maturation and tissue remodeling by embryonic valve progenitor cells: relevance for heart valve tissue engineering.* Tissue Eng Part A, 2010. **16**(11): p. 3375-83.
3. Markwald, R.R. and J.T. Butcher, *The next frontier in cardiovascular developmental biology--an integrated approach to adult disease?* Nat Clin Pract Cardiovasc Med, 2007. **4**(2): p. 60-1.

CHAPTER 3

DEVELOPMENT OF IN-VITRO BIOREACTOR TO TEST EFFECTS OF MECHANICAL STRAIN ON VALVULAR INTERSTITIAL CELLS

3.1: Summary

Many planar connective tissues exhibit complex anisotropic matrix fiber arrangements that are critical to their biomechanical function. This organized structure is created and modified by resident fibroblasts in response to mechanical forces in their environment. The directionality of applied strain fields change dramatically during development, aging, and disease, but the specific effect of strain direction on matrix remodeling is less clear. Current mechanobiological inquiry of planar tissues is limited to equibiaxial or uniaxial stretch, which inadequately simulate many in vivo environments. In this study, we implement a novel bioreactor system to demonstrate the unique effect of controlled anisotropic strain on fibroblast behavior in 3D engineered tissue environments, using aortic valve interstitial fibroblast cells (VIC) as a model system. Cell seeded 3D collagen hydrogels were subjected to cyclic anisotropic strain profiles maintained at constant areal strain magnitude for up to 96 hours at 1Hz. Increasing anisotropy of biaxial strain resulted in increased cellular orientation and collagen fiber alignment along the principal directions of strain and cell orientation was found to precede fiber reorganization. Cellular proliferation and apoptosis were both significantly enhanced under increasing biaxial strain anisotropy ($P < 0.05$). While cyclic strain reduced both vimentin and alpha-smooth muscle actin compared to unstrained controls, vimentin and alpha-smooth muscle actin expression increased with strain anisotropy and correlated with direction ($P < 0.05$). Collectively, these results suggest that strain field anisotropy is an independent regulator of fibroblast cell phenotype, turnover, and matrix reorganization, which may inform normal and pathological remodeling in soft tissues.

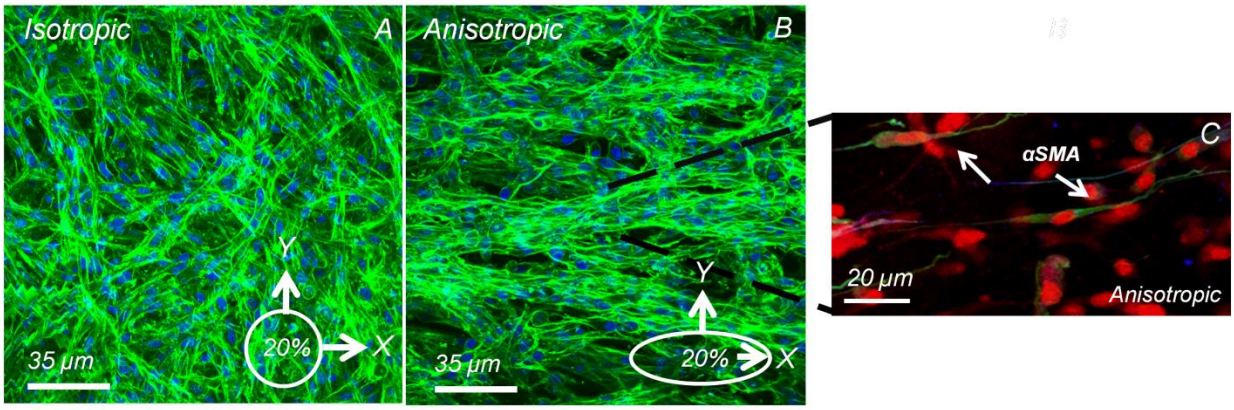

Figure 3.1 – Valvular interstitial cells rapidly reorient orthogonally with biaxial anisotropic strain, while modulating directional levels of ACTA2. (A) Orientation of valvular interstitial cells (f-actin, green) align without a preferred direction during isotropic strain (DNA, blue). (B) During anisotropic strain, cellular orientation aligns with respect to the principal directions of strain. (C) A larger degree of ACTA2 expression (green) occurs perpendicular to the first principal strain direction (DNA-red).

3.2: Introduction

Planar connective tissues such as the diaphragm, pericardium, and valve leaflets perform critical biomechanical functions under cyclic mechanical loading [1, 2]. These tissues have evolved complex multidirectional collagenous fiber orientations that result in anisotropic mechanical properties ideally suited to their local microenvironment. Resident tissue fibroblasts continuously repair and remodel their tissue microenvironment in response to these mechanical cues, including secreting and/or degrading extracellular matrix proteins, releasing soluble growth factors, and reorganizing cell-cell/cell-matrix adhesive interactions [3, 4]. Fibroblasts transition between a quiescent synthetic phenotype, characterized by homeostatic matrix turnover, to activated contractile myofibroblasts that change the underlying matrix mechanics and/or composition depending on the remodeling state of the tissue [5]. For example, during wound closure and fibrosis/scar formation, myofibroblasts elevate expression of contractile proteins and generate traction forces that create mechanical tension to pull matrix fibers together [6]. Heart valve leaflets are exposed to arguably the most demanding mechanical environment in the body, yet interstitial fibroblasts thrive and mediate significant matrix turnover

[7, 8]. Mechanical microenvironmental cues therefore provide strong inductive signals regulating tissue homeostasis and remodeling, but how they mediate healthy instead of pathological tissue remodeling remains poorly understood.

Mechanistic understanding of fibroblast mediated tissue remodeling has advanced considerably with the aid of engineered tissue models that enable testing of molecular, cellular, and tissue scale mechanisms within a well defined, repeatable, and physiologically relevant microenvironment [9]. Fibroblasts in anchored 3D hydrogels develop mechanical tension leading to increased expression of contractile proteins, enhanced matrix synthesis, and release of growth factors such as transforming growth factor-beta (TGFβ), while fibroblasts in free-floating unstressed gels remain quiescent [10]. More recently, bioreactors have been developed to apply specific mechanical strain parameters uniformly to a specimens as to isolate the underlying signaling mechanisms [11]. For example, cyclic stretching of fibroblasts in vitro induces cytoskeleton rearrangement [12], focal adhesion clustering [13], and downstream intracellular signaling cascades leading to cell and matrix fiber reorganization [14]. While the effects of strain magnitude and frequency have been studied for some time, the unique signaling from strain directionality is much less known. Cyclic uniaxial (one direction) stretch induced TGFβ1, collagen III and fibronectin gene expression in cardiac fibroblasts. Equiaxial (isotropic) strain, however, induced divergent responses in extracellular matrix (ECM) mRNA levels [15]. Fibroblasts have also been shown to align perpendicular to the direction of principal strain, while no-preferred direction occurs during equiaxial strain [16]. Given that planar tissues experience multi-axial strain patterns in vivo and exhibit anisotropic biomechanical properties rather than either of the above extremes [17], it is therefore critically important to understand how biaxial strain anisotropy independently affects molecular signaling, fibroblast phenotype, and matrix remodeling behavior

While biaxial and even triaxial stretches have been applied to tissues in cylindrical configurations, such as blood vessels [18], a similar device for planar 3D engineered tissues has not been developed. Well-defined anisotropic biaxial strain fields have to date only been applied to planar cultures on 2D substrates [19]. Biaxial (radial and circumferential) tensile strains can be applied in 2D using a vacuum-pressure (Flexcell) system, but strain magnitude varies in-homogeneously with distance from the center of the membrane [20]. Tan et al. also generated static heterogeneous anisotropic biaxial micro-strain patterns through multi-spoke and microgroove array patterned 2D substrates [21]. We previously showed that smooth muscle cells exposed to homogeneous equiaxial stretch in 3D culture dedifferentiate to synthetic myofibroblasts [22]. Studies with valve fibroblasts in 3D culture have shown heterogeneous changes in cell phenotype and matrix synthesis, but these could not be directly related to specific strain profiles [23].

The objective of this study, therefore, was to test how biaxial strain anisotropy independently controls fibroblast cell phenotype and matrix remodeling in 3D environments. We developed and implemented a novel cyclic biaxial strain bioreactor with controllable homogeneous strain field anisotropy for engineered tissue hydrogels. We hypothesized that valvular interstitial cells (VIC) would align with respect to the principal directions of strain and rapidly remodel the underlying matrix to mirror this alignment pattern. We first determined the temporal changes in cell and matrix fiber reorganization with strain anisotropy, followed by quantification of cell proliferation, apoptosis, and fibroblast phenotype.

3.3: Materials and Methods

3.3.1: Bioreactor Design and Optimization

Our challenge was to create a bioreactor test system that enabled 1) fabrication and stable anchoring of 3D hydrogels and 3) applied controlled multiaxial mechanical stimulation without

having to disturb the tissue. We hypothesized that if elliptically shaped 3D hydrogels were stretched uniformly along their outer perimeters, then the internal strain field would be homogeneous but biaxial. To evaluate this, finite element simulations (FEA, ANSYS Inc.) were first conducted to optimize geometric parameters for the bioreactor system. 20,000 prismatic rectangular elements were used with large strain hyperelastic (Mooney-Rivlin, modulus = 1 MPa) material properties performed on quarter-symmetric circular sections of silicone slab and platen. Both elliptical and circular slabs and/or platens were tested, with radii between 0.5 and 2 inches. Platen/cassette hole diameter ratios were varied between 0.5 and 0.9. Slab thickness was varied from 2-6 mm, with well depth ratios ranging from 0.5 to 0.9. Finally, well centroid within the slab was translated radially from concentric to 75% of the platen radius. Design optimization criteria were to1) maximize the number of samples testable within one cassette well, 2) maximize the size of samples testable, 3) maximize the depth of the PDMS wells, 4) maximize the possible applied strain magnitude, and 5) minimize the stress developed in the PDMS.

To fabricate these different hydrogel 3D geometries, we developed thick elastomeric slabs instead of commonly used thin membranes (described below), which were secured between two circular aluminum flanges of a cassette (Figure 3.2A). Each cassette contained four cylindrical holes (where the slabs were exposed) positioned concentrically over Teflon lined platens. Negative molds were machined from polycarbonate such that small wells would be present within the silicone slab spanning the cassette holes above the platens (Figure 3.2B). Molds were designed with ellipsoidal wells of major/minor axis ratios (hereafter X and Y respectively) of 1:1, 2:1, and 4:1. Beveled edges were machined within the ellipse to ensure uniform vertical strain fields through the well edges and to secure a compression spring (Lee Spring) for anchoring hydrogels. Polydimethylsiloxane (PDMS Sylgard 184, Dow Corning) was formed at a concentration of 20:1, degassed, poured into the negative molds, and solidified at 70°C for 12

hours. Slabs were then released from the molds, mounted within the aluminum cassettes, and autoclaved before use (Figure 3.2C). The stage was constrained to vertical motion using shafts with linear bearings. A rotary stepper motor (34Y, Anaheim Automation) drove vertical translation through a screw-pinion gear assembly (Figure 3.2D). Limit switches were mounted on either side of the translation stage to prevent overstrain and semi-automate calibration. A cold plate (CP12, Lytron) was placed underneath the stepper motor for heat transfer. Strain magnitude and frequency waveforms were applied to the motor via a controller module and custom software (DPN10601, Anaheim Automation).

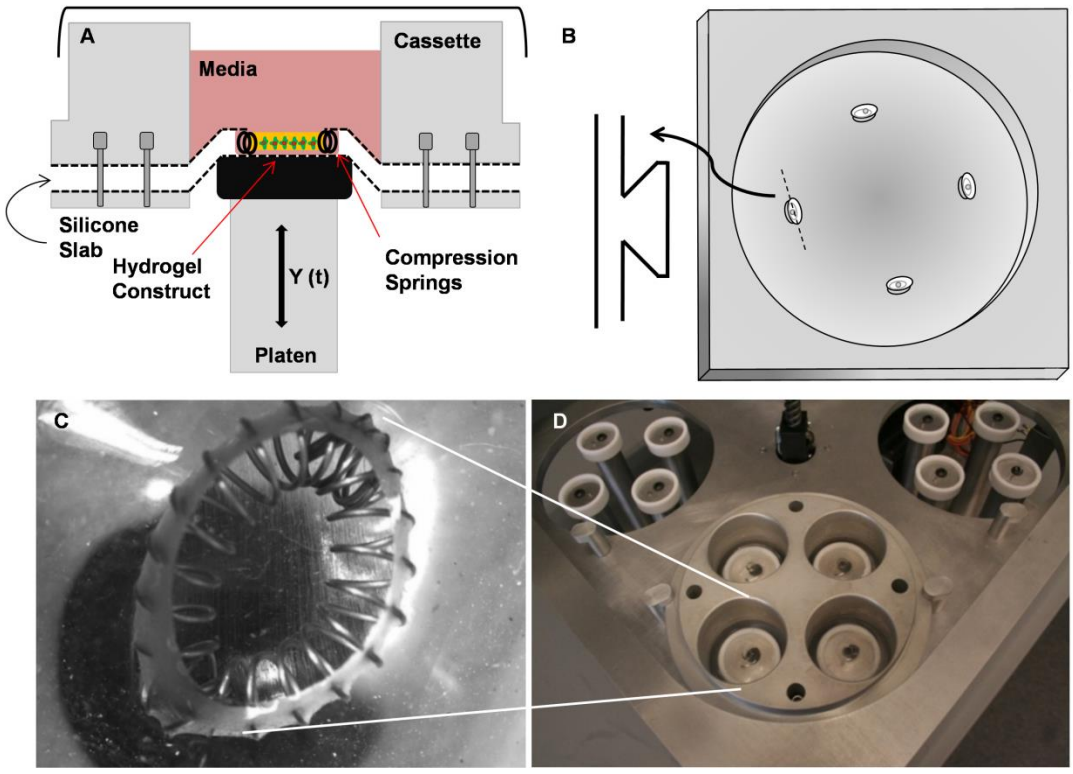

Figure 3.2 – Design of the anisotropic biaxial strain (ABS) bioreactor. (A) Conceptual schematic showing a cross-sectional view of a constrained collagen construct embedded in a silicone slab and loaded within an aluminum cassette. (B) An inverted polycarbonate negative mold with machined circular and elliptical wells used for constructing the silicone slab with embedded wells. (C) An expanded view of the elliptical well containing elliptical compression springs. (D) Macroscopic view of the bioreactor containing 4 cassettes and 16 independent wells.

3.3.2: Construction of Cassettes

To create the silicon membranes used for straining the hydrogels, a negative mold within 3/8" piece of polycarbonate was constructed. The polycarbonate was machined to form wells at a depth of 3mm, at various biaxial eccentricities. In terms of major to minor axis (x vs. y), ellipsoidal wells were generated at 1:1, 2:1, and 4:1 geometries. A bevel was also machined within the ellipse for securing the compression springs. Polydimethylsiloxane (Sylgard 184, Dow Corning, Midland, MI) was combined at a concentration of 20:1 respectively, and degassed prior to use. The silicon was poured into the negative molds and let solidify at 70°C for 12 hours. The silicon molds were then released from the polycarbonate, mounted within the cassettes, and autoclaved. The sterilized compression springs were then placed in the wells and covered with a petri dish lid (150mm).

3.3.3: FEA Analysis

Throughout the design of the bioreactor, a finite element model was used to optimize shapes and ensure homogeneous anisotropic strain patterns. Various well diameters, aspect ratios, silicon membrane depths, cassette sizes, magnitudes of strain, and frequency were all considered. The silicon membranes were modeled as a hyperelastic material using a Mooney-Rivlin two-parameter model with invariant coefficients of 0.55 and 0.14 MPa. The membranes were first generated within the plane function as 2D triangular elements. The geometry of membrane measured 25mm in radius and the platen was 20mm in radius with a filet radius of 1mm. Contact analysis using a sliding boundary condition was used for the intersection between the membrane and platen, assuming a coefficient of friction of 0.06 (Castrol, Braycote 803). For all simulations, the displacement was applied to the edge of the membrane. All finite element simulations were completed through ANSYS.

3.3.4: Cell Isolation

Adult PAVIC were isolated by a collagenase digestion method as previously described[24]. Briefly, aortic valve leaflets were obtained from a local abattoir and placed on cold Dulbecco's phosphate buffered saline (Invitrogen) for transport. The surface of the leaflets was partially digested in (600U/ml, Worthington) collagenase solution with Dulbecco's Modified Eagle's Medium (DMEM) (Gibco) for 5-10 minutes after which the endothelial layer was sheared off with a cotton swab. The remaining leaflet was then incubated for 12-18 hours in collagenase solution and homogenized with a serological pipette. Cells were then plated on tissue culture plastic, and maintained with DMEM (Gibco) supplemented with 10% fetal bovine serum (Gibco) and 1% penicillin/streptomycin (Gibco). Cultures were fed every two days and split at confluency. Cultures used for experiments were between passages 4 and 6.

3.3.5: 3D Hydrogel Formation

Three-dimensional (3D) hydrogel constructs were created using a modified procedure from that previously described[25]. Porcine aortic valve interstitial cells (PAVIC) were used as a representative planar tissue fibroblast source. A suspension of 400,000 cells/ml porcine aortic valvular interstitial cells (PAVIC) were used in 3x DMEM with 10% FBS (Gibco), 2 mg/ml type I collagen (BD), and 0.1 M NaOH to neutralize the solution. 3D cultures with 1:1, 2:1, and 4:1 aspect ratio were pre-loaded 300 steps below center of platen. This was done to shift the calibration curve to the linear portion of the graph and increase the size of the well. Once pre-loaded, wells were filled with different volumes of gels depending on the geometry (ratio of major to minor axis). For the 1:1, 2:1, 4:1, and control wells, 100µl, 125µl, 150µl, and 125µl respectively of gel was inoculated into the wells containing the compression springs, which solidified after 60 minutes. After 60 min, 18 ml of media was added to the reservoir. The hydrogels were allowed to compact around the springs over a 24 hr period after which a 20% area strain (250 step size, 2mm) was applied to all the constructs at 1Hz. This seeded

compaction process is similar to Garvin et al. such that fibroblasts suspended in collagen gels will compact around an anchor and form a stable construct [26]. Static cultures served as controls and both mechanically anchored and unanchored hydrogels were used. The unanchored controls were lifted from the well after 24 hr to allow free compaction of the gels. All materials were sterilized via autoclaving before use. The system was housed in a standard tissue culture incubator, maintained at 37°C and 5% CO_2 throughout the culture period.

3.3.6: Strain Field Calibration

Marker fields (40µm glass beads) were placed along the well bottom, gel surface, and at the compression spring attachment points **(Figure 3.3).** The stage was translated to different depths, and marker positions within multiple wells were imaged and digitally recorded using ImageJ. Assuming uniform deformation within small groups of three points, the local normal and shear strain field could be described by a system of equations as previously described [22] (see Supplementary Methods for more details**)**. Comparing multiple marker groups determined strain field homogeneity. At least three independent point groups were compared per well and experimental condition for calibration. For frequency response mapping, linear acceleration/deceleration-time commands of increasing magnitude and shorter time intervals were sent to the stepper motor, creating sinusoidal stage motion patterns. Peak sustainable frequencies were recorded for each applied strain magnitude (equiaxial configuration).

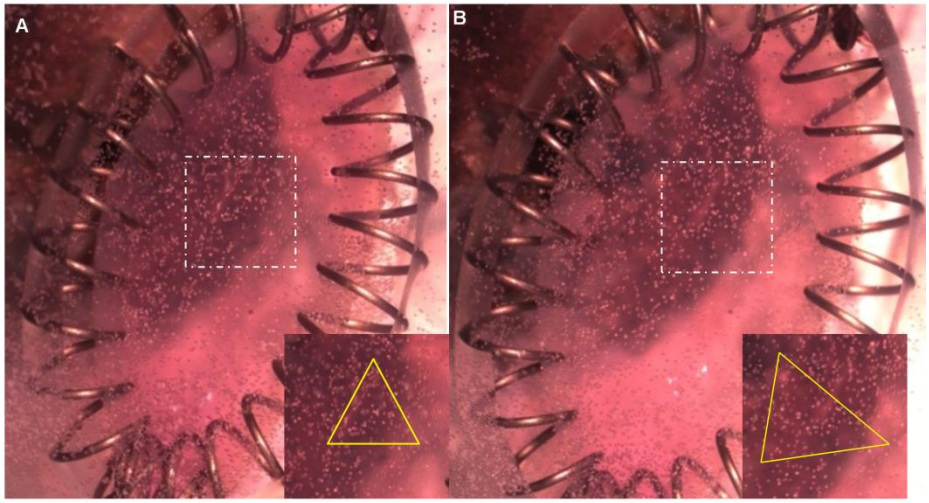

Figure 3.3 – Calibration of anisotropic strain fields. (A) 40 µm glass beads were placed within the collagen hydrogel and tracked from the undeformed to the (B) deformed configuration. Virtual triangles created with bead centroids as vertexes were used to quantitatively monitor tissue deformation and to assess the uniformity of the strain field (inset).

Strain Calibration Equations

These patterns related the undeformed (unstrained) configuration and the deformed (strained) configuration by position [27], namely:

$x_i = FX_i + B_i$, Equation (1)

where x is the deformed coordinates, and X is the undeformed coordinates. F is a deformation gradient tensor for the plane of interest, either membrane or construct surface:

$F_{ij} = \frac{dx_i}{dX_j}$, Equation (2)

By solving the system of equations in Eq. (1) relating the observed deformed and undeformed configurations of triangular bead/mark positions, the coefficients of F were obtained. These were then was used to obtain finite (Green's) strain components:

$$E = 0.5(F^T F - I), \qquad \text{Equation (3)}$$

where I is the identity tensor. Finite strain was then transformed into area strain by the following formula:

$$A/A_o = \lambda_1\lambda_2 = (2E_{11} + 1)^{0.5}(2E_{22} + 1)^{0.5}, \qquad \text{Equation (4)}$$

3.3.7: Anisotropic Strain of 3D Tissue Constructs

The device used to impose anisotropic strain is a modified version of the system described in detail by Butcher et al [22]. The system consists of four aluminium cassettes which are placed on a movable stage, and clamped concentrically over a rigid aluminium cylindrical mandrel lined with Teflon. A stepper motor (34Y, Anaheim Automation) was used to drive the movable stage down over the rigid mandrel deforming the silicon membrane at a specific magnitude and frequency. Limit switches were mounted on either side of the movable stage so that any unwanted movement would be controlled. These modifications only require one calibration of the wells and re-zeroing is recognized by the limit switches. A cooling system was also implemented to control the temperature from the stepper motor to the surrounding metal. A cold

plate (CP12, Lytron) was mounted below the stepper motor connected to a stand up freezer contained cold water. The cold water from the freezer was pumped to the cold plate and returned the heated water from the stepper motor. The magnitude and frequency of the stepper motor was controlled through a controller (DPN10601, Anaheim Automation) and various waveforms could be applied depending on the duration of current applied.

3.3.8: Quantification of Cell and Matrix Architecture

We quantified changes in cell orientation and matrix fiber reorganization at 48 and 96 hours via multiphoton microscopy. Image stacks of the collagen hydrogels were taken from the central region of each well at 5-µm vertical steps. Z-stacks encompassed at least 80% of the gel thickness in each sample, but were limited by the penetration depth of laser microscopy and slight differences in hydrogel compaction. Cell orientation angle distributions within each gels (0 degrees representing the X direction) were determined using f-actin staining (Sigma) and quantified from maximum intensity projections images using ImageJ as previously described [28]. We manually traced the shape of hundreds of cells across multiple sections for each sample, and organized them within a histogram to enable comparison with the fiber alignment data. Alignment angle distributions from each gel were normalized to the most common alignment angle, which was assigned a value of 1. Simultaneously, collagen fibril alignment angle distributions were captured using second harmonic generation (SHG) imaging using a custom-built nonlinear laser scanning microscope employing 1040-nm, 1-MHz, 300-fs pulses from a Yb-fiber chirped pulse amplifier (FCPA µJewel D-400, IMRA America, Inc.) as previously described [29]. Galvanometric mirrors were use to scan laser pulses in a raster pattern. The laser scanning and data acquisition were controlled by MPSCOPE software [30]. SHG signal was detected using a bandpass filter centered at 517 nm with 65-nm bandwidth. Images were acquired using a 0.95-numerical aperture, 20x water immersion objective (Carl Zeiss Inc., Thornwood, NY) at 10 µm section spacing. Similar to the cellular orientation quantification, fiber

angle distributions within gels (0 degrees representing the X direction) were determined using central region z-stacks and the maximum intensity projections images processed using ImageJ. ECM fibers were analyzed in total using an alignment algorithm (adapted from Bowles et al. 2010) that assessed second harmonic generation autofluorescence [31]. We observed no variation in histogram profiles with relative z-axis position, and therefore pooled all the data into single histograms for each construct.

3.3.9: Proliferation and Apoptosis Assays

5-bromo-2'-deoxyuridine (BrdU) incorporation was used to detect proliferating cells. BrdU labeling reagent (Invitrogen) was added to the culture media 12 hours prior to experiment termination (48 hours). Hydrogel constructs were fixed and targeted with a monoclonal Anti-BrdU Alexa Fluor 488 conjugate (PRB-1, Invitrogen). Total DNA was counterstained using a DRAQ-5 (Biostatus) far red nuclear dye. TUNEL (Apo-Brdu TUNEL assay kit, Invitrogen) was used to detect apoptotic cells. 48 hour stretch and control hydrogels were fixed and stained for disrupted DNA targeted by incorporation of terminal deoxynucleotidyl transferase (Tdts) and 5-Bromo-2'-deoxyuridine 5'-triphosphate (BrdUTPs). Monoclonal Ani-BrdU Alexa Fluor 488 conjugate was used to target the fragmented DNA and a propidium iodide counter stain was used to determine total cellular DNA. Positive fluorescent areas for each cell were measured using ImageJ and normalized by cell nuclei.

3.3.10: VIC Phenotype

Alpha smooth muscle actin (gene name ACTA2, marker of myofibroblastic phenotype) and vimentin protein expression (VIM, indicative of quiescent fibroblast phenotype) were compared across strain conditions at 48 hours using quantitative real-time PCR (RT-PCR, see supplemental methods) and immunohistochemistry. Antibody staining was performed as previously described [22]. Image Z-stacks (10 μm intervals) were taken with laser confocal

microscopy (TCS or Leica LSM510) at fixed gain, offset, and averaging settings. Each label occupied a different fluorescence channel, and excitation lasers were sequentially activated to negate signal bleed. Z-stacks were taken at 5-10µm sections and converted into maximum projections. Positive fluorescent areas for each color were measured using ImageJ and normalized by cell nuclei. Data was related as percentage of cells with cytoskeletal signal and compared across conditions.

3.3.11: RT-PCR

To determine gene expression changes, the hydrogel construct was isolated from the center of each well. Using a Qiagen total RNA purification kit (Qiagen, Valencia, CA), RNA was reverse transcribed to cDNA using the SuperScript III RT-PCR kit with oligo(dT) primer (Invitrogen). Sufficient quality RNA was determined by an absorbance ratio A_{260}/A_{280} of 1.8 – 2.1, while the quantity of RNA was determined by measuring the absorbance at 260nm (A_{260}). Primers were designed to detect 18S, alpha-smooth muscle actin, and vimentin in cDNA clones: 18S (R–AATGGGGTTCAACGGGTTAC, F-TAGAGGGACAAGTGGCGTTC, Amplicon 92bp, Accession DQ437859.1), VIM (F–GTACCGGAGACAGGTGCAGT, R– TTCCACGGCAAAGTTCTCTT, Amplicon 69bp, Accession XM_00213072.1), ACTA2 (F–CAGCCAGGATGTGTGAAGAA, R-TCACCCCCTGATGTCTAGGA, Amplicon 104bp, Accession NM_001164650.1). Real time PCR was performed on all samples using SYBR Green PCR master mix (Applied Biosystems, Carlsbad, CA) and a MiniOpticon Real-Time PCR Detection System (Biorad, Hercules, CA). Amplification cycle thresholds were normalized to those from 18S and melt curves compared across samples. Stable expression of 18S was observed across all mechanically stimulated conditions and GAPDH was used as a secondary housekeeping gene to verify expression level.

3.3.12: Collagen Gel Immunofluorescence

Fixed samples on collagen gels were washed for 15 minutes on a rocker 3 times with PBS, permeabilized with 0.2% Triton-X 100 (VWR International, Radnor, PA) for 10 minutes, and washed another 3 times with PBS. For the phenotype studies, samples were incubated overnight at 4^{o}C in a 1% BSA (Rockland Immunochemicals, Inc., Gilbertsville, PA) blocking solution followed by another 4^{o}C overnight incubation with mouse anti-human vimentin (VIM) 1:100 (Invitrogen) and rabbit anti-human α-SMA 1:100 (Spring Bioscience). For the orientation studies, samples were incubated with phalloidin (Invitrogen). After 3 washes for 15 minutes with PBS, samples were exposed to Alexa Fluor® 488 or 568 conjugated (Invitrogen), species specific secondary antibodies at 1:100 in 1% BSA for 2 hours at room temperature. Three more washes with PBS for 15 minutes were followed by incubation with either DRAQ5 far red nuclear stain (Enzo Life Sciences, Plymouth Meeting, PA) at 1:1000 or Hoechst (Invitrogen) at 1:10000. Samples were washed once more with 18Mohm water and stored in 18mohm water at 4^{0}C. Images were taken with a Leica TCS SP2 laser scanning spectral confocal microscope (Leica-Microsystems, Bannockburn, IL). ACTA2 and VIM was measured by creating a region of interest across the entire image. Total intensity of F-actin (green) and VIM (blue) was quantified. These values were then normalized by total nuclei within the image. All image and processing settings were consistent throughout.

Statistics

At least 6 samples per time point and treatment condition were used in each endpoint assay for statistical analysis. One-way ANOVA with Tukey's modified post-hoc tests were used to compare differences between means and data was transformed when necessary to obtain equal sample variances. For proliferation/apoptosis studies, statistical tests were implemented across treatment conditions and results are expressed as mean ± standard error. For gene/protein expression studies, statistical tests compared individual genes across treatment

conditions and results are expressed as mean ± standard deviation. $P < 0.05$ denoted statistical significance.

3.4: Results

3.4.1: Design and Optimization of the Anisotropic Biaxial Strain (ABS) Bioreactor

3D collagen gels could be anchored within cyclically deforming wells through compression springs whose lengths were adjusted to press fit inside the outer edge of the well and were secured with a 60 degree beveled edge. Preliminary finite element simulations determined that the major and minor axis lengths of an ellipsoidal well shape could independently control XX and YY strain magnitudes (Figure 3.4). Thus, by varying the eccentricity of the elliptical well, the biaxial strain profiles scaled with the major to minor axis ratio. Further simulations were done to characterize well placement within the PDMS slab and dependence upon equiaxial well diameter. Using a 1:1 geometric ratio, we found that deviations in the placement of the well, up to 60% (25mm) along the platen radius, did not significantly affect strain magnitude (Figure 3.4B). It was also determined that the strain magnitude inversely correlated with well diameter, such that a reduction of 20% to 10% radial strain occurred when increasing well diameter from 2mm to 8mm (Figure 3.4C). Finally, parametric optimization through finite element simulations predicted that for 50 cm diameter cassette holes and 6 mm wells, a silicone slab of 3/8" thickness with 3 mm deep wells, achieved a uniform 50% strain during 1 cm of stage translation. In this configuration, 4 holes could be fabricated in each cassette, and 4 cassettes could be secured on the translating stage. For these experiments, however, one well was created at the center of each cassette hole.

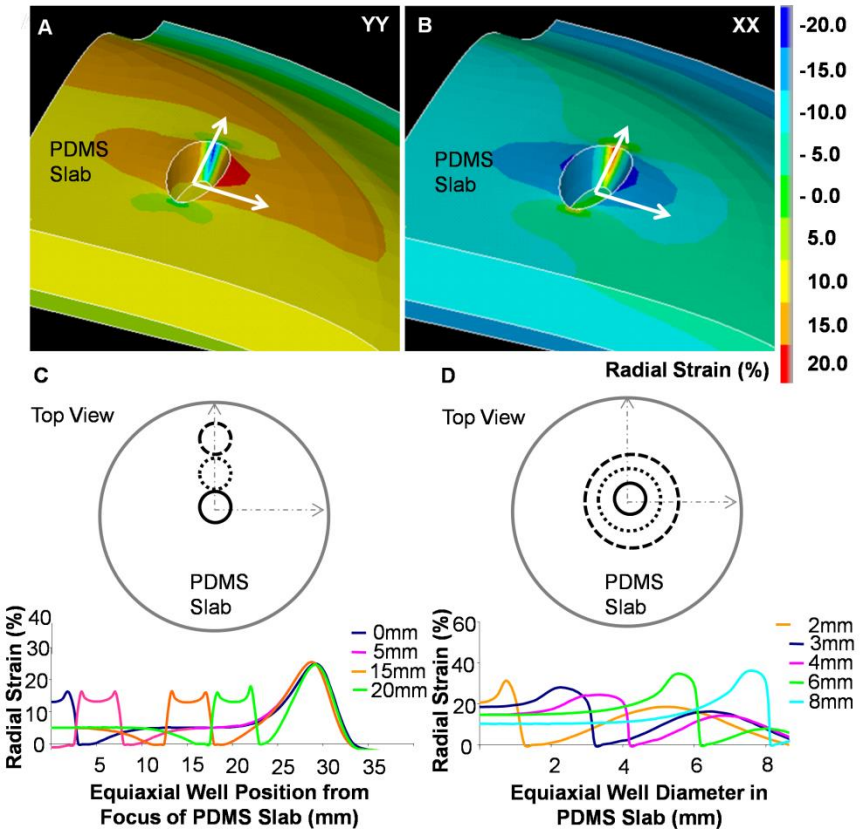

Figure 3.4 – Mechanically anchored and unanchored hydrogels regulate ACTA2 expression levels at 48 hours. Mechanically anchored hydrogels elevate ACTA2 and expression levels (2.87 fold ± 0.13) compared to unanchored hydrogels, while VIM expression is unchanged. Gene expression was measured via real-time PCR and normalized to 18S. Error bars show ±SD, n ≥ 6. Asterisks signify statistical differences according to a Student's t-test ($p \leq 0.05$).

We next compared our FEA simulations against measured strains of 3D tissues within different elliptical well geometries. Stretching a 1:1 axis ratio well to strains exceeding 25% ± 0.6% resulted in no significant differences between E_{xx} and E_{yy} (Figure 3.5A). Conversely, a 2:1 geometry created homogeneous biaxial strain fields of at least 20% ± 1.8% in the E_{xx} and 42% ± 2.1% in the E_{yy} directions, with negligible shear strain. The applied E_{xx}/E_{yy} strain ratio was consistently 2:1 regardless of applied strain magnitude or loading cycle (Figure 3.5B). Stretching 4:1 axis ratio gels introduced strains exceeding 9.1% ± 1.1% in the E_{xx} and 39% ± 1.2% in the E_{yy}, with a nearly consistent 4:1 magnitude ratio (Figure 3.5C). Experimental results confirmed FEA predicted nonlinear increases in applied biaxial strain magnitudes with stage

translation. For all gel ratios, shear strain E_{xy} varied between 0 ± 1.5% at the maximum loaded conditions and can be considered not statistically different from zero strain. We next determined the maximum stable strain magnitude as a function of frequency (Figure 3.5D). For equiaxial profiles, a maximum strain of 27%, 18%, 12%, 8%, and 5% was achieved at 1Hz, 2Hz, 3Hz, 4Hz, and 5Hz, respectively. Peak biaxial strain magnitudes in the YY direction were higher at each frequency, but proportional to the area strain during equiaxial loading. Collectively, these results establish and validate a unique and versatile high-throughput anisotropic biaxial strain bioreactor system for planar 3D tissue cultures.

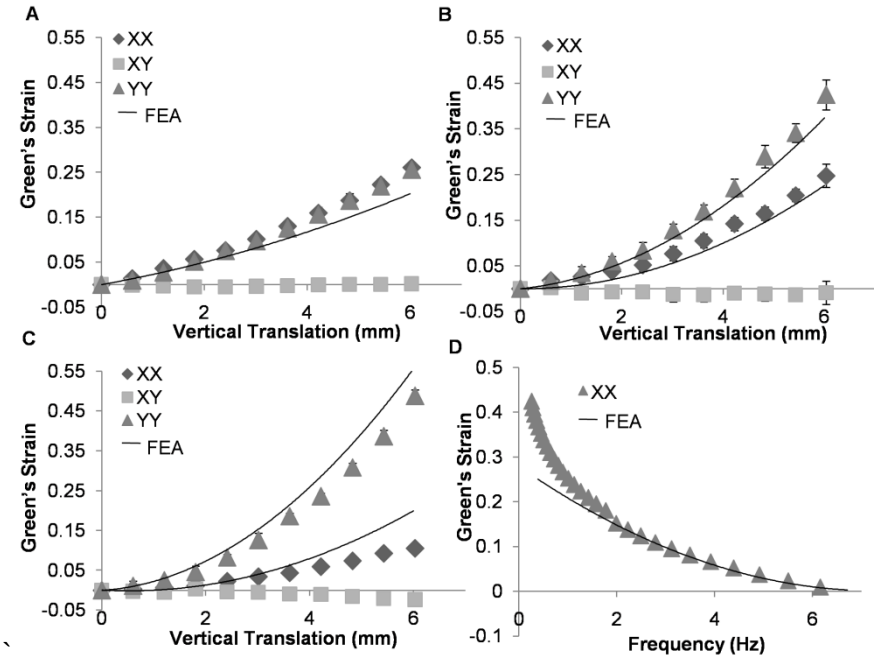

Figure 3.5 – Calibrated strain fields overlaid with FEA simulations. (A) 1:1 axis ratio circular well introduced an equiaxial strain field with minimal shear captured by FEA simulations. (B) 2:1 ellipsoidal well introduced a biaxial strain field captured by the FEA simulations. (C) 4:1 ellipsoidal well introduced a biaxial strain field that was slightly overestimated by the FEA simulations. (D) Strain vs. frequency curves for the 1:1 geometry indicates the ability to generate large deformations at high frequencies. Error bars show ± SD. N≥ 6 samples for each geometry and strain magnitude condition.

3.4.2: Biaxial Strain Anisotropy Regulates Cellular Apoptosis and Proliferation

VIC seeded 3D collagen hydrogel constructs were strained at 20% area strain, with varying biaxial anisotropies at 1Hz, and static cultures served as controls. To verify that our bioreactor was able to maintain viable cells for at least 96 hours, we performed a live/dead (green/red) assay on the hydrogel constructs. The percentage of live cells in the 1:1 (89% ± 1.3%) and 4:1 (86% ± 0.9%) geometries decreased with anisotropy compared to the percentage in anchored controls (91% ± 0.9%), but were consistently above 85% viability (Figure 3.6A-E). At 48 hrs, the number of apoptotic cells (yellow) in the 2:1 (8.5% ± 0.3%) and 4:1 (9.6% ± 0.5%) geometries increased relative to anchored controls (5% ± 0.2%) (Figure 3.6F-J). This result suggests that cell death is largely driven by strain induced apoptosis rather than bioreactor cytotoxicity. An increase in cell proliferation was also visually apparent for the mechanically stimulated conditions at 48 hrs. Using BrdU labeling, we found that with increasing biaxial anisotropy, the number of proliferative cells (green) in the 1:1 (26% ± 1.9%), 2:1 (34% ± 1.4%), and 4:1 (37% ± 1.1%) geometries statistically increased relative to anchored controls (16%, ± 1%) (Figure 3.6K-O). These findings suggest biaxial strain anisotropy enhances both cell proliferation and apoptosis, suggestive of an actively remodeling microenvironment.

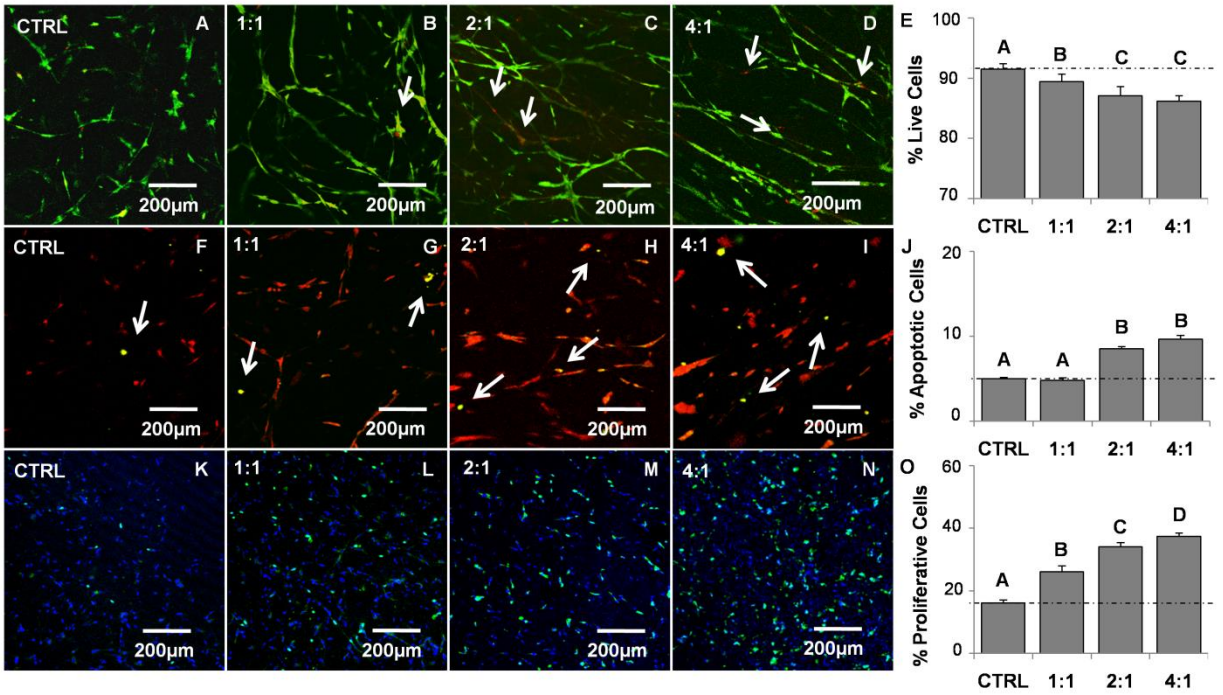

Figure 3.6 – Apoptosis and proliferation correlate with increasing biaxial anisotropy at 48hr. (A-D) Live/Dead assay reveals an increasing amount of dead cells with increasing biaxial anisotropy (live-green, dead-red). (E) Quantification of dead cells as a percentage of total cells. (F-I) Apo-BrdU assay reveals an increasing amount of apoptotic cells with increasing biaxial anisotropy (apoptotic-yellow, DNA-red). (J) Quantification of apoptotic cells as a percentage of total cells. (K-N) BrdU labeling assay reveals an increasing amount of proliferative cells with increasing biaxial anisotropy (proliferative-green, DNA-blue). (O) Quantification of proliferative cells as a percentage of total cells. Error bars show ± SE, N ≥ 6 samples per test condition. ANOVA with Tukey's post hoc testing determined statistical significance at p ≤ 0.05 thresholds. Bars that do not share letters are significantly different from each other.

3.4.3: Cell and Matrix Fibers Rapidly Reorient Orthogonally with Cyclic Strain Anisotropy

At 48 hours, significantly more f-actin labeled cells were found in cyclically stretched compared to the statically anchored controls, which partly reflects both increased matrix compaction and proliferation (Figure 3.7A-D). Static controls and 1:1 equiaxial strain revealed random orientations of cells denoted by the cytoskeletal (f-actin) filaments (Figure 3.7E-F). Normalized cell and matrix alignment index distribution curves indicate that orientation along the major X (0 degrees) and minor Y (90 degrees) axes was maintained throughout a 0.3-0.8 range (Figure 3.7M-N). In contrast, the 2:1 and 4:1 geometries revealed a cross hatched network of cells aligning along the major and minor axes with greater cross-alignment in the 4:1 geometry

(Figure 3.7G-H). Normalized alignment curves indicate that alignment along the major and minor axes ranged from 0.90-0.95 and 0.50-0.40, respectively, while the 45 degree orientation dropped to a lower fraction of 0.1-0.2 (Figure 3.7O-P). Second harmonic generation imaging of collagen fibrils showed a lack of fibril alignment regardless of strained condition (Figure 3.7I–L, M-P).

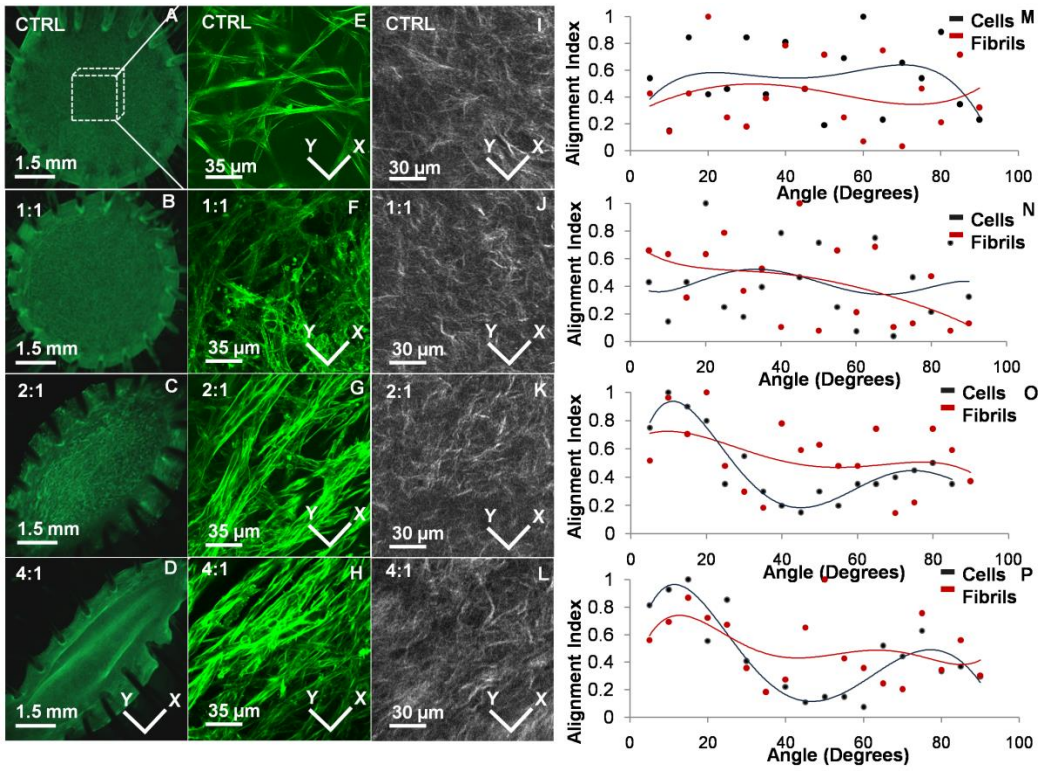

Figure 3.7 – Cell and matrix fibers rapidly reorient orthogonally with cyclic strain anisotropy at 48 hours. (A-D) Macroscopic view of collagen gels compacted within elliptical compression springs. (E-H) Orientation of AVIC associated with the anisotropic strain profiles (f-actin-green). (I-L) Orientation of collagen fibrils associated with anisotropic strain profiles (SHG imaging). (M-P) Representative alignment curves indicate orientation of VIC and coincide with respect to the principal directions of strain while minimal collagen fibril alignment has occurred.

At 96 hours, static controls and 1:1 cyclic equiaxial strain revealed random orientations of cells denoted by the cytoskeletal (f-actin) filaments (Figure 3.8A-B, E-F). Normalized cell and matrix

alignment index distribution curves indicate that orientation along the major X (0 degrees) and minor Y (90 degrees) axes was maintained throughout a 0.4-0.8 range (Figure 3.8M-N). In contrast, the 2:1 and 4:1 geometries revealed a cross hatched network of cells aligning along the major and minor axes with greater cross-alignment in the 4:1 geometry (Figure 3.8G-H). Normalized alignment curves indicate that alignment along the major and minor axes ranged from 0.85-0.95 and 0.55-0.35, respectively, while the 45 degree orientation dropped to a lower fraction of 0.1-0.2 (Figure 3.8O-P). Likewise, second harmonic generation imaging of collagen fibrils showed a similar trend such that increasing degrees of fibril alignment occurred with increasing anisotropic strain (Figure 3.8I–L, M-P). Taken together, VIC rapidly re-oriented within 48 hours of cyclic strain and maintained orientation through 96 hours. Extracellular matrix architecture, on the other hand, was poorly aligned at 48 hours regardless of the applied strain field as determined by SHG, suggesting that cell orientation precedes fiber alignment. Collectively, these results demonstrate that applied cyclic biaxial strain anisotropy drives rapid VIC cell orientation and matrix fiber alignment in a temporally regulated manner, with cell reorientation leading extracellular matrix remodeling.

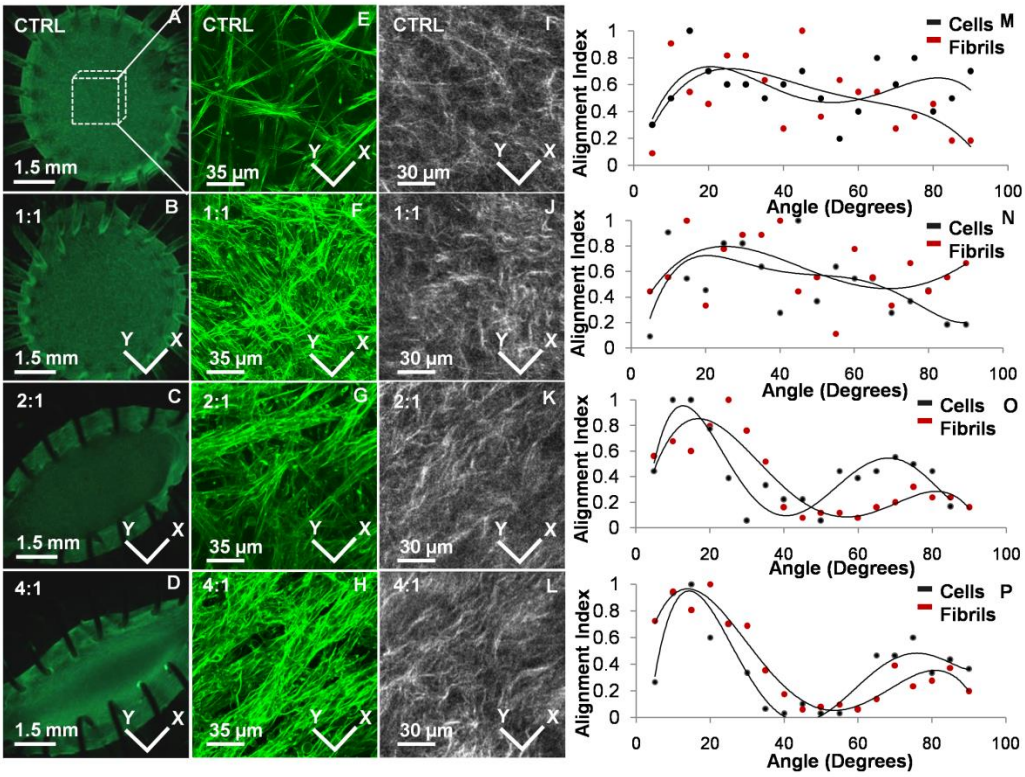

Figure 3.8 – Cell and matrix fibers rapidly reorient orthogonally with cyclic strain anisotropy at 96hr. (A-D) Macroscopic view of collagen gels compacted within elliptical compression springs. (E-H) Orientation of AVIC associated with the anisotropic strain profiles (f-actin-green). (I-L) Orientation of collagen fibrils associated with anisotropic strain profiles (SHG imaging). (M-P) Representative alignment curves indicate orientation of both VIC and collagen fibrils coincide and align with respect to the principal directions of strain. However, a larger degree cellular orientation and fiber alignment occurs perpendicular to the first principal strain direction (Y).

3.4.4: Valve Interstitial Cell Phenotype is Modulated by Biaxial Strain Anisotropy

Alpha-smooth muscle actin (ACTA2) is a key cytoskeletal filament involved in many myofibroblastic phenotype behaviors. Within unanchored 3D hydrogel cultures (free floating), VIC express low amounts of ACTA2. However, when cultured under anchored conditions (mechanically constrained), ACTA2 gene expression increased (2.87 ± 0.13 of control), indicating that tissue stress enhances myofibroblastic differentiation (Figure 3.9).

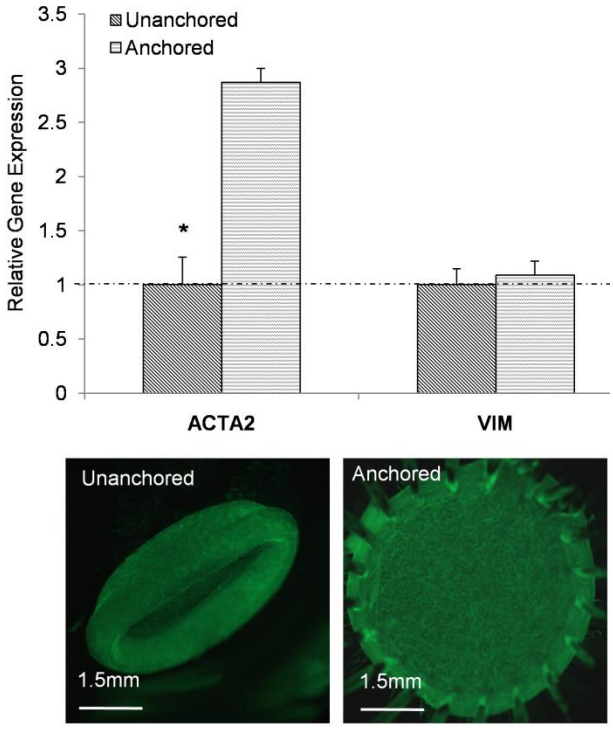

Figure 3.9 – Mechanically anchored and unanchored hydrogels regulate ACTA2 expression levels at 48 hours. Mechanically anchored hydrogels elevate ACTA2 and expression levels (2.87 fold ± 0.13) compared to unanchored hydrogels, while VIM expression is unchanged. Gene expression was measured via real-time PCR and normalized to 18S. Error bars show ±SD, n ≥ 6. Asterisks signify statistical differences according to a Student's t-test ($p \leq 0.05$).

After 48 hours of stretch at either the 1:1 or 2:1 geometries, ACTA2 gene expression was significantly downregulated with respect to anchored unstrained controls (expression 0.27-0.32 ± 0.05 fold of anchored control, no difference between). Stretch at the 4:1 geometry nearly doubled the amount of ACTA2 expression compared to equiaxial strain, but still less than half of the static anchored condition (0.47 ± 0.04 of control). Vimentin (VIM) expression was insensitive to unanchored vs. anchored conditions, but was significantly downregulated within the 1:1 or 2:1 geometries (0.62 ± 0.07 and 0.59 ± 0.13 respectively, no difference between). Stretch at the 4:1 geometry significantly increased VIM expression (1.13 ± 0.18 fold), recovering to control expression levels (Figure 3.10A). These same trends were confirmed at the protein level via immunofluorescence (Figure 3.9-F). ACTA2 protein was downregulated significantly under equiaxial strain (0.61 ± 0.07) and slightly increased with the 4:1 geometry (0.76 ± 0.05).

VIM was downregulated with equiaxial strain (0.76 ± 0.08) and then returned toward unstrained control levels with the 4:1 geometry (0.87 ± 0.06) (Figure 3.10G). Interestingly, a preponderance of cells oriented parallel to the gel major axis (thus perpendicular to the greater strain direction) expressed ACTA2 protein in the 4:1 geometry (Figure 3.10F). Together, this suggests that cyclic strain anisotropy independently contributes to VIC fibroblast-myofibroblast differentiation tendencies. Equibiaxial to mildly anisotropic stretch decreases ACTA2 and VIM gene and protein expression, while more dramatic strain anisotropy increases both ACTA2 and VIM expression.

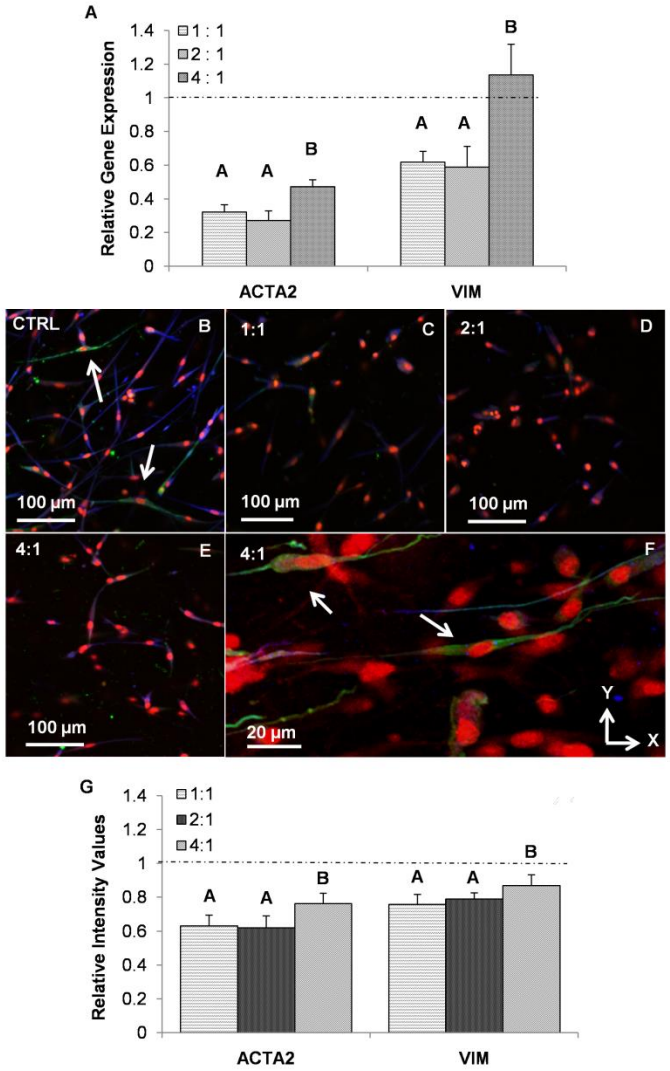

Figure 3.10 – Biaxial strain anisotropy modulates fibroblast cell phenotype at 48hr. (A) Gene expression was measured via real-time PCR, normalized to 18S, and expressed relative to unstretched anchored gel controls. ACTA2 gene expression decreased in all strain conditions, while VIM gene expression returned to control levels with 4:1 biaxial directionality. (B-F) ACTA2 (green) and VIM (blue) protein expression were measured via immunofluorescence with DNA (red) counterstain. (G) Quantification of total fluorescence was normalized to cell number and compared relative to unstretched control gels. (F) Although ACTA2 expression reduces with cyclic stretch, cells orienting perpendicular to the major axis of stretch expressed increased ACTA2 in the 4:1 geometry. Error bars show ± SD, N ≥ 6 samples per strain geometry and protein. Bars that do not share letters are significantly different from each other as determined by one-way ANOVA with Tukey's post hoc ($p \leq 0.05$).

3.5: Discussion

Anisotropic Strain in Vivo and in Vitro – Many planar connective tissues exhibit heterogeneous matrix fiber orientations that dictate anisotropic biomechanical properties which are critical for proper function. As an example, aortic heart valve cusps are very compliant in the radial direction but stiff in the circumferential direction, which greatly assists in efficient coaptation and rapid opening during the cardiac cycle. Simultaneous mechanical testing and collagen fiber distribution profiling demonstrates that anisotropic fiber splay and reorientation is a key contributor to physiological valve function [32, 33]. In altered loading environments, such as in hypertension or congenital malformation (e.g. bicuspid aortic valve), local cell and matrix architecture is modified with an increased risk of tissue degeneration [34] [35-37]. Greater understanding of how strain field anisotropy controls fibroblast cell phenotype and matrix remodeling has been challenging to study in vivo due to the confounding complexity of multiple interrelated biological signals and inherent tissue variability. Applying anisotropic strains within well-controlled 3D culture systems has been limited by 1) an inability to prescribe strain magnitudes in orthogonal directions independently, and 2) difficulties in anchoring 3D engineered tissues within bioreactors without compromising the homogeneity and consistency (over time) of the applied strain. Pneumatic actuator based elastomeric substrate deformation is commonly applied but rate-limited by the compressibility of air, rarely exceeding 1.5 Hz for physiological soft tissue strains. Alternatively, mechanical cams require constant adjustment and repeat calibration [20, 38]. Biaxial stretching of hydrogels was recently performed by molding hydrogel constructs in a cross pattern within a rotating cam [39]. However, the applied strain field was inhomogeneous and difficult to monitor over time. Furthermore, hydrogels can be adhered to elastomeric substrates via adhesive proteins, but the magnitudes of strain applicable are limited [22]. The design presented in this study overcomes these limitations by 1) prescribing strain anisotropy through eccentricity of the culture well geometry, and 2) providing uniform and stable construct attachment via compression springs. We were able to apply

homogeneous large deformation strain profiles (>30%) at high frequencies (3Hz) to engineered 3D tissues for at least 96 hours, significantly broadening the scope of 3D in vitro mechanobiological inquiry available.

Anisotropic Mechanoregulation of VIC Phenotype – Fibroblast transition between quiescent to activated myofibroblasts is controlled in part by the local mechanical environment. In the case of aortic valves, interstitial cells are largely quiescent fibroblasts in healthy tissue, but can become activated myofibroblasts and even osteoblasts in disease states [40-42]. Taylor et al. defines the quiescent valve fibroblast phenotype as one that maintains ECM composition and collagen maturity [43]. When VIC become activated myofibroblasts, they significantly upregulate contractile filaments including ACTA2, exhibit increased traction forces and migratory behavior, and secrete matrix proteins as well as their proteases and inhibitors. These factors all lead to dramatic changes in matrix composition and structural organization [40, 43]. Grinnell et al. and colleagues have used free floating (stress-free) and anchored (stressed) collagen hydrogels to show that matrix tension induces a myofibroblastic differentiation of fibroblasts from a variety of sources [6, 44, 45]. We previously found that VIC cultured in 2-D flasks expressed nearly double the amount of ACTA2 when compared to seeded within floating 3-D collagen gels, supporting this concept [24]. Similarly, we here find that mechanically anchored VIC in 3D culture expressed ACTA2 nearly 3 fold higher than unstressed controls **(Fig. S4)**. Taken together, these results suggest that VIC in anchored 3D collagen gels provide a simple positive-control model of myofibroblast like differentiation.

Fibroblast-myofibroblast transitions of VIC in the context of cyclic stretch, however, are more complex. Merryman et al. showed that cyclic uniaxial stretch of porcine aortic valve leaflets for 7-14 days produced a slight increase in ACTA2 gene expression, but a marked increase with exogenous TGFβ1 administration [46]. Thayer et al. found that increased ACTA2 expression

due to cyclic stretch could be relieved with combined loading with cyclic pressure [47]. Our findings here, using VIC in 3D hydrogel culture, show that ACTA2 expression is also independently regulated by the anisotropy of applied cyclic strain. Cyclic equiaxial strain decreases ACTA2 expression, suggesting fibroblast-like tendencies, but strong directional biaxial strain re-elevates ACTA2 toward the stressed myofibroblastic control condition. We further found that ACTA2 expression was directly related to the degree of cell alignment, which occurred perpendicular to the first principal axis of stretch. Vimentin, commonly employed as a marker for fibroblasts, is an intermediate filament expressed by mesenchymal cells and responsible for cytoskeletal integrity, but not expressed exclusively by fibroblasts [48]. We found vimentin expression changed similarly with ACTA2 under cyclic stretch, but there was no change between anchored and free-floating 3D gels, nor we did not notice a directionally dependent expression tendency like we did with ACTA2. Therefore, we are confident that vimentin was a reasonable choice as a fibroblast marker for this system, and focus our interpretations on ACTA2 and other behaviors.

Our results here demonstrate that the complete picture of fibroblast “quiescence” and “activation” should also include cell phenotype and turnover characteristics. Schnieder & Deck et al. used autoradiographic labeling in rats to demonstrate that normal cell and matrix turnover in a variety of fibroblast-populated tissues are not identical. In fact, valve leaflets exhibited naturally elevated proliferation, matrix synthesis, and degradation rates indicative of a continuous but homeostatic remodeling environment [7]. Considering that the native healthy valve contains relatively few myofibroblasts, this suggests that phenotype “quiescence” may still present dynamic matrix remodeling behavior. Our studies here suggest that one factor that can potentiate this is mechanical forces, specifically anisotropic cyclic stretch. Cyclic biaxial strain induced both VIC proliferation and apoptosis, suggesting a high degree of turnover, while equiaxial strain exhibited significantly less. Furthermore, equiaxial strain had very little effect on

matrix fiber reorganization, while cyclic anisotropic strain resulted in significantly aligned matrix fibers. Following this trend, equibiaxial stretch reduced ACTA2 expression, while anisotropic strain elevates it. Taken together, these results suggest that cyclic equiaxial strain promotes a tendency towards a quiescent fibroblastic phenotype, and increasing strain anisotropy supports a tendency towards an active myofibroblastic differentiation. We note that all these studies were performed at the same overall magnitude of area strain and frequency. While not the focus of this study, we believe that these responses are likely further altered by strain magnitude and frequency [49]. It appears that matrix remodeling lags changes in cell response to anisotropic strain, but the underlying cause is not yet known. Without live cells, however, no matrix fiber alignment occurs in any strain pattern (data not shown), suggesting that this remodeling is an active cell-mediated response to the applied strain field. Future studies considering altered matrix synthesis, degradation, or matrix fibril diameter, may help reveal the time dependent remodeling tendencies and clarify the extent of differentiation.

Accelerated Tissue Engineering via Strain Anisotropy - Modern tissue engineering approaches for load bearing tissues have sought to mimic or restore the native biological and biomechanical characteristics of replaced tissue, among them biomimetic material anisotropy [50]. Fiber reinforced scaffolds, whether electrospun, nonwoven, or woven mesh designs with biodegradable materials have been employed to create directionally dependent material behaviors [51]. Alternatively, biological polymers such as collagen and fibrin can be mechanically stimulated to evolve material heterogeneity [52, 53]. Whether this anisotropy needs to be included at the outset or evolved over time is still debated. Many bioreactors designed for whole tissues expose local regions to anisotropic strain fields, but these are difficult to quantify and challenging to relate directly to local cell differentiation and matrix remodeling [54]. Alternatively, anisotropic mechanical conditioning of 3D engineered tissue sheets could accelerate the formation of desired structural architecture and tissue biomechanics prior to

forming more complex tissue shapes [55]. Furthermore, our results suggest it may be possible to direct stem/progenitor cells towards multiple distinct phenotypes through strain anisotropy, which has a potential advantage in that these cells will also be self-organized in their environmental context. It is not yet known how cells in defined 3D matrix architectures interpret both time and directionally varying anisotropic strain fields, but our findings suggest that each component may contribute to accelerated matrix remodeling and cell differentiation.

In conclusion, we developed and implemented a novel bioreactor to investigate the relationship between anisotropic strain, cell differentiation, and matrix remodeling in 3D culture. Our findings demonstrate that applied cyclic biaxial strain anisotropy induces time dependent VIC orientation and collagen fiber alignment, which occurs at 48 hours and 96 hours, respectively. During this process, ACTA2 expression was directly related to the degree of cell alignment and occurred perpendicular to the principal axes of loading. These findings suggest biaxial strain anisotropy, independent of magnitude or frequency, is a potent regulator of rapid matrix reorganization and VIC phenotype. Controlling strain anisotropy in vivo or in vitro may be a potent means of directing adaptive tissue remodeling.

REFERENCES

1. Sacks, M.S., *Biaxial mechanical evaluation of planar biological materials.* Journal of Elasticity, 2000. **61**(1-3): p. 199-246.
2. Sacks, M.S., F.J. Schoen, and J.E. Mayer, *Bioengineering challenges for heart valve tissue engineering.* Annu Rev Biomed Eng, 2009. **11**: p. 289-313.
3. Sodian, R., et al., *Early in vivo experience with tissue-engineered trileaflet heart valves.* Circulation, 2000. **102**(19 Suppl 3): p. III22-9.
4. Rabkin-Aikawa, E., et al., *Clinical pulmonary autograft valves: pathologic evidence of adaptive remodeling in the aortic site.* J Thorac Cardiovasc Surg, 2004. **128**(4): p. 552-61.
5. Gabbiani, G., *The myofibroblast in wound healing and fibrocontractive diseases.* J Pathol, 2003. **200**(4): p. 500-3.
6. Grinnell, F., *Fibroblasts, myofibroblasts, and wound contraction.* J Cell Biol, 1994. **124**(4): p. 401-4.
7. Schneider, P.J. and J.D. Deck, *Tissue and cell renewal in the natural aortic valve of rats: an autoradiographic study.* Cardiovasc Res, 1981. **15**(4): p. 181-9.
8. Butcher, J.T., G.J. Mahler, and L.A. Hockaday, *Aortic valve disease and treatment: The need for naturally engineered solutions.* Adv Drug Deliv Rev, 2011.
9. Bell, E., B. Ivarsson, and C. Merrill, *Production of a tissue-like structure by contraction of collagen lattices by human fibroblasts of different proliferative potential in vitro.* Proc Natl Acad Sci U S A, 1979. **76**(3): p. 1274-8.
10. Grinnell, F. and C.H. Ho, *Transforming growth factor beta stimulates fibroblast-collagen matrix contraction by different mechanisms in mechanically loaded and unloaded matrices.* Exp Cell Res, 2002. **273**(2): p. 248-55.
11. Brown, T.D., *Techniques for mechanical stimulation of cells in vitro: a review.* J Biomech, 2000. **33**(1): p. 3-14.
12. Smith, P.G., et al., *Mechanical strain increases cell stiffness through cytoskeletal filament reorganization.* Am J Physiol Lung Cell Mol Physiol, 2003. **285**(2): p. L456-63.
13. Shyy, J.Y. and S. Chien, *Role of integrins in cellular responses to mechanical stress and adhesion.* Curr Opin Cell Biol, 1997. **9**(5): p. 707-13.
14. Wang, J.H., et al., *Mechanoregulation of gene expression in fibroblasts.* Gene, 2007. **391**(1-2): p. 1-15.
15. Lee, A.A., et al., *Differential responses of adult cardiac fibroblasts to in vitro biaxial strain patterns.* J Mol Cell Cardiol, 1999. **31**(10): p. 1833-43.
16. Culbertson, E.J., et al., *Loss of mechanical strain impairs abdominal wall fibroblast proliferation, orientation, and collagen contraction function.* Surgery, 2011. **150**(3): p. 410-7.
17. Ogden, R.W., *Nonlinear elasticity, anisotropy, material stability, and residual stresses in soft tissue.* CISM Courses and Lectures No. 441, ed. I.C.f.M. Sciences. 2003: Springer. 65-108.
18. Zaucha, M.T., et al., *A novel cylindrical biaxial computer-controlled bioreactor and biomechanical testing device for vascular tissue engineering.* Tissue Eng Part A, 2009. **15**(11): p. 3331-40.
19. Hornberger, T.A., et al., *Intracellular signaling specificity in response to uniaxial vs. multiaxial stretch: implications for mechanotransduction.* Am J Physiol Cell Physiol, 2005. **288**(1): p. C185-94.
20. Ku, C.H., et al., *Collagen synthesis by mesenchymal stem cells and aortic valve interstitial cells in response to mechanical stretch.* Cardiovasc Res, 2006. **71**(3): p. 548-56.

21. Tan, W., et al., *Development and evaluation of microdevices for studying anisotropic biaxial cyclic stretch on cells.* Biomed Microdevices, 2008. **10**(6): p. 869-82.
22. Butcher, J.T., B.C. Barrett, and R.M. Nerem, *Equibiaxial strain stimulates fibroblastic phenotype shift in smooth muscle cells in an engineered tissue model of the aortic wall.* Biomaterials, 2006. **27**(30): p. 5252-8.
23. Gupta, V. and K.J. Grande-Allen, *Effects of static and cyclic loading in regulating extracellular matrix synthesis by cardiovascular cells.* Cardiovasc Res, 2006. **72**(3): p. 375-83.
24. Butcher, J.T. and R.M. Nerem, *Porcine aortic valve interstitial cells in three-dimensional culture: comparison of phenotype with aortic smooth muscle cells.* J Heart Valve Dis, 2004. **13**(3): p. 478-85; discussion 485-6.
25. Stegemann, J.P. and R.M. Nerem, *Altered response of vascular smooth muscle cells to exogenous biochemical stimulation in two- and three-dimensional culture.* Exp Cell Res, 2003. **283**(2): p. 146-55.
26. Garvin, J., et al., *Novel system for engineering bioartificial tendons and application of mechanical load.* Tissue Engineering, 2003. **9**(5): p. 967-979.
27. YC, F., *A first course in continuum mechanics.* Englewood Cliffs, NJ, 1977. **Prentice Hall**.
28. Butcher, J.T., et al., *Unique morphology and focal adhesion development of valvular endothelial cells in static and fluid flow environments.* Arterioscler Thromb Vasc Biol, 2004. **24**(8): p. 1429-34.
29. Zipfel, W.R., R.M. Williams, and W.W. Webb, *Nonlinear magic: multiphoton microscopy in the biosciences.* Nat Biotechnol, 2003. **21**(11): p. 1369-77.
30. Nguyen, Q.T., P.S. Tsai, and D. Kleinfeld, *MPScope: a versatile software suite for multiphoton microscopy.* J Neurosci Methods, 2006. **156**(1-2): p. 351-9.
31. Bowles, R.D., et al., *Self-assembly of aligned tissue-engineered annulus fibrosus and intervertebral disc composite via collagen gel contraction.* Tissue Eng Part A, 2010. **16**(4): p. 1339-48.
32. Tower, T.T., M.R. Neidert, and R.T. Tranquillo, *Fiber alignment imaging during mechanical testing of soft tissues.* Ann Biomed Eng, 2002. **30**(10): p. 1221-33.
33. Sacks, M.S., D.B. Smith, and E.D. Hiester, *A small angle light scattering device for planar connective tissue microstructural analysis.* Ann Biomed Eng, 1997. **25**(4): p. 678-89.
34. Yap, C.H., et al., *Dynamic deformation characteristics of porcine aortic valve leaflet under normal and hypertensive conditions.* Am J Physiol Heart Circ Physiol, 2010. **298**(2): p. H395-405.
35. Sacks, M.S., W. David Merryman, and D.E. Schmidt, *On the biomechanics of heart valve function.* J Biomech, 2009. **42**(12): p. 1804-24.
36. Weinberg, E.J. and M.R. Kaazempur Mofrad, *A multiscale computational comparison of the bicuspid and tricuspid aortic valves in relation to calcific aortic stenosis.* J Biomech, 2008. **41**(16): p. 3482-7.
37. Robicsek, F., et al., *The congenitally bicuspid aortic valve: how does it function? Why does it fail?* Ann Thorac Surg, 2004. **77**(1): p. 177-85.
38. Banes, A.J., et al., *Culturing cells in a mechanically active environment.* Am Biotechnol Lab, 1990. **8**(7): p. 12-22.
39. Gupta, V., et al., *Synthesis of glycosaminoglycans in differently loaded regions of collagen gels seeded with valvular interstitial cells.* Tissue Eng, 2007. **13**(1): p. 41-9.
40. Rabkin-Aikawa, E., et al., *Dynamic and reversible changes of interstitial cell phenotype during remodeling of cardiac valves.* J Heart Valve Dis, 2004. **13**(5): p. 841-7.

41. Chen, J.H., et al., *Identification and characterization of aortic valve mesenchymal progenitor cells with robust osteogenic calcification potential.* Am J Pathol, 2009. **174**(3): p. 1109-19.
42. Liu, A.C., V.R. Joag, and A.I. Gotlieb, *The emerging role of valve interstitial cell phenotypes in regulating heart valve pathobiology.* Am J Pathol, 2007. **171**(5): p. 1407-18.
43. Taylor, P.M., et al., *The cardiac valve interstitial cell.* Int J Biochem Cell Biol, 2003. **35**(2): p. 113-8.
44. Grinnell, F., *Fibroblast-collagen-matrix contraction: growth-factor signalling and mechanical loading.* Trends Cell Biol, 2000. **10**(9): p. 362-5.
45. Grinnell, F., *Fibroblast biology in three-dimensional collagen matrices.* Trends in Cell Biology, 2003. **13**(5): p. 264-269.
46. Merryman, W.D., et al., *Synergistic effects of cyclic tension and transforming growth factor-beta1 on the aortic valve myofibroblast.* Cardiovasc Pathol, 2007. **16**(5): p. 268-76.
47. Thayer, P., et al., *The effects of combined cyclic stretch and pressure on the aortic valve interstitial cell phenotype.* Ann Biomed Eng, 2011. **39**(6): p. 1654-67.
48. Goldman, R.D., et al., *The function of intermediate filaments in cell shape and cytoskeletal integrity.* J Cell Biol, 1996. **134**(4): p. 971-83.
49. Arnoczky, S.P., et al., *Activation of stress-activated protein kinases (SAPK) in tendon cells following cyclic strain: the effects of strain frequency, strain magnitude, and cytosolic calcium.* J Orthop Res, 2002. **20**(5): p. 947-52.
50. Mendelson, K. and F.J. Schoen, *Heart valve tissue engineering: concepts, approaches, progress, and challenges.* Ann Biomed Eng, 2006. **34**(12): p. 1799-819.
51. Courtney, T., et al., *Design and analysis of tissue engineering scaffolds that mimic soft tissue mechanical anisotropy.* Biomaterials, 2006. **27**(19): p. 3631-8.
52. Mol, A., et al., *Fibrin as a cell carrier in cardiovascular tissue engineering applications.* Biomaterials, 2005. **26**(16): p. 3113-21.
53. Neidert, M.R. and R.T. Tranquillo, *Tissue-engineered valves with commissural alignment.* Tissue Eng, 2006. **12**(4): p. 891-903.
54. Vesely, I., *Heart valve tissue engineering.* Circ Res, 2005. **97**(8): p. 743-55.
55. L'Heureux, N., et al., *A completely biological tissue-engineered human blood vessel.* FASEB J, 1998. **12**(1): p. 47-56.

CHAPTER 4

RHOA AND RAC1 PLAY DISTINCT AND ESSENTIAL ROLES IN THE MECHANICAL REGULATION OF EMBRYONIC VALVE MORPHOGENESIS

4.1: Summary

Embryonic valves rapidly evolve from disorganized globular “cushions” to highly organized thin fibrous leaflets. These multi-scale interactions occur within a demanding hemodynamic environment and are essential to maintain unidirectional flow. The mechanisms by which mechanical forces direct cellular response to coordinate this cycle of morphogenesis and function are not known. In this study, we determined how mechanosensitive small GTPases RhoA and Rac1 coordinate atrioventricular valve (AV) differentiation and morphogenesis. RhoA activity is elevated during early cushion formation, but decreases considerably over development. In contrast, active Rac1 increases as cushions mature into valves. Using gain and loss of function assays, we determined that the RhoA-SRF pathway was essential for a myofibroblastic contractile phenotype in early cushion formation, but was surprisingly insufficient to drive matrix condensation during valve maturation. Interestingly, sustained cyclic stretch was a potent inhibitor of RhoA, and inactivation resulted in favor of Rac1 signaling. The Rac1-p38 pathway was necessary and sufficient to cause directed matrix condensation through cell polarization, leading to enhanced stress fiber alignment and adhesion necessary for valvular remodeling. Finally, we used partial atrial ligation experiments to show that altered cyclic mechanical loading *in vivo* augmented or restricted cushion growth directly through potentiation of RhoA and Rac1 activity. Together, these results demonstrate that mechanical signaling is essential to coordinate a transition from RhoA to Rac1 based signaling, to produce a thin organized leaflet with a quiescent phenotype.

4.2: Introduction

Congenital valve abnormalities affect 1-2% of all live births and predispose the tissue to early failure [1]. It is thought that the majority of valve defects occur during the maturation stage. Despite the significant public health and clinical burden posed by valve abnormalities, a basic understanding of the mechanisms orchestrating valve formation has to yet to be achieved. Valvulogenesis occurs under a continuous barrage of fluid shear stress and mechanical strain. The increasing hemodynamic loads and extension of the valves into the flow field suggests that these forces play a critical role [2]. Central to valve morphogenesis, embryonic globular "cushions" condense, and remodel into thin fibrous leaflets. This provides the necessary biomechanical structure for maintaining efficient unidirectional blood flow [3]. Interestingly, during this extensive remodeling process, residing progenitor valve cells are thought to evolve toward a quiescent phenotype [4]. While the importance of transitioning to a quiescent phenotype during development is still under investigation, numerous reports in adult diseased conditions have indicated that chronic myofibroblastic activation leads a thick and disorganized extracellular matrix (ECM) valve structure with inadequate biomechanical function [5, 6]. There is a substantial gap in understanding the phenotype transition with respect to ECM remodeling during development and the need is clear. Revealing the cellular mechanisms underlying this multi-scale process during development will shed light on the "normal" controlled process of valve maturation and function. This is may prove a necessity for developing regenerative strategies to combat dysfunctional tissue states, such as congenital defects or adult valve disease.

Hemodynamic loading within embryonic valve tissue can occur at the surface due to shear flow, or through internal constituents called tissue stretch (mechanical strain). Both forces are important during valve development, but the influence of each can change dramatically depending on the developmental stage. During early valve formation (HH25), the influence of

shear flow has been well established. For example, computational modeling using native tissue geometries and measured fluid velocities demonstrated that regions associated with early valve formation were among the highest for shear flows [7]. Likewise, in developing zebrafish, Vermot et al. found that reversing flows is important to initiate endocardial ring formation through activation of KLF2, necessary for normal valvulogenesis [8]. However, only at later stages (HH36, HH40, and beyond) does the valve primordia transition to a thin leaflet architecture capable of withstanding remarkable hemodynamic loads [3]. The fact that morphological change with increased transvalvular pressure suggest that resident valve cells are heavily influenced by cyclic mechanical strain [9]. The post-EMT valvular remodeling process has been difficult to understand because tissue strain cannot be as easily measured as shear flow. Likewise, resident cells reside within a 3D matrix, rather than a 2D substrate typically seen with endothelial layers.

Microsurgical experimental approaches have enabled the study of mechanical signaling in the post-EMT maturation process. Sedmera and colleagues employed partial left atrial ligation (LAL) to reduce ventricular preload in avian embryos [10]. They observed that this global hemodynamic change caused the AV valve primordia to remain thickened and not progress towards a thin fibrous leaflet [11]. Conversely, banding of the right atrium increased ventricular preload, and observations suggested an acceleration of valve condensation, though few details were reported [12]. The shared mechanisms responsible for accelerating or retarding valvular remodeling are not known, but strong candidates include the small GTPase proteins Rho and Rac. These proteins have been widely established as mechanosensitive, and are capable of regulating cellular differentiation and ECM remodeling through a spatial balance of expression [13]. Recent studies *in-vitro* has shown that the RhoA pathway is necessary for endocardial cell transformation, proliferation, and migration during cushion formation [14, 15]. Likewise, extracted cushions implanted within a pulsatile flow system were found to enhance fibrous ECM

accumulation and tissue stiffening through RhoA activation [16]. These results confirm the relationship between hemodynamics and small GTPase proteins, but to the extent are unknown.

The objective of this study was to understand how resident valvular interstitial cell (VIC) quiescence is achieved in conjunction with condensing and remodeling the ECM. Initial examination revealed a marked transition from RhoA to Rac1 dependent signaling during early to late cushion/valve morphogenesis (HH25, HH36, and HH40). Using in-vitro gain and loss of function assays, we determined that cyclic mechanical strain *in-vitro* inhibited myofibroblastic activation by decreasing RhoA-GTP levels, and in turn promoted the Rac1 signaling pathway. Elevated Rac1 activity resulted in strong cell polarization, stress fiber alignment, and adhesion, which is critical for enhanced matrix condensation. These effects were further confirmed *in-vivo* using ligation experiments to modulate side specific hemodynamic load. We found that specific alterations to hemodynamic inflow augmented either RhoA or Rac1 activity, which in turn retarded or accelerated valve morphogenesis.

4.3: Materials and Methods.

4.3.1: Avian Valve Cell Progenitor Isolation and Culture

AV cushions (HH25) or left AV leaflets (HH36 or HH40) were dissected from the myocardium of embryonic chick hearts and digested via trypsin (0.025%, Invitrogen) to obtain valve progenitor cells as previously described [17] and used directly in experiments (without passaging). Cells were pelleted via centrifugation and re-suspended within a neutralized collagen hydrogel (1.5 mg/mL) solution at a density of 400,000 cells/ml. Approximately 150 uL of gel was inoculated into culture wells, which solidified after 60 min. Cells were cultured in a base medium consisting of M199 (Invitrogen) supplemented with 5% chick serum (Hyclone), 250 mg/mL insulin, 25 ug/mL transferrin, and 250 ug/mL selenium (ITS; Sigma), and 1% penicillin/ streptomycin as previously established for valve mesenchyme [14].

4.3.2: Static and Cyclic Stress Experiments

A subset of collagen gels were formed around rings of compression springs as previously described [18], creating a mechanically anchored (MA) culture condition [19]. Alternatively, gels were released after 24 hours of culture so that the gel created a free floating culture condition (FF). Each resulted in either a mechanically stressed or stress-free condition during cell compaction, respectively [20, 21]. A custom designed bioreactor was implemented to apply cyclic stretch to aqueous hydrogels as previously described [18]. Gels were cultured around similar compression springs over a 24 hr period, after which 20% cyclic equiaxial strain (area strain) (225 step size, 2mm) was applied at 2.1Hz, which approximated in vivo embryonic valve cyclic strain profiles (STIM) [22]. Experiments were conducted at both short (<60 minutes) and longer (up to 48 hr) term intervals. In total three conditions were used, MA (static mechanically anchored stressed gels), FF (static stress free floating gels), and STIM (dynamic mechanically anchored strained gels).

4.3.3: RhoA/Rac1 Gain and Loss of Function Assays

To test the effect of specific activation or inhibition of RhoA or Rac1 in different environments, mesenchyme was electroporated with plasmids encoding for constitutively active RhoA (CA-RhoA, Q63L), CA-Rac1 (Q61L), dominant negative RhoA (DN-RhoA, T19N), or DN-Rac1 (T17N) using the Neon transfection system (Invitrogen, Carlsbad, CA) as previously described [23]. Cells were then embedded into collagen constructs and further cultured in 5% serum, antibiotic-free M199 for up to 48 hr after initial compaction. For inhibitor experiments, cells were embedded into collagen gels and cultured in 5% serum, 1% penicillin/streptomycin, and treated with small molecule inhibitors specific to p38 (SB203580, 10 uM, Cell Signaling), SRF (CCG-1423, 20 uM, Millipore), or ROCK (Y-27632, 10 μM, Cell Signaling) for up to 48 hr after initial compaction.

4.3.4: Measuring RhoA and Rac1 Activity

RhoA and Rac1 activity was measured using GLISA activation assay kits from Cytoskeleton according to the manufacturer's instructions. Cell extracts were added to 96-well plate coated with GST fusion of Rho binding domain. After incubation with shaking at 4°C for 30 minutes, the plate was washed 3 times with washing buffer (Cytoskeleton) before addition of antigen presenting buffer. The captured GTP-bound Rho GTPases were incubated with their corresponding anti-Rho GTPase antibodies. The GTPase-antibody conjugates were detected with horseradish peroxidase (HRP)–conjugated secondary antibody and quantified using an Epoch Microplate Spectrophotometer (Biotek).

.

4.3.5: Phenotype Assessment

Cell phenotype was assessed at both the gene and protein level (primers and proteins are included in the supplement). Briefly, gene expression was measured by extracting RNA using a Qiagen total RNA purification kit (Qiagen, Valencia, CA) and reverse transcribed to cDNA using

the SuperScript III RT-PCR kit with oligo(dT) primer (Invitrogen). Samples were amplified using the SYBR Green PCR system (Biorad, Hercules, CA) on a Biorad CFX96 cycler. For visualization of proteins, collagen constructs were fixed in 4% PFA overnight at 4C. Cells were incubated overnight with the appropriate primary/secondary antibodies, washed, and nuclear counterstained for subsequent confocal imaging. To quantify protein expression, cells were trypsinzed from the collagen constructs, fixed with 4% PFA for 10 min and then preserved in 50% methanol/PBS. Cells were further washed and incubated with appropriate primary/secondary antibodies and scanned using a Coulter Epics XL-MCL Flow Cytometer (Coulter). Adhesion testing and scratch methods are also included in the supplement.

4.3.6: In-Vivo Atrial Ligation Experiments

Fertilized White Leghorn chicken eggs were incubated in a 38°C forced-draft incubator to Hamburger-Hamilton (HH) stage 21 (3.5 days, Hamburger and Hamilton). The embryo was cultured in an ex-ovo platform previously described. Briefly, an overhand knot of 10–0 nylon suture loop was placed across either the right or left atrium and tightened, partially constricting the left or right AV orifice respectively. This diverted flow from the constricted inlet towards the untreated inlet, decreasing hemodynamic load on the one side and increasing it on the other [10, 12]. At D7 and D10, hearts and/or left AV valves were analyzed using RT-PCR, immunohistochemistry, and micro-ct.

Statistics. Statistical analysis was done using SAS and/or JMP software using a One-way or Two-way ANOVA w/ Tukey's Post Hoc. Sample size and significance are labeled within each figure legend.

4.4: Results

4.4.1: RhoA and Rac1 pathway expression patterns diverge in the AV valve region during morphogenesis. **Native** expression profiles in the developing left AV valve (HH25, HH36, and HH40) were evaluated using qPCR, ELISA, and immunofluorescence (whole mount) on freshly isolated tissue. We found that the relative gene and protein expression of alpha-smooth muscle actin (ACTA2), serum response factor (SRF), and active RhoA (RhoA-GTP) all decreased exponentially during development, while vimentin (VIM) remained unchanged. SRF nuclear localization was also found to significantly decrease as measured through co-localization with cell nuclei **(Figure 4.1A-C)**. Conversely, active Rac1 (Rac1-GTP) and β1 integrin expression significantly increased. Phospho-PAK1 expression, indicative of the active Rac1 pathway, was also elevated exclusively in later stage AV valves **(Figure 4.1D-F)**. These results support that RhoA activity dominates early AV cushion formation, but abates in favor of activated Rac1 during leaflet maturation. This divergence was concomitant with a transition from activated myofibroblast-like cushion mesenchyme in early AV cushions towards more quiescent fibroblasts in remodeled valves.

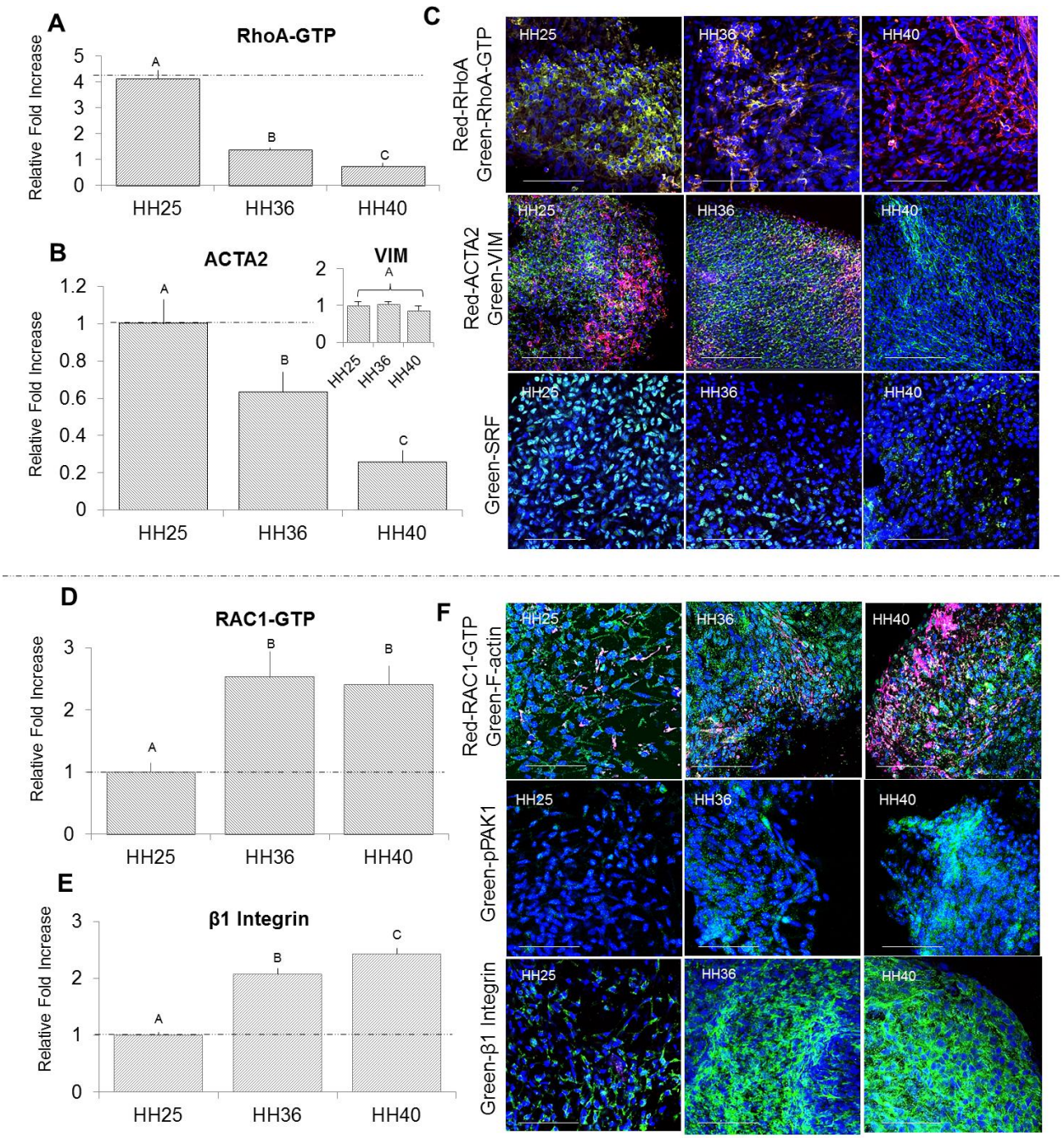

Figure 4.1 – Native expression profiles in the developing left AV valve reveal the divergence of RhoA and Rac1 pathways. (A) Protein expression of RhoA-GTP was quantified using GLISA and samples were normalized to total RhoA. (B) Gene expression of ACTA2 and Vimentin (inset) was quantified using real-time PCR. (C) Whole-mount immunofluorescence for RhoA-red, RhoA-GTP-green (top row), ACTA2-red, Vimentin-green (middle row), and SRF-green (bottom row). (D) Protein expression of Rac1-GTP was quantified using GLISA and samples were normalized to total protein. (E) Gene expression for β1 integrin was quantified using real-time PCR. (F) Whole-mount immunofluorescence for Rac1-GTP, F-actin-green (top row), phospho-Pak1-green (middle row), and β1 integrin-green (bottom row). All samples were counterstained for nuclei using Draq5-blue. Scale bars represent 100um (C,F). N≥ 8, One-way ANOVA w/ Tukey's Post Hoc. Different letters indicate statistical significance $P < 0.05$.

4.4.2: Matrix condensation capacity of AV valve mesenchyme increases during development. We isolated HH25, HH36, and HH40 left AV leaflets and optically measured thickness at the midpoint. We found that leaflets at later stages of maturation had a significant decrease in thickness (Figure 4.2A). This led us to believe that a decrease in leaflet thickness may be a function of the matrix condensation capacity in later stage valve cells. We then freshly isolated AV leaflets at HH25, HH36, and HH40 and embedded the valve progenitor cells into collagen hydrogels. After 24 hr, constructs were released and compaction area was measured during the next five days (Figure 4.2B). We found that matrix compaction was dependent on leaflet stage, and significantly increased during valve development (Figure 4.2C). Together, these results suggest that the decreased thickness of valve leaflets is due to the increased matrix condensation levels, as shown in later stage (HH36, HH40) valve cells.

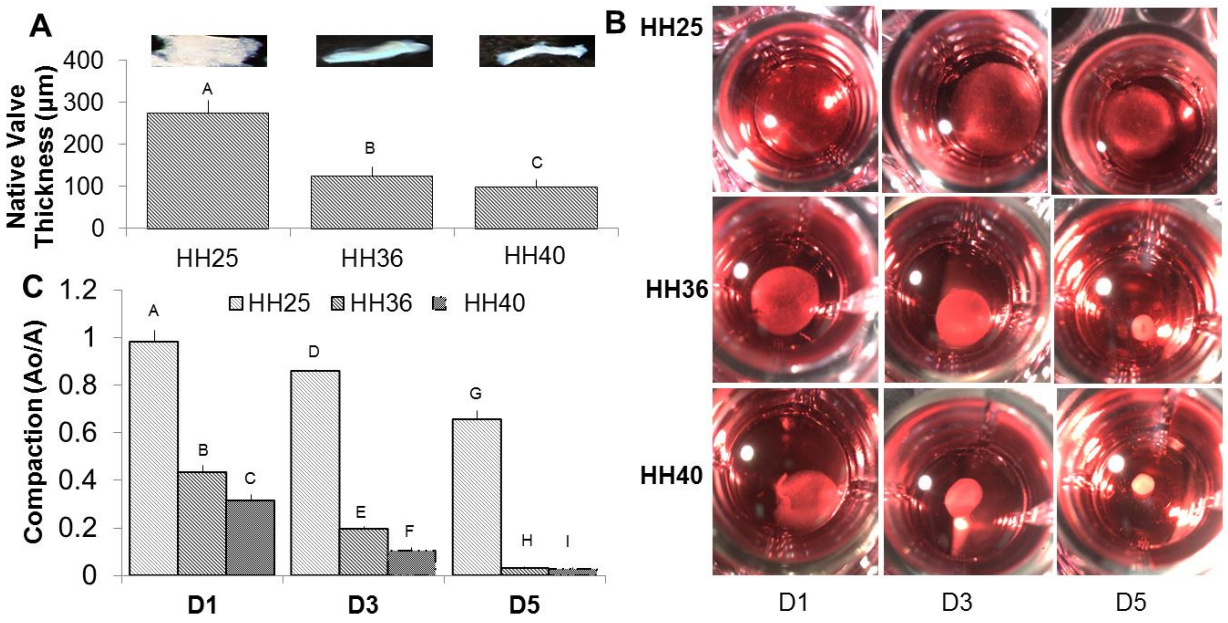

Figure 4.2 – Native embryonic left AV valve thickness decreases and correlates with matrix condensation potential. (A) Left AV valve tissue was isolated from H25, HH36, and HH40 avian embryos and thickness was determined by optical measurements. (B) AV progenitor cells were isolated and subjected to 3D collagen hydrogel compaction cultures. (C) Matrix condensation was quantified by measuring current area and normalized to initial area (A/Ao) during a 5 day period. Note the significance in compaction at later stages (HH36,HH40). N≥ 6, One-way ANOVA w/ Tukey's Post Hoc. Different letters indicate statistical significance $P < 0.05$.

4.4.3: ECM content increases in collagen/GAG ratio and valve becomes highly organized during AV valve development. HH25 mitral cushions contained equal proportions of collagens and glycosaminoglycans (GAGs), with more collagen located near the annular attachment region. At HH36, mitral leaflets were significantly more compacted at both the annular attachment and mid-zone regions. At HH40, mitral leaflets became even thinner and more organized in cross-section. The GAG/collagen architecture was starting to establish the tri-laminar structure typically found in post-natal mitral valves. The fractional ratio of collagen to GAG was quantified and increased significantly at all stages during development (Figure S4.1).

4.4.4: Myofibroblastic activation is mitigated by cyclic mechanical stretch in AV progenitor cells. Because RhoA has been previously shown to be a mechanosenstive protein, we speculated that a relationship might exist between mechanical stretch and RhoA [13, 16]. We freshly isolated HH40 leaflets, and embedded the progenitor cells into our previously described 3D bioreactors. Mechanically anchored (MA) and free-floating (FF) gels were also seeded. These control conditions are indicative of positive and negative controls for myofibroblastic activation, respectively (Figure 4.3A) [18, 21, 24]. Cells were stimulated at 20% area strain, at 2.1hz, for up to 48 hr. Gene expression of ACTA2 and SRF decreased after 12 hr, and was not significantly different from free-floating gels at 24, 48 hr (Figure 4.3B). At 48 hr, we confirmed these results using flow cytometry (Figure 4.3C).

To assess the dynamics of RhoA during mechanical strain, we performed a time dependent assay using GLISA to determine RhoA activity. STIM RhoA-GTP levels increased initially (0-3 hr), and then decreased to CTRL-FF levels thereafter, when compared to CTRL-MA gels (Figure 4.3D). Additionally we found a strong correlation between RhoA-GTP and matrix tension within the CTRL-MA gels by measuring compaction force using micro spring

transducers (Figure S4.2). These findings were confirmed via immunofluorescence at the 48 hr time-point. We also showed that SRF nuclear localization was mitigated by mechanical stretch (Figure 4.3E). Together, these results indicate that sustained cyclic stretch is a potent inhibitor of myofibroblastic activation, and RhoA-GTP levels correlate with underlying cell-matrix tension.

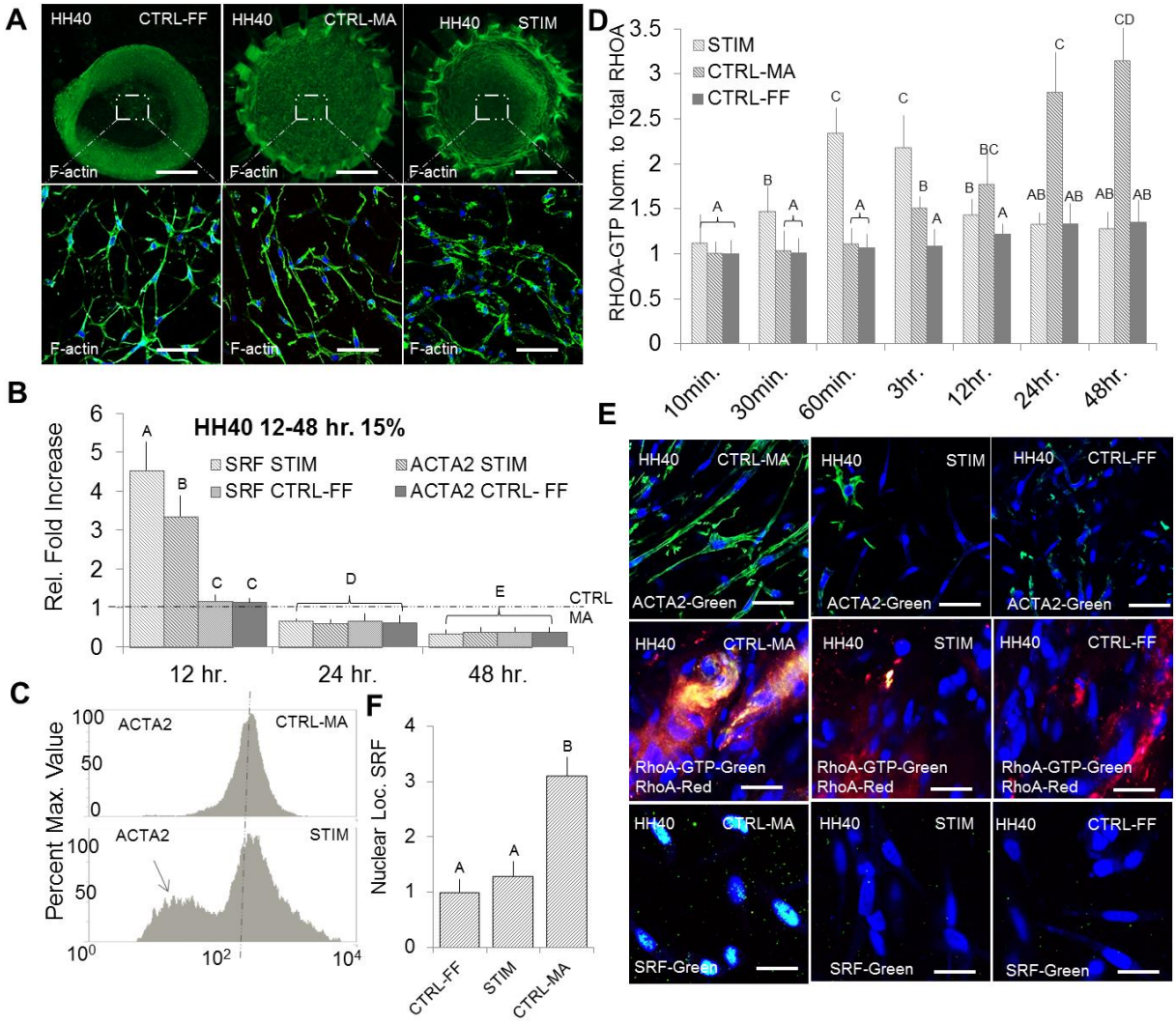

Figure 4.3 – Mechanical stretch mitigates myofibroblastic activation in HH40 AV progenitor cells. (A) Cells were isolated from left AV valve tissue and seeded into our previously described bioreactor. Free floating (FF-liberated after 24 hr) and mechanically anchored (MA-confined compaction) gels were used as control conditions. Cells were allowed to compact for 24 hr and stimulated at 20% area strain at 2.1hz (average frequency during development) in a time dependent manner (STIM). (B) After mechanical stretch, gene expression for SRF and ACTA2 was measured using real-time PCR at 12, 24, and 48 hr. (C) Flow cytometry was used to quantify the protein expression of ACTA2 between MA-CTRL and STIM conditions. (D) Dynamic protein expression of RhoA-GTP was quantified using GLISA for MA-CTRL, FF-

CTRL, and STIM conditions. (E) Immunofluorescence for ACTA2-green (top row), RhoA-GTP-green, RhoA-Red (middle row), and SRF-green (bottom row) was conducted on fixed collagen constructs at 48 hr for CTRL-MA, CTRL-FF, and STIM conditions. (F) Nuclear localization of SRF was quantified using metamorph co-localization software. All samples were counterstained for nuclei using Draq5-blue. Scale bars represent 50um (A) and 20um (E) . N≥ 6, One-way ANOVA w/ Tukey's Post Hoc. Different letters indicate statistical significance $P < 0.05$.

We next determined the role of mechanical stretch on myofibroblastic activation for different stages of development. We found that mechanical strain decreased SRF and ACTA2 expression at both the gene and protein levels in a stage-dependent manner. Together, these results indicate that mechanical stretch regulates cell quiescence in AV leaflets, especially at later stages of valve development. Lastly, because nuclear localization of SRF expression directly correlated with ACTA2 expression, and is a known regulator of the ACTA2 gene, we speculated that SRF was necessary to promote ACTA2 expression [25]. Using MA-CTRL conditions, the SRF pathway was inhibited by supplementing with a SRF pathway inhibitor (CCG-1423). Inhibition of the SRF pathway at 48 hr resulted in a quiescent phenotype at both the gene and protein level (Figure S4.3).

4.4.5: ACTA2 and SRF expression are directly controlled by RhoA Activity. To determine the relationship between RhoA and myofibroblastic activation, we performed gain- and loss-of-function experiments using CA- and DN-RhoA (Figure S4.4). Using FF gels (indicative of quiescent phenotype), transfection with CA-RhoA was found to increase myofibroblastic activity comparable to CTRL-MA gels, as shown through increased ACTA2, SRF, and CyclinB2 (proliferation marker) expression (Figure 4.4A,C). Conversely, using MA gels (indicative of myofibroblastic phenotype), transfection with DN-RhoA was found to inhibit myofibroblastic activity comparable to CTRL-FF gels, as shown through decreased ACTA2, SRF, and CyclinB2 expression at 48 hr (Figure 4.4B,D).

Additionally, we directly perturbed the role of RhoA during simulated conditions. Because mechanical stimulation was found to inhibit myofibroblastic activation, we hypothesized that elevated RhoA activity would block the effects in strained cells. We thus transfected HH40 AV mesenchyme with CA-RhoA and even after mechanical stimulation, myofibroblastic activation was non-significant from CTRL-MA gels at 48 hr (Figure 4.4E,F). Together, these results confirm the role of RhoA in regulating myofibroblastic activation through increased tension (stress-build up), while sustained cyclic mechanical strain inhibits this process.

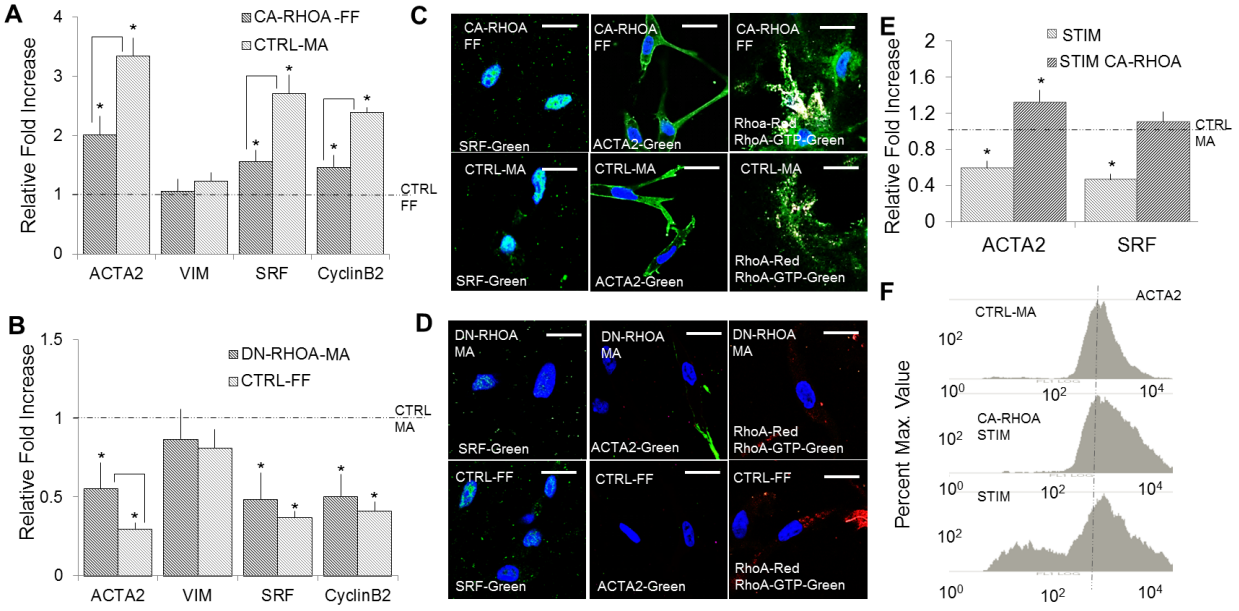

Figure 4.4 – Myofibroblastic activation in HH40 AV progenitor cells is dependent on RhoA activity. (A-B) Gene expression of ACTA2, VIM, SRF, and CyclinB2 were quantified using RT-PCR and compared to CTRL-MA or CTRL-FF conditions. Note the similarity between CA-RhoA-FF and CTRL-MA vs. DN-RhoA-MA and CTRL-FF. (C-D) Visualization of SRF-green (left column), ACTA2-green (middle column), RhoA-GTP-green, and RhoA-Red (right column) by immunofluorescence on the fixed collagen constructs. (E) Transfected CA-RhoA cells were stretched for 48 hr at 2.1hz. Gene expression of ACTA2 and SRF was quantified using RT-PCR. Flow cytometry quantified ACTA2 expression in MA-CTRL, STIM, and CA-RhoA-STIM conditions (10000 cells). All samples were counterstained for nuclei using Draq5-blue. Scale bars represent 10um (C-D). N≥ 8, Two-way ANOVA w/ Tukey's Post Hoc. Different letters indicate statistical significance P <0 .05.

4.4.6: Rac1-p38 pathway drives matrix condensation in AV valve progenitor cells. We next sought to determine whether RhoA or Rac1 was important for mediating cushion matrix condensation at 48 hr. We determined that RhoA activity (via CA-RhoA or DN-RhoA transfection, respectively) resulted in no significant change in compaction potential as compared to control conditions (Figure 4.5A). However, elevated Rac1 activity (via CA-Rac1 transfection) dramatically enhanced compaction, while suppressed Rac1 activity (via DN-Rac1 transfection) inhibited this process. Interestingly, the combination of CA-Rac1 with DN-RhoA inhibited compaction similar to controls, suggesting that basal levels of RhoA activity are still required for matrix condensation to proceed (Figure 4.5B). CA-Rac1 combined with p38 MAP kinase inhibition (via SB203580) significantly reduced compaction levels similar to control (Figure 4.5C). These results together determine that matrix condensation by AV cushion mesenchyme is dominated via the Rac1-p38 pathway.

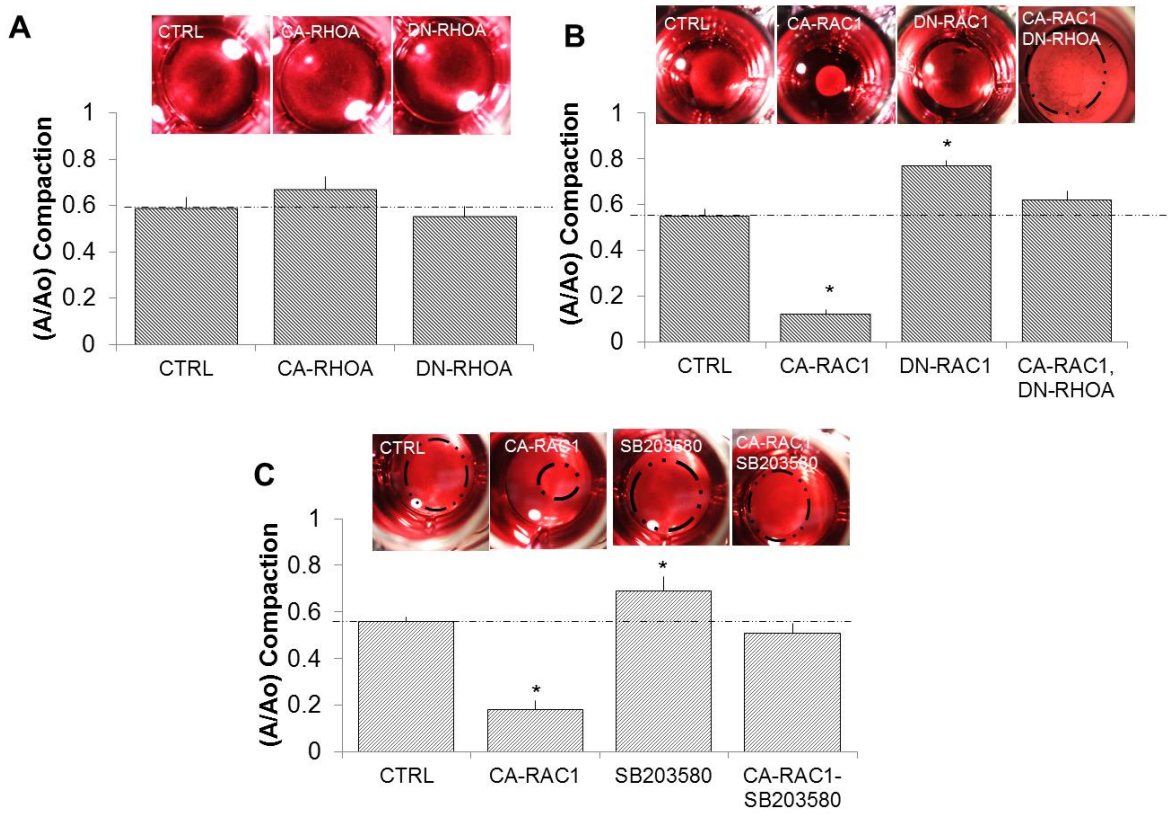

Figure 4.5 – Compaction potential of HH40 AV progenitor cells is dependent upon Rac1 via p38. (A-C) HH40 cells were isolated from left AV valve tissue and immediately transfected with CA-RhoA, DN-RhoA, CA-Rac1, DN-Rac1 (Neon Transfection system) and/or chemical inhibitors. Cells were then embedded into collagen hydrogels and allowed to compact for 24 hr. Hydrogel compaction was measured by current area over initial area (A/Ao), and determined at the end of 48 hr. N≥ 6, One-way ANOVA w/ Tukey's Post Hoc. Asterisks indicate statistical significance at $P < 0.05$.

4.4.7: Rac1 promotes matrix condensation through increased adhesion and polarity, but independent of myofibroblast behavior. To determine the mechanism through which Rac1 enhances matrix condensation, we performed gain and loss of function experiments using CA- and DN- mutants of Rac1. CA-Rac1 was found to increase myofibroblastic activity and integrin expression as measured through increased ACTA2, SRF, and β1 integrin gene expression in MA conditions (Figure 4.6A,C). Conversely, DN-Rac1 had no effect on myofibroblastic activation, but significantly decreased β1 integrin gene expression in FF conditions at 48 hr (Figure 4.6B). This indicates that Rac1 drives integrin expression independent of static mechanical tension. To test whether increased integrin expression effected adhesion, cells

were seeded in well plates and exposed to an orbital shaker at >500rpm for 15 seconds at intervals of 30 min. CA-Rac1 was found to increase the percentage of adherent cells in a time dependent manner compared to control, while DN-Rac1 had the opposite effect (Figure 4.6D,E). We next quantified a number of subcellular macromolecules that mediates the regulatory effects of cell anchorage on ECM adhesion. After 24 hr, transfection with CA-Rac1 increased the number of focal complexes at the leading edge of lamellipodium by measuring co-localization intensity of vinculin and F-actin along the periphery. Moreover, the distribution angle of F-actin and subsequent stress fibers was highly aligned indicating a polarized cell. DN-Rac1 had the opposite effect (Figure 4.6F,G). Lastly, CA-Rac1 resulted in a decreased migration potential as shown through a scratch assay (Figure S4.5). These results indicate that Rac1 increases both the number of integrin binding sites and focal complexes leading to enhanced cell polarity and adhesion, but reduced cell migration.

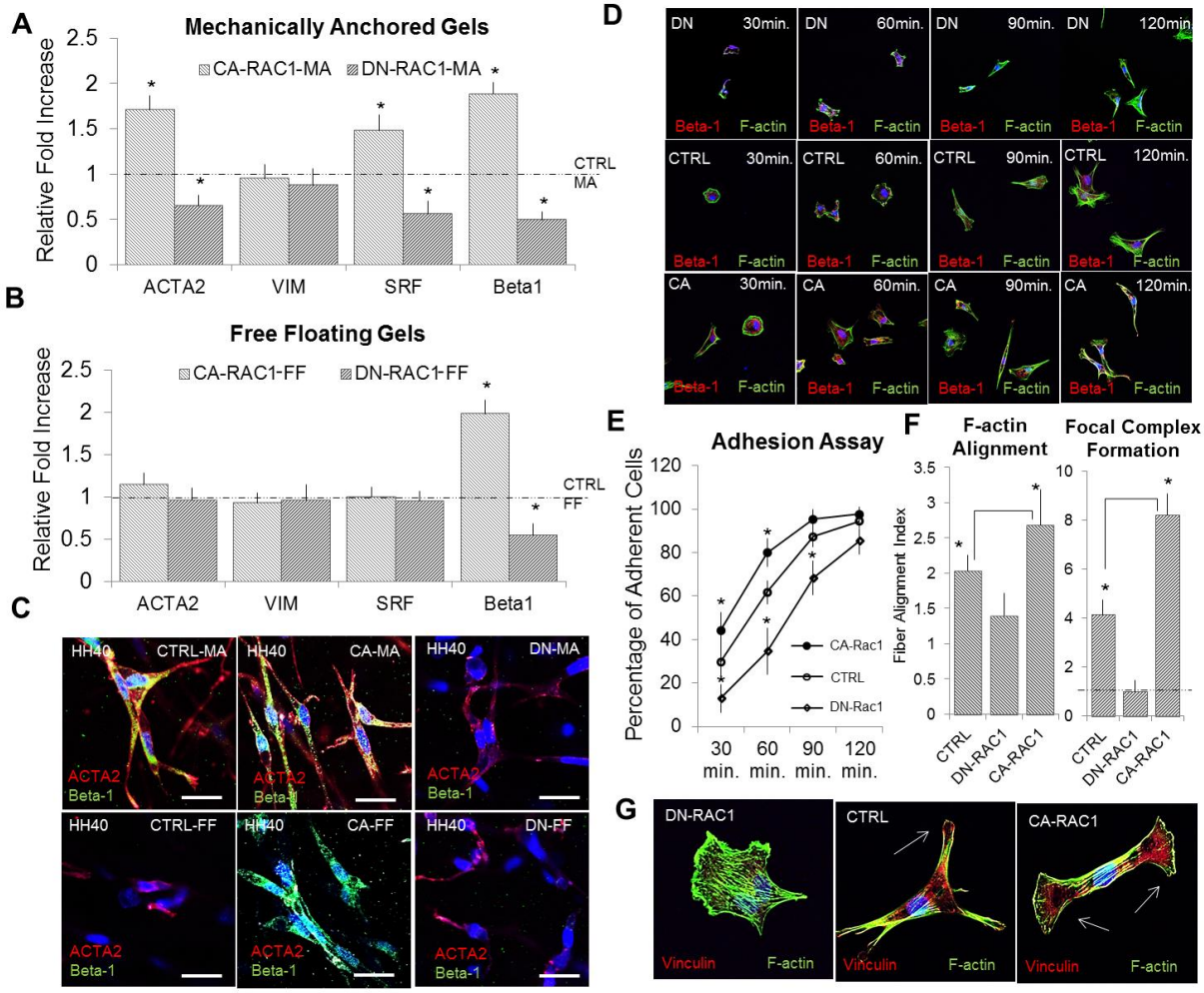

Figure 4.6 – Rac1 promotes matrix condensation through increased adhesion and polarity, but independent of myofibroblast behavior in HH40 AV progenitor cells. (A-B) Gene expression for ACTA2, Vim, SRF, and β1 integrin was quantified using RT-PCR in both CTRL-MA and CTRL-FF conditions (note myofibroblastic activation is dependent upon MA conditions). (C) Immunofluorescence for ACTA2-red and β1 integrin-green of the control (left column), CA-Rac1 (middle column), and DN-Rac1 conditions (right column row) on the fixed collagen constructs. (D) An adhesion test was performed on tissue culture plastic and the extent of spreading was visualized through immunofluorescence for β1 integrin-red and F-actin-green of DN-Rac1 (top row), control (middle row), and CA-Rac1 conditions (bottom row). (E) The percentage of adherent cells was quantified at each time interval after application of the orbital shaker. (F) At 24 hr, the extent of F-actin alignment and focal complexes were quantified for each condition. (G) Focal complexes and F-actin alignment were visualized using immunofluorescence (note the distribution angle of F-actin and subsequent stress fibers alignment within CA-Rac1). All samples were counterstained for nuclei using Draq5-blue. Scale bars represent 20um. N≥ 6, One-way ANOVA w/ Tukey's Post Hoc. Asterisks indicate statistical significance at $P < 0.05$.

4.4.8: In vivo perturbation of AV valve mechanical environment confirms the divergent roles of RhoA and Rac1 in valvular morphogenesis. To determine the importance of sustained mechanical loading on valvulogenesis *in-vivo*, we performed partial atrial ligation experiments on ex-ovo cultured chick embryos [10, 12]. Left atrial ligation (LAL) shunted hemodynamic flow into the right side of the AV canal, while right atrial ligation (RAL) diverted hemodynamic flow into the left side of the AV canal (Figure 4.7A). As a result of the altered hemodynamic loading, LAL had reduced collagen along the attachment zone, and extensive GAGs were present throughout the leaflet with a noticeable reduction in the fibrosa layer. Conversely, the RAL had increased collagen along the attachment zone and throughout the midzone of the leaflets. The collagen to GAG fractional ratio in the RAL was significantly more than the LAL, and normal leaflets suggesting a more mature leaflet in the RAL conditions (Figure S4.6). Using micro-CT, the functional consequence of these procedures was found to alter both leaflet size and left ventricular volume. RAL were found to have significantly increased leaflet area and left-ventricular volume as compared to control. Conversely, LAL had significantly decreased leaflet area and left-ventricular volume as compared to control (Figure 4.7B). Together, LAL procedures resulted in a significantly underdeveloped valve, with reduced functional characteristics. RAL had the opposite effect.

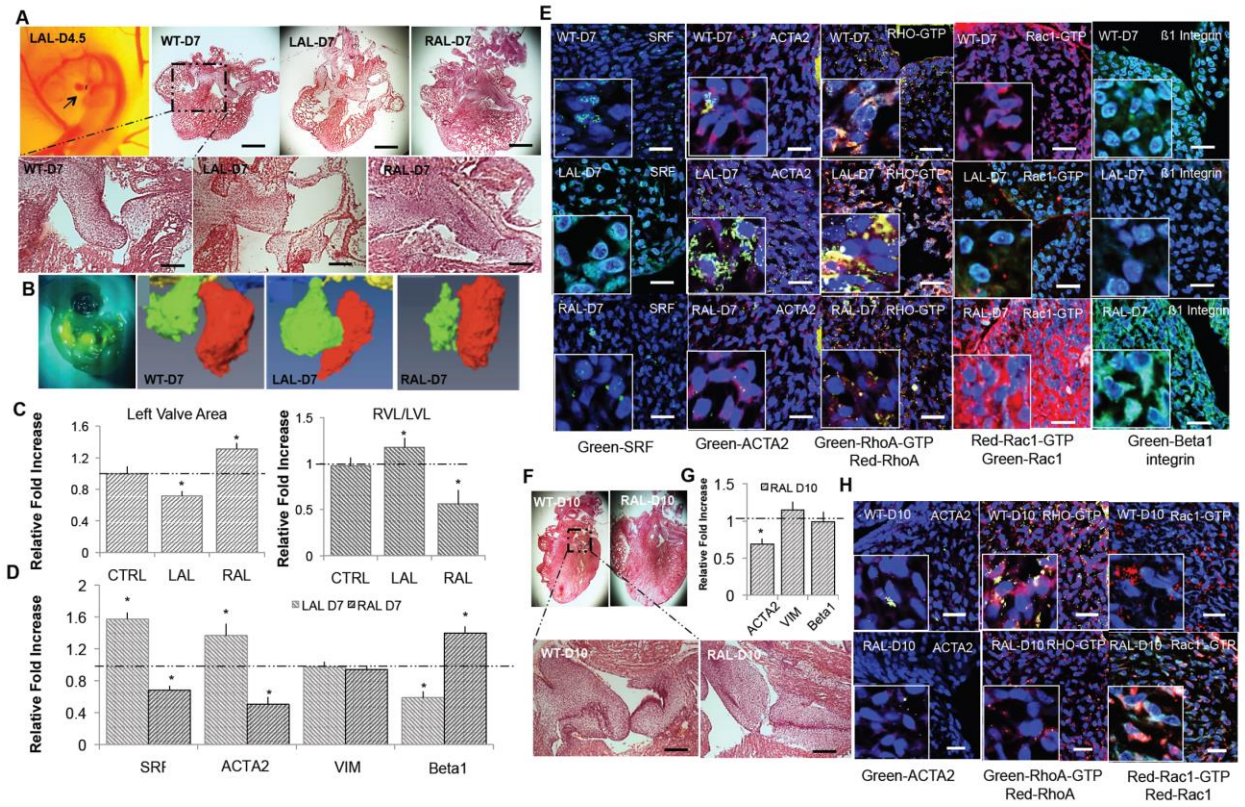

Figure 4.7 – Hemodynamic perturbation in-vivo confirms divergence of RhoA/Rac1 pathways during AV valve development. (A) Atriums of the heart were ligated using suture material between 4-5 days. Micro-CT was used to measure both the change in size of ventricular chambers, but also left AV valve geometry (ultrasound also confirmed a significant decrease in time averaged velocity and cardiac output) at D7. H&E histology stain of the heart and left AV valve structures for the control, LAL, and RAL conditions. (B) Real-time PCR for SRF, ACTA2, VIM, and β1 integrin gene expression at D7. (E) Immunohistochemistry for SRF, ACTA2, RhoA-GTP, Rac1-GTP, and β1 integrin of resident valve cells at D7 of wild-type (top row), left atrial ligation (middle row), and right atrial ligation conditions (bottom row). (F) RALs (right atrial ligation) at D10 were analyzed. H&E histology was conducted on both the left AV valve and ventricular chamber structures. (G) Real-time PCR for ACTA2, VIM, and β1 integrin gene expression at D10. (H) Immunohistochemistry staining of ACTA2, RhoA-GTP, and Rac1-GTP in resident valve cells for wild-type (top row), left atrial ligation (middle row), and right atrial ligation conditions (bottom row). All samples were counterstained for nuclei using Draq5-blue. Scale bars represent 300um (A,F) and 40um (E,H). N≥ 8, One-way ANOVA w/ Tukey's Post Hoc. Asterisks indicate statistical significance at $P < 0.05$.

As anticipated, reduced hemodynamic load in the LAL was found to enhance myofibroblastic activation in the left AV valve mesenchyme. ACTA2 and SRF gene expression was significantly elevated compared to sham controls, while RAL had the opposite effect at D7 (Figure 4.7C,D). β1 integrin gene expression also increased in the RAL conditions. Using immunohistochemistry, nuclear localization of SRF and increased RhoA-GTP activity was

clearly evident in the left AV valve of LAL treated embryos, while Rac1-GTP activity was decreased relative to sham controls. Conversely, RAL treat embryos resulted in a loss of SRF nuclear localization and decreased Rho-GTP activity, while Rac1-GTP activity was significantly elevated (Figure 4.7E). We further analyzed D10 embryos within the RAL conditions (LAL have significant lethality at D8 as previously reported [10]) to assess late stage morphogenesis (Figure 4.7F). ACTA2 expression and SRF nuclear localization significantly decreased and correlated with RhoA-GTP activity, while Rac1-GTP activity increased (Figure 4.7G,H). Furthermore, the left AV valve in the RAL treated embryos had increased in collagen/GAG content relative to sham controls. Together, these results confirm the importance of RhoA and Rac1 activity in regulating proper cell phenotype and valve morphogenesis through mechanical load. We summarized our results as illustrated in the cartoon (Figure 4.8).

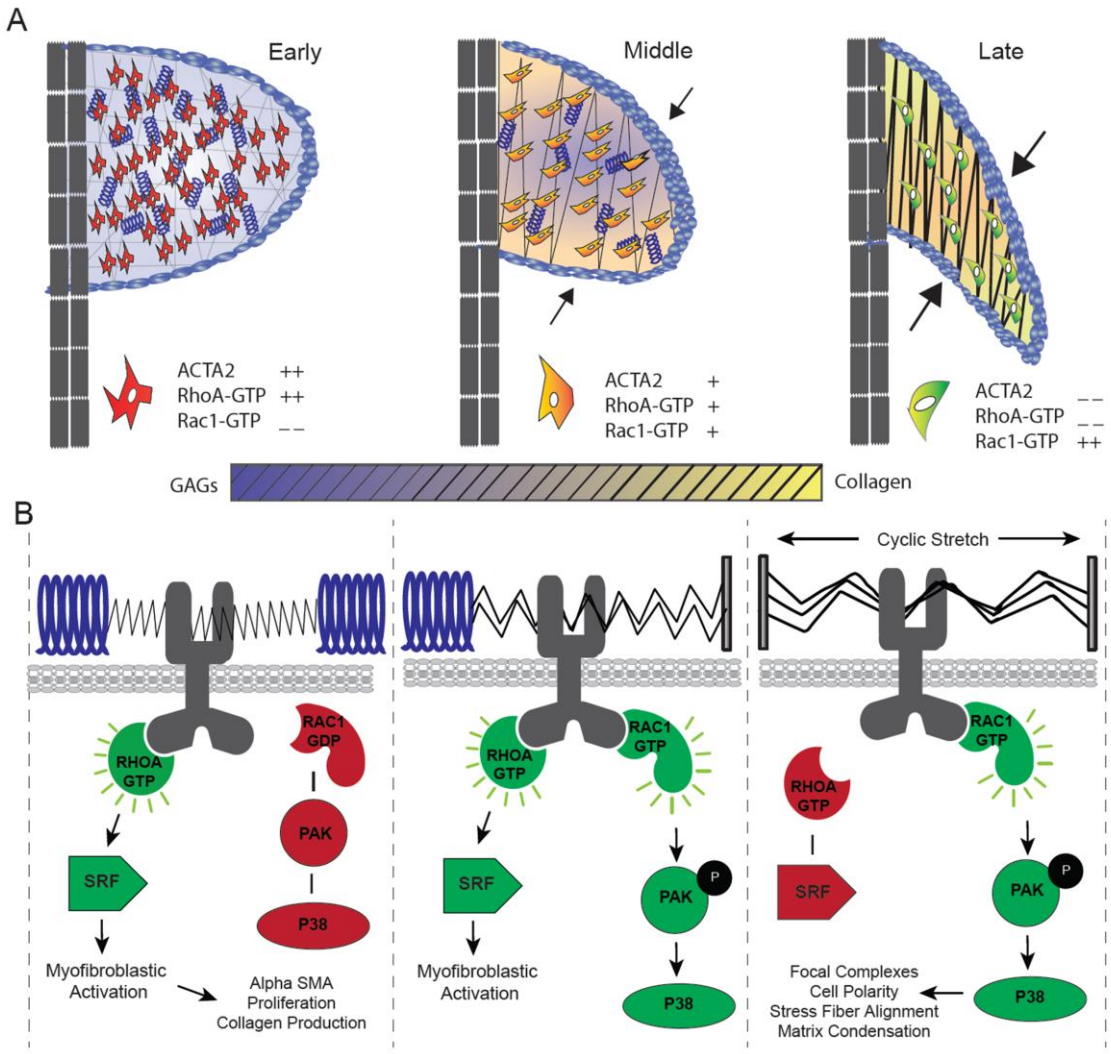

Figure 4.8 – Summary of phenotypic changes associated with cyclic stretch during valve maturation. (A) Early valve tissue resembles a globular "cushion" consisting of high GAG/collagen ratio. Resident mesenchyme cells are highly myofibroblastic as indicated by positive expression for ACTA2 and RhoA-GTP. During valve maturation, the resident cells become Rac1 positive, and transition to a highly polarized but quiescent valvular phenotype. The valve morphology changes to a thin fibrous leaflet consisting of a high collagen/GAG ratio. (B) Underlying this process, sustained cyclic stretch is necessary for directing valvular phenotype through a RhoA/Rac1 divergence "switch". At early stages, the resident cells activate the RhoA pathway and nuclear localization of SRF to enhance smooth muscle actin, collagen production, and proliferation. At later stages, significant collagen is produced and promotion of the Rac1-p38 pathway leads to enhanced ECM adhesion and cell polarization necessary for matrix condensation. Concurrently, the RhoA pathway is "switched" off by sustained cyclic stretch and cell quiescence is maintained.

4.5: Discussion

Embryonic valve primordia deform considerably as they withstand increasing hemodynamic loads while transitioning from thick endocardial cushions to thin fibrous leaflets [26, 27]. Previous studies altering intracardiac flows in vivo report a high incidence of valvular malformation [11, 28, 29]. Similarly, genetic mutant animal models with malformed valves experience a changed hemodynamic environment [30, 31]. While the importance of flow in the initiation of valve formation is well recognized, how mechanical signals participate in the transition from cushion to fibrous leaflet is poorly understood [32-34]. Morphogenic processes involve adhesion, migration, and matrix remodeling behaviors, which are all impossible without mechanosensitive action and reaction [35, 36]. Furthermore, as morphogenesis and ECM remodeling subsides, active myofibroblasts transition to quiescence for maintaining tissue homeostasis [37]. In this study, we clarify how mechanical signaling orchestrates endocardial cushion condensation into thin fibrous leaflets, while simultaneously establishing fibroblastic quiescence. Using gain and loss of function assays, we identify RhoA and Rac1 as key participants in mechanical regulation of embryonic valve remodeling. Mechanical tension promotes RhoA mediated cell migration essential for early cushion formation, but RhoA activity subsides as cushions condense into leaflets. Rac1 activity in contrast was necessary and sufficient to mediate condensation and reduction of myofibroblastic phenotype. Interestingly, cyclic mechanical stretch *in-vitro* inhibited myofibroblastic activation by decreasing RhoA-GTP levels and promoted Rac1 signaling. Rac1 activity resulted in strong cell polarization, stress fiber alignment, and adhesion, which in turn is necessary for enhanced matrix condensation. These effects were further confirmed *in-vivo* using ligation experiments to regulate side specific hemodynamic load. These results establish the importance of mechanical load on regulating valve progenitor differentiation and matrix condensation through coordinated RhoA/Rac1 signaling.

Valvular interstitial cells are predominantly quiescent fibroblasts in healthy postnatal tissue, but exhibit activated myofibroblastic behavior during embryonic remodeling or disease states [6, 38]. When VICs become activated myofibroblasts, they significantly up-regulate contractile filaments (including ACTA2), exhibit increased matrix turnover, and are highly proliferative. These factors all lead to dramatic changes in matrix composition and structural organization [4, 39]. Grinnell et al. and colleagues developed a now classic floating (stress-free) and mechanically anchored (stressed) hydrogel 3D culture system to study mechanoregulation of matrix remodeling adapted herein. They determined that fibroblasts within mechanically stressed environments generate cell tension and become activated myofibroblasts, while cells in stress-free free floating gels do not (negative control) [19, 40]. We previously confirmed a similar behavior of postnatal VICs in these model systems [18]. The mechanisms underlying this mechanosensation are incompletely understood, but involve at least in part cytoskeletal tension and RhoA signaling [41, 42]. In our system, we found that mechanical tension increases in mechanically anchored hydrogels (measured via spring transducers) and monotonically correlates with RhoA activity during a 72 hr period. Concurrently, SRF nuclear localization ensues, where it can directly bind the promoter region of ACTA2 to drive myofibroblastic differentiation [43]. We confirmed the requirement of RhoA activation by measuring myofibroblastic activation of valvular progenitors in stress-free (floating) gels with CA-RhoA conditions, which express ACTA2 and SRF similar to the stressed (mechanically anchored) condition.

The functional consequence of the transition from activated myofibroblast to quiescent fibroblast is incompletely understood, but corresponds with the remodeling of homogenous GAG rich cushion matrix at HH25 to an organized trilaminar leaflet structure consisting of collagen, elastin, and GAGs at HH40 [44, 45]. We found that disruption of this process in the form of sustained myofibroblastic activation restricts valve condensation and development of striated

architecture, which is confirmed by observations in valves with chronically activated interstitial cells [4, 37]. As demonstrated both *in-vitro* and *in-vivo*, sustained cyclic loading is a key mechanism for abating myofibroblastic activity by suppressing RhoA activity. How and why diseased postnatal valves persist in myofibroblastic activation in the presence of cyclic stretch is not fully ascertained, but is likely due to the combinatorial involvement of altered biochemical (e.g. TGFβ) and mechanical (e.q. cytoskeletal tension) conditions. Our findings support however, that decreasing RhoA activity is a potential mechanism for alleviating myofibroblastic activation of VIC in a remodeling valve.

While the extent of cell deformation during valve maturation is unknown, it is well documented that valve primordia increase their motion as they elongate [8], and tissue stretch undoubtedly occurs in proportion to the transvalvular pressure the valves experience [46, 47]. Simultaneously, tissue stiffness increases during development [22, 48]. Interestingly, we recently found that resident valve cell deformation and tissue stiffness are functionally connected, and cells in stiffer ECM environments are more sensitive to tissue stretch [49]. Given the fact that both transvalvular pressure and tissue stiffness increases during development; we speculate that sustained cyclic deformation may be more critical for maintaining a quiescent cell at later stages, possibly through tensional homeostasis [50]. Additionally, because cell-matrix interactions change during valve development (i.e. increase beta1 integrin) the sensitivity (stage independent effects) of deformation may be a function of the resident cells' ability to form stable ECM connections, possibly through increased adhesion, cell polarization, and alignment.

Our results further identify the p38-Rac1 pathway as necessary and sufficient for matrix condensation by valve progenitors. This was initially surprising, as the RhoA pathway is a well-established driver of stress fiber formation and contractility [41, 51]. However, Parsons et al.

recently demonstrated that constitutively active-Rac1 drives the formation of adhesions along the ventral surface of the cell body, which move toward those at the tip and result in contraction-like shortening and matrix compression at the base of lamellipodia [52]. Both the magnitude and direction of the adhesion motions correlate strongly with nearby matrix displacements indicating the importance of cell polarity for force generation [53]. Additionally, fibroblast-specific deletion of Rac1 in mouse resulted in delayed cutaneous wound closure, with reduced collagen production and matrix compaction [54]. Consistent with these results, we determined that colocalization of actin fibers and vinculin along the cell periphery depended on Rac1 activity. Actin stress fibers were highly aligned within the cells only when Rac1 was active, indicating strong polarization and contraction [55]. Importantly, CA-RhoA or DN-RhoA did not affect matrix condensation. However, CA-Rac1 combined with DN-RhoA completely blocked matrix condensation, suggesting that basal levels of RhoA are still needed to maintain cell contractility and traction force. We therefore conclude that Rac1 enhances cell polarization and adhesion to coordinate actin stress fiber alignment and directionally for RhoA mediated contractility. This explains at least in part the inverse relationship between matrix condensation and myofibroblastic differentiation during valve maturation that leads to thin mature quiescent valves.

Clinically, Rac1 signaling defects have been implicated in Noonan Syndrome. About 10%–15% of individuals with NS have mutations in son of sevenless 1 (*SOS1*), which encodes a RAS and RAC guanine nucleotide exchange factor (GEF) [56]. Interestingly, a retrospective study of 136 patients with Noonan Syndrome and cardiac heart defects found that 15% of these individuals had anomalies of the atrioventricular canal, and a subset with severe mitral defects [57]. Recently, mice with the Noonan Syndrome-associated Sos1E846K gain-of-function mutation were found to have hyperactive Rac1 activity, leading to extensive cardiac and valve defects [58]. While the direct mechanism by which Sos1-Rac1 leads to cardiac defects is still unclear, a

potentially deleterious combination of altered mechanical and genetic signaling cannot be overlooked. Patients with Noonan syndrome and mitral defects often have elevated blood pressure, as measured by peak-to-peak gradient and Doppler mean gradient, leading to sub-aortic stenosis and accessory fibrous mitral valve tissue [57]. Our results indicate that hemodynamic loading contributes to Rac1 activity, and reduced mechanical loading cause's dysfunctional adhesion and cell polarization, leading to immature matrix remodeling. In corroboration with previous studies, genetic mutations of Rac1 were found to result in abnormal ECM remodeling in-vitro and in-vivo [54, 59]. The mechanisms were found to include impaired adhesion as well as reduced matrix condensation [60, 61]. Together, consideration of hemodynamic loading in concert with Rac1 signaling may inform mechanistic insights in mitral valve malformation and/or premature degeneration.

In summary, these results establish that mechanical loading is essential for coordinating a transition from RhoA to Rac1 based signaling to produce a thin organized valve leaflet with a quiescent phenotype. Unbalanced RhoA/Rac1 signaling may therefore be an important predictor of abnormal valve morphogenesis. Additionally, altered hemodynamic signaling can possibly be used to control RhoA/Rac1 signaling to rescue tissue fate. These findings and innovative methodologies motivate and enable new mechanobiological hypotheses to link microenvironmental cues with genetic regulation for understanding tissue formation and remodeling.

REFERENCES

1. Go, A.S., et al., *Heart disease and stroke statistics--2013 update: a report from the American Heart Association.* Circulation, 2013. **127**(1): p. e6-e245.
2. Goodwin, R.L., et al., *Three-dimensional model system of valvulogenesis.* Dev Dyn, 2005. **233**(1): p. 122-9.
3. Butcher, J.T. and R.R. Markwald, *Valvulogenesis: the moving target.* Philos Trans R Soc Lond B Biol Sci, 2007. **362**(1484): p. 1489-503.
4. Rabkin-Aikawa, E., et al., *Dynamic and reversible changes of interstitial cell phenotype during remodeling of cardiac valves.* J Heart Valve Dis, 2004. **13**(5): p. 841-7.
5. David Merryman, W., *Mechano-potential etiologies of aortic valve disease.* J Biomech, 2010. **43**(1): p. 87-92.
6. Liu, A.C., V.R. Joag, and A.I. Gotlieb, *The emerging role of valve interstitial cell phenotypes in regulating heart valve pathobiology.* Am J Pathol, 2007. **171**(5): p. 1407-18.
7. Yalcin, H.C., et al., *Hemodynamic patterning of the avian atrioventricular valve.* Dev Dyn, 2011. **240**(1): p. 23-35.
8. Vermot, J., et al., *Reversing blood flows act through klf2a to ensure normal valvulogenesis in the developing heart.* PLoS Biol, 2009. **7**(11): p. e1000246.
9. Sacks, M.S., W. David Merryman, and D.E. Schmidt, *On the biomechanics of heart valve function.* J Biomech, 2009. **42**(12): p. 1804-24.
10. Sedmera, D., et al., *Remodeling of chick embryonic ventricular myoarchitecture under experimentally changed loading conditions.* Anat Rec, 1999. **254**(2): p. 238-52.
11. Colvee, E. and J.M. Hurle, *Malformations of the semilunar valves produced in chick embryos by mechanical interference with cardiogenesis. An experimental approach to the role of hemodynamics in valvular development.* Anat Embryol (Berl), 1983. **168**(1): p. 59-71.
12. deAlmeida, A., T. McQuinn, and D. Sedmera, *Increased ventricular preload is compensated by myocyte proliferation in normal and hypoplastic fetal chick left ventricle.* Circ Res, 2007. **100**(9): p. 1363-70.
13. Kaibuchi, K., S. Kuroda, and M. Amano, *Regulation of the cytoskeleton and cell adhesion by the Rho family GTPases in mammalian cells.* Annu Rev Biochem, 1999. **68**: p. 459-86.
14. Butcher, J.T., et al., *Periostin promotes atrioventricular mesenchyme matrix invasion and remodeling mediated by integrin signaling through Rho/PI 3-kinase.* Dev Biol, 2007. **302**(1): p. 256-66.
15. Tavares, A.L., et al., *TGF beta-mediated RhoA expression is necessary for epithelial-mesenchymal transition in the embryonic chick heart.* Dev Dyn, 2006. **235**(6): p. 1589-98.
16. Tan, H., et al., *Fluid flow forces and rhoA regulate fibrous development of the atrioventricular valves.* Dev Biol, 2013. **374**(2): p. 345-56.
17. Chiu, Y.N., et al., *Transforming growth factor beta, bone morphogenetic protein, and vascular endothelial growth factor mediate phenotype maturation and tissue remodeling by embryonic valve progenitor cells: relevance for heart valve tissue engineering.* Tissue Eng Part A, 2010. **16**(11): p. 3375-83.
18. Gould, R.A., et al., *Cyclic strain anisotropy regulates valvular interstitial cell phenotype and tissue remodeling in three-dimensional culture.* Acta Biomater, 2012. **8**(5): p. 1710-9.
19. Grinnell, F., *Fibroblast biology in three-dimensional collagen matrices.* Trends Cell Biol, 2003. **13**(5): p. 264-9.

20. Butcher, J.T., B.C. Barrett, and R.M. Nerem, *Equibiaxial strain stimulates fibroblastic phenotype shift in smooth muscle cells in an engineered tissue model of the aortic wall.* Biomaterials, 2006. **27**(30): p. 5252-8.
21. Butcher, J.T. and R.M. Nerem, *Porcine aortic valve interstitial cells in three-dimensional culture: comparison of phenotype with aortic smooth muscle cells.* J Heart Valve Dis, 2004. **13**(3): p. 478-85; discussion 485-6.
22. Butcher, J.T., et al., *Transitions in early embryonic atrioventricular valvular function correspond with changes in cushion biomechanics that are predictable by tissue composition.* Circ Res, 2007. **100**(10): p. 1503-11.
23. Mahler, G.J., E.J. Farrar, and J.T. Butcher, *Inflammatory cytokines promote mesenchymal transformation in embryonic and adult valve endothelial cells.* Arterioscler Thromb Vasc Biol, 2013. **33**(1): p. 121-30.
24. Grinnell, F., *Fibroblast biology in three-dimensional collagen matrices.* Trends in Cell Biology, 2003. **13**(5): p. 264-269.
25. Mack, C.P., et al., *Smooth muscle differentiation marker gene expression is regulated by RhoA-mediated actin polymerization.* J Biol Chem, 2001. **276**(1): p. 341-7.
26. Phoon, C.K., *Circulatory physiology in the developing embryo.* Curr Opin Pediatr, 2001. **13**(5): p. 456-64.
27. Hu, N., et al., *Diastolic filling characteristics in the stage 12 to 27 chick embryo ventricle.* Pediatr Res, 1991. **29**(4 Pt 1): p. 334-7.
28. Hove, J.R., et al., *Intracardiac fluid forces are an essential epigenetic factor for embryonic cardiogenesis.* Nature, 2003. **421**(6919): p. 172-7.
29. Hogers, B., et al., *Unilateral vitelline vein ligation alters intracardiac blood flow patterns and morphogenesis in the chick embryo.* Circ Res, 1997. **80**(4): p. 473-81.
30. Beis, D., et al., *Genetic and cellular analyses of zebrafish atrioventricular cushion and valve development.* Development, 2005. **132**(18): p. 4193-204.
31. Phoon, C.K. and D.H. Turnbull, *Ultrasound biomicroscopy-Doppler in mouse cardiovascular development.* Physiol Genomics, 2003. **14**(1): p. 3-15.
32. Bartman, T. and J. Hove, *Mechanics and function in heart morphogenesis.* Dev Dyn, 2005. **233**(2): p. 373-81.
33. Egorova, A.D., et al., *Tgfbeta/Alk5 signaling is required for shear stress induced klf2 expression in embryonic endothelial cells.* Dev Dyn, 2011. **240**(7): p. 1670-80.
34. Martin, R.T. and T. Bartman, *Analysis of heart valve development in larval zebrafish.* Dev Dyn, 2009. **238**(7): p. 1796-802.
35. Davidson, L.A., *Integrating morphogenesis with underlying mechanics and cell biology.* Curr Top Dev Biol, 2008. **81**: p. 113-33.
36. Ingber, D.E., *Mechanical control of tissue morphogenesis during embryological development.* Int J Dev Biol, 2006. **50**(2-3): p. 255-66.
37. Aikawa, E., et al., *Human semilunar cardiac valve remodeling by activated cells from fetus to adult: implications for postnatal adaptation, pathology, and tissue engineering.* Circulation, 2006. **113**(10): p. 1344-52.
38. Chen, J.H., et al., *Identification and characterization of aortic valve mesenchymal progenitor cells with robust osteogenic calcification potential.* Am J Pathol, 2009. **174**(3): p. 1109-19.
39. Taylor, P.M., et al., *The cardiac valve interstitial cell.* Int J Biochem Cell Biol, 2003. **35**(2): p. 113-8.
40. Grinnell, F., *Fibroblasts, myofibroblasts, and wound contraction.* J Cell Biol, 1994. **124**(4): p. 401-4.
41. Wozniak, M.A. and C.S. Chen, *Mechanotransduction in development: a growing role for contractility.* Nat Rev Mol Cell Biol, 2009. **10**(1): p. 34-43.

42. McBeath, R., et al., *Cell shape, cytoskeletal tension, and RhoA regulate stem cell lineage commitment.* Dev Cell, 2004. **6**(4): p. 483-95.
43. Wang, Z., et al., *Myocardin and ternary complex factors compete for SRF to control smooth muscle gene expression.* Nature, 2004. **428**(6979): p. 185-9.
44. Kruithof, B.P., S.A. Krawitz, and V. Gaussin, *Atrioventricular valve development during late embryonic and postnatal stages involves condensation and extracellular matrix remodeling.* Dev Biol, 2007. **302**(1): p. 208-17.
45. Ku, C.H., et al., *Collagen synthesis by mesenchymal stem cells and aortic valve interstitial cells in response to mechanical stretch.* Cardiovasc Res, 2006. **71**(3): p. 548-56.
46. Schoen, F.J., *Evolving concepts of cardiac valve dynamics: the continuum of development, functional structure, pathobiology, and tissue engineering.* Circulation, 2008. **118**(18): p. 1864-80.
47. Lucitti, J.L., K. Tobita, and B.B. Keller, *Arterial hemodynamics and mechanical properties after circulatory intervention in the chick embryo.* J Exp Biol, 2005. **208**(Pt 10): p. 1877-85.
48. Buskohl, P.R., R.A. Gould, and J.T. Butcher, *Quantification of embryonic atrioventricular valve biomechanics during morphogenesis.* J Biomech, 2012. **45**(5): p. 895-902.
49. Gould, R.A., et al., *Multi-scale biomechanical remodeling in aging and genetic mutant murine mitral valve leaflets: insights into Marfan syndrome.* PLoS One, 2012. **7**(9): p. e44639.
50. Ingber, D.E., *Cellular mechanotransduction: putting all the pieces together again.* FASEB J, 2006. **20**(7): p. 811-27.
51. Chrzanowska-Wodnicka, M. and K. Burridge, *Rho-stimulated contractility drives the formation of stress fibers and focal adhesions.* J Cell Biol, 1996. **133**(6): p. 1403-15.
52. Parsons, J.T., A.R. Horwitz, and M.A. Schwartz, *Cell adhesion: integrating cytoskeletal dynamics and cellular tension.* Nat Rev Mol Cell Biol, 2010. **11**(9): p. 633-43.
53. Petroll, W.M., L. Ma, and J.V. Jester, *Direct correlation of collagen matrix deformation with focal adhesion dynamics in living corneal fibroblasts.* J Cell Sci, 2003. **116**(Pt 8): p. 1481-91.
54. Liu, S., M. Kapoor, and A. Leask, *Rac1 expression by fibroblasts is required for tissue repair in vivo.* Am J Pathol, 2009. **174**(5): p. 1847-56.
55. Davidson, L.A., A.M. Ezin, and R. Keller, *Embryonic wound healing by apical contraction and ingression in Xenopus laevis.* Cell Motil Cytoskeleton, 2002. **53**(3): p. 163-76.
56. Tartaglia, M., et al., *Gain-of-function SOS1 mutations cause a distinctive form of Noonan syndrome.* Nat Genet, 2007. **39**(1): p. 75-9.
57. Marino, B., et al., *Congenital heart diseases in children with Noonan syndrome: An expanded cardiac spectrum with high prevalence of atrioventricular canal.* J Pediatr, 1999. **135**(6): p. 703-6.
58. Chen, P.C., et al., *Activation of multiple signaling pathways causes developmental defects in mice with a Noonan syndrome-associated Sos1 mutation.* J Clin Invest, 2010. **120**(12): p. 4353-65.
59. Hinz, B. and G. Gabbiani, *Cell-matrix and cell-cell contacts of myofibroblasts: role in connective tissue remodeling.* Thromb Haemost, 2003. **90**(6): p. 993-1002.
60. Berrier, A.L. and K.M. Yamada, *Cell-matrix adhesion.* J Cell Physiol, 2007. **213**(3): p. 565-73.
61. Hinz, B., *Formation and function of the myofibroblast during tissue repair.* J Invest Dermatol, 2007. **127**(3): p. 526-37.

CHAPTER 5

MULTI-SCALE BIOMECHANICAL REMODELING IN AGING AND GENETIC MUTANT MURINE MITRAL VALVE LEAFLETS: INSIGHTS INTO MARFAN SYNDROME

5.1: Summary

Mitral valve degeneration is a key component of the pathophysiology of Marfan syndrome. The biomechanical consequences of aging and genetic mutation in mitral valves are poorly understood because of limited tools to study this in mouse models. Our aim was to determine the global biomechanical and local cell-matrix deformation relationships in the aging and Marfan related *Fbn1* mutated murine mitral valve. To conduct this investigation, a novel stretching apparatus and gripping method was implemented to directly quantify both global tissue biomechanics and local cellular deformation and matrix fiber realignment in murine mitral valves. Excised mitral valve leaflets from wild-type and *Fbn1* mutant mice from 2 weeks to 10 months in age were tested in circumferential orientation under continuous laser optical imaging. Mouse mitral valves stiffen with age, correlating with increases in collagen fraction and matrix fiber alignment. *Fbn1* mutation resulted in significantly more compliant valves (modulus 1.34 ± 0.12 vs. 2.51 ± 0.31 MPa, respectively, $P<.01$) at 4 months, corresponding with an increase in proportion of GAGs and decrease in elastin fraction. Local cellular deformation and fiber alignment change linearly with global tissue stretch, and these slopes become more extreme with aging. In comparison, *Fbn1* mutated valves have decoupled cellular deformation and fiber alignment with tissue stretch. Taken together, quantitative understanding of multi-scale murine planar tissue biomechanics is essential for establishing consequences of aging and genetic mutations. Decoupling of local cell-matrix deformation kinematics with global tissue stretch may be an important mechanism of normal and pathological biomechanical remodeling in valves.

5.2: Introduction

Marfan syndrome (MFS) is an autosomal-dominant systemic disorder of connective tissue, with an estimated prevalence of 1 in 5,000 individuals [1]. It is associated with mutations in *Fbn1*, encoding fibrillin-1, the principal component of extracellular microfibrils, leading to severe cardiovascular, ocular, and skeletal defects [2]. Of these consequences, mitral valve disease is one of the leading indications for surgery and causes of death in young children with MFS. Furthermore, mitral valve prolapse is widely prevalent, affecting 2.4% of individuals in a community-based survey [3]. Currently, no medical therapies exist to prevent valve disease in predisposed individuals [4]. Despite its significant public health and clinical burden, very little is known about the biomechanical remodeling of mitral valves with age or genetic mutations, which lie at the core of its pathophysiology.

Mitral valves (MV) are fibrous leaflets whose primary function is to maintain unidirectional blood inflow into the left ventricle with each heartbeat [5]. Resident valve interstitial cells (VIC) repair and remodel the tissue to form a complex biomechanical structure capable of withstanding forces exerted by the surrounding blood and muscle walls [6]. MV tissue biomechanics is dictated in large part by local microstructure, which is comprised of stratified collagen and elastin dispersed with proteoglycans [7]. Myxomatous MV leaflets have increased production of collagens, particularly type III collagen, and glycosaminoglycans (GAGs) [8]. Some postulate that this may be the result of a leaflet response to repeated mechanical stress leading to MV dysfunction [9]. Sherratt et al. suggested that microfibrils, predominantly composed of fibrillin-1, act as stiff reinforcing filaments in elastic fibers, possibly limiting the extension of elastin and protecting these fibers from hemodynamic damage [10]. Breakdown of these microfibrils may also affect adjacent cell attachment, as an RGD sequence of fibrillin-1 has been reported to support cellular adhesion in vitro via integrin $\alpha_v\beta_3$ [11,12]. Still, the global and local

biomechanical consequences of human fibrillin-1 mutations in the mitral valve have not been fully elucidated.

Mouse models are indispensible for understanding functional consequences of fibrillin-1 mutations. Ng et al. found that MV leaflets from mice with a heterozygous cysteine-substitution mutation in fibrillin-1 exhibit postnatally acquired alterations in architecture that correlate both temporally and spatially with increased cell proliferation, decreased apoptosis, and excess TGF-β activation and signaling [13]. Mice homozygous for a hypomorphic *Fbn1* allele (mgR) die between 3 and 6 months of age from aortic dissections. This tissue mechanical failure is preceded by a series of secondary events that are spatially coincident including progressive elastic fiber degradation and disarray and aortic wall thickening due to excessive deposition of matrix elements including collagen and proteoglycans. These findings suggest that cell mediated matrix remodeling leads to gross tissue biomechanical changes. While molecular processes are easily studied in mice, no experimental devices exist for quantifying the biomechanical characteristics of these micro-scale planar soft tissues.

In this study, we implement a novel method to quantify global biomechanical and local cell-matrix relationships in small-scale planar tissues. By stretching mouse mitral valves under confocal microscopy, tissue strain was quantified concurrently with underlying cellular deformation and fiber alignment. We found that local cell and matrix kinematics are decoupled to different degrees correlating with magnitude of global valve tissue stretch. This decoupling was correlated with transitions in the proportions of collagen and GAGs, whether with age or *Fbn1* mutation.

5.3: Materials and Methods

5.3.1: Device Fabrication and Biomechanical Testing

We designed and fabricated a device that miniaturized a classical uniaxial strip test. Two challenges for very small, ultra compliant tissues are 1) measuring very small magnitude forces applied, and 2) securing the tissue to a member that can stretch without failure at the grips. We addressed the first using classical Euler cantilever beam deflection mechanics. Elastomeric posts (Polydimethylsiloxane, Sylgard184) were prepared by casting a 10:1 mix of base and curing agent in custom made negative molds and curing at 65^{o}C for 6 hours. The mold geometry (cross-section, depth) was adjusted to create posts with different force sensitivity and strain capacity. Bending stiffness was calculated analytically with the measured deflection (Figure 5.1A-B), and measured force verified independently via mass balance as previously described (*1*).

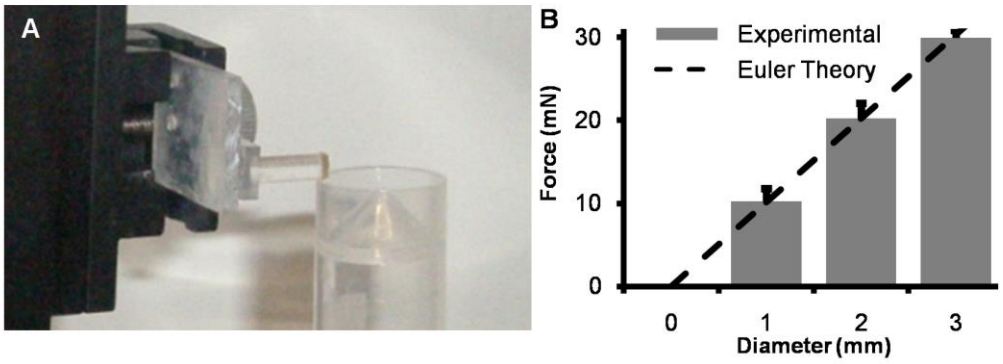

Figure 5.1 – Silicon post construction and calibration. (A) Elastomeric posts mounted on micro-manipulation and deflection force measured via weight scale. (B) Representative calibration curves for fixed aspect ratio of height to diameter (H/D) = 3 with varying diameters. Euler beam theory (dashed line) predicts a linear increase in bending stiffness with diameter. Post bending stiffness was measured for 3 diameters and agrees with theory. n = 6 (3 silicon batches), with data presented as mean± SD.

Cylindrical posts with a diameter of 2mm and axial length of 6mm were used for mitral valve testing. Once calibrated, the silicon posts were mounted on top of two L-shaped plastic beams

that traveled on linear rail guides. A screw-driven wedge enabled equal and opposite co-linear displacement of the L-beams, and thus the cantilever posts, micron resolution (Fig. 5.2). Valve tissue was secured to the post top using filter paper and a high-viscosity cyanoacrylate (454 Prism, Loctite). The tissue was kept flat prior to mounting by first placing it on a glass coverslip and removing all excess liquid, then inverting it to contact the posts. Once mounted, the entire system was placed on the stage of an upright confocal microscope (TCS SP2, Leica).

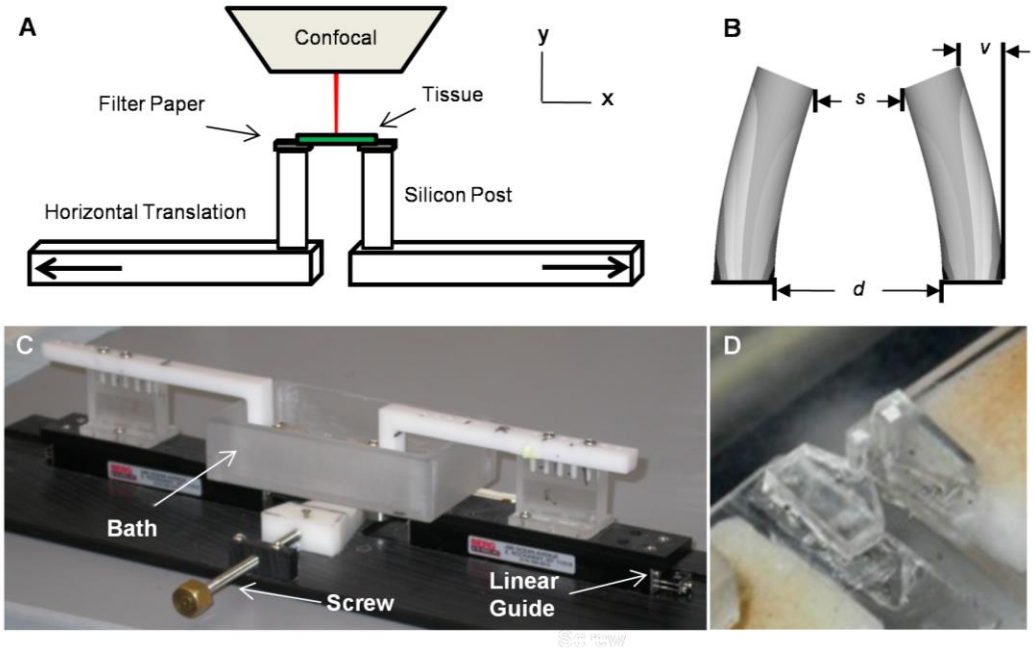

Figure 5.2 – Meso-scale uniaxial tensile device. (A) Experimental stage controls the opposite co-linear translation of two cylindrical elastomeric beams. Tissue is mounted on the top surface of the posts using filter paper. The assembly is fully submerged in a buffered saline bath, and able to be imaged continuously under an upright confocal system. (B) Silicon post defection (v), post separation (s), and horizontal translation (d) were used for the biomechanical analysis. (C) Fabricated device implements a screw-driven wedge design for separation of the two linear rail guides at micro-meter resolution. (D) Detailed view of the silicon-post setup located inside the water bath. Distance between the posts is approximately 500 um.

5.3.2: Mitral Valve Isolation and Biomechanical Testing

Wildtype (*Fbn1* +/+) and heterozygous ($^{C1039G/+}$*Fbn1*) knock-in mice between the ages of 2 weeks and 10 months were used in this study, as that reflects a broad range of murine valve growth and development [15]. Details of the human *Fbn1* knock-in mutation (C1039G/+) have been previously described [16]. Mutant mice were back-crossed into the C57BL/6J background for at least 10 generations. All animal use was approved by the Cornell University and Johns Hopkins Institutional Animal Care and Use Committee (IACUC). For valve tissue isolation, mice were then anesthetized using anintraperitoneal injection of sodium pentobarbital (125 mg/kg) and verified via toe pinch. Acranio-caudal incision was then made to expose the thoracic cavity, and the diaphragm severed. The heart was then excised above the level of the aortic valve and perfused with ice-cold saline to wash away any blood from the chamber and valve regions. Mutant mouse hearts were prepared at Johns Hopkins, placed in a 15ml conical tube containing DMEM, 10% FBS, and 0.1% ITS, and shipped on ice the same day to Cornell. Shipped mitral valve tissues were stained with Live-Dead to confirm greater than 90% cell viability (Figure 5.3. Tissues were tested immediately on arrival, which was within 24 hours after the initial isolation.

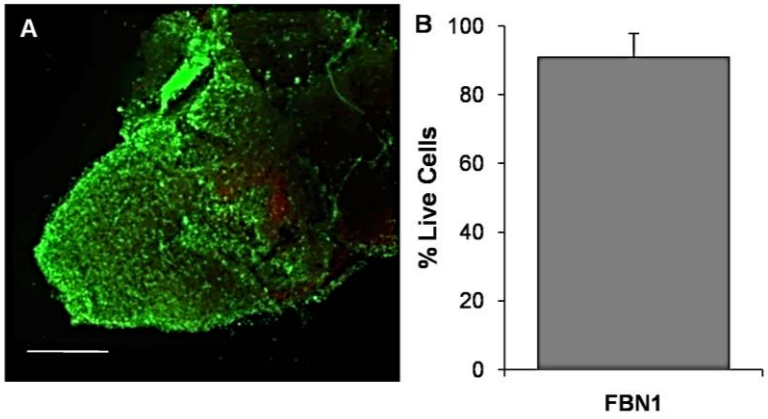

Figure 5.3 – Live/dead stain on shipped $^{C1039G/+}$*Fbn1* mitral valves. (A) Visualization of Live/dead stain. (B) Shipped FBN1 valves had over 90% viability upon arrival, similar to valves excised directly at our institution. Magnification, ×4 Scale bars: 500 μm. Error bars show ±SD, n ≥ 3 valves per time point.

The anterior mitral valve leaflet was dissected from the annular wall and trimmed to a rectangular strip using micro-scissors. The presence and architecture of cells and extracellular matrix were visualized using fluorescent vital dyes (5 µM CellTrackerRed CMPTX and 10 µM 5-DTAF, respectively, both from Invitrogen). Leaflets were then mounted to the posts in the atrialis-up configuration, immersed in a bath containing Dulbecco's phosphate buffered saline (DPBS) and placed under an upright confocal (TCS SP2, Leica). Zero-strain reference length was defined as the maximum length of tissue for which no post deflection was visible (representing a maximum tensile preload of 100 nN). Tissues were first preconditioned with 3 cycles of approximately 10% strain, followed by a single quasi-static tensile test administered at 25-micron displacement intervals. At each test position, a macroscopic tissue view of the valve was taken at 10x magnification, and microscopic z-stacks of cells and fibers at 40x, both using confocal microscopy. Simultaneously, post deflection was monitored using a digital SLR camera (D5000, Nikon) positioned at the side of the test system.

5.3.3: Determination of Local Biomechanics

Biomechanical parameters were quantified through image analysis performed using ImageJ (NIH). Global tissue deformation was measured via tip-to tip post displacement, while local tissue deformation at each incremental stretch were measured at the midline zone by tracking virtual fiducial markers using confocal microscopy as previously described (*2*). Applied force was determined by comparing measured post-deflection against the calibration curve. Tissue width and thickness was measured at the initial state using confocal microscopy (10X and 40x z-stacks, respectively). First Piola-Kirchoff stress and stretch ratio-based strain data were generated and fit to a uniaxial exponential Fung model. From this, an effective tissue modulus was determined using the two material coefficients (α,β) as previously described (*3*). Local matrix fiber alignment and cell deformation was captured at each stretch interval using 40x

confocal z-stacks (Figure 5.4). Cell shape changes were traced manually, tracked over subsequent images, and quantified as a cell circularity index (CI = 4*Pi*(Area/Perimeter^2)) as manually traced in ImageJ. Fiber alignment along the axis of stretch was quantified as an alignment index (FAI) custom algorithm through MATLAB as previously described (*4*). The Fourier Transform intensity was computed between 0^o to 180^o (angles with respect to horizontal) at 5^o intervals and presented the results in the form of a histogram as a graphic display of alignment along a particular angle. The AI integrals were approximated as the sum of these 5^o intervals. This was directly compared to the summed angles $\pm 10^o$ from the direction of stretch for a FAI.

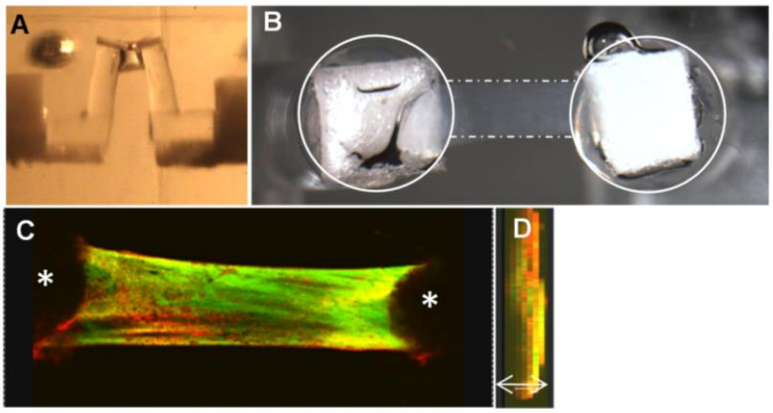

Figure 5.4 – Stretching mouse valves under continuous fluorescence imaging. (A) Post deflection used for measuring force generation. (B) Top view of post with attached tissue (center-outlined). Outline of post cross-section included as a reference (circles). (C) Macro scale valve deformation at 10X under confocal microscropy (extracellular matrix-green, cells- red). Stars denote post centroids. (D) Valve thickness measured using confocal microscopy full thickness z-stacks (40 um in this image).

5.3.4: Extracellular Matrix Composition. Additional hearts were excised and fixed in 10% buffered formalin overnight, arranged in 1.5% agar prior to paraffin embedding, and slides were prepared using 7µm sections. Sections of paraffin-embedded tissue were prepared and stained with either Movat Pentachrome, Masson's Trichrome, or Verhoff-van Gieson stain (VVG). Mitral valves were examined at 4X magnification and compared to a 200µm calibration standard

included in each image. Only sections in which the entire anterior leaflet was present were included in analyses. Colors representing different matrix constituents were separated in NIH ImageJ using an RGB or CMYK channel splitter and converted to grayscale images. These areas were then thresholded, quantified, and normalized against the area of the entire valve leaflet to determine relative fractional composition as previously described (*5*) (Figure 5.5).

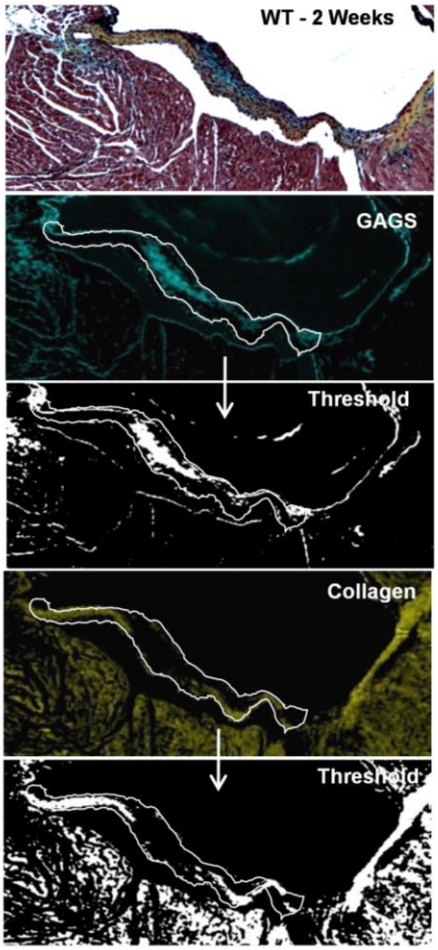

Figure 5.5 – **Digital quantification of ECM composition.** Serial sections of the mitral valves were stained with Movat's Pentachrome to identify the relative amounts of cells, collagen, and glycosaminoglycans at each age. The relative contributions changed dramatically across the length of the valve, so the entire valve area was considered (dashed contour). Colors were separated using an RGB or CMYK channel splitter. Black and white thresholds were created in NIH ImageJ and used to determine the volume fractions of each contributor.

Statistics

At least 6 independent valve specimens per time point and treatment condition were used during mechanical testing and samples from at least 3 independent valves were used for histochemical/morphologic analysis. All results are expressed as mean ± standard deviation, unless otherwise stated. One-way ANOVA with Tukey's modified post-hoc tests were used to compare differences between means and data was transformed when necessary to obtain equal sample variances. For *Fbn1*-mutant mice, Student's t-tests compared single time point across treatment conditions. $P < 0.05$ denoted statistical significance.

5.4: Results

5.4.1: Temporal biomechanical analysis of wild-type C57BL/6J mitral valves. We tested circumferentially oriented mitral valve leaflet specimens from 2 week-, 3 week-, 4 month-, and 10 month-old C57BL/6J mice, an interval during which significant physiological and morphological changes (valve thickness, mitral annulus, and blood pressure) have been observed [15]. As our objective was to compare local and global tissue deformations, tissues were stretched to a maximum of λ=1.6, which was sufficient to induce large cell shape changes but not cause fiber disruption or fracture. Macroscopically, the planar valves deformed as a typical uniaxial strip, with necking in the central region (Figure 5.6A-D). Microscopically, resident cells steadily changed shape from round to elliptical with stretch (Fig 5.6E-H), while matrix fibers progressively straightened and aligned to the loading direction (Fig. 5.6I-L).

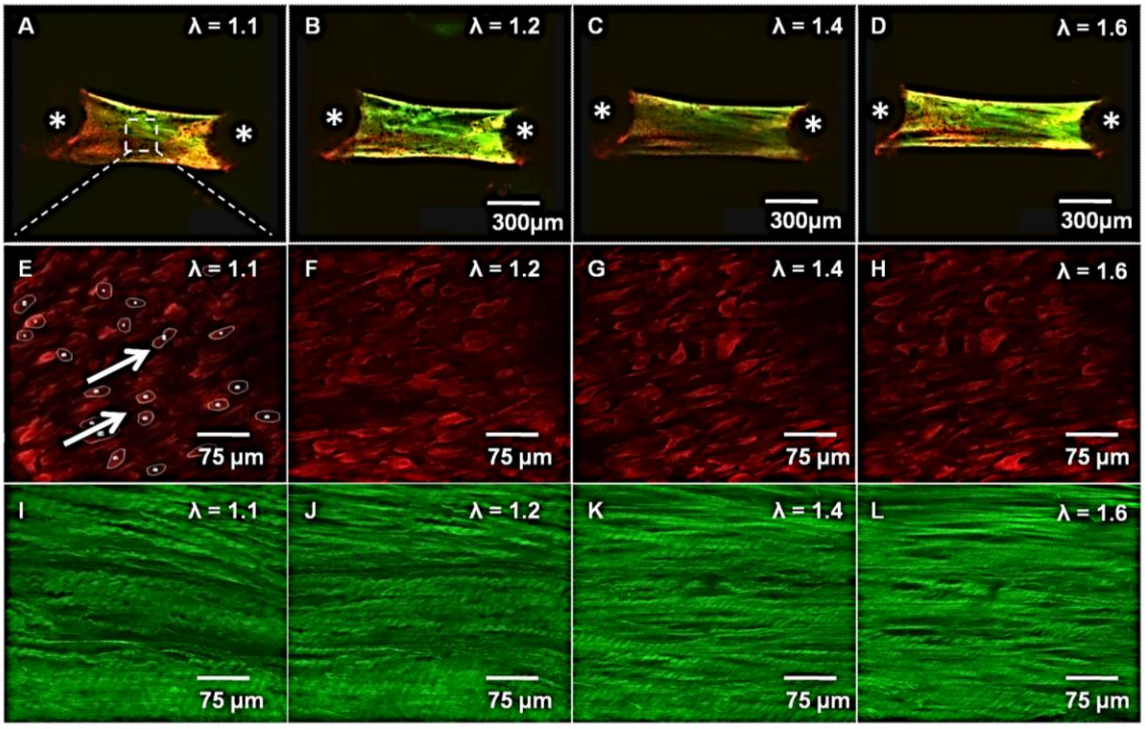

Figure 5.6 – **Macro and micro-scale tissue analysis.** (A-D) Macro scale valve deformation at varying stretch ratios (λ) viewed at 10X under confocal microscopy (Green: 5-DTAF stained matrix fibers, Red: vital dye labeled cell bodies). Stars denote centroid location of the cantilever posts. (E-H) Micro-scale cellular deformation of the same group of cells viewed during the same test at 40X under confocal microscopy. Arrows denote tracked morphology of individual cells. (I-L) Micro-scale fiber alignment from the same region viewed during the same test at 40X under confocal microscopy. Fiber un-crimping and alignment is clearly visible as stretch progresses left to right.

Biomechanically, anterior leaflets at each age exhibited nonlinear elastic material responses (Figure 5.7A). Valve leaflets significantly increased in stiffness with maturation (effective modulus of 1.04 ± 0.24MPa at 2 weeks to 2.88 ± 0.27MPa at 4 months, $P<0.05$), after which stiffness was maintained for the next 6 months of life (2.58 ± 0.28MPa at 10 months, not different from 4 months) (Figure 5.7B). Quantification of local cell deformation revealed a linear reduction in circularity index (CI) with stretch (Figure 5.7C). The slope of CI became increasingly negative over maturation (-0.11 ± 0.03 at 2 weeks to -0.32 ± 0.05 at 4 months, $P<0.05$), but leveled off at 10 months (-0.28 ± 0.4) (Figure 5.7 D). From these data, we were able to visualize a correlation between the effective tissue modulus and slope of CI, which suggests that cellular deformation increases with both stretch and tissue stiffness. Similarly, 5-

DTAF labeled extracellular matrix fibers aligned linearly with stretch, and the degree of alignment significantly increased with tissue maturation (Figure 5.7E). The slope of fiber alignment (FA) index increased from 0.46 ± 0.12 at 2 weeks to 0.93 ± 0.17 at 4 months ($P<0.05$). In contrast to cell shape, FA slope decreased significantly at 10 months (0.58 ± 0.09), which suggests that older valves have a reduced capacity for fiber reorientation with stretch, reminiscent of immature valves (Figure 5.7 F). Taken together, these results suggest that valve tissue microstructure is similarly sensitive to changes in deformation even at low strain and high stiffness zones.

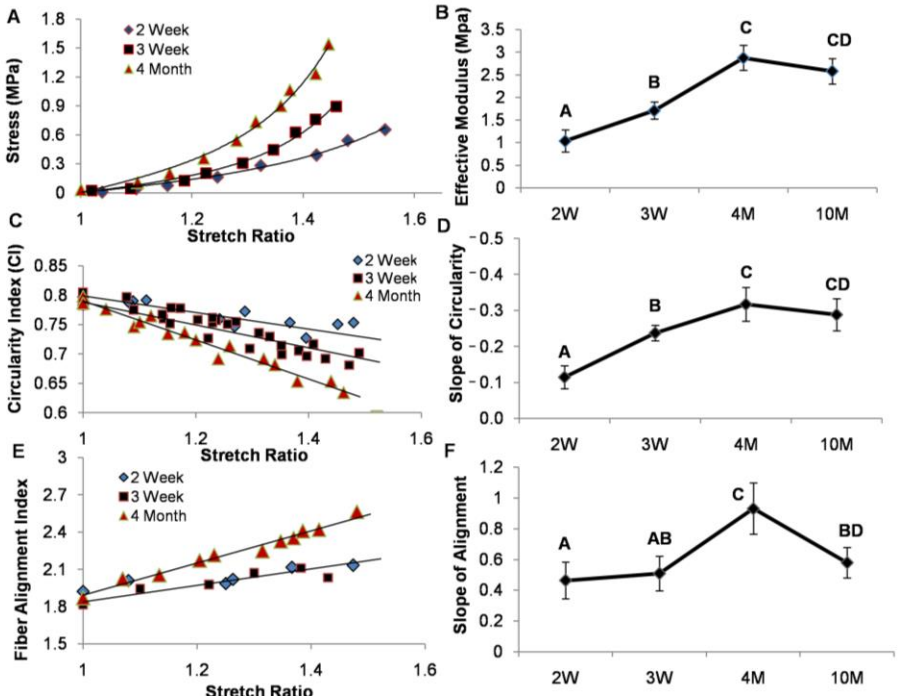

Figure 5.7 – Temporal biomechanical analysis of C57/B6J mitral valves. (A) Representative stress-strain curves of mitral valves loaded in the circumferential direction (not to failure). (B) Stress-strain data were fit to an exponential Fung model, from which coefficients were used to determine effective modulus. (C) Representative circularity index curves as defined by the ratio of $4*Pi*(Area/Perimeter^2)$. (D) Circularity-index curves were modeled as a linear fit and the negative slope was used for comparison. (E) Representative fiber-alignment curves were defined by the Fourier-Transform of collagen alignment and summed within ten degrees of the image horizontal, which was parallel to the tissue and loading direction. (F) Fiber-alignment data were fit to a linear model, the negative slope of which was used for comparison. Error bars show ±SD, n ≥ 6 for each condition. Groups that do not share letters are significantly different from each other according to a one-way ANOVA with Tukey's post hoc ($p \leq 0.05$).

5.4.2: Age dependent changes in anterior mitral valve leaflet extracellular matrix composition in wild-type C57BL/6J mice. Noticeable changes in structural organization occurred in mitral valves with age. 2-3 week old mitral leaflets contained equal proportions of collagens and GAGs, with more collagen located near the annular attachment region (Figure 5.8A-B). At 4 months, valves were significantly more compacted in both the annular attachment and mid-zone regions (Figure 5.8C). At 10-12 months, valves became thicker, more irregular in cross-section, and a larger disorganization of GAG/collagen architecture near the annulus region (Figure 5.8D). The fractional ratio of collagen to GAG increased from 2 weeks to 4 months (1.14 ± 0.78 to 2.94 ± 0.88, $P<0.05$), then tapered off in older valves (1.94 ± 0.89) (Figure 5.8E). Taken together, these results suggest that mitral valve tissue biomechanics was related to the fractional ratio of collagen to GAGs.

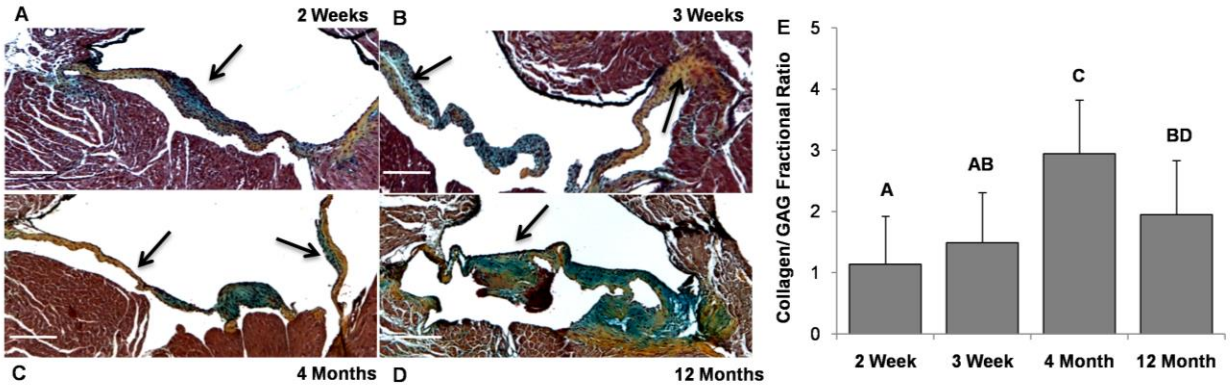

Figure 5.8 – Temporal histological examination of C57/B6J mitral valves. (A) 2 week old murine mitral valves contain similar fractional amounts of collagen and GAGs, with the majority of collagen near the attachment zones but mostly undefined architecture (Movat's stain: yellow/orange = collagen, green/blue = GAGs). (B) More collagen relative to GAGs is present in 3 week old MV, with matrix stratification developing (Arrows). (C) At 4 months, murine mitral valves have nearly 3 times the amount of collagen to GAGs, are significantly more compact, and have well defined atrialis/fibrosa strata (Arrows). (D) At 12 months, murine mitral valves have significantly less collagen to GAGs, with dramatically increased thickening and reduced structural organization. (E) Digital quantification of matrix composition using color thresholding. Data compared as the ratio of collagen to GAGs within each valve leaflet. Magnification, ×4. Scale bars: 200 μm. Error bars show ±SD, n ≥ 3 valves per time point. Bars that do not share any letters are significantly different according to a one-way ANOVA with Tukey's post hoc ($p \leq 0.05$).

5.4.3: Increased compliance of $^{C1039G/+}$Fbn1 mitral valves and its relationship to tissue microstructure. Transported $^{+/+}$*Fbn1* and $^{C1039G/+}$*Fbn1* valves had over 90% viability upon arrival, similar to valves excised and assessed without transportation. As anticipated, 4 month old $^{+/+}$*Fbn1* valves responded nonlinearly when stretched, with an effective modulus that was not significantly different from those of our locally-housed mouse valves (2.51 ± 0.31MPa). $^{C1039G/+}$*Fbn1* valves, in contrast, had significantly reduced moduli (1.34 ± 0.12MPa, $P<0.05$) (Figure 5.9A-B). At the microstructural level, we found a reduction in the negative slope of circularity index with $^{C1039G/+}$*Fbn1* mice relative to $^{+/+}$*Fbn1* (-0.23 ± 0.04 vs. -0.34 ± 0.04, $P<0.05$) (Figure 5.9C-D), suggesting that the fibrillin-1 mutation impairs local cell sensitivity to tissue stretch.

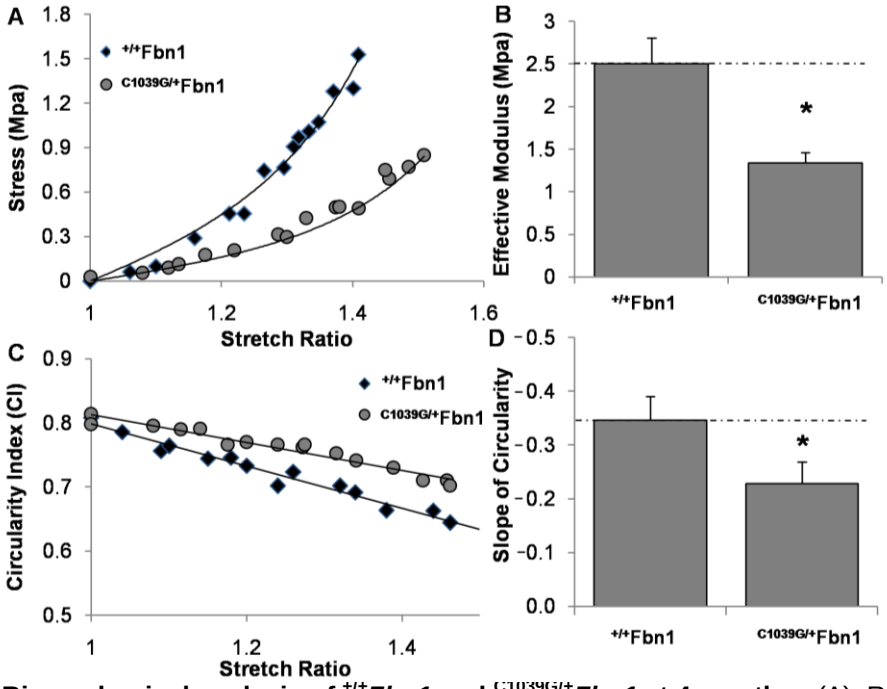

Figure 5.9 – Biomechanical analysis of $^{+/+}$*Fbn1* and $^{C1039G/+}$*Fbn1* at 4 months. (A) Representative stress-strain responses of mitral valves loaded in the circumferential direction. (B) Stress-strain data were fit to an exponential Fung model, coefficients of which were used to determine effective modulus. (C) Representative stretch induced cell shape changes responses defined by the circularity index (CI) = 4*Pi*(Area/Perimeter^2). (D) Circularity-index data were modeled as a linear fit, the negative slope of which was used for comparison. Error bars show ±SD, n ≥ 6 valves per condition. Asterisks signify statistical differences according to a Student's t-test ($p \leq 0.05$).

Likewise, fiber alignment with stretch is reduced in $^{C1039G/+}$*Fbn1* mitral valves in comparison to wildtype (0.36 ± 0.08 vs. 0.85 ± 0.12, P<0.05) (Figure 5.10). This suggests that matrix fiber reorganization with stretch is also impaired in mitral valves of $^{C1039G/+}$*Fbn1* mice, which may explain in part their reduced global tissue stiffness.

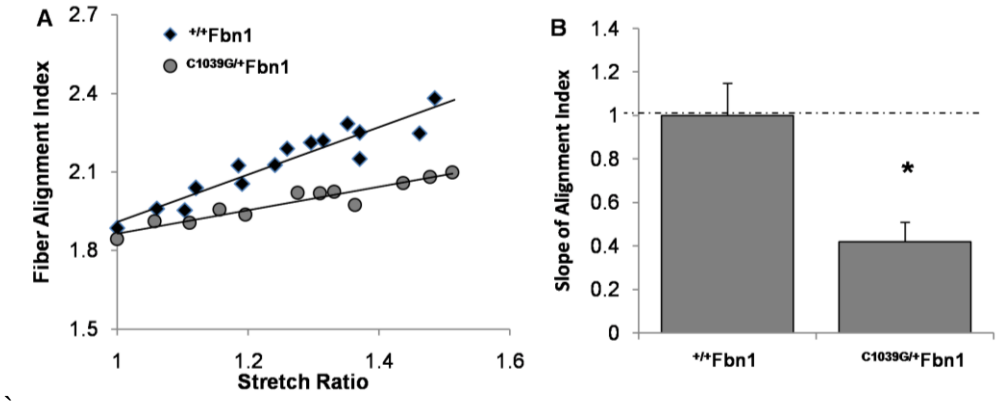

Figure 5.10 – Fiber alignment analysis of $^{+/+}$*Fbn1* and $^{C1039G/+}$*Fbn1* at 4 months. (A) Representative fiber-alignment curve as defined by the Fourier-Transform. (B) Fiber-alignment curves were modeled as a linear fit and the negative slope was used for comparison. Error bars show ±SD, n ≥ 6. Asterisks signify statistical differences according to a Student's t-test (p ≤ 0.05).

5.4.4: Fractional composition of the extracellular matrix components in the $^{C1039G/+}$Fbn1 mitral valves. The fraction of connective tissue was found significantly less in the $^{C1039G/+}$*Fbn1* (0.51 ± 0.18) compared to the $^{+/+}$*Fbn1* leaflets (1 ± 0.28, P<0.05) (Figure 5.11A-C). Less compacted collagen was present at the attachment zone, but extensive GAGs were present throughout the leaflet with a noticeable reduction in the fibrosa layer. The collagen to GAG fractional ratio was significantly less in the $^{C1039G/+}$*Fbn1* (0.44 ± 0.26) compared to the $^{+/+}$*Fbn1* (2.94 ± 0.84, P<0.05) (Figure 5.11D-F). In contrast to the layer specific elastin present in wildtype valves, mutant valves contained significantly less fraction of elastin (0.75 ± 0.17 for C1039G/+ compared to 1 ± 0.07 for wildtype, P<0.05), which was less organized throughout the

leaflet (Figure 5.11G-I). Collectively, these results indicate that decreased stiffness with *Fbn1* mutation correlates with a reduction in the amount of connective tissue fraction, elastin fraction, and collagen/GAG fractional ratio.

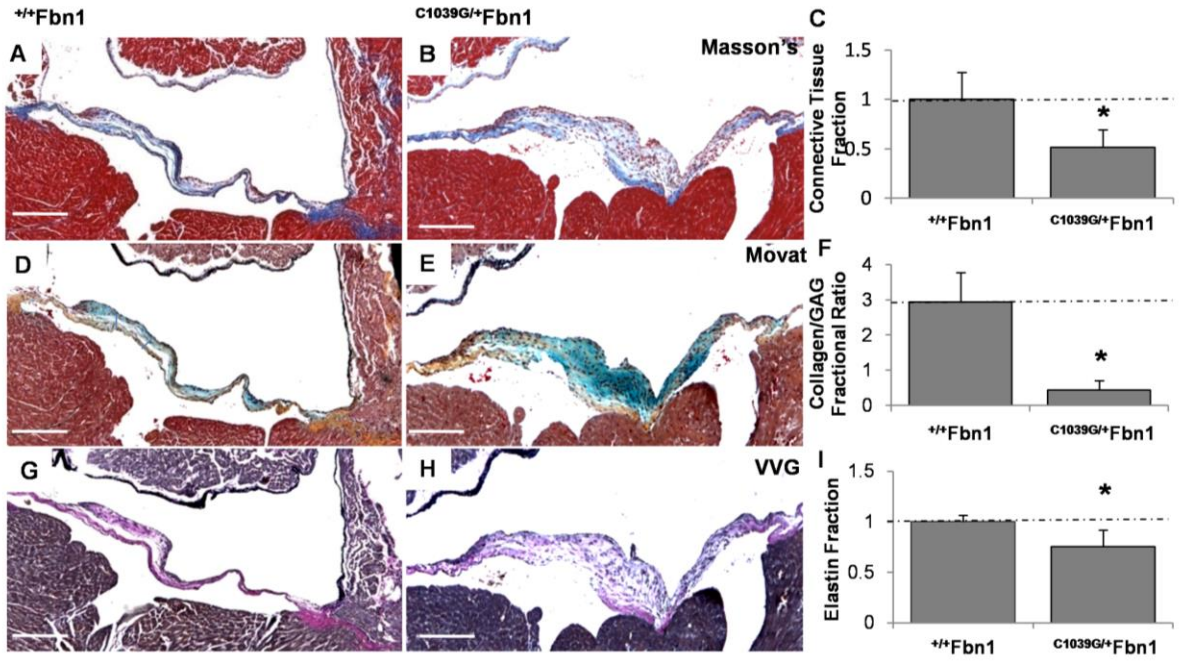

Figure 5.11 – Differences between $^{+/+}$*Fbn1* and $^{C1039G/+}$*Fbn1* mitral valve matrix composition at 4 months. (A-B) Masson's Trichrome reveals a reduction in the fractional amount of connective tissue in the marfan mitral valve compared to wildtype. (C) Digital quantification of the connective tissue composition using color thresholding, with blue regions denoting connective tissue. (D-F) Movat's stain reveals over 3-fold reduction in the fractional amount of collagen compared to GAGs in the Marfan mitral valve relative to the wildtype (yellow-collagen, blue-GAGs). (G-I) Verhoeff's–van Gieson (VVG) stain reveals a significant reduction in the fractional amount of elastin in the Marfan mitral valve compared to the wildtype (purple/black-elastin). Magnification, ×4. Scale bars: 200 μm. Error bars show ±SD, n ≥ 3 valves per condition. Asterisks denote statistical differences according to a Student's t-test ($p \leq 0.05$).

5.5: Discussion

Myxomatous degeneration of the MV with consequent valve prolapse and dysfunction is a common phenotype, affecting 2-3% of individuals in the general population [3]. Over the last decade, murine models have been indispensible for understanding many of the functional consequences of mutations in fibrillin-1 [13,21,22]. The bulk of these studies have established

the critical contribution of fibrillin-1 deficiency to disease progression through altered cell–matrix interactions and dysregulated TGFβ signaling. To further evaluate the global biomechanical and local cell-matrix relationships, we developed a novel method to evaluate mouse MV architecture during loaded conditions. We found that in the *Fbn1* mutant mice, the effective modulus was less, which was supported by our histological analysis revealing a reduction in the amount of connective tissue fraction, elastin fraction, and collagen/GAG fractional ratio. Interestingly, both valve deformation and fiber alignment were significantly reduced, suggesting that MV cell-matrix interactions become progressively more decoupled. Quantitative differences between local cell or matrix deformations and global tissue stretch may be an important contributor to pathological tissue remodeling in valves, whether originated by aging, mechanical, or genetic mutation contexts.

The ability to investigate the integration of mechanics and genetics in small animal models across multiple length scales represents a powerful tool for quantifying functional consequences of sub-lethal mutations. Historically, this has been particularly challenging due to the difficulty with attaching small tissues (0.2mm-2mm), measuring force ranges (10μN-10mN), and imaging of underlying microarchitecture. Pipette aspiration has been a classic approach for measuring the mechanical properties of small tissues. Butcher et al. used this method to measure the nonlinear pseudoelastic biomechanics of developing chick atrioventricular cushions while, Krishnamurthy et al., used a similar approach to measure the measure regional mechanical properties of mouse aortic valve tissue [20,23]. Others have used micro-indentation testing systems to determine the compressive and biphasic mechanical properties of cartilage in the small joints of the mouse using glass fibers [24]. More sophisticated devices have been designed to take advantage of the cylindrical geometry of soft tissues, such as blood vessels. Small caliber (50–5000 μm) blood vessels mounted on cannulaes provide a substrate for well-controlled mechanical loads and multiaxial mechanical tests [25]. While these approaches

provide tremendous information in small model tissue biomechanics, quantification of the underlying cell deformation is necessary for understanding the mechanobiological consequences of tissues at physiological levels. To overcome these limitations, a novel stretching apparatus and gripping method was implemented to directly quantify both global tissue biomechanics and local cellular deformation and matrix fiber realignment in murine mitral valves.

The clinical manifestation of the MV when it is affected in MFS involves redundant prolongation of one or both leaflets, often accompanied by myxomatous thickening [26]. MV prolapse and regurgitation also commonly occur in related conditions. A retrospective review and ultrasound based comparison of MV morphology at the time of MV surgery in MFS and myxomatous non-syndromic MV disease reported that individuals with MFS presented at an earlier age (41 vs. 57 years, respectively), and that the anterior MV leaflet was longer in MFS than in non-syndromic MV disease (40 vs. 33 mm, respectively) [27]. As with many phenotypic characteristics of MFS, the presence and severity of MV prolapse, thickening, and regurgitation often vary within families segregating the same *Fbn1* gene mutation [28,29]. In mice, MV leaflets heterozygous or homozygous for a *Fbn1* mutation were also shown to be both longer and thicker than in wild-type littermates, and these differences correlated with increased TGFβ signaling and increased production of collagen. Adult heterozygous mutant mice were also shown to have MV prolapse by high-resolution echocardiography [13]. Furthermore, in sheep with displaced papillary muscles (commonly used to replicate MV regurgitation), assessment of total mitral leaflet area by 3-D echo was found to increase with stretch, and was 2.8 times thicker than normal [30]. While further investigation is needed, these findings suggest that adaptive mechanisms within the MV are connected to the in-vivo physiological loads within the MV. In the case of the *Fbn1* mutation, increased leaflet length/thickness, annulus diameter, and transvalvular pressure all

govern the stress distribution within the MV (tissue deformation), which potentially leads to valve remodeling and aberrant function.

Recent studies have investigated both the in-vitro and in-vivo dynamic deformation of the MV. It was found that the MV anterior leaflet experiences large anisotropic strains, approaching stretch ratios of 1.2 in the circumferential and 1.4 in the radial direction at physiological levels [31]. Furthermore, their observations also suggest that changes in left ventricular pressure and annular geometry result in altered effective leaflet stiffness, which may be an important factor in reducing leaflet stress [32]. From our studies, the decreased compliance of *Fbn1* MV implies they may be subjected to increased strain at the same transvalvular pressures. However, we find that the interstitial cells within *Fbn1* valves do not deform to the same degree at the same strain. These two datasets suggest there may exist a balance between excess loading and altered mechanosensitivity that can initiate or exacerbate pathological cell remodeling. If the known differences in growth factor expression, particularly TGFβ, is additionally factored in, clearly uncovering the mechanobiological mechanism of MV dysfunction in MFS remains a major challenge. The additional mechanical tools generated from this study enable important new hypotheses and avenues of research in this direction.

Our histochemical analysis also revealed a large abundance of GAGs, which was not unexpected as myxomatous valves have been shown to contain more GAGs and PGs than normal [8,33]. In MV excised from human patients, myxomatous leaflets were found to have 3% more water content and 30% higher GAG concentrations than normal mitral leaflets, which are thought to influence the hydration-related "floppy" nature of these tissues [34]. Biomechanical testing of myxomatous valves have also been shown physically and mechanically different from normal MV leaflets in human patients such that they are more extensible and less stiff [35]. These findings align closely with our results, which suggest that the functional consequence of

valve thickening, reduced fiber alignment, and abnormal matrix deposition ultimately leads to a reduction in tissue stiffness. Upon substantial remodeling, the functional consequence of MV leaflets can ultimately result in prolapse and regurgitation [36]. Although several studies have reported disparate prevalence of MV prolapse among individuals with MFS, the biomechanical remodeling within the MV is substantial [37]. We suspect the underlying mechanobiological regulation of VIC is a critical component for understanding the long-term biomechanical and pathological consequences of MV disease in MFS.

Interestingly, at the cellular level, we found that both collagen fiber alignment and overall cellular deformation were significantly reduced in the *Fbn1* mutant leaflets. Although the underlying mechanism is currently unknown, cellular deformation has been shown dependent upon integrin binding and traction force generation. Numerous studies have shown that the degree of traction force is proportional to substrate stiffness, via integrins [38]. Strengthening of focal adhesions is thought to dominate on stiffer substrates as compared to soft substrates [39]. Bax et al., reported an RGD sequence of fibrillin-1 that supports cellular adhesion in vitro via integrin αvβ3. Using human dermal fibroblasts, fibrillin-1 protein fragments induced signaling events that led to cell spreading, altered cytoskeletal organization, and enhanced extracellular fibrillin-1 deposition [40]. Mutations in integrin binding also result in a unique human phenotype called “stiff skin syndrome (SSS)”. Cultured dermal fibroblasts from patients with SSS showed dysregulated amounts activated (phosphorylated) focal adhesion kinase (pFAK) [41]. Therefore, the increased GAG content, disorganized extracellular matrix, and/or altered integrin motifs may regulate traction force generation, and hence the ability to deform during mechanical load.

Few studies have investigated the mechano-regulation of VIC in response to altered pressure or strain. VIC isolated in vitro and mechanically strained at 10%, 14%, and 20% have also been shown to upregulate collagen synthesis by an increase in [3H]-proline incorporation in a strain

dependent manner [42]. Hence, collagen synthesis by VICs is dependent upon the degree and duration of stretch. Furthermore, when pulmonary VICs were exposed to aortic pressure levels, as occurs following the Ross operation, collagen and sulfated glycosaminoglycan synthesis were increased significantly [43]. This demonstrates that VICs are capable of remodeling the ECM in response to changes in strain magnitude and/or the stress state of the tissue. Comparing our findings between age and *Fbn1* mutation, we find a strong similarity between altered local cell-matrix kinematics and changes in matrix composition. Interestingly, leaflet thickness, blood pressure, and MV annulus were also correlated [15,44,45]. This suggests that elevated blood pressure magnitudes (age dependent) and/or altered valve stress states may dictate the mechano-biological response, possibly through regulating ECM composition and hence, overall cellular deformation.

Taken together, an important question previously unidentified and revealed by this study is whether these alterations in local cell-matrix interactions with stretch are a cause or consequence of valve tissue remodeling. Three possible hypotheses into the mechanical etiologies of MFS valve dysfunction include 1) the interstitial cells experience a reduced mechanical force distribution in *Fbn1* mutant vs. wild-type tissue, 2) cells in both cases experience the same loads but, the *Fbn1* mutant interstitial cell is unable to sense it correctly (e.g. its mechanotransduction processes are tuned improperly), or 3) both cells sense the same loads but the *Fbn1* mutant cells can't respond appropriately, pathologically remodeling the matrix instead of augmenting/maintaining its mature organization. Studies have shown that cytokines and growth factor signaling is altered in *Fbn1* mutant valves, but it is yet unclear whether they are genetically prescribed or the consequence of the altered mechanobiological signaling (i.e. integrin binding or expression). Further investigation systematically testing these different hypotheses is ongoing.

Our results provide a framework to explore a fibrillin-1 mutation leading to abnormal biomechanics/mechanobiology and clinical manifestations in MFS associated MV disease. The most novel and unexpected finding is that not only are extracellular matrix components altered, but the response of VIC to stress is also changed, so that cells effectively sense less stretch in MFS during normal physiological loads. This decoupling of local cell and matrix kinematics from global valve tissue stretch may have direct implications in the ability of VIC to maintain normal homeostatic cellular deformation. Pathological changes in MV matrix composition and organization ensue, which in turn weakens the tissue. These results support the potential for matrix stabilization techniques such as collagen crosslinking or radiofrequency ablation for maintaining mechanical performance and cell mechanobiology, and thereby delay pathological remodeling [46].

The mouse MV is an extremely thin piece of tissue, with an average thickness in the mid region of ≈ 30-40μm (4-5 cells thick), compared to the ≈ 500-700μm thick human MV [47]. We therefore used confocal z-stacks to capture both collagen fibers and cells across the entire thickness. With this method, we found that collagen fiber alignment and un-crimping occurred simultaneously across the valve, but potential thickness dependent inhomogeneities were not addressable. We also measured the circularity index (CI) of cells rather than nuclear aspect ratios (NAR). While CI is representative of cell morphology, cells were well spread in almost all cases, potentially limiting our sensitivity to deformation. However, using the change in CI, we were able to ascertain significant differences in local cell behavior in association with both age and *Fbn1* genotype.

In conclusion, degenerative biomechanical remodeling of the MV is a key component of Marfan syndrome. Through quantifying global biomechanical and local cell-matrix relationships in *Fbn1* mutant murine mitral valves, we found that local cell and matrix kinematics are decoupled to

different degrees correlating with magnitude of global valve tissue stretch. Changes in local cell-matrix deformation relationships may be an important metric for determining mechanisms of normal and pathological tissue remodeling in valves, as in aging or genetic mutation.

REFERENCES

1. Pyeritz RE (2000) The Marfan syndrome. Annu Rev Med 51: 481-510.
2. Dietz HC, Loeys B, Carta L, Ramirez F (2005) Recent progress towards a molecular understanding of Marfan syndrome. Am J Med Genet C Semin Med Genet 139C: 4-9.
3. Freed LA, Levy D, Levine RA, Larson MG, Evans JC, et al. (1999) Prevalence and clinical outcome of mitral-valve prolapse. N Engl J Med 341: 1-7.
4. Judge DP, Dietz HC (2008) Therapy of Marfan syndrome. Annu Rev Med 59: 43-59.
5. Mendelson K, Schoen FJ (2006) Heart valve tissue engineering: concepts, approaches, progress, and challenges. Ann Biomed Eng 34: 1799-1819.
6. Mulholland DL, Gotlieb AI (1997) Cardiac valve interstitial cells: Regulator of valve structure and function. Cardiovascular Pathology 6: 167-174.
7. Kunzelman KS, Cochran RP (1992) Stress/strain characteristics of porcine mitral valve tissue: parallel versus perpendicular collagen orientation. J Card Surg 7: 71-78.
8. Tamura K, Fukuda Y, Ishizaki M, Masuda Y, Yamanaka N, et al. (1995) Abnormalities in elastic fibers and other connective-tissue components of floppy mitral valve. Am Heart J 129: 1149-1158.
9. Durbin AD, Gotlieb AI (2002) Advances towards understanding heart valve response to injury. Cardiovascular Pathology 11: 69-77.
10. Sherratt MJ, Baldock C, Haston JL, Holmes DF, Jones CJ, et al. (2003) Fibrillin microfibrils are stiff reinforcing fibres in compliant tissues. J Mol Biol 332: 183-193.
11. Lee SS, Knott V, Jovanovic J, Harlos K, Grimes JM, et al. (2004) Structure of the integrin binding fragment from fibrillin-1 gives new insights into microfibril organization. Structure 12: 717-729.
12. Sakamoto H, Broekelmann T, Cheresh DA, Ramirez F, Rosenbloom J, et al. (1996) Cell-type specific recognition of RGD- and non-RGD-containing cell binding domains in fibrillin-1. J Biol Chem 271: 4916-4922.
13. Ng CM, Cheng A, Myers LA, Martinez-Murillo F, Jie C, et al. (2004) TGF-beta-dependent pathogenesis of mitral valve prolapse in a mouse model of Marfan syndrome. J Clin Invest 114: 1586-1592.
14. Sasoglu FM, Bohl AJ, Layton BE (2007) Design and microfabrication of a high-aspect-ratio PDMS microbeam array for parallel nanonewton force measurement and protein printing. Journal of Micromechanics and Microengineering 17: 623-632.
15. Hinton RB, Jr., Alfieri CM, Witt SA, Glascock BJ, Khoury PR, et al. (2008) Mouse heart valve structure and function: echocardiographic and morphometric analyses from the fetus through the aged adult. Am J Physiol Heart Circ Physiol 294: H2480-2488.
16. Judge DP, Biery NJ, Keene DR, Geubtner J, Myers L, et al. (2004) Evidence for a critical contribution of haploinsufficiency in the complex pathogenesis of Marfan syndrome. J Clin Invest 114: 172-181.
17. Helmke BP, Goldman RD, Davies PF (2000) Rapid displacement of vimentin intermediate filaments in living endothelial cells exposed to flow. Circ Res 86: 745-752.
18. Fung YC (1967) Elasticity of soft tissues in simple elongation. Am J Physiol 213: 1532-1544.
19. Bowles RD, Williams RM, Zipfel WR, Bonassar LJ (2010) Self-assembly of aligned tissue-engineered annulus fibrosus and intervertebral disc composite via collagen gel contraction. Tissue Eng Part A 16: 1339-1348.
20. Butcher JT, McQuinn TC, Sedmera D, Turner D, Markwald RR (2007) Transitions in early embryonic atrioventricular valvular function correspond with changes in cushion biomechanics that are predictable by tissue composition. Circ Res 100: 1503-1511.

21. Habashi JP, Doyle JJ, Holm TM, Aziz H, Schoenhoff F, et al. (2011) Angiotensin II type 2 receptor signaling attenuates aortic aneurysm in mice through ERK antagonism. Science 332: 361-365.
22. Habashi JP, Judge DP, Holm TM, Cohn RD, Loeys BL, et al. (2006) Losartan, an AT1 antagonist, prevents aortic aneurysm in a mouse model of Marfan syndrome. Science 312: 117-121.
23. Krishnamurthy VK, Guilak F, Narmoneva DA, Hinton RB (2011) Regional structure-function relationships in mouse aortic valve tissue. J Biomech 44: 77-83.
24. Cao L, Youn I, Guilak F, Setton LA (2006) Compressive properties of mouse articular cartilage determined in a novel micro-indentation test method and biphasic finite element model. J Biomech Eng 128: 766-771.
25. Gleason RL, Gray SP, Wilson E, Humphrey JD (2004) A multiaxial computer-controlled organ culture and biomechanical device for mouse carotid arteries. J Biomech Eng 126: 787-795.
26. Barlow JB, Bosman CK (1966) Aneurysmal protrusion of the posterior leaflet of the mitral valve. An auscultatory-electrocardiographic syndrome. Am Heart J 71: 166-178.
27. Bhudia SK, Troughton R, Lam BK, Rajeswaran J, Mills WR, et al. (2006) Mitral valve surgery in the adult Marfan syndrome patient. Ann Thorac Surg 81: 843-848.
28. Montgomery RA, Geraghty MT, Bull E, Gelb BD, Johnson M, et al. (1998) Multiple molecular mechanisms underlying subdiagnostic variants of Marfan syndrome. Am J Hum Genet 63: 1703-1711.
29. Aalberts JJ, Schuurman AG, Pals G, Hamel BJ, Bosman G, et al. (2010) Recurrent and founder mutations in the Netherlands: Extensive clinical variability in Marfan syndrome patients with a single novel recurrent fibrillin-1 missense mutation. Neth Heart J 18: 85-89.
30. Dal-Bianco JP, Aikawa E, Bischoff J, Guerrero JL, Handschumacher MD, et al. (2009) Active adaptation of the tethered mitral valve: insights into a compensatory mechanism for functional mitral regurgitation. Circulation 120: 334-342.
31. Grashow JS, Yoganathan AP, Sacks MS (2006) Biaixal stress-stretch behavior of the mitral valve anterior leaflet at physiologic strain rates. Ann Biomed Eng 34: 315-325.
32. Sacks MS, Enomoto Y, Graybill JR, Merryman WD, Zeeshan A, et al. (2006) In-vivo dynamic deformation of the mitral valve anterior leaflet. Ann Thorac Surg 82: 1369-1377.
33. Rabkin E, Aikawa M, Stone JR, Fukumoto Y, Libby P, et al. (2001) Activated interstitial myofibroblasts express catabolic enzymes and mediate matrix remodeling in myxomatous heart valves. Circulation 104: 2525-2532.
34. Grande-Allen KJ, Griffin BP, Ratliff NB, Cosgrove DM, Vesely I (2003) Glycosaminoglycan profiles of myxomatous mitral leaflets and chordae parallel the severity of mechanical alterations. J Am Coll Cardiol 42: 271-277.
35. Barber JE, Kasper FK, Ratliff NB, Cosgrove DM, Griffin BP, et al. (2001) Mechanical properties of myxomatous mitral valves. J Thorac Cardiovasc Surg 122: 955-962.
36. Weyman AE, Scherrer-Crosbie M (2004) Marfan syndrome and mitral valve prolapse. J Clin Invest 114: 1543-1546.
37. Judge DP, Rouf R, Habashi J, Dietz HC (2011) Mitral valve disease in marfan syndrome and related disorders. J Cardiovasc Transl Res 4: 741-747.
38. Yeung T, Georges PC, Flanagan LA, Marg B, Ortiz M, et al. (2005) Effects of substrate stiffness on cell morphology, cytoskeletal structure, and adhesion. Cell Motil Cytoskeleton 60: 24-34.
39. Hoffman BD, Grashoff C, Schwartz MA (2011) Dynamic molecular processes mediate cellular mechanotransduction. Nature 475: 316-323.

40. Bax DV, Bernard SE, Lomas A, Morgan A, Humphries J, et al. (2003) Cell adhesion to fibrillin-1 molecules and microfibrils is mediated by alpha 5 beta 1 and alpha v beta 3 integrins. J Biol Chem 278: 34605-34616.
41. Loeys BL, Gerber EE, Riegert-Johnson D, Iqbal S, Whiteman P, et al. (2010) Mutations in fibrillin-1 cause congenital scleroderma: stiff skin syndrome. Sci Transl Med 2: 23ra20.
42. Ku CH, Johnson PH, Batten P, Sarathchandra P, Chambers RC, et al. (2006) Collagen synthesis by mesenchymal stem cells and aortic valve interstitial cells in response to mechanical stretch. Cardiovasc Res 71: 548-556.
43. Ikhumetse JD, Konduri S, Warnock JN, Xing Y, Yoganathand AP (2006) Cyclic aortic pressure affects the biological properties of porcine pulmonary valve leaflets. J Heart Valve Dis 15: 295-302.
44. Tiemann K, Weyer D, Djoufack PC, Ghanem A, Lewalter T, et al. (2003) Increasing myocardial contraction and blood pressure in C57BL/6 mice during early postnatal development. Am J Physiol Heart Circ Physiol 284: H464-474.
45. Yang B, Larson DF, Watson R (1999) Age-related left ventricular function in the mouse: analysis based on in vivo pressure-volume relationships. Am J Physiol 277: H1906-1913.
46. Shawn L. Price CGN, Jeffrey L. Williams, H. Thomas McElderry, W. David Merryman (2010) Radiofrequency Ablation Directionally Alters Geometry and Biomechanical Compliance of Mitral Valve Leaflets: Refinement of a Novel Percutaneous Treatment Strategy Cardiovascular Engineering and Technology Volume 1: 194-201.
47. Sahasakul Y, Edwards WD, Naessens JM, Tajik AJ (1988) Age-related changes in aortic and mitral valve thickness: implications for two-dimensional echocardiography based on an autopsy study of 200 normal human hearts. Am J Cardiol 62: 424-430.

CHAPTER 6

HIERARCHICAL APPROACHES FOR SYSTEMS MODELING DURING CARDIAC DEVELOPMENT

6.1: Summary

Ordered cardiac morphogenesis and function is essential for all vertebrate life. The heart begins as a simple contractile tube, but quickly grows and morphs into a multi-chambered pumping organ, complete with valves, while maintaining regulation of blood flow and nutrient distribution. Though not identical, cardiac morphogenesis shares many molecular and morphological processes across vertebrate species. Quantitative data across multiple time and length scales have been gathered through decades of reductionist single variable analyses. These range from detailed molecular signaling pathways at the cellular levels to cardiac function at the tissue/organ levels. However, none of these components act in true isolation from others, and each in turn exhibits short and long-range effects in both time and space. Genetic expression networks may not just be shifted by the absence of a gene, but an entire signaling cascade left "on" or "off" depending on the condition. Also taking into account local microenvironmental changes throughout development, it is apparent that a systems level approach is an essential resource to accelerate information generation concerning the functional relationships across multiple length scales (molecular data vs. physiological function) and structural development. In this review, we discuss relevant *in vivo* and *in vitro* experimental approaches, compare different computational frameworks for systems modeling, and discuss the latest information about systems modeling of cardiac development. Lastly, we conclude with some important future directions for cardiac systems modeling.

6.2: Background

The first definitive organ to form in the embryo is the heart, whose morphogenesis, growth, and integrated function are essential to embryonic survival. The embryonic heart begins as a spontaneously contractile tube with an outer muscular (myocardial) layer and an inner endothelial (endocardial) layer. Myocardial and endocardial progenitor cells arise from bilateral populations of mesodermal cells close to the midbrain–hindbrain boundary [1]. Shortly before circulation is established, these mesodermal cells migrate medially to form a linear heart tube. This simple tube then undergoes complex morphogenetic movements that lead to the formation of a looped, multi-chambered organ complete with valves to regulate blood flow [2-4]. Though much research has highlighted roles of individual genes, the complex molecular networks that control this process are only beginning to be elucidated. Recent evidence suggests that the cardiogenic transcriptome is dependent upon the combinatorial binding of “master” transcription factors Gata4, Mef2a, Nkx2.5, and Srf. Together, these transcription factors have been targeted for regulation in over 1600 genes [5]. Only a small fraction of these genes have been investigated through the use of genetic mutant animal models, and filling this gap would consume significant time and resources Each mutation causes compensatory changes in signaling networks that may further confound understanding, especially in less pronounced phenotypes. Genetic regulation is, however, only a fraction of the story. Cells are highly sensitive to microenvironmental factors (e.g. physiological conditions such as oxygen content or pressure load) which affect molecular targets across multiple scales (e.g. transcript levels, protein modifications, histone interactions) which sometimes result in divergent effects [6, 7]. Deciphering the complexity is even more challenging when considering how features change in time (across development) and space (region of the heart).

Systems biology implements a process to identify emergent static and dynamic properties to obtain, replicate, and predict biological phenomena. The systems approach synthesizes experimental data into a computational model that not only simulates the previous data but can be used to predict previously untested interactions. These predictions in turn motivate further biological experiments; the results of which are used to then validate and improve the model [8, 9]. First, one must identify the core architecture driving a cellular process. A network is, technically speaking, a graph consisting of nodes connected by edges. In biological networks, nodes typically represent molecules like gene transcripts or proteins. Edges define the type of connection between nodes, e.g. interactions or relationships such as protein–protein interactions or transcription factor-DNA binding. Examples of biological networks are gene networks, transcription networks, protein–protein interaction networks, and metabolomic networks. This architecture can be derived from a variety of sources, including primary literature and database websites. Relationships describing the node interactions include purely empirical, statistical, or defined by continuous equations (e.g. reaction-diffusion). Once the core architecture is in place, both high and low throughput, quantitative data from multiple single or small number factor, primary experiments are gathered. The model is then trained against the primary data to determine preliminary coefficient subsets to mirror the data, such that the biological networks provide physiologically relevant information. From the newly trained network, simulations can be conducted across possible parameter sets to prioritize and identify key regulatory nodes and recognize critical pathways through robustness analysis (Figure 6A.1). The predictions are then tested on follow-up biological experiments. These results can also be applied back to re-train the model to strengthen its specificity and predicative capacity.

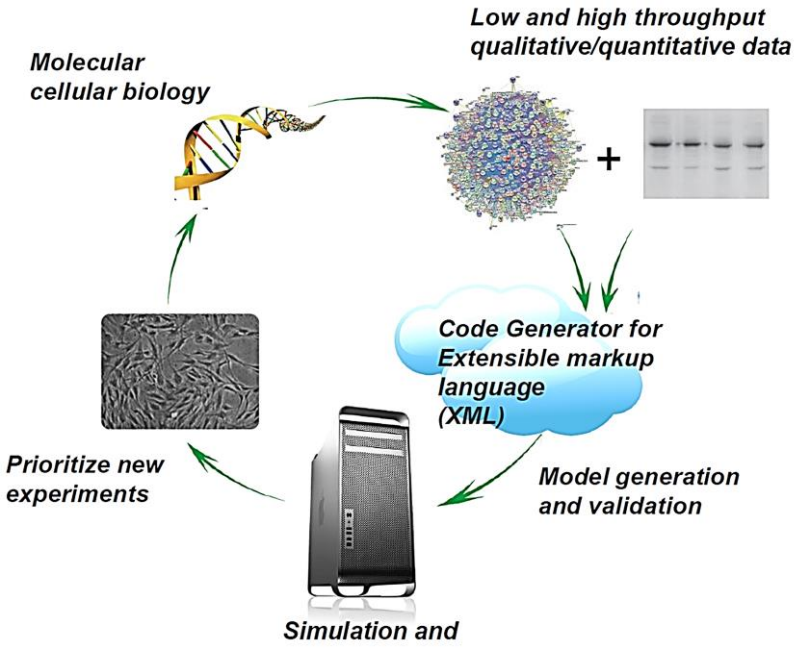

Figure 6.1 – The objective of systems biology is to integrate low- and high-throughput data with predictive computer modeling to better understand the properties of networks and cell systems important to human health. To apply such an approach, one must identify the core architecture driving a cellular process through biological networks, gather both high and low throughput quantitative data from single factor experiments, train and validate the model for physiological relevance, and run simulations in order to prioritize wet experiments.

Complex systems like the heart are composed of diverse elements constructed spatially and temporally in a hierarchical fashion [10]. Analyses of these multi-scale systems is likely most efficient by linking together different types of models that are ideal for particular scales. It is impossible and impractical to model the organ and tissue levels in the same framework as at the molecular and cellular levels, because they are driven by completely different stimuli that result in different responses [11]. A systems approach is necessary to connect, inform, and predict the functional relationships that span these length scales (e.g. molecular data versus physiological function and structural development) [12]. A cardiac developmental systems model has the potential to accelerate the discovery of key regulatory aspects of heart development and predict testable hypotheses about cardiac function eventually motivating new

approaches for congenital malformations therapy. Although the necessary framework capable of integrating such massive amounts of data is still in its infancy, recent systems approaches have shown promise for enabling the identification of critical signaling protein complexes and, moreover, for predicting tissue morphogenesis through multi-scale approaches.

6.2.1: Computational resources for data integration and model implementation

The progressive accumulation of enormous amounts of heterogeneous molecular response data has created a significant need to create databases that can organize, store, and rapidly retrieve pertinent information. In this section we will discuss the organizational framework necessary to approach a systems level question: (1) integration of heterogeneous datasets from a wide spectrum of databases, (2) standardization of systems languages to facilitate data representation and interoperability, and (3) robust integrative software tools available for systems biology research.

6.2.2: Availability of databases for integrating biological information

The emergence of large-scale biological information has driven the development of global databases. These databases are important for the future of systems biology, as they centralize quantitative and qualitative data, ranging from protein structures to signaling pathways. However, to fully take advantage of these databases (biological information in general), one would need to obtain repeatedly the information necessary to piece together the larger network, which is not at all practical [13, 14]. A comprehensive database which integrates not only "-omics" datasets from experiments and literature, but also other information such as kinetic data and existing mathematical models is invaluable given the resources currently available to researchers [15-18]. There are many resources for integrated data analysis as reviewed by Joyce and Palsson [19, 20]. To name a few, HCNet [21], GEO database [22], and Cardiac

Integrated Database Management System (CIDMS) all contain information related to genetic regulation of heart development and function.

6.2.3: Multi-scale standardization of system biology languages

As previously mentioned, a major problem in systems biology is how to establish and maintain cohesion between data derived from multiple independent experiments using different cell sources with slightly different controls, doses, time-courses, and analysis methods. Standards for the interpretation, handling, and dissemination of data should be given priority. It is crucial that individual research groups be able to exchange their models and create publicly accessible data banks and software environments that function with a broad selection of tool sets. There are many data exchange formats currently available to aid in the exchange of information such as MIAME for microarray experiments [23], PSI-MI for protein–protein interaction, BIOPAX for pathways, and MIRIAM for biochemical models [24]. SBML [25], CellML [26], and FieldML [27] are machine-readable formats and standard forms of information exchange between software tools that provide both spatially distinct qualitative and quantitative models of biochemical networks (Sauro and Bergmann 2008; Kohl 2011). On the other hand, ontologies are well-structured controlled platforms providing standard definitions and concepts, as they aid in facilitating semantic-level data integration. Systems Biology Ontology (SBO) and Systems Biology Graphical Notation (SBGN) projects are also gaining popularity and have been initiated. For example, ontologies are important to define spatial domains at both the molecular and cellular levels (GO-MF-Gene Ontology Molecular Function, CBO-Cell behavior Ontology) while their function may be determined by the physics of biology and/or phenotype and traits (OPB-Ontology of Physics for biology, PATO-Phenotype and Traits Ontology). However, the XML based languages described above have been adopted as standards for representing biological

data despite the limitation in data interoperability. There are multiple resources available that discuss the topics mentioned above in depth [28-30].

6.2.4: Example approaches for multi-scale simulation of valvulogenesis

Many examples illustrating a systematic approach could be taken from heart development, but for this purpose we will discuss heart valve morphogenesis, as it is a fundamentally important component of cardiac development and a process for which significant data exists characterizing the anatomical morphogenesis, microstructural remodeling, and molecular regulation [31] (Figure 6A.2). Briefly, valvulogenesis initiates through a process called endocardial-to-mesenchymal transition (EMT) by which the endocardial lining in specific regions of the linear heart tube (in the atrioventricular canal and outflow tract segments) differentiate into a mesenchymal phenotype and invade into the gelatinous matrix underneath called the cardiac jelly. EMT is characterized by loss of tight junctions, downregulation of cell-cell adhesive contacts (e.g. E-cadherin, PECAM1) upregulation of cell-matrix adhesions (integrins), and development of contractile cytoskeletal machinery [32]. Continued cellularization and expansion of these tissue regions creates apposing pairs of tissues dubbed “cushions” that act as primitive valves to maintain unidirectional blood flow[33] [34]. This cellular transformation of EMT has also been shown in other processes such as fibrosis and oncogenesis [35].

The need for systems biology is becoming more apparent as the complexity of EMT (both spatial and temporal fashion) remains to be fully elucidated [36]. By applying a standardized strategy through XML based languages and systematic ontologies, centralization of ideas, resources, and strategies will be critical for continual advancement of predicting complex tissue formation such as valvulogenesis. In Figure 6A.2 the different levels of spatial and temporal scales as they pertain to heart development and their associated modes of representation are

illustrated. A signaling network within the cell may be represented using an ordinary differential equation (ODE) within a markup language, such as SBML, that enable the network to be interpreted by many different modeling platforms. At the next level up, cell-cell interactions and their chemical signaling mechanisms can be represented by partial differential equations (PDEs) or Stochastic Petri Nets. For larger cell networks at the growing tissue level, some form of agent based modeling (ABM) is likely to be used. When looking at the level of the developing heart and its structural components, a finite element (FE) approach or a multiphysics simulation can be used to understand the functional relationship between the different components of the heart from its walls, valves. and vessels.

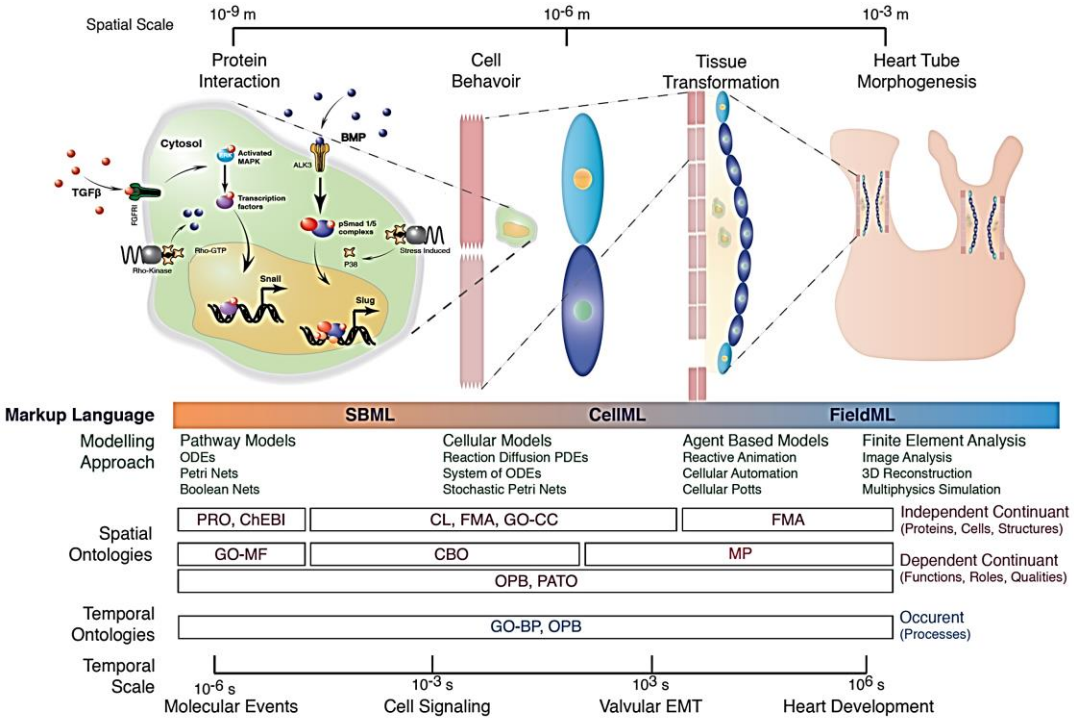

Figure 6.2 – Heart valve morphogenesis initiates through a process called epithelial-mesenchymal transition (EMT), in which endocardial cells loose cell-cell contacts (tight junctions), acquire cell-matrix adhesions, and undergo cytoskeleton rearrangement The modeling framework encompasses a wide range of spatial scales 10^{-9}m (proteins) to 10^{-3}m (the primitive heart tube), and temporal scales from 10^{-6}s (molecular events) to 10^{6}s (weeks of heart development). Multiple XML languages (SBML, CellML, FieldML) and ontology's are required for multi-scale modeling of this complex tissue formation during development. Figure adapted from [37]. *(PRO-Protein Ontology, ChEBI-Chemical Entities of Biological Interest, CL-Cell Type Ontology, FMA-Foundational Model of Anatomy, GO-CC-Gene Ontology Cellular*

6.2.5: Integrative software

There are multiple software tools available to the research community used to facilitate integration of cardiac systems data. The most useful programs (1) handle genome-size data sets, (2) integrate multiple data types obtained from systems measurements, (3) provide a way to map and model networks and pathways, and (4) contain a user friendly interface as well as visual display of both the data and models. We focus on software tools that do not require the individual to have an extensive background in computer programming but still prove to be valuable resources for cell biologists. Cytoscape, an open source bioinformatics computing environment, is used for integration, visualization, and query of biological networks [38, 39]. NAViGaTOR, another open source network visualization package, is an alternative to Cytoscape and uses Open Graphics Library (openGL) to allow for quick generation of a model and for visualization of both 2D and 3D graphical views [40]. VisANT is a lightweight network visualization tool able to run as a browser-based applet or as a standalone Java program. The name resolution feature of this tool maps all network nodes to gene names pairing the two proteins encoded by each gene simplifying the mapping feature; it is well designed with scalability concerns in mind [41]. Another open-source option is Pathway Assist. The focus of this tool is an automated natural language processing-based information extraction system for protein-protein and gene-gene functional interactions. Pathway Assist contains a built in database of protein interactions and cellular pathways [42]. CellDesigner is a structured diagram editor for drawing gene regulatory and biochemical networks stored in SBML for use in simulation packages [25, 43]. Through a graphical user interface, the dynamics of the network under defined input parameters can be observed [44]. Continuity 6 is a problem-solving environment for multi-scale modeling in bioengineering and physiology, especially cardiac

biomechanics, transport and electrophysiology, and it is distributed free for academic research [45].

6.2.6: Computational Modeling of Cardiac Development

A particularly challenging aspect of understanding the development process of cardiac formation is the complexity of information at multiple spatial scales evolving in a dynamic manner; thus, a systems approach to understand the flow of information is critical. As we move forward with cardiac model generation pertaining to cardiac development, there is considerable debate over the best strategy for biological simulation, whether it should be "bottom- up," "top-down" or some combination of the two [46, 47]. The consensus is that the approach be "middle-out," meaning that we start modeling at the level(s) at which there are rich biological data and then reach up and down to other levels [48]. In the case of the heart, we have benefited from the fact that multiple levels of quantitative data have been gathered ranging from detailed molecular signaling pathways at the cellular levels to complex 3D geometrical models of the whole organ [49, 50]. Connecting these structurally diverse and hierarchically spatial levels of interactions has been challenging. We will now discuss current cardiac models involving molecular regulation of the cardiac transcriptome, morphogenesis, and function.

6.2.7: Molecular Mechanisms Regulating the Cardiac Transcriptome

With the emergence of the human genome project and advancement of biotechniques, detailed signaling networks and systems models describing these networks have started to generate momentum. Recently, a group sought to map the molecular patterns critical to cardiogenesis through interrogated gene expression in stem cells undergoing guided differentiation, while generating genomic paradigms responsible for confinement of pluripotency. They found that examination of gene relationships revealed a non-stochastic network anchored by integrin,

WNT/β-catenin transforming growth factor β and vascular endothelial growth factor pathways, which were validated by manipulation of selected cascades that promoted or restrained cardiogenic yield. Moreover, candidate genes within anchor pathways acted as nodes that organized correlated expression profiles into functional clusters which collectively orchestrated and secured an overall cardiogenic theme [51].

Underlying these signaling pathways, a combination of key transcription factors was found to drive a wide range of gene expression essential for cardiac development [17, 52]. Using a custom Chip-chip analysis (promoter and enhancer sequenc) and cardiac myocte mRNA expression levels, it was found that the combinatorial contribution of Gata4, Mef2a, Nkx2.5, and Srf transcription factors was responsible for regulating the cardiac transcriptome. Specifically, the 91 target genes were bound by all four factors, 121 target genes were bound by three and 286 target genes were bound by two transcription factors, all targeting over 1600 genes. Surprisingly, Gata4 and Nkx2.5 had the lowest number of targets (345 for Gata4, 276 for Nkx2.5), but it was found that their co-binding to 143 genes made each transcription factor highly correlated [5] (Figure 6A.3).

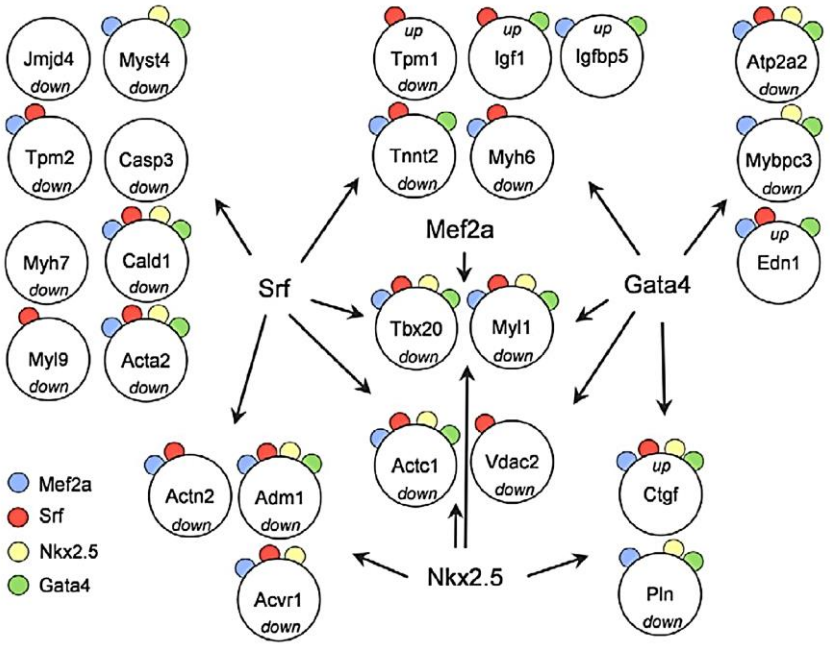

Figure 6.3 – Transcription factor network showing a selection of cardiac relevant genes (nkx 2.5, srf, gata4, mef2a) bound in ChIP-chip and/or ChIP-seq, and significantly differentially expressed in RNAi knockdown experiments of the respective factor. Up- and downregulation of genes is depicted and occurrence of ChIP binding marked by color-coded circles. Figure taken from [5].

Furthermore, histone modifications and microRNAs modulate the underlying functional consequence of these cardiac transcription factors. Histone-3 acetylation was found to have a strong correlation with Srf- and Gata4- dependent gene activation. Moreover, upon Srf knockdown, a large proportion of targets were found to regulate microRNAs (potentially explains up to 45% of indirect mRNA targets), which thus might represent an important intermediate layer of regulation. [5]. Interestingly, it was found that even these non-paralogous transcription factors can partially compensate each other's function, as shown through RNAi knockdown experiments. In addition, enzymatic complexes such as the Swi/Snf-like BAF complexes remodel chromatin to allow the transcriptional machinery access to heart-specific enhancers [53]. Through experimental observations, it was revealed that dynamic randomness of SWI/SNF occurs in the *cis* chromatin remodeling process. By applying a stochastic model, a

recent group identified the physiological properties of the chromatin remodeling process through a system of parametric microevents. Their simulations showed that SWI/SNF chromatin remodeling has low energy efficiency suggesting that the orchestrated chromatin remodeling makes few kilobase-pairs of the DNA accessible to the transcription machinery in a timely manner [54].

6.2.8: Cardiac Signaling Networks and Morphological Changes

Connecting these underlying molecular networks driving cardiac tissue morphogenesis is important for understanding aberrations, which underlie a wide spectrum of human disorders including congenital cardiac defects. A recent study sought to connect model human heart morphogenesis through dissecting the underlying functional signaling pathway. Using detailed phenotype information from deleterious mutations in 255 genes with high-confidence experimental interactome data, systematic analysis of spatio-temporal protein networks driving cardiac development were revealed. A striking temporal correlation between organ complexity and the number of discrete functional modules coordinating morphogenesis was found (Figure 6A.4). For example, abnormal myocardial trabeculae formation was found dependent upon core networks within the NOTCH, Focal Adhesion, and ERBB signaling pathways, while abnormal valve formation was found dependent upon core pathways within the ERBB, Retinoic Acid, and Neurotrophin signaling pathways. [55].

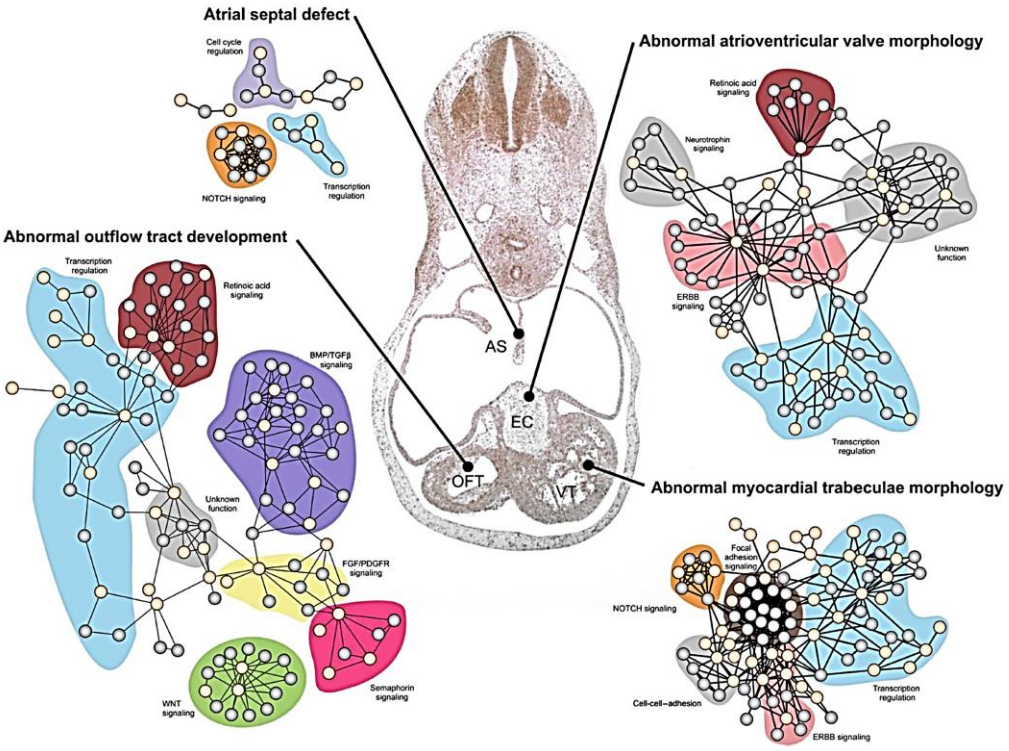

Figure 6.4 – Examples of four functional networks driving the development of different anatomical structures in the human heart. These four networks were constructed by analyzing the interaction patterns of four different sets of cardiac development (CD) proteins corresponding to the morphological groups 'atrial septal defects,' 'abnormal atrioventricular valve morphology,' 'abnormal myocardial trabeculae morphology,' and 'abnormal outflow tract development'. Centrally in the figure is a haematoxylin-eosin stained frontal section of the heart from a 37-day human embryo, where tissues affected by the four networks are marked. Figure taken from [55].

A follow up study by Lage et al. explored the relationships between congenital heart disease (CHD) risk factors and responses using datasets from similar studies of CHD in humans and model organisms. They found that CHD risk factors functionally converge in protein networks driving the development of specific anatomical structures (e.g., outflow tract, ventricular septum, and atrial septum) which are malformed by CHD. This integrative analysis of CHD risk factors and responses suggests a complex pattern of functional interactions between genomic variation and environmental exposures that modulate critical biological systems during heart development [56].

Interestingly, recapitulation of these critical signaling pathways were shown when murine embryos were exposed to high glucose, a condition known to induce cardiovascular defects in both animal models and humans. Through a mass spectrometry-based proteomics approach, critical protein clusters were found differentially expressed in embryos with defects from those with normal cardiovascular development. These protein clusters were mapped to adhesion/migration, differentiation, and insulin signaling pathways while correlating with increased protein levels observed in the amniotic fluid of human foetuses with CHD [57].

Toenjes and colleagues used a similar approach to precisely describe the variety of heart malformations observed in the patients using an integrative approach combining cardiac gene regulatory networks based on correlated gene expression and optimized prediction of transcription factor binding sites. From this combined approach, they were able to find genes that appeared to be specifically associated with certain phenotypes such as TOF-1-3 (Tetrology of Fallot), TGA (transposition of great arteries), or VSD (ventricular septal defect) [58].

6.2.9: Modeling Cardiac Function

A large number of models for cardiac function have been based proper physio-chemical or and/or biophysical principles that emphasize different levels of structural organization. Contrary to signaling networks, cellular networks use physical properties or rules that approximate individual cells into large scale combinations forming systems [15]. These models are computationally tractable and informative since predictability using intrinsic physical properties has proven reliable. For example, dynamic gap junction models coupled with cardiac cell models have proven insightful such that Ca^{2+} transients affect gap junction conductance during action potential propagation leading to potential arrhythmias [59-61]. Likewise, dynamics in

heart trabeculae with changing heart frequency (mechanical load increases during development) was found to support the hypothesis that mitochondrial matrix Ca^{2+} plays an important role in matching energy supply with mechanical demand in cardiac myocytes [62]. Other systems have focused solely on the mechanical environment leading to proper heart tube function and formation. For example, heart tube formation is driven by cytoskeletal contraction, as exposure to the myosin-II inhibitor blebbistatin arrested any shortening and also decreased both tissue stiffness (measured by microindentation) and mechanical tension (measured by cutting experiments) Finite element simulations complementing these experiments suggest that the endoderm (not the mesoderm) is the primary contractile tissue layer during this process [63].

Modeling the whole heart typically use more of a continuum approach such that these models attempt to explain the integrated function in terms of ventricular anatomy, the structure and material properties of myocardial tissue, and/or associated intra-cellular and extracellular conductivities of the tissue [64]. With the development of anatomically detailed models of ventricular geometry and associated muscle fiber architecture, models have been developed to incorporate cardiac electrical impulse propagation [65]. For example, physiologically based mathematical models of the ventricular cell, together with a realistic three-dimensional computer model of cardiac anatomy, predicted that dynamical instabilities remain a major cause of the wavebreak that drives fibrillation, even in an anatomically realistic heart [14]. Others have incorporated further model complexity by integrating continuum models of cardiac electrical impulse propagation and wall mechanics through finite element methods [66, 67]. These models have proven useful in understanding relationships between ventricular contraction and heart dilation, an important component of cardiac development [68].

6.3: Limitations and Future Directions

Cardiac development is inevitably multi-scalar and contains elements of a diverse nature constructed spatially in a hierarchical fashion. To understand this process and the origins of congenital heart defects, an integrative approach is needed to connect a diverse range of biological information and computational frameworks within a spatial hierarchy. However, some of the fundamental limitations with multi-scale analysis are biological uncertainties, lack of integrating the diverse modeling environments, and unimaginably large computational times [69, 70]. To combat these limitations, most of the systems insight has been implemented through highly focused directed models such as cardiac transcriptome networks or protein-clusters correlating with tissue morphogenesis. These have been extremely useful for understanding cardiac differentiation and connecting aberrant tissue morphogenesis to congenital heart defect.

Modularity of conserved canonical biological frameworks may help bride these gaps [71]. Having such units well defined provides for security in archiving, in model sharing and in ease of reproducibility and of selection in model construction. It also renders those units more accessible and independently modifiable. We see such modularity approaches to combine functionally integrated cell systems models of cardiac metabolism, signal transduction, and excitation-contraction coupling interactions into multi-scale models of cardiac electromechanical interactions that include hierarchical structures (cells, tissue, organs) [72, 73].

Recently, a number of groups have already sought to undertake the challenging tasks of incorporating many of the above mentioned processes into multi-scale models [49, 67, 73]. Through the generation of powerful software tools, integrating computational models for interpreting the functional or clinical significance is starting to be achieved. Continuing on with this process, the need for open source web technologies and associated informatics

approaches (i.e. Continuity 6) are important for improvements in data sharing, integration, and mining. This includes data representation (markup language, graphical), computational algorithms, and incorporating mechanical aspects such as FEA analyses packages.

In whole, connecting the phenotype of cardiac formation with the underlying molecular regulation is a grand challenge. Using both "top-down" and "bottom-up" approaches, insightful information regarding tissue morphogenesis and underlying transcription networks is being achieved [74]. As improvements within the field are made, investigations can begin to integrate the spatial hierarchy of cardiac development and to tackle difficult biological problems on unprecedented scales. Hopefully, over time, we will fully understand the origins of genetic and environmental factors leading to the majority of CHD and devise strategies for novel therapeutic and, even more importantly, preventive approaches.

REFERENCES

1. Reiter, J.F., et al., *Gata5 is required for the development of the heart and endoderm in zebrafish.* Genes Dev, 1999. **13**(22): p. 2983-95.
2. Manner, J., *Cardiac looping in the chick embryo: a morphological review with special reference to terminological and biomechanical aspects of the looping process.* Anat Rec, 2000. **259**(3): p. 248-62.
3. Stainier, D.Y., *Zebrafish genetics and vertebrate heart formation.* Nat Rev Genet, 2001. **2**(1): p. 39-48.
4. Zaffran, S. and M. Frasch, *Early signals in cardiac development.* Circ Res, 2002. **91**(6): p. 457-69.
5. Schlesinger, J., et al., *The cardiac transcription network modulated by Gata4, Mef2a, Nkx2.5, Srf, histone modifications, and microRNAs.* PLoS Genet, 2011. **7**(2): p. e1001313.
6. Brand, T., *Heart development: molecular insights into cardiac specification and early morphogenesis.* Dev Biol, 2003. **258**(1): p. 1-19.
7. Olson, E.N. and D. Srivastava, *Molecular pathways controlling heart development.* Science, 1996. **272**(5262): p. 671-6.
8. Palsson, B., *The challenges of in silico biology.* Nat Biotechnol, 2000. **18**(11): p. 1147-50.
9. Hood, L., *Systems biology: integrating technology, biology, and computation.* Mech Ageing Dev, 2003. **124**(1): p. 9-16.
10. Crampin, E.J., et al., *Computational physiology and the Physiome Project.* Exp Physiol, 2004. **89**(1): p. 1-26.
11. Bassingthwaighte, J., P. Hunter, and D. Noble, *The Cardiac Physiome: perspectives for the future.* Exp Physiol, 2009. **94**(5): p. 597-605.
12. Hunter, P.J. and T.K. Borg, *Integration from proteins to organs: the Physiome Project.* Nat Rev Mol Cell Biol, 2003. **4**(3): p. 237-43.
13. Velculescu, V.E., B. Vogelstein, and K.W. Kinzler, *Analysing uncharted transcriptomes with SAGE.* Trends Genet, 2000. **16**(10): p. 423-5.
14. Xie, F., et al., *A simulation study of the effects of cardiac anatomy in ventricular fibrillation.* J Clin Invest, 2004. **113**(5): p. 686-93.
15. Clayton, R.H., et al., *Models of cardiac tissue electrophysiology: progress, challenges and open questions.* Prog Biophys Mol Biol, 2011. **104**(1-3): p. 22-48.
16. Dal-Bianco, J.P., et al., *Active adaptation of the tethered mitral valve: insights into a compensatory mechanism for functional mitral regurgitation.* Circulation, 2009. **120**(4): p. 334-42.
17. Akazawa, H. and I. Komuro, *Cardiac transcription factor Csx/Nkx2-5: Its role in cardiac development and diseases.* Pharmacol Ther, 2005. **107**(2): p. 252-68.
18. Hubbard, T.J., et al., *Ensembl 2007.* Nucleic Acids Res, 2007. **35**(Database issue): p. D610-7.
19. Joyce, A.R. and B.O. Palsson, *The model organism as a system: integrating 'omics' data sets.* Nat Rev Mol Cell Biol, 2006. **7**(3): p. 198-210.
20. Ghosh, S., et al., *Software for systems biology: from tools to integrated platforms.* Nat Rev Genet, 2011. **12**(12): p. 821-32.
21. Hong, S.E., et al., *HCNet: a database of heart and calcium functional network.* Bioinformatics, 2006. **22**(16): p. 2053-4.

22. Yalcin, H.C., et al., *An ex-ovo chicken embryo culture system suitable for imaging and microsurgery applications.* J Vis Exp, 2010(44).
23. Brazma, A., *Minimum Information About a Microarray Experiment (MIAME)--successes, failures, challenges.* ScientificWorldJournal, 2009. **9**: p. 420-3.
24. Stromback, L. and P. Lambrix, *Representations of molecular pathways: an evaluation of SBML, PSI MI and BioPAX.* Bioinformatics, 2005. **21**(24): p. 4401-7.
25. Hucka, M., et al., *The systems biology markup language (SBML): a medium for representation and exchange of biochemical network models.* Bioinformatics, 2003. **19**(4): p. 524-31.
26. Lloyd, C.M., M.D. Halstead, and P.F. Nielsen, *CellML: its future, present and past.* Prog Biophys Mol Biol, 2004. **85**(2-3): p. 433-50.
27. Christie, G.R., et al., *FieldML: concepts and implementation.* Philos Transact A Math Phys Eng Sci, 2009. **367**(1895): p. 1869-84.
28. Wierling, C., R. Herwig, and H. Lehrach, *Resources, standards and tools for systems biology.* Brief Funct Genomic Proteomic, 2007. **6**(3): p. 240-51.
29. Klipp, E., et al., *Systems biology standards--the community speaks.* Nat Biotechnol, 2007. **25**(4): p. 390-1.
30. Stromback, L., D. Hall, and P. Lambrix, *A review of standards for data exchange within systems biology.* Proteomics, 2007. **7**(6): p. 857-67.
31. Armstrong, E.J. and J. Bischoff, *Heart valve development: endothelial cell signaling and differentiation.* Circ Res, 2004. **95**(5): p. 459-70.
32. Nakajima, Y., et al., *Expression of smooth muscle alpha-actin in mesenchymal cells during formation of avian endocardial cushion tissue: a role for transforming growth factor beta3.* Dev Dyn, 1997. **209**(3): p. 296-309.
33. Person, A.D., S.E. Klewer, and R.B. Runyan, *Cell biology of cardiac cushion development.* Int Rev Cytol, 2005. **243**: p. 287-335.
34. Moorman, A.F. and V.M. Christoffels, *Cardiac chamber formation: development, genes, and evolution.* Physiol Rev, 2003. **83**(4): p. 1223-67.
35. Thiery, J.P., *Epithelial-mesenchymal transitions in development and pathologies.* Curr Opin Cell Biol, 2003. **15**(6): p. 740-6.
36. Ahmed, S. and A. Nawshad, *Complexity in interpretation of embryonic epithelial-mesenchymal transition in response to transforming growth factor-beta signaling.* Cells Tissues Organs, 2007. **185**(1-3): p. 131-45.
37. Tariq Abdulla, R.I., Jean-Marc Schleich, Ron Summers, *Composite Annotation for Heart Development*, in *ICBO: International Conference on Biomedical Ontology*2011: Buffalo, NY. p. 47-54.
38. Cline M, S.M., Cerami E, Kuchinsky A, Landys N, et al., *Integration of biological networks and gene expression data using Cytoscape.* Nat Protoc, 2007. **2**: p. 2366-2382.
39. Shannon P, M.A., Ozier O, Baliga N, Wang J, et al. , *Cytoscape: a software environment for integrated models of biomolecular interaction networks.* Genome Res, 2003. **13**: p. 2498–2504.
40. Chin, A.J., *Analysis of two aspects of left-right patterning of the vertebrate heart. Heart tube position and heart tube chirality.* Methods Mol Biol, 2000. **136**: p. 261-70.
41. Singh, B.N., et al., *Heart of newt: a recipe for regeneration.* J Cardiovasc Transl Res, 2010. **3**(4): p. 397-409.
42. Nikitin A, E.S., Daraselia N, Mazo I, *Pathway studio—the analysis and navigation of molecular networks.* Bioinformatics, 2003. **19**: p. 2155–2157.
43. Kitano H, F.A., Matsuoka Y, Oda K., *Using process diagrams for the graphical representation of biological networks.* Nat Biotechnol, 2005. **23**: p. 961-966.

44. Funahashi A, M.Y., Jouraku A,Morohashi M, KikuchiN,Kitano H, *CellDesigner 3.5: a versatile modeling tool for biochemical networks.* Proc IEEE, 2008. **96**: p. 1254–1265.
45. Aguado-Sierra, J., Kerckhoffs, R.C.P., Lionetti, F. , Villongco, C., Hunt, D., Gonzales, M., Campbell, S., and McCulloch, A. D., *A Computational Framework for Patient-Specific Multi-Scale Cardiac Modeling*, in *Patient-Specific Modeling of the Cardiovascular System: Technology-Driven Personalized Medicine*, R.C.P. Kerckhoffs, Editor 2010, © Springer Science+Business Media. p. 203-223.
46. *Complexity in biological information processing. Proceedings of a symposium. Berlin, Germany, 4-6 July 2000.* Novartis Found Symp, 2001. **239**: p. 1-250.
47. Bruggeman, F.J. and H.V. Westerhoff, *The nature of systems biology.* Trends Microbiol, 2007. **15**(1): p. 45-50.
48. Noble, D., *Modeling the heart--from genes to cells to the whole organ.* Science, 2002. **295**(5560): p. 1678-82.
49. Hake, J., et al., *Modeling Cardiac Calcium Sparks in a Three-Dimensional Reconstruction of a Calcium Release Unit.* J Physiol, 2012.
50. Srivastava, D. and E.N. Olson, *A genetic blueprint for cardiac development.* Nature, 2000. **407**(6801): p. 221-6.
51. Faustino, R.S., et al., *Genomic chart guiding embryonic stem cell cardiopoiesis.* Genome Biol, 2008. **9**(1): p. R6.
52. Clark, K.L., K.E. Yutzey, and D.W. Benson, *Transcription factors and congenital heart defects.* Annu Rev Physiol, 2006. **68**: p. 97-121.
53. Lickert, H., et al., *Baf60c is essential for function of BAF chromatin remodelling complexes in heart development.* Nature, 2004. **432**(7013): p. 107-12.
54. Mazloom, A.R., et al., *Chromatin remodeling in silico: a stochastic model for SWI/SNF.* Biosystems, 2010. **99**(3): p. 179-91.
55. Lage, K., et al., *Dissecting spatio-temporal protein networks driving human heart development and related disorders.* Mol Syst Biol, 2010. **6**: p. 381.
56. Lage, K., et al., *Genetic and environmental risk factors in congenital heart disease functionally converge in protein networks driving heart development.* Proc Natl Acad Sci U S A, 2012. **109**(35): p. 14035-40.
57. Nath, A.K., et al., *Proteomic-based detection of a protein cluster dysregulated during cardiovascular development identifies biomarkers of congenital heart defects.* PLoS One, 2009. **4**(1): p. e4221.
58. Toenjes, M., et al., *Prediction of cardiac transcription networks based on molecular data and complex clinical phenotypes.* Mol Biosyst, 2008. **4**(6): p. 589-98.
59. Nakamura, H., et al., *Gain- and loss-of-function in chick embryos by electroporation.* Mech Dev, 2004. **121**(9): p. 1137-43.
60. Chesnutt, C. and L. Niswander, *Plasmid-based short-hairpin RNA interference in the chicken embryo.* Genesis, 2004. **39**(2): p. 73-8.
61. Oka, C., et al., *Modeling the calcium gate of cardiac gap junction channel.* J Physiol Sci, 2006. **56**(1): p. 79-85.
62. Cortassa, S., et al., *An integrated model of cardiac mitochondrial energy metabolism and calcium dynamics.* Biophys J, 2003. **84**(4): p. 2734-55.
63. Varner, V.D. and L.A. Taber, *Not just inductive: a crucial mechanical role for the endoderm during heart tube assembly.* Development, 2012. **139**(9): p. 1680-90.
64. Nordsletten, D.A., et al., *Coupling multi-physics models to cardiac mechanics.* Prog Biophys Mol Biol, 2011. **104**(1-3): p. 77-88.
65. Bishop, M.J., et al., *Development of an anatomically detailed MRI-derived rabbit ventricular model and assessment of its impact on simulations of electrophysiological function.* Am J Physiol Heart Circ Physiol, 2010. **298**(2): p. H699-718.

66. Kerckhoffs, R.C., et al., *Coupling of a 3D finite element model of cardiac ventricular mechanics to lumped systems models of the systemic and pulmonic circulation.* Ann Biomed Eng, 2007. **35**(1): p. 1-18.
67. Vetter, F.J. and A.D. McCulloch, *Three-dimensional analysis of regional cardiac function: a model of rabbit ventricular anatomy.* Prog Biophys Mol Biol, 1998. **69**(2-3): p. 157-83.
68. Voiculescu, O., C. Papanayotou, and C.D. Stern, *Spatially and temporally controlled electroporation of early chick embryos.* Nat Protoc, 2008. **3**(3): p. 419-26.
69. Bassingthwaighte, J.B., H.J. Chizeck, and L.E. Atlas, *Strategies and Tactics in Multiscale Modeling of Cell-to-Organ Systems.* Proc IEEE Inst Electr Electron Eng, 2006. **94**(4): p. 819-830.
70. Hunter, P.J., E.J. Crampin, and P.M. Nielsen, *Bioinformatics, multiscale modeling and the IUPS Physiome Project.* Brief Bioinform, 2008. **9**(4): p. 333-43.
71. Kitano, H., *Systems biology: a brief overview.* Science, 2002. **295**(5560): p. 1662-4.
72. Land, S., S.A. Niederer, and N.P. Smith, *Efficient computational methods for strongly coupled cardiac electromechanics.* IEEE Trans Biomed Eng, 2012. **59**(5): p. 1219-28.
73. McCulloch, A.D. and G. Paternostro, *Cardiac systems biology.* Ann N Y Acad Sci, 2005. **1047**: p. 283-95.
74. Csete, M.E. and J.C. Doyle, *Reverse engineering of biological complexity.* Science, 2002. **295**(5560): p. 1664-9.

Chapter 7

Phenotypic heterogeneity in EMT is controlled by NFAT and phospho-Sp1

7.1: Summary

Identifying master molecular regulators of EMT is a key pursuit for their potential as diagnostic or therapeutic targets. Though research has uncovered hundreds of genes that are involved in EMT, almost all have been studied in isolation from one another. The ability to generate a large network analysis of EMT has been suggested as an attractive approach due to the ability to rapidly screen signaling networks. We formulated and analyzed a family of mechanistic models (1700 kinetic constants and 995 initial conditions) using a detailed molecular framework to describe the induction of EMT through TGFβ isoforms. The models were trained and cross-validated to prescribe biological significance using 41 different experimental data sets taken from literature from DLD1 colon carcinoma, MDCKII, and A375 melanoma cell lines. To address parametric uncertainty in ODE-based deterministic models, we implemented an ensemble approach using POET. The ensemble of parameter sets allowed us to identify different operational paradigms within EMT (sub-populations), which provide testable hypotheses into the possible transformational aspects of cellular phenotype. After network analysis and experimental verification, our results suggest the ability of both MCF10A and DLD1 to exhibit phenotypic heterogeneity based on the simultaneous treatment of TGFβ2 and VEGFA. Underlying this heterogeneous phenotype, master regulatory complexes were found to include both the NFAT and phospho-Sp1 transcription factors. Lastly, we found that the extent of ductal branch formation during acini formation was dependent upon phenotype heterogeneity in MCF10A. Together, these results establish a predictive mechanistic model of EMT susceptibility, and reveal a novel signaling axis between phospho-Sp1/NFAT for possibly regulating carcinoma progression through an EMT vs. tubulogenesis response.

7.2: Introduction

The molecular networks orchestrating the epithelial to mesenchymal transition (EMT) remain an important area of investigation. Much promise has been focused on developing diagnostic or therapeutic agents in hopes of controlling epithelial differentiation during pathological conditions (1). Decades of work employing a reductionist approach has identified critical signaling pathways controlling EMT, including MAPK, Smad, Wnt, and NFAT (2). Each of these pathways are responsive to multiple ligands and display a high degree of cross-talk (3). For example, VEGF is critical for tumor progression through angiogenesis, while TGFβ has both protective and transformative roles, depending on the extent of disease progression (4, 5). However, the convergence of these multiple signaling components to promote or inhibit phenotypic consequences during EMT is not well understood. This is largely true because directly testing hundreds of variables is intractable with a reductionist approach. On the other hand, a systems analysis of EMT is attractive because of the ability to rapidly simulate virtual experiments involving a myriad of biological perturbations, including those for which relevant reagents are not available (6).

Previous computational models investigating EMT signaling components have focused on the effects of a single biological factor and/or simulations within a single cell. For example, Chung *et al.*, constructed an ordinary differential equation model using mass-action kinetics to investigate the mechanisms associated with TGFβ receptor activation and Smad signaling. Their model suggested that a reduction of functional TGFβ receptors in cancer cells may lead to attenuated and delayed signaling responses via Smad2 (7). Similar work by Vilar *et al.* suggested that specific changes in receptor trafficking patterns can lead to phenotypes that favor tumor progression (8). Although these models have provided useful information about receptor dynamics, complex signaling networks like EMT contain interactions at other levels, including competing second messengers and transcriptional regulators. Furthermore, because these reactions occur with varying initial conditions and unknown parameter values, significant differences may exist in the overall response of the model. In order to address these additional levels of uncertainty, recent computational algorithms and statistical approaches have been developed for application of large scale ODE modeling (9, 10).

The objective of this study was to determine the extent of EMT in normal epithelial cells exposed to pathological conditions by (1) implementing and subsequently interrogating a population based model containing canonical EMT regulatory networks, and (2) verify our mechanistic targets using established cell lines with differing induction capacities for EMT. Toward this objective, we modeled the core molecular interactions of EMT using mass-action kinetics within an ordinary differential equation (ODE) framework. A population approach was used to estimate a family or ensemble of EMT models that was consistent with the previous literature (11, 12). Using the newly predicted operational paradigms, we sought to capture the role of phospho-Sp1 and NFAT on phenotype heterogeneity during TGFβ induced EMT *in vitro* via key marker expression profiles and fate processes.

7.3: Materials and Methods

7.3.1: Formulation and Analyses of the Model. The EMT model was formulated as a set of coupled non-linear ordinary differential equations (ODEs). Equations were generated using UNIVERSAL from an SBML input file (available in the supplemental materials). UNIVERSAL is an open source Objective-C/Java code generator, available at Google Code (http://code.google.com /p/universal-code-generator). The model equations were solved using the LSODE routine in OCTAVE (v 3.0.5; www.octave.org) on an Apple workstation (Apple, Cupertino, CA; OS X v10.6.4) as previously described (13). The model has 1756 unknown parameters (1700 kinetic constants and 56 non-zero initial conditions) which were not uniquely identifiable given the training data. Instead of identifying a single best fit model, we estimated a population of likely models (each consistent with the training data) using 41 data sets generated in DLD1 colon carcinoma, MDCKII, and A375 melanoma cells taken from Medici *et al.* (12). We used the Pareto Optimal Ensemble Technique (POET) multiobjective optimization framework in combination with leave-one-out cross-validation to estimate an ensemble (9). Robustness coefficients were calculated as shown previously (13). Extended methods are included in appendix D.

7.3.2: Cell Culture DLD1 colon carcinoma, MCF10A, and HUVEC were acquired from the American Tissue Culture Collection (Manassas, VA). Cells were grown in culture with RPMI 1640 medium with 10% fetal bovine serum and 1% penicillin/streptomycin for DLD1, EBM-2 supplemented with EGM-2, 5% fetal bovine serum, and 1% penicillin/streptomycin for HUVEC, or MGEM 2 supplemented with insulin, bovine pituitary extract, cholera toxin, hEGF, hydrocortisone, 5% horse serum, and 1% penicillin/streptomycin for MCF10A. Cells were serum starved for 24 hours and removed from all experimental conditions. Recombinant VEGFA165 was also removed from culture medium prior to experimentation. Recombinant human TGFβ2 (R $\&$ D Systems, Minneapolis, MN) was added to the culture medium at a concentration of 10 ng/ml and recombinant VEGFA165 at a concentration of (5ng/ml, 50ng/ml) for all relative experiments. NFAT inhibitor (VIVIT peptide) (EMDBiosciences, Darmstadt, Germany), was added to the culture medium at a concentration of 10μM for all relative experiments. Cells were passaged 1:3 or 1:4 every 3-6 d and used between passages 4 and 8.

7.3.3: RT-PCR RNA extractions were performed using a Qiagen total RNA purification kit (Qiagen, Valencia, CA) and RNA was reverse transcribed to cDNA using the SuperScript III RT-PCR kit with oligo(dT) primer (Invitrogen). Sufficient quality RNA was determined by an absorbance ratio A260/A280 of 1.8-2.1, while the quantity of RNA was determined by measuring the absorbance at 260nm (A260). Real-time PCR experiments were conducted using the SYBR Green PCR system (Biorad, Hercules, CA) on a Biorad CFX96 cycler, with 40 cycles per sample. Cycling temperatures were as follows: denaturing, 95C; annealing, 60C; and extension, 70C. Primers were designed to detect GAPDH, ecadherin, vimentin, Slug, Sp1, and NFATc1 in cDNA clones: Sp1 (F-TTG AAA AAG GAG TTG GTG GC, R-TGC TGG TTC TGT AAG TTG GG, Accession NG030361.1), NFATc1 (F-GCA TCA CAG GGA AGA CCG TGT C, R-GAA GTT CAA TGT CGG AGT TTC TGA G, Accession NG029226.1). GAPDH, ecadherin, vimentin, and Slug primers were taken from previously published literature (Medici *et al*.) (12).

7.3.4: Antibody Staining Samples were fixed in 4% PFA overnight at 4C. Samples were then washed for 15 minutes on a rocker 3 times with PBS, permeabilized with 0.2% Triton-X 100 (VWR International, Radnor, PA) for 10 minutes, and washed another 3 times with PBS. Samples were incubated overnight at 4C in a 1% BSA (Rockland Immunochemicals, Inc., Gilbertsville, PA) blocking solution followed by another 4C overnight incubation with either rabbit anti-human ecadherin 1:100 (Abcam, ab53033), mouse anti-human phospho-Sp1 1:100 (Abcam, ab37707), mouse anti-human vimentin 1:100 (Invitrogen, V9), and rabbit anti-human NFATc1 (Santa Cruz, sc-7294) 1:100. After 3 washes for 15 minutes with PBS, samples were exposed to Alexa Fluor 488 or 568 conjugated (Invitrogen), species specific secondary antibodies at 1:100 in 1% BSA for 2 hours at room temperature. Three more washes with PBS for 15 minutes were followed by incubation with either DRAQ5 far red nuclear stain (Enzo Life Sciences, Plymouth Meeting, PA) at 1:1000.

7.3.5: FACS Flow cytometry for ecadherin 1:100 (Abcam) and vimentin 1:100 expressing cells was performed. Briefly, cells were trypsinized, fixed with 4% PFA for 10 min and then preserved in 50% methanol/PBS. Cells were kept in the -20C until antibody staining was preformed. Samples were divided into multiple aliquots in order to stain the proteins separately and compensate for secondary antibody non-specific binding. Cells were incubated for 24 hr at 4 C in primary antibody

diluted in either PBS (extracellular) or 0.2% saponin-PBS (intracellular). Cells were then washed 3 times with PBS and incubated with appropriate secondary antibodies and imaged using a Coulter Epics XL-MCL Flow Cytometer (Coulter). All samples were compensated using appropriate background subtraction and all samples were normalized using 7500 cells per flow condition.

7.3.6: Three-Dimensional Culture Assays For invasion/migration assays, cells were resuspended in culture media, and allowed to aggregate overnight in hanging drop culture (20μL; 20,000 cells). The spherical aggregates were placed on the surface of neutralized type I collagen hydrogels (1.5mg/mL) and allowed to adhere for 2h before adding treatments. Cultures were maintained for 72h, after which they were fixed in 4% PFA and slowly rehydrated using PBS. For compaction assays, cells were pelleted via centrifugation and resuspended within a neutralized collagen hydrogel (1.5mg/mL) solution at a density of 400,000 cells/mL. 250μL of gel was inoculated into culture wells, which solidified after 60min. Treatments were then added within 800μL of the culture medium without serum. Gels were liberated from the surfaces of the culture wells the next day and cultured free floating for an additional 3-7 days, exchanging serum free media with appropriate factors every 48hr.

7.3.7: Statistics Results are expressed as mean $\pm$ standard error, n$\geq$6. Data was analyzed with the GraphPad Prism version 4.00 for Windows (GraphPad Software, San Diego, CA) and SAS (Statistical Analysis Software, Cary, NC). A one-way ANOVA with Tukey's post hoc was used to compare differences between means and data was transformed when necessary to obtain equal sample variances. Differences between means were considered significant at p$\prec$0.05.

7.4 Results

Model connectivity re-creates core architecture within EMT. The EMT network connectivity (proteins, mRNA, and genes) was assembled from literature and on-line databases: String-8 (14), NetworKIN (15), and TRANSFAC (16). The model interactome contained over 1700 interactions and was not specific to a single cell line. Rather, we assembled canonical pathways involved in EMT signaling and defaulted to human connectivity when possible. Using a canonical network allowed us to explore general features of TGFβ induced EMT without cell line specific artifacts (Figure 7.1). Briefly, induction of EMT occurs through the binding of extracellular TGFβ1/2 with TGFβ surface receptors I/II (TGFβR-I/II) to initiate the assembly of an adapter complex, beginning the downstream signaling program. Central to this process, autocrine production of TGFβ3 binds to the TGFβR-I/II followed by the recruitment of activin receptor-like kinase 1 (ALK5) and TGFβ surface receptor III (TGFβR-III) to form the activated receptor complex (17). Complex assembly activates the serine/threonine kinase intracellular domain, leading to the recruitment and phosphorylation of both MAPK (Ras-Raf-Mek-Erk) and Smad partners (18). Downstream of the TGFβ signaling, nuclear pSmad2/3-Smad4 proteins form transcriptional complexes with several genes in the model, including lymphoid enhancer-binding factor 1 (LEF-1), nuclear factor of activated T-cells (NFAT), and specificity protein 1 (Sp1). Simultaneously, ERK1/2-mediated phosphorylation of the AP1 and Sp1 transcription factors can also regulate transcriptional complexes involving NFAT, Slug, and Smads. The VEGFA, BMP, Wnt, and PI3K pathways are also included in the model. The full model connectivity and inital conditions as a datafile are located in Appendix D.

7.4.1: Model population quantitatively captured key features of TGFβ induced EMT signaling. EMT signaling was modeled using mass-action kinetics within an ordinary differential equation (ODE) framework. This formulation is a common method to model biological pathways (19, 20). The EMT model had 1756 unknown parameters (1700 kinetic constants and 56 non-zero initial conditions) which were not uniquely identifiable given the training data and organized into well mixed sub-compartments. Instead of identifying a single best fit model, we estimated a population of likely models (each consistent with the training data) by minimizing the difference between simulations and 41 data sets generated in DLD1 colon carcinoma, MDCKII, and A375 melanoma

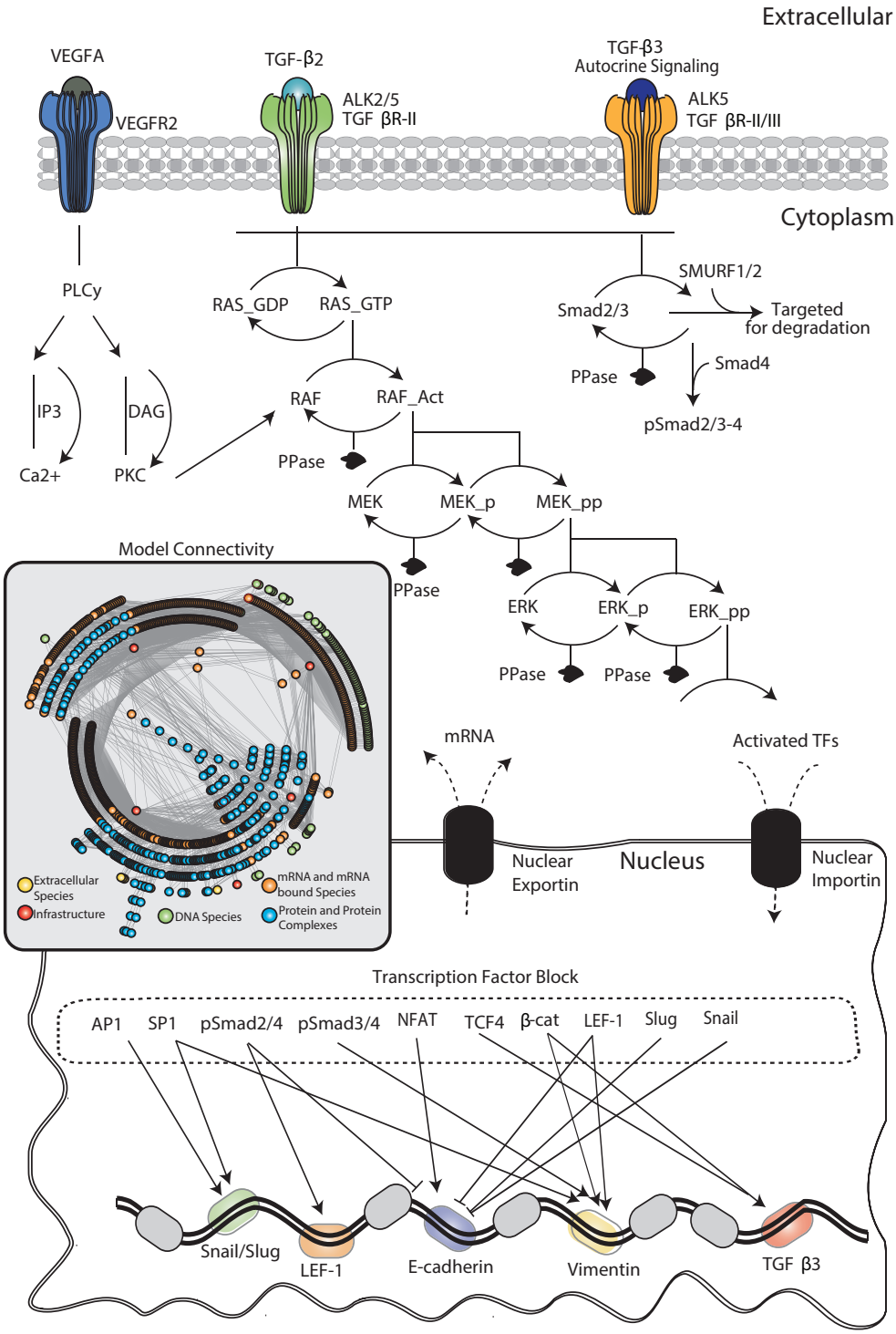

Figure 7. 1: Model population quantitatively captures TGFβ-induced EMT signaling. (A-I) The population was generated using POETs and trained using 11 different objective functions (41 data sets) taken from Medici *et al.* (12). The model was able to effectively capture the simulated experiments 78% of the time. (J-L) The model populations were also compared against untrained temporal data to measure the effectiveness as a pure prediction. The high predictability can be contributed to the leave-one-out cross validation scheme, objective functions with overlapping data, and multi-objective optimization algorithm.

cells by Medici *et al.* (12) using the Pareto Optimal Ensemble Technique (POETs) (Fig. T2). Additionally, we used POETs in combination with leave-one-out cross validation to independently calculate training and prediction error as previously described (9, 13).

POETs generated an ensemble of models which captured the multiple phases of EMT induction. Stimulation with TGFβ2 (10 a.u.) induced Snail expression, while the MEK inhibitor (U0126) blocked Snail expression by inhibiting AP1 activation. Similar results were obtained for Slug confirming initial activation through the MAPK pathway. Over-expression of Snail or Slug in the absence of ecadherin indirectly induced TGFβ3 expression through the β-catenin/TCF4 complex. Conversely, over-expression of ecadherin inhibited the TGFβ3 autocrine production by sequestering cytosolic β-catenin, thereby blocking EMT. TGFβ3 signaled through through the Smad pathway to regulate LEF1 expression and downstream target EMT genes. TGFβ3 (10 a.u.) in combination with downstream inhibitors (DN-Smad4 and DN-LEF1) completely inhibited vimentin expression, while elevating ecadherin expression (Figure 7.2). Taken together, our model was able to quantitatively capture the signaling network previously revealed by Medici *et al.* (12). A complete listing of all data used for training (including statistics) are included in appdendix D (Fig. T3).

The predictive power of the model ensemble was also tested against non-trained EMT data (11). Our model was able to capture the dynamic gene expression levels of ecadherin, pSmad2, and LEF1 within one-standard deviation (up to the 48 hr time-point) (Figure 7.2). In whole, 78% of our training objectives were statistically significant (at a 95% confidence interval) compared to the randomized parameter sets generated from the best-fit nominal set (starting point for the optimization). The high predictability can be attributed to the leave-one-out cross validation scheme, diverse objective functions, and robustness of the POETs algorithm. Further discussion of the POET residuals and prediction statistics are included in the supplement (Fig. T3).

7.4.2: Simulated TGFβ2 induction revealed heterogeneity within the model population through NFAT and phospho-Sp1. After validating our model ensemble, we used robustness analysis to generate falsifiable phenotypic predictions in response to different perturbations. Robustness coefficients with values > 1 (< 1) indicated a marker increased (decreased) compared to a base

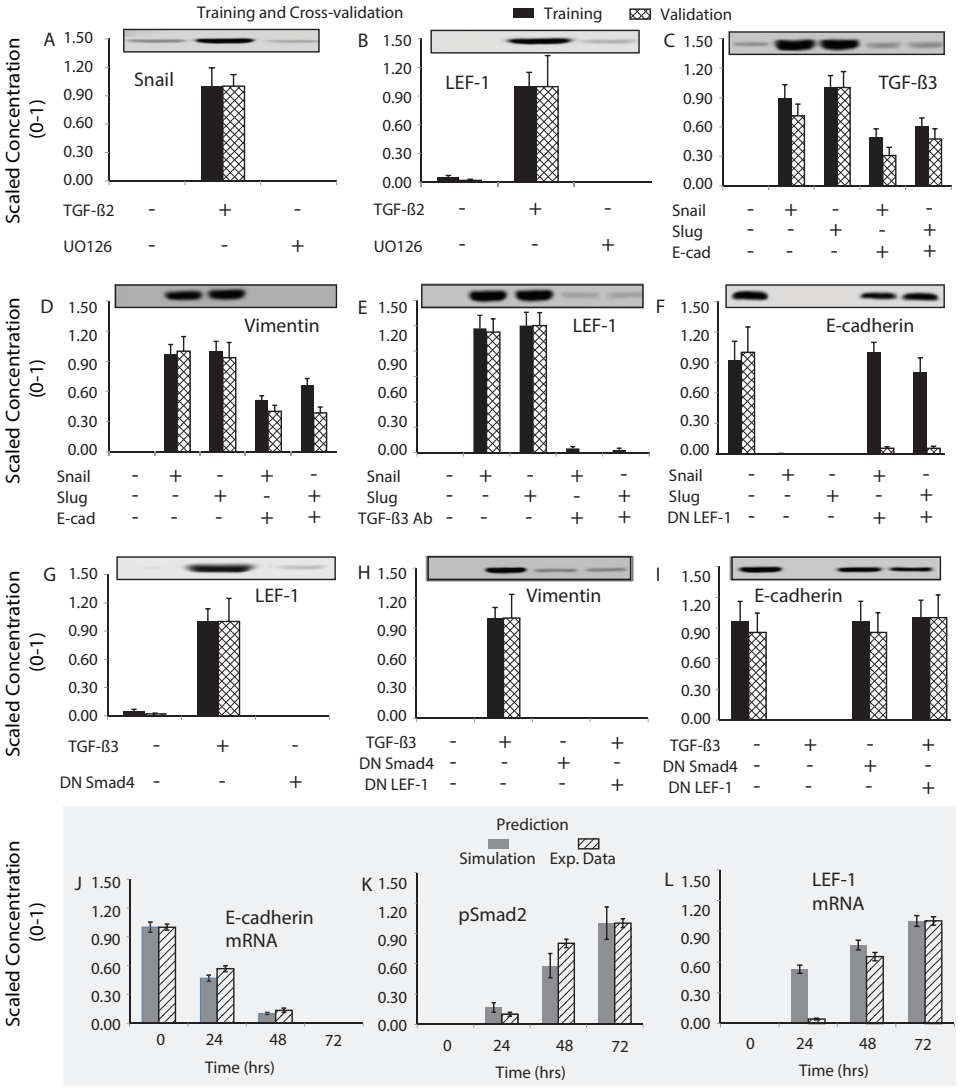

Figure 7. 2: Model population quantitatively captures TGFβ-induced EMT signaling. (A-I) The population was generated using POETs and trained using 11 different objective functions (41 data sets) taken from Medici *et al.* (12). The model was able to effectively capture the simulated experiments 78% of the time. (J-L) The model populations were also compared against untrained temporal data to measure the effectiveness as a pure prediction. The high predictability can be contributed to the leave-one-out cross validation scheme, objective functions with overlapping data, and multi-objective optimization algorithm.

state, while a value of 1 indicated approximately no change following a perturbation. Phenotypic behavior of the entire 1091 parameter ensemble was interpreted using downstream markers vimentin (mesenchymal) and ecadherin (epithelial) at 48 hrs as previously described (21).

Interestingly, POETs identified four subpopulations which responded differently to TGFβ2 induction. Cells in subpopulation one (R1) had high levels of phospho-Sp1 was responsible for the decreased ecadherin expression through Slug-mediated inhibition, and increased vimentin expression. In subpopulation two (R2), moderate levels of phospho-Sp1 (activated form) was responsible for the increased vimentin expression. In subpopulation three (R3), elevated levels of phospho-Sp1 and nuclear localization of NFAT (driven by AP1) were responsible for increased vimentin and ecadherin expression. Lastly, in subpopulation four (R4) reduced levels of AP1, phospho-Sp1, and NFAT (loss of ERK activity) were responsible for the lack of induction. In addition, by applying flow analysis, we determined that these key transcription factors (phospho-Sp1 and NFAT) were localized within the TGFβ2 and VEGFA pathways, respectively (Fig. S1). This lead use to hypothesize that phospho-Sp1 and NFAT expression levels could be driven by VEGFA and/or TGFβ2 stimulation. Specifically, simultaneous VEGFA and TGFβ2 treatment would yield an atypical and heterogeneous EMT response (similar to R3), at least *in vitro* (Figure 7.3).

7.4.3: Simulated TGFβ2 and VEGFA treatment recreated phenotype heterogeneity through NFAT. To re-create the phentoype heterogeneity as found in region three (R3), we conducted simulated treatments of TGFβ2 and/or VEGFA (as hypothesized above). Stimulation with VEGFA (50 a.u.) maintained a population of epithelial (Q4-43.6%) compared to mesenchymal phenotype (Q1-7.5%). Conversely, addition of TGFβ2 (10 a.u.) shifted the population from an epithelial (Q4-5.5%) to mesenchymal (Q1-45.6%) phenotype. Interestingly, the combined effects of TGFβ2 and VEGFA were found to increase both ecadherin and vimentin levels (Q2-45.3%). To isolate the effect of NFAT, NFAT dephosphorylation was inhibited across all conditions. NFAT inhibition with TGFβ2 treatment resulted in a loss of all ecadherin positive sets (Q2-23.5%). Likewise, NFAT inhibition with VEGFA treatment mitigated all ecadherin positive sets (Q2-19.1%). Lastly, NFAT inhibition with TGFβ2 and VEGFA mitigated nearly all ecadherin expression, shifting the population (Q2-27.3%) towards a mesenchymal phenotype (Q1-45.1%) (Figure 7.4).

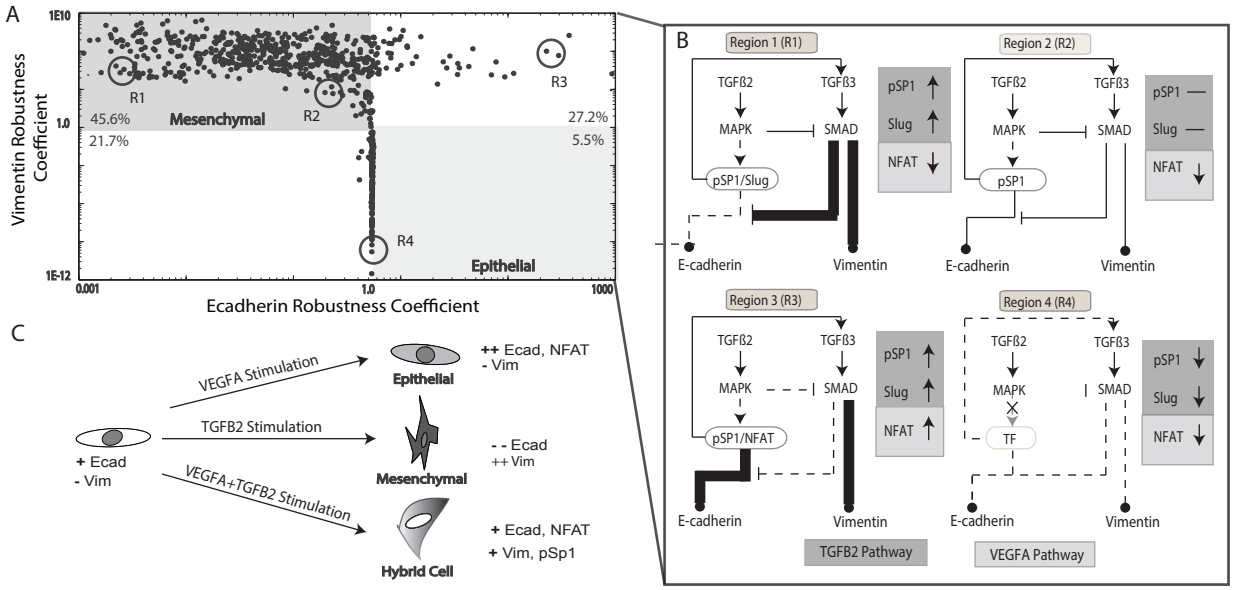

Figure 7. 3: TGFβ pertubation reveals phenotype heterogeneity within regional subpopulations of the model. Robustness coefficients were used to quantify the effect of initial condition perturbations after steady state across the population of data sets. Coefficients with values > 1 (< 1) indicated a marker increased (decreased) compared to a base state, while a value of 1 indicated approximately no change following a perturbation. Ecadherin and vimentin robustness coefficients were used as phenotypic markers. (A) After TGFβ2 perturbation, we isolated 4 distinct parameter sets known to have phenotypically different behaviors. (B) Each region has been represented by a small signaling network. From our analysis, we determined that the differences were a function of downstream transcription factors (phospho-Sp1, and NFAT) within the TGFβ2 and VEGFA pathway, respectively. (C) We hypothesized that elevated phospho-Sp1 and NFAT levels could drive phenotype heterogeneity through simultaneous TGFβ2 and VEGFA treatment, similar to region three (R3).

We further quantified the protein levels using the raw values at 48 hrs for multiple targets including ecadherin, vimentin, phospho-Sp1, nuclear NFAT, alpha-SMA, and Slug. Similar to our robustness analysis, elevated ecadherin expression was dependent upon the addition of VEGFA, while NFAT inhibition mitigated this effect. Taken together, high levels of phospho-Sp1 correlated with vimentin expression, while NFAT was found critical for maintaining ecadherin expression, although neither mutually exclusive.

7.4.4: Combined TGFβ2 and VEGFA treatment drives phenotypic heterogeneity in MCF10A and DLD1. Our simulations (robustness analysis and combined perturbations) all support the hypothesis that elevated expression levels of both NFAT and phospho-Sp1 is a master signaling axis for driving EMT phenotype heterogeneity (positive ecadherin, positive vimentin). To validate these results *in vitro*, we stimulated either quiescent epithelial/endothelial cells (MCFA10 and HUVEC) or transformed epithelial cell lines (DLD1) with TGFβ2 and/or VEGFA. Treatment with (10ng/ml) TGFβ2 increased Slug and vimentin, while ecadherin expression was inhibited at both the gene and protein level at 48 hrs. Within DLD1, a similar response occurred, although vimentin and ecadherin expression was more significant. Interestingly, HUVEC were not shown responsive to EMT with TGFβ2 addition (Fig. S3). An increase in nuclear phospho-Sp1 during EMT induction was also clearly evident, and quantified through nuclear co-localization (Figure 7.5). Morphological changes were also verified, changing from a quiescent cobblestone structure to spread spindle shaped. These results suggest TGFβ2 as a potent inducer of EMT and is cell type dependent.

Conversely, treatment with (50ng/ml) VEGFA increased both NFATc1 and ecadherin gene expression in MCF10A at both the gene and protein level at 48 hrs. In DLD1, a similar trend occurred although the expression levels of NFATc1 and ecadherin was less significant. We also found that NFATc1 nuclear localization significantly increased in both MCF10 and DLD1, while having no effect on phospho-Sp1 levels (Figure 7.5). Hence, VEGFA is a potent inducer of NFAT activation.

Combining VEGFA (50ng/ml) with TGFβ2 (10ng/ml) treatment in MCF10A, ecadherin and vimentin expression were significantly elevated at both the gene and protein level resulting in a heterogeneous response. No change in Sp1 expression was observed, although NFATc1 expres-

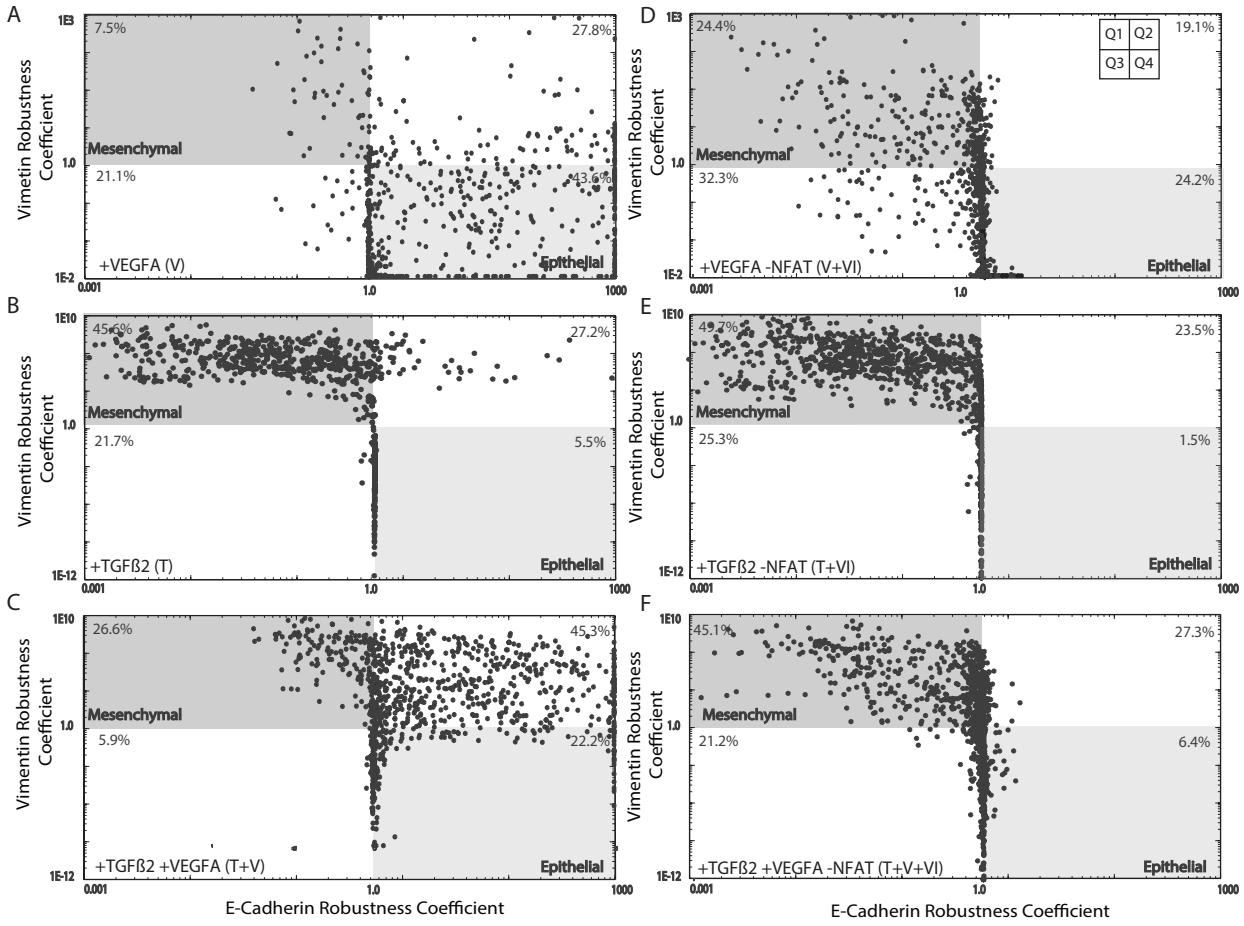

Figure 7. 4: Simulated TGFβ2 and VEGFA (known inducer of NFAT) combination re-creates phenotype heterogeneity through NFAT and phospho-Sp1. Robustness coefficients were used to quantify the shift in population at 48 hr. (A-C) Initial VEGFA (50 a.u.) treatment resulted in a popluation with enhanced epithelial (Q4) properties. This was contrary to the addition of TGFβ2 (10 a.u.), which shifted the population towards a mesenchymal phenotype (Q1). Interestingly, the combined effects of TGFβ2 and VEGFA was found to increase both ecadherin and vimentin levels, creating a heterogeneous population (Q2). (D-F) To isolate the effect of NFAT, we inhibited NFAT de-phosphorylation in combination with VEGFA. This negated the increase in ecadherin expression and shifted the population towards a mesenchymal phenotype (Q1,Q3). Likewise, combining NFAT inhibition with TGFβ mitigated all ecadherin expression (Q2) confirming their importance for population heterogeneity. Lastly, combination of TGFβ2, VEGFA, and NFAT inhibition nearly mitigated all effects of VEGFA, shifting the heterogeneous population (Q2) towards a mesenchymal phenotype (Q1). In whole, high levels of phospho-Sp1 correlated with vimentin expression, while NFAT was found largely responsible for maintaining ecadherin expression, although neither mutually exclusive.

sion was shown to increase. DLD1 underwent a similar response as NFATc1, Slug, and vimentin all significantly increased, while maintaining ecadherin levels (Fig. S3). Nuclear co-localization of both NFATc1 and phospho-Sp1 was also apparent, especially within the MCF10A (Figure 7.5). Taken together, these results suggest that combined VEGFA and TGFβ2 treatment promote phenotype heterogeneity.

7.4.5: Ecadherin expression is dependent upon NFAT. To establish the role of NFAT during EMT heterogeneity, we applied a VIVIT peptide to inhibit NFAT dephosphorylation (22). Treatment with VEGFA (50ng/ml) and VIVIT (10μM) in MCF10A resulted in significantly reduced ecadherin levels. However, treatment with TGFβ2 and VIVIT had little effect on EMT induction capacity. VIVIT in combination with TGFβ2 and VEGFA resulted in almost complete inhibition of ecadherin, while increasing Slug and vimenti nlevels. These findings were confirmed via immunofluorescence, as NFAT was shown to inhibit ecadherin expression in all three cases (Figure 7.5). Nuclear co-localization of NFAT in all three cases was mitigated (as expected), while phospho-Sp1 increased in both TGFβ conditions (Fig. S4).

Quantitative flow cytometry confirmed these results. Control cells maintained high ecadherin and low vimentin levels (Q1-99.5%). Comparable to our simulations, we found that upon TGFβ2 treatment, MCF10A cells shifted from an epithelial to mesenchymal phenotype (Q1-33.4%, Q4-42.8%). Combined TGFβ2 and VEGFA treatment increased vimentin levels (Q1-42.1%, Q2-52.3%), while positively effecting ecadherin levels (compared to TGFβ2 alone). NFAT was also found critical for maintaining these ecadherin levels (Q1-37.3%, Q4-29.0%). Together, these results suggests that NFAT are critical for regulating ecadherin expression during phenotype heterogeneity in MCF10A, but to a lesser extent in DLD1 (Fig. S4).

7.4.6: Ductal branching during acini formation is dependent upon phenotype heterogeneity in MCF10A. To determine the functional consequences of phenotype heterogeneity, we applied previously developed 3D in-vitro models of invasion, migration, compaction, and tubulogenesis (23). MCF10A and DLD1 were formed into spheroids overnight and explanted to a collagen gel for 72 hours. Within MCF10A, TGFβ2 significantly enhanced invasive and compaction proper-

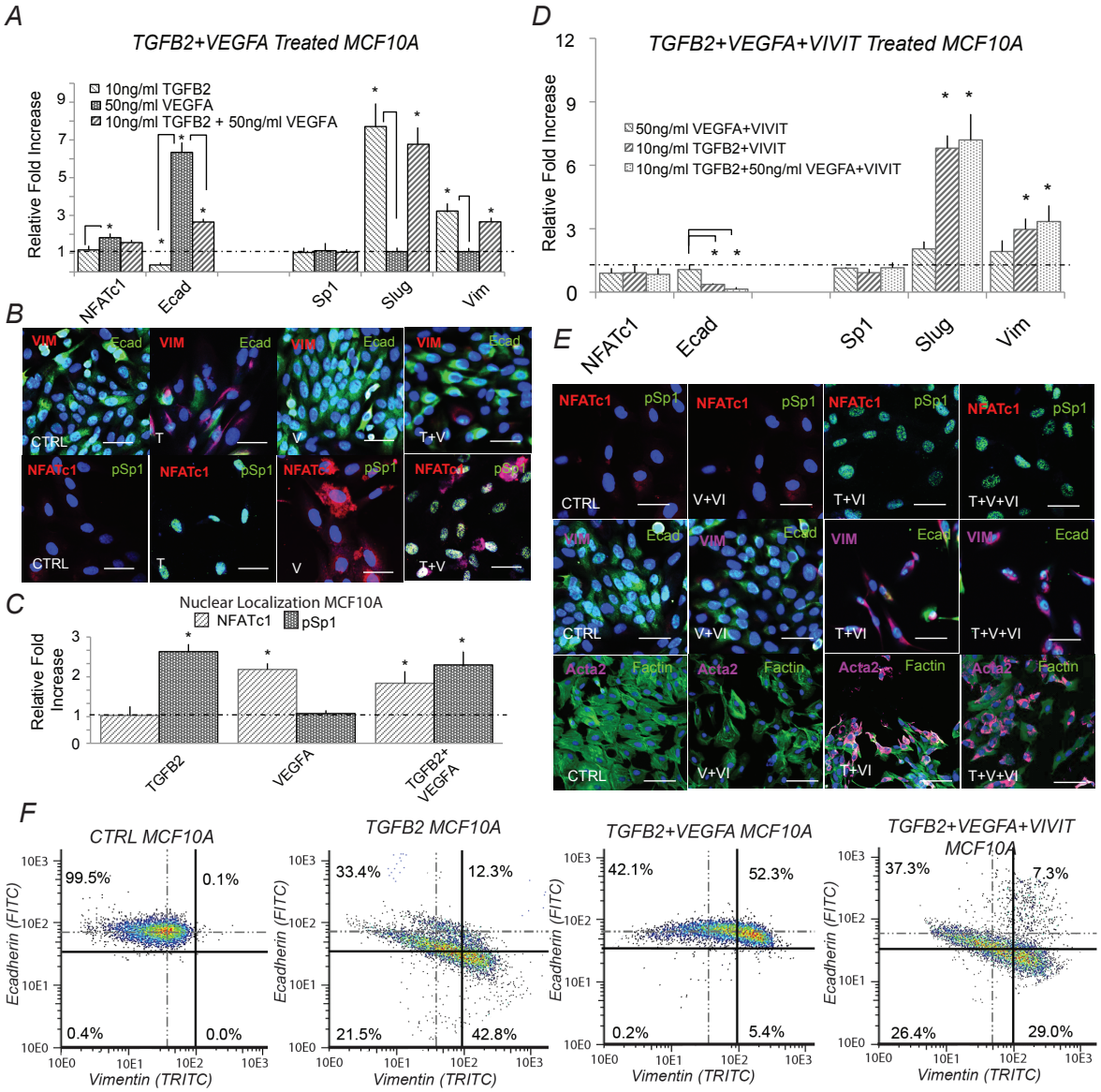

Figure 7. 5: Simultaneous TGFβ2 and VEGFA treatment induced phenotype heterogeneity and is dependent upon NFAT activity *in-vitro*. (A) In MCF10A, treatment with (10ng/ml) TGFβ2 increased Slug and vimentin, while ecadherin expression was inhibited at both the gene and protein level at 48 hrs. Conversely, VEGFA alone increased both NFATc1 and ecadherin gene expression. Simultaneous TGFβ2 (10ng/ml) and VEGFA (50ng/ml) treatment increased Slug, NFATc1, and vimentin expression, while also increasing ecadherin levels via qPCR. (B-C) Immunofluorescence confirmed these results and nuclear co-localization of both phospho-Sp1 and NFAT were found dependent upon TGFβ2 and VEGFA, respectively. (D) To isolate the effect of NFAT, treatment of VEGFA (50ng/ml) and VIVIT (10μM) reduced ecadherin expression at 48hrs (control-dashed line). Similarly, combined TGFβ2, VEGFA and VIVIT treatment increased Slug and vimentin expression, while inhibiting ecadherin levels via qPCR. (E) These findings were confirmed via immunofluorescence as the VIVIT peptide inhibited ecadherin and nuclear localization of NFATc1 in all three cases. (F) Quantitative flow cytometry also confirmed this trend. Similar experiments in DLD1 followed a similar trend (supplement). Magnification, 40x. Scale bars: 50μm. C=Control, T=TGFβ2 , V=VEGFA, VI= NFAT inhibitor (VIVIT). Asterisks signify statistical differences from each other according to a one-way ANOVA with Tukey's post hoc ($p \prec 0.05$).

ties, while VEGFA promoted migration. Mediating these effects, combined TGFβ2 and VEGFA significantly increased migration, while limiting the compaction potential. NFAT was found to be an important target of VEGFA, as the VIVIT peptide mitigated migration during VEGFA alone. Likewise, VIVIT in combination with VEGFA and TGFβ2 significantly decreased migration, while increasing invasion and compaction (Figure 7.6). DLD1 cells followed a similar trend to MCF10A, although the degree of migration, invasion, and compaction was less.

After analyzing compaction assays at 7 days, we measured cell morphology (circularity index), and was found to correlate overall with both invasion and compaction. TGFβ2 treatment resulted in an irregular and spindle shaped morphology, while VEGFA promoted round quiescent cells. Combined VEGFA and TGFβ2 promoted a hybrid morphology, while NFAT inhibition (VIVIT) significantly reduced the circularity index, similar to TGFβ2 treatment. The formation of tubular structures (acini) was also found to increase in size and number upon VEGFA treatment. However, the number of tubular branches relative to total acini was significantly increased upon combined TGFβ2 and VEGFA. These results indicate that simultaneous VEGFA and TGFβ2 treatment (hybrid phenotype) regulates acini and ductal branch formation, and is dependent upon NFAT activity (Figure 7.6). No tubular structures were identified within the DLD1 constructs during the 7 day tubulogenesis endpoints.

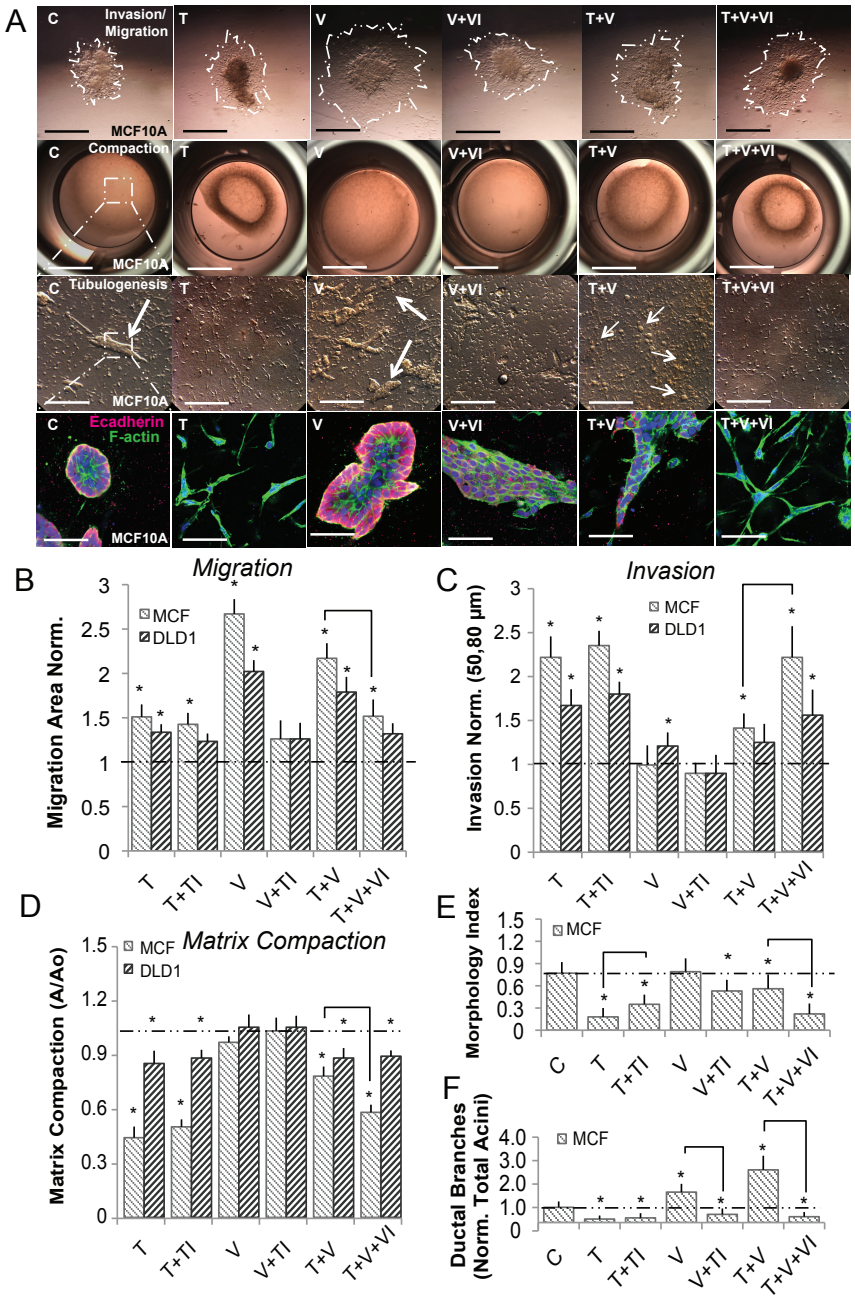

Figure 7. 6: Ductal branching is dependent upon phenotype heterogeneity within MCF10A in 3-D culture. MCF10A and DLD1 were formed into spheroids overnight and explanted to a collagen gel for 72 hrs. For compaction and tubular assays, cells were embedded into collagen gels for 72 hrs, and the extent of tubulogenesis was measured at 7 days. (A-D) Within MCF10A, TGFβ2 (10ng/ml) enhanced invasion and contractile properties while, VEGFA (50ng/ml) promoted increased migration. TGFβ2 with VEGFA significantly increased migration, while limiting with compaction. VIVIT (10μM) in combination with VEGFA and TGFβ2 decreased migration and compaction, while increasing invasion. (D) Likewise, cell morphology (circularity index) correlated with both invasion and compaction in MCF10A. (E-F) The size of tubular structures (acini) also increased significantly upon addition of VEGFA, while the number of ductal branches was most significant upon simultaneous TGFβ2 and VEGFA treatment (Red-Ecadherin, Green-Factin, Blue-Nuclear). DLD1 cells followed a similar trend, although the degree of migration, invasion, and compaction was less significant. In addition, no tubular structures were identified during the 7 day tubulogenesis endpoints. Scale bars: 500μm, 1000μm, 250μm, and 80μm, respectively. C=Control, T=TGFβ2 , V=VEGFA, VI= NFAT inhibitor (VIVIT). Asterisks signify statistical differences from each other according to a one-way ANOVA with Tukey's post hoc ($p \prec 0.05$).

7.5: Discussion

We formulated and analyzed a family of mechanistic models using a detailed molecular framework, which describes the induction of EMT. The models were trained and cross-validated to prescribe biological significance using experimental data sets taken from literature. To address parametric uncertainty in ODE-based deterministic models, we implemented an ensemble approach using POETs. The ensemble of parameter sets allowed us to identify different operational paradigms within EMT (sub-populations), which provide testable hypotheses into the possible transformational aspects of cellular phenotype. Our results suggest the ability of both MCF10A and DLD1 to exhibit phenotypic heterogeneity based on the combined treatment of TGFβ2 and VEGFA and master regulatory complexes included both the NFAT and Sp1 transcription factors. Lastly using 3D cultures, we found that the extent of ductal branching in MCF10A was dependent upon phenotype heterogeneity. Together, these results establish a predictive mechanistic model of EMT, and suggest pathogenetic phenotype outcomes of EMT through an NFAT/phospho-Sp1 signaling axis.

Classically, ODEs and mass-action kinetics are common frameworks for modeling biological pathways (19, 20, 24). However, the use of ODEs for large scale deterministic modeling has been limited. This is largely because structural and parametric uncertainty associated with this type of modeling can be substantial. Furthermore, the availability of computational algorithms capable of handling such an approach are few. We have addressed both of these ODE shortcomings by including well-mixed compartments to account for spatially localized species and processes and have considered an ensemble of models in our analysis to coarse-grain population phenomena. Regardless of model formulation, each model class requires the identification of a large number of unknown model parameters. While computationally complex, multi-objective optimization is an important tool to address qualitative conflicts in training data that arise from experimental error or cell line artifacts (25, 26). To minimize the parametric uncertainty associated with large scale deterministic networks, population based techniques can robustly capture model predictions through an ensemble of parameter sets (10).

Pathological conditions leading to tumor progression have revealed a plethora of microenvi-

ronmental factors, including soluble factors VEGF and TGFβ. VEGFA has been shown critical for tumor progression via angiogenesis, while TGFβ is thought to have both protective and transformative roles, depending on the extent of disease progression (4, 5). In the context of EMT, the combined role of both VEGFA and TGFβ has yet to be understood. Recent evidence both *in vitro* and *in vivo* have identified the ability of epithelial cells to obtain heterogeneous phenotypes, rather than the classical mesenchymal transition (2, 27). For example, studies exploring the levels of EMT markers in cancerous human epithelial cell lines were found to contain a spectrum of expression profiles, such that both ecadherin and vimentin positive cells were found (28). Furthermore, Zajchowski *et al.*, speculated that these expression profiles were important for maintaining epithelial properties, while allowing other characteristics such as proliferation and migration (29). A fundamental question often discussed is whether phenotype heterogeneity reflects the plasticity of normal cells responding to pathological conditions. Our results suggest that hybrid phenotypes are clearly evident and one possibility is through combined treatment of two growth factors commonly localized in the tumor microenvironment, VEGFA and TGFβ.

Underlying the convergence of TGFβ2 and VEGFA signaling pathways, our model identified key transcription factors (Sp1 and NFAT) critical for regulating ecadherin and vimentin expression. Specifically, we showed *in vitro* that NFAT expression and nuclear localization was critical for ecadherin expression during phenoype heterogeneity. Recent studies have suggested the importance of nuclear factor of activated T cells (NFAT) as a key transcription factors involved in cell growth, survival, invasion, angiogenesis and cancer (30). For example, proliferation and anchorage-independent growth of pancreatic tumor cells is dependent on calcineurin activity and NFATc1, which induces MYC transcription and is consistent with high levels of nuclear NFATc1 in pancreatic cancers (31). Likewise, our results found that VEGFA was a potent inducer of NFATc1 expression and may be required for epithelial cell polarization and tubulogenesis. Although NFAT isoforms were not specifically addressed in our work, our simulations suggest that NFAT is capable of mediating EMT (subset of population). Experimentally, we found that ecadherin expression levels are dependent upon NFAT dephosphorylation in response to simultaneous VEGFA and TGFβ2 treatment. These results suggest that NFAT (possibly NFATc1) plays a critical role in maintaining

cell-cell contacts, even during partial EMT.

The ability of epithelial cells to reproduce a tissue-like organization when grown inside a 3D extracellular matrix (ECM) has been widely applied for understanding tubular formation processes. MCF10A cells have been previously shown to form structures that closely resemble acini (multi-lobed cluster of cells) (32). Underlying this process, it is thought that a cellular response reminiscent of a partial epithelial mesenchymal transition ensues, stimulating further branching and formation of acini. It has been speculated that this well controlled process of tubulogenesis might be co-opted as a mechanism for tumour cells to break away from a primary lesion and invade through the stroma (33). However, because the EMT-like process is transient, clusters of tumor cells can reform at a high rate, possibly explaining why invasive human carcinomas are frequently observed to be collections of cells with varying degrees of gland-like differentiation. Based on our results, we show that that heterogeneous phenotype during EMT, is important for underlying cellular migration and invasion leading to tubular branching. However, a salient feature of partial EMT is the retention of cell-cell contacts in which cells possess migratory properties, but do not completely break away from their neighbors. By quantifying cell morphology, we were able to conclude that cells within this hybrid phenotype still maintain properties of epithelial cells, in comparison to a fully differentiated mesenchymal state. This might explain why fibroblastoid morphology, an important feature of traditional EMT, is not commonly observed in human carcinomas (34).

References

1. J. P. Thiery, “Epithelial-mesenchymal transitions in development and pathologies,” *Curr Opin Cell Biol*, vol. 15, pp. 740–6, Dec 2003.
2. K. Polyak and R. A. Weinberg, “Transitions between epithelial and mesenchymal states: acquisition of malignant and stem cell traits.,” *Nat Rev Cancer*, vol. 9, pp. 265–273, Apr 2009.
3. J. P. Thiery and J. P. Sleeman, “Complex networks orchestrate epithelial-mesenchymal transitions,” *Nat Rev Mol Cell Biol*, vol. 7, pp. 131–42, Feb 2006.
4. N. Ferrara, “Vegf and the quest for tumour angiogenesis factors,” *Nat Rev Cancer*, vol. 2, pp. 795–803, Oct 2002.
5. B. C. Willis and Z. Borok, “Tgf-beta-induced emt: mechanisms and implications for fibrotic lung disease,” *Am J Physiol Lung Cell Mol Physiol*, vol. 293, pp. L525–34, Sep 2007.
6. S. Ahmed and A. Nawshad, “Complexity in interpretation of embryonic epithelial-mesenchymal transition in response to transforming growth factor-beta signaling,” *Cells Tissues Organs*, vol. 185, no. 1-3, pp. 131–45, 2007.
7. S.-W. Chung, F. L. Miles, R. A. Sikes, C. R. Cooper, M. C. Farach-Carson, and B. A. Ogunnaike, “Quantitative modeling and analysis of the transforming growth factor beta signaling pathway,” *Biophys J*, vol. 96, pp. 1733–50, Mar 2009.
8. J. M. G. Vilar, R. Jansen, and C. Sander, “Signal processing in the tgf-beta superfamily ligand-receptor network,” *PLoS Comput Biol*, vol. 2, p. e3, Jan 2006.
9. S. O. Song, A. Chakrabarti, and J. D. Varner, “Ensembles of signal transduction models using pareto optimal ensemble techniques (poets),” *Biotechnol J*, vol. 5, pp. 768–80, Jul 2010.
10. R. N. Gutenkunst, J. J. Waterfall, F. P. Casey, K. S. Brown, C. R. Myers, and J. P. Sethna, “Universally sloppy parameter sensitivities in systems biology models,” *PLoS Comput Biol*, vol. 3, pp. 1871–78, Oct 2007.
11. D. Medici, E. D. Hay, and D. A. Goodenough, “Cooperation between snail and lef-1 transcription factors is essential for tgf-beta1-induced epithelial-mesenchymal transition,” *Mol Biol Cell*, vol. 17, pp. 1871–9, Apr 2006.
12. D. Medici, E. D. Hay, and B. R. Olsen, “Snail and slug promote epithelial-mesenchymal transi-

tion through beta-catenin-t-cell factor-4-dependent expression of transforming growth factor-beta3," *Mol Biol Cell*, vol. 19, pp. 4875–87, Nov 2008.

13. R. Tasseff, S. Nayak, S. O. Song, A. Yen, and J. D. Varner, "Modeling and analysis of retinoic acid induced differentiation of uncommitted precursor cells.," *Integr Biol (Camb)*, vol. 3, pp. 578–591, May 2011.
14. L. J. Jensen, M. Kuhn, M. Stark, S. Chaffron, C. Creevey, J. Muller, T. Doerks, P. Julien, A. Roth, M. Simonovic, P. Bork, and C. von Mering, "String 8–a global view on proteins and their functional interactions in 630 organisms," *Nucleic Acids Res*, vol. 37, pp. D412–6, Jan 2009.
15. R. Linding, L. J. Jensen, G. J. Ostheimer, M. A. T. M. van Vugt, C. Jørgensen, I. M. Miron, F. Diella, K. Colwill, L. Taylor, K. Elder, P. Metalnikov, V. Nguyen, A. Pasculescu, J. Jin, J. G. Park, L. D. Samson, J. R. Woodgett, R. B. Russell, P. Bork, M. B. Yaffe, and T. Pawson, "Systematic discovery of in vivo phosphorylation networks," *Cell*, vol. 129, pp. 1415–26, Jun 2007.
16. "Transfac: an integrated system for gene expression regulation.," *Nucleic Acids Res*, vol. 28, pp. 316–319, Jan 2000.
17. R. Derynck and Y. E. Zhang, "Smad-dependent and smad-independent pathways in tgf-beta family signalling," *Nature*, vol. 425, pp. 577–84, Oct 2003.
18. J. Massagué, J. Seoane, and D. Wotton, "Smad transcription factors," *Genes Dev*, vol. 19, pp. 2783–810, Dec 2005.
19. B. Schoeberl, C. Eichler-Jonsson, E. D. Gilles, and G. Muller, "Computational modeling of the dynamics of the MAP kinase cascade activated by surface and internalized EGF receptors.," *Nat Biotechnol*, vol. 20, pp. 370–375, Apr 2002.
20. W. W. Chen, B. Schoeberl, P. J. Jasper, M. Niepel, U. B. Nielsen, D. A. Lauffenburger, and P. K. Sorger, "Input-output behavior of ErbB signaling pathways as revealed by a mass action model trained against dynamic data.," *Mol Syst Biol*, vol. 5, p. 239, 2009.
21. R. Tasseff, S. Nayak, S. Salim, P. Kaushik, N. Rizvi, and J. D. Varner, "Analysis of the molecular networks in androgen dependent and independent prostate cancer revealed fragile and robust subsystems," *PLoS One*, vol. 5, no. 1, p. e8864, 2010.

22. J. Aramburu, M. B. Yaffe, C. L-Rodrez, L. C. Cantley, P. G. Hogan, and A. Rao, “Affinity-driven peptide selection of an nfat inhibitor more selective than cyclosporin a.,” *Science*, vol. 285, pp. 2129–2133, Sep 1999.

23. E. Dhimolea, M. V. Maffini, A. M. Soto, and C. Sonnenschein, “The role of collagen reorganization on mammary epithelial morphogenesis in a 3d culture model.,” *Biomaterials*, vol. 31, pp. 3622–3630, May 2010.

24. M. Helmy, J. Gohda, J.-I. Inoue, M. Tomita, M. Tsuchiya, and K. Selvarajoo, “Predicting novel features of toll-like receptor 3 signaling in macrophages.,” *PLoS One*, vol. 4, no. 3, p. e4661, 2009.

25. J. Handl, D. B. Kell, and J. Knowles, “Multiobjective optimization in bioinformatics and computational biology,” *IEEE/ACM Trans Comput Biol Bioinform*, vol. 4, no. 2, pp. 279–92, 2007.

26. S. O. Song and J. Varner, “Modeling and analysis of the molecular basis of pain in sensory neurons,” *PLoS One*, vol. 4, no. 9, p. e6758, 2009.

27. R. Strauss, Z.-Y. Li, Y. Liu, I. Beyer, J. Persson, P. Sova, T. Möller, S. Pesonen, A. Hemminki, P. Hamerlik, C. Drescher, N. Urban, J. Bartek, and A. Lieber, “Analysis of epithelial and mesenchymal markers in ovarian cancer reveals phenotypic heterogeneity and plasticity,” *PLoS One*, vol. 6, no. 1, p. e16186, 2011.

28. R. M. Neve, K. Chin, J. Fridlyand, J. Yeh, F. L. Baehner, T. Fevr, L. Clark, N. Bayani, J.-P. Coppe, F. Tong, T. Speed, P. T. Spellman, S. DeVries, A. Lapuk, N. J. Wang, W.-L. Kuo, J. L. Stilwell, D. Pinkel, D. G. Albertson, F. M. Waldman, F. McCormick, R. B. Dickson, M. D. Johnson, M. Lippman, S. Ethier, A. Gazdar, and J. W. Gray, “A collection of breast cancer cell lines for the study of functionally distinct cancer subtypes,” *Cancer Cell*, vol. 10, pp. 515–27, Dec 2006.

29. D. A. Zajchowski, M. F. Bartholdi, Y. Gong, L. Webster, H. L. Liu, A. Munishkin, C. Beauheim, S. Harvey, S. P. Ethier, and P. H. Johnson, “Identification of gene expression profiles that predict the aggressive behavior of breast cancer cells,” *Cancer Res*, vol. 61, pp. 5168–78, Jul 2001.

30. M. Mancini and A. Toker, “Nfat proteins: emerging roles in cancer progression.,” *Nat Rev Cancer*, vol. 9, pp. 810–820, Nov 2009.

31. “Sequential activation of nfat and c-myc transcription factors mediates the tgf-beta switch from a suppressor to a promoter of cancer cell proliferation.,” *J Biol Chem*, vol. 285, pp. 27241–27250, Aug 2010.

32. J. Debnath, S. K. Muthuswamy, and J. S. Brugge, “Morphogenesis and oncogenesis of mcf-10a mammary epithelial acini grown in three-dimensional basement membrane cultures.,” *Methods*, vol. 30, pp. 256–268, Jul 2003.

33. L. E. O’Brien, K. Tang, E. S. Kats, A. Schutz-Geschwender, J. H. Lipschutz, and K. E. Mostov, “Erk and mmps sequentially regulate distinct stages of epithelial tubule development.,” *Dev Cell*, vol. 7, pp. 21–32, Jul 2004.

34. J. Debnath and J. S. Brugge, “Modelling glandular epithelial cancers in three-dimensional cultures.,” *Nat Rev Cancer*, vol. 5, pp. 675–688, Sep 2005.

35. R. Kohavi, “A study of cross-validation and bootstrap for accuracy estimation and model selection,” in *International joint Conference on artificial intelligence*, vol. 14, pp. 1137–1145, Citeseer, 1995.

36. M. Abramoff, P. Magelhaes, and S. Ram, “Image processing with imagej,” *Biophotonics International,*, vol. 11, pp. 36–42, 2004.

37. C. Fonseca, P. Fleming, *et al.*, “Genetic algorithms for multiobjective optimization: Formulation, discussion and generalization,” in *Proceedings of the fifth international conference on genetic algorithms*, vol. 423, pp. 416–423, Citeseer, 1993.

38. K. G. Gadkar, F. J. Doyle, 3rd, T. J. Crowley, and J. D. Varner, “Cybernetic model predictive control of a continuous bioreactor with cell recycle,” *Biotechnol Prog*, vol. 19, no. 5, pp. 1487–97, 2003.

CHAPTER 8

MULTIDISCIPLINARY INQUIRY BASED LEARNING USING AN EX-OVO CHICKEN CULTURE PLATFORM TO INVESTIGATE NEO-ANGIOGENESIS IN DEVELOPMENT

8.1: Summary

Embryonic development offers a unique perspective on the function of many biological processes and their heightened sensitivity to environmental factors. This hands-on lesson investigates the effects of prostaglandin E1 (PGE1) on the morphogenesis of chick vasculature. PGE1 is applied to shell-less (ex-ovo) cultured chick embryos, which are highly accessible and intrinsically spawn inquiry. The student activities mirror the scientific research process, including review of the scientific literature, hypothesis formation, experimental design, interpretation of data, and re-evaluation of initial hypothesis. This exercise supports instruction on developmental biology, biophysics, animal research, and experimental design, and is motivated by a clinically relevant health issue.

8.2: Introduction

The cardiovascular system is a critical supplier of nutrients and oxygen for vertebrate development and homeostasis. During embryonic development, vasculature is formed by both vasculogenesis and angiogenesis. Vasculogenesis, which consists of *de novo* vessel formation from angioblasts, provides the nascent vascular network, particularly during early embryonic life. Angiogenesis, which refers to expansion of a pre-existing vascular bed through sprouting, bridging and intussusceptive growth, intervenes mostly during later stages of embryogenesis. Recent experimental studies have demonstrated that Prostaglandin E1 (PGE1) can contribute to embryonic induction of neo-angiogenesis (Ribatti and Djonov 2011).

Prostaglandins are a family of chemical messengers which are involved in local signaling within tissues and are a group of lipid compounds that are derived enzymatically from fatty acids. Specifically, every prostaglandin contains 20 carbon atoms, including a 5- ring and signals through a wide array of G-protein coupled receptors (Amano, Hayashi et al. 2003). The effects of the signal are highly dependent upon both the specific type of prostaglandin as well as the properties of the target tissue cells. For instance, the same prostaglandin may have different effects when acting upon the endothelial cells of the gastrointestinal tract than on the vasculature of inflamed tissue (Jabbour and Sales 2004). In the developing chick embryo, PGE1 has been shown a potent inducer of neo-angiogenesis which is important for developing the chorioallantoic membrane (CAM) (Dohle, Pasa et al. 2009).

The chicken embryo chorioallantoic membrane (CAM) assay has been a model for studying neovascularization since the early 1970's when it was adapted by Folkmann et al (Gimbrone, Cotran et al. 1974). While there have been many variations developed over the years, the basic assay is performed by implanting a membrane or filter paper containing the compound of interest on the chick embryo CAM through an ex-ovo platform. The subsequent incubation period ranges from 1-3 days, depending on the compound, after which time angiogenesis can be quantified via image analysis. The CAM assay is quick, technically simple, and inexpensive making it suitable for a classroom activity.

The ex-ovo culture is an intrinsically inquiry based classroom activity as the natural response of students is to ask, "What will happen to the chick embryo?" The high school lesson engages this enthusiasm by exploring the role of PGE1 on the developing chick vasculature. The teaching activities include an interactive background of PGE1 scientific literature, hypothesis driven experiments, hands-on ex-ovo culture with PGE1 treated embryos, systematic measurement of growth, and interpretation of data in the context of the reviewed literature. This

exercise supports instruction in developmental biology, molecular signaling, animal research, experimental design, and is motivated by a clinically relevant health issue using current scientific research.

8.3: Preparing for the Study

8.3.1: Materials and Methods

- Fertilized white Leghorn chicken eggs (local poultry farm)
- Egg Incubator & Rocker (HovaBator, GQF Mfg. $60-$100)
- Cling Wrap
- 70% ethanol
- Rubber bands (#16, 2.5 in)
- Rubber gloves & Safety Glasses
- 9 oz plastic cups (Dia. 3in)
- 100 mm diameter Petri dish
- Whatman Filter Paper Size 3
- 1.5 ml centrifuge tubes (optional)
- Forceps
- Prostaglandin E1 (Cayman Chemicals 13010 $15)
- USB Microscope Veho VMS-100 (~$70) or alternative large working distance scope

Safety: Prostaglandin E1 should be handled with gloves and safety glasses

Preparation of Incubator and Chick Embryos

Fertilized white Leghorn chicken eggs should be obtained from your local poultry farms. These fertilized embryos can be stored in a cooler maintained at 13 ˚C (55 ˚F) for up to 3-4 days until ready for use. Prior to the start of your activity, clean out incubator with soap and water to

remove contaminates. Dilute bleach or 70% ethanol may be used to sterilize incubator. Line base of incubator with aluminum foil for easy clean up and place thermometer inside. Pre-heat incubator to 37 ˚C (99 ˚F), and let stand 1 hour to confirm constancy of temperature. Place eggs blunt side up in incubator and turn on rocker to chick start incubation (day 0). Include a ¾ filled 9 oz cup of water inside incubator to maintain humidity.

8.3.2: Ex-ovo Culture of Chick Embryos

After 72 hours (day 3), prepare hammocks for ex-ovo culture (Figure 1). Fill ¾ of 9 oz plastic cups with warm water. Cut about 20 x 20 cm (8 x 8 in) square of cling wrap and place loosely inside the cups. Cling wrap should be in contact with water and form loose hammock. Secure cling wrap to cup with a rubber band (Figure 7.1A). Spray the plastic wrap with 70% ethanol to prevent contamination. Remove eggs from incubator after 72 hours of incubation. Sterilize eggs by spraying surface with 70% ethanol. Lay the eggs horizontally on egg carton for 1-2 minutes to allow the embryo to rotate (Figure 7.1B). Using a sharp edge (like the edge of a metal bucket or a glass beaker), tap the egg gently until there is a small dent on the underside of the egg (Figure 7.1C). Put thumbs in opposite sides of the dent and open the shell directly above hammock (Figure 7.1D). The entire yolk, egg white, and embryo should fall into the hammock softly (Figure 7.1E). If the embryo is not on top side of yolk, gently rotate egg yolk with fingers (using gloves). Place a 100 mm diameter Petri dish on top of the cup to seal the embryo. Transfer the embryo back into the incubator set at 37°C with water cup to maintain humidity (Figure 7.1F). Observe embryos as long as you would like or directed by the activity. We recommend that the students perform the ex-ovo culture under close supervision of an instructor or teaching aid.

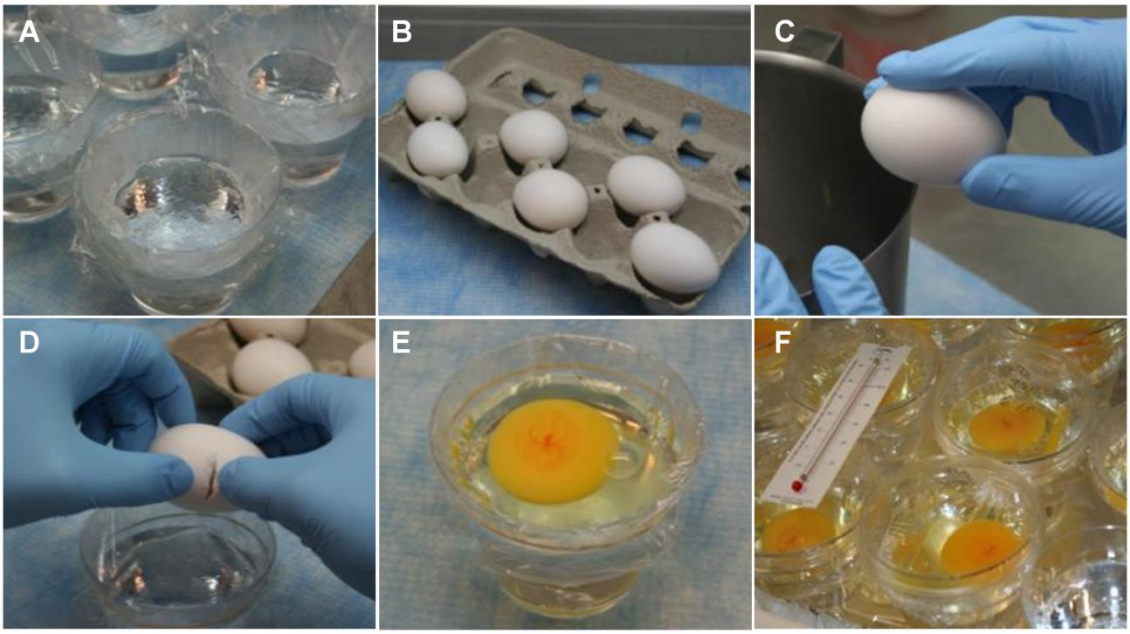

Figure 8.1 – Step-by-step ex-ovo culture technique. A) Prepare hammocks in plastic cups, B) Lay eggs on blunt side to prep for cracking, C) Use sharp edge to create narrow crack on center of egg, D) Carefully open egg shell directly above hammock and cup E) Rotate embryo to top side of egg yolk, F) Place in incubator at to 37 °C (99 °F)

8.3.3: Motivate Study and Discuss Background

Before investigating the effect of PGE1 on the embryonic chick, it is important to motivate this study. Using the information outlined in the introduction and below, attempt to connect the importance of neo-angiogenesis with the students experience or perceptions of the issue. We found this was best done through a brief, but interactive large group discussion. In addition, we recommend discussing normal embryonic development, particularly pertaining to chick development (Hamburger and Hamilton embryo atlas images provided in the supplement and/or online at www.butcherlab.com).

Sufficient background information is needed to further place neo-angiogenesis context and facilitate the students' hypothesis formation. The students were given excerpts from introduction sections of scientific and medical journal articles to analyze. Field-specific literature was paraphrased to increase the readability of the excerpts. With each excerpt we included a series of questions which assessed reading comprehension and the acquisition of scientific concepts. Though reading technical literature can be difficult for students, completion of the exercise empowered the students and broke down the false notion that scientific research can only be understood by scientists. The exercise is similar to scientific reading comprehension questions on many standardized tests. It may also be used as a graded activity, which provides early feedback for both student and teacher on the progress of the project. We recommend small groups of two or three students, preferably with a range of ability, for this exercise. An initial read-through as a large group can remove any class wide gaps in understanding.

8.3.4: Background Information Excerpt Example

Read the excerpt from (Ribatti and Djonov 2011) and answer the following questions.

"Angiogenesis is an important process by which new blood vessels are formed, both in health and disease. Starting with the hypothesis of Judah Folkman (1933-2008) that tumor growth is angiogenesis dependent, this area of research has a solid scientific foundation. More than 30 years ago, Folkman found a revolutionary new way to think about cancer. He postulated that in order to survive and grow, tumors require blood vessels and that by cutting off the blood supply; a cancer could be starved into remission. Several clinical studies have shown a positive correlation between the number of vessels in the tumor, metastasis formation and prognosis. The genetic instability of tumor cells permits the occurrence of multiple genetic alterations that facilitate tumor progression and metastasis, and cell clones with diverse biological aggressiveness may coexist within the same tumor. These two properties allow tumors to

acquire resistance to cytotoxic agents. Inhibiting angiogenesis is a major area of therapeutic development for the treatment of cancer. Whereas conventional chemotherapy, radiotherapy and immunotherapy are directed against tumor cells, antiangiogenic therapy is aimed at the vasculature of a tumor and will either cause total tumor regression or keep tumors in a state of dormancy. Even though numerous compounds inhibit angiogenesis, few of them have proved effective *in vivo*, and only a couple of agents have been able to induce tumor regression."

Table 8.1 - Background Questions to Help with Hypothesis Generation
Q#1) List the stages of chick embryonic development and illustrate normal morphology.
Q#2) What are prostaglandins and how do they signal to cells?
Q#3) Are the effects of prostaglandins tissue or cell type specific?
Q#4) What role does angiogenesis play in development?
Q#5) What does this excerpt indicate about the role of angiogenesis in cancer?
Q#6) Why would scientists target molecules which induced neo-angiogenesis in cancer?

8.3.5: Experimental Design

After reading the background material and discussing it as a class, divide the students into groups of 3-4 to prepare for experiment. Ask each group to formulate and record a hypothesis on what will happen when PGE1 is applied to the vasculature network of the ex-ovo cultured embryo as compared to a normal embryo. Remind the students to develop a testable hypothesis, considering ahead of time which metrics they will use to evaluate the hypothesis. In this module, embryo, the number of vascular branches was the morphological parameter used to compare between treatments (Figure 7.2). Other measurement ideas include CAM width, anterior vein thickness, or radius of vasculature.

8.3.6: Example Hypothesis & Proposed Metrics

We hypothesis that PGE1 administered to the embryo will create a localized neo-angiogenesis. We will use "number of vascular branches" as metric of vascular growth.

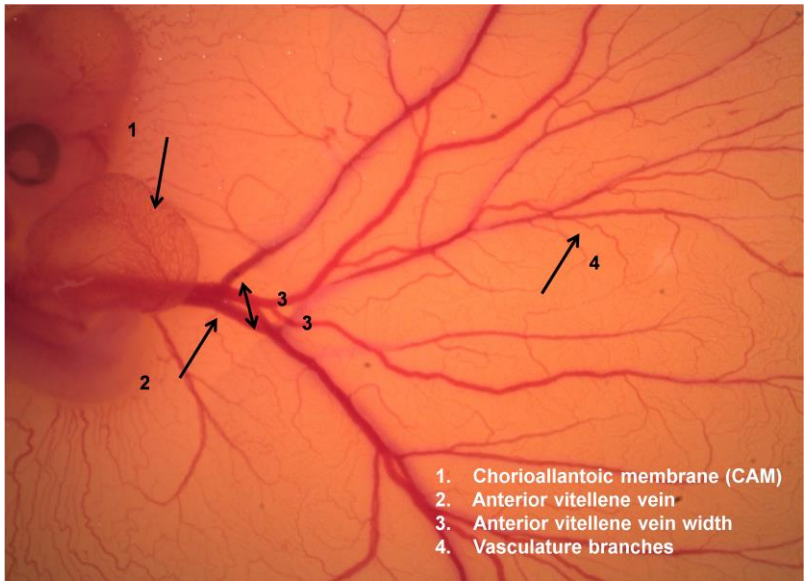

Figure 8.2 – Image of chick embryo in ex-ovo culture at 4.5 days of incubation.

Control experiments are an essential component to any well designed scientific study. Spend a brief, but intentional time explaining the types and purpose of controls with the students. Solicit their assistance in identifying the most appropriate controls for this study. We recommend two controls, an untreated group (standard control) and a filter paper with PBS (phospho-buffered saline) only (sham control). The standard control will provide the benchmark of normal development to compare with PGE1 treated, and the sham control to verify that the effects observed are not due to the filter paper or PBS.

8.4: Conducting the Investigation

8.4.1: Environment Perturbation Study - Addition of PGE1

From previous dose dependent and temporal responses, we have determined that a PGE1 concentration of 1mg/ml at applied at day 8 of incubation induces morphological changes by day 10 of incubation. We recommend that the teacher mix and administer the PGE1 treatment to the embryo. Cut the Whatman filter paper into 2-5 mm diameter punches or strips. Dilute 1mg of PGE1 in 1ml of PBS in a 1.5ml tube. Place the filter paper sections in the 1.5ml tube and let soak for 30 minutes. Using forceps, remove filter paper from PGE1 solution and place on the ex-ovo culture. We suggest placement of the filter paper on the right side of the embryo, within the vasculature (Figure 7.3). Capture images of the embryo and vasculature sequentially at day 8, day 9, and, day 10 using the USB-microscope (Veho VMS-100, Figure 7.3 and 7.4). Measure the predetermined metrics of vascular branches from these images using open source software ImageJ (NIH, http://rsbweb.nih.gov/ij/). Simple instructions for ImageJ are available at http://climb.bme.cornell.edu/embryo.php. Hand measurement using a caliper or ruler is a viable alternative. Finally, record the measurements in tables for each metric (Figure 5).

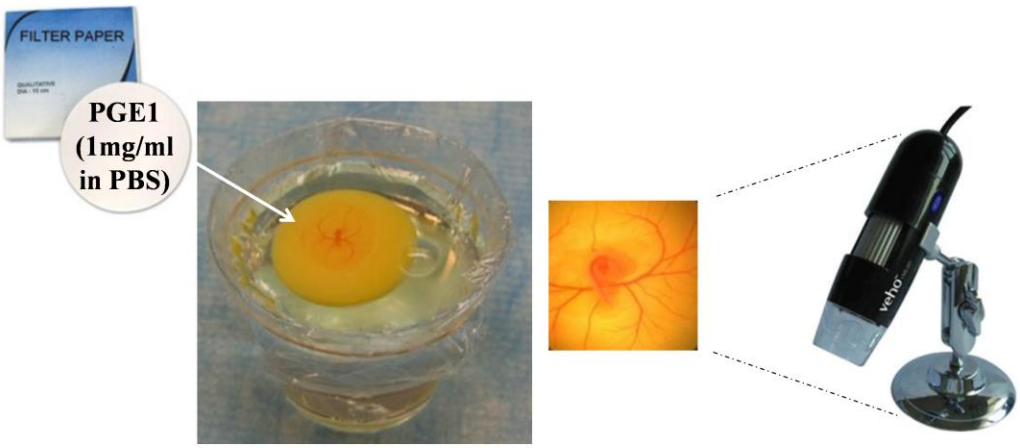

Figure 8.3 – Experimental design consists of soaking filter paper in different concentrations of prostaglandin E1 (PGE1) and placing it on the embryonic vasculature. Following several days of incubation, a USB-microscope can capture the downstream effects on development.

8.4.2: Analysis & Interpretation of PGE1 Treatment Results

An essential part of the scientific process, and often the most challenging, is to quantitatively analyze and correctly interpret the data. To assist with this task, we recommend the students plot the data, either digitally or by hand, for each output measured (Figure 7.4). Instruct the students to use the data to confirm or deny their initial hypothesis. If the hypothesis is confirmed, the students must prepare a series of arguments from the data to support their claim. If the hypothesis fails, the students must generate a new hypothesis based on the results of the study. It is also important to consider the implications of these results in a broader context. For instance, ask the students how these results might relate to wound healing or cancerous tumors.

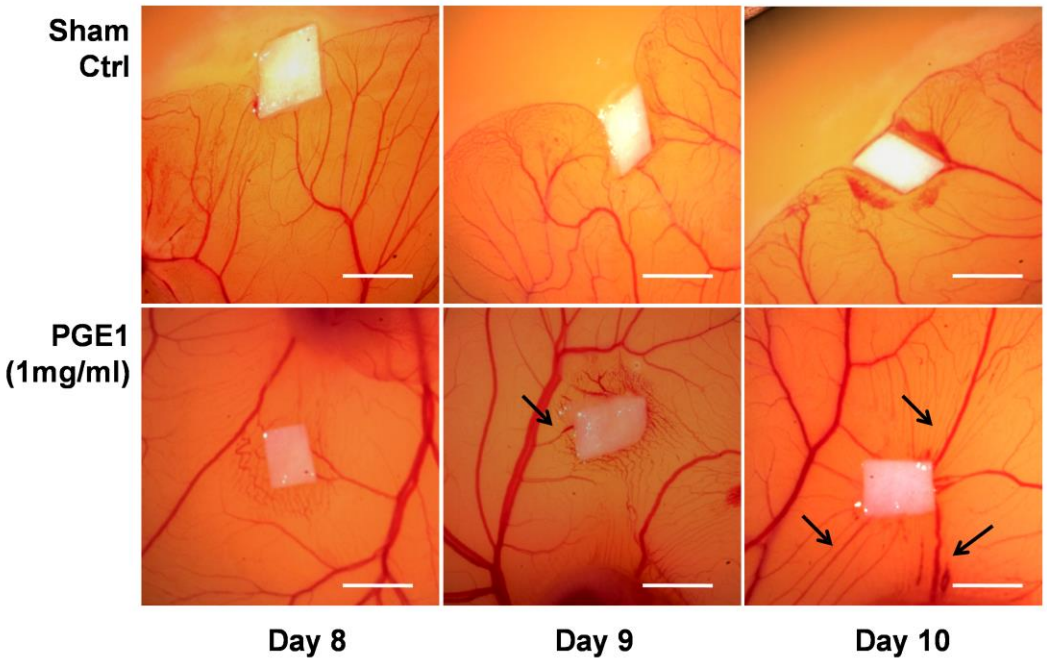

Figure 8.4 – PGE1 perturbation study data set. Array of ex-ovo chick images across treatment and over time. Treatment resulted in neo-angiogenesis over a three day period starting at day 8. Scale bar indicates 5 mm.

8.4.3: Example Data Analysis & Interpretation Worksheet

Using the generated tables, line graphs, and previous understanding of embryonic development and PGE1, work through the following questions as you analyze the data (Figure 7.5).

- **Q#1)** Compare the number of vasculature branches between the control and PGE1 treatments. Did the addition of PGE1 increase or decrease vasculature?
    - While the control and treated embryos had roughly the same number of vasculature branches, by day 10 the number of vasculature branches within the (1mg/ml) PGE1 treatment increased 2.8 times than the control. These results suggest that PGE1 has a positive effect on vasculature within the embryo.

- **Q#2)** Are the sham results different from the control? What do the sham results indicate about our method of treatment?
    - The sham results do not appear to be significantly different from the control. This indicates that the defects were not induced by the filter paper or PBS, but instead can be wholly attributed to the addition of PGE1.

- **Q#3)** Approximate the growth rate of each treatment by determining the slope of the "tip-to-tail" curves. Which condition had the fastest growth rate? Is the rate linear?
    - Control Sham – 0.25 branches/day, PGE1 1mg/ml – 4 branches/day. The control embryo had the slowest growth rate and the 1mg/ml PGE1 treatment had the fastest. The PGE1 growth rate was roughly 16 times as fast as the control treatment. This result agrees with the conclusion in question #1, that PGE1 increased the number of vasculature branches within the embryo.
    - Growth rate is exponential for the PGE1. This suggests that the embryo needs time to respond to the PGE1 and may involve a positive feedback system.

- **Q#4)** From our data, we see that PGE1 treatment effected the ***local*** development of the embryos vasculature. Do you think any effect will occur globally?
    - PGE1 is saturated in filter paper and is applied over a small area away from the embryo. However, it is placed within the blood vessel bed. This particular placement on a vessel may facilitate the spread, and uptake, of PGE1 in the embryo body. This emphasizes the substantial role the circulatory system plays in nutrient consumption and trafficking, demonstrating how even local concentrations of agents can have global consequences due to rapid transport throughout the developing embryo.

- **Q#5)** Explain why tumors need blood vessels and why my PGE1 be an important molecule underlying cancer spreading.
    - Tumors need oxygen to rapidly grow and thrive. By creating neo-angiogenesis, vasculature can be formed to supply these important nutrients. PGE1 may be up-regulated in cases of cancer since it has been shown a potent inducer of vessel formation within the developing embryo.

Number of blood vessels	Day 8	Day 9	Day 10
CTRL	5.5	4.5	6
CTRL ST. DEV.	1	1.25	2.5
PGE1 (1mg/ml)	6	8	17
PGE1 ST. DEV.	1	2.5	5

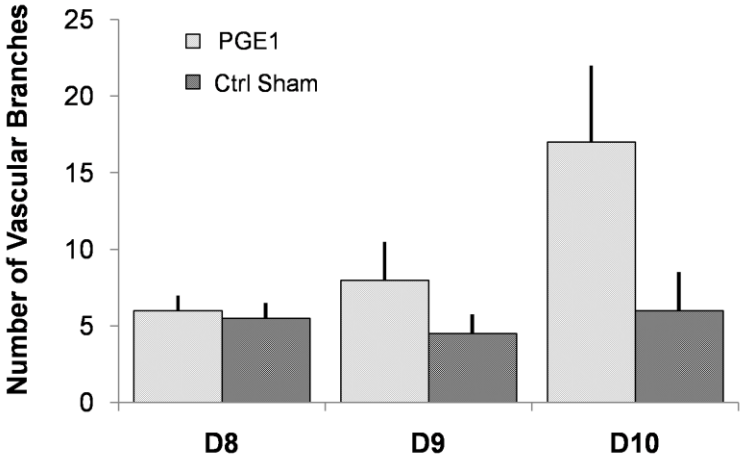

Figure 8.5 – Quantifying the number of vascular branches for PGE1 perturbation study using open source software (ImageJ) provided by the NIH.

8.5: Discussion

The embryo provides a unique lens through which to study general (cell activity, organ systems) and development specific (cell differentiation, morphogenesis) processes in biology and physics. Watching the embryo induces fundamental questioning of why some structures develop first vs. later on, how the embryo is feeding itself, and how processes change with growth. Even if just a biology classroom, the effects of physics such as diffusion, transport, and mechanical forces can be incorporated into our lesson framework. Instructional versatility enables the breadth of content to be appropriately scaled to student ability or knowledge base. For instance, observation, measurement, and prediction of normal development may be sufficient for middle school biology students, while the PGE1 perturbation model may be more appropriate for upper level high school students. In the following, we present further background information and ethical issues with animal research to extend the applicability of this lesson (Figure 7.6).

Figure 8.6 – Engagment of students during the ex-ovo chick culture and analysis of experimental results.

Metabolic and Molecular Aspects of Study – Mechanism of Action

Prostaglandin E1 activates several signal transduction pathways that have been implicated in carcinogenesis. For example, PGE1 mediated activation of E prostanoid receptors (G protein couple receptors, GPCR) leads to enhanced adenylate cyclase activity and cyclic adenosine monophosphate production (cAMPs). This in turn activates protein kinase A/cyclic adenosine monophosphate response element binding protein (PKA). Upon activation, nuclear transcription factor CREB can bind to the promoter of vascular endothelial growth factor (VEGFA) to drive neo-angiogenesis and blood vessel assembly (Figure 7.7, adapted from (Mann, Backlund et al. 2005). PGE2 and PGE3 also signal through similar signaling cascades, however, their effects may be quite different depending on cell and tissue type.

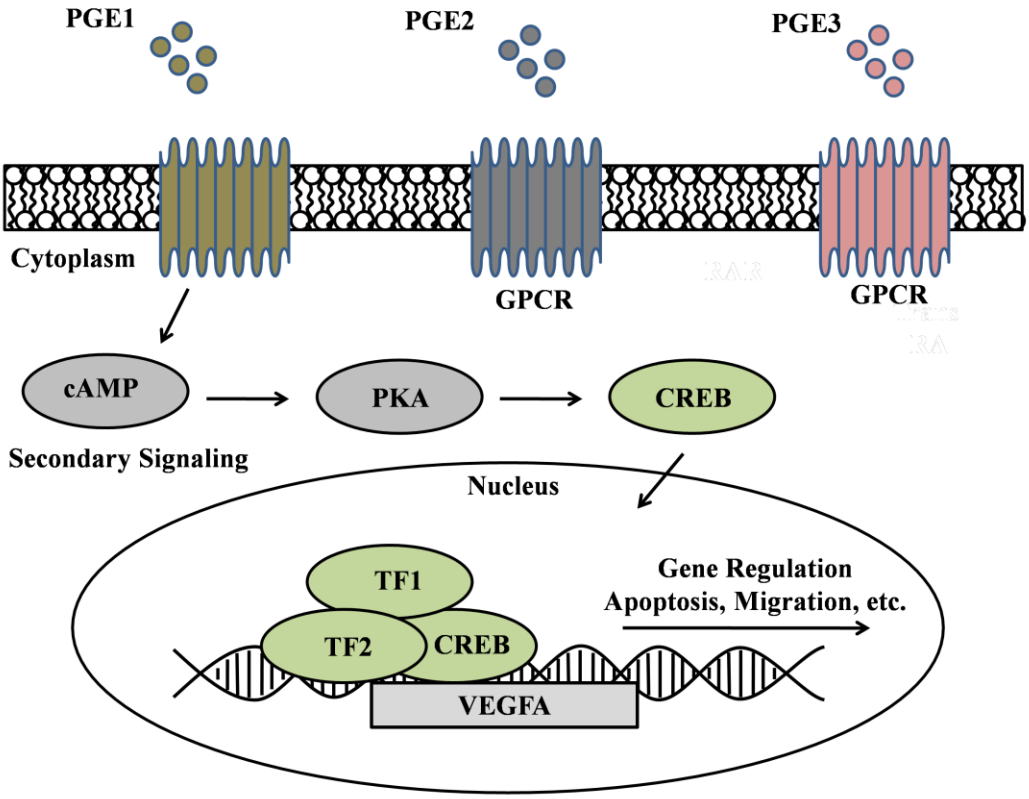

Figure 8.7 – Metabolic and molecular pathway advanced student classrooms) describing the mechanism through which PGE1 regulates gene regulation.

Bioethics of Animal Research

Using live embryos within the classroom will inevitably spark a conversation about humane treatment and ethics. We feel this is an extremely important aspect, and should not be overlooked. From a purely regulatory standpoint, all use of vertebrate animals in research, teaching and testing is regulated by the Institutional Animal Care and Use Committee (IACUC, http://www.iacuc.org/). Chick embryos younger than embryonic day 15 (E15) are assumed to be unable to experience pain, because of limited neural development. It is recommended that E14 or younger embryos be euthanized by hypothermia, typically by placing the eggs in a −20°C freezer. Chick embryos from E15 to pre-hatching should be euthanized by decapitation, anesthetic agents or another rapid and humane method. Studies using embryos within three days of hatching or hatchlings must be reviewed by the normal IACUC procedure for vertebrate animals. In our experiments, embryos will be euthanized at day 7, which is only 1/3 of the way through its 3 week hatching cycle. Therefore, the embryos cannot experience pain and are exempt from any IACUC protocols. This however, will not limit conversation about the ethics of animal research within the classroom. We encourage teachers to lead a classroom discussion on the role of animals in scientific research, and use this time effectively to discuss humane treatment and ethics. From our experience, the level of concern and opinions will vary from class to class. It is imperative to gage student sensitivity in a considerate and objective manner before conducting the experiments. Resources for animal research ethics can be found on the web: www.ethics.org.

References

Amano, H., I. Hayashi, et al. (2003). "Host prostaglandin E(2)-EP3 signaling regulates tumor-associated angiogenesis and tumor growth." J Exp Med **197**(2): 221-232.

Dohle, D. S., S. D. Pasa, et al. (2009). "Chick ex ovo culture and ex ovo CAM assay: how it really works." J Vis Exp(33).

Gimbrone, M. A., Jr., R. S. Cotran, et al. (1974). "Tumor growth and neovascularization: an experimental model using the rabbit cornea." J Natl Cancer Inst **52**(2): 413-427.

Jabbour, H. N. and K. J. Sales (2004). "Prostaglandin receptor signalling and function in human endometrial pathology." Trends Endocrinol Metab **15**(8): 398-404.

Mann, J. R., M. G. Backlund, et al. (2005). "Mechanisms of disease: Inflammatory mediators and cancer prevention." Nat Clin Pract Oncol **2**(4): 202-210.

Ribatti, D. and V. Djonov (2011). "Angiogenesis in development and cancer today." Int J Dev Biol **55**(4-5): 343-344.

Davey MG, Tickle C (2007) The chicken as a model for embryonic development. Cytogenet Genome Res 117:231-239. doi:10.1159/000103184

Yalcin HC, Shekhar A, Rane AA, Butcher JT. (2010) An ex-ovo chicken embryo culture system suitable for imaging and microsurgery applications. J Vis Exp (44). pii: 2154. doi(44): 10.3791/2154.

Table 8.2 - Addressing the National Science Education Standards

Standard	Value of this Activity
Teachers should successfully convey unifying concepts of science.	Students will successfully design, conduct, report and evaluate the effects of PGE1 on embryonic development. Using mathematics, students will process and report data to understand the origin of congenital defects through environmental factors.
Teachers should engage students in various methods and active learning through scientific inquiry.	During our investigation, we implement multiple methods of inquiry leading to scientific knowledge. Students determine the effects of PGE1 on embryonic development that require them to develop concepts and relationships from their observations, data, and inferences in a scientific manner
Teachers should organize safe and effective learning environments that promote the success of students and the welfare of all living things	Students will treat all living organisms used in the classroom or found in the field in a safe, humane, and ethical manner and respect legal restrictions on their collection, keeping, and use. Classroom discussions on using animals for experimental systems have been highlighted.
Teachers should create a community of diverse learners who construct meaning from their science experiences for further exploration and learning.	The experiments have been organized to engage students in a collaborative learning environment. In addition, technological tools such as (NIH) Image J, allow students to collect, process data, and facilitate the learning of science.

CHAPTER 9

DISCUSSION

9.1 Congenital Valve Malformations and Treatment

As presented in Chapter 1, the clinical incidence of congenital heart disease is approximately 1% of all births, with 20-30% directly related to valves in the US [1]. This statistic underestimates the true incidence of congenital valve defects, as a significant portion of these defects are not diagnosed until adulthood [2]. The most common is human bicuspid aortic valve, where the valve forms only two leaflets instead of three. Although it may function normally during development, during later stages of life BAV is prone to disease such as calcification and aortic stenosis [3]. Specific abnormalities in valve structural proteins present at birth can also contribute to valve dysfunction and disease later in life, making the distinction between congenital and acquired valve disease unclear [4]. Marfan syndrome is an example where dysfunctional expression of the fibrillin-1 gene leads to a wide spectrum of clinical phenotypes, including valve regurgitation, thickening, and prolapse. The current treatment for heart valve defects is replacement, and approximately 95,000 valve replacement surgeries are performed in the United States annually [5]. The majority of aortic valves that are replaced at any age have congenital malformations, including BAV, further supporting developmental origins of adult valve dysfunction and disease [6]. This clinical data demonstrates a serious problem of valve related disease and its etiologies.

Ongoing studies have been directed toward identifying genetic components responsible for congenital valve malformation and disease [7]. Genetic syndromes including Williams, Marfan, Trisomy 21, Alagille, Turner, and Noonan are all examples where valve malformation are prevelant [8-10]. Mitral valve prolapse is not traditionally considered a congenital malformation,

however it is heritable and be diagnosed at birth [11]. Likewise, heart malformations such as tetralogy of Fallot, hypoplastic left heart syndrome, or Ebsteins's anamoly have a strong presence of valve related defects [12]. Several gene loci have been associated valve defects, such as Notch1 in BAV, filamin-A in MVP, and fibrillin-1 in MFS [13-15].

While congenital valve malformation and disease may have a genetic component, other factors are likely to be involved. In many cases, nonsyndromic valve malformations are idiopathic and the origins are unknown. However, evidence over the last decade has suggested the importance of hemodynamics during valve development. For example, in zebrafish and chick, altered blood flow lead to dysfunctional leaflet morphogenesis [16]. The molecular mechanisms through which hemodynamics regulates valve maturation is poorly understood, especially at later stages of development. Interestingly, the genetic association of BAV with hypoplastic left heart syndrome suggests that normal valve hemodynamics is required for ventricular chamber morphogenesis [17]. Additionally, there is increasing evidence that the coordinated function of the myocardium and valves is necessary for normal prenatal heart development [18]. This creates a complicated situation such that the congenital heart malformations likely lie at the multi-scale interface of genetics and mechanics.

Currently, the treatment options for congenital valve defects are limited. In most cases, total replacements of the valve are done using mechanical valves. However, this is expensive and extremely evasive. Additionally, as the patient grows, multiple heart surgeries need to be conducted in order to accommodate for the increased size of the heart and aortic vessel. Current diagnostic tools for valve dysfunction rely on echocardiography and while the fetus is in the developing womb, there is not much that can be done. While a therapy is needed in these situations, applying a strategy to understand the mechanistic development of these abnormalities may be an effective research path [19]. That way, diagnostic tools and targeted

therapies can be developed for these underlying causes, effectively removing the need for any kind of prosthetic valvular replacement.

The paradigm for biological research in the 20th century was the use of animal models. While having the advantage of systemic circulation and immune response these models are expensive, require long development times, and often offer little mechanistic data. While animal models are need evaluate preclinical safety and confirm efficacy of drugs/devices, other technologies such as tissue engineering and in-vitro bioreactors are needed to understand cellular action in response to biological and physiological cues. Experimental research over the last 20-30 years has been developing along these lines. Tissue engineering has now been useful generating 3D constructs to more effectively model and capture the native environment. Likewise, bioreactors are important for applying controlled physiological stimulation such as electrical, chemical, or mechanical. Together, by utilizing combined approaches with animal models, tissue engineering [20], and in-vitro bioreactors [21, 22] we may begin to better understand the biological and mechanical factors which drive the embryonic valve morphogenesis and related congenital malformations.

9.2: Embryonic Valve Mechanics and Biology

Valve leaflets are critical for maintaining unidirectional blood flow during embryonic development. These tissues have evolved complex multidirectional collagenous fiber orientations that result in anisotropic mechanical properties ideally suited to their local microenvironment. Underlying this process, resident tissue fibroblasts continuously repair and remodel their tissue microenvironment in response to these mechanical cues, including secreting and/or degrading extracellular matrix proteins, releasing soluble growth factors, and reorganizing cell-cell/cell-matrix adhesive interaction. Developing leaflets are exposed to arguably the most demanding mechanical environment in the body, yet interstitial fibroblasts

thrive and mediate significant matrix turnover [19, 23]. Cyclic loading my therefore provide strong inductive signals towards resident valve cells for regulating tissue formation and homeostasis [24]. However, deciphering the role of cyclic stretch on valve phenotype combined with tissue remodeling presents a situation that is both technically challenging and theoretically difficult; some have even suggested it as a “moving” target [24].

We are beginning to understand more about embryonic valve biology and the effects of mechanical cues on their behavior. Techniques to isolate and culture these cells have only recently been developed, and to date use of these cells in tissue engineered constructs (i.e. collagen hydrogel) are becoming a more popular method to study cellular phenomenons. In Chapter 2 of this work, detailed protocols were developed to isolate pure populations of avian progenitor endocardial cells [25]. These cells were characterized through functional assays and compare favorably to other reports in the literature. The avian endocardial cells were used as the model cell source to determine biological response to mechanical forces and the effects in 3-D culture, the results of which are discussed in Chapter 5. However, before these cells could be used for that application, we developed and implemented a bioreactor capable of applying homogeneous strain field anisotropy within engineered tissue hydrogels as presented in Chapter 3. This platform was essential to enable testing of molecular, cellular, and tissue scale mechanisms within a well-defined, repeatable, and physiologically relevant microenvironment [26].

A central theme throughout this thesis was to understand the role of mechanical stretch on valvular differentiation combined with multi-scale tissue morphogenesis. However, deciphering the role of mechanical stretch during valve formation is extremely complicated due to changes in magnitude, duration, and frequency during valvular morphogenesis. Additionally, as pointed out in Chapter 6, residing valvular interstitial cell-matrix kinematics can vary in normal and

pathological conditions [27]. This leads to differences in the extent of both cell and tissue deformation. These dynamic conditions make experimental testing a difficult challenge and while it is not feasible to test every condition (nor would anyone want to), insight and clever design is needed. The purpose of this chapter is then to combine some of the results of different chapters to provide future direction into the biological responses of resident valve interstitial cells. Two prominent themes developed, and they are addressed in the following paragraphs. First expanding the definition of embryonic valve phenotype and second, understanding the role of anisotropic strain.

9.2.1: Expanding and Describing the Embryonic Valve Cell Phenotype

As demonstrated in Chapter 3 and Chapter 4, sustained cyclic stretch was a potent inhibitor of valvular myofibroblastic differentiation in a stage independent manner. The mechanism was found that stretch directly mitigates RhoA-GTP levels to inactivate SRF (serum response factor) and hence, downstream smooth muscle actin [28]. Although the regulation of a myofibroblastic to quiescent phenotype is critical for valve formation, regulation of these factors alone does not fully describe the phenotype which is seen during leaflet formation. We and others suspect that both FGF and BMP pathways play a large role in driving the mesenchymal-transformation through Sox9 and Scx transcription factors [29, 30]. Using IHC and real-time PCR, we found that the FGF and BMP pathways dramatically diverge during AV valve formation (Figure 8.1).

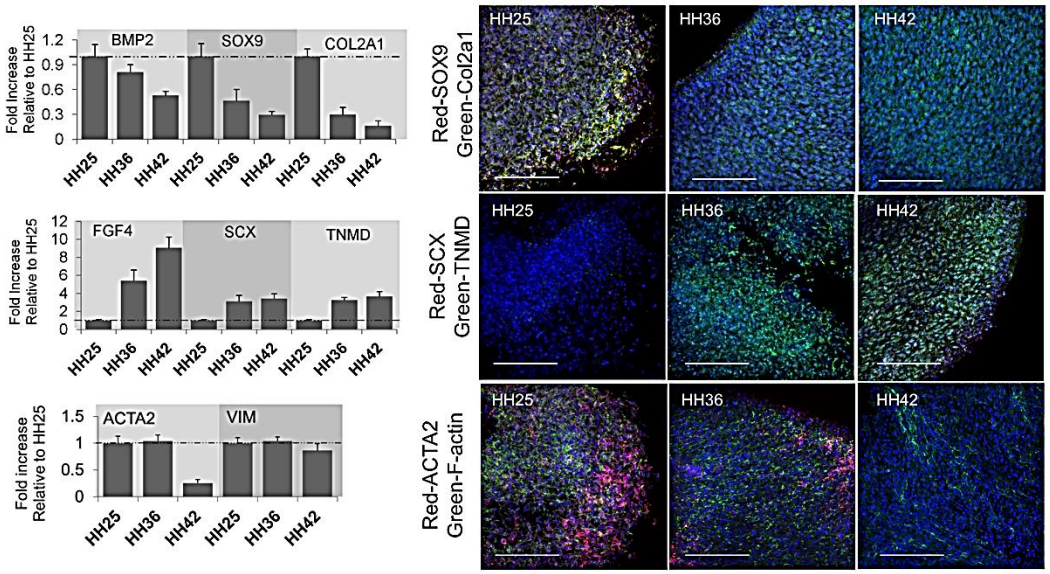

Figure 9.1 - Native expression profiles in the developing AV valve reveal the divergence of the BMP/FGF. Avian embryonic left mitral valve tissue (AV) was harvested at HH25, HH36, and HH42, and subjected to whole mount (IF) analysis.

Interestingly, Sox9 is thought to be a master regulator required for endocardial cushion cell lineage expansion, as well as differentiation associated with cartilage progenitor cells [31, 32]. In both chick and mouse, Sox9 is expressed within the endocardial cushions and remodeling leaflets. BMP2 activates expression of Sox9 and the cartilage differentiation marker Col2a1, which has been observed in cultured avian endocardial cushion cells [30]. Upon gene knockout of Sox9 in mice, embryonic lethality occurs between E11.5 and E12.5 with hypoplastic endocardial cushions. It is thought that loss of Sox9 inhibits EMT after delamination and initial migration, but before definitive mesenchymal transformation [33]. Upon targeted loss of Sox9 with Col2a1Cre in the remodeling valve, decreased expression of cartilage-associated proteins Col2a1 occurs. In adult mice, heterozygous loss of Sox9 in Col2a1Cre results in thickened valve leaflets and calcification characteristic of valve disease [32].

Furthermore, recent results demonstrate a new interaction that directly links ROCK to increased cartilage matrix production via activation of SOX9 in response to mechanical and growth factor stimulation. It was found that ROCK can directly phosphorylate SOX9 at Ser181 leading to enhanced transcription [34]. As stated previously, the activity of RhoA and Rho kinase (ROCK) has profound effects on the actin cytoskeleton, and these effects are instrumental in determining the phenotype and differentiation of vavlular interstitial cells [35]. This begs the question, is RhoA a master regulator of both myofibroblastic differentiation and fibroblast transformation? Furthermore, if mechanical strain inhibits RhoA-GTP levels, does it also effect Sox9 expression? While we were not able to directly answer this question, we conducted a few preliminary tests to evaluate the potential of this hypothesis.

Resident valve cells isolated from HH25, HH36, and HH42 avian leaflets were exposed to 20% area strain at 2.1 Hz (approximating a range between the in vivo HH23-HH36 AV valves [36]) for 24 hours with static cultures as controls. In vitro mechanical stimulation resulted in significant ($P<0.05$, normalized to 18S) differences in SOX9, COL2A1, relative to control (mechanically constrained). These results indicated that mechanical stimulation can modulate the transcription factors and ECM markers of progenitor AV cells. At early staging (HH25, HH36) mechanical strain mitigates levels of SOX9 expression (and COL2A1) (Figure 8.2).

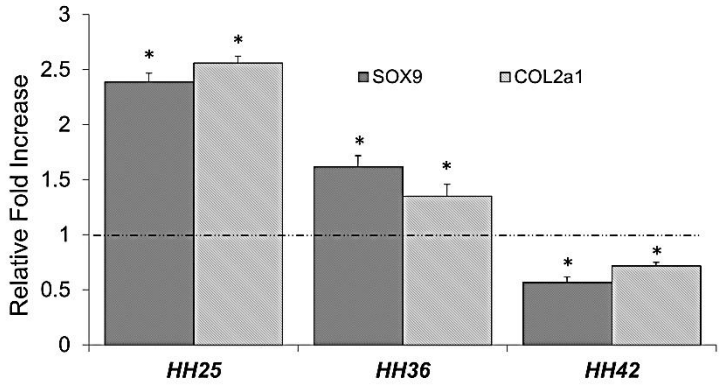

Figure 9.2 – Equiaxial strain regulates Sox9 and Col2a1 expression in a stage independent manner.

Conversely, at later stages (HH42) mechanical strain mitigates levels of SOX9 expression (and COL2A1) (Figure 8.2). While these preliminary experiments confirm the mechno-sensitivity of Sox9, expression is stage dependent effect. This is contrary to what has been shown with myofibroblastic differentiation. This suggests that although RhoA may regulate Sox9 inhibition, it does not fully explain why Sox9 expression increases at early stages (mesenchymal) and decrease at later stages (fibroblast) upon mechanical strain. Further experiments investigating the mechanism of this switch will be extremely important for understanding the complete picture of mesenchymal-fibroblast phenotype change, with respect to mechanical strain.

As a final thought, Sox9 has been shown to regulate expression of the LEF1 gene by interacting with the bcatenin pathway [37]. This is particularly interesting because the bcatenin/LEF1 pathway can directly regulate myofibroblastic differentiation through alpha-SMA expression [38]. Bcatenin has been shown elevated within the developing cushions, especially when the progenitor valve cells are of strong mesenchymal phenotype (HH25) [39]. Recently, a study LEF1 was found essential for valve endocardial cell proliferation and extracellular matrix development, but is not required for initiation of EMT [40]. While the role of bcatenin and LEF1 in valve maturation remains under investigation, the relative levels of bcatenin may help to explain why Sox9 expression increases at early stages (mesenchymal), but then decreases at later stages (fibroblast) upon mechanical strain. For example, myofibroblastic differentiation may have to precede the fibroblast transition in order to free up cytosolic Sox9 levels from the beta-catenin complex. This is because Sox9 is a potent inhibitor of bcatenin via the ubiquitination/proteasome pathway [38]. Once myofibroblastic transformation is complete, Sox9 inhibition may occur via integrin transduction and downstream cytoskeletal rearrangement.

9.2.2: Role of Strain Directionality in Embryonic Valves

Valve leaflets experience cyclic strain every cardiac cycle. Replicating these strain patterns in controlled in vitro test beds has been challenging because physiological profiles are highly anisotropic and heterogeneous [41]. The vast majority of studies have focused on modulating the magnitude and frequency of cyclic strain. However, these aspects do not change as much in vivo compared to the stretch directionality in the developing valve [42]. In Chapter 3, we implemented a novel bioreactor to investigate the relationship between anisotropic strain, cell differentiation, and matrix remodeling in 3D culture. Our findings demonstrated that applied cyclic biaxial strain anisotropy induces time dependent VIC orientation and collagen fiber alignment. During this process, ACTA2 expression was directly related to the degree of cell alignment and expression occurred perpendicular to the principal axes of loading. These findings suggest biaxial strain anisotropy, independent of magnitude or frequency is a potent regulator of rapid matrix reorganization and VIC phenotype. During development, directional mediated stretch on resident valve cells has been hypothesized, although the extent of anisotropic stretch in a stage dependent manner has yet to be invested. Furthermore, the effect of anisotropic stretch on embryonic valve progenitor differentiation is unknown.

Therefore, as a preliminary study, we sought to measure the in-vivo deformation of avian valve leaflets. Identification of the mechanical environment of developing valves is particularly challenging because of their small size, complex geometries, and rapid movements. We have developed ultrasound techniques using combined imaging modalities to characterize strain profiles on developing valve surfaces for approximating developing cushion tissue deformations [43].

Briefly, time dependent cushion specific time, 2D long axis videos (55 fps) of AV cushion/leaflet motions were digitized using NIH Image, traced, and finite strain equations were solved at each

time point across the cardiac cycle. Strain tensors were then converted into the principal strains. Strain profiles were generated from HH23-32 septal mitral leaflets and deformation was found to exceed in both magnitude over development. Furthermore, at later stages HH30-32, strain was found anisotropic (20% in the XX and 40% in the YY direction), suggesting that strain directionality is important during leaflet formation (Figure 9.3).

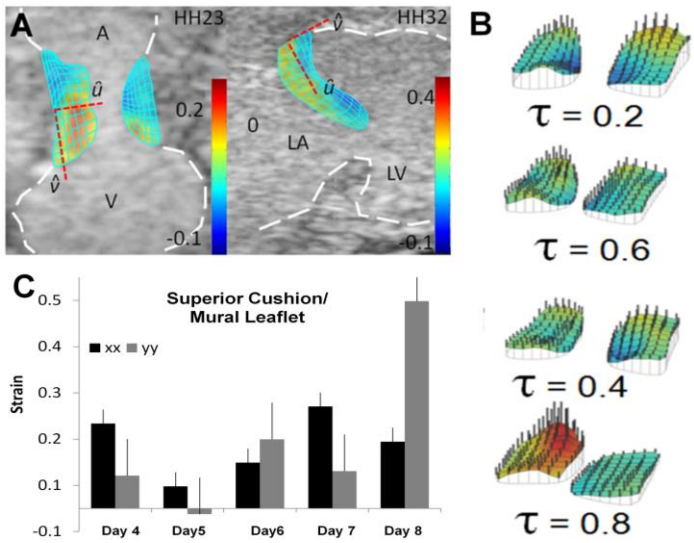

Figure 9.3 – Estimated in-vivo stain profiles of avian AV leaflets suggest a significant increase in strain anisotropy within the AV valve during development.

To examine the extent of fiber anisotropy during valve development in correlation with the estimated strain fields, we excised AV valves from day 5, day 8, and day 12 chicks. We stained each valve with 5-DTAF, a molecule capable of staining the entire extracellular matrix. From our results, it was found that the degree of fiber orientation and complexity of remodeling increased dramatically from day 5 to day 12 day. Day 5 was found to be isotropic with little alignment, while day 8 was found to have a fiber network of ECM proteins occurring perpendicular to the long axis of the AV valve. Day 12 was heavily aligned with a large network of ECM proteins occurring perpendicular to the long axis of the AV valve. We suspect that this fiber anisotropy within the developing valve is a function of anisotropic strain profiles. In

Chapter 3, we found that increasing anisotropy of biaxial strain resulted in increased cellular orientation and collagen fiber alignment along the principal directions of strain and cell orientation was found to precede fiber reorganization. However, this matrix remodeling has yet to be confirmed in embryonic valves.

As a last preliminary experiment to understand how anisotropic fibers develop in the embryonic leaflet, we subjected multi-axial strain profiles at 2.1 Hz, while maintaining a 20% area strain. HH36 AV cells (Day 10) were shown to increase their degree of cellular orientation and align perpendicular to the applied strain field (Figure 9.4). Therefore, we are confident that strain directionality proves a potent inducer of valve cellular orientation and also suggests similarities between the global remodeling process in embryonic AVC and adult VIC.

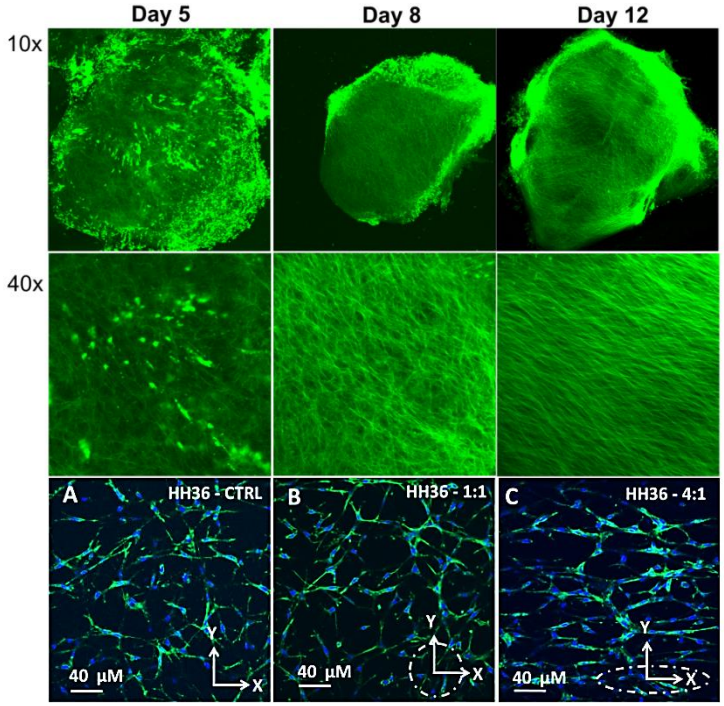

Figure 9.4 – Fibers increase in anisotropy from day 5 to day 12. Likewise, AV cells subjected to anisotropic strain profiles orient into a network that closely resembles that of underlying native tissue architecture.

Lastly, while we have yet to determine the exact mechanism by which VIC orient and remodeling the underlying matrix architecture, our previous results in Chapter 3 suggest that directionality controls gene expression of resident cells in a spatial manner. During anisotropic strain, VIC aligning perpendicular to the major strain field axis exhibit higher amounts of alpha-SMA when compared to VIC in parallel alignment. Therefore, investigation into the specific spatial localization of proteins (i.e. RhoA, Rac, pSmad) may prove as an effective means towards understanding the ability of VIC to orient and differentiation with respect to directionality.

9.3: Recapitulation of Embryonic Process in Adult Disease States

Developmental biologists are now beginning to connect the balance between signaling proteins, transcription factors, and the environment. The orchestrations of these factors are critical for determining the formation and homeostasis of tissue with its associated structure and function [44]. Interestingly, with the abundance of data now gathered at the embryonic and adult level, it is becoming evident that developmental process can be re-capitulated during pathological conditions (at least some aspect) [45].

9.3.1: Epithelial to Mesenchymal Transition

Among the key discoveries in the embryonic heart valve development with relevance to adult cardiovascular disease is the process called epithelial to mesenchymal transition. This phenomenon is associated with a loss of epithelial traits, such as E-cadherin expression, and the acquisition of mesenchymal characteristics, such as Vimentin, and Fibronectin expression [46]. TGFβ is an important inducer of this process as seen by the initiating the formation of endocardial cushions in the atrioventricular valves and mediating palate fusion of medial epithelial cells [47-49]. In this context, EMT terminates and has been suggested as a highly

controlled process [50]. EMT is also important under pathological conditions, prominently in fibrosis and in invasion and metastasis of carcinomas [51]. Recent work by Medici et al. has revealed a key molecular framework through which sequential activation of TGFβ isoforms induces EMT, culminating decades of work within the field [52]. In Chapter 6, we sought to synergize the EMT data generated by Medici et al by generating a family of mechanistic ODE models. After analyzing this ensemble, three main predications were found. In the following paragraphs, we will discuss these hypothesis, and there potential importance in embryonic development.

1. NFAT Hypothesis

While much investigation has been focused on determining the molecular factors associated with mesenchymal transformation, equally important is determining the molecular cues which regulate epithelial quiescence. Based on our simulations and experimental data, NFATs were found as major contributors for maintaining an epithelial phenotype. Specifically, we correlated the NFATc1 isoform with nuclear localization during VEGFA treatment and knockdown of NFATs resulted in a significant decrease in ecadherin protein levels. Interestingly, these results complement many processes found during embryonic EMT. For example, in developing endocardial cells, Wu et al. found that loss of NFATc1 function leads to enhanced EMT and decreased proliferation of valve endocardium and mesenchyme. Using blastocyst complementation assays they showed that NFATc1 inhibits EMT in a cell-autonomous manner. It was proposed that NFATc1 suppresses transcription of Snail and Slug, the key transcriptional factors for initiation of EMT [53]. Furthermore, Bmp7 expression through NFATc1 transcription plays an important role in embryonic kidney branching morphogenesis and recently, BMP-7 expression has been shown to reverse TGFβ1 EMT by re-induction of ecadherin [54, 55]. Although the direct mechanism has yet to be identified and/or confirmed through targeted perturbation studies, these findings suggest the importance of NFATc1 in maintaining epithelial

phenotype (ecadherin expression). Hence, future modeling and experimental studies surrounding NFAT biology may reveal critical therapeutic targets for controlling pathological EMT.

2. MAPK Phophotase Hypothesis

The ERK-MAPK pathway has been shown to modify TGFβ signaling at multiple levels. One such way is that the activated Ras pathway inhibits the TGFβ induced nuclear accumulation of Smad2/3, as seen in epithelial cells [56]. ERK kinases have been shown to phosphorylate Smad2 and Smad3 at specific sites in the region linking the MH1 and MH2 domains. These sites are separate from the TGFβ receptor phosphorylation sites which activate Smad nuclear translocation [57]. The effect of interaction between ERKs and Smads is the subject of some controversy, with data suggesting that such an interaction either enhances or inhibits downstream events. A hyperactive Ras pathway has been shown to effectively counteract the antiproliferative activity of TGFβ through attenuation of Smad accumulation in the nucleus [56]. In contrast, Ras signals strongly cooperated with Smads for invasion of human carcinoma cells [58]. The regulation of MAPK phosphatase is highly specific and tightly controlled through dual specificity. Four unique sub-groups have been shown to regulate specific complexes within ERK, JNK, and p38 cascades. It has been speculated that a role of an additional N-terminal domain within the type III subgroup could provide a cross-talk between MAPK and other signaling pathways [59]. Interestingly, our model suggests that upon TGFβ stimulation, high levels of MAPK do not affect the TGFβ3 response and inhibition of pSmads is limited. A possibility is through selective dephosphorylation of the MAPK/ERK complexes targeting pSmads. This may prove as a positive feedback mechanism, which allows the TGFβ3 autocrine response to ensue. Why and how this happens may prove important for understanding differences between pathological and controlled EMT.

3. Dual Inhibition of Snail and pSMAD Hypothesis

Recent evidence has suggested the sequential role of Snail and LEF1 for stimulation of EMT. Both transcription factors are expressed in tissues that undergo EMT during embryogenesis [48, 60] and have been described to promote the invasive phenotype in cancer cells [61]. Snail repression of E-cadherin has been well established and directly correlated with EMT. However, upon blocking LEF1, epithelial cells fail to undergo mesenchymal transition. The role of LEF1 has become increasingly complex as it can bind with b-catenin to regulate mesenchymal markers, form transcriptional complexes with pSmad2/4 to directly repress the E-cadherin gene, and negatively regulated by the Groucho/TLE complex [62, 63]. Our model is capable of capturing the necessary role of both Snail and pSmad2/4LEF1 E-cadherin repression. We found that during TGFβ2 stimulated computer stimulation, E-cadherin reduces substrate affinity for beta-catenin and accumulation of free cytosolic beta-catenin ensues. When blocking TGFβ3, low levels of free cytosolic beta-catenin still accumulate. This suggests that Snail acts as a primer to release membrane bound beta-catenin. However, the pSmad2/4/LEF1 complex is needed to fully repress E-cadherin for complete mesenchymal phenotype shift, suggesting that the pSmad2/4/LEF1 complex is very robust to the negative feedback. Hence, a dual block of the Snail and pSmad2 may be needed to terminate EMT.

9.3.2: Myofibroblastic activation during mitral valve degeneration

VICs continuously remodel their environment in response to mechanical cues by secreting and degrading ECM, releasing growth factors and cytokines, and reorganizing adhesive interactions. As shown in Chapter 3, embryonic AVC transition from a highly contractile myofibroblast phenotype during cushion development to a quiescent phenotype at later stages of maturation. Underlying this phenotype, transition RhoA-GTP levels dramatically decrease causing a direct reduction in alpha smooth muscle actin. Without this transition, leaflet maturation would not ensue, and a thick fibrous tissue would form. Interestingly, this thick fibrous leaflet and

consequent valve dysfunction is found in a number of mitral valve diseases such as Marfan syndrome and Myxomatus degeneration [64]. In these conditions, the diseased mitral VIC express contractile filaments like αSMA, matrix metalloproteinases, and exhibit increased traction for matrix remodeling, all features of activated myofibroblasts [65, 66]. This prompts the question, what are the contributing factors to this mitral valve degeneration and can we apply any of the molecular blue-print found during the myofibroblastic transition during embryonic development?

Over the last decade, significant progress has been made on understanding the functional consequences of mitral valve degeneration [67]. The bulk of these studies have established the critical contribution of ECM deficiency through altered cell–matrix interactions and dysregulated TGFβ signaling [64, 68]. For example, in Chapter 6 we showed those cell-matrix deformation kinematics are decoupled in Marfan mutated valves. This "decoupling" in cell-matrix deformation kinematics suggests that they are unable to sense or respond appropriately to their local microenvironment. While we have yet to fully investigate the mechanism, one possible explanation is that TGFβ upregulation is altering adhesive and contractile elements in the VICs, which leads to this phenotype transition pathological remodeling of their microenvironment [69]. From our previous results in Chapter 3 and 4, both embryonic and aortic valve interstitial cells seeded in unstressed hydrogels remain quiescent while when free floating in hydrogels. However, during mechanically anchored conditions, the cells develop tension and upregulate contractile expression, TGFβ, and matrix remodeling. We found that mechanical strain regulates this process by regulating αSMA and vimentin expression. Interestingly, strain directionality was found to potentiate this process by elevating αSMA and vimentin expression. Furthermore, we determined that both TGFB1 expression and smad2 phosphorylation were specifically activated by biaxial strain patterns. Coupled with the known dysregulation of TGFβ1

in mitral valve degeneration, these findings may indicate that dysregulation in TGFβ signaling in MVIC may be controlled by altered mechanobiological signaling in cell-matrix interaction.

Hence, further investigation into how strain controls fibroblast-myofibroblast transition in VICs through adhesive TGF-β signaling should be considered. As revealed in Chapter 4, potential downstream targets effecting embryonic phenotype transition and matrix remodeling include the mechano-sensitive small GTP proteins RhoA and Rac1. RhoA regulates actin cytoskeleton and stress fiber formation, while Rac1 regulates cell-cell adhesion, actin polymerization, and cytoskeletal polarity [70]. These proteins may be the mechanobiological mechanisms of myofibroblast activation and remodeling in the mitral valve. Advances in our understanding of mechanobiological processes may lead to mechanics based treatments to attenuate pathological signaling and future uses of our dynamic bioreactor may be to screen for diseases mechanically at a cellular level.

9.4 Sustained Cyclic Deformation a Key for Tissue Homeostasis?

During development, a constant barrage of hemodynamic occurs concomitantly with increasing mechanical force. It is speculated that heart valve interstitial cells (VICs) maintain valvular tissue homeostasis through mechnoregulated extracellular matrix (primarily collagen) biosynthesis. In mice, both blood pressure and myocardial contraction have been shown to significantly increase at 2 weeks, 3 weeks, and 4months, implying that the stresses on the valves are also increasing [71]. Our work has shown that the effective modulus of AV valves increase significantly during this period. This is complemented by the histochemical sections revealing collagen compaction and a significant increase in the collagen to GAG fractional ratio during this period. Previous studies in chick, have found that both AV cushions increased in effective modulus between HH17 and HH25, which correlated with increased blood velocity and

myocardial contraction. Enzymatic digestion of major structural constituent collagens or glycosaminoglycans resulted in distinctly different stress-strain curves suggestive of their individual contributions [36]. In mice, extracellular matrix remodeling and production of mature collagen between N11.5 and 8 weeks supports the notion of that matrix composition and fiber alignment/compaction is critical to the growth and function of heart valves [72]. Further work by Aikawa et al., visualized the extent of collagen remodeling during human development. It was found that during early fetal, late fetal, child, and adult, both collagen fiber thickness and alignment increase in the valves, while in diseased state reverted back to an immature form [73].

The precise mechanisms by which macroscopic stress effects cell to ECM interactions remains under investigation. Our work has shown that in post-natal development and diseased states, tissue stiffness correlates with cellular deformation. We speculate that ECM composition, fiber alignment, and compaction, play a key role in regulating the degree of cellular deformation. As collagen fibers are recruited, alignment and compaction results in tissue stiffness and cell lengthening [74]. In the heterozygous C1039G mice, we found tissue stiffness to be almost identical to that of a 3 week wild-type valve, suggesting an immature leaflet undergoing extensive remodeling. Our histochemical analysis revealed a large abundance of GAGs, which was not unexpected as myxomatous valves have been shown to contain more GAGs and PGs than normal [65, 75]. Previous work using the C1039G mice had also found that the mitral valves were much thicker than C57/B6J, which could possibly be contributed to the swelling nature of GAGs [68]. This lack of collagen organization and increased GAG content may prove to limit the overall amount of cellular deformation under mechanical load. Furthermore, the reduction in tissue stiffness may also play a role in traction force generation. Numerous studies have shown that the degree of traction force is proportional to substrate stiffness, via integrins [76]. Recent work by Bax et al., reported an RGD sequence of fibrillin-1 has been reported to

support cellular adhesion in vitro via integrin avb3 [77]. Therefore, the increased GAG content and disorganized extracellular matrix may prove to regulate traction force generation, and hence the ability to deform during mechanical load.

9.4.1: Hypothetical Scheme of Conserved Deformation

To understand the physiological relevance of these findings, we computationally simulated the in-vivo macro-scale valve mechanics to predict an overall amount of micro-scale cellular deformation. Valve stress states were estimated using a spherical pressure vessel model (hoop stress) as suggested by Thubrikar et al. Membrane stress in the circumferential direction is defined by $\sigma_m = ((P_v-P_a)*R_d)/T$, where P_v-P_a is the transvalular pressure, R_d is the radius of deformation, and T is the thickness at the mid-zone. [78]. Previous literature values were used to estimate blood pressure and diameter of mitral annulus (1/2 annulus diameter annulus was used for radius of deformation) [71, 79, 80]. Valve thickness was determined through histological morphometery and confocal z-stacks **(Table 9.1).**

Table S1

	Systolic BP (mmHG)	Diameter Mitral Annulus (μm)	Anterior Mitral Thickness (μm)	Estimated Stress State (KPa)
2 Week	70	1250	37 ± 8	157.64
3 Week	86	1400	27 ± 7	297.26
4 Month	115	1700	21 ± 5	620.58
10 Month	120	1750	25 ± 6	559.95
C1039G/+	115	2000	38 ± 8	403.48
FBN1+/+	115	1700	21 ± 5	620.58

Table 9.1 – Supplement Table 1. In-vivo physiological parameters used for estimated stress states of mitral valves. Systolic blood pressure and mitral valve annulus measurements were gathered from various literature sources while, mitral valve thickness was estimated using histological morphometry and confocal z-stack measurements.

According to our stress-strain curves, hypothetical stretch ratios were found to converge upon a stretch ratio of 1.3 during maturation in the *C57/B6J* mitral valve leaflets (Figure 9.5A). Likewise, transposing these stretch ratios onto cellular deformation curves, we found that the circularity index converged upon a deformation of 0.71 (Figure 9.5B).

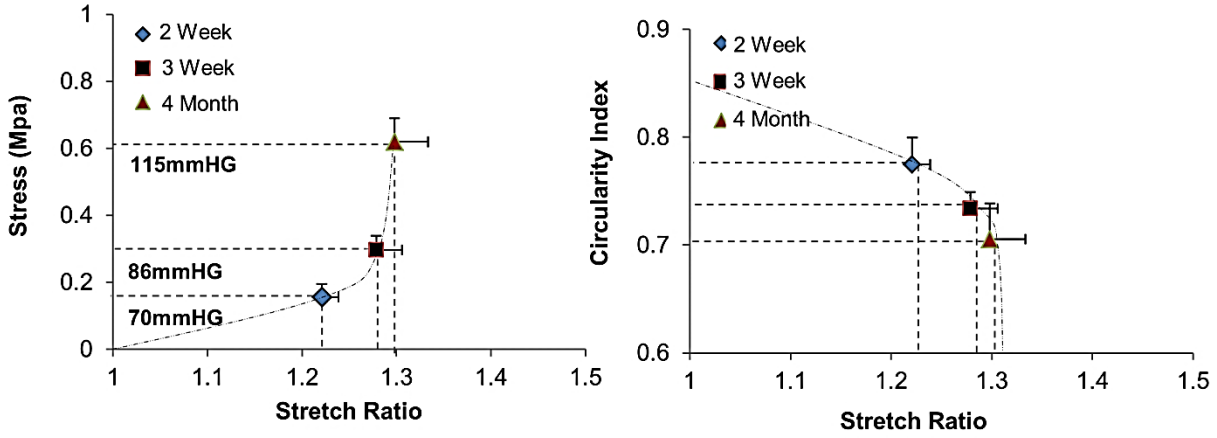

Figure 9.5 –Microscale deformation under macroscale stretch. (A) In-vivo train states for different aged valves were estimated using physiological stress states (Table S1). Upon maturation, the marfan mitral valve leaflet converges to a stretch ratio of 1.3. **(B)** Strain states for each valve were mapped against respective circularity index curves for estimating overall deformation. Upon maturation, cell deformation converges upon a circularity index of 0.7.

In the case of the mutant valves, hypothetical tissue stretch ratios were λ=1.25 and λ=1.37 in the $^{+/+}$*Fbn1* and $^{C1039G/+}$*Fbn1*, respectively **(Figure 9.6A).** Transposing these stretch ratios onto the cellular deformation curves, we found that the projected cellular deformations between the two cases are identically CI=0.71 **(Figure 9.6B)**. This suggests that mechanisms of remodeling could stem from intrinsic cell properties governed by a specific strain. Depending on the stress-state observed on the mitral valve, the valvular interstitial cells will remodel the matrix to maintain a desired level of deformation (or strain) **(Figure 9.6C)**.

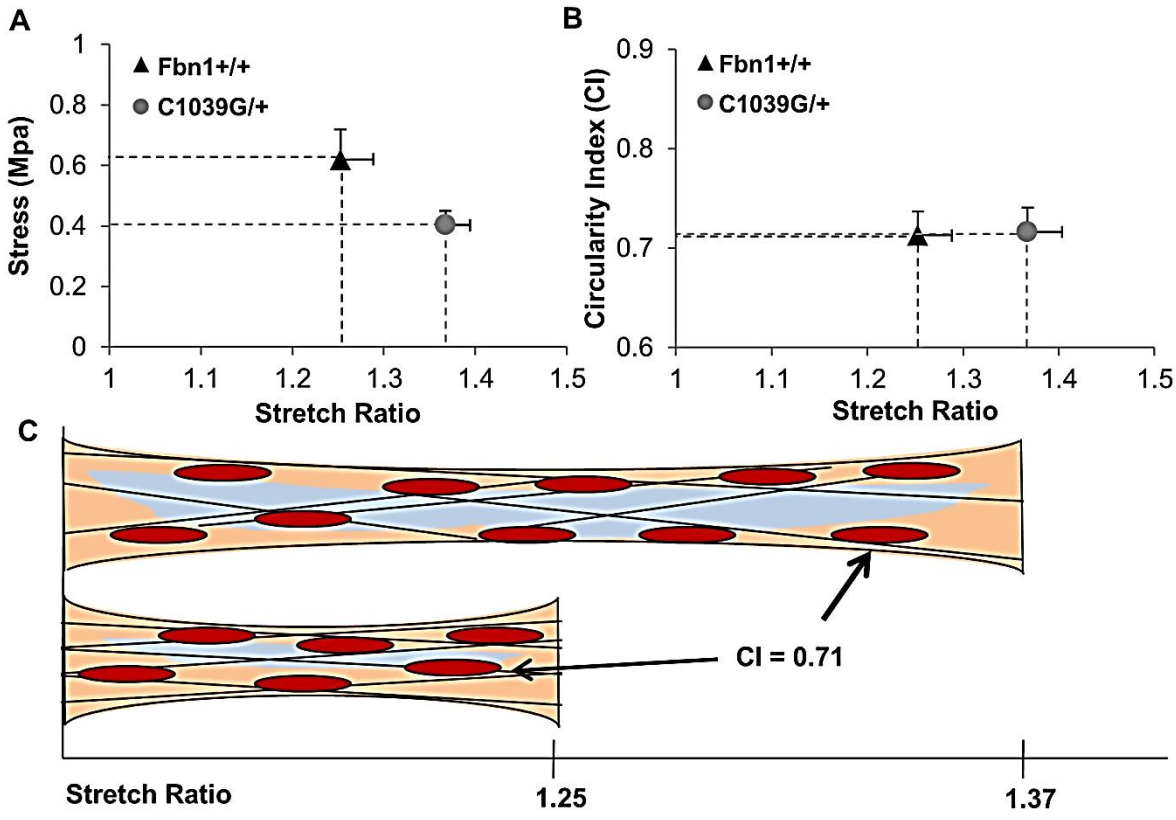

Figure 9.6 – Microscale deformation under macroscale stretch. **(A)** In-vivo strain states for both wildtype and mutant mitral valves were estimated using physiological stress states (Table S1). At physiological loading states (115mmHg), the marfan mitral valve leaflet will stretch significantly more than wild-type ($\lambda = 1.37$ vs. $\lambda = 1.25$). **(B)** Mapping stretch states for each valve to circularity index suggests that cell deformation is identical in wildtype and marfan valve despite the elevated stretch. **(C)** We hypothesize that indigenous valve fibroblasts may remodel their matrix microenvironment to to maintain a homeostatic morphology (in this case CI = 0.71).

In the case of the *Fbn1* mutation, VIC may therefore pathologically degenerate the matrix in order to achieve the homeostatic deformation state, which in turn weakens the tissue further in a vicious cycle leading to structural failure. Due to loss of mechanical competence and increased surface area of the mitral valve leaflets, this disease leads to regurgitation and cardiac dysfunction. There is a strong clinical need for percutaneous treatment of patients with mitral valve disease and regurgitation as an alternative to open-chest surgery [81]. This raises the possibility that matrix stabilization such as collagen crosslinking or radiofrequency ablation could be used to maintain mechanical performance and thereby delay remodeling [82].

Few studies have investigated the mechano-regulation of VIC in response to altered pressure or strain. Work by Merryman et al., used micropipette aspiration to assess VIC cellular stiffness and cytoskeleton composition from 4 different heart valves. It was found that the VICs from the aortic and mitral valves were significantly stiffer than those from the pulmonary and tricuspid valves and left-side isolated VICs and correlated with the different transvalvular pressures [83]. VIC isolated in vitro and mechanically strained were found to increase collagen synthesis upon the degree and duration of stretch. Furthermore, when pulmonary VICs were exposed to aortic pressure levels, as occurs following the Ross operation, collagen and sulfated glycosaminoglycan synthesis were increased significantly [84]. This demonstrates that VICs are capable of remodeling the ECM in response to changes in the mechanical environment. We speculate that mechanobiolgical consequences of hemodynamic load may play in important part in regulating matrix remodeling such that VIC will remodel accordingly to maintain a desired level of deformation. In the case of pathological conditions, this may lead to altered ECM production and hence, dysfunction tissue biomechanics.

In summary, elucidating the specific roles of mechanical force and extracellular matrix cues on valvular cells may potentially lead to an effective protocol for clinically applicable strategies. Understanding the embryonic pathway focuses on the “controlled” and direct process through which progenitor cells become mature quiescent valve cells. To our advantage, homeostatic baselines during development rapidly transition (epithelial-mesencymal-fibroblast), and in many cases recapitulate partial events that in adult diseases’, such as valvular calcification. Additionally, by mapping the molecular blueprint “roadmap” during development, we may begin to solidify biological thresholds for normal vs. pathogenic cellular events during the valve development and aging process. My hope is that these newly generated hypotheses and findings will bring use one step closer to developing novel regenerative agents.

REFERENCES

1. Go, A.S., et al., *Heart disease and stroke statistics--2013 update: a report from the American Heart Association.* Circulation, 2013. **127**(1): p. e6-e245.
2. Hoffman, J.I. and S. Kaplan, *The incidence of congenital heart disease.* J Am Coll Cardiol, 2002. **39**(12): p. 1890-900.
3. Robicsek, F., et al., *The congenitally bicuspid aortic valve: how does it function? Why does it fail?* Ann Thorac Surg, 2004. **77**(1): p. 177-85.
4. Markwald, R.R., et al., *Developmental basis of adult cardiovascular diseases: valvular heart diseases.* Ann N Y Acad Sci, 2010. **1188**: p. 177-83.
5. Redberg, R.F., et al., *AHA/ACCF [corrected] 2009 performance measures for primary prevention of cardiovascular disease in adults: a report of the American College of Cardiology Foundation/American Heart Association task force on performance measures (writing committee to develop performance measures for primary prevention of cardiovascular disease): developed in collaboration with the American Academy of Family Physicians; American Association of Cardiovascular and Pulmonary Rehabilitation; and Preventive Cardiovascular Nurses Association: endorsed by the American College of Preventive Medicine, American College of Sports Medicine, and Society for Women's Health Research.* Circulation, 2009. **120**(13): p. 1296-336.
6. Roberts, W.C. and J.M. Ko, *Frequency by decades of unicuspid, bicuspid, and tricuspid aortic valves in adults having isolated aortic valve replacement for aortic stenosis, with or without associated aortic regurgitation.* Circulation, 2005. **111**(7): p. 920-5.
7. Srivastava, D. and E.N. Olson, *A genetic blueprint for cardiac development.* Nature, 2000. **407**(6801): p. 221-6.
8. Natowicz, M., et al., *Genetic disorders and major extracardiac anomalies associated with the hypoplastic left heart syndrome.* Pediatrics, 1988. **82**(5): p. 698-706.
9. Dukes-McEwan, J., *A foundation for future research: the developmental genetics of congenital heart disease in animals.* Vet J, 2006. **171**(2): p. 195-7.
10. Bruneau, B.G., *The developmental genetics of congenital heart disease.* Nature, 2008. **451**(7181): p. 943-8.
11. Freed, L.A., et al., *Prevalence and clinical outcome of mitral-valve prolapse.* N Engl J Med, 1999. **341**(1): p. 1-7.
12. Gittenberger-de Groot, A.C., et al., *Basics of cardiac development for the understanding of congenital heart malformations.* Pediatr Res, 2005. **57**(2): p. 169-76.
13. Mohamed, S.A., et al., *Novel missense mutations (p.T596M and p.P1797H) in NOTCH1 in patients with bicuspid aortic valve.* Biochem Biophys Res Commun, 2006. **345**(4): p. 1460-5.
14. Pereira, L., et al., *Targetting of the gene encoding fibrillin-1 recapitulates the vascular aspect of Marfan syndrome.* Nat Genet, 1997. **17**(2): p. 218-22.
15. Norris, R.A., et al., *Expression of the familial cardiac valvular dystrophy gene, filamin-A, during heart morphogenesis.* Dev Dyn, 2010. **239**(7): p. 2118-27.
16. Hove, J.R., et al., *Intracardiac fluid forces are an essential epigenetic factor for embryonic cardiogenesis.* Nature, 2003. **421**(6919): p. 172-7.
17. Hinton, R.B., Jr., et al., *Extracellular matrix remodeling and organization in developing and diseased aortic valves.* Circ Res, 2006. **98**(11): p. 1431-8.
18. Glickman, N.S. and D. Yelon, *Cardiac development in zebrafish: coordination of form and function.* Semin Cell Dev Biol, 2002. **13**(6): p. 507-13.
19. Butcher, J.T., G.J. Mahler, and L.A. Hockaday, *Aortic valve disease and treatment: The need for naturally engineered solutions.* Adv Drug Deliv Rev, 2011.

20. Engelmayr, G.C., Jr., et al., *The independent role of cyclic flexure in the early in vitro development of an engineered heart valve tissue.* Biomaterials, 2005. **26**(2): p. 175-87.
21. Syedain, Z.H. and R.T. Tranquillo, *Controlled cyclic stretch bioreactor for tissue-engineered heart valves.* Biomaterials, 2009. **30**(25): p. 4078-84.
22. Seliktar, D., et al., *Dynamic mechanical conditioning of collagen-gel blood vessel constructs induces remodeling in vitro.* Ann Biomed Eng, 2000. **28**(4): p. 351-62.
23. Schneider, P.J. and J.D. Deck, *Tissue and cell renewal in the natural aortic valve of rats: an autoradiographic study.* Cardiovasc Res, 1981. **15**(4): p. 181-9.
24. Butcher, J.T. and R.R. Markwald, *Valvulogenesis: the moving target.* Philos Trans R Soc Lond B Biol Sci, 2007. **362**(1484): p. 1489-503.
25. Mahler, G., R. Gould, and J. Butcher, *Isolation and culture of avian embryonic valvular progenitor cells.* J Vis Exp, 2010(44).
26. Bell, E., B. Ivarsson, and C. Merrill, *Production of a tissue-like structure by contraction of collagen lattices by human fibroblasts of different proliferative potential in vitro.* Proc Natl Acad Sci U S A, 1979. **76**(3): p. 1274-8.
27. Gould, R.A., et al., *Multi-scale biomechanical remodeling in aging and genetic mutant murine mitral valve leaflets: insights into Marfan syndrome.* PLoS One, 2012. **7**(9): p. e44639.
28. Mack, C.P., et al., *Smooth muscle differentiation marker gene expression is regulated by RhoA-mediated actin polymerization.* J Biol Chem, 2001. **276**(1): p. 341-7.
29. Zhang, J., et al., *The FGF-BMP signaling axis regulates outflow tract valve primordium formation by promoting cushion neural crest cell differentiation.* Circ Res, 2010. **107**(10): p. 1209-19.
30. Lincoln, J., C.M. Alfieri, and K.E. Yutzey, *BMP and FGF regulatory pathways control cell lineage diversification of heart valve precursor cells.* Dev Biol, 2006. **292**(2): p. 292-302.
31. Wehrli, B.M., et al., *Sox9, a master regulator of chondrogenesis, distinguishes mesenchymal chondrosarcoma from other small blue round cell tumors.* Hum Pathol, 2003. **34**(3): p. 263-9.
32. Lincoln, J., et al., *Sox9 is required for precursor cell expansion and extracellular matrix organization during mouse heart valve development.* Dev Biol, 2007. **305**(1): p. 120-32.
33. Akiyama, H., et al., *Essential role of Sox9 in the pathway that controls formation of cardiac valves and septa.* Proc Natl Acad Sci U S A, 2004. **101**(17): p. 6502-7.
34. Haudenschild, D.R., et al., *Rho kinase-dependent activation of SOX9 in chondrocytes.* Arthritis Rheum, 2010. **62**(1): p. 191-200.
35. Maekawa, M., et al., *Signaling from Rho to the actin cytoskeleton through protein kinases ROCK and LIM-kinase.* Science, 1999. **285**(5429): p. 895-8.
36. Butcher, J.T., et al., *Transitions in early embryonic atrioventricular valvular function correspond with changes in cushion biomechanics that are predictable by tissue composition.* Circ Res, 2007. **100**(10): p. 1503-11.
37. Mertin, S., S.G. McDowall, and V.R. Harley, *The DNA-binding specificity of SOX9 and other SOX proteins.* Nucleic Acids Res, 1999. **27**(5): p. 1359-64.
38. Yano, F., et al., *The canonical Wnt signaling pathway promotes chondrocyte differentiation in a Sox9-dependent manner.* Biochem Biophys Res Commun, 2005. **333**(4): p. 1300-8.
39. Hurlstone, A.F., et al., *The Wnt/beta-catenin pathway regulates cardiac valve formation.* Nature, 2003. **425**(6958): p. 633-7.
40. Cai, X., et al., *Tbx20 acts upstream of Wnt signaling to regulate endocardial cushion formation and valve remodeling during mouse cardiogenesis.* Development, 2013. **140**(15): p. 3176-87.
41. Sacks, M.S., et al., *In-vivo dynamic deformation of the mitral valve anterior leaflet.* Ann Thorac Surg, 2006. **82**(4): p. 1369-77.

42. May-Newman, K. and F.C. Yin, *Biaxial mechanical behavior of excised porcine mitral valve leaflets.* Am J Physiol, 1995. **269**(4 Pt 2): p. H1319-27.
43. Butcher, J.T., et al., *Quantitative volumetric analysis of cardiac morphogenesis assessed through micro-computed tomography.* Dev Dyn, 2007. **236**(3): p. 802-9.
44. Zaffran, S. and M. Frasch, *Early signals in cardiac development.* Circ Res, 2002. **91**(6): p. 457-69.
45. Van Vliet, P., et al., *Early cardiac development: a view from stem cells to embryos.* Cardiovasc Res, 2012. **96**(3): p. 352-62.
46. Thiery, J.P. and J.P. Sleeman, *Complex networks orchestrate epithelial-mesenchymal transitions.* Nat Rev Mol Cell Biol, 2006. **7**(2): p. 131-42.
47. Zavadil, J. and E.P. Bottinger, *TGF-beta and epithelial-to-mesenchymal transitions.* Oncogene, 2005. **24**(37): p. 5764-74.
48. Nawshad, A. and E.D. Hay, *TGFbeta3 signaling activates transcription of the LEF1 gene to induce epithelial mesenchymal transformation during mouse palate development.* J Cell Biol, 2003. **163**(6): p. 1291-301.
49. Nawshad, A., et al., *TGFbeta3 inhibits E-cadherin gene expression in palate medial-edge epithelial cells through a Smad2-Smad4-LEF1 transcription complex.* J Cell Sci, 2007. **120**(Pt 9): p. 1646-53.
50. Lee, J.M., et al., *The epithelial-mesenchymal transition: new insights in signaling, development, and disease.* J Cell Biol, 2006. **172**(7): p. 973-81.
51. Thiery, J.P., *Epithelial-mesenchymal transitions in tumour progression.* Nat Rev Cancer, 2002. **2**(6): p. 442-54.
52. Medici, D., E.D. Hay, and B.R. Olsen, *Snail and Slug promote epithelial-mesenchymal transition through beta-catenin-T-cell factor-4-dependent expression of transforming growth factor-beta3.* Mol Biol Cell, 2008. **19**(11): p. 4875-87.
53. Wu, B., et al., *Nfatc1 coordinates valve endocardial cell lineage development required for heart valve formation.* Circ Res, 2011. **109**(2): p. 183-92.
54. Zeisberg, M., et al., *BMP-7 counteracts TGF-beta1-induced epithelial-to-mesenchymal transition and reverses chronic renal injury.* Nat Med, 2003. **9**(7): p. 964-8.
55. Buijs, J.T., et al., *TGF-beta and BMP7 interactions in tumour progression and bone metastasis.* Clin Exp Metastasis, 2007. **24**(8): p. 609-17.
56. Kretzschmar, M., et al., *A mechanism of repression of TGFbeta/ Smad signaling by oncogenic Ras.* Genes Dev, 1999. **13**(7): p. 804-16.
57. Kretzschmar, M. and J. Massague, *SMADs: mediators and regulators of TGF-beta signaling.* Curr Opin Genet Dev, 1998. **8**(1): p. 103-11.
58. Oft, M., R.J. Akhurst, and A. Balmain, *Metastasis is driven by sequential elevation of H-ras and Smad2 levels.* Nat Cell Biol, 2002. **4**(7): p. 487-94.
59. Farooq, A. and M.M. Zhou, *Structure and regulation of MAPK phosphatases.* Cell Signal, 2004. **16**(7): p. 769-79.
60. Vega, S., et al., *Snail blocks the cell cycle and confers resistance to cell death.* Genes Dev, 2004. **18**(10): p. 1131-43.
61. Singh, A. and J. Settleman, *EMT, cancer stem cells and drug resistance: an emerging axis of evil in the war on cancer.* Oncogene, 2010. **29**(34): p. 4741-51.
62. Arce, L., N.N. Yokoyama, and M.L. Waterman, *Diversity of LEF/TCF action in development and disease.* Oncogene, 2006. **25**(57): p. 7492-504.
63. Arce, L., K.T. Pate, and M.L. Waterman, *Groucho binds two conserved regions of LEF-1 for HDAC-dependent repression.* BMC Cancer, 2009. **9**: p. 159.
64. Judge, D.P., et al., *Mitral valve disease in marfan syndrome and related disorders.* J Cardiovasc Transl Res, 2011. **4**(6): p. 741-7.

65. Rabkin, E., et al., *Activated interstitial myofibroblasts express catabolic enzymes and mediate matrix remodeling in myxomatous heart valves.* Circulation, 2001. **104**(21): p. 2525-32.
66. Rabkin-Aikawa, E., et al., *Dynamic and reversible changes of interstitial cell phenotype during remodeling of cardiac valves.* J Heart Valve Dis, 2004. **13**(5): p. 841-7.
67. Pai, R.G., *Degenerative valve disease.* J Am Coll Cardiol, 2006. **48**(12): p. 2601; author reply 2602.
68. Ng, C.M., et al., *TGF-beta-dependent pathogenesis of mitral valve prolapse in a mouse model of Marfan syndrome.* J Clin Invest, 2004. **114**(11): p. 1586-92.
69. Walker, G.A., et al., *Valvular myofibroblast activation by transforming growth factor-beta: implications for pathological extracellular matrix remodeling in heart valve disease.* Circ Res, 2004. **95**(3): p. 253-60.
70. Parsons, J.T., A.R. Horwitz, and M.A. Schwartz, *Cell adhesion: integrating cytoskeletal dynamics and cellular tension.* Nat Rev Mol Cell Biol, 2010. **11**(9): p. 633-43.
71. Tiemann, K., et al., *Increasing myocardial contraction and blood pressure in C57BL/6 mice during early postnatal development.* Am J Physiol Heart Circ Physiol, 2003. **284**(2): p. H464-74.
72. Kruithof, B.P., S.A. Krawitz, and V. Gaussin, *Atrioventricular valve development during late embryonic and postnatal stages involves condensation and extracellular matrix remodeling.* Dev Biol, 2007. **302**(1): p. 208-17.
73. Aikawa, E., et al., *Human semilunar cardiac valve remodeling by activated cells from fetus to adult: implications for postnatal adaptation, pathology, and tissue engineering.* Circulation, 2006. **113**(10): p. 1344-52.
74. Sacks, M.S., W. David Merryman, and D.E. Schmidt, *On the biomechanics of heart valve function.* J Biomech, 2009. **42**(12): p. 1804-24.
75. Tamura, K., et al., *Abnormalities in elastic fibers and other connective-tissue components of floppy mitral valve.* Am Heart J, 1995. **129**(6): p. 1149-58.
76. Yeung, T., et al., *Effects of substrate stiffness on cell morphology, cytoskeletal structure, and adhesion.* Cell Motil Cytoskeleton, 2005. **60**(1): p. 24-34.
77. Bax, D.V., et al., *Cell adhesion to fibrillin-1 molecules and microfibrils is mediated by alpha 5 beta 1 and alpha v beta 3 integrins.* J Biol Chem, 2003. **278**(36): p. 34605-16.
78. Thubrikar, M. and R.T. Eppink, *A method for analysis of bending and shearing deformations in biological tissue.* J Biomech, 1982. **15**(7): p. 529-35.
79. Hinton, R.B., Jr., et al., *Mouse heart valve structure and function: echocardiographic and morphometric analyses from the fetus through the aged adult.* Am J Physiol Heart Circ Physiol, 2008. **294**(6): p. H2480-8.
80. Yang, B., D.F. Larson, and R. Watson, *Age-related left ventricular function in the mouse: analysis based on in vivo pressure-volume relationships.* Am J Physiol, 1999. **277**(5 Pt 2): p. H1906-13.
81. Nkomo, V.T., et al., *Burden of valvular heart diseases: a population-based study.* Lancet, 2006. **368**(9540): p. 1005-11.
82. Shawn L. Price, C.G.N., Jeffrey L. Williams, H. Thomas McElderry and W. David Merryman, *Radiofrequency Ablation Directionally Alters Geometry and Biomechanical Compliance of Mitral Valve Leaflets: Refinement of a Novel Percutaneous Treatment Strategy* Cardiovascular Engineering and Technology, 2010. **Volume 1**(3): p. 194-201.
83. Merryman, W.D., et al., *Differences in tissue-remodeling potential of aortic and pulmonary heart valve interstitial cells.* Tissue Eng, 2007. **13**(9): p. 2281-9.
84. Ikhumetse, J.D., et al., *Cyclic aortic pressure affects the biological properties of porcine pulmonary valve leaflets.* J Heart Valve Dis, 2006. **15**(2): p. 295-302.

CHAPTER 10

CONCLUSIONS AND FUTURE RECCOMMENDATIONS

Over 200,000 years of productive life before the age of 55 are lost due to CHD in the US each year and the annual direct cost for valve disease in the US is $1 billion (Nkomo et al., 2006). While failure to initiate the formation of valves is uniformly lethal in early gestation, clinically serious malformations arise from improper structural maturation of the valvuloseptal apparatus and outflow tract, including tetralogy of fallot, left heart hypoplasia, bicuspid aortic valve, and ventricular septal defects (Srivastava, 2006). Nearly all study of mechanical action on cellular function focuses on the “normal and pathological” adult age. This neglects key stages in the functional life cycle of tissues where remodeling is most active yet, controlled, early development. Until the basic interactions between cells and their microenvironment are understood in this context, our ability to understand congenital malformation and manipulate these phenomena remains limited. By using a developmentally inspired approach, I hope that my work eventually lead to efficient strategies for control tissue adaptation and remodeling as well as accelerate the construction of cardiovascular tissue replacements.

Pure populations of progenitor endocardial cells and valve mesenchyme were isolated using the protocols developed in Chapter 2. Eventually, we expanded these protocols to isolate cells later stage AV valves ranging from HH29-HH42. While the protocols were generally suitable for these cells, we did find that two important factors were critical during this isolation process. Both the concentration of chick serum and seeding technique dramatically regulated cell survival and growth. We initially found that 1% chick serum from passage HH14- was sufficient to culture the endocardial progenitor cells. This was of optimal concentration since higher amounts are thought to potentially shift the native phenotype. However, during initial experimentation, 1%

was not sufficient for culturing HH25 mesenchymal progenitor cells. In this case, we needed to increase the concentration to 5%. We believe this was due to the fact that HH25 cells were embedded within a 1.5mg/ml collagen hydrogel, while the HH14 were seeded on top of the gel. While there may be multiple explanations for this observation, we feel that embedding of valve progenitor cells at HH25 into collagen gels was too harsh due to either 1) lack of cell-cell contacts needed for cell survival, 2) collagen gel stuffiness was much higher than native tissue at that stage, or 3) collagen itself (cell-ECM) lacked the necessary binding potential for these cells. Hence, further investigation into how and why tissue stiffness or ECM components affect this progenitor cell phenotype/homeostasis should be considered. Possibly adding a certain percentage of HA (Hylurounic Acid) may help with cell binding, or changing collagen concentration (to a lower amount) may be useful.

In Chapter 3, it was shown that directionally of mechanical stretch can mediate the proliferation, differentiation, and remodeling process of aortic valve interstitial cells in a collagen construct. While we established an important model of cellular remodeling with respect to phenotype (mechanically anchored vs. free floating conditions), this was of no means exhaustive. Further investigation into the remodeling processes associated with stretch directionality should be considered. For example, how do the resident valve cells actually remodeling the collagen constructs? Possibilities include 1) secretion of MMPs (MMP2, MMP9), 2) cell contractility to compact fibers, 3) cell polarization to organize fibers or, 4) secretion of new ECM (mature vs. immature fibrils, collagen, elastin, GAGs, etc.). Concurrently, understanding the time course in which this happens is important. Do the cells align first and then orient the underlying matrix second, or do the cells align and then degrade/secrete new matrix. By using this this established model, an informative study would be useful for understand the possibly mechanisms by which normal and abnormal remodeling occurs during directionally mediated mechanical stretch.

Using the previously developed bioreactor and mechanically anchored vs. stress free gel models, in Chapter 4 we sought to understand how matrix condensation occurs simultaneously with phenotype quiescence typically seen in mature valves. We found both in-vitro and in-vivo that RhoA/Rac1 divergence driven by mechanical stretch is central to this process. While this study was fairly in-depth and comprehensive, there are still areas that could be improved and/or investigated. First, understanding the myofibroblastic differentiation of valve interstitial cells by expanding the RhoA-SRF signaling pathway. Recent evidence implicates serum response factor (SRF) and the myocardin-related transcription factors (MRTFs) as key mediators of the contractile gene program in response to TGF-β1 or RhoA signaling. It has been suggested that a signaling axis between MRTF and SRF can regulate ACTA2 transcription through various levels of F-actin and G-actin. Mechanical stretch and directionality most likely plays a large role in regulating these different types actin polymerization and is likely a good place to investigate. Second, at later stages of development Rac1 (HH40) was localized to the endothelial layer of the fibrosis valve layer. At later stages of the adult life, this layer is prone to calcification. It would be interesting to observe whether Rac1 is altered in any diseased conditions, compared to normal conditions within these endothelial cells. Rac1 could possibly serve as a protective of the endothelial layer as it recently has been found to regulate ROS expression. Third, the dynamics between RhoA and Rac1 are important for regulating myofibriblastic vs. quiescent activity. However, the full phenotype of a valve progenitor cells has not yet fully been established. I suspect that controlling the transcription factors Sox9 and Scx will be equally important, shown to be driven by FGF and BMP growth factors. Recent evidence has also shown that Sox9-bcatenin pathway is regulated by actin polymerization and mechanical stimulation, possibly connecting the role of Small GTPases with Sox9.

In Chapter 4, we investigated the post-natal AV valve multi-scale interactions between tissue stretch and underlying cell-matrix deformations. We found that tissue stretch correlates strongly with bulk stiffness, cell deformation, and alignment. However, in diseased conditions such as Marfan syndrome, the underlying tissue deformation and tissue stretch becomes decoupled leading to dysfunctional mechanobiology and biomechanics. An important question previously unidentified and revealed by this study is whether these alterations in local cell-matrix interactions with stretch are a cause or consequence of valve tissue remodeling. Three possible hypotheses into the mechanical etiologies of valve dysfunction include 1) the interstitial cells experience a reduced mechanical force distribution, 2) cells experience the normal loading but, the interstitial cell is unable to sense it correctly (e.g. its mechanotransduction processes are tuned improperly), or 3) the cells sense the normal loading but can't respond appropriately, hence pathologically remodeling the matrix instead of augmenting/maintaining its mature organization. Further investigation systematically testing these different hypotheses should be considered.

The complexity of cellular signaling is overwhelming due to the large numbers of interacting protein complexes, complicated feedback mechanisms, and cross-talk between multiple signaling pathways. As a result, even predicting the fundamental regulation of cellular fate processes remains difficult. Hence, systems biology has been suggested as an essential tool. In Chapter 6, we sought to model the epithelial-mesenchyme transition (EMT) phenomenon, the first step of valve formation. Using a systems approach, we established a predictive mechanistic model of EMT susceptibility, and revealed a novel signaling axis between phospho-Sp1/NFAT for possibly regulating a normal mesenchymal invasion potential of endocardial cells vs. metastatic carcinoma. In addition to the possible hypothesis discussed in Chapter 7, we have also developed a second generation model of valve differentiation (included in the supplement). Within this model, we have included the small GTPases RhoA, Rac1, and FGF

signaling pathways. Together these factors represent the entire differentiation spectrum associated with interstitial valve progenitors. For future studies, I suggest training this model on our preliminary data captured in Chapter 4. Once trained this model can then be used as a model to analyze molecular pathways, or apply towards multi-scale finite element analysis.

In the final chapter 8, we developed a hands-on lesson to investigate the effects of an angiogenesis factor (prostaglandin E1) on the morphogenesis of chick vasculature. The student activities mirror the scientific research process, including review of the scientific literature, hypothesis formation, experimental design, interpretation of data, and re-evaluation of initial hypothesis. The exercise supports instruction on developmental biology, biophysics, animal research, and experimental design, and is motivated by a clinically relevant health issue. While this lesson was inquiry and comprehensive, the application of using engineering technologies to teach students is not limited. A few other ideas include growing zebrafish to understand congential defects (i.e. aquarium with zebra which can be spiked with chemical mutation at any time), pacing an avian embryo to understand the role cardiac rhythm in humans (i.e. hooking up electrodes within the ex-ovo culture and applying a certain voltage/frequency), development of pressure devices to understand the purpose of valves in the heart (i.e. using tubing and other materials, fabricate a homemade valve that can withstand the large pressures and maintain unidirectional flow), or teaching students about the role of mechano-transduction (i.e. create a computer program which can push and pull cell membrane, then cell has certain decision to make). By developing these outreach activities, we hope to inspire and teach students about the engineering process (or science) so that they become interested in science, and maybe one day pursue such a career.

In summary, a more developed understanding of valvular cell interactions in developmental conditions will help map a “blueprint” for developing targeted diagnostic and therapeutic

strategies. Eventually we may be able alleviate congenital valve dysfunction before it progresses to tissue failure, potentially removing the need for valvular replacement or repair entirely.

APPENDIX A

Relevant Protocols

Protocol 1.1 - 3D Culture assay protocols for embryonic chick AV cushion mesenchyme

1. Preparation
    a. Incubate 5 dozen fertilized chick eggs at 37 C and 40-50% humidity for 4.5 days.
    b. Autoclave in a covered instrument tray the following items:
        i. Serrated tissue forceps – for grabbing membranes around embryo
        ii. Tissue scissors (8 cm) – For cutting membranes around embryo
        iii. Dumont #55 forceps (2 pair) – for microdissection of tissues. Make sure the tips are acceptable before autoclaving.
    c. Make sterile EBSS solution
        i. 10X liquid stock, dilute 100 ml 1:9 in milliQ water.
        ii. Add 2.2 g of sodium bicarbonate
        iii. pH to 7.0.
        iv. Sterile filter or autoclave. If autoclaving, pH to 7.2 (filter raises pH ~0.2).
        v. Label as sterile and place in fridge until use.
    d. Make sterile 3X M199 solution
        i. Power stock, dissolve one packet in 333 ml. Use the last 33 ml to swish around the packet to get all powder.
        ii. Add sodium bicarbonate as indicated on package
        iii. pH to 7.0
        iv. Sterile filter (no autoclaving).
        v. Label as sterile and place in fridge until use.
    e. Make sterile 1X M199 solution
        i. Power stock, dissolve one packet in 1000 ml. Use the last 25 ml to swish around the packet to get all powder.
        ii. Add sodium bicarbonate as indicated on package
        iii. pH to 7.0
        iv. Add 1% Penicillin/Streptomycin (P/S in freezer)
        v. Sterile filter (no autoclaving).
        vi. Label as sterile and place in fridge until use.
    f. Make chick cell culture medium (normally 100 ml at a time in autoclaved glass bottle)
        i. Sterile 1X M199 +P/S
        ii. + 1% Chick Serum (aliquots in freezer)
        iii. +ITS (aliquots in freezer)
        iv. Should be sterile already b/c components sterile

2. AV Cushion cell isolation
    a. Clean up nasty clean bench, remove anything not being used especially for this experiment. Should be just the scope, an ice bucket, chick bucket, absorbent pad, some 100 mm culture dishes, and reagents. Wipe surfaces with ethanol before putting down pad. Have bench circulating for 10+ mins before working.
    b. Wear gloves and lab coat. Don't be coughing/sneezing into the workspace.
    c. Take one 100mm dish and add ice cold EBSS. Keep on ice. No need for lid but be sterile.
    d. Take another 100mm dish and use for cracking eggs into.
    e. Spray eggs with ethanol and allow to air dry or wipe off. Can do all eggs at once.
    f. One at a time, crack egg into dish and remove embryo. Place embryo in EBSS on ice.

g. Do all 60 eggs. You may need to empty egg bucket once. Do it before ¾ full or you'll have a big mess on your hands.
h. Take dish with embryos and place under dissecting scope.
i. Pull hearts from all the embryos and place in a specific location near the edge of the dish. You will have to move embryos around as you go through them.
j. Using a sterile transfer pipet, transfer the hearts to a new dish with fresh cold sterile EBSS.
k. Isolate the AV region from all hearts at once in assembly fashion. Place the AVs in a specific region in the dish. If you want, you can also isolate the ventricle and/or outflow tract and place them in separate places. Ventricle cells are a nice comparison with AV and outflow tract cells are useful as well, especially as positive controls for Westerns. You may want to gently shake each AV to get all the blood out. Blood is bad, not fatal though.
l. Again, sterilely transfer the AVs to a new dish with fresh cold EBSS.
m. Sequentially isolate the cushions from the AV. Make sure there is no myocardium present.
n. Every 15 or so cushions, sterilely transfer them to a 15 ml conical tube that is on ice. Be careful that none of them get stuck in the tube.
o. Once all the cushions are in the tube, gently spin cushions to the bottom (300 rpm for 3 min in bucket centrifuge).
p. Take a 1000 ul pipet (blue tips, sterile) and remove as much EBSS as possible without disturbing the cushions.
q. Add 1 ml of prewarmed 0.25% Trypsin (freezer or fridge). Place in water bath at 37C for 5 min. Pipet up and down with 1 ml tip until completely dissolved. Add 100 ul chick serum to quench.
r. Pellet cells at 1000 rpm for 5 mins. Remove supernatant with 1000 ul tip.
s. Resuspend in 5 ml of culture medium and mix by pipetting. Take 10 ul of suspension and count on hemacytometer. Calculate the number of cells you have.

3. Invasion/migration assay.
   a. Reconstitute cells in 1000 cells/ul suspension.
   b. Pipet 20 ul boluses of this suspension in an array on a 100 mm culture lid. Be careful to not get any air into the droplets (i.e. set the pipet to 22 ul and don't push all the way down). Also, place the droplets in a circle around the central region of the lid.
   c. Fill the culture dish (not the lid) with sterile EBSS.
   d. In a smooth yet quick motion, flip the lid back on the culture dish.
   e. Incubate overnight (18 hours) in the incubator (37C, 5% CO2). The cells should aggregate by gravity into a small sphere inside the droplet.
   f. Next day: Make collagen gels according to the protocol in the clean bench. Anywhere between 1.0 and 2.0 mg/ml can be used for different stiffnesses, but my standard is 1.5 mg/ml and 250 ul volume/gel. Let solidify in the incubator for 60 mins. Do not liberate them or add media yet.
   g. Place the dish with the hanging drops and the collagen gels in the clean bench.
   h. Using a 20 ul pipet tip, gently suck up the drop and place down on top of a gel, slightly off center. Up to 3 drops can be placed on each gel, but 2 is standard. They should be far enough apart to not interact with each other.
   i. Let drops adhere for at least 1 hour (2 hours more ideal).
   j. Using 200 ul pipet, gently add culture media from the edge of the well, making sure to not introduce any sudden gushes. The drop should be adhered, but be very gentle, the slightest nudge can wreck it.
   k. Do one 4-well at a time, and put the finished ones in the incubator. Only have out of the incubator the drops you are using for that well plate.
   l. Culture for 72 hours or according to experiment.

4. Collagen compaction assay

a. Using worksheet, determine how many gels you will make based on the number of cells you have isolated. Typically 48 well plates are used for making gels with 1.5 mg/ml collagen and 250 ul gel volume.
b. Pellet cells and pipet off supernatant.
c. Using protocol, add 3X M199, Water, Serum, Treatment (if any), Collagen, and NaOH in that order. Mix by gentle pipetting.
d. Inoculate 250 ul into each well. Work quickly.
e. Let solidify in the incubator for 1 hour.
f. Add 400 ul of culture media. Incubate overnight.
g. Next day, liberate gels under dissection scope using 200 ul pipet tip.
h. Culture until experiment ends.

Protocol 1.2 - Cyclic Stretch Bioreactor

Making molds (PDMS)

1. Using the Sylgard 184 silicone elastomer kit, pour **66.5 grams** of elastomer base into a plastic cup
2. Add **3.5 grams** of elastomer curing agent into the cup, for a total of 70 grams (1:20 dilution)
3. Mix thoroughly with metal spatula (mixture should be white and bubbly)
4. Place cup in the vacuum chamber and de-gas the mixture (will take 30-45 minutes)

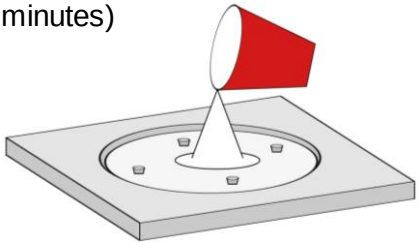

5. Pour one cup of mixture (70 grams) into one plastic mold. Make sure to scrape off as much of the mixture from cup as possible.
6. Use leftover PDMS to re-coat the edges of the wells on previously made silicone molds.
7. Heat in oven at 65°C for at least 6 hours (usually leave in overnight)

***Note**: to make large rectangle control mold, use two cups of PDMS mixture (70 grams each)

Cleaning cassettes and springs

1. Using tissue punch, punch out holes in PDMS mold where the screws will attach the top and bottom cassettes, with the PDMS sandwiched in between.
2. In warm water with soap, soak and scrub aluminum cassettes (especially the inner walls of the wells), bottom cassette pieces, and PDMS molds. Make sure that the wells are very clean, then rinse with DI water. Set to air dry.
3. Wash the springs by shaking in a 50ml centrifuge tube with warm water and soap. Rinse thoroughly with DI water. You may have to do this several times until completely clean. Set out to dry.
4. Preparing springs:
   For 1:1 strain: Fold one 1" spring into a circular shape (hook one end of the spring onto the other)
   For 2:1 strain: Attach two 0.625" springs at the ends to form an oval shape
   For 4:1 strain: Attach two 0.75" springs at the ends to form an oval shape

Prepping cassettes and molds

1. Place PDMS mold on top of the bottom cassette piece so the open wells are facing up, and they are in the middle of the holes in the cassette (so the platens will hit wells in the middle for an even stretch)

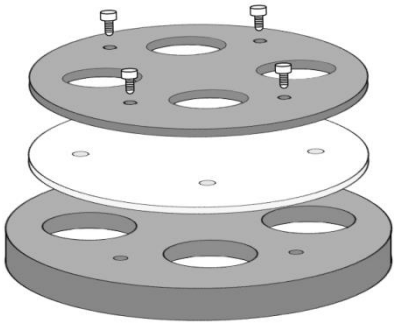

2. Place top cassette on top of the PDMS mold, then screw tightly into place using an Allen wrench.
3. Make up an autoclave bag for each cassette.

4. Trim off any PDMS overhanging the cassette edge with a straight edge blade, and place **one spring into each well** (to be inserted after autoclaving).

5. Seal autoclave bag, label with name and autoclave tape.

Preparing materials for experiment

1. Place extra washed springs into autoclave-appropriate boxes
2. Place gloves into a box to be autoclaved (these will be used to insert the springs)
3. Place forceps into a box to be autoclaved
4. Prepare spring controls:
   (a) Wash and dry squares of the control PDMS molds
   (b) Place washed springs into each control well (it won't matter if they crack in the autoclave because they are controls)
   (c) Put these controls in a box to be autoclaved

5. Gather cassettes (in their bags), springs, gloves, controls, and forceps and place in an autoclave bucket

6. Put cassettes on top of boxes so the bottom of the bags won't get wet

7. Autoclave setting: **GRAVITY 25:00 min sterilize, 11:00 min dry**

Pre-experiment: Checking settings on the bioreactor

Prepare bioreactor

1. Coat white plastic platens with braycote (804) rubbing on **smoothly** with finger

2. Use a small screwdriver to make sure that the small holes drilled into the sides of the platens are clear (drilled holes prevent bubbles from forming under the gel)

3. Pour lubricant into large middle screw and into all four ball bearings

Check software program

1. Plug bioreactor into the controller
2. Plug controller into the wall

} **This order is extremely important**

3. Plug controller into the computer

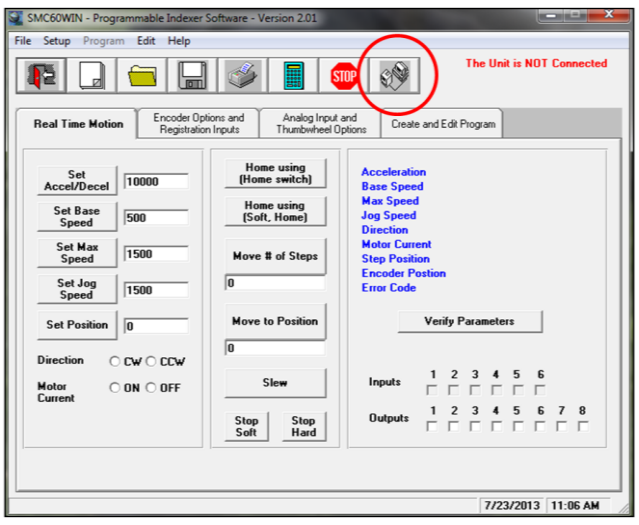

4. Open **SMC60WIN** (controller software)

5. Connect the unit (top right)
*Note: This is **very important:** make sure unit is connected before you load any program to the controller

6. Upload program from controller

7. Send the program back to the controller (so it will know its starting point)

8. **Run** the program to see if motor and bioreactor is running smoothly

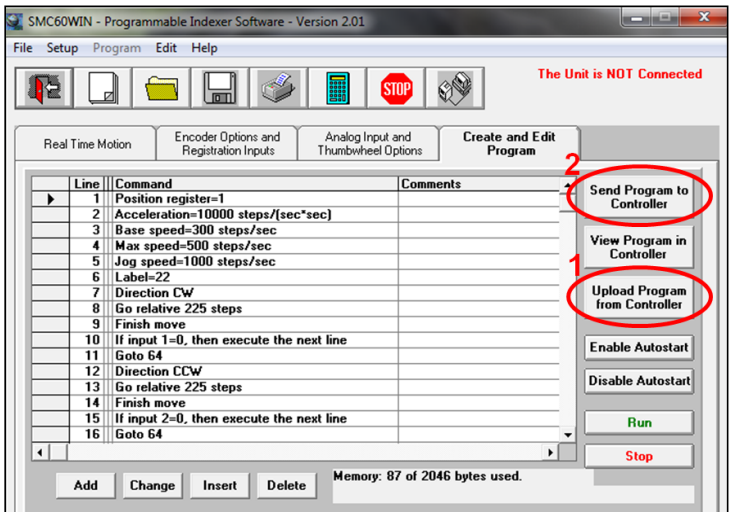

Troubleshooting:
1. Make sure screws are tight on the motor (or else the gears won't connect – no torque): tighten using hex screwdriver and attachment
2. For a tighter grip between gears, add grease to the gears

9. Set the plate manually until it is flush with the platens

10. Move plate up 200 steps (counter clockwise): this is where the cassettes will be loaded

9. Set to flush position

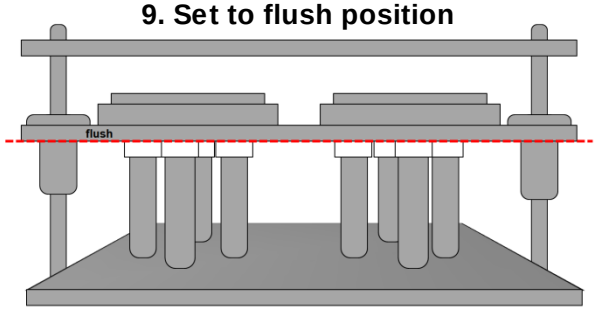

10. Up 200 steps to load cassettes

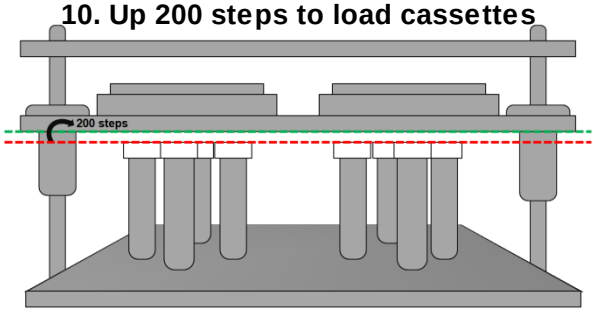

Insertion of springs into wells

**All of these procedures should take place in the laminar flow hood*

1. Open all autoclave bags with cassettes so you will be able to easily remove them later (do not touch cassettes yet)

2. Put on new pair of autoclaved gloves. Touch only the very edges of the gloves (do not touch the fingers). Put the right glove on first, then the left glove. The left-hand fingers and the **most important** to keep clean (they will be touching the springs)

3. Remove the cassettes with autoclaved gloves

4. Insert the springs by pushing up on mold with your right thumb from the bottom, and carefully place the spring into the well with your left thumb and fingers

5. Cover each cassette with a sterile plastic dish cover

6. Once all springs have been loaded, load each cassette into bioreactor (which should be set at 200 steps above flush)

7. Lock in cassettes with the screw-clamps

8. Place the cassettes diagonally so the loading does not unbalance the bioreactor

**Once cassettes are loaded (after springs are inserted*)*

1. Go down 200 steps until flush
2. Go down 400 steps where gels will be loaded (this will be the starting point for the experiment)

1. Reset to flush position

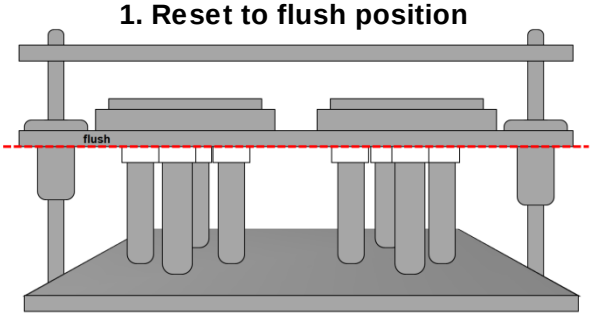

2. Go down 400 steps to load gels

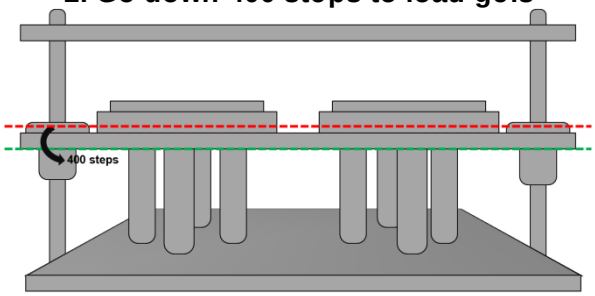

9. Turn on large incubator (37°C, around 3.6-3.7% CO_2)

10. Place bioreactor in large incubator while making collagen gels

Making the Collagen Gel.

Reagents (cell culture)
Dulbecco's modified eagle's medium (DMEM)
0.25% Trypsin-EDTA
1X Phosphate buffered saline (PBS)
Reagents (collagen gel)
3X DMEM
18 mΩ H_2O
Fetal Bovine Serum (FBS)
Collagen type I (rat tail)
0.1M NaOH
Cell source
Valve interstitial cells (use between passage 4-8)

1. Take a T75 flask of VIC out of the incubator, wash once with 10 ml of warm PBS

2. Add 4 ml of trypsin to the flask to trypsinize the cells (37°C) for 5 minutes

3. Add three times the amount of DMEM to terminate the digestion (12 ml). Transfer to a centrifuge tube. **DO NOT** centrifuge.

4. Count the cells using a hemocytometer.

5. Calculate the desired volume of cell suspension using ***collagen only disk template*** file.
**Example: for VIC gels, use 400,000 cells/ml*

6. Transfer the desired volume of cell suspension into a 15 ml tube; centrifuge at 1000 rpm for 5 minutes

7. Prepare a bowl of ice. Put collagen, 0.1M NaOH, 18 mΩ H_2O, FBS, and 3X DMEM on ice

8. After centrifuge, aspirate the supernatant, add **in order** to the cell pellet
   3X DMEM
   18 mΩ H_2O
   FBS
   Collagen
   NaOH

**Mix well with each step. Especially make sure the NaOH is well mixed with the collagen on the last step*

Seeding springs

**Best to start in back and move forward*

1. For **1:1** gels, add about 120µl
2. For **2:1** gels, add about 140µl

Make sure gel is completely within the coils of the springs so the gel will compact correctly. Try to suck out the air from the coils, which will bring the collagen into the spring

3. For **4:1** gels, add about 150µl

4. After seeding bioreactor, seed controls (and if needed, the released gels ~150 µl in a 46-well plate, released 12 hours later)

5. Set bioreactor in incubator, let gels sit for one hour

6. Add media to gels (bioreactor and controls)

7. Let gels compact around gels for 24 hours

Starting bioreactor

1. Attach water hoses to the cooling plate beneath the bioreactor

2. Plug the controller into the computer (it should already be attached to the bioreactor)

3. **Connect unit**

4. Upload program from controller, then send it back (this sets starting position)

5. **Run** the program (them remove USB connection from controller)

6. Turn on power strip where water pump in freezer is attached

**Make sure incubator is at 37°C, around 3.6-3.7% C*

Materials:

Bioreactor materials
Sylgard 184 silicone elastomer kit (Dow Corning, 3097358-1004)
Castrol braycote (804) grease (SPI supplies, 05133-AB)
Lubricating oil

Compression springs
1" springs (Lee Spring Co., CI 010B 13 S316)
0.75" springs (Lee Spring Co., CI 008B 11 S316)
0.625" springs (Lee Spring Co., CI 008B 09 S316)

Collagen gel and media reagents
Dulbecco's modified eagle's medium, DMEM (Invitrogen, 12100-046)
Fetal bovine serum, FBS (GemCell 100-500)
Penicillin-streptomycin (Invitrogen, 15070-063)
Collagen Type I, Rat Tail (BD, 354236)
0.25% Trypsin-EDTA (Invitrogen, 25200072)

Example bioreactor program (20%strain, 1 Hz)

Line	Address	SMC_Command	Command
1	0	Z1	Position register=1
2	5	A10000	Acceleration=10000 steps/(sec*sec)
3	10	B300	Base speed=300 steps/sec
4	14	M500	Max speed=500 steps/sec
5	18	J1000	Jog speed=1000 steps/sec
6	22	L22	Label=22
7	22	+	Direction CW
8	24	N225 @0G	Go relative 225 steps
9	31	F	Finish move
10	33	&10	If input 1=0, then execute the next line
11	37	X64	Goto 64
12	41	-	Direction CCW
13	43	N225 @0G	Go relative 225 steps
14	50	F	Finish move
15	52	&20	If input 2=0, then execute the next line
16	56	X64	Goto 64
17	60	X22	Goto 22
18	64	L64	Label=64
19	64	W2000	Wait 2000 msec
20	69	P1 @0G	Go to position 1
21	76	W45000	Wait 45000 msec
22	81	X22	Goto 22
23	85	Q	End of program

Protocol 1.3 - Phalloidin (F-Actin) Staining

Phalloidin stock should be prepared by dissolving in 1.5 mL methanol to yield a final concentration of 200 U/mL (which is about 6.6 µM)

Method:

1. Fix cells in 4% PFA overnight at 4°C

2. Wash once with PBS and store at 4°C in 70% EtOH

3. Wash 3 times with PBS
    - 15 minutes each on rotator

4. Permeabilize with 0.2% Triton-X
    - ex. 20µL per 10mL PBS
    - 10 minutes on rotator

5. Wash 3 times with PBS
    - 15 minutes each on rotator

6. Block in 1% BSA in PBS at 4°C
    - Either overnight at 4°C or for 1 hour at 37°C

7. Remove 1% BSA solution

8. Add 5 µL stock dye to 200 µL 1% BSA (1:40 dilution) for each gel to be stained
    - 100 µL per gel sample
    - Incubate for 30 minutes at room temperature in the dark

9. Wash 3 times with PBS
    - 15 minutes each on rotator

10. Add Draq 5 nuclear stain at 1:1000 dilution
    - 100 µL per gel sample
    - Incubate 30 minutes at room temperature in the dark

    **Note: this step can be done with the phalloidin stain step to save time*

11. Wash once in 1X PBS
    - 15 minutes on rotator

12. Image with either confocal (Leica or Zeiss)

    **Note: Images are best if taken within 24 hours of staining*

13. Store in 18 MΩ water at 4°C covered in foil

Protocol 1.4 - Isolation of Endothelial Layer from Porcine Leaflet

Protocol

1. Preparation
    1. Autoclave in a covered instrument tray the following items:
        1. Serrated tissue forceps - For handling the leaflet tissue
        2. Tissue scissors (8 cm) - For trimming leaflet tissue and cusps
        3. Cotton Swabs - For isolating the endothelial layer from the leaflet or cusp
    2. Make sterile collagenase solution
        1. Add 4.0 grams of powdered DMEM to 250 mL of 18 MΩ water.
        2. Add 1.11 grams of sodium bicarbonate.
        3. Add (600 U/mL) 180,000 units of collagenase.
        4. Add 1% (3mL) Penicillin/Streptomycin.
        5. Adjust the pH of the solution to 7.2.
        6. Bring the solution up to 270 mL.
        7. Sterilize the solution by passing through a 0.2 µm filter.
        8. Add 10% (30mL) of sterile fetal bovine serum.
    3. Make sterile endothelial cell medium
        1. Add 6.7 grams of powdered DMEM to 400 mL of 18 MΩ water.
        2. Add 1.85 grams of sodium bicarbonate.
        3. Add (50 U/mL) 25,000 units of heparin.
        4. Add 1% (5mL) Penicillin/Streptomycin.
        5. Adjust the pH of the solution to 7.2.
        6. Bring the solution up to 450 mL.
        7. Sterilize the solution by passing through a 0.2 µm filter.
        8. Add 10% (50mL) of sterile fetal bovine serum.
    4. Make sterile interstitial cell medium
        1. Add 13.37 grams of powdered DMEM to 800 mL of 18 MΩ water.
        2. Add 3.7 grams of sodium bicarbonate.
        3. Add 1% (10mL) Penicillin/Streptomycin.
        4. Adjust the pH of the solution to 7.2.
        5. Bring the solution up to 900 mL.
        6. Sterilize the solution by passing through a 0.2 µm filter.
        7. Add 10% (100mL) of sterile bovine serum.

2. Isolation of Heart Valve Leaflets
    1. Excise the aortic root immediately and aseptically from the heart after sacrifice.
    2. Thoroughly rinse the aortic root of blood with cold sterile DPBS. It is imperative to remove all blood components as soon as possible to limit VEC death and bacterial contamination. Antibiotics and antimycotics are not advised at this stage since they are potentially harmful to the VEC.
    3. Isolate valve leaflets (3 per valve) directly from the root and place in a sterile 15 mL conical tube filled with 12 mL cold DPBS. Shake several times to remove debris and refill with fresh DPBS.
    4. Transport back to the lab on ice.
    5. Upon arrival at the laboratory, place the container with the tissue under the sterile hood.

3. Isolation of Endothelial Layer
    1. Fill a sterile 35mm dish with 3mL of cold collagenase solution per valve (3 leaflets).

2. Place all three leaflets from the 15 mL tube into the dish filled with the collagenase solution.
3. Incubate the tissue for 5-10 minutes at 37 C.
4. Gently remove the endothelial layer by rotating a dry sterile swab onto the surface of the leaflet. The direction of rotation and amount of shear applied is critical for the purity of your sample. The rotation of the swab should be in an opposite direction to linear motion of your hand creating a controlled shear. This shear is what lifts the endothelial cells from the tissue. The amount of force applied should be enough to feel the resistance of the tissue but, not penetrate the basement membrane.
5. Occasionally, dab the swab within the collagenase solution to dislodge cells from the tip fibers. After swabbing is complete, the texture of the endothelial layer should feel slightly smoother than before.
6. Collect the cell suspension/collagenase and transfer to a new sterile 15mL tube.
7. Centrifuge the tubes at 1000 rpm for 5 minutes to pellet any isolated cells and aspirate supernatant. If isolating interstitial cells as well, perform that protocol while these cells are being centrifuged.
8. Add 3 mL of endothelial porcine medium to the 15 mL tubes, centrifuge a second time, and aspirate media. This second centrifugation helps filter some of the unwanted material such as tip fibers.
9. Re-suspend the centrifuged endothelial cells in 5 mL of endothelial porcine medium and plate the cells in a pre-coated T-25 flask with collagen (use 1 flask per centrifuge tube).
10. Let the cells grow at least 2-3 days before changing the endothelial medium. This helps the cells recover and divide since the isolation process is fairly harsh and the cell yield may be low. It is critical to passage cells near confluence since contact inhibition could lead to cell transformation.

4. Preparation of 60 mm Culture Dish for Side Specific Isolation
1. Line the 60 mm glass petri dishes with aluminum foil (2 glass dishes per leaflet). The aluminum foil helps to remove the paraffin, so that the glass petri dish can be reused for other isolations.
2. Place paraffin beads within the dishes, about half full, and cover for autoclaving.
3. Once the autoclaving is complete and paraffin is melted, move the dish ensemble to a cool flat surface. As the paraffin cools, it will harden and create a layer that will support needle punctures.
4. After 30 minutes, the sterilized dish can then be used as an isolation chamber to immobilize the leaflet tissue.

5. Isolation of Side Specific Endothelial Layer
1. Remove the leaflets from the 15mL tubes and place on prepared 60mm culture dish for side specific isolation.
2. Manipulate the leaflet so that the ventricularis side is face down on the paraffin surface leaving the fibrosa side exposed. Pin the edges of the leaflet to expose the endothelial layer.
3. Place a few drops of cold collagenase on each (upwards-facing) endothelial surface and incubate the tissue for 5-10 minutes at 37 C.
4. As before, gently remove the endothelial layer by rotating a dry sterile swab onto the surface of the leaflet. The direction of rotation and amount of shear applied is critical for the purity of your sample. The rotation of the swab should be in an opposite direction to linear motion of your hand creating a controlled shear. This shear is what lifts the endothelial cells from the tissue and nothing else. The amount of force applied should be enough to feel the resistance of the tissue but, does not penetrate within the tissue.

5. Occasionally, dab the swab within the collagenase solution to dislodge cells from the tip fibers. After swabbing is complete, the texture of the endothelial layer should feel slightly smoother than before.
6. Collect the cell suspension/collagenase and transfer to a new sterile 15mL tube. Indicate side specificity on label (leaflets from the same valve can be pooled together).
7. Transfer the leaflets to a new culture dish so that the ventricularis side is now exposed and repeat steps (5.3-5.6).
8. Once all cell suspension/collagenase is collected, centrifuge the tubes at 1000 rpm for 5minutes to pellet any isolated cells and aspirate supernatant. If isolating interstitial cells as well, perform that protocol while these cells are being centrifuged.
9. Add 3 mL of endothelial porcine medium to the tubes, centrifuge a second time, and aspirate media. This second centrifugation helps filter some of the unwanted material such as tip fibers.
10. Re-suspend the centrifuged endothelial cells in 5 mL of endothelial porcine medium and plate the cells in a pre-coated T-25 flask with collage (use 1 flask per centrifuge tube).
11. Let the cells grow at least 2-3 days before changing the endothelial medium. This helps the cells recover and divide since the isolation process is fairly harsh. If you notice the yield to be very low, consider moving to a smaller flask or well plate since cell-cell adhesion promotes cell growth. Remember to passage near confluence since contact inhibition could lead to cell transformation.

6. Isolation of Interstitial Cells
    1. Fill a sterile 15 mL centrifuge tube with 10 mL of collagenase solution per valve (3 leaflets).
    2. After swabbing the leaflets of endothelial cells, immediately place them in the appropriate 15mL tube with the collagenase solution.
    3. Incubate for approximately 12 to 18 hours (agitate gently if desired).
    4. Mix the degraded tissue gently with a serological pipette until cell suspension/collagenase becomes homogenized. This homogenization helps break up the tissue and release the interstitial cells.
    5. Centrifuge the digested tissue for 5 minutes at 1000 rpm and aspirate the supernatant.
    6. Add 5 mL interstitial porcine medium to the 15mL tubes, centrifuge a second time, and aspirate supernate.
    7. Re-suspend the centrifuged endothelial cells in 5 mL of interstitial porcine medium and plate the cells in a T-75 flask (use 1 flask per centrifuge tube).
    8. Let the cells grow at least 1-2 days before changing the interstitial cell medium. There will be much more tissue debris than with the endothelial cells but, that is expected. The cells should also grow to confluence faster than the endothelial cells because of the cell yield and their nature.

Protocol 1.5 - Masson's Trichrome Stain

Stock Solutions (all can be stored at room temperature for up to one year)

Bouin's Solution (Flammable cabinet). Add glacial acetic acid (to 5% just before use) ; dispose of in container

25ml x 5% = 1.25 ml to 23.75 ml

Alcoholic Hematoxylin Stock (Weigert's)

Hematoxylin (Sigma H9627) 5g
95% Ethanol 500ml
Dissolve over gentle heat, store in corrosive cabinet

10 % Ferric Chloride Stock

Ferric chloride Hexahydrate 9.67g
Milli-pure water 495 ml
Glacial acetic acid 5 ml
Dissolve ferric chloride in 50ml water, then dilute; store in corrosive cabinet

Acid Fuchsin, 1% aqueous stock

Acid Fuchsin, 1g [0.5g]
Milli-pure water 100 ml [50 ml]

Beibrich Scarlet, 1% aqueous Stock

Biebrich Scarlet 10g [5 g]
Milli-pure water 1000 ml [50 ml]

Aniline Blue Stock

Aniline Blue 1.25g
Glacial acetic acid 1 ml
Di Water 50ml

Phosphomolybdic-Phosphotungstic Acid

Phosphomolybdic acid, 0.625 g
Phosphotungstic acid, 0.625 g
DI Water 50 ml

Working Solutions

1% Acetic Acid

Glacial acetic acid, 0.5 ml [0.25 ml]
Di water, 49.5 ml [24.75 ml]
Make fresh just before use

Weigert's Hematoxylin

Alcoholic Hematoxylin Stock, 25 ml [12.5 ml]
10% Ferric Chloride Stock, 25 ml [12.5 ml]
Prepare just before use, discard in "Hematoxylin Waste" container

Biebrich Scarlet-Acid Fuschin Solution

Beibrich scarlet, 1% stock, 44.5ml [22.25 ml]
Acid fuschin, 1% stock, 5.0 ml [2.5 ml]
Glacial acetic acid, 0.5 ml [0.25 ml]
Prepare just before use, discard after 24 hours

Aniline Blue Working Solution

Aniline Blue stock 50 ml [25 ml]
Glacial acetic acid, 1.0 ml [0.5 ml]

Procedure

1. Deparaffinize and re-hydrate to H2O
    a. Xylene, 100% EtOH, 95% EtOH, 70% EtOH, ddH2O
2. Bouin's Solution 56 degrees (RT overnight)……..…1 hour
3. Running tap water rinse until yellow clears……..……1 min
4. Distilled water rinse…….…….……1 min
5. Weigert's Hematoxylin …….…….…..…….10 min
    a. Stains nuclei blue/black
6. Running tap water rinse…….……..…..……10 min
7. Distilled water rinse…….…….…….……1 min
8. Biebrich scarlet-acid fuchsin…….…….……5 min
    a. Stains cytoplasm and muscle red
9. Distilled water rinse…….…….……..….quick dip only
10. Phosphomolybdic-phosphotungstic acid solution……15-20 min
    a. Until collagen is not red, allows for uptake of aniline blue
11. Aniline blue solution…….…….……15 min
    a. Stains collagen blue
12. Distilled water rinse…….…….……...…quick dip only
13. 1% Acetic acid solution…….……..…..4 min
14. Dehydrate to xylene, mount with permount

Collagen – blue
Nuclei – black
Muscle, cytoplasm, keratin - red

Protocol 1.6 - Russel-Movat Pentachrome Stain

Time: ~3 hours
Background: Performing stain with American MasterTech kit.
Verhoeff's Elastic Stain expires after 24 hours, and is prepared with 6.25 mL of each of the following:
1. 10% Alcoholic Hematoxylin
2. Reagent Alcohol (not in kit, use 100% EtOH)
3. 10% Ferric Chloride
4. Universal Iodine Solution

Protocol:
1. Deparaffinize slides and hydrate through alcohols
    a. 3 changes of Xylene, 3 min. each
    b. 100% ethanol 5 min., 95% ethanol 2 min., 70% ethanol 2 min.
2. Rinse in running water for 2 min., followed by diH_2O for 2 min.
3. Place slide in **Verhoeff's Elastic Stain** for 15 min.
4. Rinse in lukewarm running water for 5 min., followed by 2 min. diH_2O
5. Differentiate in **2% Ferric Chloride** for 30 sec. Looking for black fibers, gray background
6. Rinse slide in diH_2O for 2 min. and place in **5% Sodium Thiosulfate** for 1 min.
7. Rinse in lukewarm running water for 5 min.
8. Place in **3% Acetic Acid** for 3 min.
9. Place in **1% Alcan Blue Solution** for 20 min.
10. Rinse in lukewarm running water for 1 min., then in diH_2O for 2 min.
11. Place in **Crocein Scarlet-Acid Fuchsin** for 2 min.
12. Rinse through 3 changes of diH_2O, 1 min. each
13. Dip slide 5 times in **1% Acetic Acid**
14. Place in 2 changes of **5% Phosphotungstic Acid** for 2 min. each. Collagen is now a pale pink, ground substance turns from red to bluish. Check under microscope, and stop differentiation when connective tissue is clear but before the elastic fibers are de-stained
15. Dip slide 5 times in **1% Acetic Acid**
16. Dehydrate through 3 changes of 100% EtOH, 2 min. each
17. Place in **Alcoholic Saffron Solution** for 15 min. →collagen turns yellow
18. Dehydrate through 3 changes of 100% EtOH, 1 min. each
19. Clear slide through 3 changes of Xylene, 1 min. each
20. Coverslip using permanent mounting media

Results
Elastic fibers, nuclei: **BLACK**
Collagen: **YELLOW**
Mucins: **BLUE TO GREEN**
Muscle: **RED**
Fibrinoid: **INTENSE RED**

Protocol 1.7 –H&E Stain (H&E)

Paraffin sections (see back for cryostat sections) Reviewed 7/07 MN

Station	Solution	Time (in minutes)
1	Xylene	4
2	Xylene	4
3	Xylene	4
4	100% Ethyl Alcohol (ETOH)	5
5	95% ETOH	2
6	70% ETOH	2
7	Deionized water	2
8	(Anatech, Ltd. brand cat. #842) Harris' Hematolyxin	6
9	running Tap water	3
10	0.2% Acid alcohol	20 seconds
11	running Tap water	1.5
12	1% Ammonia water	1
13	running Tap water	1.5
14	70% ETOH	1
15	(Harleco brand, VWR cat. #15204-132) 1% Alcoholic Eosin Y	1
16	95% ETOH	1
17	95% ETOH	1
18	100% ETOH	1
19	100% ETOH	1
20	Xylene	3

SOLUTIONS:

Harris' Hematoxylin (prepared)

Anatech, Ltd. brand - **FILTER EVERY MONDAY OR MORE OFTEN AS NECESSARY.**

Change after 2 weeks (10 working days) of use.

0.2% Acid Alcohol

	(per Varistain container)	(4000 ml. bottle)
70% ETOH ----------	680 ml.	2720 ml.
1% Acid alcohol --------	170 ml.	680 ml.

1% Ammonia Water

	(per Varistain container)	(4000 ml. bottle)
Deionized water ----------	800 ml.	3000 ml.
Ammonium Hydroxide (28%) ---------	8 ml.	30 ml.

1% Alcoholic Eosin Y (prepared)

Harleco brand, order from VWR Scientific (cat # 15204-132)

Add 0.5 ml. glacial acetic acid per 750 ml. 1% Eosin Y solution before using the stain for the first time.

Change after 2 weeks (10 working days) of use.

CHANGING SCHEDULE

Monday: all solutions

Tuesday thru Friday: rotate 100% ETOH in stations 4 & 5

Change: deionized water
1% ammonia water and 0.2% acid alcohol
95% ETOH in stations 17 & 18
100% ETOH in stations 19 & 20 (rotate last alcohol to station 19)

CONTROLS:

Run control slide once a week on Monday and in between whenever the Hematoxylin and/or
Eosin are changed or if a problem is suspected.
Label slide with date, your initials, and with the time in both hematoxylin and eosin solutions and lot number of Hematoxylin.
Check control slide under microscope for stain quality. Give control slide to Lab Supervisor for review.

RAPID H&E FOR CRYOSTAT SECTIONS

1.	10% neutral buffered formalin (for fresh,unfixed tissue).....	1 min.
If tissue is fixed start at step 2:		
2.	70% ETOH.....	brief rinse
3.	Deionized water.....	brief rinse
4.	Harris' Hematoxylin*.....	1 min.
5.	Tap water.....	brief rinse
6.	0.2%Acid alcohol.....	2-5 sec (1 dip)
7.	Tap water wash.....	1 min.
8.	1% ammonia water to blue.....	2-5 sec. (few dips)
9.	Tap water wash.....	1 min.
10.	1% alcoholic Eosin Y.....	10 sec.
11.	95% ETOH (agitate slides).....	few dips
12.	100% ETOH (agitate slides).....	few dips
13.	Xylene.....	1 min.
14.	Propar.....	1 min.
15.	Mount/coverslip with Permount.	

Reference:

Preece, A., A Manual for Histologic Technicians, Third Edition, Boston 1972, p. 100.

*Harris Hematoxylin time increased to 1 min from 20-30 sec. 7/25/02 (MN per BASummers)

Protocol 1.8 - Protocol for Making 4% PFA Solution

Objective:
Prepare 4% PFA Solutions from powder, aliquote, and store in -20C Freezer.

Materials:

1) Balance (portable)
2) Hotplate with magnetic stirrer and thermometer
3) Stirbar
4) 1L Bottle
5) 1000mL of 1X PBS
6) 40 g of Paraformaldehyde powder (Sigma Aldrich P6 148-500 Grams)
7) 50ml Serological pipettes
8) Automatic pipette
9) Orange cap 15ml centrifuge tubes

Prepare 4% w/v PFA in 1X PBS:
Work in the Chemical Safety Hood and wear gloves

1) Move balance and hot plate into Chemical Safety Hood and plug in
2) Fill bottle with 1000mL of 1X PBS
3) Add stir bar to bottle and place on hotplate
4) Weigh out 40g of PFA powder
5) Add PFA into bottle
6) Stir and Heat at 60C until completely dissolved
7) Use serological pipette to aliquot 10ml of 4% solution into each centrifuge tube.
    a. 1000/10 = 100 tubes of 4% PFA

Protocol 1.9 – Protocol: BrdU Labeling of Paraffin Sections

1) Deparaffinize and re-hydrate to H_2O.
    a. Heat at 60° until wax melts (~15 minutes).
    b. Xylene 1…...…10-15 minutes
    c. Xylene 2……..…5-10 minutes
    d. Xylene 3……..…5 minutes
    e. 100% EtOH.….5 minutes
    f. 95% EtOH.…...3-5 minutes
    g. 70% EtOH.……3 minutes
    h. Tap water
2) HCl incubation – put directly on slides
    a. Incubate slides in 2N HCl at 37° for 10 minutes
    b. Rinse in 0.1M Borate Buffer [pH 8.5] for 12 minutes at room temperature
    c. Rinse 3x5 min PBS
3) Blocking- put directly on slides
    a. Incubate with 10% goat serum in 1% BSA for 30 min at room temperature.
4) Primary Antibody – put directly on slides
    a. Incubate with 1:100 dilution of primary antibody in 1% BSA for 1 hour at room temperature or overnight at 4°. [mouse anti-Brdu]
5) Wash slides 3x5 min in PBS in coplin jar
6) Secondary Antibody – put directly on slides
    a. Incubate with 1:300 dilution of secondary antibody in PBS for 30 minutes at room temperature. [goat anti-mouse]
7) Wash slides 3x5 min in PBS in coplin jar
    a. DAB Kit (*light sensitive, do this step in the dark. *Excess DAB is a biohazard.*)
    b. 1 ml tap water
    c. 1 drop solution 1 (green)
    d. Vortex
    e. 1 drop solution 2 (brown)
    f. 1 drop solution 3 (white)
    g. Vortex and place on slides for 2-5 minutes; watch under microscope.
8) Rinse slides with PBS and then tap water in coplin jar.
9) Counter-stain in methyl green for 10-30 seconds
10) Quickly dehydrate to Xylene and mount using *Permount.*

Borate Buffer: 3.09g Boric Acid
500 ml ddH2O
Mix to dissolve. Adjust pH to 8.5 with NaOH pellets
Store at room temperature.

1% BSA is in PBS.

Protocol 1.10 - Immunohistochemistry (Paraffin Sections)

Melt wax by placing slides in 55C oven for ~10 minutes

*Set slides on their side, against the wall of a box, so that wax melts down, off the sample

Deparaffanization and Rehydration

1. Xylene, 3 changes for **3 minutes each**
2. 100% ethanol, 1 changes, **5 minutes**
3. 95% ethanol, 1 change, **2 minutes**
4. 70% ethanol, 1 change, **2 minutes**
5. Rinse gently in de-ionized water (gently pipette and aspirate dH_2O on sample)

- Circle each sample with hydrophobic pen, let dry
- Optional antigen retrieval (protocol developed by Jingjing Zhou and Caitlin Bowen, Summer 2012):
    - Lay slides flat in container
    - Pipet enough 2N HCl to cover samples onto each slide
    - Incubate for 70 minutes at 37C
    - Aspirate 2N HCl
    - Pipet enough 0.1M Sodium Borate (pH 8.5) to cover samples onto each slide
    - Incubate for 12 minutes at Room Temp
    - Rinse 3x in PBS for 5 minutes each
- Alternative antigen retrieval (developed by Jingjing Zhou)
    - Tri-sodium citrate buffer:
        - Weigh out 2.94g Tri-Sodium Citrate
        - Add 1000mL distilled water
        - pH to 6.0 with 1M HCl
        - Add 0.5mL Tween-20
    - Add Sodium Citrate buffer to tip box
    - Warm buffer by heating in microwave on High for 1 min
    - Add slides to dish
    - 5 min on “warm”
    - 5 min rest
    - 5 mini on “warm”
    - 2 min rest
    - 2 min on “warm”
    - 20 min cool to RT
    - Rinse 1x in PBS
- Apply enough 10% Goat serum (in 1X PBS) to cover sample (about 75uL per sample)
- Incubate 60 min at 37°C or overnight at 4°C

Primary antibody application:

1. Make 100µL per sample of 1° antibody (1:500 in antibody dilution buffer)
   Antibody dilution buffer: 1% BSA in 1x PBS +0.3% Triton-X (Cell Signaling Tech)
   *Note: If in doubt of pipetting small volumes, err on the side of higher concentration
2. Gently aspirate 1% BSA

3. Dry slide very carefully with a kim wipe by touching a corner of the wipe to the edge of the liquid on your sample
    *Do NOT touch your samples with the kim wipe
4. Apply primary antibody
5. Incubate overnight (at least 8 hr) at 4°C

Secondary antibody application:
Aspirate 1° ab solution
Place slide(s) in dish (ex: pipet box lid) with enough PBS to cover
Wash 3x in PBS on shaker, 5 minutes each
While shaking, prepare 2° ab solution:
    Fluorescent antibody: 1:200
    Draq 5: 1:1000
    In solution of 1% BSA+PBS
        Ex: 2.5uL goat anti-rabbit 568 + .5uL Draq 5 + 497uL 1% BSA+PBS = 500uL 2° ab solution
Apply 100uL 2° ab solution to each sample
Incubate for 30 minutes at room temperature, *cover with foil*
3 washes
Wash 3x in PBS on shaker, 5 minutes each

Dehydration (optional, unclear from the literature if this degrades your fluorescent signal or not):
    70% ethanol, 1 change, 3 min
    95% ethanol, 1 change, 3 min
    100% ethanol, 2 changes, 3 min each
    Xylene, 3 changes, 3 min each
Rinse gently in deionized water

Mounting
Remove ProLong Gold antifade reagent (Invitrogen P36934) from freezer, allow to come to room temp
    Do not apply external heat
Remove excess liquid from specimen using kim wipe, as described above
Apply 1 drop of medium to the sample
    Or to the slide if sample was mounted on a coverslip
Gently lower coverslip onto slide, avoid trapping air bubbles
Allow slides to cure 24 hrs at room temperature. *Protect from light!*
If necessary, seal the edges of the coverslip with nail polish (clear) or hot wax

Long term storage: RT, fridge, or -20 freezer

Protocol 1.11 - Expedited IHC protocol

Day 1
Fixation & Blocking

1. Aspirate medium
2. Wash once with PBS (repeat until pink color is gone from solution)
3. Add 4% PFA, incubate at least 4 hours at 4°C
    - PFA moves approximately 1 mm per hour
4. Aspirate 4% PFA, add PBS (or 70% EtOH if you want to store them for up to 2 wks)
5. Transfer gels from 4-well to 6-well plate (carefully, maintain up/down orientation)
6. Wash gels 3X in lots of PBS, 15 minutes each on rotator
7. Permeabilize with 0.2% Triton-X 100 for 10 minutes on rotator
   (10 mL PBS, 20 µL Triton-X)
8. Wash 3X with PBS, 15 minutes each on rotator
9. Add blocking solution, incubate overnight at 4°C, **or 1 hour at 37°C**
    - 1% BSA in PBS (blocking solution, 2 mL/well)

Day 2

10. Transfer gels back to 4-well plate
11. Aspirate blocking solution and add primary antibodies in PBS, 50 µL/well
    - αSMA (spring biosciences, rabbit anti-human, 1:100)
    - QH1, for quail (mouse anti-human, 1:100)
    - *ex. Have 4 x 7 gels = 28 gels*
      28 x 50 µL = 1400 uL (make 1600 uL)
      16 µL QH1 antibody
      16 µL αSMA antibody
      1568 µL PBS
12. Incubate with primary antibody overnight at 4°C in a humidified chamber (fridge)

Day 3

13. Transfer gels to 6-well plate (maintain up/down orientation)
14. Wash 3X with PBS, 15 minutes each on rotator
15. Transfer gels back to 4-well plate
16. Add secondary antibody at 1:100 dilution in PBS + 1% BSA
    - 100 µL per gel, 3 mL PBS, 30 µL secondary antibodies
      (QH1: goat anti-mouse 568
      αSMA: goat anti-rabbit 488)
17. Incubate with secondary antibody for 2 hours at RT
18. Transfer gels to 6-well plate
19. Wash 3X with PBS, 15 minutes each on rotator
20. Transfer gels back to 4-well plate
21. Add Draq 5, 1:1000, 100 µL per gel
    - 3 mL PBS, 3 µL Draq 5
22. Incubate for 30 minutes at RT
23. Store in 2 mL PBS

After final Draq 5 staining, to prepare gels for imaging:

If using Zeiss (images from bottom)

- Transfer gels to a 6-well plate, in plenty of 18 MOhm deionized water
- Bring downstairs:
  - 6-well plate with gels
  - squirt bottle of 18 MO water
  - a few slides or coverslips
  - disposable spatula
  - 4-well plates (with some PBS in them) for storing gels after imaging
  - Flash drive
- Once downstairs, move gel carefully from well to slide, maintaining orientation
- Squirt enough water onto the gel to keep it from sliding around… will this work? Practice before confocal training
- Place slide carefully onto microscope stage
- After imaging, transfer gel into its well in the 4-well plate, re-use slide

Protocol 1.12 - Immunofluorescence of cells on slides:

Cell culture: PAVEC

Divide slide into three sections and outline outer edge with hydrophobic pen
Sterilize under UV for > 30min
Apply ~100uL collagen (50ug/mL) to each section
Incubate at 37C for >20 min
Meanwhile, trypsinize and spin down cells
Resuspend cells in 200uL x (# of sections)
    Ex. For 3 slides = 9 sections = 1.8mL
Aspirate excess collagen
Apply cells to each section
Let adhere for > 2 hours (until cell spreading is observed)
Ideally, let grow overnight.

Immunofluorescence:

Rinse with PBS
Fix in 4% PFA for 20 min at 37C or overnight at 4C
Rinse with PBS
Permeabilize with 0.5% Triton-X for 10 min on rotator
    1 mL PBS + 5uL Triton-X
Wash 3x with PBS for 5 min on rotator
Block in 1% BSA for 30 min at room temp
Make primary antibody solution
    1:100 primary antibody
    +PBS
Aspirate BSA
Apply 100uL primary ab to each section, at 1:100 dilution
Incubate 1 hr at Room Temp
Wash 2x in PBS for 5 min on rotator
Make secondary antibody solution
    1:100 secondary antibody
    +1:100 Draq 5
    +1% BSA
Apply 100uL secondary antibody to each section, at 1:100 dilution
Incubate 30 min at Room Temp
Apply small drop of ProLong Gold anti-fade mounting medium
Carefully apply coverslip
Fix for 24 hrs

Protocol 1.13 - Designing primers for qPCR

1. Look up desired gene (Ensembl or PubMed)
    a. Type in gene name and species (e.g. Sus Scrofa = pig)
2. In ensemble, Click on the red box where they have identified your gene
    a. click on Transcript ID
    b. choose cDNA in the left hand menu
    c. hyperlink to FASTA sequence
3. Copy and paste the whole FASTA sequence into Word
4. ENSMBL gene transcript annotation to locate exon boundaries in first ~500pb and change the color of alternating exons between black/blue
5. Copy and paste ~500bp of 5' sequence into Primer3
    a. Sequence ID: animal name and gene name (e.g. Pig CDH11)
    b. Product size: 125-150 (number of base pairs)
    c. Click "pick primers"
6. Primers are chosen, denoted by >>> and <<<
    a. Amplicon (PCR product) is the entire sequence from start of forward primer to the end of the reverse primer
    b. Reverse primer is backwards and complementary to the section underlined by <<<<

Notes:
* Don't create primers near the end of the mRNA sequence
* Avoid sequences with long repetitions of G or C –could get primer dimmers or folding
* Ideally, have G or C clamps at the end of your primers for secure bonding

7. Copy and paste chosen primer info into Word
8. Find where primers are located in gene sequence (Ctl+F) (…reverse complement!)
    a. Amplicon should span blue/black region: this makes sure it crosses an intron-exon boundary, which excludes genomic DNA from amplification
    b. cDNA doesn't have introns, so spanning a boundary between two exons insures you're only amplifying your cDNA
9. BLAST the primers using NCBI primer-BLAST
    a. Select species of interest
    b. Paste forward and reverse primers in the respective fields
    c. Should see 100% match in the gene of interest
    d. Check that there are no other 100% matched

Protocol 1.14 - RNA Isolation

Time: ~1 hour

Materials (located by RNase free bench unless otherwise noted):
RNA isolation kit (includes QIAshredders with caps, RNeasy spin columns, RW1, RPE, 1.5 mL collection tubes), RNase Zap, RNase free water, RNase free 70% EtOH (Emily's bench), 1 mL pipette with RNase free tips, 1 mL RNase free centrifuge tubes, waste beaker (cabinet), kimwipe (Emily's bench), tube racks

Background:
Porcine Aortic Valve Leaflets were excised from pigs and placed in vessels for disruption and homogenization. Samples were flash frozen with LN_2 and broken down with a mortar and pestle, and stored at 4C.

Protocol:

1. Retrieve samples from -80C (2^{nd} shelf down, right hand side)
2. Wipe down area and samples with RNase Zap
3. Vortex samples to mix
4. Centrifuge 30 seconds at 15,000 rpm
5. Transfer the supernatant (lysate, ~350 uL) to a QIAshredder spin column for each sample
6. Centrifuge 2 min. at 15,000 rpm
7. Remove QIAshredder from centrifuge, remove membrane and replace it with a lid from the kit (label the lids)
8. Centrifuge 3 min at 15,000 rpm to get protein/remaining contaminants to the bottom of the tube.
9. Return aortic valve leaflets to the -80C freezer
10. Transfer 300 uL of each sample to a RNase free centrifuge tubes
11. Transfer 300 uL (1 volume) of 70% EtOH to each tube, pipette up and down until viscosity change is no longer visible. DO NOT CENTRIFUGE
12. Transfer the volume (600 uL) to RNeasy spin columns
13. Centrifuge for 30 sec at 8,000 rcf
14. Discard flow through into a waste beaker (pour out of clear tube, tap the tube on a kimwipe to remove any excess)
15. Add 700 uL RW1 to each sample, use the same tip as long as you don't touch
16. Centrifuge 30 sec at 8,000 rcf
17. Remove the flow through as before
18. Add 500 uL RPE Buffer to each sample and centrifuge 30 sec at 8,000 rcm
19. Remove the flow through as before
20. Add 500 uL RPE Buffer to each sample and centrifuge for 2 min at 8,000 rcf
21. Transfer RNeasy spin column (pink membrane) into 2 mL collection tubes
22. Centrifuge for 1 min at full speed
23. Place RNeasy spin column into 1.5 mL collection tubes from the kit
24. Dilute with 30 uL RNase free water by adding directly to the membrane
25. Place tubes in centrifuge with clear lid facing inwards. Centrifuge for 1 min at 8,000 rcf
26. Wash the waste beaker, then use RNase Zap on hands
27. RNA solution is collected in 1.5 mL tubes after centrifugation. Add 2 uL of each sample to 0.5 mL tubes (black box above the RNA station) to be used with the NanoDrop
28. Store RNA samples at -80C

NanoDrop Protocol:

1. Put 2 uL samples on ice, take to the NanoDrop (Weill 130, LER) with gloves and RNase free water
2. Open NanoDrop 2,000 software→Nucleic Acid→No→Okay
3. Change “type” to RNA, type in sample ID, load 1 uL RNase free water onto the stage and click blank
4. Wipe the stage with a kimwipe, add 1 uL sample, and click measure. Repeat this step for all samples. When saving, use the date and nucleic acid, but add the sample name
5. Click Report, Export, and save as a Report, Excel SML spreadsheet (*.xml).

Protocol 1.15 - Apoptosis Assay (APO-BrdU TUNEL Assay)

Materials:

- **APO-BrdU TUNEL Assay Kit** (Invitrogen A23210)
  - **Positive control cells** (Component A, brown cap), fixed human lymphoma cell line (5 ml)
  - **Negative control cells** (Component B, white cap), fixed human lymphoma cell line (5 ml)
  - **Terminal deoxynucleotidyl transferase** (Component C, yellow cap) (45 µl)
  - **5-Bromo-2'-deoxyuridine 5'-triphosphate (brdUTP) (**Component D, violet cap) (480 µl)
  - Anti-BrdU mouse monoclonal antibody PRB-1, Alexa Fluor 488 conjugate (Component E, orange cap) (350 µl)
  - **Propidium iodide/RNase A staining buffer** (Component F, amber bottle) (30 ml)
  - **Reaction buffer** (Componet G, green cap) (0.6 ml)
  - **Wash buffer** (Component H, blue cap) (120 ml)
  - **Rinse bugger** (Component I, red cap) (120 ml)
- **1X Phosphate Buffered Saline (PBS)**
- **Draq5** (Biostatus Limited)

Method:

1. Wash gels once with warm PBS, then fix in 4% PFA for 24 hours (store at 4°C)

2. Aspirate 4% PFA, store gels at 4°C in 70% EtOH (until staining begins)

3. Aspirate EtOH, wash 3X in wash buffer (blue cap) on shaker for 5 minutes each (1X PBS is also ok)

4. Prepare a DNA labeling solution (total volume 50 µl per gel)
   - 10 µl reaction buffer (green cap)
   - 0.75 µl TdT enzyme (yellow cap)
   - 8.0 µl BrdUP (violet cap)
   - 31.25 µl dH_20
   - Note: this makes up 50 µl of labeling solution – scale up volumes as needed for multiple samples

5. Incubate gels with 50 µl DNA labeling solution for 2 hours at 37°C (oven or incubator)
   - Note: Incubation of labeling solution can also be carried out at room temperature overnight

6. Rinse with rinse buffer (red cap), 5 minutes on shaker

7. Aspirate, rinse once more with rinse buffer (red cap), 5 minutes on shaker

8. Add 100 µl antibody (1:50 dilution in rinse buffer) to each gel, incubate for 1 hour in dark at room temperature

9. Incubate samples with 1:1000 dilution Draq5 in 1X PBS for 30 minutes
    - Note: this step can be combined with the previous (add Draq5 to the BrdU antibody solution)

10. Add 200 µl of propidium iodine (amber bottle) to each sample, incubate in dark at room temperature for 30 minutes

11. Store in 1X PBS at 4°C until imaging
    - Note: samples are best imaged within 24 hours of staining

Protocol 1.16 - Proliferation Assay (BrdU Labeling)

Materials:

- **BrdU Labeling Reagent** (15 ml; Invitrogen 00-0103)
- **10X Phosphate Buffered Saline (PBS)**
- **1.5 M Hydrochloric Acid**
- **Blocking Buffer** (1X PBS / 5% BSA / 0.3% Triton X-100)
    - To make 500 ml of blocking buffer:
        - 50 ml 10X PBS
        - 25 ml 5% BSA (1.25 g BSA in 25 ml 1X PBS)
        - 420 ml dH_20
        - 1.5 ml Triton X-100
    - Mix well, store at 4°C
- **Antibody Dilution Buffer** (1% BSA in 1X PBS)
    - To make 100 ml of buffer:
        - 1 g BSA
        - 100 ml 1X PBS
    - Mix well, store at 4°C
- **Anti-BrdU mouse monoclonal antibody, Alexa Fluor 488 conjugate** (350 µl; Invitrogen B35130)
- **Draq5** (Biostatus Limited)

Method (Part 1) – Adding BrdU to Experiment

1. Add BrdU labeling reagent (1:100 dilution) to cell culture media

2. Sterile filter BrdU media before adding to gels

3. Add BrdU media to gels 12 hours prior to fixation (other cell types may need doubling time to be determined)

4. Incubate at 37°C

Method (Part 2) – Fixation and Staining

12. After 12 hours incubation with BrdU, aspirate media, wash once with warm PBS, then fix in 4% PFA for 24 hours (store at 4°C)

13. Aspirate 4% PFA, store gels at 4°C in 70% EtOH (until staining begins)

14. Aspirate EtOH, wash 3X in 1X PBS on shaker for 5 minutes each.

15. Add 1.5M HCl and incubate for 30 minutes at room temperature.

16. Aspirate HCl and wash 2X with 1X PBS on shaker for 5 minutes each.

17. Block samples in Blocking Buffer for 60 minutes at room temperature.

18. Aspirate blocking buffer, add conjugated antibody (anti-BrdU 488) to each sample

- 1:100 dilution of antibody in 1% BSA
- Add 50 µl to each sample
- Incubate at room temperature in the dark for 2 hours

19. Incubate samples with 1:1000 dilution Draq5 in 1X PBS for 30 minutes
    - Note: this step can be combined with the previous (add Draq5 to the BrdU antibody solution)

20. Store in 1X PBS at 4°C until imaging
    - Note: samples are best imaged within 24 hours of staining

Protocol 1.17 – Plasmid transfection into AVC via electroporation

Transfection

1. Cells should be transfected a day after passaging, when cells are still in exponential growth phase.
2. Prepare biosafety hood, wipe area with 70% ethanol.
   a. Warm electroporation culture media for AVC, 1X PBS (25 mL 10X PBS in 225 mL 18M mΩ water, autoclaved), and trypsin in EDTA *(located on middle shelf in large –20 C fridge)* in water bath.
   b. Wipe empty beaker with ethanol, fill with 50-100 mL 100% bleach and place in hood.
3. Wipe closed package of desired well-plate *(located in drawer next to biosafety hood)* and place into hood. Do not open outside of hood or sterility will be lost. The number of desired experiments or predicted number of cells determines number of wells on plate. Refer to Neon Transfection System manual for appropriate well-plate size as a function of cell count.
4. Wells must be coated with 0.500 mL collagen (125 uL stock collagen type I/10 mL 1X PBS) 30 minutes prior to plating to allow proper adhesion. Apply collagen to flask at least 10 minutes prior to beginning harvesting process.
5. Aspirate media from current old flask and dispose into waste bleach beaker.
6. Add 10 mL 1X PBS to flask to rinse cells. Remove PBS and dispose in waste beaker.
7. Add 3 mL trypsin in EDTA to flask to remove the cells from the plate surface. Tap flask to aid in removal. Be mindful of time in contact with trypsin because excessive exposure will destroy the cells.
8. Place in dry 37 C incubator for 3 minutes (no more than 5 minutes or cells will die).
9. Take flask out of incubator and continue tapping. Solution should be cloudy with cells. Quickly check under light microscope to verify cells have been detached from plate bottom.
10. Deactivate trypsin by adding 3X volume (9 mL) warm electroporation PAVEC media to flask. Pipette up and down to homogenize.
11. Transfer cell suspension to 15 mL conical tube. Count cells at this stage to determine how much of suspension with proper number of cells must be used in electroporation experiment.
12. Once required volume of suspension is determined, aliquot that amount and centrifuge at 1000 rpm for 5 minutes.
13. After centrifugation, aspirate supernatant carefully without disturbing the pellet and dispose in waste beaker.

*Release and pellet cells, **Start here**

14. **Resuspend cells in 11 uL x # rxns of Buffer R** (provided in Neon Kit) and transfer to sterile 1.5 mL microcentrifuge tube.
15. Obtain plasmid *(located in small –20 C fridge)* and thaw immediately.
16. **Slowly add 1.0 ug of plasmid per reaction to be done to cell suspension**. Do not mix or pipette vigorously or the DNA will be lysed.
17. **Apply 10 uL Neon transfection tip** (refer to Neon Transfection manual for proper attachment) and take up cell/DNA suspension, being careful to not take in any

bubbles. Place in microinjector station and run diagnostics. Troubleshoot as necessary.

18. Prepare well plate by removing collagen and adding 2.5 mL warm electroporation PAVEC media to each well being used.
19. Set following parameters for optimal PAVEC transfection (tested with pmaxFP-C)
    a. Parameter 15 (Database -> PAVEC -> Load)
        i. Voltage: 1650 V
        ii. Pulse width: 20 ms
        iii. Pulse number: 2
    b. Press Start
        i. Watch carefully for arcing (small orange flash)
20. Remove microinjector from station and apply the cells in tip evenly in a single well. Repeat transfection for number of desired experiments.
21. Each gold Neon tip can be used **ONLY TWICE** before contamination is unacceptable. Dispose tip after two uses.
    a. Dispose electroporation chamber after 10 uses
22. Label plate properly with name, date, cell type, etc.
23. Place in dry 37 C incubator.

Protocol 1.18 - Preparation of LB Broth

Bacterial Transformation of Plasmid in *E. coli*

1. Obtain clean and dry 500 mL glass vial (with screw-top lid).
2. Add 500 mL 18M mΩ water.
3. Add 10 g LB Broth powder *(located on shelf above pH meter).*
4. Prepare for autoclaving by partially sealing top with autoclave tape and labeling flask with name, date, solution type, etc.
5. Choose appropriate autoclave program (20-30 minutes). Make sure lid is slightly loosened or pressurization will result in explosion.

Preparation of LB Agar Plates (in laminar flow hood)

1. Add 50 mL18M mΩ water into a clean beaker for every plate to be poured.
2. Add 1 LB agar tablet (located on shelf above pH meter) for every 50 mL of water.
3. Prepare for autoclaving by partially sealing top with autoclave tape and autoclave using appropriate program.
4. Thaw appropriate antibiotic.
   a. Pencillin/streptomyocin *(located in mid-shelf in large –20 C freezer)*
   b. 100X Kanamycin *(located in door shelf in large –20 C freezer)*
   c. 1000x Ampicillin
5. After autoclaving, let LB agar solution cool to approximately 55 C. *(~55C is reached when you can touch the beaker with gloved hands for 3 seconds before it gets too hot)*
6. Add appropriate amount to achieve standard final concentrations for respective antibiotic.
   a. Pencillin/streptomyocin – 100 ug/mL
   b. 100X Kanamycin – 0.25-0.50 ug/mL
   c. 1000x Ampicillin – 1 ul/mL
7. Open sterile petri dishes under laminar flow hood. (be sure to reseal before putting back)
8. While LB broth+agar+antibiotic mixture is still fluid and warm, pour ~40-50 mL of mixture into each Petri dish and let cool with cover half on to prevent condensation under lid.
9. Leave in hood until solid prior to applying competent *E. coli* cells. For long term storage, store at 4 C *(good for at least 6 months).*

Transformation in NovaBlue competent cells (protocol also provided by manufacturer)

1. Create an ice bucket *(ice located in autoclave room)*
2. Create 42 C water bath. Use heat block and add 18M mΩ water to rack.
3. For each n set of plasmids being mass-produced, [*OPTIONAL*] obtain n+1 number of tubes of competent cells from NovaBlue Singles Competent cells kit *(located on third shelf of –80 C freezer in NovaBlue box)*. One tube will be used for the Test Plasmid.

Also take out tube of SOC medium found in the kit and warm at room temperature prior to starting. SOC medium can also be stored at – 20 C so it takes less time to thaw.

4. Place tubes on ice and thaw for 2-5 minutes.
5. Flick tubes 1-2 times to resuspend cells and shake once or twice with hands to get any liquid back to the bottom.
6. [*OPTIONAL*] To one tube of competent cells, add 1 uL (0.2 ng) Test Plasmid, gently stir and return to ice bucket.
7. To other tubes, add *10 uL* of ligation reaction or *0.5 uL* pure plasmid DNA (approximately 1-10 ng) and return to ice.
8. Incubate all tubes on ice for 5-10 minutes.
9. Without shaking, place tubes in 42 C water bath for *exactly* 30 seconds.
10. Place tubes back on ice for 2 minutes.
11. Add 250-300 uL SOC medium at room temperature to each tube. Return tube to ice.
12. If selecting for kanamycin, streptomycin, or spectinomycin resistance, shake at 37 C for 30 minutes prior to next steps. If selecting for ampicillin or chloramphenicol resistance, continue directly to step 13.
13. Spin down the bacteria at 1000 RPM for 1 minute in the table top centrifuge.
14. Remove all but 50 uL of the supernatant to create a concentrated mixture and resuspend.
15. Transfer the remaining 50 uL of mixture to center of cool LB agar plate prepared with selective media in previous steps. With blue cell spreader (under electrophoresis machines), spread cell mixture until dry.
16. Place cover-side down in 37 C bacterial incubator *(located in Weill B07, contact Dr Archer for access/permission)* 12-16 hours (overnight).

Selecting single colony for MiniPrep

1. In the morning of the next day, warm LB broth at room temperature and transfer 5 mL to 15 mL conical tube for every plate (done in the laminar flow hood to maintain sterility of the LB broth)
2. [Optional] Add appropriate antibiotic to have final concentration listed previously. Make sure this concentration matches that applied to the selective media in the LB agar plates.
3. Retrieve LB agar plates from incubator and with sterile pipette, transfer one single large colony to each conical tube (only one colony per tube) and leave pipette/transferring stick in the conical tube.
4. Keep at 4 degrees until ready to place in incubator.
5. Securely place in shaking incubator at 37 C (top incubator) and resume shaking. Shake overnight. Be sure to leave cap *slightly* open to allow for air to get in, without allowing any media to spill.
6. Keep LB agar plates at 4 C until you are sure that you have isolated your plasmid.

MiniPrep (QIAGEN)

1. Take 1.2 ml from 5 ml of bacterial culture and place in microcentrifuge tube. Spin at 13,000 RPM for 1 minute.
2. Remove supernatant and resuspend in 250 uL Buffer P1. Vortex for at least 3 minutes. *If you want to pause, freeze bacterial pellet at – 80 C before resuspension.*
3. Add 250 uL Buffer P2 and mix thoroughly by inverting tube 4-6 times. Solution should turn blue due to LyseBlue reagent. Do not let reaction to proceed for more than 5 minutes

4. Add 350 uL Buffer N3 and mix immediately by inverting tube 4-6 times. Solution should turn colorless. Leave on ice for a few minutes.
5. Centrifuge for 10 minutes at 13,000 RPM.
6. Apply the supernatant (850 uL) to the QIAprep spin column by pipetting. Make sure not to get any of the white pellet into the spin column.
7. Centrifuge for 1 minute at 13,000 RPM and discard flow-through.
8. Wash spin column by adding 750 uL Buffer PE and centrifuge for 1 minute at 13,000 RPM. Discard flow-through.
9. Centrifuge for 1 minute at 13,000 RPM to dry membrane.
10. Add column to a clean microcentrifuge tube. Add 20-30 uL ddH2O to the center of the spin column and let stand for 1 minute.
11. Centrifuge for 1 minute. Expected NanoDrop reading is 90-110 ng/uL.

Inoculation of colony

12. Warm LB broth and transfer 100 mL to sterile Erlenmeyer flask. Use one flask for every colony selected/conical tube used previously. For Midi Prep, use 25 mL volume split into two 50 mL conical tubes (11.5 ml LB media, 1 ml cells to each).
13. Add appropriate antibiotic to have final concentration listed previously. Make sure this concentration matches that applied to the selective media in the LB agar plates.
14. Transfer 1-2 mL of bacterial cell mixture in conical in shaking incubator to 100 mL of newly prepared LB broth in Erlenmeyer flask. Return to shaking incubator and incubate at 37 C overnight.

Purification of plasmid from *E. coli*

1. Obtain two 50-mL Oak Ridge round-bottom ultracentrifuge tubes (from Dr. Reinhart-King's lab, ask permission or order if unobtainable) and autoclave before proceeding with purification. These tubes are necessary to withstand high centrifugation speeds used in later steps of purification.
2. Retrieve flasks from shaking incubator and return to Weill 304.
3. Transfer 800 uL of mixture to cryotube and add 200 uL glycerol (4:1 ratio) and place in –80 C freezer for later use.
4. Use QIAGEN Endonuclease-Free MaxiPrep kit to purify. Follow manufacturer's protocol.
5. Locate appropriate centrifuges needed in purification steps *(ultracentrifuge located in Dr. Shuler's lab, ask Paula Miller for permission).*
6. Once purified, determine final DNA concentration *(see Nanodrop analysis protocol).*

Protocol 1.19 - Pierce 660 nm Protein Assay

Time: ~30 min

Materials: Protein samples, microcentrifuge tubes, 660 nm Pierce Reagent, Ionic Detergent Compatibility Reagent (IDCR), Laemmli Buffer, 96-well plates

Background: The standard was already made (2,000 ug/mL Bovine Syrum Albumin (BSA), diluted 1:1 in Laemmli Buffer) and the assay performed.
In this assay we will study the affects of TNFα, TNFα + superoxide dismutase (SOD), and osteogenic media (OGM) proteins. TNFα is inflammatory, and OGM allows for or induces calcification (not clear which). I will perform the assay on TNFα + SOD.

Hypothesis: SOD mitigates the pathological affect of TNFα on Porcine Aortic Valves (PAVs).

Protocol:

To make reagent: 500 mg IDCR + 10 mL 660 nm protein reagent (Western blotting shelf, above electrophoresis equipment)

1. Thaw protein samples from the -80 at room temperature
2. Vortex the protein sample and add 5 uL to the walls of microcentrifuge tubes
3. Wash the protein sample down with 45 uL of Laemmli Buffer
4. Pipette up and down to mix, and add 10 uL of the solution to the wells of a 96-well plate (N=4)
5. Add 150 uL of reagent (see above) to each well
6. Cover the well plate in Parafilm, shake to mix
7. Turn the plate reader on (Putnam Lab)
8. Open Gen5 software
9. Create new item: Experiment→Butcher_660 nm→Right click Plate1→Read
10. Plate ID: date, sample
11. Wait for tray to come out and computer to prompt you to load the plate. Remove Parafilm and load, read
12. Save experiment under Desktop→Butcher Lab→Emily→660 nm Assay
13. Export to Microsoft Excel and save the experiment the same way, email to yourself

The experiment was repeated 3 times:
1. Not enough of the protein sample was added (low results)
2. Poor mixing of protein sample with Laemmli Buffer (wide range of results)
3. Appropriate results

Protocol 1.20 - Protocol for preparing EBSS

To prepare 1000 mL of 10X EBSS, the following materials will be used:

- Calcium chloride dihydrate ($CaCl_2 \cdot 2H_2O$, Sigma #C7902) – 2.65 g
- Potassium chloride (KCl, Sigma #P5405) – 4.0 g
- Magnesium sulfate($MgSO_4$, Sigma #M2643) – 0.9767 g
- Sodium chloride (NaCl, Sigma #S5886) – 68.0 g
- Sodium phosphate monobasic ($NaH_2PO_4 \cdot H_2O$, Sigma #S5011) – 1.4 g
- D-glucose ($C_6H_{12}O_6$, Sigma #G7021) – 10 g
- ddH_2O – 1000 mL

1.) Mix all components and 700 mL ddH_2O in a 1000 mL beaker with a magnetic stirrer on a stir plate.
2.) Use a graduated cylinder to bring the volume of the solution to 1000 mL.
3.) Using a 0.22m bottle top filter, filter-sterilize the 10X solution into a 1000 mL bottle.
4.) Store the sterile salt solution at 4C.

To prepare 1000 mL of 1X EBSS, the following materials will be used:

- 10X EBSS liquid – 100 mL
- Sodium bicarbonate ($NaHCO_3$, Sigma #S5761) – 2.2 g
- ddH_2O – 900 mL

1.) In a sterile cell culture hood, pour 100 mL 10X EBSS into a graduated cylinder.
2.) Add 600 mL ddH_2O.
3.) Transfer the solution to a 1000 mL beaker.
4.) Add 2.2 g sodium bicarbonate to the solution and mix with a magnetic stirrer on a stir plate.
5.) Adjust the pH of the solution to 7.2 using 1 M NaOH or 1 M HCl.
6.) Use a graduated cylinder to bring the volume of the solution to 1000 mL.
7.) Using a 0.22m bottle top filter, filter-sterilize the 1X solution into a 1000 mL bottle.
8.) Store the sterile salt solution at 4C.

Reference

Earl, WR. (1943) The mouse fibroblast cultures and changes seen in the living cells. J. Nat. Cancer Inst. 4: 165-169.

Protocol 1.21 - Live & Dead Assay Viability/Cytotoxicity Assay

Live and Dead Viability/Cytotoxicity Kit (Molecular Probes) was used to simultaneously visualize live and dead cells. The cytoplasm of the live cells is stained in green by converting the calcein AM into green fluorescent calcein through intracellular esterases, while ethidium homodimer-1 (EthD-1) can entered dead cells through damaged membranes to bind deoxyribonucleic acid (DNA) and produce a bright red fluorescence in dead cells.

1. Remove the LIVE/DEAD reagent stock solutions from the freezer and allow them to warm to room temperature.

2. Add 10 µL of the supplied 2 mM EthD-1 stock solution to 5 mL of sterilized PBS, vortexing to ensure thorough mixing. This gives an approximately 4 µM EthD-1 solution.

3. Add 2.5 µL of the supplied 4 mM calcein AM stock solution to the 5 mL EthD-1 solution. This gives an approximately 2 µM calcein AM solution. Vortex the resulting solution to ensure thorough mixing. The working solution is for 10 samples.

4. Remove the culture medium and wash the sample with PBS. Withdraw PBS.

5. Add 0.5 ml the working solution (approximately 2 µM calcein AM and 4 µM EthD-1) directly to the sample.

6. Incubate the samples for 30 min in the incubator (37 °C, 5% CO_2).

7. Transfer the stained sample(s) to medium (if imaging process takes several hours)

*Note that aqueous solutions of calcein AM are susceptible to hydrolysis (see Storage and Handling of Reagents). Aqueous working solutions should therefore be used within one day.

EthD-1(powder form) from Invitrogen

Dissolve 1 mg EthD-1 in DMSO/H2O (1:4 v/v, 0.117 ml DMSO and 0.468 ml H2O) to have 2 mM stock solution (Stock solution is in Dr. Shuler lab)

Calcein AM (powder form) from Invitrogen

Dissolve 50 ug calcein AM in 12.5 ul DMSO to have 4 mM stock solution (stock solution is in our lab or Dr. Shuler lab)

Exiction/Emmision

- Calcein = 494/517 nm
- Ethidium homodimer-1 in the presence of DNA = 528/617 nm

APPENDIX B

SUPPLEMENTAL FIGURES FROM CHAPTER 4

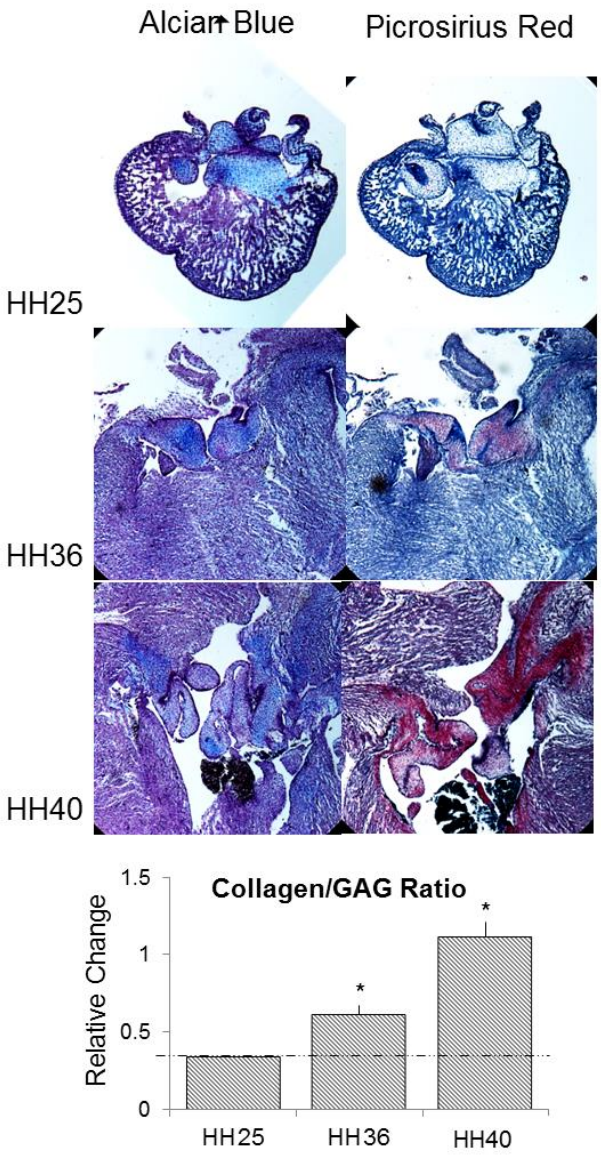

Figure S4.1. Collagen to GAG ratio increases during valve maturation. HH25, HH36, and HH40 hearts were isolated, fixed, and embedded. Serial sections of the left AV left were stained using Picrosirius Red and Alcian blue to identify the relative amounts of collagen and glycosaminoglycans (GAGs), respectively. The relative contributions changed dramatically across the length of the valve, so the entire valve area was considered (dashed contour). Colors were separated using an RGB or CMYK channel splitter.

Black and white thresholds were created in NIH ImageJ and used to determine the volume fractions of each contributor. N ≥ 3, One-way ANOVA w/ Tukey's Post Hoc. P < .05, Asterisks indicate statistical significance.

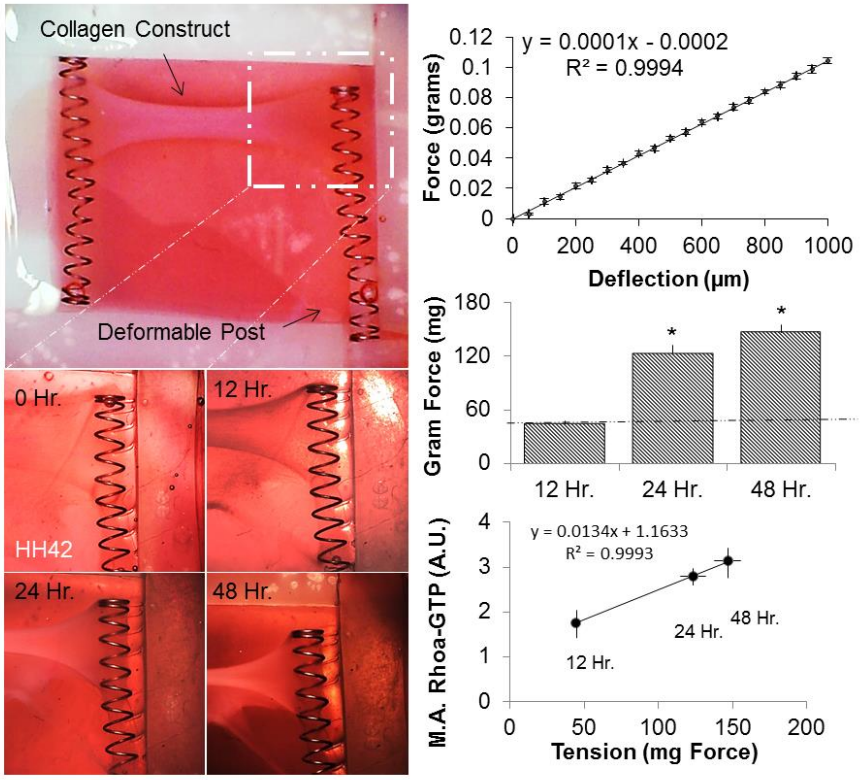

Figure S4.2. Isotropic tension increased within the mechanically anchored collagen construct over time. (A) Collagen construct was seeded within fabricated well, consisting of a rigid compression spring, and a spring attached to a silicon deformable post. As the collagen constructs condenses, the spring attached to the deformable posts bends, producing significant deformation at 12 hr., 24 hr., and 48 hr., after initial compaction. To measure the force exerted by the collagen gel, the silicon posts were calibrated using a weight scale. We then fit a linear curve to the amount of bending deflection (um), to force grams. After, measuring the bending deflection at each time point, we converted to a gram force which was found to increase significantly at each time point. Lastly, we generated a correlative graph between RhoA-GTP activation and tension within the hydrogel. We found a very strong (R2=.99) correlation between RhoA-GTP levels and tension, suggesting a relationship between the two variables. N ≥ 6, One-way ANOVA w/ Tukey's Post Hoc. P < .05, Asterisks indicate statistical significance.

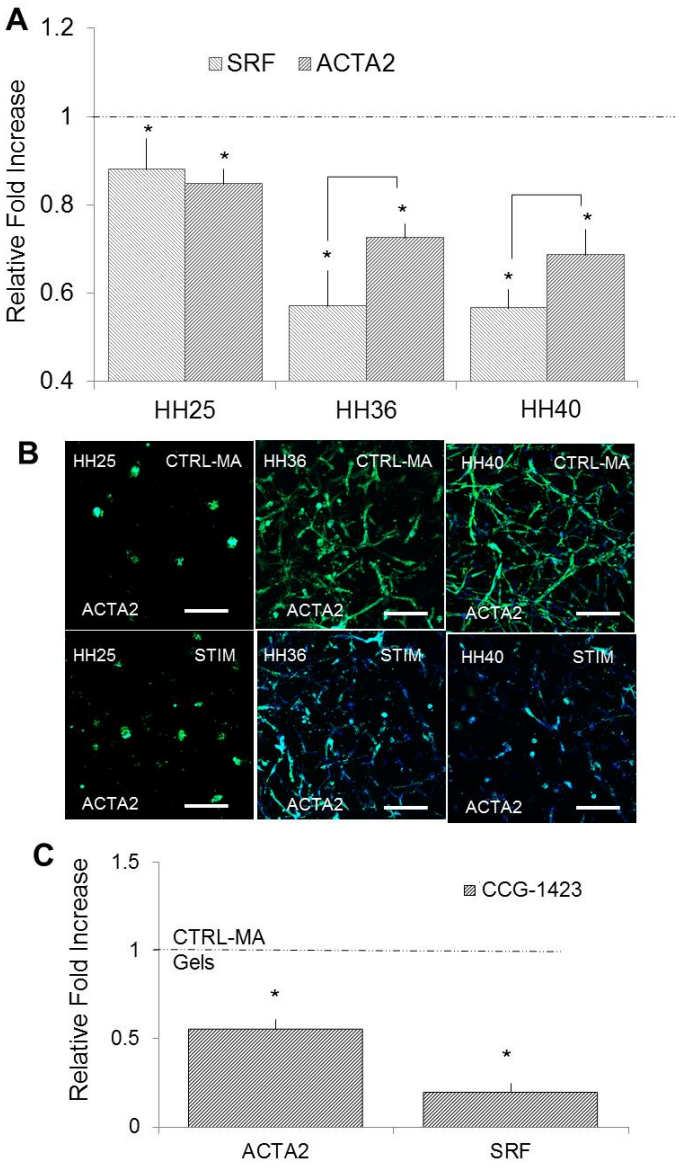

Figure S4.3. Mechanical stretch mitigates myofibroblastic activation in a stage dependent manner. (A) HH25, HH36, and HH40 cells were isolated and seeded into the bioreactor. Cells were allowed to compact for 24hrs. and stimulated at 20% area strain at 2.1hz (average frequency during development) for 48hrs. After mechanical stretch, ACTA2 gene expression significantly decreased as compared to MA gels (HH36 and HH40 was also found significantly decrease compared to HH25). (B) We confirmed ACTA2 expression levels at 48hr. via immuno-fluorescence, and ACTA2 was found significantly decrease in mechanically stretched gels. (C) SRF pathway was inhibited in the CTRL-MA conditions and ACTA2 gene expression was measured at 48 hours. Myofibroblastic activation was inhibited confirming the importance of the SRF pathway. Scale bars represent 100um. $N \geq 6$, One-way ANOVA w/ Tukey's Post Hoc. $P < .05$, Different letters indicate statistical significance

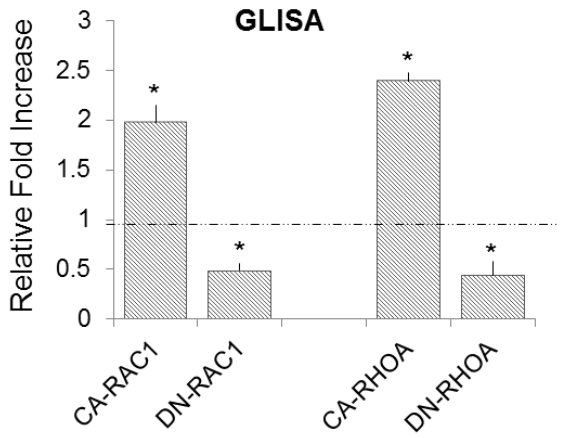

Figure S4.4. Confirmation of RhoA and Rac1 efficiency using GLISA. N ≥ 3, Student t-test. P < .05, Asterisks indicate statistical significance.

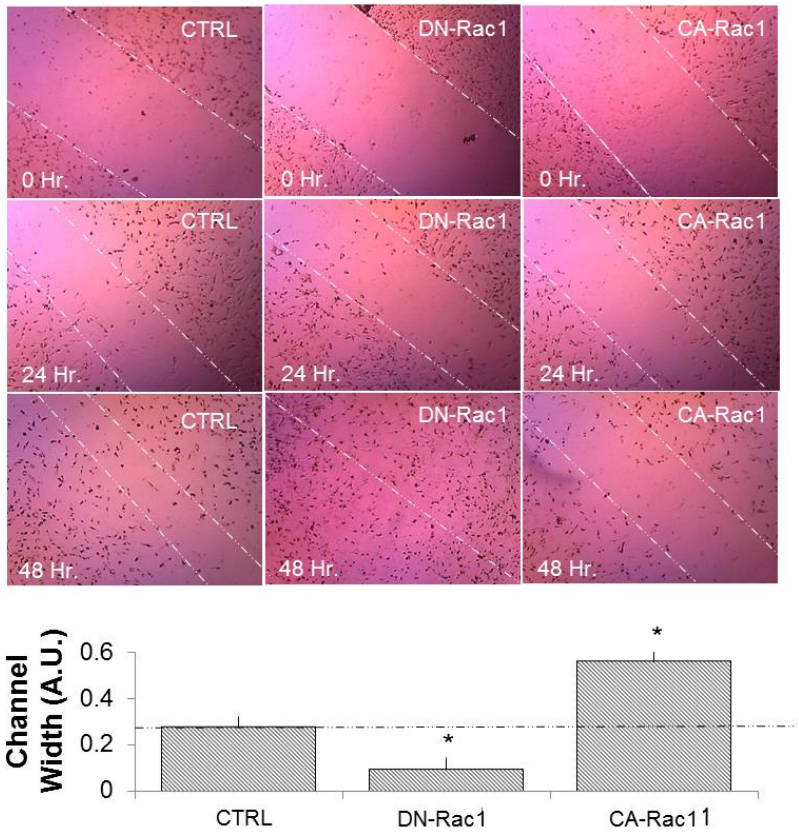

Figure S4.5. Rac1 inhibits migration of HH40 AV cells.. (A) HH40 AV cells were transfected with either CA-Rac1 or DN-Rac1 and seeded onto a tissue culture plastic. At 48 hrs. a scratch was introduced into each well using a 200um pipette tip. Channel width (a.u.) was measured every 24 hours for 2 days. Relative to the initial channel width, DN-Rac1 was found to significantly increase the migration potential, while CA-Rac1 mitigated this effect at 48hrs. N ≥ 6, One-way ANOVA w/ Tukey's Post Hoc. P < .05, Asterisks indicate statistical significance.

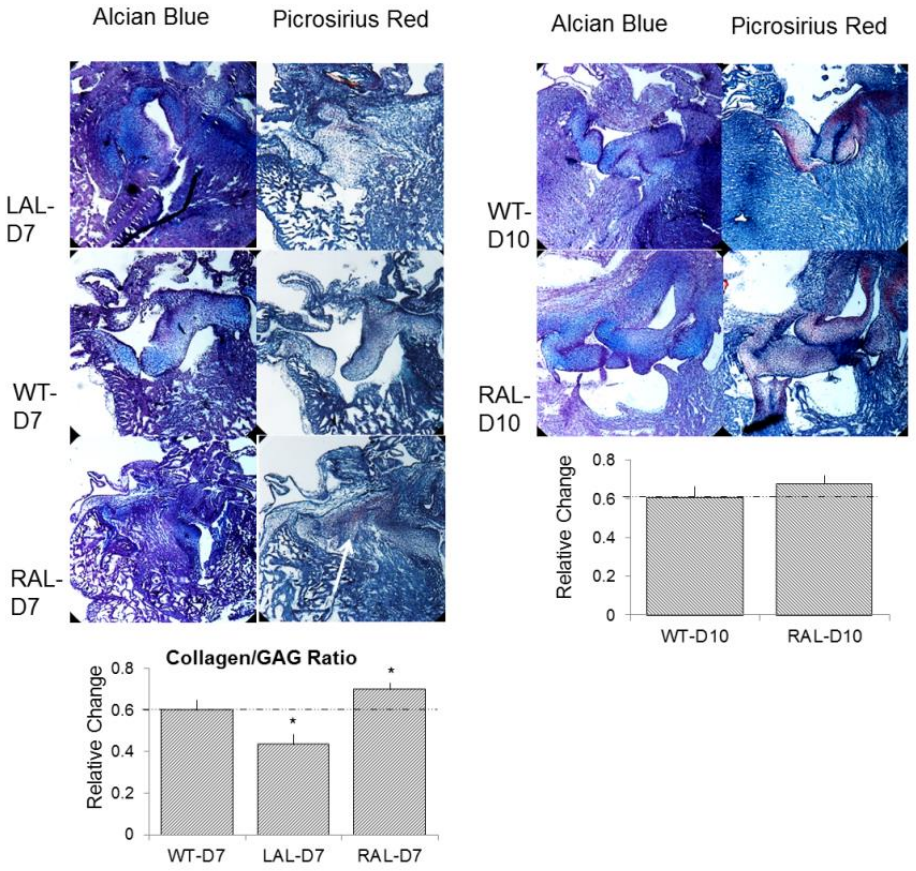

Figure S4.6. In-vivo mechanical load regulates ECM content by increasing the collagen/GAG ratio. Hearts at D7 and D10 were isolated, fixed, and embedded. Serial sections of the left AV left were stained using Picrosirius Red and Alcian blue to identify the relative amounts of collagen and glycosaminoglycans (GAGs), respectively. The relative contributions changed dramatically across the length of the valve, so the entire valve area was considered (dashed contour). Colors were separated using an RGB or CMYK channel splitter. Black and white thresholds were created in NIH ImageJ and used to determine the volume fractions of each contributor. N≥ 4, One-way ANOVA w/ Tukey's Post Hoc. P < .05, Asterisks indicate statistical significance.

Extended Methods.

RT-PCR. RNA extractions were performed using a Qiagen total RNA purification kit (Qiagen, Valencia, CA) and RNA was reverse transcribed to cDNA using the SuperScript III RT-PCR kit with oligo(dT) primer (Invitrogen). Sufficient quality RNA was determined by an absorbance ratio

A260/A280 of 1.8-2.1, while the quantity of RNA was determined by measuring the absorbance at 260nm (A260). Real-time PCR experiments were conducted using the SYBR Green PCR system (Biorad, Hercules, CA) on a Biorad CFX96 cycler, with 40 cycles per sample. Cycling temperatures were as follows: denaturing, 95C; annealing, 60C; and extension, 70C. Primers were normalized to β-actin and 18S rRNA. A list of all primer sequences used in this study is included below.

Gene	Forward 5'-3'	Reverse 5'-3'	Accession
18S	CGGAGAGGGAGCCTGCGAA	CGCCAGCTCGATCCCAAGA	AF173612.1
bactin	ATCACAGGGGTGTGGGTGTT	AATGAGAGGTTCAGGTGCCC	NM_205518.1
ACTA2	CAGTTTTCCCTTCCATCGTG	TGGGGTATTTCAAGGTCAGG	NM_001031229.1
VIM	TCTTAGCAGCAACGCTTTCA	CGACAGGATGTTGACAATGC	NM_001048076.1
Cyclinβ2	AGGGGTGGAGAATGCCGTGA	TGCCAGGTCCTTTCGTAGCCTT	NM_001004369.1
β1 Integrin	TGTTTGTGGGGACCAGATTG	CCAGGTGACACTTCCCATCA	NM_001039254.2
SRF	Purchased From Qiagen Quantitect Gg_SRF_2_SG Catalog No QT01495872		XM_427988

Antibody Staining. Samples were fixed in 4% PFA overnight at 4C. Samples were then washed for 15 minutes on a rocker 3 times with PBS, permeabilized with 0.2\% Triton-X 100 (VWR International, Radnor, PA) for 10 minutes, and washed another 3 times with PBS. Samples were incubated overnight at 4C in a 1% BSA (Rockland Immunochemicals, Inc., Gilbertsville, PA) blocking solution followed by another 4C overnight incubation with either rabbit ACTA2 1:100 (Springer), rabbit SRF 1:100 (Santa Cruz, sc-13029), mouse vimentin 1:100 (Invitrogen, V9), and mouse vinculin (Santa Cruz, sc-73614) 1:100, rabbit RhoA 1:100 (Cell Signaling, 67B9), rabbit Rac1 1:100 (Santa Cruz, sc-217), mouse Rac1-GTP 1:100 (NewEast Bioscience), mouse RhoA-GTP 1:100 (NewEast Bioscience), rabbit phospho-PAK1 1:100 (Cell Signaling, T402), or rabbit beta1 (Abcam, 52971). After 3 washes for 15 minutes with PBS, samples were exposed to Alexa Fluor 488 or 568 conjugated (Invitrogen), species specific secondary antibodies at 1:100 in 1% BSA for 2 hours at room temperature. Three more washes with PBS for 15 minutes were followed by incubation with either DRAQ5 far red nuclear stain (Enzo Life Sciences, Plymouth Meeting, PA) at 1:1000.

FACS. Flow cytometry for ACTA2 1:100 (Abcam) was performed. Briefly, cells were trypsinized, fixed with 4% PFA for 10 min and then preserved in 50% methanol/PBS. Cells were

kept in the -20C until antibody staining was performed. Samples were divided into multiple aliquots in order to stain the proteins separately and compensate for secondary antibody non-specific binding. Cells were incubated for 24 hr at 4 C in primary antibody diluted in either PBS (extracellular) or 0.2% saponin-PBS (intracellular). Cells were then washed 3 times with PBS and incubated with appropriate secondary antibodies and imaged using a Coulter Epics XL-MCL Flow Cytometer (Coulter). All samples were compensated using appropriate background subtraction and all samples were normalized using 10000 cells per flow condition.

In-Vivo Atrial Ligation Experiments. Fertilized White Leghorn chicken eggs were incubated blunt end up in a 38°C forced-draft incubator to Hamburger-Hamilton (HH) stage 21 (3.5 days, Hamburger and Hamilton). The embryo was cultured in an ex-ovo platform previously described. The egg was positioned under a nikon brightfield microscope, and the embryos outer membrane was removed to expose the embryo. The embryo was gently turned to the left side up position, and a slit-like opening was made in its thoracic wall using a pair of fine forceps. An overhand knot of 10–0 nylon suture loop was placed across either the right or left atrium and tightened, partially constricting the left or right atrioventricular orifice respectively. This diverted flow from the constricted inlet towards the untreated inlet, decreasing hemodynamic load on the one side and increasing it on the other. The embryo was then gently flipped to its original right side up position and cultured for an additional 4 days.

Three-dimensional Stereology via Microcomputed Tomography. Microcomputed tomography (micro-CT) analysis was performed according to described protocols (4). Briefly, 50 µm glass microneedles were used to perfuse a polymerizing CT dense contrast agent microfil (Flow-Tech, Carver, MA) at a ratio of 20:75:5 (agent, diluent, and catalyst) through the ventricular apex region of the chicks. Microfil polymerized into a cast within 15 min, after which the entire embryo was fixed in 4% paraformaldehyde. Embryos were typically imaged within 48 hr after fixation via micro-CT (eXplore CT 120, GE Healthcare) at a 25 µm voxel resolution. Datasets were processed using Microview (GE Healthcare) and Osirix (Osirix). Individual cardiac chamber volumes were segmented and quantified as previously described (*1, 2*).

ELISA. Activation of RhoA and Rac1 were also followed using G-LISA activation assay kits from Cytoskeleton according to the manufacturer's instructions with a minor modification. Cell extracts were added to 96-well plate coated with GST fusion of Rho binding domain. After incubation with light shaking at 4°C for 30 minutes, the plate was washed 3 times with washing

buffer (Cytoskeleton) before addition of antigen presenting buffer (Cytoskeleton). The captured GTP-bound Rho GTPases were incubated with their corresponding anti-Rho GTPase antibodies. The GTPase-antibody conjugates were detected with horseradish peroxidase (HRP)–conjugated secondary antibody and quantified using the Epoch spectrophotometer (Biotek) .

Scratch assay. Freshly isolated cells were transfected and seeded into 24 well plates at $50*10^4$ cells/cm^2. After 24 hrs. a scratch through the central axis of the plate was gently made using a pipette tip. Migration of the cells into the scratch was observed at time points of 24 hr. and 48 hr. Subsequent analysis and image processing was done using ImageJ. Initial channel length was measured and used to normalize migration length at subsequent time intervals.

Adhesion Assay. Freshly isolated cells were isolated and transfected and seeded into 24 well plates at $50*10^4$ cells/cm^2. After 24 hours, cells were trypsinized and re-plated onto 4 well tissue culture dishes at $5*10^4$ cells/cm^2. The plates were then exposed to an orbital shaker at 500rpm for 15 seconds at intervals of 30 min up to 120min. A control set of plates with each condition was used to quantify total cells and were not exposed to an orbital shaker. All cells were counterstained using Draq5 and each condition (time interval) was analyzed via ImageJ. Cells exposed to the orbital shaker were normalized to total cells, generating a percentage of adherent cells. Conditions were then compared via ANOVA for statistical significance.

Extent of Cell Alignment and Nascent Focal Complexes. We quantified changes in cell alignment at 24 hrs. via multiphoton microscopy. Hundreds of cell images (CA-Rac1, DN-Rac1, and control conditions) were collected and analyzed. The angle distributions within each cell were determined using f-actin staining as previously described through a fiber alignment index (1 equals not aligned, while 5 equals highly aligned) (*3, 4*). Focal complexes were quantified be measuring the co-localization of vinculin and F-actin along the periphery using metamorph software.

REFERENCES

1. H. C. Yalcin, A. Shekhar, A. A. Rane, J. T. Butcher, An ex-ovo chicken embryo culture system suitable for imaging and microsurgery applications. *J Vis Exp*, (2010).
2. H. C. Yalcin *et al.*, Two-photon microscopy-guided femtosecond-laser photoablation of avian cardiogenesis: noninvasive creation of localized heart defects. *Am J Physiol Heart Circ Physiol* **299**, H1728 (Nov, 2010).
3. R. A. Gould *et al.*, Multi-scale biomechanical remodeling in aging and genetic mutant murine mitral valve leaflets: insights into Marfan syndrome. *PLoS One* **7**, e44639 (2012).
4. J. T. Butcher, A. M. Penrod, A. J. Garcia, R. M. Nerem, Unique morphology and focal adhesion development of valvular endothelial cells in static and fluid flow environments. *Arterioscler Thromb Vasc Biol* **24**, 1429 (Aug, 2004).

APPENDIX C

LDATAFILE

```
function DF=LDataFile(TSTART,TSTOP,Ts,INDEX)
% Machine generated by Universal.

% Load the stoichiometric matrix --
S=load('Network.dat');
[NROWS,NCOLS]=size(S);

% Formulate the rate constant vector k --
k=zeros(NCOLS,1);

% Parameter vector --
k=[
        0.5201765399659437      ;       %       1       EXEXPORT_CYTOSOL + TGFB3_CYTOSOL = EXEXPORT_TGFB3_CYTOSOL
        EXEXPORT_CYTOSOL+TGFB3_CYTOSOL = EXEXPORT_TGFB3_CYTOSOL
        0.08259715142623342     ;       %       2       EXEXPORT_TGFB3_CYTOSOL = EXEXPORT_CYTOSOL + TGFB3_CYTOSOL
        EXEXPORT_TGFB3_CYTOSOL = EXEXPORT_CYTOSOL+TGFB3_CYTOSOL
        0.3383175807457527      ;       %       3       EXEXPORT_TGFB3_CYTOSOL = EXEXPORT_CYTOSOL + TGFB3_EXTRACELLULAR
        EXEXPORT_TGFB3_CYTOSOL = EXEXPORT_CYTOSOL+TGFB3_EXTRACELLULAR
        0.4374046487299713      ;       %       4       EXEXPORT_CYTOSOL + TGFB2_CYTOSOL = EXEXPORT_TGFB2_CYTOSOL
        EXEXPORT_CYTOSOL+TGFB2_CYTOSOL = EXEXPORT_TGFB2_CYTOSOL
        0.0785125247401077      ;       %       5       EXEXPORT_TGFB2_CYTOSOL = EXEXPORT_CYTOSOL + TGFB2_CYTOSOL
        EXEXPORT_TGFB2_CYTOSOL = EXEXPORT_CYTOSOL+TGFB2_CYTOSOL
        0.9864417788655951      ;       %       6       EXEXPORT_TGFB2_CYTOSOL = EXEXPORT_CYTOSOL + TGFB2_EXTRACELLULAR
        EXEXPORT_TGFB2_CYTOSOL = EXEXPORT_CYTOSOL+TGFB2_EXTRACELLULAR
        0.9044308564376912      ;       %       7       DNA_SMURF1_NUCLEAR + RNAP_NUCLEAR = DNA_SMURF1_RNAP_NUCLEAR
        DNA_SMURF1_NUCLEAR+RNAP_NUCLEAR = DNA_SMURF1_RNAP_NUCLEAR
        0.04457378621682241     ;       %       8       DNA_SMURF1_RNAP_NUCLEAR = DNA_SMURF1_NUCLEAR + RNAP_NUCLEAR
        DNA_SMURF1_RNAP_NUCLEAR = DNA_SMURF1_NUCLEAR+RNAP_NUCLEAR
        0.9854681450664591      ;       %       9       DNA_SMURF1_RNAP_NUCLEAR = DNA_SMURF1_NUCLEAR + RNAP_NUCLEAR +
MRNA_SMURF1_NUCLEAR     DNA_SMURF1_RNAP_NUCLEAR = DNA_SMURF1_NUCLEAR+RNAP_NUCLEAR+MRNA_SMURF1_NUCLEAR
        0.17878441863520556     ;       %       10      MRNA_SMURF1_NUCLEAR + NEXPORT_NUCLEAR =
MRNA_SMURF1_NEXPORT_NUCLEAR     MRNA_SMURF1_NUCLEAR+NEXPORT_NUCLEAR = MRNA_SMURF1_NEXPORT_NUCLEAR
        0.03949756944048011     ;       %       11      MRNA_SMURF1_NEXPORT_NUCLEAR = MRNA_SMURF1_NUCLEAR +
NEXPORT_NUCLEAR MRNA_SMURF1_NEXPORT_NUCLEAR = MRNA_SMURF1_NUCLEAR+NEXPORT_NUCLEAR
        0.06913703105616786     ;       %       12      MRNA_SMURF1_NEXPORT_NUCLEAR = MRNA_SMURF1_CYTOSOL +
NEXPORT_NUCLEAR MRNA_SMURF1_NEXPORT_NUCLEAR = MRNA_SMURF1_CYTOSOL+NEXPORT_NUCLEAR
        0.46623710874896274     ;       %       13      MRNA_SMURF1_CYTOSOL + RIBOSOME_CYTOSOL =
MRNA_SMURF1_RIBOSOME_CYTOSOL    MRNA_SMURF1_CYTOSOL+RIBOSOME_CYTOSOL = MRNA_SMURF1_RIBOSOME_CYTOSOL
        0.010722949313692755    ;       %       14      MRNA_SMURF1_RIBOSOME_CYTOSOL = MRNA_SMURF1_CYTOSOL +
RIBOSOME_CYTOSOL        MRNA_SMURF1_RIBOSOME_CYTOSOL = MRNA_SMURF1_CYTOSOL+RIBOSOME_CYTOSOL
        0.3257990411263175      ;       %       15      MRNA_SMURF1_RIBOSOME_CYTOSOL =
MRNA_SMURF1_START_RIBOSOME_CYTOSOL      MRNA_SMURF1_RIBOSOME_CYTOSOL = MRNA_SMURF1_START_RIBOSOME_CYTOSOL
        0.10795192932789754     ;       %       16      MRNA_SMURF1_START_RIBOSOME_CYTOSOL = RIBOSOME_CYTOSOL +
SMURF1_CYTOSOL + MRNA_SMURF1_CYTOSOL    MRNA_SMURF1_START_RIBOSOME_CYTOSOL =
RIBOSOME_CYTOSOL+SMURF1_CYTOSOL+MRNA_SMURF1_CYTOSOL
        0.08729144081002116     ;       %       17      MRNA_SMURF1_CYTOSOL = []        MRNA_SMURF1_CYTOSOL = []
        0.05261779092635993     ;       %       18      SMURF1_CYTOSOL = []     SMURF1_CYTOSOL = []
        0.0026085744121078547   ;       %       19      DNA_SMURF2_NUCLEAR + RNAP_NUCLEAR = DNA_SMURF2_RNAP_NUCLEAR
        DNA_SMURF2_NUCLEAR+RNAP_NUCLEAR = DNA_SMURF2_RNAP_NUCLEAR
        0.7758758897719407      ;       %       20      DNA_SMURF2_RNAP_NUCLEAR = DNA_SMURF2_NUCLEAR + RNAP_NUCLEAR
        DNA_SMURF2_RNAP_NUCLEAR = DNA_SMURF2_NUCLEAR+RNAP_NUCLEAR
        0.7413921306133238      ;       %       21      DNA_SMURF2_RNAP_NUCLEAR = DNA_SMURF2_NUCLEAR + RNAP_NUCLEAR +
MRNA_SMURF2_NUCLEAR     DNA_SMURF2_RNAP_NUCLEAR = DNA_SMURF2_NUCLEAR+RNAP_NUCLEAR+MRNA_SMURF2_NUCLEAR
        0.5823680389491563      ;       %       22      MRNA_SMURF2_NUCLEAR + NEXPORT_NUCLEAR =
MRNA_SMURF2_NEXPORT_NUCLEAR     MRNA_SMURF2_NUCLEAR+NEXPORT_NUCLEAR = MRNA_SMURF2_NEXPORT_NUCLEAR
        0.01805033511707348     ;       %       23      MRNA_SMURF2_NEXPORT_NUCLEAR = MRNA_SMURF2_NUCLEAR +
NEXPORT_NUCLEAR MRNA_SMURF2_NEXPORT_NUCLEAR = MRNA_SMURF2_NUCLEAR+NEXPORT_NUCLEAR
        0.12038690090260429     ;       %       24      MRNA_SMURF2_NEXPORT_NUCLEAR = MRNA_SMURF2_CYTOSOL +
NEXPORT_NUCLEAR MRNA_SMURF2_NEXPORT_NUCLEAR = MRNA_SMURF2_CYTOSOL+NEXPORT_NUCLEAR
        0.3942156686103949      ;       %       25      MRNA_SMURF2_CYTOSOL + RIBOSOME_CYTOSOL =
MRNA_SMURF2_RIBOSOME_CYTOSOL    MRNA_SMURF2_CYTOSOL+RIBOSOME_CYTOSOL = MRNA_SMURF2_RIBOSOME_CYTOSOL
        0.09155943143875152     ;       %       26      MRNA_SMURF2_RIBOSOME_CYTOSOL = MRNA_SMURF2_CYTOSOL +
RIBOSOME_CYTOSOL        MRNA_SMURF2_RIBOSOME_CYTOSOL = MRNA_SMURF2_CYTOSOL+RIBOSOME_CYTOSOL
        0.2210759746367258      ;       %       27      MRNA_SMURF2_RIBOSOME_CYTOSOL =
MRNA_SMURF2_START_RIBOSOME_CYTOSOL      MRNA_SMURF2_RIBOSOME_CYTOSOL = MRNA_SMURF2_START_RIBOSOME_CYTOSOL
        0.9697132759997918      ;       %       28      MRNA_SMURF2_START_RIBOSOME_CYTOSOL = RIBOSOME_CYTOSOL +
SMURF2_CYTOSOL + MRNA_SMURF2_CYTOSOL    MRNA_SMURF2_START_RIBOSOME_CYTOSOL =
RIBOSOME_CYTOSOL+SMURF2_CYTOSOL+MRNA_SMURF2_CYTOSOL
        0.02905293365148076     ;       %       29      MRNA_SMURF2_CYTOSOL = []        MRNA_SMURF2_CYTOSOL = []
        0.059200472491522604    ;       %       30      SMURF2_CYTOSOL = []     SMURF2_CYTOSOL = []
        0.90889829530306456     ;       %       31      DNA_SMAD1_NUCLEAR + RNAP_NUCLEAR = DNA_SMAD1_RNAP_NUCLEAR
        DNA_SMAD1_NUCLEAR+RNAP_NUCLEAR = DNA_SMAD1_RNAP_NUCLEAR
        0.047263836564669495    ;       %       32      DNA_SMAD1_RNAP_NUCLEAR = DNA_SMAD1_NUCLEAR + RNAP_NUCLEAR
        DNA_SMAD1_RNAP_NUCLEAR = DNA_SMAD1_NUCLEAR+RNAP_NUCLEAR
        0.3730313009057662      ;       %       33      DNA_SMAD1_RNAP_NUCLEAR = DNA_SMAD1_NUCLEAR + RNAP_NUCLEAR +
MRNA_SMAD1_NUCLEAR      DNA_SMAD1_RNAP_NUCLEAR = DNA_SMAD1_NUCLEAR+RNAP_NUCLEAR+MRNA_SMAD1_NUCLEAR
        0.18851918962290348     ;       %       34      MRNA_SMAD1_NUCLEAR + NEXPORT_NUCLEAR =
MRNA_SMAD1_NEXPORT_NUCLEAR      MRNA_SMAD1_NUCLEAR+NEXPORT_NUCLEAR = MRNA_SMAD1_NEXPORT_NUCLEAR
        0.028697769420319277    ;       %       35      MRNA_SMAD1_NEXPORT_NUCLEAR = MRNA_SMAD1_NUCLEAR +
NEXPORT_NUCLEAR MRNA_SMAD1_NEXPORT_NUCLEAR = MRNA_SMAD1_NUCLEAR+NEXPORT_NUCLEAR
```

0.6929672623408051 ; % 36 MRNA_SMAD1_NEXPORT_NUCLEAR = MRNA_SMAD1_CYTOSOL + NEXPORT_NUCLEAR MRNA_SMAD1_NEXPORT_NUCLEAR = MRNA_SMAD1_CYTOSOL+NEXPORT_NUCLEAR
0.3848574589775263 ; % 37 MRNA_SMAD1_CYTOSOL + RIBOSOME_CYTOSOL = MRNA_SMAD1_RIBOSOME_CYTOSOL MRNA_SMAD1_CYTOSOL+RIBOSOME_CYTOSOL = MRNA_SMAD1_RIBOSOME_CYTOSOL
0.05086799912991296 ; % 38 MRNA_SMAD1_RIBOSOME_CYTOSOL = MRNA_SMAD1_CYTOSOL + RIBOSOME_CYTOSOL MRNA_SMAD1_RIBOSOME_CYTOSOL = MRNA_SMAD1_CYTOSOL+RIBOSOME_CYTOSOL
0.3641523397132931 ; % 39 MRNA_SMAD1_RIBOSOME_CYTOSOL = MRNA_SMAD1_START_RIBOSOME_CYTOSOL MRNA_SMAD1_RIBOSOME_CYTOSOL = MRNA_SMAD1_START_RIBOSOME_CYTOSOL
0.5222354221734035 ; % 40 MRNA_SMAD1_START_RIBOSOME_CYTOSOL = RIBOSOME_CYTOSOL + SMAD1_CYTOSOL + MRNA_SMAD1_CYTOSOL MRNA_SMAD1_START_RIBOSOME_CYTOSOL = RIBOSOME_CYTOSOL+SMAD1_CYTOSOL+MRNA_SMAD1_CYTOSOL
0.1757259455531941 ; % 41 MRNA_SMAD1_CYTOSOL = [] MRNA_SMAD1_CYTOSOL = []
0.027350417929296378 ; % 42 SMAD1_CYTOSOL = [] SMAD1_CYTOSOL = []
0.9041212052161975 ; % 43 DNA_SMAD2_NUCLEAR + RNAP_NUCLEAR = DNA_SMAD2_RNAP_NUCLEAR DNA_SMAD2_NUCLEAR+RNAP_NUCLEAR = DNA_SMAD2_RNAP_NUCLEAR
0.03822475396948191 ; % 44 DNA_SMAD2_RNAP_NUCLEAR = DNA_SMAD2_NUCLEAR + RNAP_NUCLEAR DNA_SMAD2_RNAP_NUCLEAR = DNA_SMAD2_NUCLEAR+RNAP_NUCLEAR
0.44629345187005465 ; % 45 DNA_SMAD2_RNAP_NUCLEAR = DNA_SMAD2_NUCLEAR + RNAP_NUCLEAR + MRNA_SMAD2_NUCLEAR DNA_SMAD2_RNAP_NUCLEAR = DNA_SMAD2_NUCLEAR+RNAP_NUCLEAR+MRNA_SMAD2_NUCLEAR
0.4513403620669495 ; % 46 MRNA_SMAD2_NUCLEAR + NEXPORT_NUCLEAR = MRNA_SMAD2_NEXPORT_NUCLEAR MRNA_SMAD2_NUCLEAR+NEXPORT_NUCLEAR = MRNA_SMAD2_NEXPORT_NUCLEAR
0.07157408191243762 ; % 47 MRNA_SMAD2_NEXPORT_NUCLEAR = MRNA_SMAD2_NUCLEAR + NEXPORT_NUCLEAR MRNA_SMAD2_NEXPORT_NUCLEAR = MRNA_SMAD2_NUCLEAR+NEXPORT_NUCLEAR
0.8032926823377786 ; % 48 MRNA_SMAD2_NEXPORT_NUCLEAR = MRNA_SMAD2_CYTOSOL + NEXPORT_NUCLEAR MRNA_SMAD2_NEXPORT_NUCLEAR = MRNA_SMAD2_CYTOSOL+NEXPORT_NUCLEAR
0.1390346908996929 ; % 49 MRNA_SMAD2_CYTOSOL + RIBOSOME_CYTOSOL = MRNA_SMAD2_RIBOSOME_CYTOSOL MRNA_SMAD2_CYTOSOL+RIBOSOME_CYTOSOL = MRNA_SMAD2_RIBOSOME_CYTOSOL
0.010873960569937348 ; % 50 MRNA_SMAD2_RIBOSOME_CYTOSOL = MRNA_SMAD2_CYTOSOL + RIBOSOME_CYTOSOL MRNA_SMAD2_RIBOSOME_CYTOSOL = MRNA_SMAD2_CYTOSOL+RIBOSOME_CYTOSOL
0.10616696808269332 ; % 51 MRNA_SMAD2_RIBOSOME_CYTOSOL = MRNA_SMAD2_START_RIBOSOME_CYTOSOL MRNA_SMAD2_RIBOSOME_CYTOSOL = MRNA_SMAD2_START_RIBOSOME_CYTOSOL
0.9843890522927627 ; % 52 MRNA_SMAD2_START_RIBOSOME_CYTOSOL = RIBOSOME_CYTOSOL + SMAD2_CYTOSOL + MRNA_SMAD2_CYTOSOL MRNA_SMAD2_START_RIBOSOME_CYTOSOL = RIBOSOME_CYTOSOL+SMAD2_CYTOSOL+MRNA_SMAD2_CYTOSOL
0.34289372071924584 ; % 53 MRNA_SMAD2_CYTOSOL = [] MRNA_SMAD2_CYTOSOL = []
0.3854504902821078 ; % 54 SMAD2_CYTOSOL = [] SMAD2_CYTOSOL = []
0.914865152695174078 ; % 55 DNA_SMAD3_NUCLEAR + RNAP_NUCLEAR = DNA_SMAD3_RNAP_NUCLEAR DNA_SMAD3_NUCLEAR+RNAP_NUCLEAR = DNA_SMAD3_RNAP_NUCLEAR
0.008686705548544708 ; % 56 DNA_SMAD3_RNAP_NUCLEAR = DNA_SMAD3_NUCLEAR + RNAP_NUCLEAR DNA_SMAD3_RNAP_NUCLEAR = DNA_SMAD3_NUCLEAR+RNAP_NUCLEAR
0.47147151497316553 ; % 57 DNA_SMAD3_RNAP_NUCLEAR = DNA_SMAD3_NUCLEAR + RNAP_NUCLEAR + MRNA_SMAD3_NUCLEAR DNA_SMAD3_RNAP_NUCLEAR = DNA_SMAD3_NUCLEAR+RNAP_NUCLEAR+MRNA_SMAD3_NUCLEAR
0.8125392997761574 ; % 58 MRNA_SMAD3_NUCLEAR + NEXPORT_NUCLEAR = MRNA_SMAD3_NEXPORT_NUCLEAR MRNA_SMAD3_NUCLEAR+NEXPORT_NUCLEAR = MRNA_SMAD3_NEXPORT_NUCLEAR
0.05592088462837061 ; % 59 MRNA_SMAD3_NEXPORT_NUCLEAR = MRNA_SMAD3_NUCLEAR + NEXPORT_NUCLEAR MRNA_SMAD3_NEXPORT_NUCLEAR = MRNA_SMAD3_NUCLEAR+NEXPORT_NUCLEAR
0.10003411121437822 ; % 60 MRNA_SMAD3_NEXPORT_NUCLEAR = MRNA_SMAD3_CYTOSOL + NEXPORT_NUCLEAR MRNA_SMAD3_NEXPORT_NUCLEAR = MRNA_SMAD3_CYTOSOL+NEXPORT_NUCLEAR
0.9123869868761132 ; % 61 MRNA_SMAD3_CYTOSOL + RIBOSOME_CYTOSOL = MRNA_SMAD3_RIBOSOME_CYTOSOL MRNA_SMAD3_CYTOSOL+RIBOSOME_CYTOSOL = MRNA_SMAD3_RIBOSOME_CYTOSOL
0.05317720099206461 ; % 62 MRNA_SMAD3_RIBOSOME_CYTOSOL = MRNA_SMAD3_CYTOSOL + RIBOSOME_CYTOSOL MRNA_SMAD3_RIBOSOME_CYTOSOL = MRNA_SMAD3_CYTOSOL+RIBOSOME_CYTOSOL
0.6913295756938763 ; % 63 MRNA_SMAD3_RIBOSOME_CYTOSOL = MRNA_SMAD3_START_RIBOSOME_CYTOSOL MRNA_SMAD3_RIBOSOME_CYTOSOL = MRNA_SMAD3_START_RIBOSOME_CYTOSOL
0.4664249516408243 ; % 64 MRNA_SMAD3_START_RIBOSOME_CYTOSOL = RIBOSOME_CYTOSOL + SMAD3_CYTOSOL + MRNA_SMAD3_CYTOSOL MRNA_SMAD3_START_RIBOSOME_CYTOSOL = RIBOSOME_CYTOSOL+SMAD3_CYTOSOL+MRNA_SMAD3_CYTOSOL
0.12462045242650488 ; % 65 MRNA_SMAD3_CYTOSOL = [] MRNA_SMAD3_CYTOSOL = []
0.25174914469340764 ; % 66 SMAD3_CYTOSOL = [] SMAD3_CYTOSOL = []
0.9910788552173622 ; % 67 DNA_SMAD4_NUCLEAR + RNAP_NUCLEAR = DNA_SMAD4_RNAP_NUCLEAR DNA_SMAD4_NUCLEAR+RNAP_NUCLEAR = DNA_SMAD4_RNAP_NUCLEAR
0.008064508441874563 ; % 68 DNA_SMAD4_RNAP_NUCLEAR = DNA_SMAD4_NUCLEAR + RNAP_NUCLEAR DNA_SMAD4_RNAP_NUCLEAR = DNA_SMAD4_NUCLEAR+RNAP_NUCLEAR
0.8391790107174769 ; % 69 DNA_SMAD4_RNAP_NUCLEAR = DNA_SMAD4_NUCLEAR + RNAP_NUCLEAR + MRNA_SMAD4_NUCLEAR DNA_SMAD4_RNAP_NUCLEAR = DNA_SMAD4_NUCLEAR+RNAP_NUCLEAR+MRNA_SMAD4_NUCLEAR
0.7819499123822488 ; % 70 MRNA_SMAD4_NUCLEAR + NEXPORT_NUCLEAR = MRNA_SMAD4_NEXPORT_NUCLEAR MRNA_SMAD4_NUCLEAR+NEXPORT_NUCLEAR = MRNA_SMAD4_NEXPORT_NUCLEAR
0.09014065569063816 ; % 71 MRNA_SMAD4_NEXPORT_NUCLEAR = MRNA_SMAD4_NUCLEAR + NEXPORT_NUCLEAR MRNA_SMAD4_NEXPORT_NUCLEAR = MRNA_SMAD4_NUCLEAR+NEXPORT_NUCLEAR
0.6013277866184339 ; % 72 MRNA_SMAD4_NEXPORT_NUCLEAR = MRNA_SMAD4_CYTOSOL + NEXPORT_NUCLEAR MRNA_SMAD4_NEXPORT_NUCLEAR = MRNA_SMAD4_CYTOSOL+NEXPORT_NUCLEAR
0.48994453138996064 ; % 73 MRNA_SMAD4_CYTOSOL + RIBOSOME_CYTOSOL = MRNA_SMAD4_RIBOSOME_CYTOSOL MRNA_SMAD4_CYTOSOL+RIBOSOME_CYTOSOL = MRNA_SMAD4_RIBOSOME_CYTOSOL
0.03707791628521362 ; % 74 MRNA_SMAD4_RIBOSOME_CYTOSOL = MRNA_SMAD4_CYTOSOL + RIBOSOME_CYTOSOL MRNA_SMAD4_RIBOSOME_CYTOSOL = MRNA_SMAD4_CYTOSOL+RIBOSOME_CYTOSOL
0.950156194331962 ; % 75 MRNA_SMAD4_RIBOSOME_CYTOSOL = MRNA_SMAD4_START_RIBOSOME_CYTOSOL MRNA_SMAD4_RIBOSOME_CYTOSOL = MRNA_SMAD4_START_RIBOSOME_CYTOSOL
0.25472827492419114 ; % 76 MRNA_SMAD4_START_RIBOSOME_CYTOSOL = RIBOSOME_CYTOSOL + SMAD4_CYTOSOL + MRNA_SMAD4_CYTOSOL MRNA_SMAD4_START_RIBOSOME_CYTOSOL = RIBOSOME_CYTOSOL+SMAD4_CYTOSOL+MRNA_SMAD4_CYTOSOL
0.4850524206985869 ; % 77 MRNA_SMAD4_CYTOSOL = [] MRNA_SMAD4_CYTOSOL = []
0.4575910513624255 ; % 78 SMAD4_CYTOSOL = [] SMAD4_CYTOSOL = []
0.6962224032949356 ; % 79 DNA_SMAD5_NUCLEAR + RNAP_NUCLEAR = DNA_SMAD5_RNAP_NUCLEAR DNA_SMAD5_NUCLEAR+RNAP_NUCLEAR = DNA_SMAD5_RNAP_NUCLEAR
0.02822397745420642 ; % 80 DNA_SMAD5_RNAP_NUCLEAR = DNA_SMAD5_NUCLEAR + RNAP_NUCLEAR DNA_SMAD5_RNAP_NUCLEAR = DNA_SMAD5_NUCLEAR+RNAP_NUCLEAR
0.07635875719358298 ; % 81 DNA_SMAD5_RNAP_NUCLEAR = DNA_SMAD5_NUCLEAR + RNAP_NUCLEAR + MRNA_SMAD5_NUCLEAR DNA_SMAD5_RNAP_NUCLEAR = DNA_SMAD5_NUCLEAR+RNAP_NUCLEAR+MRNA_SMAD5_NUCLEAR
0.012938441340032969 ; % 82 MRNA_SMAD5_NUCLEAR + NEXPORT_NUCLEAR = MRNA_SMAD5_NEXPORT_NUCLEAR MRNA_SMAD5_NUCLEAR+NEXPORT_NUCLEAR = MRNA_SMAD5_NEXPORT_NUCLEAR
0.008821196161891488 ; % 83 MRNA_SMAD5_NEXPORT_NUCLEAR = MRNA_SMAD5_NUCLEAR + NEXPORT_NUCLEAR MRNA_SMAD5_NEXPORT_NUCLEAR = MRNA_SMAD5_NUCLEAR+NEXPORT_NUCLEAR

0.709050526371447 ; % 84 MRNA_SMAD5_NEXPORT_NUCLEAR = MRNA_SMAD5_CYTOSOL + NEXPORT_NUCLEAR MRNA_SMAD5_NEXPORT_NUCLEAR = MRNA_SMAD5_CYTOSOL+NEXPORT_NUCLEAR
0.5422561944543943 ; % 85 MRNA_SMAD5_CYTOSOL + RIBOSOME_CYTOSOL = MRNA_SMAD5_RIBOSOME_CYTOSOL MRNA_SMAD5_CYTOSOL+RIBOSOME_CYTOSOL = MRNA_SMAD5_RIBOSOME_CYTOSOL
0.08898818046594906 ; % 86 MRNA_SMAD5_RIBOSOME_CYTOSOL = MRNA_SMAD5_CYTOSOL + RIBOSOME_CYTOSOL MRNA_SMAD5_RIBOSOME_CYTOSOL = MRNA_SMAD5_CYTOSOL+RIBOSOME_CYTOSOL
0.4301939312988523 ; % 87 MRNA_SMAD5_RIBOSOME_CYTOSOL = MRNA_SMAD5_START_RIBOSOME_CYTOSOL MRNA_SMAD5_RIBOSOME_CYTOSOL = MRNA_SMAD5_START_RIBOSOME_CYTOSOL
0.006116266289741157 ; % 88 MRNA_SMAD5_START_RIBOSOME_CYTOSOL = RIBOSOME_CYTOSOL + SMAD5_CYTOSOL + MRNA_SMAD5_CYTOSOL MRNA_SMAD5_START_RIBOSOME_CYTOSOL = RIBOSOME_CYTOSOL+SMAD5_CYTOSOL+MRNA_SMAD5_CYTOSOL
0.31611646239580793 ; % 89 MRNA_SMAD5_CYTOSOL = [] MRNA_SMAD5_CYTOSOL = []
0.2200985768385944 ; % 90 SMAD5_CYTOSOL = [] SMAD5_CYTOSOL = []
0.02118208936560032 ; % 91 DNA_SMAD6_NUCLEAR + RNAP_NUCLEAR = DNA_SMAD6_RNAP_NUCLEAR DNA_SMAD6_NUCLEAR+RNAP_NUCLEAR = DNA_SMAD6_RNAP_NUCLEAR
0.0300629815807156 ; % 92 DNA_SMAD6_RNAP_NUCLEAR = DNA_SMAD6_NUCLEAR + RNAP_NUCLEAR DNA_SMAD6_RNAP_NUCLEAR = DNA_SMAD6_NUCLEAR+RNAP_NUCLEAR
0.4806835110109028 ; % 93 DNA_SMAD6_RNAP_NUCLEAR = DNA_SMAD6_NUCLEAR + RNAP_NUCLEAR + MRNA_SMAD6_NUCLEAR DNA_SMAD6_RNAP_NUCLEAR = DNA_SMAD6_NUCLEAR+RNAP_NUCLEAR+MRNA_SMAD6_NUCLEAR
0.793074870186985 ; % 94 MRNA_SMAD6_NUCLEAR + NEXPORT_NUCLEAR = MRNA_SMAD6_NEXPORT_NUCLEAR MRNA_SMAD6_NUCLEAR+NEXPORT_NUCLEAR = MRNA_SMAD6_NEXPORT_NUCLEAR
0.06790478627548091 ; % 95 MRNA_SMAD6_NEXPORT_NUCLEAR = MRNA_SMAD6_NUCLEAR + NEXPORT_NUCLEAR MRNA_SMAD6_NEXPORT_NUCLEAR = MRNA_SMAD6_NUCLEAR+NEXPORT_NUCLEAR
0.2794276654358169 ; % 96 MRNA_SMAD6_NEXPORT_NUCLEAR = MRNA_SMAD6_CYTOSOL + NEXPORT_NUCLEAR MRNA_SMAD6_NEXPORT_NUCLEAR = MRNA_SMAD6_CYTOSOL+NEXPORT_NUCLEAR
0.10786537377208982 ; % 97 MRNA_SMAD6_CYTOSOL + RIBOSOME_CYTOSOL = MRNA_SMAD6_RIBOSOME_CYTOSOL MRNA_SMAD6_CYTOSOL+RIBOSOME_CYTOSOL = MRNA_SMAD6_RIBOSOME_CYTOSOL
0.06346339723634625 ; % 98 MRNA_SMAD6_RIBOSOME_CYTOSOL = MRNA_SMAD6_CYTOSOL + RIBOSOME_CYTOSOL MRNA_SMAD6_RIBOSOME_CYTOSOL = MRNA_SMAD6_CYTOSOL+RIBOSOME_CYTOSOL
0.1968710012795719 ; % 99 MRNA_SMAD6_RIBOSOME_CYTOSOL = MRNA_SMAD6_START_RIBOSOME_CYTOSOL MRNA_SMAD6_RIBOSOME_CYTOSOL = MRNA_SMAD6_START_RIBOSOME_CYTOSOL
0.8252809333373334 ; % 100 MRNA_SMAD6_START_RIBOSOME_CYTOSOL = RIBOSOME_CYTOSOL + SMAD6_CYTOSOL + MRNA_SMAD6_CYTOSOL MRNA_SMAD6_START_RIBOSOME_CYTOSOL = RIBOSOME_CYTOSOL+SMAD6_CYTOSOL+MRNA_SMAD6_CYTOSOL
0.2863738069696536 ; % 101 MRNA_SMAD6_CYTOSOL = [] MRNA_SMAD6_CYTOSOL = []
0.2438297232078887 ; % 102 SMAD6_CYTOSOL = [] SMAD6_CYTOSOL = []
0.018695377267448043 ; % 103 DNA_SMAD7_NUCLEAR + RNAP_NUCLEAR = DNA_SMAD7_RNAP_NUCLEAR DNA_SMAD7_NUCLEAR+RNAP_NUCLEAR = DNA_SMAD7_RNAP_NUCLEAR
0.07277758852471339 ; % 104 DNA_SMAD7_RNAP_NUCLEAR = DNA_SMAD7_NUCLEAR + RNAP_NUCLEAR DNA_SMAD7_RNAP_NUCLEAR = DNA_SMAD7_NUCLEAR+RNAP_NUCLEAR
0.9074885664202607 ; % 105 DNA_SMAD7_RNAP_NUCLEAR = DNA_SMAD7_NUCLEAR + RNAP_NUCLEAR + MRNA_SMAD7_NUCLEAR DNA_SMAD7_RNAP_NUCLEAR = DNA_SMAD7_NUCLEAR+RNAP_NUCLEAR+MRNA_SMAD7_NUCLEAR
0.03158187167159987 ; % 106 MRNA_SMAD7_NUCLEAR + NEXPORT_NUCLEAR = MRNA_SMAD7_NEXPORT_NUCLEAR MRNA_SMAD7_NUCLEAR+NEXPORT_NUCLEAR = MRNA_SMAD7_NEXPORT_NUCLEAR
0.031070285385804076 ; % 107 MRNA_SMAD7_NEXPORT_NUCLEAR = MRNA_SMAD7_NUCLEAR + NEXPORT_NUCLEAR MRNA_SMAD7_NEXPORT_NUCLEAR = MRNA_SMAD7_NUCLEAR+NEXPORT_NUCLEAR
0.5184976500489137 ; % 108 MRNA_SMAD7_NEXPORT_NUCLEAR = MRNA_SMAD7_CYTOSOL + NEXPORT_NUCLEAR MRNA_SMAD7_NEXPORT_NUCLEAR = MRNA_SMAD7_CYTOSOL+NEXPORT_NUCLEAR
0.31904601839283064 ; % 109 MRNA_SMAD7_CYTOSOL + RIBOSOME_CYTOSOL = MRNA_SMAD7_RIBOSOME_CYTOSOL MRNA_SMAD7_CYTOSOL+RIBOSOME_CYTOSOL = MRNA_SMAD7_RIBOSOME_CYTOSOL
0.033125994432657034 ; % 110 MRNA_SMAD7_RIBOSOME_CYTOSOL = MRNA_SMAD7_CYTOSOL + RIBOSOME_CYTOSOL MRNA_SMAD7_RIBOSOME_CYTOSOL = MRNA_SMAD7_CYTOSOL+RIBOSOME_CYTOSOL
0.6123023288133863 ; % 111 MRNA_SMAD7_RIBOSOME_CYTOSOL = MRNA_SMAD7_START_RIBOSOME_CYTOSOL MRNA_SMAD7_RIBOSOME_CYTOSOL = MRNA_SMAD7_START_RIBOSOME_CYTOSOL
0.594487459601517 ; % 112 MRNA_SMAD7_START_RIBOSOME_CYTOSOL = RIBOSOME_CYTOSOL + SMAD7_CYTOSOL + MRNA_SMAD7_CYTOSOL MRNA_SMAD7_START_RIBOSOME_CYTOSOL = RIBOSOME_CYTOSOL+SMAD7_CYTOSOL+MRNA_SMAD7_CYTOSOL
0.32024730784036487 ; % 113 MRNA_SMAD7_CYTOSOL = [] MRNA_SMAD7_CYTOSOL = []
0.26775482993514105 ; % 114 SMAD7_CYTOSOL = [] SMAD7_CYTOSOL = []
0.5364092853877909 ; % 115 DNA_ENDOGLIN_NUCLEAR + RNAP_NUCLEAR = DNA_ENDOGLIN_RNAP_NUCLEAR DNA_ENDOGLIN_NUCLEAR+RNAP_NUCLEAR = DNA_ENDOGLIN_RNAP_NUCLEAR
0.03144525856077001 ; % 116 DNA_ENDOGLIN_RNAP_NUCLEAR = DNA_ENDOGLIN_NUCLEAR + RNAP_NUCLEAR DNA_ENDOGLIN_RNAP_NUCLEAR = DNA_ENDOGLIN_NUCLEAR+RNAP_NUCLEAR
0.16794541590701806 ; % 117 DNA_ENDOGLIN_RNAP_NUCLEAR = DNA_ENDOGLIN_NUCLEAR + RNAP_NUCLEAR + MRNA_ENDOGLIN_NUCLEAR DNA_ENDOGLIN_RNAP_NUCLEAR = DNA_ENDOGLIN_NUCLEAR+RNAP_NUCLEAR+MRNA_ENDOGLIN_NUCLEAR
0.20495643986700485 ; % 118 MRNA_ENDOGLIN_NUCLEAR + NEXPORT_NUCLEAR = MRNA_ENDOGLIN_NEXPORT_NUCLEAR MRNA_ENDOGLIN_NUCLEAR+NEXPORT_NUCLEAR = MRNA_ENDOGLIN_NEXPORT_NUCLEAR
0.009165947890536541 ; % 119 MRNA_ENDOGLIN_NEXPORT_NUCLEAR = MRNA_ENDOGLIN_NUCLEAR + NEXPORT_NUCLEAR MRNA_ENDOGLIN_NEXPORT_NUCLEAR = MRNA_ENDOGLIN_NUCLEAR+NEXPORT_NUCLEAR
0.6789653704657468 ; % 120 MRNA_ENDOGLIN_NEXPORT_NUCLEAR = MRNA_ENDOGLIN_CYTOSOL + NEXPORT_NUCLEAR MRNA_ENDOGLIN_NEXPORT_NUCLEAR = MRNA_ENDOGLIN_CYTOSOL+NEXPORT_NUCLEAR
0.8285323341864742 ; % 121 MRNA_ENDOGLIN_CYTOSOL + RIBOSOME_CYTOSOL = MRNA_ENDOGLIN_RIBOSOME_CYTOSOL MRNA_ENDOGLIN_CYTOSOL+RIBOSOME_CYTOSOL = MRNA_ENDOGLIN_RIBOSOME_CYTOSOL
0.0933669607223379 ; % 122 MRNA_ENDOGLIN_RIBOSOME_CYTOSOL = MRNA_ENDOGLIN_CYTOSOL + RIBOSOME_CYTOSOL MRNA_ENDOGLIN_RIBOSOME_CYTOSOL = MRNA_ENDOGLIN_CYTOSOL+RIBOSOME_CYTOSOL
0.9438271934274336 ; % 123 MRNA_ENDOGLIN_RIBOSOME_CYTOSOL = MRNA_ENDOGLIN_START_RIBOSOME_CYTOSOL MRNA_ENDOGLIN_RIBOSOME_CYTOSOL = MRNA_ENDOGLIN_START_RIBOSOME_CYTOSOL
0.5388958714570403 ; % 124 MRNA_ENDOGLIN_START_RIBOSOME_CYTOSOL = RIBOSOME_CYTOSOL + ENDOGLIN_CYTOSOL + MRNA_ENDOGLIN_CYTOSOL MRNA_ENDOGLIN_START_RIBOSOME_CYTOSOL = RIBOSOME_CYTOSOL+ENDOGLIN_CYTOSOL+MRNA_ENDOGLIN_CYTOSOL
0.04537559222842208 ; % 125 MRNA_ENDOGLIN_CYTOSOL = [] MRNA_ENDOGLIN_CYTOSOL = []
0.17008546230349786 ; % 126 ENDOGLIN_CYTOSOL = [] ENDOGLIN_CYTOSOL = []
0.8914284372552602 ; % 127 DNA_ALK1_NUCLEAR + RNAP_NUCLEAR = DNA_ALK1_RNAP_NUCLEAR DNA_ALK1_NUCLEAR+RNAP_NUCLEAR = DNA_ALK1_RNAP_NUCLEAR
0.0015580093673532747 ; % 128 DNA_ALK1_RNAP_NUCLEAR = DNA_ALK1_NUCLEAR + RNAP_NUCLEAR DNA_ALK1_RNAP_NUCLEAR = DNA_ALK1_NUCLEAR+RNAP_NUCLEAR
0.15050700132760975 ; % 129 DNA_ALK1_RNAP_NUCLEAR = DNA_ALK1_NUCLEAR + RNAP_NUCLEAR + MRNA_ALK1_NUCLEAR DNA_ALK1_RNAP_NUCLEAR = DNA_ALK1_NUCLEAR+RNAP_NUCLEAR+MRNA_ALK1_NUCLEAR
0.8207925143528575 ; % 130 MRNA_ALK1_NUCLEAR + NEXPORT_NUCLEAR = MRNA_ALK1_NEXPORT_NUCLEAR MRNA_ALK1_NUCLEAR+NEXPORT_NUCLEAR = MRNA_ALK1_NEXPORT_NUCLEAR
1.752330751385034E-4 ; % 131 MRNA_ALK1_NEXPORT_NUCLEAR = MRNA_ALK1_NUCLEAR + NEXPORT_NUCLEAR MRNA_ALK1_NEXPORT_NUCLEAR = MRNA_ALK1_NUCLEAR+NEXPORT_NUCLEAR

0.9617341264993546 ; % 132 MRNA_ALK1_NEXPORT_NUCLEAR = MRNA_ALK1_CYTOSOL + NEXPORT_NUCLEAR
MRNA_ALK1_NEXPORT_NUCLEAR = MRNA_ALK1_CYTOSOL+NEXPORT_NUCLEAR
0.7045453617232692 ; % 133 MRNA_ALK1_CYTOSOL + RIBOSOME_CYTOSOL = MRNA_ALK1_RIBOSOME_CYTOSOL
MRNA_ALK1_CYTOSOL+RIBOSOME_CYTOSOL = MRNA_ALK1_RIBOSOME_CYTOSOL
0.06819913947769468 ; % 134 MRNA_ALK1_RIBOSOME_CYTOSOL = MRNA_ALK1_CYTOSOL + RIBOSOME_CYTOSOL
MRNA_ALK1_RIBOSOME_CYTOSOL = MRNA_ALK1_CYTOSOL+RIBOSOME_CYTOSOL
0.6667502681252524 ; % 135 MRNA_ALK1_RIBOSOME_CYTOSOL = MRNA_ALK1_START_RIBOSOME_CYTOSOL
MRNA_ALK1_RIBOSOME_CYTOSOL = MRNA_ALK1_START_RIBOSOME_CYTOSOL
0.8438816499691592 ; % 136 MRNA_ALK1_START_RIBOSOME_CYTOSOL = RIBOSOME_CYTOSOL + ALK1_CYTOSOL
+ MRNA_ALK1_CYTOSOL MRNA_ALK1_START_RIBOSOME_CYTOSOL = RIBOSOME_CYTOSOL+ALK1_CYTOSOL+MRNA_ALK1_CYTOSOL
0.028757248046415607 ; % 137 MRNA_ALK1_CYTOSOL = [] MRNA_ALK1_CYTOSOL = []
0.19905565797917152 ; % 138 ALK1_CYTOSOL = [] ALK1_CYTOSOL = []
0.9759085893754013 ; % 139 DNA_ALK2_NUCLEAR + RNAP_NUCLEAR = DNA_ALK2_RNAP_NUCLEAR
DNA_ALK2_NUCLEAR+RNAP_NUCLEAR = DNA_ALK2_RNAP_NUCLEAR
0.03850708039319317 ; % 140 DNA_ALK2_RNAP_NUCLEAR = DNA_ALK2_NUCLEAR + RNAP_NUCLEAR
DNA_ALK2_RNAP_NUCLEAR = DNA_ALK2_NUCLEAR+RNAP_NUCLEAR
0.3997244629439337 ; % 141 DNA_ALK2_RNAP_NUCLEAR = DNA_ALK2_NUCLEAR + RNAP_NUCLEAR +
MRNA_ALK2_NUCLEAR DNA_ALK2_RNAP_NUCLEAR = DNA_ALK2_NUCLEAR+RNAP_NUCLEAR+MRNA_ALK2_NUCLEAR
0.7772152927770049 ; % 142 MRNA_ALK2_NUCLEAR + NEXPORT_NUCLEAR = MRNA_ALK2_NEXPORT_NUCLEAR
MRNA_ALK2_NUCLEAR+NEXPORT_NUCLEAR = MRNA_ALK2_NEXPORT_NUCLEAR
0.009717462703479597 ; % 143 MRNA_ALK2_NEXPORT_NUCLEAR = MRNA_ALK2_NUCLEAR + NEXPORT_NUCLEAR
MRNA_ALK2_NEXPORT_NUCLEAR = MRNA_ALK2_NUCLEAR+NEXPORT_NUCLEAR
0.6709136175427387 ; % 144 MRNA_ALK2_NEXPORT_NUCLEAR = MRNA_ALK2_CYTOSOL + NEXPORT_NUCLEAR
MRNA_ALK2_NEXPORT_NUCLEAR = MRNA_ALK2_CYTOSOL+NEXPORT_NUCLEAR
0.8397405381709364 ; % 145 MRNA_ALK2_CYTOSOL + RIBOSOME_CYTOSOL = MRNA_ALK2_RIBOSOME_CYTOSOL
MRNA_ALK2_CYTOSOL+RIBOSOME_CYTOSOL = MRNA_ALK2_RIBOSOME_CYTOSOL
0.07599945719313639 ; % 146 MRNA_ALK2_RIBOSOME_CYTOSOL = MRNA_ALK2_CYTOSOL + RIBOSOME_CYTOSOL
MRNA_ALK2_RIBOSOME_CYTOSOL = MRNA_ALK2_CYTOSOL+RIBOSOME_CYTOSOL
0.8072028481983483 ; % 147 MRNA_ALK2_RIBOSOME_CYTOSOL = MRNA_ALK2_START_RIBOSOME_CYTOSOL
MRNA_ALK2_RIBOSOME_CYTOSOL = MRNA_ALK2_START_RIBOSOME_CYTOSOL
0.1924892696569287 ; % 148 MRNA_ALK2_START_RIBOSOME_CYTOSOL = RIBOSOME_CYTOSOL + ALK2_CYTOSOL
+ MRNA_ALK2_CYTOSOL MRNA_ALK2_START_RIBOSOME_CYTOSOL = RIBOSOME_CYTOSOL+ALK2_CYTOSOL+MRNA_ALK2_CYTOSOL
0.08963404070656744 ; % 149 MRNA_ALK2_CYTOSOL = [] MRNA_ALK2_CYTOSOL = []
0.21269670831972332 ; % 150 ALK2_CYTOSOL = [] ALK2_CYTOSOL = []
0.9186315393659695 ; % 151 DNA_ALK3_NUCLEAR + RNAP_NUCLEAR = DNA_ALK3_RNAP_NUCLEAR
DNA_ALK3_NUCLEAR+RNAP_NUCLEAR = DNA_ALK3_RNAP_NUCLEAR
0.04764104832408128 ; % 152 DNA_ALK3_RNAP_NUCLEAR = DNA_ALK3_NUCLEAR + RNAP_NUCLEAR
DNA_ALK3_RNAP_NUCLEAR = DNA_ALK3_NUCLEAR+RNAP_NUCLEAR
0.477356468978543 ; % 153 DNA_ALK3_RNAP_NUCLEAR = DNA_ALK3_NUCLEAR + RNAP_NUCLEAR +
MRNA_ALK3_NUCLEAR DNA_ALK3_RNAP_NUCLEAR = DNA_ALK3_NUCLEAR+RNAP_NUCLEAR+MRNA_ALK3_NUCLEAR
0.5314710377148251 ; % 154 MRNA_ALK3_NUCLEAR + NEXPORT_NUCLEAR = MRNA_ALK3_NEXPORT_NUCLEAR
MRNA_ALK3_NUCLEAR+NEXPORT_NUCLEAR = MRNA_ALK3_NEXPORT_NUCLEAR
0.011479686156112324 ; % 155 MRNA_ALK3_NEXPORT_NUCLEAR = MRNA_ALK3_NUCLEAR + NEXPORT_NUCLEAR
MRNA_ALK3_NEXPORT_NUCLEAR = MRNA_ALK3_NUCLEAR+NEXPORT_NUCLEAR
0.5353596485852495 ; % 156 MRNA_ALK3_NEXPORT_NUCLEAR = MRNA_ALK3_CYTOSOL + NEXPORT_NUCLEAR
MRNA_ALK3_NEXPORT_NUCLEAR = MRNA_ALK3_CYTOSOL+NEXPORT_NUCLEAR
0.1667698541714553 ; % 157 MRNA_ALK3_CYTOSOL + RIBOSOME_CYTOSOL = MRNA_ALK3_RIBOSOME_CYTOSOL
MRNA_ALK3_CYTOSOL+RIBOSOME_CYTOSOL = MRNA_ALK3_RIBOSOME_CYTOSOL
0.0581155476256232 ; % 158 MRNA_ALK3_RIBOSOME_CYTOSOL = MRNA_ALK3_CYTOSOL + RIBOSOME_CYTOSOL
MRNA_ALK3_RIBOSOME_CYTOSOL = MRNA_ALK3_CYTOSOL+RIBOSOME_CYTOSOL
0.6212360530656802 ; % 159 MRNA_ALK3_RIBOSOME_CYTOSOL = MRNA_ALK3_START_RIBOSOME_CYTOSOL
MRNA_ALK3_RIBOSOME_CYTOSOL = MRNA_ALK3_START_RIBOSOME_CYTOSOL
0.361659504745071 ; % 160 MRNA_ALK3_START_RIBOSOME_CYTOSOL = RIBOSOME_CYTOSOL + ALK3_CYTOSOL
+ MRNA_ALK3_CYTOSOL MRNA_ALK3_START_RIBOSOME_CYTOSOL = RIBOSOME_CYTOSOL+ALK3_CYTOSOL+MRNA_ALK3_CYTOSOL
0.4287215785085048 ; % 161 MRNA_ALK3_CYTOSOL = [] MRNA_ALK3_CYTOSOL = []
0.48496332924758145 ; % 162 ALK3_CYTOSOL = [] ALK3_CYTOSOL = []
0.21852698429551676 ; % 163 DNA_ALK5_NUCLEAR + RNAP_NUCLEAR = DNA_ALK5_RNAP_NUCLEAR
DNA_ALK5_NUCLEAR+RNAP_NUCLEAR = DNA_ALK5_RNAP_NUCLEAR
0.008195100041991144 ; % 164 DNA_ALK5_RNAP_NUCLEAR = DNA_ALK5_NUCLEAR + RNAP_NUCLEAR
DNA_ALK5_RNAP_NUCLEAR = DNA_ALK5_NUCLEAR+RNAP_NUCLEAR
0.9902617384007653 ; % 165 DNA_ALK5_RNAP_NUCLEAR = DNA_ALK5_NUCLEAR + RNAP_NUCLEAR +
MRNA_ALK5_NUCLEAR DNA_ALK5_RNAP_NUCLEAR = DNA_ALK5_NUCLEAR+RNAP_NUCLEAR+MRNA_ALK5_NUCLEAR
0.2460988216357486 ; % 166 MRNA_ALK5_NUCLEAR + NEXPORT_NUCLEAR = MRNA_ALK5_NEXPORT_NUCLEAR
MRNA_ALK5_NUCLEAR+NEXPORT_NUCLEAR = MRNA_ALK5_NEXPORT_NUCLEAR
0.03324562499557674 ; % 167 MRNA_ALK5_NEXPORT_NUCLEAR = MRNA_ALK5_NUCLEAR + NEXPORT_NUCLEAR
MRNA_ALK5_NEXPORT_NUCLEAR = MRNA_ALK5_NUCLEAR+NEXPORT_NUCLEAR
0.1928083789465429 ; % 168 MRNA_ALK5_NEXPORT_NUCLEAR = MRNA_ALK5_CYTOSOL + NEXPORT_NUCLEAR
MRNA_ALK5_NEXPORT_NUCLEAR = MRNA_ALK5_CYTOSOL+NEXPORT_NUCLEAR
0.1889736024079035 ; % 169 MRNA_ALK5_CYTOSOL + RIBOSOME_CYTOSOL = MRNA_ALK5_RIBOSOME_CYTOSOL
MRNA_ALK5_CYTOSOL+RIBOSOME_CYTOSOL = MRNA_ALK5_RIBOSOME_CYTOSOL
0.08942552312317859 ; % 170 MRNA_ALK5_RIBOSOME_CYTOSOL = MRNA_ALK5_CYTOSOL + RIBOSOME_CYTOSOL
MRNA_ALK5_RIBOSOME_CYTOSOL = MRNA_ALK5_CYTOSOL+RIBOSOME_CYTOSOL
0.32520373955515725 ; % 171 MRNA_ALK5_RIBOSOME_CYTOSOL = MRNA_ALK5_START_RIBOSOME_CYTOSOL
MRNA_ALK5_RIBOSOME_CYTOSOL = MRNA_ALK5_START_RIBOSOME_CYTOSOL
0.5051299282938028 ; % 172 MRNA_ALK5_START_RIBOSOME_CYTOSOL = RIBOSOME_CYTOSOL + ALK5_CYTOSOL
+ MRNA_ALK5_CYTOSOL MRNA_ALK5_START_RIBOSOME_CYTOSOL = RIBOSOME_CYTOSOL+ALK5_CYTOSOL+MRNA_ALK5_CYTOSOL
0.2494315719060336 ; % 173 MRNA_ALK5_CYTOSOL = [] MRNA_ALK5_CYTOSOL = []
0.1692605933623273 ; % 174 ALK5_CYTOSOL = [] ALK5_CYTOSOL = []
0.6551766834104369 ; % 175 DNA_ALK6_NUCLEAR + RNAP_NUCLEAR = DNA_ALK6_RNAP_NUCLEAR
DNA_ALK6_NUCLEAR+RNAP_NUCLEAR = DNA_ALK6_RNAP_NUCLEAR
0.003940006017138765 ; % 176 DNA_ALK6_RNAP_NUCLEAR = DNA_ALK6_NUCLEAR + RNAP_NUCLEAR
DNA_ALK6_RNAP_NUCLEAR = DNA_ALK6_NUCLEAR+RNAP_NUCLEAR
0.6978861900884743 ; % 177 DNA_ALK6_RNAP_NUCLEAR = DNA_ALK6_NUCLEAR + RNAP_NUCLEAR +
MRNA_ALK6_NUCLEAR DNA_ALK6_RNAP_NUCLEAR = DNA_ALK6_NUCLEAR+RNAP_NUCLEAR+MRNA_ALK6_NUCLEAR
0.05474368423048548 ; % 178 MRNA_ALK6_NUCLEAR + NEXPORT_NUCLEAR = MRNA_ALK6_NEXPORT_NUCLEAR
MRNA_ALK6_NUCLEAR+NEXPORT_NUCLEAR = MRNA_ALK6_NEXPORT_NUCLEAR
0.027332160031823028 ; % 179 MRNA_ALK6_NEXPORT_NUCLEAR = MRNA_ALK6_NUCLEAR + NEXPORT_NUCLEAR
MRNA_ALK6_NEXPORT_NUCLEAR = MRNA_ALK6_NUCLEAR+NEXPORT_NUCLEAR
0.13442677206550535 ; % 180 MRNA_ALK6_NEXPORT_NUCLEAR = MRNA_ALK6_CYTOSOL + NEXPORT_NUCLEAR
MRNA_ALK6_NEXPORT_NUCLEAR = MRNA_ALK6_CYTOSOL+NEXPORT_NUCLEAR
0.5192858441901614 ; % 181 MRNA_ALK6_CYTOSOL + RIBOSOME_CYTOSOL = MRNA_ALK6_RIBOSOME_CYTOSOL
MRNA_ALK6_CYTOSOL+RIBOSOME_CYTOSOL = MRNA_ALK6_RIBOSOME_CYTOSOL

0.07792791454221999 ; % 182 MRNA_ALK6_RIBOSOME_CYTOSOL = MRNA_ALK6_CYTOSOL + RIBOSOME_CYTOSOL
MRNA_ALK6_RIBOSOME_CYTOSOL = MRNA_ALK6_CYTOSOL+RIBOSOME_CYTOSOL
0.48018771946149486 ; % 183 MRNA_ALK6_RIBOSOME_CYTOSOL = MRNA_ALK6_START_RIBOSOME_CYTOSOL
MRNA_ALK6_RIBOSOME_CYTOSOL = MRNA_ALK6_START_RIBOSOME_CYTOSOL
0.45891570311066965 ; % 184 MRNA_ALK6_START_RIBOSOME_CYTOSOL = RIBOSOME_CYTOSOL + ALK6_CYTOSOL
+ MRNA_ALK6_CYTOSOL MRNA_ALK6_START_RIBOSOME_CYTOSOL = RIBOSOME_CYTOSOL+ALK6_CYTOSOL+MRNA_ALK6_CYTOSOL
0.4671396689399151 ; % 185 MRNA_ALK6_CYTOSOL = [] MRNA_ALK6_CYTOSOL = []
0.40348688107890374 ; % 186 ALK6_CYTOSOL = [] ALK6_CYTOSOL = []
0.4807109387000512 ; % 187 DNA_SHC_NUCLEAR + RNAP_NUCLEAR = DNA_SHC_RNAP_NUCLEAR
DNA_SHC_NUCLEAR+RNAP_NUCLEAR = DNA_SHC_RNAP_NUCLEAR
0.044825069081376345 ; % 188 DNA_SHC_RNAP_NUCLEAR = DNA_SHC_NUCLEAR + RNAP_NUCLEAR
DNA_SHC_RNAP_NUCLEAR = DNA_SHC_NUCLEAR+RNAP_NUCLEAR
0.6092263251413107 ; % 189 DNA_SHC_RNAP_NUCLEAR = DNA_SHC_NUCLEAR + RNAP_NUCLEAR +
MRNA_SHC_NUCLEAR DNA_SHC_RNAP_NUCLEAR = DNA_SHC_NUCLEAR+RNAP_NUCLEAR+MRNA_SHC_NUCLEAR
0.28205307116886635 ; % 190 MRNA_SHC_NUCLEAR + NEXPORT_NUCLEAR = MRNA_SHC_NEXPORT_NUCLEAR
MRNA_SHC_NUCLEAR+NEXPORT_NUCLEAR = MRNA_SHC_NEXPORT_NUCLEAR
0.00426326926286178 ; % 191 MRNA_SHC_NEXPORT_NUCLEAR = MRNA_SHC_NUCLEAR + NEXPORT_NUCLEAR
MRNA_SHC_NEXPORT_NUCLEAR = MRNA_SHC_NUCLEAR+NEXPORT_NUCLEAR
0.9281073050782441 ; % 192 MRNA_SHC_NEXPORT_NUCLEAR = MRNA_SHC_CYTOSOL + NEXPORT_NUCLEAR
MRNA_SHC_NEXPORT_NUCLEAR = MRNA_SHC_CYTOSOL+NEXPORT_NUCLEAR
0.27375912383082757 ; % 193 MRNA_SHC_CYTOSOL + RIBOSOME_CYTOSOL = MRNA_SHC_RIBOSOME_CYTOSOL
MRNA_SHC_CYTOSOL+RIBOSOME_CYTOSOL = MRNA_SHC_RIBOSOME_CYTOSOL
0.02030209246420305 ; % 194 MRNA_SHC_RIBOSOME_CYTOSOL = MRNA_SHC_CYTOSOL + RIBOSOME_CYTOSOL
MRNA_SHC_RIBOSOME_CYTOSOL = MRNA_SHC_CYTOSOL+RIBOSOME_CYTOSOL
0.9896630727587311 ; % 195 MRNA_SHC_RIBOSOME_CYTOSOL = MRNA_SHC_START_RIBOSOME_CYTOSOL
MRNA_SHC_RIBOSOME_CYTOSOL = MRNA_SHC_START_RIBOSOME_CYTOSOL
0.3320351365115597 ; % 196 MRNA_SHC_START_RIBOSOME_CYTOSOL = RIBOSOME_CYTOSOL + SHC_CYTOSOL
+ MRNA_SHC_CYTOSOL MRNA_SHC_START_RIBOSOME_CYTOSOL = RIBOSOME_CYTOSOL+SHC_CYTOSOL+MRNA_SHC_CYTOSOL
0.007338159922264609 ; % 197 MRNA_SHC_CYTOSOL = [] MRNA_SHC_CYTOSOL = []
0.2931501744453865 ; % 198 SHC_CYTOSOL = [] SHC_CYTOSOL = []
0.7419435994042889 ; % 199 DNA_GRB2_NUCLEAR + RNAP_NUCLEAR = DNA_GRB2_RNAP_NUCLEAR
DNA_GRB2_NUCLEAR+RNAP_NUCLEAR = DNA_GRB2_RNAP_NUCLEAR
0.09719010597020415 ; % 200 DNA_GRB2_RNAP_NUCLEAR = DNA_GRB2_NUCLEAR + RNAP_NUCLEAR
DNA_GRB2_RNAP_NUCLEAR = DNA_GRB2_NUCLEAR+RNAP_NUCLEAR
0.44497073590791714 ; % 201 DNA_GRB2_RNAP_NUCLEAR = DNA_GRB2_NUCLEAR + RNAP_NUCLEAR +
MRNA_GRB2_NUCLEAR DNA_GRB2_RNAP_NUCLEAR = DNA_GRB2_NUCLEAR+RNAP_NUCLEAR+MRNA_GRB2_NUCLEAR
0.8632318663781365 ; % 202 MRNA_GRB2_NUCLEAR + NEXPORT_NUCLEAR = MRNA_GRB2_NEXPORT_NUCLEAR
MRNA_GRB2_NUCLEAR+NEXPORT_NUCLEAR = MRNA_GRB2_NEXPORT_NUCLEAR
0.0754059508115241 ; % 203 MRNA_GRB2_NEXPORT_NUCLEAR = MRNA_GRB2_NUCLEAR + NEXPORT_NUCLEAR
MRNA_GRB2_NEXPORT_NUCLEAR = MRNA_GRB2_NUCLEAR+NEXPORT_NUCLEAR
0.2780944944291569 ; % 204 MRNA_GRB2_NEXPORT_NUCLEAR = MRNA_GRB2_CYTOSOL + NEXPORT_NUCLEAR
MRNA_GRB2_NEXPORT_NUCLEAR = MRNA_GRB2_CYTOSOL+NEXPORT_NUCLEAR
0.2881833612160266 ; % 205 MRNA_GRB2_CYTOSOL + RIBOSOME_CYTOSOL =
MRNA_GRB2_RIBOSOME_CYTOSOL MRNA_GRB2_CYTOSOL+RIBOSOME_CYTOSOL = MRNA_GRB2_RIBOSOME_CYTOSOL
0.012117753382413866 ; % 206 MRNA_GRB2_RIBOSOME_CYTOSOL = MRNA_GRB2_CYTOSOL +
RIBOSOME_CYTOSOL MRNA_GRB2_RIBOSOME_CYTOSOL = MRNA_GRB2_CYTOSOL+RIBOSOME_CYTOSOL
0.49479703952495957 ; % 207 MRNA_GRB2_RIBOSOME_CYTOSOL = MRNA_GRB2_START_RIBOSOME_CYTOSOL
MRNA_GRB2_RIBOSOME_CYTOSOL = MRNA_GRB2_START_RIBOSOME_CYTOSOL
0.7906528700130084 ; % 208 MRNA_GRB2_START_RIBOSOME_CYTOSOL = RIBOSOME_CYTOSOL +
GRB2_CYTOSOL + MRNA_GRB2_CYTOSOL MRNA_GRB2_START_RIBOSOME_CYTOSOL = RIBOSOME_CYTOSOL+GRB2_CYTOSOL+MRNA_GRB2_CYTOSOL
0.08267280950330064 ; % 209 MRNA_GRB2_CYTOSOL = [] MRNA_GRB2_CYTOSOL = []
0.12093093088159534 ; % 210 GRB2_CYTOSOL = [] GRB2_CYTOSOL = []
0.5630371608878857 ; % 211 DNA_SOS_NUCLEAR + RNAP_NUCLEAR = DNA_SOS_RNAP_NUCLEAR
DNA_SOS_NUCLEAR+RNAP_NUCLEAR = DNA_SOS_RNAP_NUCLEAR
0.09529736083139052 ; % 212 DNA_SOS_RNAP_NUCLEAR = DNA_SOS_NUCLEAR + RNAP_NUCLEAR
DNA_SOS_RNAP_NUCLEAR = DNA_SOS_NUCLEAR+RNAP_NUCLEAR
0.27509190112175863 ; % 213 DNA_SOS_RNAP_NUCLEAR = DNA_SOS_NUCLEAR + RNAP_NUCLEAR +
MRNA_SOS_NUCLEAR DNA_SOS_RNAP_NUCLEAR = DNA_SOS_NUCLEAR+RNAP_NUCLEAR+MRNA_SOS_NUCLEAR
0.3387132879576339 ; % 214 MRNA_SOS_NUCLEAR + NEXPORT_NUCLEAR = MRNA_SOS_NEXPORT_NUCLEAR
MRNA_SOS_NUCLEAR+NEXPORT_NUCLEAR = MRNA_SOS_NEXPORT_NUCLEAR
0.06406211652109715 ; % 215 MRNA_SOS_NEXPORT_NUCLEAR = MRNA_SOS_NUCLEAR + NEXPORT_NUCLEAR
MRNA_SOS_NEXPORT_NUCLEAR = MRNA_SOS_NUCLEAR+NEXPORT_NUCLEAR
0.436536951080606 ; % 216 MRNA_SOS_NEXPORT_NUCLEAR = MRNA_SOS_CYTOSOL + NEXPORT_NUCLEAR
MRNA_SOS_NEXPORT_NUCLEAR = MRNA_SOS_CYTOSOL+NEXPORT_NUCLEAR
0.2170949164855861 ; % 217 MRNA_SOS_CYTOSOL + RIBOSOME_CYTOSOL = MRNA_SOS_RIBOSOME_CYTOSOL
MRNA_SOS_CYTOSOL+RIBOSOME_CYTOSOL = MRNA_SOS_RIBOSOME_CYTOSOL
0.014985336433125596 ; % 218 MRNA_SOS_RIBOSOME_CYTOSOL = MRNA_SOS_CYTOSOL + RIBOSOME_CYTOSOL
MRNA_SOS_RIBOSOME_CYTOSOL = MRNA_SOS_CYTOSOL+RIBOSOME_CYTOSOL
0.24572023457940018 ; % 219 MRNA_SOS_RIBOSOME_CYTOSOL = MRNA_SOS_START_RIBOSOME_CYTOSOL
MRNA_SOS_RIBOSOME_CYTOSOL = MRNA_SOS_START_RIBOSOME_CYTOSOL
0.8080710180502351 ; % 220 MRNA_SOS_START_RIBOSOME_CYTOSOL = RIBOSOME_CYTOSOL + SOS_CYTOSOL
+ MRNA_SOS_CYTOSOL MRNA_SOS_START_RIBOSOME_CYTOSOL = RIBOSOME_CYTOSOL+SOS_CYTOSOL+MRNA_SOS_CYTOSOL
0.2123985429089661 ; % 221 MRNA_SOS_CYTOSOL = [] MRNA_SOS_CYTOSOL = []
0.10225640548432885 ; % 222 SOS_CYTOSOL = [] SOS_CYTOSOL = []
0.669185385759699 ; % 223 DNA_BMPRII_NUCLEAR + RNAP_NUCLEAR = DNA_BMPRII_RNAP_NUCLEAR
DNA_BMPRII_NUCLEAR+RNAP_NUCLEAR = DNA_BMPRII_RNAP_NUCLEAR
0.08398493054352466 ; % 224 DNA_BMPRII_RNAP_NUCLEAR = DNA_BMPRII_NUCLEAR + RNAP_NUCLEAR
DNA_BMPRII_RNAP_NUCLEAR = DNA_BMPRII_NUCLEAR+RNAP_NUCLEAR
0.5454808353301231 ; % 225 DNA_BMPRII_RNAP_NUCLEAR = DNA_BMPRII_NUCLEAR + RNAP_NUCLEAR +
MRNA_BMPRII_NUCLEAR DNA_BMPRII_RNAP_NUCLEAR = DNA_BMPRII_NUCLEAR+RNAP_NUCLEAR+MRNA_BMPRII_NUCLEAR
0.6480369075520682 ; % 226 MRNA_BMPRII_NUCLEAR + NEXPORT_NUCLEAR =
MRNA_BMPRII_NEXPORT_NUCLEAR MRNA_BMPRII_NUCLEAR+NEXPORT_NUCLEAR = MRNA_BMPRII_NEXPORT_NUCLEAR
0.005155026174519273 ; % 227 MRNA_BMPRII_NEXPORT_NUCLEAR = MRNA_BMPRII_NUCLEAR +
NEXPORT_NUCLEAR MRNA_BMPRII_NEXPORT_NUCLEAR = MRNA_BMPRII_NUCLEAR+NEXPORT_NUCLEAR
0.659317665100542 ; % 228 MRNA_BMPRII_NEXPORT_NUCLEAR = MRNA_BMPRII_CYTOSOL +
NEXPORT_NUCLEAR MRNA_BMPRII_NEXPORT_NUCLEAR = MRNA_BMPRII_CYTOSOL+NEXPORT_NUCLEAR
0.6340416115945492 ; % 229 MRNA_BMPRII_CYTOSOL + RIBOSOME_CYTOSOL =
MRNA_BMPRII_RIBOSOME_CYTOSOL MRNA_BMPRII_CYTOSOL+RIBOSOME_CYTOSOL = MRNA_BMPRII_RIBOSOME_CYTOSOL
0.058427545483033784 ; % 230 MRNA_BMPRII_RIBOSOME_CYTOSOL = MRNA_BMPRII_CYTOSOL +
RIBOSOME_CYTOSOL MRNA_BMPRII_RIBOSOME_CYTOSOL = MRNA_BMPRII_CYTOSOL+RIBOSOME_CYTOSOL
0.2898037292354786 ; % 231 MRNA_BMPRII_RIBOSOME_CYTOSOL = MRNA_BMPRII_START_RIBOSOME_CYTOSOL
MRNA_BMPRII_RIBOSOME_CYTOSOL = MRNA_BMPRII_START_RIBOSOME_CYTOSOL

0.23600663634812646 ; % 232 MRNA_BMPRII_START_RIBOSOME_CYTOSOL = RIBOSOME_CYTOSOL + BMPRII_CYTOSOL + MRNA_BMPRII_CYTOSOL MRNA_BMPRII_START_RIBOSOME_CYTOSOL = RIBOSOME_CYTOSOL+BMPRII_CYTOSOL+MRNA_BMPRII_CYTOSOL
0.10569858272248728 ; % 233 MRNA_BMPRII_CYTOSOL = [] MRNA_BMPRII_CYTOSOL = []
0.3370176935426546 ; % 234 BMPRII_CYTOSOL = [] BMPRII_CYTOSOL = []
0.35074566108378613 ; % 235 DNA_TGFBRII_NUCLEAR + RNAP_NUCLEAR = DNA_TGFBRII_RNAP_NUCLEAR DNA_TGFBRII_NUCLEAR+RNAP_NUCLEAR = DNA_TGFBRII_RNAP_NUCLEAR
0.04116916773635426 ; % 236 DNA_TGFBRII_RNAP_NUCLEAR = DNA_TGFBRII_NUCLEAR + RNAP_NUCLEAR DNA_TGFBRII_RNAP_NUCLEAR = DNA_TGFBRII_NUCLEAR+RNAP_NUCLEAR
0.07928751883383911 ; % 237 DNA_TGFBRII_RNAP_NUCLEAR = DNA_TGFBRII_NUCLEAR + RNAP_NUCLEAR + MRNA_TGFBRII_NUCLEAR DNA_TGFBRII_RNAP_NUCLEAR = DNA_TGFBRII_NUCLEAR+RNAP_NUCLEAR+MRNA_TGFBRII_NUCLEAR
0.5144064252298072 ; % 238 MRNA_TGFBRII_NUCLEAR + NEXPORT_NUCLEAR = MRNA_TGFBRII_NEXPORT_NUCLEAR MRNA_TGFBRII_NUCLEAR+NEXPORT_NUCLEAR = MRNA_TGFBRII_NEXPORT_NUCLEAR
0.06116832137600162 ; % 239 MRNA_TGFBRII_NEXPORT_NUCLEAR = MRNA_TGFBRII_NUCLEAR + NEXPORT_NUCLEAR MRNA_TGFBRII_NEXPORT_NUCLEAR = MRNA_TGFBRII_NUCLEAR+NEXPORT_NUCLEAR
0.7940226237698634 ; % 240 MRNA_TGFBRII_NEXPORT_NUCLEAR = MRNA_TGFBRII_CYTOSOL + NEXPORT_NUCLEAR MRNA_TGFBRII_NEXPORT_NUCLEAR = MRNA_TGFBRII_CYTOSOL+NEXPORT_NUCLEAR
0.2802899339829855 ; % 241 MRNA_TGFBRII_CYTOSOL + RIBOSOME_CYTOSOL = MRNA_TGFBRII_RIBOSOME_CYTOSOL MRNA_TGFBRII_CYTOSOL+RIBOSOME_CYTOSOL = MRNA_TGFBRII_RIBOSOME_CYTOSOL
0.0016153712784381 73 ; % 242 MRNA_TGFBRII_RIBOSOME_CYTOSOL = MRNA_TGFBRII_CYTOSOL + RIBOSOME_CYTOSOL MRNA_TGFBRII_RIBOSOME_CYTOSOL = MRNA_TGFBRII_CYTOSOL+RIBOSOME_CYTOSOL
0.04942176198443571 ; % 243 MRNA_TGFBRII_RIBOSOME_CYTOSOL = MRNA_TGFBRII_START_RIBOSOME_CYTOSOL MRNA_TGFBRII_RIBOSOME_CYTOSOL = MRNA_TGFBRII_START_RIBOSOME_CYTOSOL
0.3543511154106803 ; % 244 MRNA_TGFBRII_START_RIBOSOME_CYTOSOL = RIBOSOME_CYTOSOL + TGFBRII_CYTOSOL + MRNA_TGFBRII_CYTOSOL MRNA_TGFBRII_START_RIBOSOME_CYTOSOL = RIBOSOME_CYTOSOL+TGFBRII_CYTOSOL+MRNA_TGFBRII_CYTOSOL
0.372596879120297 ; % 245 MRNA_TGFBRII_CYTOSOL = [] MRNA_TGFBRII_CYTOSOL = []
0.2975019991021161 ; % 246 TGFBRII_CYTOSOL = [] TGFBRII_CYTOSOL = []
0.4549484803241236 ; % 247 DNA_TGFBRIII_NUCLEAR + RNAP_NUCLEAR = DNA_TGFBRIII_RNAP_NUCLEAR DNA_TGFBRIII_NUCLEAR+RNAP_NUCLEAR = DNA_TGFBRIII_RNAP_NUCLEAR
0.04972422993617496 ; % 248 DNA_TGFBRIII_RNAP_NUCLEAR = DNA_TGFBRIII_NUCLEAR + RNAP_NUCLEAR DNA_TGFBRIII_RNAP_NUCLEAR = DNA_TGFBRIII_NUCLEAR+RNAP_NUCLEAR
0.97944995420092 ; % 249 DNA_TGFBRIII_RNAP_NUCLEAR = DNA_TGFBRIII_NUCLEAR + RNAP_NUCLEAR + MRNA_TGFBRIII_NUCLEAR DNA_TGFBRIII_RNAP_NUCLEAR = DNA_TGFBRIII_NUCLEAR+RNAP_NUCLEAR+MRNA_TGFBRIII_NUCLEAR
0.4975339957761852 ; % 250 MRNA_TGFBRIII_NUCLEAR + NEXPORT_NUCLEAR = MRNA_TGFBRIII_NEXPORT_NUCLEAR MRNA_TGFBRIII_NUCLEAR+NEXPORT_NUCLEAR = MRNA_TGFBRIII_NEXPORT_NUCLEAR
0.03639029675479395 ; % 251 MRNA_TGFBRIII_NEXPORT_NUCLEAR = MRNA_TGFBRIII_NUCLEAR + NEXPORT_NUCLEAR MRNA_TGFBRIII_NEXPORT_NUCLEAR = MRNA_TGFBRIII_NUCLEAR+NEXPORT_NUCLEAR
0.7021655227051585 ; % 252 MRNA_TGFBRIII_NEXPORT_NUCLEAR = MRNA_TGFBRIII_CYTOSOL + NEXPORT_NUCLEAR MRNA_TGFBRIII_NEXPORT_NUCLEAR = MRNA_TGFBRIII_CYTOSOL+NEXPORT_NUCLEAR
0.6062312011917435 ; % 253 MRNA_TGFBRIII_CYTOSOL + RIBOSOME_CYTOSOL = MRNA_TGFBRIII_RIBOSOME_CYTOSOL MRNA_TGFBRIII_CYTOSOL+RIBOSOME_CYTOSOL = MRNA_TGFBRIII_RIBOSOME_CYTOSOL
0.09935036394228859 ; % 254 MRNA_TGFBRIII_RIBOSOME_CYTOSOL = MRNA_TGFBRIII_CYTOSOL + RIBOSOME_CYTOSOL MRNA_TGFBRIII_RIBOSOME_CYTOSOL = MRNA_TGFBRIII_CYTOSOL+RIBOSOME_CYTOSOL
0.061874091778540974 ; % 255 MRNA_TGFBRIII_RIBOSOME_CYTOSOL = MRNA_TGFBRIII_START_RIBOSOME_CYTOSOL MRNA_TGFBRIII_RIBOSOME_CYTOSOL = MRNA_TGFBRIII_START_RIBOSOME_CYTOSOL
0.5771160356390984 ; % 256 MRNA_TGFBRIII_START_RIBOSOME_CYTOSOL = RIBOSOME_CYTOSOL + TGFBRIII_CYTOSOL + MRNA_TGFBRIII_CYTOSOL MRNA_TGFBRIII_START_RIBOSOME_CYTOSOL = RIBOSOME_CYTOSOL+TGFBRIII_CYTOSOL+MRNA_TGFBRIII_CYTOSOL
0.3528539199833046 ; % 257 MRNA_TGFBRIII_CYTOSOL = [] MRNA_TGFBRIII_CYTOSOL = []
0.2419292745046377 ; % 258 TGFBRIII_CYTOSOL = [] TGFBRIII_CYTOSOL = []
0.8487577622464618 ; % 259 DNA_MSX1_NUCLEAR + RNAP_NUCLEAR = DNA_MSX1_RNAP_NUCLEAR DNA_MSX1_NUCLEAR+RNAP_NUCLEAR = DNA_MSX1_RNAP_NUCLEAR
0.030942764767411746 ; % 260 DNA_MSX1_RNAP_NUCLEAR = DNA_MSX1_NUCLEAR + RNAP_NUCLEAR DNA_MSX1_RNAP_NUCLEAR = DNA_MSX1_NUCLEAR+RNAP_NUCLEAR
0.66846587580812 ; % 261 DNA_MSX1_RNAP_NUCLEAR = DNA_MSX1_NUCLEAR + RNAP_NUCLEAR + MRNA_MSX1_NUCLEAR DNA_MSX1_RNAP_NUCLEAR = DNA_MSX1_NUCLEAR+RNAP_NUCLEAR+MRNA_MSX1_NUCLEAR
0.7972598510247131 ; % 262 MRNA_MSX1_NUCLEAR + NEXPORT_NUCLEAR = MRNA_MSX1_NEXPORT_NUCLEAR MRNA_MSX1_NUCLEAR+NEXPORT_NUCLEAR = MRNA_MSX1_NEXPORT_NUCLEAR
0.07278553699450864 ; % 263 MRNA_MSX1_NEXPORT_NUCLEAR = MRNA_MSX1_NUCLEAR + NEXPORT_NUCLEAR MRNA_MSX1_NEXPORT_NUCLEAR = MRNA_MSX1_NUCLEAR+NEXPORT_NUCLEAR
0.0507943699482335 ; % 264 MRNA_MSX1_NEXPORT_NUCLEAR = MRNA_MSX1_CYTOSOL + NEXPORT_NUCLEAR MRNA_MSX1_NEXPORT_NUCLEAR = MRNA_MSX1_CYTOSOL+NEXPORT_NUCLEAR
0.7155633869701031 ; % 265 MRNA_MSX1_CYTOSOL + RIBOSOME_CYTOSOL = MRNA_MSX1_RIBOSOME_CYTOSOL MRNA_MSX1_CYTOSOL+RIBOSOME_CYTOSOL = MRNA_MSX1_RIBOSOME_CYTOSOL
0.0077881268101971275 ; % 266 MRNA_MSX1_RIBOSOME_CYTOSOL = MRNA_MSX1_CYTOSOL + RIBOSOME_CYTOSOL MRNA_MSX1_RIBOSOME_CYTOSOL = MRNA_MSX1_CYTOSOL+RIBOSOME_CYTOSOL
0.8230884066017365 ; % 267 MRNA_MSX1_RIBOSOME_CYTOSOL = MRNA_MSX1_START_RIBOSOME_CYTOSOL MRNA_MSX1_RIBOSOME_CYTOSOL = MRNA_MSX1_START_RIBOSOME_CYTOSOL
0.7315265602181441 ; % 268 MRNA_MSX1_START_RIBOSOME_CYTOSOL = RIBOSOME_CYTOSOL + MSX1_CYTOSOL + MRNA_MSX1_CYTOSOL MRNA_MSX1_START_RIBOSOME_CYTOSOL = RIBOSOME_CYTOSOL+MSX1_CYTOSOL+MRNA_MSX1_CYTOSOL
0.16427100936968125 ; % 269 MRNA_MSX1_CYTOSOL = [] MRNA_MSX1_CYTOSOL = []
0.3516737269073221 ; % 270 MSX1_CYTOSOL = [] MSX1_CYTOSOL = []
0.12164946607853167 ; % 271 DNA_AP1_NUCLEAR + RNAP_NUCLEAR = DNA_AP1_RNAP_NUCLEAR DNA_AP1_NUCLEAR+RNAP_NUCLEAR = DNA_AP1_RNAP_NUCLEAR
0.016332488772395404 ; % 272 DNA_AP1_RNAP_NUCLEAR = DNA_AP1_NUCLEAR + RNAP_NUCLEAR DNA_AP1_RNAP_NUCLEAR = DNA_AP1_NUCLEAR+RNAP_NUCLEAR
0.5797802270389988 ; % 273 DNA_AP1_RNAP_NUCLEAR = DNA_AP1_NUCLEAR + RNAP_NUCLEAR + MRNA_AP1_NUCLEAR DNA_AP1_RNAP_NUCLEAR = DNA_AP1_NUCLEAR+RNAP_NUCLEAR+MRNA_AP1_NUCLEAR
0.6140689448643276 ; % 274 MRNA_AP1_NUCLEAR + NEXPORT_NUCLEAR = MRNA_AP1_NEXPORT_NUCLEAR MRNA_AP1_NUCLEAR+NEXPORT_NUCLEAR = MRNA_AP1_NEXPORT_NUCLEAR
0.05896060026957333 ; % 275 MRNA_AP1_NEXPORT_NUCLEAR = MRNA_AP1_NUCLEAR + NEXPORT_NUCLEAR MRNA_AP1_NEXPORT_NUCLEAR = MRNA_AP1_NUCLEAR+NEXPORT_NUCLEAR
0.060363627386177954 ; % 276 MRNA_AP1_NEXPORT_NUCLEAR = MRNA_AP1_CYTOSOL + NEXPORT_NUCLEAR MRNA_AP1_NEXPORT_NUCLEAR = MRNA_AP1_CYTOSOL+NEXPORT_NUCLEAR
0.7568961191456829 ; % 277 MRNA_AP1_CYTOSOL + RIBOSOME_CYTOSOL = MRNA_AP1_RIBOSOME_CYTOSOL MRNA_AP1_CYTOSOL+RIBOSOME_CYTOSOL = MRNA_AP1_RIBOSOME_CYTOSOL
0.028386328619030156 ; % 278 MRNA_AP1_RIBOSOME_CYTOSOL = MRNA_AP1_CYTOSOL + RIBOSOME_CYTOSOL MRNA_AP1_RIBOSOME_CYTOSOL = MRNA_AP1_CYTOSOL+RIBOSOME_CYTOSOL
0.3144174844663822 ; % 279 MRNA_AP1_RIBOSOME_CYTOSOL = MRNA_AP1_START_RIBOSOME_CYTOSOL MRNA_AP1_RIBOSOME_CYTOSOL = MRNA_AP1_START_RIBOSOME_CYTOSOL
0.7852322590891565 ; % 280 MRNA_AP1_START_RIBOSOME_CYTOSOL = RIBOSOME_CYTOSOL + AP1_CYTOSOL + MRNA_AP1_CYTOSOL MRNA_AP1_START_RIBOSOME_CYTOSOL = RIBOSOME_CYTOSOL+AP1_CYTOSOL+MRNA_AP1_CYTOSOL

0.3672384371498366 ; % 281 MRNA_AP1_CYTOSOL = [] MRNA_AP1_CYTOSOL = []
0.15831682535404873 ; % 282 AP1_CYTOSOL = [] AP1_CYTOSOL = []
0.0910227505414073 ; % 283 DNA_GPASE_NUCLEAR + RNAP_NUCLEAR = DNA_GPASE_RNAP_NUCLEAR
DNA_GPASE_NUCLEAR+RNAP_NUCLEAR = DNA_GPASE_RNAP_NUCLEAR
0.02092921163145871 ; % 284 DNA_GPASE_RNAP_NUCLEAR = DNA_GPASE_NUCLEAR + RNAP_NUCLEAR
DNA_GPASE_RNAP_NUCLEAR = DNA_GPASE_NUCLEAR+RNAP_NUCLEAR
0.2622330754808647 ; % 285 DNA_GPASE_RNAP_NUCLEAR = DNA_GPASE_NUCLEAR + RNAP_NUCLEAR +
MRNA_GPASE_NUCLEAR DNA_GPASE_RNAP_NUCLEAR = DNA_GPASE_NUCLEAR+RNAP_NUCLEAR+MRNA_GPASE_NUCLEAR
0.315009632721578 ; % 286 MRNA_GPASE_NUCLEAR + NEXPORT_NUCLEAR =
MRNA_GPASE_NEXPORT_NUCLEAR MRNA_GPASE_NUCLEAR+NEXPORT_NUCLEAR = MRNA_GPASE_NEXPORT_NUCLEAR
0.07870993767487008 ; % 287 MRNA_GPASE_NEXPORT_NUCLEAR = MRNA_GPASE_NUCLEAR +
NEXPORT_NUCLEAR MRNA_GPASE_NEXPORT_NUCLEAR = MRNA_GPASE_NUCLEAR+NEXPORT_NUCLEAR
0.06626303322305627 ; % 288 MRNA_GPASE_NEXPORT_NUCLEAR = MRNA_GPASE_CYTOSOL +
NEXPORT_NUCLEAR MRNA_GPASE_NEXPORT_NUCLEAR = MRNA_GPASE_CYTOSOL+NEXPORT_NUCLEAR
0.7107459115002046 ; % 289 MRNA_GPASE_CYTOSOL + RIBOSOME_CYTOSOL =
MRNA_GPASE_RIBOSOME_CYTOSOL MRNA_GPASE_CYTOSOL+RIBOSOME_CYTOSOL = MRNA_GPASE_RIBOSOME_CYTOSOL
0.023423759248070275 ; % 290 MRNA_GPASE_RIBOSOME_CYTOSOL = MRNA_GPASE_CYTOSOL +
RIBOSOME_CYTOSOL MRNA_GPASE_RIBOSOME_CYTOSOL = MRNA_GPASE_CYTOSOL+RIBOSOME_CYTOSOL
0.8982920418747153 ; % 291 MRNA_GPASE_RIBOSOME_CYTOSOL = MRNA_GPASE_START_RIBOSOME_CYTOSOL
MRNA_GPASE_RIBOSOME_CYTOSOL = MRNA_GPASE_START_RIBOSOME_CYTOSOL
0.573362254236925 ; % 292 MRNA_GPASE_START_RIBOSOME_CYTOSOL = RIBOSOME_CYTOSOL +
GPASE_CYTOSOL + MRNA_GPASE_CYTOSOL MRNA_GPASE_START_RIBOSOME_CYTOSOL =
RIBOSOME_CYTOSOL+GPASE_CYTOSOL+MRNA_GPASE_CYTOSOL
0.4221479437146893 ; % 293 MRNA_GPASE_CYTOSOL = [] MRNA_GPASE_CYTOSOL = []
0.45412032716368966 ; % 294 GPASE_CYTOSOL = [] GPASE_CYTOSOL = []
0.9356524043934121 ; % 295 DNA_TCF4_NUCLEAR + RNAP_NUCLEAR = DNA_TCF4_RNAP_NUCLEAR
DNA_TCF4_NUCLEAR+RNAP_NUCLEAR = DNA_TCF4_RNAP_NUCLEAR
0.0896076113196335 ; % 296 DNA_TCF4_RNAP_NUCLEAR = DNA_TCF4_NUCLEAR + RNAP_NUCLEAR
DNA_TCF4_RNAP_NUCLEAR = DNA_TCF4_NUCLEAR+RNAP_NUCLEAR
0.8748319509489678 ; % 297 DNA_TCF4_RNAP_NUCLEAR = DNA_TCF4_NUCLEAR + RNAP_NUCLEAR +
MRNA_TCF4_NUCLEAR DNA_TCF4_RNAP_NUCLEAR = DNA_TCF4_NUCLEAR+RNAP_NUCLEAR+MRNA_TCF4_NUCLEAR
0.8146514210009796 ; % 298 MRNA_TCF4_NUCLEAR + NEXPORT_NUCLEAR = MRNA_TCF4_NEXPORT_NUCLEAR
MRNA_TCF4_NUCLEAR+NEXPORT_NUCLEAR = MRNA_TCF4_NEXPORT_NUCLEAR
0.0675228203944938 ; % 299 MRNA_TCF4_NEXPORT_NUCLEAR = MRNA_TCF4_NUCLEAR + NEXPORT_NUCLEAR
MRNA_TCF4_NEXPORT_NUCLEAR = MRNA_TCF4_NUCLEAR+NEXPORT_NUCLEAR
0.24065253601488534 ; % 300 MRNA_TCF4_NEXPORT_NUCLEAR = MRNA_TCF4_CYTOSOL + NEXPORT_NUCLEAR
MRNA_TCF4_NEXPORT_NUCLEAR = MRNA_TCF4_CYTOSOL+NEXPORT_NUCLEAR
0.3919599812502418 ; % 301 MRNA_TCF4_CYTOSOL + RIBOSOME_CYTOSOL = MRNA_TCF4_RIBOSOME_CYTOSOL
MRNA_TCF4_CYTOSOL+RIBOSOME_CYTOSOL = MRNA_TCF4_RIBOSOME_CYTOSOL
0.04317530808179448 ; % 302 MRNA_TCF4_RIBOSOME_CYTOSOL = MRNA_TCF4_CYTOSOL + RIBOSOME_CYTOSOL
MRNA_TCF4_RIBOSOME_CYTOSOL = MRNA_TCF4_CYTOSOL+RIBOSOME_CYTOSOL
0.8436846857435523 ; % 303 MRNA_TCF4_RIBOSOME_CYTOSOL = MRNA_TCF4_START_RIBOSOME_CYTOSOL
MRNA_TCF4_RIBOSOME_CYTOSOL = MRNA_TCF4_START_RIBOSOME_CYTOSOL
0.9726602996328213 ; % 304 MRNA_TCF4_START_RIBOSOME_CYTOSOL = RIBOSOME_CYTOSOL + TCF4_CYTOSOL
+ MRNA_TCF4_CYTOSOL MRNA_TCF4_START_RIBOSOME_CYTOSOL = RIBOSOME_CYTOSOL+TCF4_CYTOSOL+MRNA_TCF4_CYTOSOL
0.38045011507169896 ; % 305 MRNA_TCF4_CYTOSOL = [] MRNA_TCF4_CYTOSOL = []
0.36632379137665433 ; % 306 TCF4_CYTOSOL = [] TCF4_CYTOSOL = []
0.5140366963266814 ; % 307 DNA_NOTCH1_NUCLEAR + RNAP_NUCLEAR = DNA_NOTCH1_RNAP_NUCLEAR
DNA_NOTCH1_NUCLEAR+RNAP_NUCLEAR = DNA_NOTCH1_RNAP_NUCLEAR
0.01804688184243222 ; % 308 DNA_NOTCH1_RNAP_NUCLEAR = DNA_NOTCH1_NUCLEAR + RNAP_NUCLEAR
DNA_NOTCH1_RNAP_NUCLEAR = DNA_NOTCH1_NUCLEAR+RNAP_NUCLEAR
0.23368361323224796 ; % 309 DNA_NOTCH1_RNAP_NUCLEAR = DNA_NOTCH1_NUCLEAR + RNAP_NUCLEAR +
MRNA_NOTCH1_NUCLEAR DNA_NOTCH1_RNAP_NUCLEAR = DNA_NOTCH1_NUCLEAR+RNAP_NUCLEAR+MRNA_NOTCH1_NUCLEAR
0.4606023259883263 ; % 310 MRNA_NOTCH1_NUCLEAR + NEXPORT_NUCLEAR =
MRNA_NOTCH1_NEXPORT_NUCLEAR MRNA_NOTCH1_NUCLEAR+NEXPORT_NUCLEAR = MRNA_NOTCH1_NEXPORT_NUCLEAR
0.034201503485383124 ; % 311 MRNA_NOTCH1_NEXPORT_NUCLEAR = MRNA_NOTCH1_NUCLEAR +
NEXPORT_NUCLEAR MRNA_NOTCH1_NEXPORT_NUCLEAR = MRNA_NOTCH1_NUCLEAR+NEXPORT_NUCLEAR
0.5292601015675116 ; % 312 MRNA_NOTCH1_NEXPORT_NUCLEAR = MRNA_NOTCH1_CYTOSOL +
NEXPORT_NUCLEAR MRNA_NOTCH1_NEXPORT_NUCLEAR = MRNA_NOTCH1_CYTOSOL+NEXPORT_NUCLEAR
0.32842652869697253 ; % 313 MRNA_NOTCH1_CYTOSOL + RIBOSOME_CYTOSOL =
MRNA_NOTCH1_RIBOSOME_CYTOSOL MRNA_NOTCH1_CYTOSOL+RIBOSOME_CYTOSOL = MRNA_NOTCH1_RIBOSOME_CYTOSOL
0.08344095489628048 ; % 314 MRNA_NOTCH1_RIBOSOME_CYTOSOL = MRNA_NOTCH1_CYTOSOL +
RIBOSOME_CYTOSOL MRNA_NOTCH1_RIBOSOME_CYTOSOL = MRNA_NOTCH1_CYTOSOL+RIBOSOME_CYTOSOL
0.7862863423626023 ; % 315 MRNA_NOTCH1_RIBOSOME_CYTOSOL =
MRNA_NOTCH1_START_RIBOSOME_CYTOSOL MRNA_NOTCH1_RIBOSOME_CYTOSOL = MRNA_NOTCH1_START_RIBOSOME_CYTOSOL
0.08419219281252754 ; % 316 MRNA_NOTCH1_START_RIBOSOME_CYTOSOL = RIBOSOME_CYTOSOL +
NOTCH1_CYTOSOL + MRNA_NOTCH1_CYTOSOL MRNA_NOTCH1_START_RIBOSOME_CYTOSOL =
RIBOSOME_CYTOSOL+NOTCH1_CYTOSOL+MRNA_NOTCH1_CYTOSOL
0.4986726390749206 ; % 317 MRNA_NOTCH1_CYTOSOL = [] MRNA_NOTCH1_CYTOSOL = []
0.12186270634565638 ; % 318 NOTCH1_CYTOSOL = [] NOTCH1_CYTOSOL = []
0.6246903477626534 ; % 319 DNA_SEL1_NUCLEAR + RNAP_NUCLEAR = DNA_SEL1_RNAP_NUCLEAR
DNA_SEL1_NUCLEAR+RNAP_NUCLEAR = DNA_SEL1_RNAP_NUCLEAR
0.0020591225212280963 ; % 320 DNA_SEL1_RNAP_NUCLEAR = DNA_SEL1_NUCLEAR + RNAP_NUCLEAR
DNA_SEL1_RNAP_NUCLEAR = DNA_SEL1_NUCLEAR+RNAP_NUCLEAR
0.7262400058685857 ; % 321 DNA_SEL1_RNAP_NUCLEAR = DNA_SEL1_NUCLEAR + RNAP_NUCLEAR +
MRNA_SEL1_NUCLEAR DNA_SEL1_RNAP_NUCLEAR = DNA_SEL1_NUCLEAR+RNAP_NUCLEAR+MRNA_SEL1_NUCLEAR
0.3117387285750173 ; % 322 MRNA_SEL1_NUCLEAR + NEXPORT_NUCLEAR = MRNA_SEL1_NEXPORT_NUCLEAR
MRNA_SEL1_NUCLEAR+NEXPORT_NUCLEAR = MRNA_SEL1_NEXPORT_NUCLEAR
0.04038546739317104 ; % 323 MRNA_SEL1_NEXPORT_NUCLEAR = MRNA_SEL1_NUCLEAR + NEXPORT_NUCLEAR
MRNA_SEL1_NEXPORT_NUCLEAR = MRNA_SEL1_NUCLEAR+NEXPORT_NUCLEAR
0.7845572573170222 ; % 324 MRNA_SEL1_NEXPORT_NUCLEAR = MRNA_SEL1_CYTOSOL + NEXPORT_NUCLEAR
MRNA_SEL1_NEXPORT_NUCLEAR = MRNA_SEL1_CYTOSOL+NEXPORT_NUCLEAR
0.9864998430957428 ; % 325 MRNA_SEL1_CYTOSOL + RIBOSOME_CYTOSOL = MRNA_SEL1_RIBOSOME_CYTOSOL
MRNA_SEL1_CYTOSOL+RIBOSOME_CYTOSOL = MRNA_SEL1_RIBOSOME_CYTOSOL
0.04261518755259619 ; % 326 MRNA_SEL1_RIBOSOME_CYTOSOL = MRNA_SEL1_CYTOSOL + RIBOSOME_CYTOSOL
MRNA_SEL1_RIBOSOME_CYTOSOL = MRNA_SEL1_CYTOSOL+RIBOSOME_CYTOSOL
0.9409916167570932 ; % 327 MRNA_SEL1_RIBOSOME_CYTOSOL = MRNA_SEL1_START_RIBOSOME_CYTOSOL
MRNA_SEL1_RIBOSOME_CYTOSOL = MRNA_SEL1_START_RIBOSOME_CYTOSOL
0.3191266782287694 ; % 328 MRNA_SEL1_START_RIBOSOME_CYTOSOL = RIBOSOME_CYTOSOL + SEL1_CYTOSOL
+ MRNA_SEL1_CYTOSOL MRNA_SEL1_START_RIBOSOME_CYTOSOL = RIBOSOME_CYTOSOL+SEL1_CYTOSOL+MRNA_SEL1_CYTOSOL
0.19762510204795392 ; % 329 MRNA_SEL1_CYTOSOL = [] MRNA_SEL1_CYTOSOL = []
0.2346698267468269 ; % 330 SEL1_CYTOSOL = [] SEL1_CYTOSOL = []

0.634377546469198 ; % 331 DNA_CSL_NUCLEAR + RNAP_NUCLEAR = DNA_CSL_RNAP_NUCLEAR
DNA_CSL_NUCLEAR+RNAP_NUCLEAR = DNA_CSL_RNAP_NUCLEAR
0.042914159399753495 ; % 332 DNA_CSL_RNAP_NUCLEAR = DNA_CSL_NUCLEAR + RNAP_NUCLEAR
DNA_CSL_RNAP_NUCLEAR = DNA_CSL_NUCLEAR+RNAP_NUCLEAR
0.5300841324139278 ; % 333 DNA_CSL_RNAP_NUCLEAR = DNA_CSL_NUCLEAR + RNAP_NUCLEAR +
MRNA_CSL_NUCLEAR DNA_CSL_RNAP_NUCLEAR = DNA_CSL_NUCLEAR+RNAP_NUCLEAR+MRNA_CSL_NUCLEAR
0.014683872107830176 ; % 334 MRNA_CSL_NUCLEAR + NEXPORT_NUCLEAR = MRNA_CSL_NEXPORT_NUCLEAR
MRNA_CSL_NUCLEAR+NEXPORT_NUCLEAR = MRNA_CSL_NEXPORT_NUCLEAR
0.013296013375077487 ; % 335 MRNA_CSL_NEXPORT_NUCLEAR = MRNA_CSL_NUCLEAR + NEXPORT_NUCLEAR
MRNA_CSL_NEXPORT_NUCLEAR = MRNA_CSL_NUCLEAR+NEXPORT_NUCLEAR
0.22223507158314815 ; % 336 MRNA_CSL_NEXPORT_NUCLEAR = MRNA_CSL_CYTOSOL + NEXPORT_NUCLEAR
MRNA_CSL_NEXPORT_NUCLEAR = MRNA_CSL_CYTOSOL+NEXPORT_NUCLEAR
0.5918893335491664 ; % 337 MRNA_CSL_CYTOSOL + RIBOSOME_CYTOSOL = MRNA_CSL_RIBOSOME_CYTOSOL
MRNA_CSL_CYTOSOL+RIBOSOME_CYTOSOL = MRNA_CSL_RIBOSOME_CYTOSOL
0.06984653096550035 ; % 338 MRNA_CSL_RIBOSOME_CYTOSOL = MRNA_CSL_CYTOSOL + RIBOSOME_CYTOSOL
MRNA_CSL_RIBOSOME_CYTOSOL = MRNA_CSL_CYTOSOL+RIBOSOME_CYTOSOL
0.8657346021215516 ; % 339 MRNA_CSL_RIBOSOME_CYTOSOL = MRNA_CSL_START_RIBOSOME_CYTOSOL
MRNA_CSL_RIBOSOME_CYTOSOL = MRNA_CSL_START_RIBOSOME_CYTOSOL
0.8338480348185241 ; % 340 MRNA_CSL_START_RIBOSOME_CYTOSOL = RIBOSOME_CYTOSOL + CSL_CYTOSOL +
MRNA_CSL_CYTOSOL MRNA_CSL_START_RIBOSOME_CYTOSOL = RIBOSOME_CYTOSOL+CSL_CYTOSOL+MRNA_CSL_CYTOSOL
0.006301815977498182 ; % 341 MRNA_CSL_CYTOSOL = [] MRNA_CSL_CYTOSOL = []
0.41266335390498404 ; % 342 CSL_CYTOSOL = [] CSL_CYTOSOL = []
0.0379748813757681 ; % 343 DNA_RAS_NUCLEAR + RNAP_NUCLEAR = DNA_RAS_RNAP_NUCLEAR
DNA_RAS_NUCLEAR+RNAP_NUCLEAR = DNA_RAS_RNAP_NUCLEAR
0.032095222794560375 ; % 344 DNA_RAS_RNAP_NUCLEAR = DNA_RAS_NUCLEAR + RNAP_NUCLEAR
DNA_RAS_RNAP_NUCLEAR = DNA_RAS_NUCLEAR+RNAP_NUCLEAR
0.6643010011505557 ; % 345 DNA_RAS_RNAP_NUCLEAR = DNA_RAS_NUCLEAR + RNAP_NUCLEAR +
MRNA_RAS_NUCLEAR DNA_RAS_RNAP_NUCLEAR = DNA_RAS_NUCLEAR+RNAP_NUCLEAR+MRNA_RAS_NUCLEAR
0.5202033885570895 ; % 346 MRNA_RAS_NUCLEAR + NEXPORT_NUCLEAR = MRNA_RAS_NEXPORT_NUCLEAR
MRNA_RAS_NUCLEAR+NEXPORT_NUCLEAR = MRNA_RAS_NEXPORT_NUCLEAR
0.09641014622914124 ; % 347 MRNA_RAS_NEXPORT_NUCLEAR = MRNA_RAS_NUCLEAR + NEXPORT_NUCLEAR
MRNA_RAS_NEXPORT_NUCLEAR = MRNA_RAS_NUCLEAR+NEXPORT_NUCLEAR
0.6921609018135282 ; % 348 MRNA_RAS_NEXPORT_NUCLEAR = MRNA_RAS_CYTOSOL + NEXPORT_NUCLEAR
MRNA_RAS_NEXPORT_NUCLEAR = MRNA_RAS_CYTOSOL+NEXPORT_NUCLEAR
0.541831343851341 ; % 349 MRNA_RAS_CYTOSOL + RIBOSOME_CYTOSOL = MRNA_RAS_RIBOSOME_CYTOSOL
MRNA_RAS_CYTOSOL+RIBOSOME_CYTOSOL = MRNA_RAS_RIBOSOME_CYTOSOL
0.09007513402168991 ; % 350 MRNA_RAS_RIBOSOME_CYTOSOL = MRNA_RAS_CYTOSOL + RIBOSOME_CYTOSOL
MRNA_RAS_RIBOSOME_CYTOSOL = MRNA_RAS_CYTOSOL+RIBOSOME_CYTOSOL
0.025912427039287644 ; % 351 MRNA_RAS_RIBOSOME_CYTOSOL = MRNA_RAS_START_RIBOSOME_CYTOSOL
MRNA_RAS_RIBOSOME_CYTOSOL = MRNA_RAS_START_RIBOSOME_CYTOSOL
0.531167134816863 ; % 352 MRNA_RAS_START_RIBOSOME_CYTOSOL = RIBOSOME_CYTOSOL + RAS_CYTOSOL +
MRNA_RAS_CYTOSOL MRNA_RAS_START_RIBOSOME_CYTOSOL = RIBOSOME_CYTOSOL+RAS_CYTOSOL+MRNA_RAS_CYTOSOL
0.3316535214840465 ; % 353 MRNA_RAS_CYTOSOL = [] MRNA_RAS_CYTOSOL = []
0.40584248387188787 ; % 354 RAS_CYTOSOL = [] RAS_CYTOSOL = []
0.12010013059839253 ; % 355 DNA_RAF_NUCLEAR + RNAP_NUCLEAR = DNA_RAF_RNAP_NUCLEAR
DNA_RAF_NUCLEAR+RNAP_NUCLEAR = DNA_RAF_RNAP_NUCLEAR
0.056595720187166756 ; % 356 DNA_RAF_RNAP_NUCLEAR = DNA_RAF_NUCLEAR + RNAP_NUCLEAR
DNA_RAF_RNAP_NUCLEAR = DNA_RAF_NUCLEAR+RNAP_NUCLEAR
0.4610500800545444 ; % 357 DNA_RAF_RNAP_NUCLEAR = DNA_RAF_NUCLEAR + RNAP_NUCLEAR +
MRNA_RAF_NUCLEAR DNA_RAF_RNAP_NUCLEAR = DNA_RAF_NUCLEAR+RNAP_NUCLEAR+MRNA_RAF_NUCLEAR
0.6360695987940695 ; % 358 MRNA_RAF_NUCLEAR + NEXPORT_NUCLEAR = MRNA_RAF_NEXPORT_NUCLEAR
MRNA_RAF_NUCLEAR+NEXPORT_NUCLEAR = MRNA_RAF_NEXPORT_NUCLEAR
0.01904206240201144 ; % 359 MRNA_RAF_NEXPORT_NUCLEAR = MRNA_RAF_NUCLEAR + NEXPORT_NUCLEAR
MRNA_RAF_NEXPORT_NUCLEAR = MRNA_RAF_NUCLEAR+NEXPORT_NUCLEAR
0.8380040293474278 ; % 360 MRNA_RAF_NEXPORT_NUCLEAR = MRNA_RAF_CYTOSOL + NEXPORT_NUCLEAR
MRNA_RAF_NEXPORT_NUCLEAR = MRNA_RAF_CYTOSOL+NEXPORT_NUCLEAR
0.120183198746036 ; % 361 MRNA_RAF_CYTOSOL + RIBOSOME_CYTOSOL = MRNA_RAF_RIBOSOME_CYTOSOL
MRNA_RAF_CYTOSOL+RIBOSOME_CYTOSOL = MRNA_RAF_RIBOSOME_CYTOSOL
0.0578496894050759 ; % 362 MRNA_RAF_RIBOSOME_CYTOSOL = MRNA_RAF_CYTOSOL + RIBOSOME_CYTOSOL
MRNA_RAF_RIBOSOME_CYTOSOL = MRNA_RAF_CYTOSOL+RIBOSOME_CYTOSOL
0.3275788227864429 ; % 363 MRNA_RAF_RIBOSOME_CYTOSOL = MRNA_RAF_START_RIBOSOME_CYTOSOL
MRNA_RAF_RIBOSOME_CYTOSOL = MRNA_RAF_START_RIBOSOME_CYTOSOL
0.8336545649746165 ; % 364 MRNA_RAF_START_RIBOSOME_CYTOSOL = RIBOSOME_CYTOSOL + RAF_CYTOSOL +
MRNA_RAF_CYTOSOL MRNA_RAF_START_RIBOSOME_CYTOSOL = RIBOSOME_CYTOSOL+RAF_CYTOSOL+MRNA_RAF_CYTOSOL
0.08143476565310692 ; % 365 MRNA_RAF_CYTOSOL = [] MRNA_RAF_CYTOSOL = []
0.300601913788011 ; % 366 RAF_CYTOSOL = [] RAF_CYTOSOL = []
0.9638373379979768 ; % 367 DNA_MEK_NUCLEAR + RNAP_NUCLEAR = DNA_MEK_RNAP_NUCLEAR
DNA_MEK_NUCLEAR+RNAP_NUCLEAR = DNA_MEK_RNAP_NUCLEAR
0.005418121344759053 ; % 368 DNA_MEK_RNAP_NUCLEAR = DNA_MEK_NUCLEAR + RNAP_NUCLEAR
DNA_MEK_RNAP_NUCLEAR = DNA_MEK_NUCLEAR+RNAP_NUCLEAR
0.07327517572197062 ; % 369 DNA_MEK_RNAP_NUCLEAR = DNA_MEK_NUCLEAR + RNAP_NUCLEAR +
MRNA_MEK_NUCLEAR DNA_MEK_RNAP_NUCLEAR = DNA_MEK_NUCLEAR+RNAP_NUCLEAR+MRNA_MEK_NUCLEAR
0.8865788640236085 ; % 370 MRNA_MEK_NUCLEAR + NEXPORT_NUCLEAR = MRNA_MEK_NEXPORT_NUCLEAR
MRNA_MEK_NUCLEAR+NEXPORT_NUCLEAR = MRNA_MEK_NEXPORT_NUCLEAR
0.08895523842290107 ; % 371 MRNA_MEK_NEXPORT_NUCLEAR = MRNA_MEK_NUCLEAR + NEXPORT_NUCLEAR
MRNA_MEK_NEXPORT_NUCLEAR = MRNA_MEK_NUCLEAR+NEXPORT_NUCLEAR
0.02147663065288341 ; % 372 MRNA_MEK_NEXPORT_NUCLEAR = MRNA_MEK_CYTOSOL + NEXPORT_NUCLEAR
MRNA_MEK_NEXPORT_NUCLEAR = MRNA_MEK_CYTOSOL+NEXPORT_NUCLEAR
0.9116491837178491 ; % 373 MRNA_MEK_CYTOSOL + RIBOSOME_CYTOSOL = MRNA_MEK_RIBOSOME_CYTOSOL
MRNA_MEK_CYTOSOL+RIBOSOME_CYTOSOL = MRNA_MEK_RIBOSOME_CYTOSOL
0.029813185773912954 ; % 374 MRNA_MEK_RIBOSOME_CYTOSOL = MRNA_MEK_CYTOSOL + RIBOSOME_CYTOSOL
MRNA_MEK_RIBOSOME_CYTOSOL = MRNA_MEK_CYTOSOL+RIBOSOME_CYTOSOL
0.1752854062332635 ; % 375 MRNA_MEK_RIBOSOME_CYTOSOL = MRNA_MEK_START_RIBOSOME_CYTOSOL
MRNA_MEK_RIBOSOME_CYTOSOL = MRNA_MEK_START_RIBOSOME_CYTOSOL
0.6431283489009955 ; % 376 MRNA_MEK_START_RIBOSOME_CYTOSOL = RIBOSOME_CYTOSOL + MEK_CYTOSOL
+ MRNA_MEK_CYTOSOL MRNA_MEK_START_RIBOSOME_CYTOSOL = RIBOSOME_CYTOSOL+MEK_CYTOSOL+MRNA_MEK_CYTOSOL
0.3377432368960164 ; % 377 MRNA_MEK_CYTOSOL = [] MRNA_MEK_CYTOSOL = []
0.40844335314139213 ; % 378 MEK_CYTOSOL = [] MEK_CYTOSOL = []
0.5958345637166482 ; % 379 DNA_ERK_NUCLEAR + RNAP_NUCLEAR = DNA_ERK_RNAP_NUCLEAR
DNA_ERK_NUCLEAR+RNAP_NUCLEAR = DNA_ERK_RNAP_NUCLEAR
0.01936173809170738 ; % 380 DNA_ERK_RNAP_NUCLEAR = DNA_ERK_NUCLEAR + RNAP_NUCLEAR
DNA_ERK_RNAP_NUCLEAR = DNA_ERK_NUCLEAR+RNAP_NUCLEAR

0.6315586058954646 ; % 381 DNA_ERK_RNAP_NUCLEAR = DNA_ERK_NUCLEAR + RNAP_NUCLEAR + MRNA_ERK_NUCLEAR DNA_ERK_RNAP_NUCLEAR = DNA_ERK_NUCLEAR+RNAP_NUCLEAR+MRNA_ERK_NUCLEAR
0.34128892100459995 ; % 382 MRNA_ERK_NUCLEAR + NEXPORT_NUCLEAR = MRNA_ERK_NEXPORT_NUCLEAR MRNA_ERK_NUCLEAR+NEXPORT_NUCLEAR = MRNA_ERK_NEXPORT_NUCLEAR
0.08214751297466921 ; % 383 MRNA_ERK_NEXPORT_NUCLEAR = MRNA_ERK_NUCLEAR + NEXPORT_NUCLEAR MRNA_ERK_NEXPORT_NUCLEAR = MRNA_ERK_NUCLEAR+NEXPORT_NUCLEAR
0.9076433302687152 ; % 384 MRNA_ERK_NEXPORT_NUCLEAR = MRNA_ERK_CYTOSOL + NEXPORT_NUCLEAR MRNA_ERK_NEXPORT_NUCLEAR = MRNA_ERK_CYTOSOL+NEXPORT_NUCLEAR
0.9646687070610893 ; % 385 MRNA_ERK_CYTOSOL + RIBOSOME_CYTOSOL = MRNA_ERK_RIBOSOME_CYTOSOL MRNA_ERK_CYTOSOL+RIBOSOME_CYTOSOL = MRNA_ERK_RIBOSOME_CYTOSOL
0.055610304651031076 ; % 386 MRNA_ERK_RIBOSOME_CYTOSOL = MRNA_ERK_CYTOSOL + RIBOSOME_CYTOSOL MRNA_ERK_RIBOSOME_CYTOSOL = MRNA_ERK_CYTOSOL+RIBOSOME_CYTOSOL
0.46689362455327843 ; % 387 MRNA_ERK_RIBOSOME_CYTOSOL = MRNA_ERK_START_RIBOSOME_CYTOSOL MRNA_ERK_RIBOSOME_CYTOSOL = MRNA_ERK_START_RIBOSOME_CYTOSOL
0.327085742831167 ; % 388 MRNA_ERK_START_RIBOSOME_CYTOSOL = RIBOSOME_CYTOSOL + ERK_CYTOSOL + MRNA_ERK_CYTOSOL MRNA_ERK_START_RIBOSOME_CYTOSOL = RIBOSOME_CYTOSOL+ERK_CYTOSOL+MRNA_ERK_CYTOSOL
0.4336529888094435 ; % 389 MRNA_ERK_CYTOSOL = [] MRNA_ERK_CYTOSOL = []
0.3997036867423405 ; % 390 ERK_CYTOSOL = [] ERK_CYTOSOL = []
0.06974555787036896 ; % 391 DNA_SPK_NUCLEAR + RNAP_NUCLEAR = DNA_SPK_RNAP_NUCLEAR DNA_SPK_NUCLEAR+RNAP_NUCLEAR = DNA_SPK_RNAP_NUCLEAR
0.009486977749145276 ; % 392 DNA_SPK_RNAP_NUCLEAR = DNA_SPK_NUCLEAR + RNAP_NUCLEAR DNA_SPK_RNAP_NUCLEAR = DNA_SPK_NUCLEAR+RNAP_NUCLEAR
0.6289463824352108 ; % 393 DNA_SPK_RNAP_NUCLEAR = DNA_SPK_NUCLEAR + RNAP_NUCLEAR + MRNA_SPK_NUCLEAR DNA_SPK_RNAP_NUCLEAR = DNA_SPK_NUCLEAR+RNAP_NUCLEAR+MRNA_SPK_NUCLEAR
0.9866766139638768 ; % 394 MRNA_SPK_NUCLEAR + NEXPORT_NUCLEAR = MRNA_SPK_NEXPORT_NUCLEAR MRNA_SPK_NUCLEAR+NEXPORT_NUCLEAR = MRNA_SPK_NEXPORT_NUCLEAR
0.020846206245687483 ; % 395 MRNA_SPK_NEXPORT_NUCLEAR = MRNA_SPK_NUCLEAR + NEXPORT_NUCLEAR MRNA_SPK_NEXPORT_NUCLEAR = MRNA_SPK_NUCLEAR+NEXPORT_NUCLEAR
0.8470115492015456 ; % 396 MRNA_SPK_NEXPORT_NUCLEAR = MRNA_SPK_CYTOSOL + NEXPORT_NUCLEAR MRNA_SPK_NEXPORT_NUCLEAR = MRNA_SPK_CYTOSOL+NEXPORT_NUCLEAR
0.37456649477015747 ; % 397 MRNA_SPK_CYTOSOL + RIBOSOME_CYTOSOL = MRNA_SPK_RIBOSOME_CYTOSOL MRNA_SPK_CYTOSOL+RIBOSOME_CYTOSOL = MRNA_SPK_RIBOSOME_CYTOSOL
0.0687075744060228 ; % 398 MRNA_SPK_RIBOSOME_CYTOSOL = MRNA_SPK_CYTOSOL + RIBOSOME_CYTOSOL MRNA_SPK_RIBOSOME_CYTOSOL = MRNA_SPK_CYTOSOL+RIBOSOME_CYTOSOL
0.26287578356347996 ; % 399 MRNA_SPK_RIBOSOME_CYTOSOL = MRNA_SPK_START_RIBOSOME_CYTOSOL MRNA_SPK_RIBOSOME_CYTOSOL = MRNA_SPK_START_RIBOSOME_CYTOSOL
0.2183768047703819 ; % 400 MRNA_SPK_START_RIBOSOME_CYTOSOL = RIBOSOME_CYTOSOL + SPK_CYTOSOL + MRNA_SPK_CYTOSOL MRNA_SPK_START_RIBOSOME_CYTOSOL = RIBOSOME_CYTOSOL+SPK_CYTOSOL+MRNA_SPK_CYTOSOL
0.4245033271132099 ; % 401 MRNA_SPK_CYTOSOL = [] MRNA_SPK_CYTOSOL = []
0.194735614316004 ; % 402 SPK_CYTOSOL = [] SPK_CYTOSOL = []
0.7714322465668915 ; % 403 DNA_PLCG_NUCLEAR + RNAP_NUCLEAR = DNA_PLCG_RNAP_NUCLEAR DNA_PLCG_NUCLEAR+RNAP_NUCLEAR = DNA_PLCG_RNAP_NUCLEAR
0.07481941879993896 ; % 404 DNA_PLCG_RNAP_NUCLEAR = DNA_PLCG_NUCLEAR + RNAP_NUCLEAR DNA_PLCG_RNAP_NUCLEAR = DNA_PLCG_NUCLEAR+RNAP_NUCLEAR
0.04714170778547633 ; % 405 DNA_PLCG_RNAP_NUCLEAR = DNA_PLCG_NUCLEAR + RNAP_NUCLEAR + MRNA_PLCG_NUCLEAR DNA_PLCG_RNAP_NUCLEAR = DNA_PLCG_NUCLEAR+RNAP_NUCLEAR+MRNA_PLCG_NUCLEAR
0.8442982525740508 ; % 406 MRNA_PLCG_NUCLEAR + NEXPORT_NUCLEAR = MRNA_PLCG_NEXPORT_NUCLEAR MRNA_PLCG_NUCLEAR+NEXPORT_NUCLEAR = MRNA_PLCG_NEXPORT_NUCLEAR
0.0945197471611141 ; % 407 MRNA_PLCG_NEXPORT_NUCLEAR = MRNA_PLCG_NUCLEAR + NEXPORT_NUCLEAR MRNA_PLCG_NEXPORT_NUCLEAR = MRNA_PLCG_NUCLEAR+NEXPORT_NUCLEAR
0.6481219362708843 ; % 408 MRNA_PLCG_NEXPORT_NUCLEAR = MRNA_PLCG_CYTOSOL + NEXPORT_NUCLEAR MRNA_PLCG_NEXPORT_NUCLEAR = MRNA_PLCG_CYTOSOL+NEXPORT_NUCLEAR
0.5493859632729868 ; % 409 MRNA_PLCG_CYTOSOL + RIBOSOME_CYTOSOL = MRNA_PLCG_RIBOSOME_CYTOSOL MRNA_PLCG_CYTOSOL+RIBOSOME_CYTOSOL = MRNA_PLCG_RIBOSOME_CYTOSOL
0.012230613771801414 ; % 410 MRNA_PLCG_RIBOSOME_CYTOSOL = MRNA_PLCG_CYTOSOL + RIBOSOME_CYTOSOL MRNA_PLCG_RIBOSOME_CYTOSOL = MRNA_PLCG_CYTOSOL+RIBOSOME_CYTOSOL
0.6615687456036196 ; % 411 MRNA_PLCG_RIBOSOME_CYTOSOL = MRNA_PLCG_START_RIBOSOME_CYTOSOL MRNA_PLCG_RIBOSOME_CYTOSOL = MRNA_PLCG_START_RIBOSOME_CYTOSOL
0.9786752152546898 ; % 412 MRNA_PLCG_START_RIBOSOME_CYTOSOL = RIBOSOME_CYTOSOL + PLCG_CYTOSOL + MRNA_PLCG_CYTOSOL MRNA_PLCG_START_RIBOSOME_CYTOSOL = RIBOSOME_CYTOSOL+PLCG_CYTOSOL+MRNA_PLCG_CYTOSOL
0.06894051672217255 ; % 413 MRNA_PLCG_CYTOSOL = [] MRNA_PLCG_CYTOSOL = []
0.34616801812835685 ; % 414 PLCG_CYTOSOL = [] PLCG_CYTOSOL = []
0.17953992005603714 ; % 415 DNA_RAF_PASE_NUCLEAR + RNAP_NUCLEAR = DNA_RAF_PASE_RNAP_NUCLEAR DNA_RAF_PASE_NUCLEAR+RNAP_NUCLEAR = DNA_RAF_PASE_RNAP_NUCLEAR
0.07690785644593728 ; % 416 DNA_RAF_PASE_RNAP_NUCLEAR = DNA_RAF_PASE_NUCLEAR + RNAP_NUCLEAR DNA_RAF_PASE_RNAP_NUCLEAR = DNA_RAF_PASE_NUCLEAR+RNAP_NUCLEAR
0.6407842658097708 ; % 417 DNA_RAF_PASE_RNAP_NUCLEAR = DNA_RAF_PASE_NUCLEAR + RNAP_NUCLEAR + MRNA_RAF_PASE_NUCLEAR DNA_RAF_PASE_RNAP_NUCLEAR = DNA_RAF_PASE_NUCLEAR+RNAP_NUCLEAR+MRNA_RAF_PASE_NUCLEAR
0.3876685692030051 ; % 418 MRNA_RAF_PASE_NUCLEAR + NEXPORT_NUCLEAR = MRNA_RAF_PASE_NEXPORT_NUCLEAR MRNA_RAF_PASE_NUCLEAR+NEXPORT_NUCLEAR = MRNA_RAF_PASE_NEXPORT_NUCLEAR
0.08935688947114832 ; % 419 MRNA_RAF_PASE_NEXPORT_NUCLEAR = MRNA_RAF_PASE_NUCLEAR + NEXPORT_NUCLEAR MRNA_RAF_PASE_NEXPORT_NUCLEAR = MRNA_RAF_PASE_NUCLEAR+NEXPORT_NUCLEAR
0.011116016170332421 ; % 420 MRNA_RAF_PASE_NEXPORT_NUCLEAR = MRNA_RAF_PASE_CYTOSOL + NEXPORT_NUCLEAR MRNA_RAF_PASE_NEXPORT_NUCLEAR = MRNA_RAF_PASE_CYTOSOL+NEXPORT_NUCLEAR
0.9803966537325371 ; % 421 MRNA_RAF_PASE_CYTOSOL + RIBOSOME_CYTOSOL = MRNA_RAF_PASE_RIBOSOME_CYTOSOL MRNA_RAF_PASE_CYTOSOL+RIBOSOME_CYTOSOL = MRNA_RAF_PASE_RIBOSOME_CYTOSOL
0.06041114457360476 ; % 422 MRNA_RAF_PASE_RIBOSOME_CYTOSOL = MRNA_RAF_PASE_CYTOSOL + RIBOSOME_CYTOSOL MRNA_RAF_PASE_RIBOSOME_CYTOSOL = MRNA_RAF_PASE_CYTOSOL+RIBOSOME_CYTOSOL
0.674538988740089 ; % 423 MRNA_RAF_PASE_RIBOSOME_CYTOSOL = MRNA_RAF_PASE_START_RIBOSOME_CYTOSOL MRNA_RAF_PASE_RIBOSOME_CYTOSOL = MRNA_RAF_PASE_START_RIBOSOME_CYTOSOL
0.2593093208063608 ; % 424 MRNA_RAF_PASE_START_RIBOSOME_CYTOSOL = RIBOSOME_CYTOSOL + RAF_PASE_CYTOSOL + MRNA_RAF_PASE_CYTOSOL MRNA_RAF_PASE_START_RIBOSOME_CYTOSOL = RIBOSOME_CYTOSOL+RAF_PASE_CYTOSOL+MRNA_RAF_PASE_CYTOSOL
0.042719294614261494 ; % 425 MRNA_RAF_PASE_CYTOSOL = [] MRNA_RAF_PASE_CYTOSOL = []
0.22643998500500095 ; % 426 RAF_PASE_CYTOSOL = [] RAF_PASE_CYTOSOL = []
0.7340028046157084 ; % 427 DNA_MEK_PASE_NUCLEAR + RNAP_NUCLEAR = DNA_MEK_PASE_RNAP_NUCLEAR DNA_MEK_PASE_NUCLEAR+RNAP_NUCLEAR = DNA_MEK_PASE_RNAP_NUCLEAR
0.0777762124470637 ; % 428 DNA_MEK_PASE_RNAP_NUCLEAR = DNA_MEK_PASE_NUCLEAR + RNAP_NUCLEAR DNA_MEK_PASE_RNAP_NUCLEAR = DNA_MEK_PASE_NUCLEAR+RNAP_NUCLEAR
0.6686032725605533 ; % 429 DNA_MEK_PASE_RNAP_NUCLEAR = DNA_MEK_PASE_NUCLEAR + RNAP_NUCLEAR + MRNA_MEK_PASE_NUCLEAR DNA_MEK_PASE_RNAP_NUCLEAR = DNA_MEK_PASE_NUCLEAR+RNAP_NUCLEAR+MRNA_MEK_PASE_NUCLEAR
0.8774564776836914 ; % 430 MRNA_MEK_PASE_NUCLEAR + NEXPORT_NUCLEAR = MRNA_MEK_PASE_NEXPORT_NUCLEAR MRNA_MEK_PASE_NUCLEAR+NEXPORT_NUCLEAR = MRNA_MEK_PASE_NEXPORT_NUCLEAR

0.049184086002964526 ; % 431 MRNA_MEK_PASE_NEXPORT_NUCLEAR = MRNA_MEK_PASE_NUCLEAR + NEXPORT_NUCLEAR MRNA_MEK_PASE_NEXPORT_NUCLEAR = MRNA_MEK_PASE_NUCLEAR+NEXPORT_NUCLEAR
0.7882664640933238 ; % 432 MRNA_MEK_PASE_NEXPORT_NUCLEAR = MRNA_MEK_PASE_CYTOSOL + NEXPORT_NUCLEAR MRNA_MEK_PASE_NEXPORT_NUCLEAR = MRNA_MEK_PASE_CYTOSOL+NEXPORT_NUCLEAR
0.8675866423143938 ; % 433 MRNA_MEK_PASE_CYTOSOL + RIBOSOME_CYTOSOL = MRNA_MEK_PASE_RIBOSOME_CYTOSOL MRNA_MEK_PASE_CYTOSOL+RIBOSOME_CYTOSOL = MRNA_MEK_PASE_RIBOSOME_CYTOSOL
0.09359969976851115 ; % 434 MRNA_MEK_PASE_RIBOSOME_CYTOSOL = MRNA_MEK_PASE_CYTOSOL + RIBOSOME_CYTOSOL MRNA_MEK_PASE_RIBOSOME_CYTOSOL = MRNA_MEK_PASE_CYTOSOL+RIBOSOME_CYTOSOL
0.6276638992378004 ; % 435 MRNA_MEK_PASE_RIBOSOME_CYTOSOL = MRNA_MEK_PASE_START_RIBOSOME_CYTOSOL MRNA_MEK_PASE_RIBOSOME_CYTOSOL = MRNA_MEK_PASE_START_RIBOSOME_CYTOSOL
0.3947749345555097 ; % 436 MRNA_MEK_PASE_START_RIBOSOME_CYTOSOL = RIBOSOME_CYTOSOL + MEK_PASE_CYTOSOL + MRNA_MEK_PASE_CYTOSOL MRNA_MEK_PASE_START_RIBOSOME_CYTOSOL = RIBOSOME_CYTOSOL+MEK_PASE_CYTOSOL+MRNA_MEK_PASE_CYTOSOL
0.20055688635541719 ; % 437 MRNA_MEK_PASE_CYTOSOL = [] MRNA_MEK_PASE_CYTOSOL = []
0.2747433862525737 ; % 438 MEK_PASE_CYTOSOL = [] MEK_PASE_CYTOSOL = []
0.35273225617408466 ; % 439 DNA_ERK_PASE_NUCLEAR + RNAP_NUCLEAR = DNA_ERK_PASE_RNAP_NUCLEAR DNA_ERK_PASE_NUCLEAR+RNAP_NUCLEAR = DNA_ERK_PASE_RNAP_NUCLEAR
0.018610043998967575 ; % 440 DNA_ERK_PASE_RNAP_NUCLEAR = DNA_ERK_PASE_NUCLEAR + RNAP_NUCLEAR DNA_ERK_PASE_RNAP_NUCLEAR = DNA_ERK_PASE_NUCLEAR+RNAP_NUCLEAR
0.20105220964797732 ; % 441 DNA_ERK_PASE_RNAP_NUCLEAR = DNA_ERK_PASE_NUCLEAR + RNAP_NUCLEAR + MRNA_ERK_PASE_NUCLEAR DNA_ERK_PASE_RNAP_NUCLEAR = DNA_ERK_PASE_NUCLEAR+RNAP_NUCLEAR+MRNA_ERK_PASE_NUCLEAR
0.02072878527185662 ; % 442 MRNA_ERK_PASE_NUCLEAR + NEXPORT_NUCLEAR = MRNA_ERK_PASE_NEXPORT_NUCLEAR MRNA_ERK_PASE_NUCLEAR+NEXPORT_NUCLEAR = MRNA_ERK_PASE_NEXPORT_NUCLEAR
0.095186141436726 ; % 443 MRNA_ERK_PASE_NEXPORT_NUCLEAR = MRNA_ERK_PASE_NUCLEAR + NEXPORT_NUCLEAR MRNA_ERK_PASE_NEXPORT_NUCLEAR = MRNA_ERK_PASE_NUCLEAR+NEXPORT_NUCLEAR
0.3517126027391111 ; % 444 MRNA_ERK_PASE_NEXPORT_NUCLEAR = MRNA_ERK_PASE_CYTOSOL + NEXPORT_NUCLEAR MRNA_ERK_PASE_NEXPORT_NUCLEAR = MRNA_ERK_PASE_CYTOSOL+NEXPORT_NUCLEAR
0.4475219532227488 ; % 445 MRNA_ERK_PASE_CYTOSOL + RIBOSOME_CYTOSOL = MRNA_ERK_PASE_RIBOSOME_CYTOSOL MRNA_ERK_PASE_CYTOSOL+RIBOSOME_CYTOSOL = MRNA_ERK_PASE_RIBOSOME_CYTOSOL
0.054038232608305675 ; % 446 MRNA_ERK_PASE_RIBOSOME_CYTOSOL = MRNA_ERK_PASE_CYTOSOL + RIBOSOME_CYTOSOL MRNA_ERK_PASE_RIBOSOME_CYTOSOL = MRNA_ERK_PASE_CYTOSOL+RIBOSOME_CYTOSOL
0.8137280411184259 ; % 447 MRNA_ERK_PASE_RIBOSOME_CYTOSOL = MRNA_ERK_PASE_START_RIBOSOME_CYTOSOL MRNA_ERK_PASE_RIBOSOME_CYTOSOL = MRNA_ERK_PASE_START_RIBOSOME_CYTOSOL
0.3847582461286283 ; % 448 MRNA_ERK_PASE_START_RIBOSOME_CYTOSOL = RIBOSOME_CYTOSOL + ERK_PASE_CYTOSOL + MRNA_ERK_PASE_CYTOSOL MRNA_ERK_PASE_START_RIBOSOME_CYTOSOL = RIBOSOME_CYTOSOL+ERK_PASE_CYTOSOL+MRNA_ERK_PASE_CYTOSOL
0.2779916890670523 ; % 449 MRNA_ERK_PASE_CYTOSOL = [] MRNA_ERK_PASE_CYTOSOL = []
0.3568257331691212 ; % 450 ERK_PASE_CYTOSOL = [] ERK_PASE_CYTOSOL = []
0.4931860403925228 ; % 451 DNA_SP1_NUCLEAR + RNAP_NUCLEAR = DNA_SP1_RNAP_NUCLEAR DNA_SP1_NUCLEAR+RNAP_NUCLEAR = DNA_SP1_RNAP_NUCLEAR
0.009194092429826361 ; % 452 DNA_SP1_RNAP_NUCLEAR = DNA_SP1_NUCLEAR + RNAP_NUCLEAR DNA_SP1_RNAP_NUCLEAR = DNA_SP1_NUCLEAR+RNAP_NUCLEAR
0.9436038887775245 ; % 453 DNA_SP1_RNAP_NUCLEAR = DNA_SP1_NUCLEAR + RNAP_NUCLEAR + MRNA_SP1_NUCLEAR DNA_SP1_RNAP_NUCLEAR = DNA_SP1_NUCLEAR+RNAP_NUCLEAR+MRNA_SP1_NUCLEAR
0.8648561577156606 ; % 454 MRNA_SP1_NUCLEAR + NEXPORT_NUCLEAR = MRNA_SP1_NEXPORT_NUCLEAR MRNA_SP1_NUCLEAR+NEXPORT_NUCLEAR = MRNA_SP1_NEXPORT_NUCLEAR
0.08306476598564705 ; % 455 MRNA_SP1_NEXPORT_NUCLEAR = MRNA_SP1_NUCLEAR + NEXPORT_NUCLEAR MRNA_SP1_NEXPORT_NUCLEAR = MRNA_SP1_NUCLEAR+NEXPORT_NUCLEAR
0.6816522571593553 ; % 456 MRNA_SP1_NEXPORT_NUCLEAR = MRNA_SP1_CYTOSOL + NEXPORT_NUCLEAR MRNA_SP1_NEXPORT_NUCLEAR = MRNA_SP1_CYTOSOL+NEXPORT_NUCLEAR
0.33677466224504204 ; % 457 MRNA_SP1_CYTOSOL + RIBOSOME_CYTOSOL = MRNA_SP1_RIBOSOME_CYTOSOL MRNA_SP1_CYTOSOL+RIBOSOME_CYTOSOL = MRNA_SP1_RIBOSOME_CYTOSOL
0.05070013084692987 ; % 458 MRNA_SP1_RIBOSOME_CYTOSOL = MRNA_SP1_CYTOSOL + RIBOSOME_CYTOSOL MRNA_SP1_RIBOSOME_CYTOSOL = MRNA_SP1_CYTOSOL+RIBOSOME_CYTOSOL
0.7912798958193928 ; % 459 MRNA_SP1_RIBOSOME_CYTOSOL = MRNA_SP1_START_RIBOSOME_CYTOSOL MRNA_SP1_RIBOSOME_CYTOSOL = MRNA_SP1_START_RIBOSOME_CYTOSOL
0.15975572183917663 ; % 460 MRNA_SP1_START_RIBOSOME_CYTOSOL = RIBOSOME_CYTOSOL + SP1_CYTOSOL + MRNA_SP1_CYTOSOL MRNA_SP1_START_RIBOSOME_CYTOSOL = RIBOSOME_CYTOSOL+SP1_CYTOSOL+MRNA_SP1_CYTOSOL
0.48623451956903985 ; % 461 MRNA_SP1_CYTOSOL = [] MRNA_SP1_CYTOSOL = []
0.4497961347623364 ; % 462 SP1_CYTOSOL = [] SP1_CYTOSOL = []
0.4807115890142398 ; % 463 DNA_CJUN_NUCLEAR + RNAP_NUCLEAR = DNA_CJUN_RNAP_NUCLEAR DNA_CJUN_NUCLEAR+RNAP_NUCLEAR = DNA_CJUN_RNAP_NUCLEAR
0.012668144947803628 ; % 464 DNA_CJUN_RNAP_NUCLEAR = DNA_CJUN_NUCLEAR + RNAP_NUCLEAR DNA_CJUN_RNAP_NUCLEAR = DNA_CJUN_NUCLEAR+RNAP_NUCLEAR
0.293204739040981 ; % 465 DNA_CJUN_RNAP_NUCLEAR = DNA_CJUN_NUCLEAR + RNAP_NUCLEAR + MRNA_CJUN_NUCLEAR DNA_CJUN_RNAP_NUCLEAR = DNA_CJUN_NUCLEAR+RNAP_NUCLEAR+MRNA_CJUN_NUCLEAR
0.060327747658482256 ; % 466 MRNA_CJUN_NUCLEAR + NEXPORT_NUCLEAR = MRNA_CJUN_NEXPORT_NUCLEAR MRNA_CJUN_NUCLEAR+NEXPORT_NUCLEAR = MRNA_CJUN_NEXPORT_NUCLEAR
0.07441423051525971 ; % 467 MRNA_CJUN_NEXPORT_NUCLEAR = MRNA_CJUN_NUCLEAR + NEXPORT_NUCLEAR MRNA_CJUN_NEXPORT_NUCLEAR = MRNA_CJUN_NUCLEAR+NEXPORT_NUCLEAR
0.3399980159954541 ; % 468 MRNA_CJUN_NEXPORT_NUCLEAR = MRNA_CJUN_CYTOSOL + NEXPORT_NUCLEAR MRNA_CJUN_NEXPORT_NUCLEAR = MRNA_CJUN_CYTOSOL+NEXPORT_NUCLEAR
0.6386920318077327 ; % 469 MRNA_CJUN_CYTOSOL + RIBOSOME_CYTOSOL = MRNA_CJUN_RIBOSOME_CYTOSOL MRNA_CJUN_CYTOSOL+RIBOSOME_CYTOSOL = MRNA_CJUN_RIBOSOME_CYTOSOL
0.0944934042616978 ; % 470 MRNA_CJUN_RIBOSOME_CYTOSOL = MRNA_CJUN_CYTOSOL + RIBOSOME_CYTOSOL MRNA_CJUN_RIBOSOME_CYTOSOL = MRNA_CJUN_CYTOSOL+RIBOSOME_CYTOSOL
0.862189050584555 ; % 471 MRNA_CJUN_RIBOSOME_CYTOSOL = MRNA_CJUN_START_RIBOSOME_CYTOSOL MRNA_CJUN_RIBOSOME_CYTOSOL = MRNA_CJUN_START_RIBOSOME_CYTOSOL
0.08338570246694132 ; % 472 MRNA_CJUN_START_RIBOSOME_CYTOSOL = RIBOSOME_CYTOSOL + CJUN_CYTOSOL + MRNA_CJUN_CYTOSOL MRNA_CJUN_START_RIBOSOME_CYTOSOL = RIBOSOME_CYTOSOL+CJUN_CYTOSOL+MRNA_CJUN_CYTOSOL
0.4984102174361913 ; % 473 MRNA_CJUN_CYTOSOL = [] MRNA_CJUN_CYTOSOL = []
0.3821437651748239 ; % 474 CJUN_CYTOSOL = [] CJUN_CYTOSOL = []
0.11950229219725061 ; % 475 DNA_CPLA2_NUCLEAR + RNAP_NUCLEAR = DNA_CPLA2_RNAP_NUCLEAR DNA_CPLA2_NUCLEAR+RNAP_NUCLEAR = DNA_CPLA2_RNAP_NUCLEAR
0.04659427912596445 ; % 476 DNA_CPLA2_RNAP_NUCLEAR = DNA_CPLA2_NUCLEAR + RNAP_NUCLEAR DNA_CPLA2_RNAP_NUCLEAR = DNA_CPLA2_NUCLEAR+RNAP_NUCLEAR
0.09245693886674011 ; % 477 DNA_CPLA2_RNAP_NUCLEAR = DNA_CPLA2_NUCLEAR + RNAP_NUCLEAR + MRNA_CPLA2_NUCLEAR DNA_CPLA2_RNAP_NUCLEAR = DNA_CPLA2_NUCLEAR+RNAP_NUCLEAR+MRNA_CPLA2_NUCLEAR
0.5691044872307691 ; % 478 MRNA_CPLA2_NUCLEAR + NEXPORT_NUCLEAR = MRNA_CPLA2_NEXPORT_NUCLEAR MRNA_CPLA2_NUCLEAR+NEXPORT_NUCLEAR = MRNA_CPLA2_NEXPORT_NUCLEAR
0.04411282295577443 ; % 479 MRNA_CPLA2_NEXPORT_NUCLEAR = MRNA_CPLA2_NUCLEAR + NEXPORT_NUCLEAR MRNA_CPLA2_NEXPORT_NUCLEAR = MRNA_CPLA2_NUCLEAR+NEXPORT_NUCLEAR

0.2650146912610394 ; % 480 MRNA_CPLA2_NEXPORT_NUCLEAR = MRNA_CPLA2_CYTOSOL + NEXPORT_NUCLEAR
MRNA_CPLA2_NEXPORT_NUCLEAR = MRNA_CPLA2_CYTOSOL+NEXPORT_NUCLEAR
0.9645988610915756 ; % 481 MRNA_CPLA2_CYTOSOL + RIBOSOME_CYTOSOL =
MRNA_CPLA2_RIBOSOME_CYTOSOLMRNA_CPLA2_CYTOSOL+RIBOSOME_CYTOSOL = MRNA_CPLA2_RIBOSOME_CYTOSOL
0.02998612332112296 ; % 482 MRNA_CPLA2_RIBOSOME_CYTOSOL = MRNA_CPLA2_CYTOSOL +
RIBOSOME_CYTOSOL MRNA_CPLA2_RIBOSOME_CYTOSOL = MRNA_CPLA2_CYTOSOL+RIBOSOME_CYTOSOL
0.8667892847075997 ; % 483 MRNA_CPLA2_RIBOSOME_CYTOSOL = MRNA_CPLA2_START_RIBOSOME_CYTOSOL
MRNA_CPLA2_RIBOSOME_CYTOSOL = MRNA_CPLA2_START_RIBOSOME_CYTOSOL
0.8212433953710983 ; % 484 MRNA_CPLA2_START_RIBOSOME_CYTOSOL = RIBOSOME_CYTOSOL +
CPLA2_CYTOSOL + MRNA_CPLA2_CYTOSOL MRNA_CPLA2_START_RIBOSOME_CYTOSOL =
RIBOSOME_CYTOSOL+CPLA2_CYTOSOL+MRNA_CPLA2_CYTOSOL
0.35537245949829016 ; % 485 MRNA_CPLA2_CYTOSOL = [] MRNA_CPLA2_CYTOSOL = []
0.23661960823952843 ; % 486 CPLA2_CYTOSOL = [] CPLA2_CYTOSOL = []
0.3647003144245555 ; % 487 DNA_GSK3B_NUCLEAR + RNAP_NUCLEAR = DNA_GSK3B_RNAP_NUCLEAR
DNA_GSK3B_NUCLEAR+RNAP_NUCLEAR = DNA_GSK3B_RNAP_NUCLEAR
0.07962926662694797 ; % 488 DNA_GSK3B_RNAP_NUCLEAR = DNA_GSK3B_NUCLEAR + RNAP_NUCLEAR
DNA_GSK3B_RNAP_NUCLEAR = DNA_GSK3B_NUCLEAR+RNAP_NUCLEAR
0.2619184226345602 ; % 489 DNA_GSK3B_RNAP_NUCLEAR = DNA_GSK3B_NUCLEAR + RNAP_NUCLEAR +
MRNA_GSK3B_NUCLEAR DNA_GSK3B_RNAP_NUCLEAR = DNA_GSK3B_NUCLEAR+RNAP_NUCLEAR+MRNA_GSK3B_NUCLEAR
0.5562733301414404 ; % 490 MRNA_GSK3B_NUCLEAR + NEXPORT_NUCLEAR =
MRNA_GSK3B_NEXPORT_NUCLEAR MRNA_GSK3B_NUCLEAR+NEXPORT_NUCLEAR = MRNA_GSK3B_NEXPORT_NUCLEAR
0.03742332469136391 ; % 491 MRNA_GSK3B_NEXPORT_NUCLEAR = MRNA_GSK3B_NUCLEAR +
NEXPORT_NUCLEAR MRNA_GSK3B_NEXPORT_NUCLEAR = MRNA_GSK3B_NUCLEAR+NEXPORT_NUCLEAR
0.31171196037930027 ; % 492 MRNA_GSK3B_NEXPORT_NUCLEAR = MRNA_GSK3B_CYTOSOL +
NEXPORT_NUCLEAR MRNA_GSK3B_NEXPORT_NUCLEAR = MRNA_GSK3B_CYTOSOL+NEXPORT_NUCLEAR
0.8925965166597075 ; % 493 MRNA_GSK3B_CYTOSOL + RIBOSOME_CYTOSOL =
MRNA_GSK3B_RIBOSOME_CYTOSOL MRNA_GSK3B_CYTOSOL+RIBOSOME_CYTOSOL = MRNA_GSK3B_RIBOSOME_CYTOSOL
0.086551404520 8902 ; % 494 MRNA_GSK3B_RIBOSOME_CYTOSOL = MRNA_GSK3B_CYTOSOL +
RIBOSOME_CYTOSOL MRNA_GSK3B_RIBOSOME_CYTOSOL = MRNA_GSK3B_CYTOSOL+RIBOSOME_CYTOSOL
0.5106884150317391 ; % 495 MRNA_GSK3B_RIBOSOME_CYTOSOL = MRNA_GSK3B_START_RIBOSOME_CYTOSOL
MRNA_GSK3B_RIBOSOME_CYTOSOL = MRNA_GSK3B_START_RIBOSOME_CYTOSOL
0.10166015018369057 ; % 496 MRNA_GSK3B_START_RIBOSOME_CYTOSOL = RIBOSOME_CYTOSOL +
GSK3B_CYTOSOL + MRNA_GSK3B_CYTOSOL MRNA_GSK3B_START_RIBOSOME_CYTOSOL =
RIBOSOME_CYTOSOL+GSK3B_CYTOSOL+MRNA_GSK3B_CYTOSOL
0.3334351233115636 ; % 497 MRNA_GSK3B_CYTOSOL = [] MRNA_GSK3B_CYTOSOL = []
0.26044860907358003 ; % 498 GSK3B_CYTOSOL = [] GSK3B_CYTOSOL = []
0.06562544528032555 ; % 499 DNA_CK1_NUCLEAR + RNAP_NUCLEAR = DNA_CK1_RNAP_NUCLEAR
DNA_CK1_NUCLEAR+RNAP_NUCLEAR = DNA_CK1_RNAP_NUCLEAR
0.08327177422444106 ; % 500 DNA_CK1_RNAP_NUCLEAR = DNA_CK1_NUCLEAR + RNAP_NUCLEAR
DNA_CK1_RNAP_NUCLEAR = DNA_CK1_NUCLEAR+RNAP_NUCLEAR
0.17547994393011201 ; % 501 DNA_CK1_RNAP_NUCLEAR = DNA_CK1_NUCLEAR + RNAP_NUCLEAR +
MRNA_CK1_NUCLEAR DNA_CK1_RNAP_NUCLEAR = DNA_CK1_NUCLEAR+RNAP_NUCLEAR+MRNA_CK1_NUCLEAR
0.5826477036096949 ; % 502 MRNA_CK1_NUCLEAR + NEXPORT_NUCLEAR = MRNA_CK1_NEXPORT_NUCLEAR
MRNA_CK1_NUCLEAR+NEXPORT_NUCLEAR = MRNA_CK1_NEXPORT_NUCLEAR
0.029265302694367036 ; % 503 MRNA_CK1_NEXPORT_NUCLEAR = MRNA_CK1_NUCLEAR + NEXPORT_NUCLEAR
MRNA_CK1_NEXPORT_NUCLEAR = MRNA_CK1_NUCLEAR+NEXPORT_NUCLEAR
0.6707741084697666 ; % 504 MRNA_CK1_NEXPORT_NUCLEAR = MRNA_CK1_CYTOSOL + NEXPORT_NUCLEAR
MRNA_CK1_NEXPORT_NUCLEAR = MRNA_CK1_CYTOSOL+NEXPORT_NUCLEAR
0.7279411795313381 ; % 505 MRNA_CK1_CYTOSOL + RIBOSOME_CYTOSOL = MRNA_CK1_RIBOSOME_CYTOSOL
MRNA_CK1_CYTOSOL+RIBOSOME_CYTOSOL = MRNA_CK1_RIBOSOME_CYTOSOL
4.4262449354500746E-4 ; % 506 MRNA_CK1_RIBOSOME_CYTOSOL = MRNA_CK1_CYTOSOL + RIBOSOME_CYTOSOL
MRNA_CK1_RIBOSOME_CYTOSOL = MRNA_CK1_CYTOSOL+RIBOSOME_CYTOSOL
0.9812710416782421 ; % 507 MRNA_CK1_RIBOSOME_CYTOSOL = MRNA_CK1_START_RIBOSOME_CYTOSOL
MRNA_CK1_RIBOSOME_CYTOSOL = MRNA_CK1_START_RIBOSOME_CYTOSOL
0.507984281184241 ; % 508 MRNA_CK1_START_RIBOSOME_CYTOSOL = RIBOSOME_CYTOSOL + CK1_CYTOSOL +
MRNA_CK1_CYTOSOL MRNA_CK1_START_RIBOSOME_CYTOSOL = RIBOSOME_CYTOSOL+CK1_CYTOSOL+MRNA_CK1_CYTOSOL
0.31489832219649555 ; % 509 MRNA_CK1_CYTOSOL = [] MRNA_CK1_CYTOSOL = []
0.2235307574673836 ; % 510 CK1_CYTOSOL = [] CK1_CYTOSOL = []
0.49030465720622074 ; % 511 DNA_APC_NUCLEAR + RNAP_NUCLEAR = DNA_APC_RNAP_NUCLEAR
DNA_APC_NUCLEAR+RNAP_NUCLEAR = DNA_APC_RNAP_NUCLEAR
2.0474080100499892E-4 ; % 512 DNA_APC_RNAP_NUCLEAR = DNA_APC_NUCLEAR + RNAP_NUCLEAR
DNA_APC_RNAP_NUCLEAR = DNA_APC_NUCLEAR+RNAP_NUCLEAR
0.29709960949383385 ; % 513 DNA_APC_RNAP_NUCLEAR = DNA_APC_NUCLEAR + RNAP_NUCLEAR +
MRNA_APC_NUCLEAR DNA_APC_RNAP_NUCLEAR = DNA_APC_NUCLEAR+RNAP_NUCLEAR+MRNA_APC_NUCLEAR
0.314592216915593 ; % 514 MRNA_APC_NUCLEAR + NEXPORT_NUCLEAR = MRNA_APC_NEXPORT_NUCLEAR
MRNA_APC_NUCLEAR+NEXPORT_NUCLEAR = MRNA_APC_NEXPORT_NUCLEAR
0.02376649055849528 ; % 515 MRNA_APC_NEXPORT_NUCLEAR = MRNA_APC_NUCLEAR + NEXPORT_NUCLEAR
MRNA_APC_NEXPORT_NUCLEAR = MRNA_APC_NUCLEAR+NEXPORT_NUCLEAR
0.7255667655393416 ; % 516 MRNA_APC_NEXPORT_NUCLEAR = MRNA_APC_CYTOSOL + NEXPORT_NUCLEAR
MRNA_APC_NEXPORT_NUCLEAR = MRNA_APC_CYTOSOL+NEXPORT_NUCLEAR
0.7385551591350612 ; % 517 MRNA_APC_CYTOSOL + RIBOSOME_CYTOSOL = MRNA_APC_RIBOSOME_CYTOSOL
MRNA_APC_CYTOSOL+RIBOSOME_CYTOSOL = MRNA_APC_RIBOSOME_CYTOSOL
0.059797702615856055 ; % 518 MRNA_APC_RIBOSOME_CYTOSOL = MRNA_APC_CYTOSOL + RIBOSOME_CYTOSOL
MRNA_APC_RIBOSOME_CYTOSOL = MRNA_APC_CYTOSOL+RIBOSOME_CYTOSOL
0.6246155414365662 ; % 519 MRNA_APC_RIBOSOME_CYTOSOL = MRNA_APC_START_RIBOSOME_CYTOSOL
MRNA_APC_RIBOSOME_CYTOSOL = MRNA_APC_START_RIBOSOME_CYTOSOL
0.27500941046422145 ; % 520 MRNA_APC_START_RIBOSOME_CYTOSOL = RIBOSOME_CYTOSOL + APC_CYTOSOL +
MRNA_APC_CYTOSOL MRNA_APC_START_RIBOSOME_CYTOSOL = RIBOSOME_CYTOSOL+APC_CYTOSOL+MRNA_APC_CYTOSOL
0.18515766467762163 ; % 521 MRNA_APC_CYTOSOL = [] MRNA_APC_CYTOSOL = []
0.12085623385174765 ; % 522 APC_CYTOSOL = [] APC_CYTOSOL = []
0.510421802242996 ; % 523 DNA_LRP_NUCLEAR + RNAP_NUCLEAR = DNA_LRP_RNAP_NUCLEAR
DNA_LRP_NUCLEAR+RNAP_NUCLEAR = DNA_LRP_RNAP_NUCLEAR
0.014679083664155025 ; % 524 DNA_LRP_RNAP_NUCLEAR = DNA_LRP_NUCLEAR + RNAP_NUCLEAR
DNA_LRP_RNAP_NUCLEAR = DNA_LRP_NUCLEAR+RNAP_NUCLEAR
0.21924488481646065 ; % 525 DNA_LRP_RNAP_NUCLEAR = DNA_LRP_NUCLEAR + RNAP_NUCLEAR +
MRNA_LRP_NUCLEAR DNA_LRP_RNAP_NUCLEAR = DNA_LRP_NUCLEAR+RNAP_NUCLEAR+MRNA_LRP_NUCLEAR
0.7847327629308031 ; % 526 MRNA_LRP_NUCLEAR + NEXPORT_NUCLEAR = MRNA_LRP_NEXPORT_NUCLEAR
MRNA_LRP_NUCLEAR+NEXPORT_NUCLEAR = MRNA_LRP_NEXPORT_NUCLEAR
0.0647201149091531 ; % 527 MRNA_LRP_NEXPORT_NUCLEAR = MRNA_LRP_NUCLEAR + NEXPORT_NUCLEAR
MRNA_LRP_NEXPORT_NUCLEAR = MRNA_LRP_NUCLEAR+NEXPORT_NUCLEAR
0.5522683287502911 ; % 528 MRNA_LRP_NEXPORT_NUCLEAR = MRNA_LRP_CYTOSOL + NEXPORT_NUCLEAR
MRNA_LRP_NEXPORT_NUCLEAR = MRNA_LRP_CYTOSOL+NEXPORT_NUCLEAR

0.31754483859918825 ; % 529 MRNA_LRP_CYTOSOL + RIBOSOME_CYTOSOL = MRNA_LRP_RIBOSOME_CYTOSOL
MRNA_LRP_CYTOSOL+RIBOSOME_CYTOSOL = MRNA_LRP_RIBOSOME_CYTOSOL
0.09693467348583537 ; % 530 MRNA_LRP_RIBOSOME_CYTOSOL = MRNA_LRP_CYTOSOL + RIBOSOME_CYTOSOL
MRNA_LRP_RIBOSOME_CYTOSOL = MRNA_LRP_CYTOSOL+RIBOSOME_CYTOSOL
0.9349922515362089 ; % 531 MRNA_LRP_RIBOSOME_CYTOSOL = MRNA_LRP_START_RIBOSOME_CYTOSOL
MRNA_LRP_RIBOSOME_CYTOSOL = MRNA_LRP_START_RIBOSOME_CYTOSOL
0.11393404609432467 ; % 532 MRNA_LRP_START_RIBOSOME_CYTOSOL = RIBOSOME_CYTOSOL + LRP_CYTOSOL +
MRNA_LRP_CYTOSOL MRNA_LRP_START_RIBOSOME_CYTOSOL = RIBOSOME_CYTOSOL+LRP_CYTOSOL+MRNA_LRP_CYTOSOL
0.24747033094469317 ; % 533 MRNA_LRP_CYTOSOL = [] MRNA_LRP_CYTOSOL = []
0.430300843122893 ; % 534 LRP_CYTOSOL = [] LRP_CYTOSOL = []
0.9635031311666712 ; % 535 DNA_AXIN_NUCLEAR + RNAP_NUCLEAR = DNA_AXIN_RNAP_NUCLEAR
DNA_AXIN_NUCLEAR+RNAP_NUCLEAR = DNA_AXIN_RNAP_NUCLEAR
0.05618570665559345 ; % 536 DNA_AXIN_RNAP_NUCLEAR = DNA_AXIN_NUCLEAR + RNAP_NUCLEAR
DNA_AXIN_RNAP_NUCLEAR = DNA_AXIN_NUCLEAR+RNAP_NUCLEAR
0.8342131283928055 ; % 537 DNA_AXIN_RNAP_NUCLEAR = DNA_AXIN_NUCLEAR + RNAP_NUCLEAR +
MRNA_AXIN_NUCLEAR DNA_AXIN_RNAP_NUCLEAR = DNA_AXIN_NUCLEAR+RNAP_NUCLEAR+MRNA_AXIN_NUCLEAR
0.7733452453183899 ; % 538 MRNA_AXIN_NUCLEAR + NEXPORT_NUCLEAR = MRNA_AXIN_NEXPORT_NUCLEAR
MRNA_AXIN_NUCLEAR+NEXPORT_NUCLEAR = MRNA_AXIN_NEXPORT_NUCLEAR
0.006969517725743069 ; % 539 MRNA_AXIN_NEXPORT_NUCLEAR = MRNA_AXIN_NUCLEAR + NEXPORT_NUCLEAR
MRNA_AXIN_NEXPORT_NUCLEAR = MRNA_AXIN_NUCLEAR+NEXPORT_NUCLEAR
0.1324312104007933 ; % 540 MRNA_AXIN_NEXPORT_NUCLEAR = MRNA_AXIN_CYTOSOL + NEXPORT_NUCLEAR
MRNA_AXIN_NEXPORT_NUCLEAR = MRNA_AXIN_CYTOSOL+NEXPORT_NUCLEAR
0.7716695072829305 ; % 541 MRNA_AXIN_CYTOSOL + RIBOSOME_CYTOSOL = MRNA_AXIN_RIBOSOME_CYTOSOL
MRNA_AXIN_CYTOSOL+RIBOSOME_CYTOSOL = MRNA_AXIN_RIBOSOME_CYTOSOL
0.09653901273074186 ; % 542 MRNA_AXIN_RIBOSOME_CYTOSOL = MRNA_AXIN_CYTOSOL + RIBOSOME_CYTOSOL
MRNA_AXIN_RIBOSOME_CYTOSOL = MRNA_AXIN_CYTOSOL+RIBOSOME_CYTOSOL
0.05930465304785759 ; % 543 MRNA_AXIN_RIBOSOME_CYTOSOL = MRNA_AXIN_START_RIBOSOME_CYTOSOL
MRNA_AXIN_RIBOSOME_CYTOSOL = MRNA_AXIN_START_RIBOSOME_CYTOSOL
0.360743459853207 ; % 544 MRNA_AXIN_START_RIBOSOME_CYTOSOL = RIBOSOME_CYTOSOL + AXIN_CYTOSOL
+ MRNA_AXIN_CYTOSOL MRNA_AXIN_START_RIBOSOME_CYTOSOL = RIBOSOME_CYTOSOL+AXIN_CYTOSOL+MRNA_AXIN_CYTOSOL
0.09811166276676891 ; % 545 MRNA_AXIN_CYTOSOL = [] MRNA_AXIN_CYTOSOL = []
0.3112845280499388 ; % 546 AXIN_CYTOSOL = [] AXIN_CYTOSOL = []
0.8155988724972729 ; % 547 DNA_PKC_NUCLEAR + RNAP_NUCLEAR = DNA_PKC_RNAP_NUCLEAR
DNA_PKC_NUCLEAR+RNAP_NUCLEAR = DNA_PKC_RNAP_NUCLEAR
0.03533850904146805 ; % 548 DNA_PKC_RNAP_NUCLEAR = DNA_PKC_NUCLEAR + RNAP_NUCLEAR
DNA_PKC_RNAP_NUCLEAR = DNA_PKC_NUCLEAR+RNAP_NUCLEAR
0.9290711225232582 ; % 549 DNA_PKC_RNAP_NUCLEAR = DNA_PKC_NUCLEAR + RNAP_NUCLEAR +
MRNA_PKC_NUCLEAR DNA_PKC_RNAP_NUCLEAR = DNA_PKC_NUCLEAR+RNAP_NUCLEAR+MRNA_PKC_NUCLEAR
0.13509991956918632 ; % 550 MRNA_PKC_NUCLEAR + NEXPORT_NUCLEAR = MRNA_PKC_NEXPORT_NUCLEAR
MRNA_PKC_NUCLEAR+NEXPORT_NUCLEAR = MRNA_PKC_NEXPORT_NUCLEAR
0.02501095805030459 ; % 551 MRNA_PKC_NEXPORT_NUCLEAR = MRNA_PKC_NUCLEAR + NEXPORT_NUCLEAR
MRNA_PKC_NEXPORT_NUCLEAR = MRNA_PKC_NUCLEAR+NEXPORT_NUCLEAR
0.4302864838648909 ; % 552 MRNA_PKC_NEXPORT_NUCLEAR = MRNA_PKC_CYTOSOL + NEXPORT_NUCLEAR
MRNA_PKC_NEXPORT_NUCLEAR = MRNA_PKC_CYTOSOL+NEXPORT_NUCLEAR
0.650525440699793 ; % 553 MRNA_PKC_CYTOSOL + RIBOSOME_CYTOSOL = MRNA_PKC_RIBOSOME_CYTOSOL
MRNA_PKC_CYTOSOL+RIBOSOME_CYTOSOL = MRNA_PKC_RIBOSOME_CYTOSOL
0.00445642220896193 ; % 554 MRNA_PKC_RIBOSOME_CYTOSOL = MRNA_PKC_CYTOSOL + RIBOSOME_CYTOSOL
MRNA_PKC_RIBOSOME_CYTOSOL = MRNA_PKC_CYTOSOL+RIBOSOME_CYTOSOL
0.4377811251555236 ; % 555 MRNA_PKC_RIBOSOME_CYTOSOL = MRNA_PKC_START_RIBOSOME_CYTOSOL
MRNA_PKC_RIBOSOME_CYTOSOL = MRNA_PKC_START_RIBOSOME_CYTOSOL
0.2321632009657847 ; % 556 MRNA_PKC_START_RIBOSOME_CYTOSOL = RIBOSOME_CYTOSOL + PKC_CYTOSOL +
MRNA_PKC_CYTOSOL MRNA_PKC_START_RIBOSOME_CYTOSOL = RIBOSOME_CYTOSOL+PKC_CYTOSOL+MRNA_PKC_CYTOSOL
0.34069132484649184 ; % 557 MRNA_PKC_CYTOSOL = [] MRNA_PKC_CYTOSOL = []
0.16346735279768265 ; % 558 PKC_CYTOSOL = [] PKC_CYTOSOL = []
0.3229166179981863 ; % 559 DNA_BTRCP_NUCLEAR + RNAP_NUCLEAR = DNA_BTRCP_RNAP_NUCLEAR
DNA_BTRCP_NUCLEAR+RNAP_NUCLEAR = DNA_BTRCP_RNAP_NUCLEAR
4.4194115107316635E-4 ; % 560 DNA_BTRCP_RNAP_NUCLEAR = DNA_BTRCP_NUCLEAR + RNAP_NUCLEAR
DNA_BTRCP_RNAP_NUCLEAR = DNA_BTRCP_NUCLEAR+RNAP_NUCLEAR
0.023275440330029262 ; % 561 DNA_BTRCP_RNAP_NUCLEAR = DNA_BTRCP_NUCLEAR + RNAP_NUCLEAR +
MRNA_BTRCP_NUCLEAR DNA_BTRCP_RNAP_NUCLEAR = DNA_BTRCP_NUCLEAR+RNAP_NUCLEAR+MRNA_BTRCP_NUCLEAR
0.8694705171201336 ; % 562 MRNA_BTRCP_NUCLEAR + NEXPORT_NUCLEAR =
MRNA_BTRCP_NEXPORT_NUCLEAR MRNA_BTRCP_NUCLEAR+NEXPORT_NUCLEAR = MRNA_BTRCP_NEXPORT_NUCLEAR
0.008250027517403325 ; % 563 MRNA_BTRCP_NEXPORT_NUCLEAR = MRNA_BTRCP_NUCLEAR +
NEXPORT_NUCLEAR MRNA_BTRCP_NEXPORT_NUCLEAR = MRNA_BTRCP_NUCLEAR+NEXPORT_NUCLEAR
0.7888626475217473 ; % 564 MRNA_BTRCP_NEXPORT_NUCLEAR = MRNA_BTRCP_CYTOSOL +
NEXPORT_NUCLEAR MRNA_BTRCP_NEXPORT_NUCLEAR = MRNA_BTRCP_CYTOSOL+NEXPORT_NUCLEAR
0.7157797308819791 ; % 565 MRNA_BTRCP_CYTOSOL + RIBOSOME_CYTOSOL =
MRNA_BTRCP_RIBOSOME_CYTOSOL MRNA_BTRCP_CYTOSOL+RIBOSOME_CYTOSOL = MRNA_BTRCP_RIBOSOME_CYTOSOL
0.009793162363255815 ; % 566 MRNA_BTRCP_RIBOSOME_CYTOSOL = MRNA_BTRCP_CYTOSOL +
RIBOSOME_CYTOSOL MRNA_BTRCP_RIBOSOME_CYTOSOL = MRNA_BTRCP_CYTOSOL+RIBOSOME_CYTOSOL
0.08991983007205961 ; % 567 MRNA_BTRCP_RIBOSOME_CYTOSOL = MRNA_BTRCP_START_RIBOSOME_CYTOSOL
MRNA_BTRCP_RIBOSOME_CYTOSOL = MRNA_BTRCP_START_RIBOSOME_CYTOSOL
0.6813412260114982 ; % 568 MRNA_BTRCP_START_RIBOSOME_CYTOSOL = RIBOSOME_CYTOSOL +
BTRCP_CYTOSOL + MRNA_BTRCP_CYTOSOL MRNA_BTRCP_START_RIBOSOME_CYTOSOL =
RIBOSOME_CYTOSOL+BTRCP_CYTOSOL+MRNA_BTRCP_CYTOSOL
0.4388079400406425 ; % 569 MRNA_BTRCP_CYTOSOL = [] MRNA_BTRCP_CYTOSOL = []
0.35772324066169153 ; % 570 BTRCP_CYTOSOL = [] BTRCP_CYTOSOL = []
0.4348078910304565 ; % 571 DNA_FRIZZLED_NUCLEAR + RNAP_NUCLEAR = DNA_FRIZZLED_RNAP_NUCLEAR
DNA_FRIZZLED_NUCLEAR+RNAP_NUCLEAR = DNA_FRIZZLED_RNAP_NUCLEAR
0.01464236685779179 ; % 572 DNA_FRIZZLED_RNAP_NUCLEAR = DNA_FRIZZLED_NUCLEAR + RNAP_NUCLEAR
DNA_FRIZZLED_RNAP_NUCLEAR = DNA_FRIZZLED_NUCLEAR+RNAP_NUCLEAR
0.7651047235130854 ; % 573 DNA_FRIZZLED_RNAP_NUCLEAR = DNA_FRIZZLED_NUCLEAR + RNAP_NUCLEAR +
MRNA_FRIZZLED_NUCLEAR DNA_FRIZZLED_RNAP_NUCLEAR = DNA_FRIZZLED_NUCLEAR+RNAP_NUCLEAR+MRNA_FRIZZLED_NUCLEAR
0.42549998483725293 ; % 574 MRNA_FRIZZLED_NUCLEAR + NEXPORT_NUCLEAR =
MRNA_FRIZZLED_NEXPORT_NUCLEAR MRNA_FRIZZLED_NUCLEAR+NEXPORT_NUCLEAR = MRNA_FRIZZLED_NEXPORT_NUCLEAR
0.012366653319528098 ; % 575 MRNA_FRIZZLED_NEXPORT_NUCLEAR = MRNA_FRIZZLED_NUCLEAR +
NEXPORT_NUCLEAR MRNA_FRIZZLED_NEXPORT_NUCLEAR = MRNA_FRIZZLED_NUCLEAR+NEXPORT_NUCLEAR
0.6194977281645392 ; % 576 MRNA_FRIZZLED_NEXPORT_NUCLEAR = MRNA_FRIZZLED_CYTOSOL +
NEXPORT_NUCLEAR MRNA_FRIZZLED_NEXPORT_NUCLEAR = MRNA_FRIZZLED_CYTOSOL+NEXPORT_NUCLEAR
0.8031093564446155 ; % 577 MRNA_FRIZZLED_CYTOSOL + RIBOSOME_CYTOSOL =
MRNA_FRIZZLED_RIBOSOME_CYTOSOL MRNA_FRIZZLED_CYTOSOL+RIBOSOME_CYTOSOL = MRNA_FRIZZLED_RIBOSOME_CYTOSOL
0.03288918413272725 ; % 578 MRNA_FRIZZLED_RIBOSOME_CYTOSOL = MRNA_FRIZZLED_CYTOSOL +
RIBOSOME_CYTOSOL MRNA_FRIZZLED_RIBOSOME_CYTOSOL = MRNA_FRIZZLED_CYTOSOL+RIBOSOME_CYTOSOL

0.4111347998387943 ; % 579 MRNA_FRIZZLED_RIBOSOME_CYTOSOL = MRNA_FRIZZLED_START_RIBOSOME_CYTOSOL MRNA_FRIZZLED_RIBOSOME_CYTOSOL = MRNA_FRIZZLED_START_RIBOSOME_CYTOSOL
0.27217337085512006 ; % 580 MRNA_FRIZZLED_START_RIBOSOME_CYTOSOL = RIBOSOME_CYTOSOL + FRIZZLED_CYTOSOL + MRNA_FRIZZLED_CYTOSOL MRNA_FRIZZLED_START_RIBOSOME_CYTOSOL = RIBOSOME_CYTOSOL+FRIZZLED_CYTOSOL+MRNA_FRIZZLED_CYTOSOL
0.4110065904856119 ; % 581 MRNA_FRIZZLED_CYTOSOL = [] MRNA_FRIZZLED_CYTOSOL = []
0.20407381597920576 ; % 582 FRIZZLED_CYTOSOL = [] FRIZZLED_CYTOSOL = []
0.019320407080464452 ; % 583 DNA_BCATENIN_NUCLEAR + RNAP_NUCLEAR = DNA_BCATENIN_RNAP_NUCLEAR DNA_BCATENIN_NUCLEAR+RNAP_NUCLEAR = DNA_BCATENIN_RNAP_NUCLEAR
0.08686332907914834 ; % 584 DNA_BCATENIN_RNAP_NUCLEAR = DNA_BCATENIN_NUCLEAR + RNAP_NUCLEAR DNA_BCATENIN_RNAP_NUCLEAR = DNA_BCATENIN_NUCLEAR+RNAP_NUCLEAR
0.06688561411283234 ; % 585 DNA_BCATENIN_RNAP_NUCLEAR = DNA_BCATENIN_NUCLEAR + RNAP_NUCLEAR + MRNA_BCATENIN_NUCLEAR DNA_BCATENIN_RNAP_NUCLEAR = DNA_BCATENIN_NUCLEAR+RNAP_NUCLEAR+MRNA_BCATENIN_NUCLEAR
0.14274839828791142 ; % 586 MRNA_BCATENIN_NUCLEAR + NEXPORT_NUCLEAR = MRNA_BCATENIN_NEXPORT_NUCLEAR MRNA_BCATENIN_NUCLEAR+NEXPORT_NUCLEAR = MRNA_BCATENIN_NEXPORT_NUCLEAR
0.0031381404465271826 ; % 587 MRNA_BCATENIN_NEXPORT_NUCLEAR = MRNA_BCATENIN_NUCLEAR + NEXPORT_NUCLEAR MRNA_BCATENIN_NEXPORT_NUCLEAR = MRNA_BCATENIN_NUCLEAR+NEXPORT_NUCLEAR
0.09858092459299284 ; % 588 MRNA_BCATENIN_NEXPORT_NUCLEAR = MRNA_BCATENIN_CYTOSOL + NEXPORT_NUCLEAR MRNA_BCATENIN_NEXPORT_NUCLEAR = MRNA_BCATENIN_CYTOSOL+NEXPORT_NUCLEAR
0.09515702779338212 ; % 589 MRNA_BCATENIN_CYTOSOL + RIBOSOME_CYTOSOL = MRNA_BCATENIN_RIBOSOME_CYTOSOL MRNA_BCATENIN_CYTOSOL+RIBOSOME_CYTOSOL = MRNA_BCATENIN_RIBOSOME_CYTOSOL
0.0834676746882981 ; % 590 MRNA_BCATENIN_RIBOSOME_CYTOSOL = MRNA_BCATENIN_CYTOSOL + RIBOSOME_CYTOSOL MRNA_BCATENIN_RIBOSOME_CYTOSOL = MRNA_BCATENIN_CYTOSOL+RIBOSOME_CYTOSOL
0.1707465706967607 ; % 591 MRNA_BCATENIN_RIBOSOME_CYTOSOL = MRNA_BCATENIN_START_RIBOSOME_CYTOSOL MRNA_BCATENIN_RIBOSOME_CYTOSOL = MRNA_BCATENIN_START_RIBOSOME_CYTOSOL
0.636694812630464 ; % 592 MRNA_BCATENIN_START_RIBOSOME_CYTOSOL = RIBOSOME_CYTOSOL + BCATENIN_CYTOSOL + MRNA_BCATENIN_CYTOSOL MRNA_BCATENIN_START_RIBOSOME_CYTOSOL = RIBOSOME_CYTOSOL+BCATENIN_CYTOSOL+MRNA_BCATENIN_CYTOSOL
0.5611635119092241 ; % 593 MRNA_BCATENIN_CYTOSOL = [] MRNA_BCATENIN_CYTOSOL = []
0.5330804424036437 ; % 594 BCATENIN_CYTOSOL = [] BCATENIN_CYTOSOL = []
0.8650435973223999 ; % 595 DNA_DISHEVELLED_NUCLEAR + RNAP_NUCLEAR = DNA_DISHEVELLED_RNAP_NUCLEAR DNA_DISHEVELLED_NUCLEAR+RNAP_NUCLEAR = DNA_DISHEVELLED_RNAP_NUCLEAR
0.044900547505071234 ; % 596 DNA_DISHEVELLED_RNAP_NUCLEAR = DNA_DISHEVELLED_NUCLEAR + RNAP_NUCLEAR DNA_DISHEVELLED_RNAP_NUCLEAR = DNA_DISHEVELLED_NUCLEAR+RNAP_NUCLEAR
0.40932804396189093 ; % 597 DNA_DISHEVELLED_RNAP_NUCLEAR = DNA_DISHEVELLED_NUCLEAR + RNAP_NUCLEAR + MRNA_DISHEVELLED_NUCLEAR DNA_DISHEVELLED_RNAP_NUCLEAR = DNA_DISHEVELLED_NUCLEAR+RNAP_NUCLEAR+MRNA_DISHEVELLED_NUCLEAR
0.8601301182182971 ; % 598 MRNA_DISHEVELLED_NUCLEAR + NEXPORT_NUCLEAR = MRNA_DISHEVELLED_NEXPORT_NUCLEAR MRNA_DISHEVELLED_NUCLEAR+NEXPORT_NUCLEAR = MRNA_DISHEVELLED_NEXPORT_NUCLEAR
0.0428392936701838 ; % 599 MRNA_DISHEVELLED_NEXPORT_NUCLEAR = MRNA_DISHEVELLED_NUCLEAR + NEXPORT_NUCLEAR MRNA_DISHEVELLED_NEXPORT_NUCLEAR = MRNA_DISHEVELLED_NUCLEAR+NEXPORT_NUCLEAR
0.5433688167229335 ; % 600 MRNA_DISHEVELLED_NEXPORT_NUCLEAR = MRNA_DISHEVELLED_CYTOSOL + NEXPORT_NUCLEAR MRNA_DISHEVELLED_NEXPORT_NUCLEAR = MRNA_DISHEVELLED_CYTOSOL+NEXPORT_NUCLEAR
0.26594276518030346 ; % 601 MRNA_DISHEVELLED_CYTOSOL + RIBOSOME_CYTOSOL = MRNA_DISHEVELLED_RIBOSOME_CYTOSOL MRNA_DISHEVELLED_CYTOSOL+RIBOSOME_CYTOSOL = MRNA_DISHEVELLED_RIBOSOME_CYTOSOL
0.05687789676857311 ; % 602 MRNA_DISHEVELLED_RIBOSOME_CYTOSOL = MRNA_DISHEVELLED_CYTOSOL + RIBOSOME_CYTOSOL MRNA_DISHEVELLED_RIBOSOME_CYTOSOL = MRNA_DISHEVELLED_CYTOSOL+RIBOSOME_CYTOSOL
0.6959057779444638 ; % 603 MRNA_DISHEVELLED_RIBOSOME_CYTOSOL = MRNA_DISHEVELLED_START_RIBOSOME_CYTOSOL MRNA_DISHEVELLED_RIBOSOME_CYTOSOL = MRNA_DISHEVELLED_START_RIBOSOME_CYTOSOL
0.44421795554638155 ; % 604 MRNA_DISHEVELLED_START_RIBOSOME_CYTOSOL = RIBOSOME_CYTOSOL + DISHEVELLED_CYTOSOL + MRNA_DISHEVELLED_CYTOSOL MRNA_DISHEVELLED_START_RIBOSOME_CYTOSOL = RIBOSOME_CYTOSOL+DISHEVELLED_CYTOSOL+MRNA_DISHEVELLED_CYTOSOL
0.010957434341422212 ; % 605 MRNA_DISHEVELLED_CYTOSOL = [] MRNA_DISHEVELLED_CYTOSOL = []
0.13838453876286722 ; % 606 DISHEVELLED_CYTOSOL = [] DISHEVELLED_CYTOSOL = []
0.001 ; % 607 DNA_ECADHERIN_NUCLEAR + RNAP_NUCLEAR = DNA_ECADHERIN_RNAP_NUCLEAR DNA_ECADHERIN_NUCLEAR+RNAP_NUCLEAR = DNA_ECADHERIN_RNAP_NUCLEAR
0.0016103325301803206 ; % 608 DNA_ECADHERIN_RNAP_NUCLEAR = DNA_ECADHERIN_NUCLEAR + RNAP_NUCLEAR DNA_ECADHERIN_RNAP_NUCLEAR = DNA_ECADHERIN_NUCLEAR+RNAP_NUCLEAR
0.9343147628317134 ; % 609 DNA_ECADHERIN_RNAP_NUCLEAR = DNA_ECADHERIN_NUCLEAR + RNAP_NUCLEAR + MRNA_ECADHERIN_NUCLEAR DNA_ECADHERIN_RNAP_NUCLEAR = DNA_ECADHERIN_NUCLEAR+RNAP_NUCLEAR+MRNA_ECADHERIN_NUCLEAR
0.729815026780462 ; % 610 MRNA_ECADHERIN_NUCLEAR + NEXPORT_NUCLEAR = MRNA_ECADHERIN_NEXPORT_NUCLEAR MRNA_ECADHERIN_NUCLEAR+NEXPORT_NUCLEAR = MRNA_ECADHERIN_NEXPORT_NUCLEAR
0.0029983174011490355 ; % 611 MRNA_ECADHERIN_NEXPORT_NUCLEAR = MRNA_ECADHERIN_NUCLEAR + NEXPORT_NUCLEAR MRNA_ECADHERIN_NEXPORT_NUCLEAR = MRNA_ECADHERIN_NUCLEAR+NEXPORT_NUCLEAR
0.71547797619050744 ; % 612 MRNA_ECADHERIN_NEXPORT_NUCLEAR = MRNA_ECADHERIN_CYTOSOL + NEXPORT_NUCLEAR MRNA_ECADHERIN_NEXPORT_NUCLEAR = MRNA_ECADHERIN_CYTOSOL+NEXPORT_NUCLEAR
0.7168387993532837 ; % 613 MRNA_ECADHERIN_CYTOSOL + RIBOSOME_CYTOSOL = MRNA_ECADHERIN_RIBOSOME_CYTOSOL MRNA_ECADHERIN_CYTOSOL+RIBOSOME_CYTOSOL = MRNA_ECADHERIN_RIBOSOME_CYTOSOL
0.0011836445065569379 ; % 614 MRNA_ECADHERIN_RIBOSOME_CYTOSOL = MRNA_ECADHERIN_CYTOSOL + RIBOSOME_CYTOSOL MRNA_ECADHERIN_RIBOSOME_CYTOSOL = MRNA_ECADHERIN_CYTOSOL+RIBOSOME_CYTOSOL
0.9887339825831304 ; % 615 MRNA_ECADHERIN_RIBOSOME_CYTOSOL = MRNA_ECADHERIN_START_RIBOSOME_CYTOSOL MRNA_ECADHERIN_RIBOSOME_CYTOSOL = MRNA_ECADHERIN_START_RIBOSOME_CYTOSOL
0.939049427939938 ; % 616 MRNA_ECADHERIN_START_RIBOSOME_CYTOSOL = RIBOSOME_CYTOSOL + ECADHERIN_CYTOSOL + MRNA_ECADHERIN_CYTOSOL MRNA_ECADHERIN_START_RIBOSOME_CYTOSOL = RIBOSOME_CYTOSOL+ECADHERIN_CYTOSOL+MRNA_ECADHERIN_CYTOSOL
0.0189974731661657 ; % 617 MRNA_ECADHERIN_CYTOSOL = [] MRNA_ECADHERIN_CYTOSOL = []
0.01865222458534326 ; % 618 ECADHERIN_CYTOSOL = [] ECADHERIN_CYTOSOL = []
0.48018516661682487 ; % 619 DNA_VECADHERIN_NUCLEAR + RNAP_NUCLEAR = DNA_VECADHERIN_RNAP_NUCLEAR DNA_VECADHERIN_NUCLEAR+RNAP_NUCLEAR = DNA_VECADHERIN_RNAP_NUCLEAR
0.07999472940198185 ; % 620 DNA_VECADHERIN_RNAP_NUCLEAR = DNA_VECADHERIN_NUCLEAR + RNAP_NUCLEAR DNA_VECADHERIN_RNAP_NUCLEAR = DNA_VECADHERIN_NUCLEAR+RNAP_NUCLEAR
0.9008432220651773 ; % 621 DNA_VECADHERIN_RNAP_NUCLEAR = DNA_VECADHERIN_NUCLEAR + RNAP_NUCLEAR + MRNA_VECADHERIN_NUCLEAR DNA_VECADHERIN_RNAP_NUCLEAR = DNA_VECADHERIN_NUCLEAR+RNAP_NUCLEAR+MRNA_VECADHERIN_NUCLEAR
0.5860817849523475 ; % 622 MRNA_VECADHERIN_NUCLEAR + NEXPORT_NUCLEAR = MRNA_VECADHERIN_NEXPORT_NUCLEAR MRNA_VECADHERIN_NUCLEAR+NEXPORT_NUCLEAR = MRNA_VECADHERIN_NEXPORT_NUCLEAR
0.010685549893641856 ; % 623 MRNA_VECADHERIN_NEXPORT_NUCLEAR = MRNA_VECADHERIN_NUCLEAR + NEXPORT_NUCLEAR MRNA_VECADHERIN_NEXPORT_NUCLEAR = MRNA_VECADHERIN_NUCLEAR+NEXPORT_NUCLEAR
0.4961642916747795 ; % 624 MRNA_VECADHERIN_NEXPORT_NUCLEAR = MRNA_VECADHERIN_CYTOSOL + NEXPORT_NUCLEAR MRNA_VECADHERIN_NEXPORT_NUCLEAR = MRNA_VECADHERIN_CYTOSOL+NEXPORT_NUCLEAR
0.6743154062538891 ; % 625 MRNA_VECADHERIN_CYTOSOL + RIBOSOME_CYTOSOL = MRNA_VECADHERIN_RIBOSOME_CYTOSOL MRNA_VECADHERIN_CYTOSOL+RIBOSOME_CYTOSOL = MRNA_VECADHERIN_RIBOSOME_CYTOSOL

0.020435370741104433 ; % 626 MRNA_VECADHERIN_RIBOSOME_CYTOSOL = MRNA_VECADHERIN_CYTOSOL + RIBOSOME_CYTOSOL MRNA_VECADHERIN_RIBOSOME_CYTOSOL = MRNA_VECADHERIN_CYTOSOL+RIBOSOME_CYTOSOL
0.7554106836416242 ; % 627 MRNA_VECADHERIN_RIBOSOME_CYTOSOL = MRNA_VECADHERIN_START_RIBOSOME_CYTOSOL MRNA_VECADHERIN_RIBOSOME_CYTOSOL = MRNA_VECADHERIN_START_RIBOSOME_CYTOSOL
0.5442208822246483 ; % 628 MRNA_VECADHERIN_START_RIBOSOME_CYTOSOL = RIBOSOME_CYTOSOL + VECADHERIN_CYTOSOL + MRNA_VECADHERIN_CYTOSOL MRNA_VECADHERIN_START_RIBOSOME_CYTOSOL = RIBOSOME_CYTOSOL+VECADHERIN_CYTOSOL+MRNA_VECADHERIN_CYTOSOL
0.3334622739594081 ; % 629 MRNA_VECADHERIN_CYTOSOL = [] MRNA_VECADHERIN_CYTOSOL = []
0.26712101370744057 ; % 630 VECADHERIN_CYTOSOL = [] VECADHERIN_CYTOSOL = []
0.1722294691693581 ; % 631 DNA_PECAM1_NUCLEAR + RNAP_NUCLEAR = DNA_PECAM1_RNAP_NUCLEAR DNA_PECAM1_NUCLEAR+RNAP_NUCLEAR = DNA_PECAM1_RNAP_NUCLEAR
0.07798379629722597 ; % 632 DNA_PECAM1_RNAP_NUCLEAR = DNA_PECAM1_NUCLEAR + RNAP_NUCLEAR DNA_PECAM1_RNAP_NUCLEAR = DNA_PECAM1_NUCLEAR+RNAP_NUCLEAR
0.22643374256599802 ; % 633 DNA_PECAM1_RNAP_NUCLEAR = DNA_PECAM1_NUCLEAR + RNAP_NUCLEAR + MRNA_PECAM1_NUCLEAR DNA_PECAM1_RNAP_NUCLEAR = DNA_PECAM1_NUCLEAR+RNAP_NUCLEAR+MRNA_PECAM1_NUCLEAR
0.8964840105347499 ; % 634 MRNA_PECAM1_NUCLEAR + NEXPORT_NUCLEAR = MRNA_PECAM1_NEXPORT_NUCLEAR MRNA_PECAM1_NUCLEAR+NEXPORT_NUCLEAR = MRNA_PECAM1_NEXPORT_NUCLEAR
0.03433067584415483 ; % 635 MRNA_PECAM1_NEXPORT_NUCLEAR = MRNA_PECAM1_NUCLEAR + NEXPORT_NUCLEAR MRNA_PECAM1_NEXPORT_NUCLEAR = MRNA_PECAM1_NUCLEAR+NEXPORT_NUCLEAR
0.19175691791162586 ; % 636 MRNA_PECAM1_NEXPORT_NUCLEAR = MRNA_PECAM1_CYTOSOL + NEXPORT_NUCLEAR MRNA_PECAM1_NEXPORT_NUCLEAR = MRNA_PECAM1_CYTOSOL+NEXPORT_NUCLEAR
0.9985788506930559 ; % 637 MRNA_PECAM1_CYTOSOL + RIBOSOME_CYTOSOL = MRNA_PECAM1_RIBOSOME_CYTOSOL MRNA_PECAM1_CYTOSOL+RIBOSOME_CYTOSOL = MRNA_PECAM1_RIBOSOME_CYTOSOL
4.2389667377137343E-4 ; % 638 MRNA_PECAM1_RIBOSOME_CYTOSOL = MRNA_PECAM1_CYTOSOL + RIBOSOME_CYTOSOL MRNA_PECAM1_RIBOSOME_CYTOSOL = MRNA_PECAM1_CYTOSOL+RIBOSOME_CYTOSOL
0.02613113753808549 ; % 639 MRNA_PECAM1_RIBOSOME_CYTOSOL = MRNA_PECAM1_START_RIBOSOME_CYTOSOL MRNA_PECAM1_RIBOSOME_CYTOSOL = MRNA_PECAM1_START_RIBOSOME_CYTOSOL
0.3132215628152324 ; % 640 MRNA_PECAM1_START_RIBOSOME_CYTOSOL = RIBOSOME_CYTOSOL + PECAM1_CYTOSOL + MRNA_PECAM1_CYTOSOL MRNA_PECAM1_START_RIBOSOME_CYTOSOL = RIBOSOME_CYTOSOL+PECAM1_CYTOSOL+MRNA_PECAM1_CYTOSOL
0.3317653953214866 ; % 641 MRNA_PECAM1_CYTOSOL = [] MRNA_PECAM1_CYTOSOL = []
0.28626257073631317 ; % 642 PECAM1_CYTOSOL = [] PECAM1_CYTOSOL = []
0.3365219212523929 ; % 643 DNA_AKT_NUCLEAR + RNAP_NUCLEAR = DNA_AKT_RNAP_NUCLEAR DNA_AKT_NUCLEAR+RNAP_NUCLEAR = DNA_AKT_RNAP_NUCLEAR
0.007998689235941037 ; % 644 DNA_AKT_RNAP_NUCLEAR = DNA_AKT_NUCLEAR + RNAP_NUCLEAR DNA_AKT_RNAP_NUCLEAR = DNA_AKT_NUCLEAR+RNAP_NUCLEAR
0.9667732759570121 ; % 645 DNA_AKT_RNAP_NUCLEAR = DNA_AKT_NUCLEAR + RNAP_NUCLEAR + MRNA_AKT_NUCLEAR DNA_AKT_RNAP_NUCLEAR = DNA_AKT_NUCLEAR+RNAP_NUCLEAR+MRNA_AKT_NUCLEAR
0.5448946068658 56 ; % 646 MRNA_AKT_NUCLEAR + NEXPORT_NUCLEAR = MRNA_AKT_NEXPORT_NUCLEAR MRNA_AKT_NUCLEAR+NEXPORT_NUCLEAR = MRNA_AKT_NEXPORT_NUCLEAR
0.027485532884027265 ; % 647 MRNA_AKT_NEXPORT_NUCLEAR = MRNA_AKT_NUCLEAR + NEXPORT_NUCLEAR MRNA_AKT_NEXPORT_NUCLEAR = MRNA_AKT_NUCLEAR+NEXPORT_NUCLEAR
0.16062266371714906 ; % 648 MRNA_AKT_NEXPORT_NUCLEAR = MRNA_AKT_CYTOSOL + NEXPORT_NUCLEAR MRNA_AKT_NEXPORT_NUCLEAR = MRNA_AKT_CYTOSOL+NEXPORT_NUCLEAR
0.4156424014309258 ; % 649 MRNA_AKT_CYTOSOL + RIBOSOME_CYTOSOL = MRNA_AKT_RIBOSOME_CYTOSOL MRNA_AKT_CYTOSOL+RIBOSOME_CYTOSOL = MRNA_AKT_RIBOSOME_CYTOSOL
0.030883685285236186 ; % 650 MRNA_AKT_RIBOSOME_CYTOSOL = MRNA_AKT_CYTOSOL + RIBOSOME_CYTOSOL MRNA_AKT_RIBOSOME_CYTOSOL = MRNA_AKT_CYTOSOL+RIBOSOME_CYTOSOL
0.21380512568558685 ; % 651 MRNA_AKT_RIBOSOME_CYTOSOL = MRNA_AKT_START_RIBOSOME_CYTOSOL MRNA_AKT_RIBOSOME_CYTOSOL = MRNA_AKT_START_RIBOSOME_CYTOSOL
0.7228873643748891 ; % 652 MRNA_AKT_START_RIBOSOME_CYTOSOL = RIBOSOME_CYTOSOL + AKT_CYTOSOL + MRNA_AKT_CYTOSOL MRNA_AKT_START_RIBOSOME_CYTOSOL = RIBOSOME_CYTOSOL+AKT_CYTOSOL+MRNA_AKT_CYTOSOL
0.05179729595704907 ; % 653 MRNA_AKT_CYTOSOL = [] MRNA_AKT_CYTOSOL = []
0.15376695582387934 ; % 654 AKT_CYTOSOL = [] AKT_CYTOSOL = []
0.6636683871535423 ; % 655 DNA_PI3K_NUCLEAR + RNAP_NUCLEAR = DNA_PI3K_RNAP_NUCLEAR DNA_PI3K_NUCLEAR+RNAP_NUCLEAR = DNA_PI3K_RNAP_NUCLEAR
0.09642061807909302 ; % 656 DNA_PI3K_RNAP_NUCLEAR = DNA_PI3K_NUCLEAR + RNAP_NUCLEAR DNA_PI3K_RNAP_NUCLEAR = DNA_PI3K_NUCLEAR+RNAP_NUCLEAR
0.8713400820847678 ; % 657 DNA_PI3K_RNAP_NUCLEAR = DNA_PI3K_NUCLEAR + RNAP_NUCLEAR + MRNA_PI3K_NUCLEAR DNA_PI3K_RNAP_NUCLEAR = DNA_PI3K_NUCLEAR+RNAP_NUCLEAR+MRNA_PI3K_NUCLEAR
0.39797364821783254 ; % 658 MRNA_PI3K_NUCLEAR + NEXPORT_NUCLEAR = MRNA_PI3K_NEXPORT_NUCLEAR MRNA_PI3K_NUCLEAR+NEXPORT_NUCLEAR = MRNA_PI3K_NEXPORT_NUCLEAR
0.008154200428734538 ; % 659 MRNA_PI3K_NEXPORT_NUCLEAR = MRNA_PI3K_NUCLEAR + NEXPORT_NUCLEAR MRNA_PI3K_NEXPORT_NUCLEAR = MRNA_PI3K_NUCLEAR+NEXPORT_NUCLEAR
0.5047940764198364 ; % 660 MRNA_PI3K_NEXPORT_NUCLEAR = MRNA_PI3K_CYTOSOL + NEXPORT_NUCLEAR MRNA_PI3K_NEXPORT_NUCLEAR = MRNA_PI3K_CYTOSOL+NEXPORT_NUCLEAR
0.41729907209083983 ; % 661 MRNA_PI3K_CYTOSOL + RIBOSOME_CYTOSOL = MRNA_PI3K_RIBOSOME_CYTOSOL MRNA_PI3K_CYTOSOL+RIBOSOME_CYTOSOL = MRNA_PI3K_RIBOSOME_CYTOSOL
0.01540597827480057 ; % 662 MRNA_PI3K_RIBOSOME_CYTOSOL = MRNA_PI3K_CYTOSOL + RIBOSOME_CYTOSOL MRNA_PI3K_RIBOSOME_CYTOSOL = MRNA_PI3K_CYTOSOL+RIBOSOME_CYTOSOL
0.09706140892433335 ; % 663 MRNA_PI3K_RIBOSOME_CYTOSOL = MRNA_PI3K_START_RIBOSOME_CYTOSOL MRNA_PI3K_RIBOSOME_CYTOSOL = MRNA_PI3K_START_RIBOSOME_CYTOSOL
0.9187229860562889 ; % 664 MRNA_PI3K_START_RIBOSOME_CYTOSOL = RIBOSOME_CYTOSOL + PI3K_CYTOSOL + MRNA_PI3K_CYTOSOL MRNA_PI3K_START_RIBOSOME_CYTOSOL = RIBOSOME_CYTOSOL+PI3K_CYTOSOL+MRNA_PI3K_CYTOSOL
0.014704045424866252 ; % 665 MRNA_PI3K_CYTOSOL = [] MRNA_PI3K_CYTOSOL = []
0.0341202560542474 ; % 666 PI3K_CYTOSOL = [] PI3K_CYTOSOL = []
0.2901077962112357 ; % 667 DNA_PTEN_NUCLEAR + RNAP_NUCLEAR = DNA_PTEN_RNAP_NUCLEAR DNA_PTEN_NUCLEAR+RNAP_NUCLEAR = DNA_PTEN_RNAP_NUCLEAR
0.026124027449041888 ; % 668 DNA_PTEN_RNAP_NUCLEAR = DNA_PTEN_NUCLEAR + RNAP_NUCLEAR DNA_PTEN_RNAP_NUCLEAR = DNA_PTEN_NUCLEAR+RNAP_NUCLEAR
0.32612468733598443 ; % 669 DNA_PTEN_RNAP_NUCLEAR = DNA_PTEN_NUCLEAR + RNAP_NUCLEAR + MRNA_PTEN_NUCLEAR DNA_PTEN_RNAP_NUCLEAR = DNA_PTEN_NUCLEAR+RNAP_NUCLEAR+MRNA_PTEN_NUCLEAR
0.2663101499864593 ; % 670 MRNA_PTEN_NUCLEAR + NEXPORT_NUCLEAR = MRNA_PTEN_NEXPORT_NUCLEAR MRNA_PTEN_NUCLEAR+NEXPORT_NUCLEAR = MRNA_PTEN_NEXPORT_NUCLEAR
0.057483581743710446 ; % 671 MRNA_PTEN_NEXPORT_NUCLEAR = MRNA_PTEN_NUCLEAR + NEXPORT_NUCLEAR MRNA_PTEN_NEXPORT_NUCLEAR = MRNA_PTEN_NUCLEAR+NEXPORT_NUCLEAR
0.43990294803349783 ; % 672 MRNA_PTEN_NEXPORT_NUCLEAR = MRNA_PTEN_CYTOSOL + NEXPORT_NUCLEAR MRNA_PTEN_NEXPORT_NUCLEAR = MRNA_PTEN_CYTOSOL+NEXPORT_NUCLEAR
0.7665484066776502 ; % 673 MRNA_PTEN_CYTOSOL + RIBOSOME_CYTOSOL = MRNA_PTEN_RIBOSOME_CYTOSOL MRNA_PTEN_CYTOSOL+RIBOSOME_CYTOSOL = MRNA_PTEN_RIBOSOME_CYTOSOL
0.0917421291214164 ; % 674 MRNA_PTEN_RIBOSOME_CYTOSOL = MRNA_PTEN_CYTOSOL + RIBOSOME_CYTOSOL MRNA_PTEN_RIBOSOME_CYTOSOL = MRNA_PTEN_CYTOSOL+RIBOSOME_CYTOSOL

0.31956862174545586 ; % 675 MRNA_PTEN_RIBOSOME_CYTOSOL = MRNA_PTEN_START_RIBOSOME_CYTOSOL MRNA_PTEN_RIBOSOME_CYTOSOL = MRNA_PTEN_START_RIBOSOME_CYTOSOL
0.6726000482770923 ; % 676 MRNA_PTEN_START_RIBOSOME_CYTOSOL = RIBOSOME_CYTOSOL + PTEN_CYTOSOL + MRNA_PTEN_CYTOSOL MRNA_PTEN_START_RIBOSOME_CYTOSOL = RIBOSOME_CYTOSOL+PTEN_CYTOSOL+MRNA_PTEN_CYTOSOL
0.3589483582792025 ; % 677 MRNA_PTEN_CYTOSOL = [] MRNA_PTEN_CYTOSOL = []
0.49748881324214 ; % 678 PTEN_CYTOSOL = [] PTEN_CYTOSOL = []
0.5635529850701433 ; % 679 DNA_PDK1_NUCLEAR + RNAP_NUCLEAR = DNA_PDK1_RNAP_NUCLEAR DNA_PDK1_NUCLEAR+RNAP_NUCLEAR = DNA_PDK1_RNAP_NUCLEAR
0.007729396007185196 ; % 680 DNA_PDK1_RNAP_NUCLEAR = DNA_PDK1_NUCLEAR + RNAP_NUCLEAR DNA_PDK1_RNAP_NUCLEAR = DNA_PDK1_NUCLEAR+RNAP_NUCLEAR
0.5531447742760895 ; % 681 DNA_PDK1_RNAP_NUCLEAR = DNA_PDK1_NUCLEAR + RNAP_NUCLEAR + MRNA_PDK1_NUCLEAR DNA_PDK1_RNAP_NUCLEAR = DNA_PDK1_NUCLEAR+RNAP_NUCLEAR+MRNA_PDK1_NUCLEAR
0.42396034476102173 ; % 682 MRNA_PDK1_NUCLEAR + NEXPORT_NUCLEAR = MRNA_PDK1_NEXPORT_NUCLEAR MRNA_PDK1_NUCLEAR+NEXPORT_NUCLEAR = MRNA_PDK1_NEXPORT_NUCLEAR
0.007926199239987386 ; % 683 MRNA_PDK1_NEXPORT_NUCLEAR = MRNA_PDK1_NUCLEAR + NEXPORT_NUCLEAR MRNA_PDK1_NEXPORT_NUCLEAR = MRNA_PDK1_NUCLEAR+NEXPORT_NUCLEAR
0.6463181079041799 ; % 684 MRNA_PDK1_NEXPORT_NUCLEAR = MRNA_PDK1_CYTOSOL + NEXPORT_NUCLEAR MRNA_PDK1_NEXPORT_NUCLEAR = MRNA_PDK1_CYTOSOL+NEXPORT_NUCLEAR
0.5924579936657168 ; % 685 MRNA_PDK1_CYTOSOL + RIBOSOME_CYTOSOL = MRNA_PDK1_RIBOSOME_CYTOSOL MRNA_PDK1_CYTOSOL+RIBOSOME_CYTOSOL = MRNA_PDK1_RIBOSOME_CYTOSOL
0.09363738238502645 ; % 686 MRNA_PDK1_RIBOSOME_CYTOSOL = MRNA_PDK1_CYTOSOL + RIBOSOME_CYTOSOL MRNA_PDK1_RIBOSOME_CYTOSOL = MRNA_PDK1_CYTOSOL+RIBOSOME_CYTOSOL
0.5728786001905815 ; % 687 MRNA_PDK1_RIBOSOME_CYTOSOL = MRNA_PDK1_START_RIBOSOME_CYTOSOL MRNA_PDK1_RIBOSOME_CYTOSOL = MRNA_PDK1_START_RIBOSOME_CYTOSOL
0.4723278391329575 ; % 688 MRNA_PDK1_START_RIBOSOME_CYTOSOL = RIBOSOME_CYTOSOL + PDK1_CYTOSOL + MRNA_PDK1_CYTOSOL MRNA_PDK1_START_RIBOSOME_CYTOSOL = RIBOSOME_CYTOSOL+PDK1_CYTOSOL+MRNA_PDK1_CYTOSOL
0.3495585368586248 ; % 689 MRNA_PDK1_CYTOSOL = [] MRNA_PDK1_CYTOSOL = []
0.07443972100782537 ; % 690 PDK1_CYTOSOL = [] PDK1_CYTOSOL = []
0.015788089733100197 ; % 691 DNA_AKT_PASE_NUCLEAR + RNAP_NUCLEAR = DNA_AKT_PASE_RNAP_NUCLEAR DNA_AKT_PASE_NUCLEAR+RNAP_NUCLEAR = DNA_AKT_PASE_RNAP_NUCLEAR
0.01135072980644193 ; % 692 DNA_AKT_PASE_RNAP_NUCLEAR = DNA_AKT_PASE_NUCLEAR + RNAP_NUCLEAR DNA_AKT_PASE_RNAP_NUCLEAR = DNA_AKT_PASE_NUCLEAR+RNAP_NUCLEAR
0.9939551907047479 ; % 693 DNA_AKT_PASE_RNAP_NUCLEAR = DNA_AKT_PASE_NUCLEAR + RNAP_NUCLEAR + MRNA_AKT_PASE_NUCLEAR DNA_AKT_PASE_RNAP_NUCLEAR = DNA_AKT_PASE_NUCLEAR+RNAP_NUCLEAR+MRNA_AKT_PASE_NUCLEAR
0.47531877233734376 ; % 694 MRNA_AKT_PASE_NUCLEAR + NEXPORT_NUCLEAR = MRNA_AKT_PASE_NEXPORT_NUCLEAR MRNA_AKT_PASE_NUCLEAR+NEXPORT_NUCLEAR = MRNA_AKT_PASE_NEXPORT_NUCLEAR
0.09563535074466248 ; % 695 MRNA_AKT_PASE_NEXPORT_NUCLEAR = MRNA_AKT_PASE_NUCLEAR + NEXPORT_NUCLEAR MRNA_AKT_PASE_NEXPORT_NUCLEAR = MRNA_AKT_PASE_NUCLEAR+NEXPORT_NUCLEAR
0.4123947255323268 ; % 696 MRNA_AKT_PASE_NEXPORT_NUCLEAR = MRNA_AKT_PASE_CYTOSOL + NEXPORT_NUCLEAR MRNA_AKT_PASE_NEXPORT_NUCLEAR = MRNA_AKT_PASE_CYTOSOL+NEXPORT_NUCLEAR
0.4618973121622628 ; % 697 MRNA_AKT_PASE_CYTOSOL + RIBOSOME_CYTOSOL = MRNA_AKT_PASE_RIBOSOME_CYTOSOL MRNA_AKT_PASE_CYTOSOL+RIBOSOME_CYTOSOL = MRNA_AKT_PASE_RIBOSOME_CYTOSOL
0.0491710368600744 ; % 698 MRNA_AKT_PASE_RIBOSOME_CYTOSOL = MRNA_AKT_PASE_CYTOSOL + RIBOSOME_CYTOSOL MRNA_AKT_PASE_RIBOSOME_CYTOSOL = MRNA_AKT_PASE_CYTOSOL+RIBOSOME_CYTOSOL
0.6739427835810264 ; % 699 MRNA_AKT_PASE_RIBOSOME_CYTOSOL = MRNA_AKT_PASE_START_RIBOSOME_CYTOSOL MRNA_AKT_PASE_RIBOSOME_CYTOSOL = MRNA_AKT_PASE_START_RIBOSOME_CYTOSOL
0.9156949901762825 ; % 700 MRNA_AKT_PASE_START_RIBOSOME_CYTOSOL = RIBOSOME_CYTOSOL + AKT_PASE_CYTOSOL + MRNA_AKT_PASE_CYTOSOL MRNA_AKT_PASE_START_RIBOSOME_CYTOSOL = RIBOSOME_CYTOSOL+AKT_PASE_CYTOSOL+MRNA_AKT_PASE_CYTOSOL
0.09500616615701973 ; % 701 MRNA_AKT_PASE_CYTOSOL = [] MRNA_AKT_PASE_CYTOSOL = []
0.14121866256792542 ; % 702 AKT_PASE_CYTOSOL = [] AKT_PASE_CYTOSOL = []
0.206121934376435 ; % 703 DNA_IKB_NUCLEAR + RNAP_NUCLEAR = DNA_IKB_RNAP_NUCLEAR DNA_IKB_NUCLEAR+RNAP_NUCLEAR = DNA_IKB_RNAP_NUCLEAR
0.02817067983041819 ; % 704 DNA_IKB_RNAP_NUCLEAR = DNA_IKB_NUCLEAR + RNAP_NUCLEAR DNA_IKB_RNAP_NUCLEAR = DNA_IKB_NUCLEAR+RNAP_NUCLEAR
0.598558375069083 ; % 705 DNA_IKB_RNAP_NUCLEAR = DNA_IKB_NUCLEAR + RNAP_NUCLEAR + MRNA_IKB_NUCLEAR DNA_IKB_RNAP_NUCLEAR = DNA_IKB_NUCLEAR+RNAP_NUCLEAR+MRNA_IKB_NUCLEAR
0.11372525676219403 ; % 706 MRNA_IKB_NUCLEAR + NEXPORT_NUCLEAR = MRNA_IKB_NEXPORT_NUCLEAR MRNA_IKB_NUCLEAR+NEXPORT_NUCLEAR = MRNA_IKB_NEXPORT_NUCLEAR
0.060512398992232735 ; % 707 MRNA_IKB_NEXPORT_NUCLEAR = MRNA_IKB_NUCLEAR + NEXPORT_NUCLEAR MRNA_IKB_NEXPORT_NUCLEAR = MRNA_IKB_NUCLEAR+NEXPORT_NUCLEAR
0.7074996608299391 ; % 708 MRNA_IKB_NEXPORT_NUCLEAR = MRNA_IKB_CYTOSOL + NEXPORT_NUCLEAR MRNA_IKB_NEXPORT_NUCLEAR = MRNA_IKB_CYTOSOL+NEXPORT_NUCLEAR
0.30482266581803674 ; % 709 MRNA_IKB_CYTOSOL + RIBOSOME_CYTOSOL = MRNA_IKB_RIBOSOME_CYTOSOL MRNA_IKB_CYTOSOL+RIBOSOME_CYTOSOL = MRNA_IKB_RIBOSOME_CYTOSOL
0.05041435505269384 ; % 710 MRNA_IKB_RIBOSOME_CYTOSOL = MRNA_IKB_CYTOSOL + RIBOSOME_CYTOSOL MRNA_IKB_RIBOSOME_CYTOSOL = MRNA_IKB_CYTOSOL+RIBOSOME_CYTOSOL
0.26114855742019316 ; % 711 MRNA_IKB_RIBOSOME_CYTOSOL = MRNA_IKB_START_RIBOSOME_CYTOSOL MRNA_IKB_RIBOSOME_CYTOSOL = MRNA_IKB_START_RIBOSOME_CYTOSOL
0.4597330484516561 ; % 712 MRNA_IKB_START_RIBOSOME_CYTOSOL = RIBOSOME_CYTOSOL + IKB_CYTOSOL + MRNA_IKB_CYTOSOL MRNA_IKB_START_RIBOSOME_CYTOSOL = RIBOSOME_CYTOSOL+IKB_CYTOSOL+MRNA_IKB_CYTOSOL
0.09706347309916408 ; % 713 MRNA_IKB_CYTOSOL = [] MRNA_IKB_CYTOSOL = []
0.19587262887170026 ; % 714 IKB_CYTOSOL = [] IKB_CYTOSOL = []
0.7677422719871354 ; % 715 DNA_NFKB_NUCLEAR + RNAP_NUCLEAR = DNA_NFKB_RNAP_NUCLEAR DNA_NFKB_NUCLEAR+RNAP_NUCLEAR = DNA_NFKB_RNAP_NUCLEAR
0.00510189387106974 ; % 716 DNA_NFKB_RNAP_NUCLEAR = DNA_NFKB_NUCLEAR + RNAP_NUCLEAR DNA_NFKB_RNAP_NUCLEAR = DNA_NFKB_NUCLEAR+RNAP_NUCLEAR
0.8631903428434667 ; % 717 DNA_NFKB_RNAP_NUCLEAR = DNA_NFKB_NUCLEAR + RNAP_NUCLEAR + MRNA_NFKB_NUCLEAR DNA_NFKB_RNAP_NUCLEAR = DNA_NFKB_NUCLEAR+RNAP_NUCLEAR+MRNA_NFKB_NUCLEAR
0.63359410444367 ; % 718 MRNA_NFKB_NUCLEAR + NEXPORT_NUCLEAR = MRNA_NFKB_NEXPORT_NUCLEAR MRNA_NFKB_NUCLEAR+NEXPORT_NUCLEAR = MRNA_NFKB_NEXPORT_NUCLEAR
0.05984556108274203 ; % 719 MRNA_NFKB_NEXPORT_NUCLEAR = MRNA_NFKB_NUCLEAR + NEXPORT_NUCLEAR MRNA_NFKB_NEXPORT_NUCLEAR = MRNA_NFKB_NUCLEAR+NEXPORT_NUCLEAR
0.4679857831862664 ; % 720 MRNA_NFKB_NEXPORT_NUCLEAR = MRNA_NFKB_CYTOSOL + NEXPORT_NUCLEAR MRNA_NFKB_NEXPORT_NUCLEAR = MRNA_NFKB_CYTOSOL+NEXPORT_NUCLEAR
0.8481116369277054 ; % 721 MRNA_NFKB_CYTOSOL + RIBOSOME_CYTOSOL = MRNA_NFKB_RIBOSOME_CYTOSOL MRNA_NFKB_CYTOSOL+RIBOSOME_CYTOSOL = MRNA_NFKB_RIBOSOME_CYTOSOL
0.05158092957350179 ; % 722 MRNA_NFKB_RIBOSOME_CYTOSOL = MRNA_NFKB_CYTOSOL + RIBOSOME_CYTOSOL MRNA_NFKB_RIBOSOME_CYTOSOL = MRNA_NFKB_CYTOSOL+RIBOSOME_CYTOSOL
0.8141671432833532 ; % 723 MRNA_NFKB_RIBOSOME_CYTOSOL = MRNA_NFKB_START_RIBOSOME_CYTOSOL MRNA_NFKB_RIBOSOME_CYTOSOL = MRNA_NFKB_START_RIBOSOME_CYTOSOL
0.12771024200127867 ; % 724 MRNA_NFKB_START_RIBOSOME_CYTOSOL = RIBOSOME_CYTOSOL + NFKB_CYTOSOL + MRNA_NFKB_CYTOSOL MRNA_NFKB_START_RIBOSOME_CYTOSOL = RIBOSOME_CYTOSOL+NFKB_CYTOSOL+MRNA_NFKB_CYTOSOL

0.4762764848661685 ; % 725 MRNA_NFKB_CYTOSOL = [] MRNA_NFKB_CYTOSOL = []
0.15044625924287008 ; % 726 NFKB_CYTOSOL = [] NFKB_CYTOSOL = []
0.1269111562699613 ; % 727 DNA_VEGFR2_NUCLEAR + RNAP_NUCLEAR = DNA_VEGFR2_RNAP_NUCLEAR
DNA_VEGFR2_NUCLEAR+RNAP_NUCLEAR = DNA_VEGFR2_RNAP_NUCLEAR
0.09159408492880033 ; % 728 DNA_VEGFR2_RNAP_NUCLEAR = DNA_VEGFR2_NUCLEAR + RNAP_NUCLEAR
DNA_VEGFR2_RNAP_NUCLEAR = DNA_VEGFR2_NUCLEAR+RNAP_NUCLEAR
0.5512778757504175 ; % 729 DNA_VEGFR2_RNAP_NUCLEAR = DNA_VEGFR2_NUCLEAR + RNAP_NUCLEAR +
MRNA_VEGFR2_NUCLEAR DNA_VEGFR2_RNAP_NUCLEAR = DNA_VEGFR2_NUCLEAR+RNAP_NUCLEAR+MRNA_VEGFR2_NUCLEAR
0.09398369291933706 ; % 730 MRNA_VEGFR2_NUCLEAR + NEXPORT_NUCLEAR =
MRNA_VEGFR2_NEXPORT_NUCLEAR MRNA_VEGFR2_NUCLEAR+NEXPORT_NUCLEAR = MRNA_VEGFR2_NEXPORT_NUCLEAR
0.09087402816206167 ; % 731 MRNA_VEGFR2_NEXPORT_NUCLEAR = MRNA_VEGFR2_NUCLEAR +
NEXPORT_NUCLEAR MRNA_VEGFR2_NEXPORT_NUCLEAR = MRNA_VEGFR2_NUCLEAR+NEXPORT_NUCLEAR
0.7435454002104683 ; % 732 MRNA_VEGFR2_NEXPORT_NUCLEAR = MRNA_VEGFR2_CYTOSOL +
NEXPORT_NUCLEAR MRNA_VEGFR2_NEXPORT_NUCLEAR = MRNA_VEGFR2_CYTOSOL+NEXPORT_NUCLEAR
0.9600163857745057 ; % 733 MRNA_VEGFR2_CYTOSOL + RIBOSOME_CYTOSOL =
MRNA_VEGFR2_RIBOSOME_CYTOSOL MRNA_VEGFR2_CYTOSOL+RIBOSOME_CYTOSOL = MRNA_VEGFR2_RIBOSOME_CYTOSOL
0.047082479243831334 ; % 734 MRNA_VEGFR2_RIBOSOME_CYTOSOL = MRNA_VEGFR2_CYTOSOL +
RIBOSOME_CYTOSOL MRNA_VEGFR2_RIBOSOME_CYTOSOL = MRNA_VEGFR2_CYTOSOL+RIBOSOME_CYTOSOL
0.15309996252186853 ; % 735 MRNA_VEGFR2_RIBOSOME_CYTOSOL =
MRNA_VEGFR2_START_RIBOSOME_CYTOSOL MRNA_VEGFR2_RIBOSOME_CYTOSOL = MRNA_VEGFR2_START_RIBOSOME_CYTOSOL
0.5468719432161087 ; % 736 MRNA_VEGFR2_START_RIBOSOME_CYTOSOL = RIBOSOME_CYTOSOL +
VEGFR2_CYTOSOL + MRNA_VEGFR2_CYTOSOL MRNA_VEGFR2_START_RIBOSOME_CYTOSOL =
RIBOSOME_CYTOSOL+VEGFR2_CYTOSOL+MRNA_VEGFR2_CYTOSOL
0.41735022100299374 ; % 737 MRNA_VEGFR2_CYTOSOL = [] MRNA_VEGFR2_CYTOSOL = []
0.1887972211652128 ; % 738 VEGFR2_CYTOSOL = [] VEGFR2_CYTOSOL = []
0.0 ; % 739 DNA_SNAIL_NUCLEAR + RNAP_NUCLEAR =
DNA_SNAIL_RNAP_NUCLEAR DNA_SNAIL_NUCLEAR+RNAP_NUCLEAR = DNA_SNAIL_RNAP_NUCLEAR
0.05532204643858868 ; % 740 DNA_SNAIL_RNAP_NUCLEAR = DNA_SNAIL_NUCLEAR + RNAP_NUCLEAR
DNA_SNAIL_RNAP_NUCLEAR = DNA_SNAIL_NUCLEAR+RNAP_NUCLEAR
0.09143303200805941 ; % 741 DNA_SNAIL_RNAP_NUCLEAR = DNA_SNAIL_NUCLEAR + RNAP_NUCLEAR +
MRNA_SNAIL_NUCLEAR DNA_SNAIL_RNAP_NUCLEAR = DNA_SNAIL_NUCLEAR+RNAP_NUCLEAR+MRNA_SNAIL_NUCLEAR
0.7864082337915235 ; % 742 MRNA_SNAIL_NUCLEAR + NEXPORT_NUCLEAR = MRNA_SNAIL_NEXPORT_NUCLEAR
MRNA_SNAIL_NUCLEAR+NEXPORT_NUCLEAR = MRNA_SNAIL_NEXPORT_NUCLEAR
0.0938808180071812 ; % 743 MRNA_SNAIL_NEXPORT_NUCLEAR = MRNA_SNAIL_NUCLEAR + NEXPORT_NUCLEAR
MRNA_SNAIL_NEXPORT_NUCLEAR = MRNA_SNAIL_NUCLEAR+NEXPORT_NUCLEAR
0.9343811227617576 ; % 744 MRNA_SNAIL_NEXPORT_NUCLEAR = MRNA_SNAIL_CYTOSOL + NEXPORT_NUCLEAR
MRNA_SNAIL_NEXPORT_NUCLEAR = MRNA_SNAIL_CYTOSOL+NEXPORT_NUCLEAR
0.023125202169479442 ; % 745 MRNA_SNAIL_CYTOSOL + RIBOSOME_CYTOSOL =
MRNA_SNAIL_RIBOSOME_CYTOSOL MRNA_SNAIL_CYTOSOL+RIBOSOME_CYTOSOL = MRNA_SNAIL_RIBOSOME_CYTOSOL
0.04701628360928337 ; % 746 MRNA_SNAIL_RIBOSOME_CYTOSOL = MRNA_SNAIL_CYTOSOL +
RIBOSOME_CYTOSOL MRNA_SNAIL_RIBOSOME_CYTOSOL = MRNA_SNAIL_CYTOSOL+RIBOSOME_CYTOSOL
0.491356065745466 ; % 747 MRNA_SNAIL_RIBOSOME_CYTOSOL = MRNA_SNAIL_START_RIBOSOME_CYTOSOL
MRNA_SNAIL_RIBOSOME_CYTOSOL = MRNA_SNAIL_START_RIBOSOME_CYTOSOL
0.6792018388881008 ; % 748 MRNA_SNAIL_START_RIBOSOME_CYTOSOL = RIBOSOME_CYTOSOL +
SNAIL_CYTOSOL + MRNA_SNAIL_CYTOSOL MRNA_SNAIL_START_RIBOSOME_CYTOSOL =
RIBOSOME_CYTOSOL+SNAIL_CYTOSOL+MRNA_SNAIL_CYTOSOL
0.06477737776019549 ; % 749 MRNA_SNAIL_CYTOSOL = [] MRNA_SNAIL_CYTOSOL = []
0.023267268404074948 ; % 750 SNAIL_CYTOSOL = [] SNAIL_CYTOSOL = []
0.0 ; % 751 DNA_SLUG_NUCLEAR + RNAP_NUCLEAR =
DNA_SLUG_RNAP_NUCLEAR DNA_SLUG_NUCLEAR+RNAP_NUCLEAR = DNA_SLUG_RNAP_NUCLEAR
0.06304061486430344 ; % 752 DNA_SLUG_RNAP_NUCLEAR = DNA_SLUG_NUCLEAR + RNAP_NUCLEAR
DNA_SLUG_RNAP_NUCLEAR = DNA_SLUG_NUCLEAR+RNAP_NUCLEAR
0.6746711786167137 ; % 753 DNA_SLUG_RNAP_NUCLEAR = DNA_SLUG_NUCLEAR + RNAP_NUCLEAR +
MRNA_SLUG_NUCLEAR DNA_SLUG_RNAP_NUCLEAR = DNA_SLUG_NUCLEAR+RNAP_NUCLEAR+MRNA_SLUG_NUCLEAR
0.13332611400128025 ; % 754 MRNA_SLUG_NUCLEAR + NEXPORT_NUCLEAR = MRNA_SLUG_NEXPORT_NUCLEAR
MRNA_SLUG_NUCLEAR+NEXPORT_NUCLEAR = MRNA_SLUG_NEXPORT_NUCLEAR
0.030562300003852228 ; % 755 MRNA_SLUG_NEXPORT_NUCLEAR = MRNA_SLUG_NUCLEAR + NEXPORT_NUCLEAR
MRNA_SLUG_NEXPORT_NUCLEAR = MRNA_SLUG_NUCLEAR+NEXPORT_NUCLEAR
0.15139031866343033 ; % 756 MRNA_SLUG_NEXPORT_NUCLEAR = MRNA_SLUG_CYTOSOL + NEXPORT_NUCLEAR
MRNA_SLUG_NEXPORT_NUCLEAR = MRNA_SLUG_CYTOSOL+NEXPORT_NUCLEAR
0.1382918366813053 ; % 757 MRNA_SLUG_CYTOSOL + RIBOSOME_CYTOSOL =
MRNA_SLUG_RIBOSOME_CYTOSOL MRNA_SLUG_CYTOSOL+RIBOSOME_CYTOSOL = MRNA_SLUG_RIBOSOME_CYTOSOL
0.0055988157016919286 ; % 758 MRNA_SLUG_RIBOSOME_CYTOSOL = MRNA_SLUG_CYTOSOL +
RIBOSOME_CYTOSOL MRNA_SLUG_RIBOSOME_CYTOSOL = MRNA_SLUG_CYTOSOL+RIBOSOME_CYTOSOL
0.5043881564228239 ; % 759 MRNA_SLUG_RIBOSOME_CYTOSOL = MRNA_SLUG_START_RIBOSOME_CYTOSOL
MRNA_SLUG_RIBOSOME_CYTOSOL = MRNA_SLUG_START_RIBOSOME_CYTOSOL
0.815486122632909 ; % 760 MRNA_SLUG_START_RIBOSOME_CYTOSOL = RIBOSOME_CYTOSOL +
SLUG_CYTOSOL + MRNA_SLUG_CYTOSOL MRNA_SLUG_START_RIBOSOME_CYTOSOL = RIBOSOME_CYTOSOL+SLUG_CYTOSOL+MRNA_SLUG_CYTOSOL
0.2694520497047603 ; % 761 MRNA_SLUG_CYTOSOL = [] MRNA_SLUG_CYTOSOL = []
0.02651208018954665 ; % 762 SLUG_CYTOSOL = [] SLUG_CYTOSOL = []
0.9864814129830222 ; % 763 DNA_YREG1_NUCLEAR + RNAP_NUCLEAR = DNA_YREG1_RNAP_NUCLEAR
DNA_YREG1_NUCLEAR+RNAP_NUCLEAR = DNA_YREG1_RNAP_NUCLEAR
0.08431837554107385 ; % 764 DNA_YREG1_RNAP_NUCLEAR = DNA_YREG1_NUCLEAR + RNAP_NUCLEAR
DNA_YREG1_RNAP_NUCLEAR = DNA_YREG1_NUCLEAR+RNAP_NUCLEAR
0.1701091065927868 ; % 765 DNA_YREG1_RNAP_NUCLEAR = DNA_YREG1_NUCLEAR + RNAP_NUCLEAR +
MRNA_YREG1_NUCLEAR DNA_YREG1_RNAP_NUCLEAR = DNA_YREG1_NUCLEAR+RNAP_NUCLEAR+MRNA_YREG1_NUCLEAR
0.33612163678062446 ; % 766 MRNA_YREG1_NUCLEAR + NEXPORT_NUCLEAR =
MRNA_YREG1_NEXPORT_NUCLEAR MRNA_YREG1_NUCLEAR+NEXPORT_NUCLEAR = MRNA_YREG1_NEXPORT_NUCLEAR
0.002441830205072793 ; % 767 MRNA_YREG1_NEXPORT_NUCLEAR = MRNA_YREG1_NUCLEAR +
NEXPORT_NUCLEAR MRNA_YREG1_NEXPORT_NUCLEAR = MRNA_YREG1_NUCLEAR+NEXPORT_NUCLEAR
0.7520668329315655 ; % 768 MRNA_YREG1_NEXPORT_NUCLEAR = MRNA_YREG1_CYTOSOL +
NEXPORT_NUCLEAR MRNA_YREG1_NEXPORT_NUCLEAR = MRNA_YREG1_CYTOSOL+NEXPORT_NUCLEAR
0.615312849591274 ; % 769 MRNA_YREG1_CYTOSOL + RIBOSOME_CYTOSOL =
MRNA_YREG1_RIBOSOME_CYTOSOL MRNA_YREG1_CYTOSOL+RIBOSOME_CYTOSOL = MRNA_YREG1_RIBOSOME_CYTOSOL
0.06792336385063377 ; % 770 MRNA_YREG1_RIBOSOME_CYTOSOL = MRNA_YREG1_CYTOSOL +
RIBOSOME_CYTOSOL MRNA_YREG1_RIBOSOME_CYTOSOL = MRNA_YREG1_CYTOSOL+RIBOSOME_CYTOSOL
0.7328603303654573 ; % 771 MRNA_YREG1_RIBOSOME_CYTOSOL = MRNA_YREG1_START_RIBOSOME_CYTOSOL
MRNA_YREG1_RIBOSOME_CYTOSOL = MRNA_YREG1_START_RIBOSOME_CYTOSOL
0.8297200781405897 ; % 772 MRNA_YREG1_START_RIBOSOME_CYTOSOL = RIBOSOME_CYTOSOL +
YREG1_CYTOSOL + MRNA_YREG1_CYTOSOL MRNA_YREG1_START_RIBOSOME_CYTOSOL =
RIBOSOME_CYTOSOL+YREG1_CYTOSOL+MRNA_YREG1_CYTOSOL
0.24179522894951005 ; % 773 MRNA_YREG1_CYTOSOL = [] MRNA_YREG1_CYTOSOL = []
0.21723442793006137 ; % 774 YREG1_CYTOSOL = [] YREG1_CYTOSOL = []

0.8530502567415338 ; % 775 DNA_LOADING_NUCLEAR + RNAP_NUCLEAR = DNA_LOADING_RNAP_NUCLEAR DNA_LOADING_NUCLEAR+RNAP_NUCLEAR = DNA_LOADING_RNAP_NUCLEAR
0.05916266996790825 ; % 776 DNA_LOADING_RNAP_NUCLEAR = DNA_LOADING_NUCLEAR + RNAP_NUCLEAR DNA_LOADING_RNAP_NUCLEAR = DNA_LOADING_NUCLEAR+RNAP_NUCLEAR
0.54422008429545918 ; % 777 DNA_LOADING_RNAP_NUCLEAR = DNA_LOADING_NUCLEAR + RNAP_NUCLEAR + MRNA_LOADING_NUCLEAR DNA_LOADING_RNAP_NUCLEAR = DNA_LOADING_NUCLEAR+RNAP_NUCLEAR+MRNA_LOADING_NUCLEAR
0.0025305384013382115 ; % 778 MRNA_LOADING_NUCLEAR + NEXPORT_NUCLEAR = MRNA_LOADING_NEXPORT_NUCLEAR MRNA_LOADING_NUCLEAR+NEXPORT_NUCLEAR = MRNA_LOADING_NEXPORT_NUCLEAR
0.0909894921043891 ; % 779 MRNA_LOADING_NEXPORT_NUCLEAR = MRNA_LOADING_NUCLEAR + NEXPORT_NUCLEAR MRNA_LOADING_NEXPORT_NUCLEAR = MRNA_LOADING_NUCLEAR+NEXPORT_NUCLEAR
0.34408180130399924 ; % 780 MRNA_LOADING_NEXPORT_NUCLEAR = MRNA_LOADING_CYTOSOL + NEXPORT_NUCLEAR MRNA_LOADING_NEXPORT_NUCLEAR = MRNA_LOADING_CYTOSOL+NEXPORT_NUCLEAR
0.8282032197383241 ; % 781 MRNA_LOADING_CYTOSOL + RIBOSOME_CYTOSOL = MRNA_LOADING_RIBOSOME_CYTOSOL MRNA_LOADING_CYTOSOL+RIBOSOME_CYTOSOL = MRNA_LOADING_RIBOSOME_CYTOSOL
0.08215773932368264 ; % 782 MRNA_LOADING_RIBOSOME_CYTOSOL = MRNA_LOADING_CYTOSOL + RIBOSOME_CYTOSOL MRNA_LOADING_RIBOSOME_CYTOSOL = MRNA_LOADING_CYTOSOL+RIBOSOME_CYTOSOL
0.9640156814374676 ; % 783 MRNA_LOADING_RIBOSOME_CYTOSOL = MRNA_LOADING_START_RIBOSOME_CYTOSOL MRNA_LOADING_RIBOSOME_CYTOSOL = MRNA_LOADING_START_RIBOSOME_CYTOSOL
0.3364049175843329 ; % 784 MRNA_LOADING_START_RIBOSOME_CYTOSOL = RIBOSOME_CYTOSOL + LOADING_CYTOSOL + MRNA_LOADING_CYTOSOL MRNA_LOADING_START_RIBOSOME_CYTOSOL = RIBOSOME_CYTOSOL+LOADING_CYTOSOL+MRNA_LOADING_CYTOSOL
0.23060790146383713 ; % 785 MRNA_LOADING_CYTOSOL = [] MRNA_LOADING_CYTOSOL = []
0.244038144616249064 ; % 786 LOADING_CYTOSOL = [] LOADING_CYTOSOL = []
0.6312828213643952 ; % 787 MRNA_TBX20_NUCLEAR + NEXPORT_NUCLEAR = MRNA_TBX20_NEXPORT_NUCLEAR MRNA_TBX20_NUCLEAR+NEXPORT_NUCLEAR = MRNA_TBX20_NEXPORT_NUCLEAR
0.07572429636781931 ; % 788 MRNA_TBX20_NEXPORT_NUCLEAR = MRNA_TBX20_NUCLEAR + NEXPORT_NUCLEAR MRNA_TBX20_NEXPORT_NUCLEAR = MRNA_TBX20_NUCLEAR+NEXPORT_NUCLEAR
0.0032933796056262565 ; % 789 MRNA_TBX20_NEXPORT_NUCLEAR = MRNA_TBX20_CYTOSOL + NEXPORT_NUCLEAR MRNA_TBX20_NEXPORT_NUCLEAR = MRNA_TBX20_CYTOSOL+NEXPORT_NUCLEAR
0.6133415925129372 ; % 790 MRNA_TBX20_CYTOSOL + RIBOSOME_CYTOSOL = MRNA_TBX20_RIBOSOME_CYTOSOL MRNA_TBX20_CYTOSOL+RIBOSOME_CYTOSOL = MRNA_TBX20_RIBOSOME_CYTOSOL
0.06487945362981005 ; % 791 MRNA_TBX20_RIBOSOME_CYTOSOL = MRNA_TBX20_CYTOSOL + RIBOSOME_CYTOSOL MRNA_TBX20_RIBOSOME_CYTOSOL = MRNA_TBX20_CYTOSOL+RIBOSOME_CYTOSOL
0.006512874830618354 ; % 792 MRNA_TBX20_RIBOSOME_CYTOSOL = MRNA_TBX20_START_RIBOSOME_CYTOSOL MRNA_TBX20_RIBOSOME_CYTOSOL = MRNA_TBX20_START_RIBOSOME_CYTOSOL
0.10374090053065299 ; % 793 MRNA_TBX20_START_RIBOSOME_CYTOSOL = RIBOSOME_CYTOSOL + TBX20_CYTOSOL + MRNA_TBX20_CYTOSOL MRNA_TBX20_START_RIBOSOME_CYTOSOL = RIBOSOME_CYTOSOL+TBX20_CYTOSOL+MRNA_TBX20_CYTOSOL
0.3895571865105913 ; % 794 MRNA_TBX20_CYTOSOL = [] MRNA_TBX20_CYTOSOL = []
0.014478797279110056 ; % 795 TBX20_CYTOSOL = [] TBX20_CYTOSOL = []
0.25754033899176065 ; % 796 DNA_TBX20_NUCLEAR + TWIST_NUCLEAR = DNA_TBX20_TWIST_NUCLEAR DNA_TBX20_NUCLEAR+TWIST_NUCLEAR = DNA_TBX20_TWIST_NUCLEAR
0.014834299624726566 ; % 797 DNA_TBX20_TWIST_NUCLEAR = DNA_TBX20_NUCLEAR + TWIST_NUCLEAR DNA_TBX20_TWIST_NUCLEAR = DNA_TBX20_NUCLEAR+TWIST_NUCLEAR
0.6071171669747513 ; % 798 DNA_TBX20_TWIST_NUCLEAR + RNAP_NUCLEAR = DNA_TBX20_TWIST_RNAP_NUCLEAR DNA_TBX20_TWIST_NUCLEAR+RNAP_NUCLEAR = DNA_TBX20_TWIST_RNAP_NUCLEAR
0.07622710159964612 ; % 799 DNA_TBX20_TWIST_RNAP_NUCLEAR = DNA_TBX20_TWIST_NUCLEAR + RNAP_NUCLEAR DNA_TBX20_TWIST_RNAP_NUCLEAR = DNA_TBX20_TWIST_NUCLEAR+RNAP_NUCLEAR
0.31321006525429296 ; % 800 TWIST_CYTOSOL + NIMPORT_NUCLEAR = TWIST_NIMPORT_NUCLEAR TWIST_CYTOSOL+NIMPORT_NUCLEAR = TWIST_NIMPORT_NUCLEAR
0.058206518467817915 ; % 801 TWIST_NIMPORT_NUCLEAR = TWIST_CYTOSOL + NIMPORT_NUCLEAR TWIST_NIMPORT_NUCLEAR = TWIST_CYTOSOL+NIMPORT_NUCLEAR
0.03684031299606638 ; % 802 TWIST_NIMPORT_NUCLEAR = NIMPORT_NUCLEAR + TWIST_NUCLEAR TWIST_NIMPORT_NUCLEAR = NIMPORT_NUCLEAR+TWIST_NUCLEAR
0.1046101355936444 ; % 803 TWIST_NUCLEAR + NEXPORT_NUCLEAR = TWIST_NEXPORT_NUCLEAR TWIST_NUCLEAR+NEXPORT_NUCLEAR = TWIST_NEXPORT_NUCLEAR
0.015544936228771823 ; % 804 TWIST_NEXPORT_NUCLEAR = TWIST_NUCLEAR + NEXPORT_NUCLEAR TWIST_NEXPORT_NUCLEAR = TWIST_NUCLEAR+NEXPORT_NUCLEAR
0.8715211365340421 ; % 805 TWIST_NEXPORT_NUCLEAR = NEXPORT_NUCLEAR + TWIST_CYTOSOL TWIST_NEXPORT_NUCLEAR = NEXPORT_NUCLEAR+TWIST_CYTOSOL
0.36989895899002656 ; % 806 DNA_TBX20_TWIST_RNAP_NUCLEAR = DNA_TBX20_NUCLEAR + TWIST_NUCLEAR + RNAP_NUCLEAR + MRNA_TBX20_NUCLEAR DNA_TBX20_TWIST_RNAP_NUCLEAR = DNA_TBX20_NUCLEAR+TWIST_NUCLEAR+RNAP_NUCLEAR+MRNA_TBX20_NUCLEAR
0.7162533996226281 ; % 807 DNA_PTEN_NUCLEAR + ACTIVE_NCID_CSL_NUCLEAR = DNA_PTEN_ACTIVE_NCID_CSL_NUCLEAR DNA_PTEN_NUCLEAR+ACTIVE_NCID_CSL_NUCLEAR = DNA_PTEN_ACTIVE_NCID_CSL_NUCLEAR
0.0389125848628376 2 ; % 808 DNA_PTEN_ACTIVE_NCID_CSL_NUCLEAR = DNA_PTEN_NUCLEAR + ACTIVE_NCID_CSL_NUCLEAR DNA_PTEN_ACTIVE_NCID_CSL_NUCLEAR = DNA_PTEN_NUCLEAR+ACTIVE_NCID_CSL_NUCLEAR
0.9296691298250067 ; % 809 DNA_PTEN_ACTIVE_NCID_CSL_NUCLEAR + RNAP_NUCLEAR = DNA_PTEN_ACTIVE_NCID_CSL_RNAP_NUCLEAR DNA_PTEN_ACTIVE_NCID_CSL_NUCLEAR+RNAP_NUCLEAR = DNA_PTEN_ACTIVE_NCID_CSL_RNAP_NUCLEAR
0.0023957344136982806 ; % 810 DNA_PTEN_ACTIVE_NCID_CSL_RNAP_NUCLEAR = DNA_PTEN_ACTIVE_NCID_CSL_NUCLEAR + RNAP_NUCLEAR DNA_PTEN_ACTIVE_NCID_CSL_RNAP_NUCLEAR = DNA_PTEN_ACTIVE_NCID_CSL_NUCLEAR+RNAP_NUCLEAR
0.30758961054213585 ; % 811 DNA_PTEN_ACTIVE_NCID_CSL_RNAP_NUCLEAR = DNA_PTEN_NUCLEAR + ACTIVE_NCID_CSL_NUCLEAR + RNAP_NUCLEAR + MRNA_PTEN_NUCLEAR DNA_PTEN_ACTIVE_NCID_CSL_RNAP_NUCLEAR = DNA_PTEN_NUCLEAR+ACTIVE_NCID_CSL_NUCLEAR+RNAP_NUCLEAR+MRNA_PTEN_NUCLEAR
0.989447052591121 ; % 812 ACTIVE_NCID_CYTOSOL + CSL_CYTOSOL = ACTIVE_NCID_CSL_CYTOSOL ACTIVE_NCID_CYTOSOL+CSL_CYTOSOL = ACTIVE_NCID_CSL_CYTOSOL
0.03735595388732662 ; % 813 ACTIVE_NCID_CSL_CYTOSOL = ACTIVE_NCID_CYTOSOL + CSL_CYTOSOL ACTIVE_NCID_CSL_CYTOSOL = ACTIVE_NCID_CYTOSOL+CSL_CYTOSOL
0.36684278668228576 ; % 814 ACTIVE_NCID_CSL_CYTOSOL + NIMPORT_NUCLEAR = ACTIVE_NCID_CSL_NIMPORT_NUCLEAR ACTIVE_NCID_CSL_CYTOSOL+NIMPORT_NUCLEAR = ACTIVE_NCID_CSL_NIMPORT_NUCLEAR
0.09903888249717843 ; % 815 ACTIVE_NCID_CSL_NIMPORT_NUCLEAR = ACTIVE_NCID_CSL_CYTOSOL + NIMPORT_NUCLEAR ACTIVE_NCID_CSL_NIMPORT_NUCLEAR = ACTIVE_NCID_CSL_CYTOSOL+NIMPORT_NUCLEAR
0.3762082536956671 ; % 816 ACTIVE_NCID_CSL_NIMPORT_NUCLEAR = NIMPORT_NUCLEAR + ACTIVE_NCID_CSL_NUCLEAR ACTIVE_NCID_CSL_NIMPORT_NUCLEAR = NIMPORT_NUCLEAR+ACTIVE_NCID_CSL_NUCLEAR
0.8320822340862823 ; % 817 ACTIVE_NCID_CSL_NUCLEAR + NEXPORT_NUCLEAR = ACTIVE_NCID_CSL_NEXPORT_NUCLEAR ACTIVE_NCID_CSL_NUCLEAR+NEXPORT_NUCLEAR = ACTIVE_NCID_CSL_NEXPORT_NUCLEAR
0.08011679501047485 ; % 818 ACTIVE_NCID_CSL_NEXPORT_NUCLEAR = ACTIVE_NCID_CSL_NUCLEAR + NEXPORT_NUCLEAR ACTIVE_NCID_CSL_NEXPORT_NUCLEAR = ACTIVE_NCID_CSL_NUCLEAR+NEXPORT_NUCLEAR
0.23371498680193037 ; % 819 ACTIVE_NCID_CSL_NEXPORT_NUCLEAR = NEXPORT_NUCLEAR + ACTIVE_NCID_CSL_CYTOSOL ACTIVE_NCID_CSL_NEXPORT_NUCLEAR = NEXPORT_NUCLEAR+ACTIVE_NCID_CSL_CYTOSOL
0.8587420257024541 ; % 820 MRNA_ALPHASMA_NUCLEAR + NEXPORT_NUCLEAR = MRNA_ALPHASMA_NEXPORT_NUCLEAR MRNA_ALPHASMA_NUCLEAR+NEXPORT_NUCLEAR = MRNA_ALPHASMA_NEXPORT_NUCLEAR

0.017398412003889197 ; % 821 MRNA_ALPHASMA_NEXPORT_NUCLEAR = MRNA_ALPHASMA_NUCLEAR + NEXPORT_NUCLEAR MRNA_ALPHASMA_NEXPORT_NUCLEAR = MRNA_ALPHASMA_NUCLEAR+NEXPORT_NUCLEAR
0.3684129105966647 ; % 822 MRNA_ALPHASMA_NEXPORT_NUCLEAR = MRNA_ALPHASMA_CYTOSOL + NEXPORT_NUCLEAR MRNA_ALPHASMA_NEXPORT_NUCLEAR = MRNA_ALPHASMA_CYTOSOL+NEXPORT_NUCLEAR
0.18000435834687356 ; % 823 MRNA_ALPHASMA_CYTOSOL + RIBOSOME_CYTOSOL = MRNA_ALPHASMA_RIBOSOME_CYTOSOL MRNA_ALPHASMA_CYTOSOL+RIBOSOME_CYTOSOL = MRNA_ALPHASMA_RIBOSOME_CYTOSOL
0.092218106702465 ; % 824 MRNA_ALPHASMA_RIBOSOME_CYTOSOL = MRNA_ALPHASMA_CYTOSOL + RIBOSOME_CYTOSOL MRNA_ALPHASMA_RIBOSOME_CYTOSOL = MRNA_ALPHASMA_CYTOSOL+RIBOSOME_CYTOSOL
0.8359966402801728 ; % 825 MRNA_ALPHASMA_RIBOSOME_CYTOSOL = MRNA_ALPHASMA_START_RIBOSOME_CYTOSOL MRNA_ALPHASMA_RIBOSOME_CYTOSOL = MRNA_ALPHASMA_START_RIBOSOME_CYTOSOL
0.14630104884385053 ; % 826 MRNA_ALPHASMA_START_RIBOSOME_CYTOSOL = RIBOSOME_CYTOSOL + ALPHASMA_CYTOSOL + MRNA_ALPHASMA_CYTOSOL MRNA_ALPHASMA_START_RIBOSOME_CYTOSOL = RIBOSOME_CYTOSOL+ALPHASMA_CYTOSOL+MRNA_ALPHASMA_CYTOSOL
0.044764211431845835 ; % 827 MRNA_ALPHASMA_CYTOSOL = [] MRNA_ALPHASMA_CYTOSOL = []
0.3293269500175904 ; % 828 ALPHASMA_CYTOSOL = [] ALPHASMA_CYTOSOL = []
0.3967337738496455 ; % 829 DNA_ALPHASMA_NUCLEAR + BCATENIN_LEF1_NUCLEAR = DNA_ALPHASMA_BCATENIN_LEF1_NUCLEAR DNA_ALPHASMA_NUCLEAR+BCATENIN_LEF1_NUCLEAR = DNA_ALPHASMA_BCATENIN_LEF1_NUCLEAR
0.0624436135256576076 ; % 830 DNA_ALPHASMA_BCATENIN_LEF1_NUCLEAR = DNA_ALPHASMA_NUCLEAR + BCATENIN_LEF1_NUCLEAR DNA_ALPHASMA_BCATENIN_LEF1_NUCLEAR = DNA_ALPHASMA_NUCLEAR+BCATENIN_LEF1_NUCLEAR
0.8504056453243294 ; % 831 DNA_ALPHASMA_BCATENIN_LEF1_NUCLEAR + RNAP_NUCLEAR = DNA_ALPHASMA_BCATENIN_LEF1_RNAP_NUCLEAR DNA_ALPHASMA_BCATENIN_LEF1_NUCLEAR+RNAP_NUCLEAR = DNA_ALPHASMA_BCATENIN_LEF1_RNAP_NUCLEAR
0.08862904991902518 ; % 832 DNA_ALPHASMA_BCATENIN_LEF1_RNAP_NUCLEAR = DNA_ALPHASMA_BCATENIN_LEF1_NUCLEAR + RNAP_NUCLEAR DNA_ALPHASMA_BCATENIN_LEF1_RNAP_NUCLEAR = DNA_ALPHASMA_BCATENIN_LEF1_NUCLEAR+RNAP_NUCLEAR
0.1640912016293663 ; % 833 DNA_ALPHASMA_BCATENIN_LEF1_RNAP_NUCLEAR = DNA_ALPHASMA_NUCLEAR + BCATENIN_LEF1_NUCLEAR + RNAP_NUCLEAR + MRNA_ALPHASMA_NUCLEAR DNA_ALPHASMA_BCATENIN_LEF1_RNAP_NUCLEAR = DNA_ALPHASMA_NUCLEAR+BCATENIN_LEF1_NUCLEAR+RNAP_NUCLEAR+MRNA_ALPHASMA_NUCLEAR
0.60549994501548854 ; % 834 BCATENIN_CYTOSOL + LEF1_CYTOSOL = BCATENIN_LEF1_CYTOSOL BCATENIN_CYTOSOL+LEF1_CYTOSOL = BCATENIN_LEF1_CYTOSOL
0.001165218645340047 ; % 835 BCATENIN_LEF1_CYTOSOL = BCATENIN_CYTOSOL + LEF1_CYTOSOL BCATENIN_LEF1_CYTOSOL = BCATENIN_CYTOSOL+LEF1_CYTOSOL
0.4442267360641858 ; % 836 BCATENIN_LEF1_CYTOSOL + NIMPORT_NUCLEAR = BCATENIN_LEF1_NIMPORT_NUCLEAR BCATENIN_LEF1_CYTOSOL+NIMPORT_NUCLEAR = BCATENIN_LEF1_NIMPORT_NUCLEAR
0.008221976456294572 ; % 837 BCATENIN_LEF1_NIMPORT_NUCLEAR = BCATENIN_LEF1_CYTOSOL + NIMPORT_NUCLEAR BCATENIN_LEF1_NIMPORT_NUCLEAR = BCATENIN_LEF1_CYTOSOL+NIMPORT_NUCLEAR
0.43343951665823 ; % 838 BCATENIN_LEF1_NIMPORT_NUCLEAR = NIMPORT_NUCLEAR + BCATENIN_LEF1_NUCLEAR BCATENIN_LEF1_NIMPORT_NUCLEAR = NIMPORT_NUCLEAR+BCATENIN_LEF1_NUCLEAR
0.0171641038310812 ; % 839 BCATENIN_LEF1_NUCLEAR + NEXPORT_NUCLEAR = BCATENIN_LEF1_NEXPORT_NUCLEAR BCATENIN_LEF1_NUCLEAR+NEXPORT_NUCLEAR = BCATENIN_LEF1_NEXPORT_NUCLEAR
0.08051226042975167 ; % 840 BCATENIN_LEF1_NEXPORT_NUCLEAR = BCATENIN_LEF1_NUCLEAR + NEXPORT_NUCLEAR BCATENIN_LEF1_NEXPORT_NUCLEAR = BCATENIN_LEF1_NUCLEAR+NEXPORT_NUCLEAR
0.011853971719184953 ; % 841 BCATENIN_LEF1_NEXPORT_NUCLEAR = NEXPORT_NUCLEAR + BCATENIN_LEF1_CYTOSOL BCATENIN_LEF1_NEXPORT_NUCLEAR = NEXPORT_NUCLEAR+BCATENIN_LEF1_CYTOSOL
0.11778912355119375 ; % 842 DNA_ALPHASMA_NUCLEAR + ACTIVE_NCID_CSL_NUCLEAR = DNA_ALPHASMA_ACTIVE_NCID_CSL_NUCLEAR DNA_ALPHASMA_NUCLEAR+ACTIVE_NCID_CSL_NUCLEAR = DNA_ALPHASMA_ACTIVE_NCID_CSL_NUCLEAR
0.001986798964149339 ; % 843 DNA_ALPHASMA_ACTIVE_NCID_CSL_NUCLEAR = DNA_ALPHASMA_NUCLEAR + ACTIVE_NCID_CSL_NUCLEAR DNA_ALPHASMA_ACTIVE_NCID_CSL_NUCLEAR = DNA_ALPHASMA_NUCLEAR+ACTIVE_NCID_CSL_NUCLEAR
0.9992294288753857 ; % 844 DNA_ALPHASMA_ACTIVE_NCID_CSL_NUCLEAR + RNAP_NUCLEAR = DNA_ALPHASMA_ACTIVE_NCID_CSL_RNAP_NUCLEAR DNA_ALPHASMA_ACTIVE_NCID_CSL_NUCLEAR+RNAP_NUCLEAR = DNA_ALPHASMA_ACTIVE_NCID_CSL_RNAP_NUCLEAR
0.016270204030746728 ; % 845 DNA_ALPHASMA_ACTIVE_NCID_CSL_RNAP_NUCLEAR = DNA_ALPHASMA_ACTIVE_NCID_CSL_NUCLEAR + RNAP_NUCLEAR DNA_ALPHASMA_ACTIVE_NCID_CSL_RNAP_NUCLEAR = DNA_ALPHASMA_ACTIVE_NCID_CSL_NUCLEAR+RNAP_NUCLEAR
0.8648839666237395 ; % 846 DNA_ALPHASMA_ACTIVE_NCID_CSL_RNAP_NUCLEAR = DNA_ALPHASMA_NUCLEAR + ACTIVE_NCID_CSL_NUCLEAR + RNAP_NUCLEAR + MRNA_ALPHASMA_NUCLEAR DNA_ALPHASMA_ACTIVE_NCID_CSL_RNAP_NUCLEAR = DNA_ALPHASMA_NUCLEAR+ACTIVE_NCID_CSL_NUCLEAR+RNAP_NUCLEAR+MRNA_ALPHASMA_NUCLEAR
0.9219245335771723 ; % 847 DNA_VEGFR2_NUCLEAR + NFACT1_NUCLEAR = DNA_VEGFR2_NFACT1_NUCLEAR DNA_VEGFR2_NUCLEAR+NFACT1_NUCLEAR = DNA_VEGFR2_NFACT1_NUCLEAR
0.09192728412078055 ; % 848 DNA_VEGFR2_NFACT1_NUCLEAR = DNA_VEGFR2_NUCLEAR + NFACT1_NUCLEAR DNA_VEGFR2_NFACT1_NUCLEAR = DNA_VEGFR2_NUCLEAR+NFACT1_NUCLEAR
0.1552343924327515 ; % 849 DNA_VEGFR2_NFACT1_NUCLEAR + RNAP_NUCLEAR = DNA_VEGFR2_NFACT1_RNAP_NUCLEAR DNA_VEGFR2_NFACT1_NUCLEAR+RNAP_NUCLEAR = DNA_VEGFR2_NFACT1_RNAP_NUCLEAR
0.027025033126824385 ; % 850 DNA_VEGFR2_NFACT1_RNAP_NUCLEAR = DNA_VEGFR2_NFACT1_NUCLEAR + RNAP_NUCLEAR DNA_VEGFR2_NFACT1_RNAP_NUCLEAR = DNA_VEGFR2_NFACT1_NUCLEAR+RNAP_NUCLEAR
0.0961869002953819 ; % 851 NFACT1_CYTOSOL + NIMPORT_NUCLEAR = NFACT1_NIMPORT_NUCLEAR NFACT1_CYTOSOL+NIMPORT_NUCLEAR = NFACT1_NIMPORT_NUCLEAR
0.03322099046634835 ; % 852 NFACT1_NIMPORT_NUCLEAR = NFACT1_CYTOSOL + NIMPORT_NUCLEAR NFACT1_NIMPORT_NUCLEAR = NFACT1_CYTOSOL+NIMPORT_NUCLEAR
0.2684783492575904 ; % 853 NFACT1_NIMPORT_NUCLEAR = NIMPORT_NUCLEAR + NFACT1_NUCLEAR NFACT1_NIMPORT_NUCLEAR = NIMPORT_NUCLEAR+NFACT1_NUCLEAR
0.5645816747302705 ; % 854 NFACT1_NUCLEAR + NEXPORT_NUCLEAR = NFACT1_NEXPORT_NUCLEAR NFACT1_NUCLEAR+NEXPORT_NUCLEAR = NFACT1_NEXPORT_NUCLEAR
0.04232636040033009 ; % 855 NFACT1_NEXPORT_NUCLEAR = NFACT1_NUCLEAR + NEXPORT_NUCLEAR NFACT1_NEXPORT_NUCLEAR = NFACT1_NUCLEAR+NEXPORT_NUCLEAR
0.8116488258257147 ; % 856 NFACT1_NEXPORT_NUCLEAR = NEXPORT_NUCLEAR + NFACT1_CYTOSOL NFACT1_NEXPORT_NUCLEAR = NEXPORT_NUCLEAR+NFACT1_CYTOSOL
0.9607559417022024 ; % 857 DNA_VEGFR2_NFACT1_RNAP_NUCLEAR = DNA_VEGFR2_NUCLEAR + NFACT1_NUCLEAR + RNAP_NUCLEAR + MRNA_VEGFR2_NUCLEAR DNA_VEGFR2_NFACT1_RNAP_NUCLEAR = DNA_VEGFR2_NUCLEAR+NFACT1_NUCLEAR+RNAP_NUCLEAR+MRNA_VEGFR2_NUCLEAR
0.9738404829793373 ; % 858 DNA_VEGFR2_NUCLEAR + ACTIVE_NCID_CSL_NUCLEAR = DNA_VEGFR2_ACTIVE_NCID_CSL_NUCLEAR DNA_VEGFR2_NUCLEAR+ACTIVE_NCID_CSL_NUCLEAR = DNA_VEGFR2_ACTIVE_NCID_CSL_NUCLEAR
0.020487944395096682 ; % 859 DNA_VEGFR2_ACTIVE_NCID_CSL_NUCLEAR = DNA_VEGFR2_NUCLEAR + ACTIVE_NCID_CSL_NUCLEAR DNA_VEGFR2_ACTIVE_NCID_CSL_NUCLEAR = DNA_VEGFR2_NUCLEAR+ACTIVE_NCID_CSL_NUCLEAR
0.2822419714756935 ; % 860 DNA_VEGFR2_ACTIVE_NCID_CSL_NUCLEAR + RNAP_NUCLEAR = DNA_VEGFR2_ACTIVE_NCID_CSL_RNAP_NUCLEAR DNA_VEGFR2_ACTIVE_NCID_CSL_NUCLEAR+RNAP_NUCLEAR = DNA_VEGFR2_ACTIVE_NCID_CSL_RNAP_NUCLEAR
0.022114313138316334 ; % 861 DNA_VEGFR2_ACTIVE_NCID_CSL_RNAP_NUCLEAR = DNA_VEGFR2_ACTIVE_NCID_CSL_NUCLEAR + RNAP_NUCLEAR DNA_VEGFR2_ACTIVE_NCID_CSL_RNAP_NUCLEAR = DNA_VEGFR2_ACTIVE_NCID_CSL_NUCLEAR+RNAP_NUCLEAR
0.9782340946202698 ; % 862 DNA_VEGFR2_ACTIVE_NCID_CSL_RNAP_NUCLEAR = DNA_VEGFR2_NUCLEAR + ACTIVE_NCID_CSL_NUCLEAR + RNAP_NUCLEAR + MRNA_VEGFR2_NUCLEAR DNA_VEGFR2_ACTIVE_NCID_CSL_RNAP_NUCLEAR = DNA_VEGFR2_NUCLEAR+ACTIVE_NCID_CSL_NUCLEAR+RNAP_NUCLEAR+MRNA_VEGFR2_NUCLEAR

0.7721310426335485 ; % 863 MRNA_CYCLINB2_NUCLEAR + NEXPORT_NUCLEAR = MRNA_CYCLINB2_NEXPORT_NUCLEAR MRNA_CYCLINB2_NUCLEAR+NEXPORT_NUCLEAR = MRNA_CYCLINB2_NEXPORT_NUCLEAR
0.09581876702569035 ; % 864 MRNA_CYCLINB2_NEXPORT_NUCLEAR = MRNA_CYCLINB2_NUCLEAR + NEXPORT_NUCLEAR MRNA_CYCLINB2_NEXPORT_NUCLEAR = MRNA_CYCLINB2_NUCLEAR+NEXPORT_NUCLEAR
0.11412154449318801 ; % 865 MRNA_CYCLINB2_NEXPORT_NUCLEAR = MRNA_CYCLINB2_CYTOSOL + NEXPORT_NUCLEAR MRNA_CYCLINB2_NEXPORT_NUCLEAR = MRNA_CYCLINB2_CYTOSOL+NEXPORT_NUCLEAR
0.746381511311346 ; % 866 MRNA_CYCLINB2_CYTOSOL + RIBOSOME_CYTOSOL = MRNA_CYCLINB2_RIBOSOME_CYTOSOL MRNA_CYCLINB2_CYTOSOL+RIBOSOME_CYTOSOL = MRNA_CYCLINB2_RIBOSOME_CYTOSOL
0.09775590764418816 ; % 867 MRNA_CYCLINB2_RIBOSOME_CYTOSOL = MRNA_CYCLINB2_CYTOSOL + RIBOSOME_CYTOSOL MRNA_CYCLINB2_RIBOSOME_CYTOSOL = MRNA_CYCLINB2_CYTOSOL+RIBOSOME_CYTOSOL
0.6532881545763847 ; % 868 MRNA_CYCLINB2_RIBOSOME_CYTOSOL = MRNA_CYCLINB2_START_RIBOSOME_CYTOSOL MRNA_CYCLINB2_RIBOSOME_CYTOSOL = MRNA_CYCLINB2_START_RIBOSOME_CYTOSOL
0.5217217260960831 ; % 869 MRNA_CYCLINB2_START_RIBOSOME_CYTOSOL = RIBOSOME_CYTOSOL + CYCLINB2_CYTOSOL + MRNA_CYCLINB2_CYTOSOL MRNA_CYCLINB2_START_RIBOSOME_CYTOSOL = RIBOSOME_CYTOSOL+CYCLINB2_CYTOSOL+MRNA_CYCLINB2_CYTOSOL
0.44235818872910254 ; % 870 MRNA_CYCLINB2_CYTOSOL = [] MRNA_CYCLINB2_CYTOSOL = []
0.3957023468988833 ; % 871 CYCLINB2_CYTOSOL = []CYCLINB2_CYTOSOL = []
0.7417692338665055 ; % 872 DNA_CYCLINB2_NUCLEAR + TBX20_NUCLEAR = DNA_CYCLINB2_TBX20_NUCLEAR DNA_CYCLINB2_NUCLEAR+TBX20_NUCLEAR = DNA_CYCLINB2_TBX20_NUCLEAR
0.016534190088099733 ; % 873 DNA_CYCLINB2_TBX20_NUCLEAR = DNA_CYCLINB2_NUCLEAR + TBX20_NUCLEAR DNA_CYCLINB2_TBX20_NUCLEAR = DNA_CYCLINB2_NUCLEAR+TBX20_NUCLEAR
0.522053892102061 ; % 874 DNA_CYCLINB2_TBX20_NUCLEAR + RNAP_NUCLEAR = DNA_CYCLINB2_TBX20_RNAP_NUCLEAR DNA_CYCLINB2_TBX20_NUCLEAR+RNAP_NUCLEAR = DNA_CYCLINB2_TBX20_RNAP_NUCLEAR
0.011011276825401163 ; % 875 DNA_CYCLINB2_TBX20_RNAP_NUCLEAR = DNA_CYCLINB2_TBX20_NUCLEAR + RNAP_NUCLEAR DNA_CYCLINB2_TBX20_RNAP_NUCLEAR = DNA_CYCLINB2_TBX20_NUCLEAR+RNAP_NUCLEAR
0.7570746509211372 ; % 876 TBX20_CYTOSOL + NIMPORT_NUCLEAR = TBX20_NIMPORT_NUCLEAR TBX20_CYTOSOL+NIMPORT_NUCLEAR = TBX20_NIMPORT_NUCLEAR
0.08302464666407369 ; % 877 TBX20_NIMPORT_NUCLEAR = TBX20_CYTOSOL + NIMPORT_NUCLEAR TBX20_NIMPORT_NUCLEAR = TBX20_CYTOSOL+NIMPORT_NUCLEAR
0.535382633560636 ; % 878 TBX20_NIMPORT_NUCLEAR = NIMPORT_NUCLEAR + TBX20_NUCLEAR TBX20_NIMPORT_NUCLEAR = NIMPORT_NUCLEAR+TBX20_NUCLEAR
0.9290902637855062 ; % 879 TBX20_NUCLEAR + NEXPORT_NUCLEAR = TBX20_NEXPORT_NUCLEAR TBX20_NUCLEAR+NEXPORT_NUCLEAR = TBX20_NEXPORT_NUCLEAR
0.07301061828594169 ; % 880 TBX20_NEXPORT_NUCLEAR = TBX20_NUCLEAR + NEXPORT_NUCLEAR TBX20_NEXPORT_NUCLEAR = TBX20_NUCLEAR+NEXPORT_NUCLEAR
0.21281847135837206 ; % 881 TBX20_NEXPORT_NUCLEAR = NEXPORT_NUCLEAR + TBX20_CYTOSOL TBX20_NEXPORT_NUCLEAR = NEXPORT_NUCLEAR+TBX20_CYTOSOL
0.4153250000221488 ; % 882 DNA_CYCLINB2_TBX20_RNAP_NUCLEAR = DNA_CYCLINB2_NUCLEAR + TBX20_NUCLEAR + RNAP_NUCLEAR + MRNA_CYCLINB2_NUCLEAR DNA_CYCLINB2_TBX20_RNAP_NUCLEAR = DNA_CYCLINB2_NUCLEAR+TBX20_NUCLEAR+RNAP_NUCLEAR+MRNA_CYCLINB2_NUCLEAR
0.2319227256399079 ; % 883 DNA_CYCLINB2_NUCLEAR + TWIST_NUCLEAR = DNA_CYCLINB2_TWIST_NUCLEAR DNA_CYCLINB2_NUCLEAR+TWIST_NUCLEAR = DNA_CYCLINB2_TWIST_NUCLEAR
0.08888880662540699 ; % 884 DNA_CYCLINB2_TWIST_NUCLEAR = DNA_CYCLINB2_NUCLEAR + TWIST_NUCLEAR DNA_CYCLINB2_TWIST_NUCLEAR = DNA_CYCLINB2_NUCLEAR+TWIST_NUCLEAR
0.9639609831708342 ; % 885 DNA_CYCLINB2_TWIST_NUCLEAR + RNAP_NUCLEAR = DNA_CYCLINB2_TWIST_RNAP_NUCLEAR DNA_CYCLINB2_TWIST_NUCLEAR+RNAP_NUCLEAR = DNA_CYCLINB2_TWIST_RNAP_NUCLEAR
0.08683421969366728 ; % 886 DNA_CYCLINB2_TWIST_RNAP_NUCLEAR = DNA_CYCLINB2_TWIST_NUCLEAR + RNAP_NUCLEAR DNA_CYCLINB2_TWIST_RNAP_NUCLEAR = DNA_CYCLINB2_TWIST_NUCLEAR+RNAP_NUCLEAR
0.3046978090150483 ; % 887 DNA_CYCLINB2_TWIST_RNAP_NUCLEAR = DNA_CYCLINB2_NUCLEAR + TWIST_NUCLEAR + RNAP_NUCLEAR + MRNA_CYCLINB2_NUCLEAR DNA_CYCLINB2_TWIST_RNAP_NUCLEAR = DNA_CYCLINB2_NUCLEAR+TWIST_NUCLEAR+RNAP_NUCLEAR+MRNA_CYCLINB2_NUCLEAR
0.2683926229963859 ; % 888 DNA_CYCLINB2_NUCLEAR + BCATENIN_LEF1_NUCLEAR = DNA_CYCLINB2_BCATENIN_LEF1_NUCLEAR DNA_CYCLINB2_NUCLEAR+BCATENIN_LEF1_NUCLEAR = DNA_CYCLINB2_BCATENIN_LEF1_NUCLEAR
0.031161249664524427 ; % 889 DNA_CYCLINB2_BCATENIN_LEF1_NUCLEAR = DNA_CYCLINB2_NUCLEAR + BCATENIN_LEF1_NUCLEAR DNA_CYCLINB2_BCATENIN_LEF1_NUCLEAR = DNA_CYCLINB2_NUCLEAR+BCATENIN_LEF1_NUCLEAR
0.7576437145728612 ; % 890 DNA_CYCLINB2_BCATENIN_LEF1_NUCLEAR + RNAP_NUCLEAR = DNA_CYCLINB2_BCATENIN_LEF1_RNAP_NUCLEAR DNA_CYCLINB2_BCATENIN_LEF1_NUCLEAR+RNAP_NUCLEAR = DNA_CYCLINB2_BCATENIN_LEF1_RNAP_NUCLEAR
0.06967799568397806 ; % 891 DNA_CYCLINB2_BCATENIN_LEF1_RNAP_NUCLEAR = DNA_CYCLINB2_BCATENIN_LEF1_NUCLEAR + RNAP_NUCLEAR DNA_CYCLINB2_BCATENIN_LEF1_RNAP_NUCLEAR = DNA_CYCLINB2_BCATENIN_LEF1_NUCLEAR+RNAP_NUCLEAR
0.11227107260311642 ; % 892 DNA_CYCLINB2_BCATENIN_LEF1_RNAP_NUCLEAR = DNA_CYCLINB2_NUCLEAR + BCATENIN_LEF1_NUCLEAR + RNAP_NUCLEAR + MRNA_CYCLINB2_NUCLEAR DNA_CYCLINB2_BCATENIN_LEF1_RNAP_NUCLEAR = DNA_CYCLINB2_NUCLEAR+BCATENIN_LEF1_NUCLEAR+RNAP_NUCLEAR+MRNA_CYCLINB2_NUCLEAR
0.11116156717189962 ; % 893 DNA_PECAM1_NUCLEAR + NFATC1_NUCLEAR = DNA_PECAM1_NFATC1_NUCLEAR DNA_PECAM1_NUCLEAR+NFATC1_NUCLEAR = DNA_PECAM1_NFATC1_NUCLEAR
0.03958927151747034 ; % 894 DNA_PECAM1_NFATC1_NUCLEAR = DNA_PECAM1_NUCLEAR + NFATC1_NUCLEAR DNA_PECAM1_NFATC1_NUCLEAR = DNA_PECAM1_NUCLEAR+NFATC1_NUCLEAR
0.718325239387041 ; % 895 DNA_PECAM1_NFATC1_NUCLEAR + RNAP_NUCLEAR = DNA_PECAM1_NFATC1_RNAP_NUCLEAR DNA_PECAM1_NFATC1_NUCLEAR+RNAP_NUCLEAR = DNA_PECAM1_NFATC1_RNAP_NUCLEAR
0.06874921201108153 ; % 896 DNA_PECAM1_NFATC1_RNAP_NUCLEAR = DNA_PECAM1_NFATC1_NUCLEAR + RNAP_NUCLEAR DNA_PECAM1_NFATC1_RNAP_NUCLEAR = DNA_PECAM1_NFATC1_NUCLEAR+RNAP_NUCLEAR
0.29461671132381695 ; % 897 NFATC1_CYTOSOL + NIMPORT_NUCLEAR = NFATC1_NIMPORT_NUCLEAR NFATC1_CYTOSOL+NIMPORT_NUCLEAR = NFATC1_NIMPORT_NUCLEAR
0.05201823826283674 ; % 898 NFATC1_NIMPORT_NUCLEAR = NFATC1_CYTOSOL + NIMPORT_NUCLEAR NFATC1_NIMPORT_NUCLEAR = NFATC1_CYTOSOL+NIMPORT_NUCLEAR
0.1900210750283109 ; % 899 NFATC1_NIMPORT_NUCLEAR = NIMPORT_NUCLEAR + NFATC1_NUCLEAR NFATC1_NIMPORT_NUCLEAR = NIMPORT_NUCLEAR+NFATC1_NUCLEAR
0.2783981007240266 ; % 900 NFATC1_NUCLEAR + NEXPORT_NUCLEAR = NFATC1_NEXPORT_NUCLEAR NFATC1_NUCLEAR+NEXPORT_NUCLEAR = NFATC1_NEXPORT_NUCLEAR
0.0467707138791599 ; % 901 NFATC1_NEXPORT_NUCLEAR = NFATC1_NUCLEAR + NEXPORT_NUCLEAR NFATC1_NEXPORT_NUCLEAR = NFATC1_NUCLEAR+NEXPORT_NUCLEAR
0.5033911876080657 ; % 902 NFATC1_NEXPORT_NUCLEAR = NEXPORT_NUCLEAR + NFATC1_CYTOSOL NFATC1_NEXPORT_NUCLEAR = NEXPORT_NUCLEAR+NFATC1_CYTOSOL
0.14198099026384603 ; % 903 DNA_PECAM1_NFATC1_RNAP_NUCLEAR = DNA_PECAM1_NUCLEAR + NFATC1_NUCLEAR + RNAP_NUCLEAR + MRNA_PECAM1_NUCLEAR DNA_PECAM1_NFATC1_RNAP_NUCLEAR = DNA_PECAM1_NUCLEAR+NFATC1_NUCLEAR+RNAP_NUCLEAR+MRNA_PECAM1_NUCLEAR
0.9926918199265051 ; % 904 DNA_SLUG_NUCLEAR + P_AP1_NUCLEAR = DNA_SLUG_P_AP1_NUCLEAR DNA_SLUG_NUCLEAR+P_AP1_NUCLEAR = DNA_SLUG_P_AP1_NUCLEAR
0.007123050762836125 ; % 905 DNA_SLUG_P_AP1_NUCLEAR = DNA_SLUG_NUCLEAR + P_AP1_NUCLEAR DNA_SLUG_P_AP1_NUCLEAR = DNA_SLUG_NUCLEAR+P_AP1_NUCLEAR
0.9922356396172567 ; % 906 DNA_SLUG_P_AP1_NUCLEAR + RNAP_NUCLEAR = DNA_SLUG_P_AP1_RNAP_NUCLEAR DNA_SLUG_P_AP1_NUCLEAR+RNAP_NUCLEAR = DNA_SLUG_P_AP1_RNAP_NUCLEAR

0.0069099040732254 47 ; % 907 DNA_SLUG_P_AP1_RNAP_NUCLEAR = DNA_SLUG_P_AP1_NUCLEAR + RNAP_NUCLEAR DNA_SLUG_P_AP1_RNAP_NUCLEAR = DNA_SLUG_P_AP1_NUCLEAR+RNAP_NUCLEAR
0.2597192319632444 ; % 908 P_AP1_CYTOSOL + NIMPORT_NUCLEAR = P_AP1_NIMPORT_NUCLEAR P_AP1_CYTOSOL+NIMPORT_NUCLEAR = P_AP1_NIMPORT_NUCLEAR
0.017490630470009216 ; % 909 P_AP1_NIMPORT_NUCLEAR = P_AP1_CYTOSOL + NIMPORT_NUCLEAR P_AP1_NIMPORT_NUCLEAR = P_AP1_CYTOSOL+NIMPORT_NUCLEAR
0.7028254979235711 ; % 910 P_AP1_NIMPORT_NUCLEAR = NIMPORT_NUCLEAR + P_AP1_NUCLEAR P_AP1_NIMPORT_NUCLEAR = NIMPORT_NUCLEAR+P_AP1_NUCLEAR
0.7523032287830684 ; % 911 P_AP1_NUCLEAR + NEXPORT_NUCLEAR = P_AP1_NEXPORT_NUCLEAR P_AP1_NUCLEAR+NEXPORT_NUCLEAR = P_AP1_NEXPORT_NUCLEAR
0.05829523836192474 ; % 912 P_AP1_NEXPORT_NUCLEAR = P_AP1_NUCLEAR + NEXPORT_NUCLEAR P_AP1_NEXPORT_NUCLEAR = P_AP1_NUCLEAR+NEXPORT_NUCLEAR
0.18267704853841282 ; % 913 P_AP1_NEXPORT_NUCLEAR = NEXPORT_NUCLEAR + P_AP1_CYTOSOL P_AP1_NEXPORT_NUCLEAR = NEXPORT_NUCLEAR+P_AP1_CYTOSOL
0.13463967103491348 ; % 914 DNA_SLUG_P_AP1_RNAP_NUCLEAR = DNA_SLUG_NUCLEAR + P_AP1_NUCLEAR + RNAP_NUCLEAR + MRNA_SLUG_NUCLEAR DNA_SLUG_P_AP1_RNAP_NUCLEAR = DNA_SLUG_NUCLEAR+P_AP1_NUCLEAR+RNAP_NUCLEAR+MRNA_SLUG_NUCLEAR
0.994973930290365 ; % 915 DNA_SLUG_NUCLEAR + P_SP1_NUCLEAR = DNA_SLUG_P_SP1_NUCLEAR DNA_SLUG_NUCLEAR+P_SP1_NUCLEAR = DNA_SLUG_P_SP1_NUCLEAR
0.002331303667152923 ; % 916 DNA_SLUG_P_SP1_NUCLEAR = DNA_SLUG_NUCLEAR + P_SP1_NUCLEAR DNA_SLUG_P_SP1_NUCLEAR = DNA_SLUG_NUCLEAR+P_SP1_NUCLEAR
0.9116136962923388 ; % 917 DNA_SLUG_P_SP1_NUCLEAR + RNAP_NUCLEAR = DNA_SLUG_P_SP1_RNAP_NUCLEAR DNA_SLUG_P_SP1_NUCLEAR+RNAP_NUCLEAR = DNA_SLUG_P_SP1_RNAP_NUCLEAR
0.005864601716626418 ; % 918 DNA_SLUG_P_SP1_RNAP_NUCLEAR = DNA_SLUG_P_SP1_NUCLEAR + RNAP_NUCLEAR DNA_SLUG_P_SP1_RNAP_NUCLEAR = DNA_SLUG_P_SP1_NUCLEAR+RNAP_NUCLEAR
0.10865258878649187 ; % 919 P_SP1_CYTOSOL + NIMPORT_NUCLEAR = P_SP1_NIMPORT_NUCLEAR P_SP1_CYTOSOL+NIMPORT_NUCLEAR = P_SP1_NIMPORT_NUCLEAR
0.0957786705195906 ; % 920 P_SP1_NIMPORT_NUCLEAR = P_SP1_CYTOSOL + NIMPORT_NUCLEAR P_SP1_NIMPORT_NUCLEAR = P_SP1_CYTOSOL+NIMPORT_NUCLEAR
0.03401609851811638 ; % 921 P_SP1_NIMPORT_NUCLEAR = NIMPORT_NUCLEAR + P_SP1_NUCLEAR P_SP1_NIMPORT_NUCLEAR = NIMPORT_NUCLEAR+P_SP1_NUCLEAR
0.363386992746613 ; % 922 P_SP1_NUCLEAR + NEXPORT_NUCLEAR = P_SP1_NEXPORT_NUCLEAR P_SP1_NUCLEAR+NEXPORT_NUCLEAR = P_SP1_NEXPORT_NUCLEAR
0.03497764464826358 ; % 923 P_SP1_NEXPORT_NUCLEAR = P_SP1_NUCLEAR + NEXPORT_NUCLEAR P_SP1_NEXPORT_NUCLEAR = P_SP1_NUCLEAR+NEXPORT_NUCLEAR
0.5682959350530288 ; % 924 P_SP1_NEXPORT_NUCLEAR = NEXPORT_NUCLEAR + P_SP1_CYTOSOL P_SP1_NEXPORT_NUCLEAR = NEXPORT_NUCLEAR+P_SP1_CYTOSOL
0.8567472278827303 ; % 925 DNA_SLUG_P_SP1_RNAP_NUCLEAR = DNA_SLUG_NUCLEAR + P_SP1_NUCLEAR + RNAP_NUCLEAR + MRNA_SLUG_NUCLEAR DNA_SLUG_P_SP1_RNAP_NUCLEAR = DNA_SLUG_NUCLEAR+P_SP1_NUCLEAR+RNAP_NUCLEAR+MRNA_SLUG_NUCLEAR
0.0001 ; % 926 DNA_SLUG_NUCLEAR + BCATENIN_TCF4_NUCLEAR = DNA_SLUG_BCATENIN_TCF4_NUCLEAR DNA_SLUG_NUCLEAR+BCATENIN_TCF4_NUCLEAR = DNA_SLUG_BCATENIN_TCF4_NUCLEAR
0.09191658543414892 ; % 927 DNA_SLUG_BCATENIN_TCF4_NUCLEAR = DNA_SLUG_NUCLEAR + BCATENIN_TCF4_NUCLEAR DNA_SLUG_BCATENIN_TCF4_NUCLEAR = DNA_SLUG_NUCLEAR+BCATENIN_TCF4_NUCLEAR
0.0001 ; % 928 DNA_SLUG_BCATENIN_TCF4_NUCLEAR + RNAP_NUCLEAR = DNA_SLUG_BCATENIN_TCF4_RNAP_NUCLEAR DNA_SLUG_BCATENIN_TCF4_NUCLEAR+RNAP_NUCLEAR = DNA_SLUG_BCATENIN_TCF4_RNAP_NUCLEAR
0.030600169187593375 ; % 929 DNA_SLUG_BCATENIN_TCF4_RNAP_NUCLEAR = DNA_SLUG_BCATENIN_TCF4_NUCLEAR + RNAP_NUCLEAR DNA_SLUG_BCATENIN_TCF4_RNAP_NUCLEAR = DNA_SLUG_BCATENIN_TCF4_NUCLEAR+RNAP_NUCLEAR
0.48634329702546797 ; % 930 DNA_SLUG_BCATENIN_TCF4_RNAP_NUCLEAR = DNA_SLUG_NUCLEAR + BCATENIN_TCF4_NUCLEAR + RNAP_NUCLEAR + MRNA_SLUG_NUCLEAR DNA_SLUG_BCATENIN_TCF4_RNAP_NUCLEAR = DNA_SLUG_NUCLEAR+BCATENIN_TCF4_NUCLEAR+RNAP_NUCLEAR+MRNA_SLUG_NUCLEAR
0.9866179073697999 ; % 931 BCATENIN_CYTOSOL + TCF4_CYTOSOL = BCATENIN_TCF4_CYTOSOL BCATENIN_CYTOSOL+TCF4_CYTOSOL = BCATENIN_TCF4_CYTOSOL
0.00056425647523732125; % 932 BCATENIN_TCF4_CYTOSOL = BCATENIN_CYTOSOL + TCF4_CYTOSOL BCATENIN_TCF4_CYTOSOL = BCATENIN_CYTOSOL+TCF4_CYTOSOL
0.2108842395850017 ; % 933 BCATENIN_TCF4_CYTOSOL + NIMPORT_NUCLEAR = BCATENIN_TCF4_NIMPORT_NUCLEAR BCATENIN_TCF4_CYTOSOL+NIMPORT_NUCLEAR = BCATENIN_TCF4_NIMPORT_NUCLEAR
0.018159480329432775 ; % 934 BCATENIN_TCF4_NIMPORT_NUCLEAR = BCATENIN_TCF4_CYTOSOL + NIMPORT_NUCLEAR BCATENIN_TCF4_NIMPORT_NUCLEAR = BCATENIN_TCF4_CYTOSOL+NIMPORT_NUCLEAR
0.9568593369355222 ; % 935 BCATENIN_TCF4_NIMPORT_NUCLEAR = NIMPORT_NUCLEAR + BCATENIN_TCF4_NUCLEAR BCATENIN_TCF4_NIMPORT_NUCLEAR = NIMPORT_NUCLEAR+BCATENIN_TCF4_NUCLEAR
0.3491443745080983 ; % 936 BCATENIN_TCF4_NUCLEAR + NEXPORT_NUCLEAR = BCATENIN_TCF4_NEXPORT_NUCLEAR BCATENIN_TCF4_NUCLEAR+NEXPORT_NUCLEAR = BCATENIN_TCF4_NEXPORT_NUCLEAR
0.027266969211490324 ; % 937 BCATENIN_TCF4_NEXPORT_NUCLEAR = BCATENIN_TCF4_NUCLEAR + NEXPORT_NUCLEAR BCATENIN_TCF4_NEXPORT_NUCLEAR = BCATENIN_TCF4_NUCLEAR+NEXPORT_NUCLEAR
0.5898200492149793 ; % 938 BCATENIN_TCF4_NEXPORT_NUCLEAR = NEXPORT_NUCLEAR + BCATENIN_TCF4_CYTOSOL BCATENIN_TCF4_NEXPORT_NUCLEAR = NEXPORT_NUCLEAR+BCATENIN_TCF4_CYTOSOL
0.23168796596449515 ; % 939 DNA_SLUG_NUCLEAR + ACTIVE_NCID_CSL_NUCLEAR = DNA_SLUG_ACTIVE_NCID_CSL_NUCLEAR DNA_SLUG_NUCLEAR+ACTIVE_NCID_CSL_NUCLEAR = DNA_SLUG_ACTIVE_NCID_CSL_NUCLEAR
0.015844665359885168 ; % 940 DNA_SLUG_ACTIVE_NCID_CSL_NUCLEAR = DNA_SLUG_NUCLEAR + ACTIVE_NCID_CSL_NUCLEAR DNA_SLUG_ACTIVE_NCID_CSL_NUCLEAR = DNA_SLUG_NUCLEAR+ACTIVE_NCID_CSL_NUCLEAR
0.6974357988191648 ; % 941 DNA_SLUG_ACTIVE_NCID_CSL_NUCLEAR + RNAP_NUCLEAR = DNA_SLUG_ACTIVE_NCID_CSL_RNAP_NUCLEAR DNA_SLUG_ACTIVE_NCID_CSL_NUCLEAR+RNAP_NUCLEAR = DNA_SLUG_ACTIVE_NCID_CSL_RNAP_NUCLEAR
0.03837750027455855 ; % 942 DNA_SLUG_ACTIVE_NCID_CSL_RNAP_NUCLEAR = DNA_SLUG_ACTIVE_NCID_CSL_NUCLEAR + RNAP_NUCLEAR DNA_SLUG_ACTIVE_NCID_CSL_RNAP_NUCLEAR = DNA_SLUG_ACTIVE_NCID_CSL_NUCLEAR+RNAP_NUCLEAR
0.07153365223971597 ; % 943 DNA_SLUG_ACTIVE_NCID_CSL_RNAP_NUCLEAR = DNA_SLUG_NUCLEAR + ACTIVE_NCID_CSL_NUCLEAR + RNAP_NUCLEAR + MRNA_SLUG_NUCLEAR DNA_SLUG_ACTIVE_NCID_CSL_RNAP_NUCLEAR = DNA_SLUG_NUCLEAR+ACTIVE_NCID_CSL_NUCLEAR+RNAP_NUCLEAR+MRNA_SLUG_NUCLEAR
0.96866493395302977 ; % 944 DNA_SNAIL_NUCLEAR + P_AP1_NUCLEAR = DNA_SNAIL_P_AP1_NUCLEAR DNA_SNAIL_NUCLEAR+P_AP1_NUCLEAR = DNA_SNAIL_P_AP1_NUCLEAR
0.00168311384473153 ; % 945 DNA_SNAIL_P_AP1_NUCLEAR = DNA_SNAIL_NUCLEAR + P_AP1_NUCLEAR DNA_SNAIL_P_AP1_NUCLEAR = DNA_SNAIL_NUCLEAR+P_AP1_NUCLEAR
0.96475879080509743 ; % 946 DNA_SNAIL_P_AP1_NUCLEAR + RNAP_NUCLEAR = DNA_SNAIL_P_AP1_RNAP_NUCLEAR DNA_SNAIL_P_AP1_NUCLEAR+RNAP_NUCLEAR = DNA_SNAIL_P_AP1_RNAP_NUCLEAR
0.003667940765602734 ; % 947 DNA_SNAIL_P_AP1_RNAP_NUCLEAR = DNA_SNAIL_P_AP1_NUCLEAR + RNAP_NUCLEAR DNA_SNAIL_P_AP1_RNAP_NUCLEAR = DNA_SNAIL_P_AP1_NUCLEAR+RNAP_NUCLEAR
0.24025881428390417 ; % 948 DNA_SNAIL_P_AP1_RNAP_NUCLEAR = DNA_SNAIL_NUCLEAR + P_AP1_NUCLEAR + RNAP_NUCLEAR + MRNA_SNAIL_NUCLEAR DNA_SNAIL_P_AP1_RNAP_NUCLEAR = DNA_SNAIL_NUCLEAR+P_AP1_NUCLEAR+RNAP_NUCLEAR+MRNA_SNAIL_NUCLEAR
0.92506006411360093 ; % 949 DNA_SNAIL_NUCLEAR + P_SP1_NUCLEAR = DNA_SNAIL_P_SP1_NUCLEAR DNA_SNAIL_NUCLEAR+P_SP1_NUCLEAR = DNA_SNAIL_P_SP1_NUCLEAR

0.00265324056466929 ; % 950 DNA_SNAIL_P_SP1_NUCLEAR = DNA_SNAIL_NUCLEAR + P_SP1_NUCLEAR
DNA_SNAIL_P_SP1_NUCLEAR = DNA_SNAIL_NUCLEAR+P_SP1_NUCLEAR
0.990202740246663 ; % 951 DNA_SNAIL_P_SP1_NUCLEAR + RNAP_NUCLEAR =
DNA_SNAIL_P_SP1_RNAP_NUCLEAR DNA_SNAIL_P_SP1_NUCLEAR+RNAP_NUCLEAR = DNA_SNAIL_P_SP1_RNAP_NUCLEAR
0.004975689082538155 ; % 952 DNA_SNAIL_P_SP1_RNAP_NUCLEAR = DNA_SNAIL_P_SP1_NUCLEAR +
RNAP_NUCLEAR DNA_SNAIL_P_SP1_RNAP_NUCLEAR = DNA_SNAIL_P_SP1_NUCLEAR+RNAP_NUCLEAR
0.5197376813926342 ; % 953 DNA_SNAIL_P_SP1_RNAP_NUCLEAR = DNA_SNAIL_NUCLEAR + P_SP1_NUCLEAR +
RNAP_NUCLEAR + MRNA_SNAIL_NUCLEAR DNA_SNAIL_P_SP1_RNAP_NUCLEAR =
DNA_SNAIL_NUCLEAR+P_SP1_NUCLEAR+RNAP_NUCLEAR+MRNA_SNAIL_NUCLEAR
0.0001; % 954 DNA_SNAIL_NUCLEAR + BCATENIN_TCF4_NUCLEAR = DNA_SNAIL_BCATENIN_TCF4_NUCLEAR
DNA_SNAIL_NUCLEAR+BCATENIN_TCF4_NUCLEAR = DNA_SNAIL_BCATENIN_TCF4_NUCLEAR
0.02869540256626072 ; % 955 DNA_SNAIL_BCATENIN_TCF4_NUCLEAR = DNA_SNAIL_NUCLEAR +
BCATENIN_TCF4_NUCLEAR DNA_SNAIL_BCATENIN_TCF4_NUCLEAR = DNA_SNAIL_NUCLEAR+BCATENIN_TCF4_NUCLEAR
0.0001; % 956 DNA_SNAIL_BCATENIN_TCF4_NUCLEAR + RNAP_NUCLEAR = DNA_SNAIL_BCATENIN_TCF4_RNAP_NUCLEAR
DNA_SNAIL_BCATENIN_TCF4_NUCLEAR+RNAP_NUCLEAR = DNA_SNAIL_BCATENIN_TCF4_RNAP_NUCLEAR
0.01500874762580181 ; % 957 DNA_SNAIL_BCATENIN_TCF4_RNAP_NUCLEAR =
DNA_SNAIL_BCATENIN_TCF4_NUCLEAR + RNAP_NUCLEAR DNA_SNAIL_BCATENIN_TCF4_RNAP_NUCLEAR =
DNA_SNAIL_BCATENIN_TCF4_NUCLEAR+RNAP_NUCLEAR
0.8747034502103713 ; % 958 DNA_SNAIL_BCATENIN_TCF4_RNAP_NUCLEAR = DNA_SNAIL_NUCLEAR +
BCATENIN_TCF4_NUCLEAR + RNAP_NUCLEAR + MRNA_SNAIL_NUCLEAR DNA_SNAIL_BCATENIN_TCF4_RNAP_NUCLEAR =
DNA_SNAIL_NUCLEAR+BCATENIN_TCF4_NUCLEAR+RNAP_NUCLEAR+MRNA_SNAIL_NUCLEAR
0.21460525891919335 ; % 959 DNA_SNAIL_NUCLEAR + ACTIVE_NCID_CSL_NUCLEAR =
DNA_SNAIL_ACTIVE_NCID_CSL_NUCLEAR DNA_SNAIL_NUCLEAR+ACTIVE_NCID_CSL_NUCLEAR = DNA_SNAIL_ACTIVE_NCID_CSL_NUCLEAR
0.026428411043530886 ; % 960 DNA_SNAIL_ACTIVE_NCID_CSL_NUCLEAR = DNA_SNAIL_NUCLEAR +
ACTIVE_NCID_CSL_NUCLEAR DNA_SNAIL_ACTIVE_NCID_CSL_NUCLEAR = DNA_SNAIL_NUCLEAR+ACTIVE_NCID_CSL_NUCLEAR
0.1480247985809341 ; % 961 DNA_SNAIL_ACTIVE_NCID_CSL_NUCLEAR + RNAP_NUCLEAR =
DNA_SNAIL_ACTIVE_NCID_CSL_RNAP_NUCLEAR DNA_SNAIL_ACTIVE_NCID_CSL_NUCLEAR+RNAP_NUCLEAR =
DNA_SNAIL_ACTIVE_NCID_CSL_RNAP_NUCLEAR
0.07113134186296476 ; % 962 DNA_SNAIL_ACTIVE_NCID_CSL_RNAP_NUCLEAR =
DNA_SNAIL_ACTIVE_NCID_CSL_NUCLEAR + RNAP_NUCLEAR DNA_SNAIL_ACTIVE_NCID_CSL_RNAP_NUCLEAR =
DNA_SNAIL_ACTIVE_NCID_CSL_NUCLEAR+RNAP_NUCLEAR
0.5279286510021809 ; % 963 DNA_SNAIL_ACTIVE_NCID_CSL_RNAP_NUCLEAR = DNA_SNAIL_NUCLEAR +
ACTIVE_NCID_CSL_NUCLEAR + RNAP_NUCLEAR + MRNA_SNAIL_NUCLEAR DNA_SNAIL_ACTIVE_NCID_CSL_RNAP_NUCLEAR =
DNA_SNAIL_NUCLEAR+ACTIVE_NCID_CSL_NUCLEAR+RNAP_NUCLEAR+MRNA_SNAIL_NUCLEAR
0.64155574306432 ; % 964 MRNA_LEF1_NUCLEAR + NEXPORT_NUCLEAR = MRNA_LEF1_NEXPORT_NUCLEAR
MRNA_LEF1_NUCLEAR+NEXPORT_NUCLEAR = MRNA_LEF1_NEXPORT_NUCLEAR
0.044598989951473156 ; % 965 MRNA_LEF1_NEXPORT_NUCLEAR = MRNA_LEF1_NUCLEAR + NEXPORT_NUCLEAR
MRNA_LEF1_NEXPORT_NUCLEAR = MRNA_LEF1_NUCLEAR+NEXPORT_NUCLEAR
0.4606824018781721 ; % 966 MRNA_LEF1_NEXPORT_NUCLEAR = MRNA_LEF1_CYTOSOL + NEXPORT_NUCLEAR
MRNA_LEF1_NEXPORT_NUCLEAR = MRNA_LEF1_CYTOSOL+NEXPORT_NUCLEAR
0.13532995344825194 ; % 967 MRNA_LEF1_CYTOSOL + RIBOSOME_CYTOSOL = MRNA_LEF1_RIBOSOME_CYTOSOL
MRNA_LEF1_CYTOSOL+RIBOSOME_CYTOSOL = MRNA_LEF1_RIBOSOME_CYTOSOL
0.06013032058588437 ; % 968 MRNA_LEF1_RIBOSOME_CYTOSOL = MRNA_LEF1_CYTOSOL + RIBOSOME_CYTOSOL
MRNA_LEF1_RIBOSOME_CYTOSOL = MRNA_LEF1_CYTOSOL+RIBOSOME_CYTOSOL
0.8699641851750547 ; % 969 MRNA_LEF1_RIBOSOME_CYTOSOL = MRNA_LEF1_START_RIBOSOME_CYTOSOL
MRNA_LEF1_RIBOSOME_CYTOSOL = MRNA_LEF1_START_RIBOSOME_CYTOSOL
0.40328427740659945 ; % 970 MRNA_LEF1_START_RIBOSOME_CYTOSOL = RIBOSOME_CYTOSOL + LEF1_CYTOSOL
+ MRNA_LEF1_CYTOSOL MRNA_LEF1_START_RIBOSOME_CYTOSOL = RIBOSOME_CYTOSOL+LEF1_CYTOSOL+MRNA_LEF1_CYTOSOL
0.020573474813859627 ; % 971 MRNA_LEF1_CYTOSOL = [] MRNA_LEF1_CYTOSOL = []
0.3245253207582558 ; % 972 LEF1_CYTOSOL = [] LEF1_CYTOSOL = []
0.00036924036280513 ; % 973 DNA_LEF1_NUCLEAR + P_SP1_NUCLEAR = DNA_LEF1_P_SP1_NUCLEAR
DNA_LEF1_NUCLEAR+P_SP1_NUCLEAR = DNA_LEF1_P_SP1_NUCLEAR
0.659965185878266 ; % 974 DNA_LEF1_P_SP1_NUCLEAR = DNA_LEF1_NUCLEAR + P_SP1_NUCLEAR
DNA_LEF1_P_SP1_NUCLEAR = DNA_LEF1_NUCLEAR+P_SP1_NUCLEAR
0.00093208578737944787; % 975 DNA_LEF1_P_SP1_NUCLEAR + RNAP_NUCLEAR = DNA_LEF1_P_SP1_RNAP_NUCLEAR
DNA_LEF1_P_SP1_NUCLEAR+RNAP_NUCLEAR = DNA_LEF1_P_SP1_RNAP_NUCLEAR
0.56545678129179704 ; % 976 DNA_LEF1_P_SP1_RNAP_NUCLEAR = DNA_LEF1_P_SP1_NUCLEAR + RNAP_NUCLEAR
DNA_LEF1_P_SP1_RNAP_NUCLEAR = DNA_LEF1_P_SP1_NUCLEAR+RNAP_NUCLEAR
0.7830563296197833 ; % 977 DNA_LEF1_P_SP1_RNAP_NUCLEAR = DNA_LEF1_NUCLEAR + P_SP1_NUCLEAR +
RNAP_NUCLEAR + MRNA_LEF1_NUCLEAR DNA_LEF1_P_SP1_RNAP_NUCLEAR =
DNA_LEF1_NUCLEAR+P_SP1_NUCLEAR+RNAP_NUCLEAR+MRNA_LEF1_NUCLEAR
0.0001543146375926685 ; % 978 DNA_LEF1_NUCLEAR + P_AP1_NUCLEAR = DNA_LEF1_P_AP1_NUCLEAR
DNA_LEF1_NUCLEAR+P_AP1_NUCLEAR = DNA_LEF1_P_AP1_NUCLEAR
0.662481631069402 ; % 979 DNA_LEF1_P_AP1_NUCLEAR = DNA_LEF1_NUCLEAR + P_AP1_NUCLEAR
DNA_LEF1_P_AP1_NUCLEAR = DNA_LEF1_NUCLEAR+P_AP1_NUCLEAR
0.0009017374606204481 ; % 980 DNA_LEF1_P_AP1_NUCLEAR + RNAP_NUCLEAR = DNA_LEF1_P_AP1_RNAP_NUCLEAR
DNA_LEF1_P_AP1_NUCLEAR+RNAP_NUCLEAR = DNA_LEF1_P_AP1_RNAP_NUCLEAR
0.4023809622349879 ; % 981 DNA_LEF1_P_AP1_RNAP_NUCLEAR = DNA_LEF1_P_AP1_NUCLEAR + RNAP_NUCLEAR
DNA_LEF1_P_AP1_RNAP_NUCLEAR = DNA_LEF1_P_AP1_NUCLEAR+RNAP_NUCLEAR
0.9183818553334551 ; % 982 DNA_LEF1_P_AP1_RNAP_NUCLEAR = DNA_LEF1_NUCLEAR + P_AP1_NUCLEAR +
RNAP_NUCLEAR + MRNA_LEF1_NUCLEAR DNA_LEF1_P_AP1_RNAP_NUCLEAR =
DNA_LEF1_NUCLEAR+P_AP1_NUCLEAR+RNAP_NUCLEAR+MRNA_LEF1_NUCLEAR
0.6796486388720944 ; % 983 DNA_LEF1_NUCLEAR + YREG1_NUCLEAR = DNA_LEF1_YREG1_NUCLEAR
DNA_LEF1_NUCLEAR+YREG1_NUCLEAR = DNA_LEF1_YREG1_NUCLEAR
0.007854445931635087 ; % 984 DNA_LEF1_YREG1_NUCLEAR = DNA_LEF1_NUCLEAR + YREG1_NUCLEAR
DNA_LEF1_YREG1_NUCLEAR = DNA_LEF1_NUCLEAR+YREG1_NUCLEAR
0.9849948106923009 ; % 985 YREG1_CYTOSOL + NIMPORT_NUCLEAR = YREG1_NIMPORT_NUCLEAR
YREG1_CYTOSOL+NIMPORT_NUCLEAR = YREG1_NIMPORT_NUCLEAR
0.005110431898005731 ; % 986 YREG1_NIMPORT_NUCLEAR = YREG1_CYTOSOL + NIMPORT_NUCLEAR
YREG1_NIMPORT_NUCLEAR = YREG1_CYTOSOL+NIMPORT_NUCLEAR
0.6378155895561209 ; % 987 YREG1_NIMPORT_NUCLEAR = NIMPORT_NUCLEAR + YREG1_NUCLEAR
YREG1_NIMPORT_NUCLEAR = NIMPORT_NUCLEAR+YREG1_NUCLEAR
0.037459570865114933 ; % 988 YREG1_NUCLEAR + NEXPORT_NUCLEAR = YREG1_NEXPORT_NUCLEAR
YREG1_NUCLEAR+NEXPORT_NUCLEAR = YREG1_NEXPORT_NUCLEAR
0.06099730366904002 ; % 989 YREG1_NEXPORT_NUCLEAR = YREG1_NUCLEAR + NEXPORT_NUCLEAR
YREG1_NEXPORT_NUCLEAR = YREG1_NUCLEAR+NEXPORT_NUCLEAR
0.0507265896782332 ; % 990 YREG1_NEXPORT_NUCLEAR = NEXPORT_NUCLEAR + YREG1_CYTOSOL
YREG1_NEXPORT_NUCLEAR = NEXPORT_NUCLEAR+YREG1_CYTOSOL
0.00001290152514927544; % 991 DNA_LEF1_NUCLEAR + BCATENIN_TCF4_NUCLEAR =
DNA_LEF1_BCATENIN_TCF4_NUCLEAR DNA_LEF1_NUCLEAR+BCATENIN_TCF4_NUCLEAR = DNA_LEF1_BCATENIN_TCF4_NUCLEAR
0.023740649512587444 ; % 992 DNA_LEF1_BCATENIN_TCF4_NUCLEAR = DNA_LEF1_NUCLEAR +
BCATENIN_TCF4_NUCLEAR DNA_LEF1_BCATENIN_TCF4_NUCLEAR = DNA_LEF1_NUCLEAR+BCATENIN_TCF4_NUCLEAR

0.00004700333191116176; % 993 DNA_LEF1_BCATENIN_TCF4_NUCLEAR + RNAP_NUCLEAR =
DNA_LEF1_BCATENIN_TCF4_RNAP_NUCLEAR DNA_LEF1_BCATENIN_TCF4_NUCLEAR+RNAP_NUCLEAR = DNA_LEF1_BCATENIN_TCF4_RNAP_NUCLEAR
0.08716514430037481 ; % 994 DNA_LEF1_BCATENIN_TCF4_RNAP_NUCLEAR =
DNA_LEF1_BCATENIN_TCF4_NUCLEAR + RNAP_NUCLEAR DNA_LEF1_BCATENIN_TCF4_RNAP_NUCLEAR =
DNA_LEF1_BCATENIN_TCF4_NUCLEAR+RNAP_NUCLEAR
0.2208336482279667 ; % 995 DNA_LEF1_BCATENIN_TCF4_RNAP_NUCLEAR = DNA_LEF1_NUCLEAR +
BCATENIN_TCF4_NUCLEAR + RNAP_NUCLEAR + MRNA_LEF1_NUCLEAR DNA_LEF1_BCATENIN_TCF4_RNAP_NUCLEAR =
DNA_LEF1_NUCLEAR+BCATENIN_TCF4_NUCLEAR+RNAP_NUCLEAR+MRNA_LEF1_NUCLEAR
0.9038626132762561 ; % 996 DNA_LEF1_NUCLEAR + PSMAD2_SMAD4_NUCLEAR =
DNA_LEF1_PSMAD2_SMAD4_NUCLEAR DNA_LEF1_NUCLEAR+PSMAD2_SMAD4_NUCLEAR = DNA_LEF1_PSMAD2_SMAD4_NUCLEAR
0.0001833889101410521 ; % 997 DNA_LEF1_PSMAD2_SMAD4_NUCLEAR = DNA_LEF1_NUCLEAR +
PSMAD2_SMAD4_NUCLEAR DNA_LEF1_PSMAD2_SMAD4_NUCLEAR = DNA_LEF1_NUCLEAR+PSMAD2_SMAD4_NUCLEAR
0.684396272214844 ; % 998 DNA_LEF1_PSMAD2_SMAD4_NUCLEAR + RNAP_NUCLEAR =
DNA_LEF1_PSMAD2_SMAD4_RNAP_NUCLEAR DNA_LEF1_PSMAD2_SMAD4_NUCLEAR+RNAP_NUCLEAR = DNA_LEF1_PSMAD2_SMAD4_RNAP_NUCLEAR
0.0008832960714437582 ; % 999 DNA_LEF1_PSMAD2_SMAD4_RNAP_NUCLEAR =
DNA_LEF1_PSMAD2_SMAD4_NUCLEAR + RNAP_NUCLEAR DNA_LEF1_PSMAD2_SMAD4_RNAP_NUCLEAR =
DNA_LEF1_PSMAD2_SMAD4_NUCLEAR+RNAP_NUCLEAR
0.9993140868262271 ; % 1000 DNA_LEF1_PSMAD2_SMAD4_RNAP_NUCLEAR = DNA_LEF1_NUCLEAR +
PSMAD2_SMAD4_NUCLEAR + RNAP_NUCLEAR + MRNA_LEF1_NUCLEAR DNA_LEF1_PSMAD2_SMAD4_RNAP_NUCLEAR =
DNA_LEF1_NUCLEAR+PSMAD2_SMAD4_NUCLEAR+RNAP_NUCLEAR+MRNA_LEF1_NUCLEAR
0.5827869322306561 ; % 1001 PSMAD2_CYTOSOL + SMAD4_CYTOSOL = PSMAD2_SMAD4_CYTOSOL
PSMAD2_CYTOSOL+SMAD4_CYTOSOL = PSMAD2_SMAD4_CYTOSOL
0.008659421027035985 ; % 1002 PSMAD2_SMAD4_CYTOSOL = PSMAD2_CYTOSOL + SMAD4_CYTOSOL
PSMAD2_SMAD4_CYTOSOL = PSMAD2_CYTOSOL+SMAD4_CYTOSOL
0.6193994131883749 ; % 1003 PSMAD2_SMAD4_CYTOSOL + NIMPORT_NUCLEAR =
PSMAD2_SMAD4_NIMPORT_NUCLEAR PSMAD2_SMAD4_CYTOSOL+NIMPORT_NUCLEAR = PSMAD2_SMAD4_NIMPORT_NUCLEAR
0.07856214474732792 ; % 1004 PSMAD2_SMAD4_NIMPORT_NUCLEAR = PSMAD2_SMAD4_CYTOSOL +
NIMPORT_NUCLEAR PSMAD2_SMAD4_NIMPORT_NUCLEAR = PSMAD2_SMAD4_CYTOSOL+NIMPORT_NUCLEAR
0.6625485915323986 ; % 1005 PSMAD2_SMAD4_NIMPORT_NUCLEAR = NIMPORT_NUCLEAR +
PSMAD2_SMAD4_NUCLEAR PSMAD2_SMAD4_NIMPORT_NUCLEAR = NIMPORT_NUCLEAR+PSMAD2_SMAD4_NUCLEAR
0.09766889561146144 ; % 1006 PSMAD2_SMAD4_NUCLEAR + NEXPORT_NUCLEAR =
PSMAD2_SMAD4_NEXPORT_NUCLEAR PSMAD2_SMAD4_NUCLEAR+NEXPORT_NUCLEAR = PSMAD2_SMAD4_NEXPORT_NUCLEAR
0.013787815981760744 ; % 1007 PSMAD2_SMAD4_NEXPORT_NUCLEAR = PSMAD2_SMAD4_NUCLEAR +
NEXPORT_NUCLEAR PSMAD2_SMAD4_NEXPORT_NUCLEAR = PSMAD2_SMAD4_NUCLEAR+NEXPORT_NUCLEAR
0.07849644722521144 ; % 1008 PSMAD2_SMAD4_NEXPORT_NUCLEAR = NEXPORT_NUCLEAR +
PSMAD2_SMAD4_CYTOSOL PSMAD2_SMAD4_NEXPORT_NUCLEAR = NEXPORT_NUCLEAR+PSMAD2_SMAD4_CYTOSOL
0.8114984141007076 ; % 1009 DNA_LEF1_NUCLEAR + PSMAD3_SMAD4_NUCLEAR =
DNA_LEF1_PSMAD3_SMAD4_NUCLEAR DNA_LEF1_NUCLEAR+PSMAD3_SMAD4_NUCLEAR = DNA_LEF1_PSMAD3_SMAD4_NUCLEAR
0.0004105271269438591 ; % 1010 DNA_LEF1_PSMAD3_SMAD4_NUCLEAR = DNA_LEF1_NUCLEAR +
PSMAD3_SMAD4_NUCLEAR DNA_LEF1_PSMAD3_SMAD4_NUCLEAR = DNA_LEF1_NUCLEAR+PSMAD3_SMAD4_NUCLEAR
0.5532195234135988 ; % 1011 DNA_LEF1_PSMAD3_SMAD4_NUCLEAR + RNAP_NUCLEAR =
DNA_LEF1_PSMAD3_SMAD4_RNAP_NUCLEAR DNA_LEF1_PSMAD3_SMAD4_NUCLEAR+RNAP_NUCLEAR = DNA_LEF1_PSMAD3_SMAD4_RNAP_NUCLEAR
0.008752776269006068 ; % 1012 DNA_LEF1_PSMAD3_SMAD4_RNAP_NUCLEAR =
DNA_LEF1_PSMAD3_SMAD4_NUCLEAR + RNAP_NUCLEAR DNA_LEF1_PSMAD3_SMAD4_RNAP_NUCLEAR =
DNA_LEF1_PSMAD3_SMAD4_NUCLEAR+RNAP_NUCLEAR
0.66298925999519784 ; % 1013 DNA_LEF1_PSMAD3_SMAD4_RNAP_NUCLEAR = DNA_LEF1_NUCLEAR +
PSMAD3_SMAD4_NUCLEAR + RNAP_NUCLEAR + MRNA_LEF1_NUCLEAR DNA_LEF1_PSMAD3_SMAD4_RNAP_NUCLEAR =
DNA_LEF1_NUCLEAR+PSMAD3_SMAD4_NUCLEAR+RNAP_NUCLEAR+MRNA_LEF1_NUCLEAR
0.8495767718676666 ; % 1014 PSMAD3_CYTOSOL + SMAD4_CYTOSOL = PSMAD3_SMAD4_CYTOSOL
PSMAD3_CYTOSOL+SMAD4_CYTOSOL = PSMAD3_SMAD4_CYTOSOL
0.0020438923808302745 ; % 1015 PSMAD3_SMAD4_CYTOSOL = PSMAD3_CYTOSOL + SMAD4_CYTOSOL
PSMAD3_SMAD4_CYTOSOL = PSMAD3_CYTOSOL+SMAD4_CYTOSOL
0.50835719190732747 ; % 1016 PSMAD3_SMAD4_CYTOSOL + NIMPORT_NUCLEAR =
PSMAD3_SMAD4_NIMPORT_NUCLEAR PSMAD3_SMAD4_CYTOSOL+NIMPORT_NUCLEAR = PSMAD3_SMAD4_NIMPORT_NUCLEAR
0.003528014643126919 ; % 1017 PSMAD3_SMAD4_NIMPORT_NUCLEAR = PSMAD3_SMAD4_CYTOSOL +
NIMPORT_NUCLEAR PSMAD3_SMAD4_NIMPORT_NUCLEAR = PSMAD3_SMAD4_CYTOSOL+NIMPORT_NUCLEAR
0.34071586620842966 ; % 1018 PSMAD3_SMAD4_NIMPORT_NUCLEAR = NIMPORT_NUCLEAR +
PSMAD3_SMAD4_NUCLEAR PSMAD3_SMAD4_NIMPORT_NUCLEAR = NIMPORT_NUCLEAR+PSMAD3_SMAD4_NUCLEAR
0.0946424274434269 ; % 1019 PSMAD3_SMAD4_NUCLEAR + NEXPORT_NUCLEAR =
PSMAD3_SMAD4_NEXPORT_NUCLEAR PSMAD3_SMAD4_NUCLEAR+NEXPORT_NUCLEAR = PSMAD3_SMAD4_NEXPORT_NUCLEAR
0.07420319971944565 ; % 1020 PSMAD3_SMAD4_NEXPORT_NUCLEAR = PSMAD3_SMAD4_NUCLEAR +
NEXPORT_NUCLEAR PSMAD3_SMAD4_NEXPORT_NUCLEAR = PSMAD3_SMAD4_NUCLEAR+NEXPORT_NUCLEAR
0.06915133141781196 ; % 1021 PSMAD3_SMAD4_NEXPORT_NUCLEAR = NEXPORT_NUCLEAR +
PSMAD3_SMAD4_CYTOSOL PSMAD3_SMAD4_NEXPORT_NUCLEAR = NEXPORT_NUCLEAR+PSMAD3_SMAD4_CYTOSOL
0.909139794615169 ; % 1022 DNA_YREG1_NUCLEAR + SNAIL_NUCLEAR = DNA_YREG1_SNAIL_NUCLEAR
DNA_YREG1_NUCLEAR+SNAIL_NUCLEAR = DNA_YREG1_SNAIL_NUCLEAR
0.06879944055708677 ; % 1023 DNA_YREG1_SNAIL_NUCLEAR = DNA_YREG1_NUCLEAR + SNAIL_NUCLEAR
DNA_YREG1_SNAIL_NUCLEAR = DNA_YREG1_NUCLEAR+SNAIL_NUCLEAR
0.7792358587398225 ; % 1024 SNAIL_CYTOSOL + NIMPORT_NUCLEAR = SNAIL_NIMPORT_NUCLEAR
SNAIL_CYTOSOL+NIMPORT_NUCLEAR = SNAIL_NIMPORT_NUCLEAR
0.07300115165415934 ; % 1025 SNAIL_NIMPORT_NUCLEAR = SNAIL_CYTOSOL + NIMPORT_NUCLEAR
SNAIL_NIMPORT_NUCLEAR = SNAIL_CYTOSOL+NIMPORT_NUCLEAR
0.4642230978204308 ; % 1026 SNAIL_NIMPORT_NUCLEAR = NIMPORT_NUCLEAR + SNAIL_NUCLEAR
SNAIL_NIMPORT_NUCLEAR = NIMPORT_NUCLEAR+SNAIL_NUCLEAR
0.02322970200022778 ; % 1027 SNAIL_NUCLEAR + NEXPORT_NUCLEAR = SNAIL_NEXPORT_NUCLEAR
SNAIL_NUCLEAR+NEXPORT_NUCLEAR = SNAIL_NEXPORT_NUCLEAR
0.07258042671074526 ; % 1028 SNAIL_NEXPORT_NUCLEAR = SNAIL_NUCLEAR + NEXPORT_NUCLEAR
SNAIL_NEXPORT_NUCLEAR = SNAIL_NUCLEAR+NEXPORT_NUCLEAR
0.025129962322406052 ; % 1029 SNAIL_NEXPORT_NUCLEAR = NEXPORT_NUCLEAR + SNAIL_CYTOSOL
SNAIL_NEXPORT_NUCLEAR = NEXPORT_NUCLEAR+SNAIL_CYTOSOL
0.812985228726991 ; % 1030 DNA_YREG1_NUCLEAR + SLUG_NUCLEAR = DNA_YREG1_SLUG_NUCLEAR
DNA_YREG1_NUCLEAR+SLUG_NUCLEAR = DNA_YREG1_SLUG_NUCLEAR
0.0037556445604581268 ; % 1031 DNA_YREG1_SLUG_NUCLEAR = DNA_YREG1_NUCLEAR + SLUG_NUCLEAR
DNA_YREG1_SLUG_NUCLEAR = DNA_YREG1_NUCLEAR+SLUG_NUCLEAR
0.8057558443262969 ; % 1032 SLUG_CYTOSOL + NIMPORT_NUCLEAR = SLUG_NIMPORT_NUCLEAR
SLUG_CYTOSOL+NIMPORT_NUCLEAR = SLUG_NIMPORT_NUCLEAR
0.07969757345270201 ; % 1033 SLUG_NIMPORT_NUCLEAR = SLUG_CYTOSOL + NIMPORT_NUCLEAR
SLUG_NIMPORT_NUCLEAR = SLUG_CYTOSOL+NIMPORT_NUCLEAR
0.80446135534356968 ; % 1034 SLUG_NIMPORT_NUCLEAR = NIMPORT_NUCLEAR + SLUG_NUCLEAR
SLUG_NIMPORT_NUCLEAR = NIMPORT_NUCLEAR+SLUG_NUCLEAR
0.07549790829130268 ; % 1035 SLUG_NUCLEAR + NEXPORT_NUCLEAR = SLUG_NEXPORT_NUCLEAR
SLUG_NUCLEAR+NEXPORT_NUCLEAR = SLUG_NEXPORT_NUCLEAR

0.0479385015198228 ; % 1036 SLUG_NEXPORT_NUCLEAR = SLUG_NUCLEAR + NEXPORT_NUCLEAR
SLUG_NEXPORT_NUCLEAR = SLUG_NUCLEAR+NEXPORT_NUCLEAR
0.011032143643005121 ; % 1037 SLUG_NEXPORT_NUCLEAR = NEXPORT_NUCLEAR + SLUG_CYTOSOL
SLUG_NEXPORT_NUCLEAR = NEXPORT_NUCLEAR+SLUG_CYTOSOL
0.6563516012250837 ; % 1038 DNA_YREG1_NUCLEAR + TWIST_NUCLEAR = DNA_YREG1_TWIST_NUCLEAR
DNA_YREG1_NUCLEAR+TWIST_NUCLEAR = DNA_YREG1_TWIST_NUCLEAR
0.023819137080219654 ; % 1039 DNA_YREG1_TWIST_NUCLEAR = DNA_YREG1_NUCLEAR + TWIST_NUCLEAR
DNA_YREG1_TWIST_NUCLEAR = DNA_YREG1_NUCLEAR+TWIST_NUCLEAR
0.4287972565918152 ; % 1040 DNA_TGFBRIII_NUCLEAR + P_SP1_NUCLEAR = DNA_TGFBRIII_P_SP1_NUCLEAR
DNA_TGFBRIII_NUCLEAR+P_SP1_NUCLEAR = DNA_TGFBRIII_P_SP1_NUCLEAR
0.07095133801109646 ; % 1041 DNA_TGFBRIII_P_SP1_NUCLEAR = DNA_TGFBRIII_NUCLEAR + P_SP1_NUCLEAR
DNA_TGFBRIII_P_SP1_NUCLEAR = DNA_TGFBRIII_NUCLEAR+P_SP1_NUCLEAR
0.605894081297111 ; % 1042 DNA_TGFBRIII_P_SP1_NUCLEAR + PSMAD3_SMAD4_NUCLEAR =
DNA_TGFBRIII_P_SP1_PSMAD3_SMAD4_NUCLEAR DNA_TGFBRIII_P_SP1_NUCLEAR+PSMAD3_SMAD4_NUCLEAR =
DNA_TGFBRIII_P_SP1_PSMAD3_SMAD4_NUCLEAR
0.0053095088183134805 ; % 1043 DNA_TGFBRIII_P_SP1_PSMAD3_SMAD4_NUCLEAR = DNA_TGFBRIII_P_SP1_NUCLEAR
+ PSMAD3_SMAD4_NUCLEAR DNA_TGFBRIII_P_SP1_PSMAD3_SMAD4_NUCLEAR = DNA_TGFBRIII_P_SP1_NUCLEAR+PSMAD3_SMAD4_NUCLEAR
0.18593148318478914 ; % 1044 DNA_TGFBRIII_P_SP1_PSMAD3_SMAD4_NUCLEAR + RNAP_NUCLEAR =
DNA_TGFBRIII_P_SP1_PSMAD3_SMAD4_RNAP_NUCLEAR DNA_TGFBRIII_P_SP1_PSMAD3_SMAD4_NUCLEAR+RNAP_NUCLEAR =
DNA_TGFBRIII_P_SP1_PSMAD3_SMAD4_RNAP_NUCLEAR
0.01896652305266401 ; % 1045 DNA_TGFBRIII_P_SP1_PSMAD3_SMAD4_RNAP_NUCLEAR =
DNA_TGFBRIII_P_SP1_PSMAD3_SMAD4_NUCLEAR + RNAP_NUCLEAR DNA_TGFBRIII_P_SP1_PSMAD3_SMAD4_RNAP_NUCLEAR =
DNA_TGFBRIII_P_SP1_PSMAD3_SMAD4_NUCLEAR+RNAP_NUCLEAR
0.7371386880382716 ; % 1046 DNA_TGFBRIII_P_SP1_PSMAD3_SMAD4_RNAP_NUCLEAR = DNA_TGFBRIII_NUCLEAR
+ P_SP1_NUCLEAR + PSMAD3_SMAD4_NUCLEAR + RNAP_NUCLEAR + MRNA_TGFBRIII_NUCLEAR DNA_TGFBRIII_P_SP1_PSMAD3_SMAD4_RNAP_NUCLEAR =
DNA_TGFBRIII_NUCLEAR+P_SP1_NUCLEAR+PSMAD3_SMAD4_NUCLEAR+RNAP_NUCLEAR+MRNA_TGFBRIII_NUCLEAR
0.665750012435797 ; % 1047 MRNA_CREB_NUCLEAR + NEXPORT_NUCLEAR = MRNA_CREB_NEXPORT_NUCLEAR
MRNA_CREB_NUCLEAR+NEXPORT_NUCLEAR = MRNA_CREB_NEXPORT_NUCLEAR
0.05674904016431015 ; % 1048 MRNA_CREB_NEXPORT_NUCLEAR = MRNA_CREB_NUCLEAR + NEXPORT_NUCLEAR
MRNA_CREB_NEXPORT_NUCLEAR = MRNA_CREB_NUCLEAR+NEXPORT_NUCLEAR
0.4964775975686876 ; % 1049 MRNA_CREB_NEXPORT_NUCLEAR = MRNA_CREB_CYTOSOL + NEXPORT_NUCLEAR
MRNA_CREB_NEXPORT_NUCLEAR = MRNA_CREB_CYTOSOL+NEXPORT_NUCLEAR
0.4055352909361867 ; % 1050 MRNA_CREB_CYTOSOL + RIBOSOME_CYTOSOL =
MRNA_CREB_RIBOSOME_CYTOSOL MRNA_CREB_CYTOSOL+RIBOSOME_CYTOSOL = MRNA_CREB_RIBOSOME_CYTOSOL
0.03524739018999985 ; % 1051 MRNA_CREB_RIBOSOME_CYTOSOL = MRNA_CREB_CYTOSOL +
RIBOSOME_CYTOSOL MRNA_CREB_RIBOSOME_CYTOSOL = MRNA_CREB_CYTOSOL+RIBOSOME_CYTOSOL
0.30411257048958884 ; % 1052 MRNA_CREB_RIBOSOME_CYTOSOL = MRNA_CREB_START_RIBOSOME_CYTOSOL
MRNA_CREB_RIBOSOME_CYTOSOL = MRNA_CREB_START_RIBOSOME_CYTOSOL
0.7128434240185748 ; % 1053 MRNA_CREB_START_RIBOSOME_CYTOSOL = RIBOSOME_CYTOSOL +
CREB_CYTOSOL + MRNA_CREB_CYTOSOL MRNA_CREB_START_RIBOSOME_CYTOSOL =
RIBOSOME_CYTOSOL+CREB_CYTOSOL+MRNA_CREB_CYTOSOL
0.43955515132567996 ; % 1054 MRNA_CREB_CYTOSOL = [] MRNA_CREB_CYTOSOL = []
0.18637865591300284 ; % 1055 CREB_CYTOSOL = [] CREB_CYTOSOL = []
0.7954254033985687 ; % 1056 DNA_CREB_NUCLEAR + SNAIL_NUCLEAR = DNA_CREB_SNAIL_NUCLEAR
DNA_CREB_NUCLEAR+SNAIL_NUCLEAR = DNA_CREB_SNAIL_NUCLEAR
0.0712470302943861 ; % 1057 DNA_CREB_SNAIL_NUCLEAR = DNA_CREB_NUCLEAR + SNAIL_NUCLEAR
DNA_CREB_SNAIL_NUCLEAR = DNA_CREB_NUCLEAR+SNAIL_NUCLEAR
0.17939456103718765 ; % 1058 DNA_CREB_NUCLEAR + SLUG_NUCLEAR = DNA_CREB_SLUG_NUCLEAR
DNA_CREB_NUCLEAR+SLUG_NUCLEAR = DNA_CREB_SLUG_NUCLEAR
0.047985228020168136 ; % 1059 DNA_CREB_SLUG_NUCLEAR = DNA_CREB_NUCLEAR + SLUG_NUCLEAR
DNA_CREB_SLUG_NUCLEAR = DNA_CREB_NUCLEAR+SLUG_NUCLEAR
0.7666837272945636 ; % 1060 MRNA_TGFB3_NUCLEAR + NEXPORT_NUCLEAR = MRNA_TGFB3_NEXPORT_NUCLEAR
MRNA_TGFB3_NUCLEAR+NEXPORT_NUCLEAR = MRNA_TGFB3_NEXPORT_NUCLEAR
0.05390706317068598 ; % 1061 MRNA_TGFB3_NEXPORT_NUCLEAR = MRNA_TGFB3_NUCLEAR + NEXPORT_NUCLEAR
MRNA_TGFB3_NEXPORT_NUCLEAR = MRNA_TGFB3_NUCLEAR+NEXPORT_NUCLEAR
0.5605855961675164 ; % 1062 MRNA_TGFB3_NEXPORT_NUCLEAR = MRNA_TGFB3_CYTOSOL + NEXPORT_NUCLEAR
MRNA_TGFB3_NEXPORT_NUCLEAR = MRNA_TGFB3_CYTOSOL+NEXPORT_NUCLEAR
0.32534027511968344 ; % 1063 MRNA_TGFB3_CYTOSOL + RIBOSOME_CYTOSOL =
MRNA_TGFB3_RIBOSOME_CYTOSOL MRNA_TGFB3_CYTOSOL+RIBOSOME_CYTOSOL = MRNA_TGFB3_RIBOSOME_CYTOSOL
0.03796365960382067 ; % 1064 MRNA_TGFB3_RIBOSOME_CYTOSOL = MRNA_TGFB3_CYTOSOL +
RIBOSOME_CYTOSOL MRNA_TGFB3_RIBOSOME_CYTOSOL = MRNA_TGFB3_CYTOSOL+RIBOSOME_CYTOSOL
0.30424085754544217 ; % 1065 MRNA_TGFB3_RIBOSOME_CYTOSOL = MRNA_TGFB3_START_RIBOSOME_CYTOSOL
MRNA_TGFB3_RIBOSOME_CYTOSOL = MRNA_TGFB3_START_RIBOSOME_CYTOSOL
0.295309242494041 ; % 1066 MRNA_TGFB3_START_RIBOSOME_CYTOSOL = RIBOSOME_CYTOSOL +
TGFB3_CYTOSOL + MRNA_TGFB3_CYTOSOL MRNA_TGFB3_START_RIBOSOME_CYTOSOL =
RIBOSOME_CYTOSOL+TGFB3_CYTOSOL+MRNA_TGFB3_CYTOSOL
0.275839644207659 ; % 1067 MRNA_TGFB3_CYTOSOL = [] MRNA_TGFB3_CYTOSOL = []
0.2041367153131641 ; % 1068 TGFB3_CYTOSOL = [] TGFB3_CYTOSOL = []
0.08879715445996236 ; % 1069 DNA_TGFB3_NUCLEAR + YREG1_NUCLEAR = DNA_TGFB3_YREG1_NUCLEAR
DNA_TGFB3_NUCLEAR+YREG1_NUCLEAR = DNA_TGFB3_YREG1_NUCLEAR
0.29714793513157001 ; % 1070 DNA_TGFB3_YREG1_NUCLEAR = DNA_TGFB3_NUCLEAR + YREG1_NUCLEAR
DNA_TGFB3_YREG1_NUCLEAR = DNA_TGFB3_NUCLEAR+YREG1_NUCLEAR
0.8606759737568547 ; % 1071 DNA_TGFB3_NUCLEAR + SNAIL_NUCLEAR = DNA_TGFB3_SNAIL_NUCLEAR
DNA_TGFB3_NUCLEAR+SNAIL_NUCLEAR = DNA_TGFB3_SNAIL_NUCLEAR
0.055435733674386366 ; % 1072 DNA_TGFB3_SNAIL_NUCLEAR = DNA_TGFB3_NUCLEAR + SNAIL_NUCLEAR
DNA_TGFB3_SNAIL_NUCLEAR = DNA_TGFB3_NUCLEAR+SNAIL_NUCLEAR
2.7728002664714843 ; % 1073 DNA_TGFB3_SNAIL_NUCLEAR + BCATENIN_TCF4_NUCLEAR =
DNA_TGFB3_SNAIL_BCATENIN_TCF4_NUCLEAR DNA_TGFB3_SNAIL_NUCLEAR+BCATENIN_TCF4_NUCLEAR = DNA_TGFB3_SNAIL_BCATENIN_TCF4_NUCLEAR
0.0009471364518100901 ; % 1074 DNA_TGFB3_SNAIL_BCATENIN_TCF4_NUCLEAR = DNA_TGFB3_SNAIL_NUCLEAR +
BCATENIN_TCF4_NUCLEAR DNA_TGFB3_SNAIL_BCATENIN_TCF4_NUCLEAR = DNA_TGFB3_SNAIL_NUCLEAR+BCATENIN_TCF4_NUCLEAR
0.9602340018246602 ; % 1075 DNA_TGFB3_SNAIL_BCATENIN_TCF4_NUCLEAR + RNAP_NUCLEAR =
DNA_TGFB3_SNAIL_BCATENIN_TCF4_RNAP_NUCLEAR DNA_TGFB3_SNAIL_BCATENIN_TCF4_NUCLEAR+RNAP_NUCLEAR =
DNA_TGFB3_SNAIL_BCATENIN_TCF4_RNAP_NUCLEAR
0.008481623654728794 ; % 1076 DNA_TGFB3_SNAIL_BCATENIN_TCF4_RNAP_NUCLEAR =
DNA_TGFB3_SNAIL_BCATENIN_TCF4_NUCLEAR + RNAP_NUCLEAR DNA_TGFB3_SNAIL_BCATENIN_TCF4_RNAP_NUCLEAR =
DNA_TGFB3_SNAIL_BCATENIN_TCF4_NUCLEAR+RNAP_NUCLEAR
0.9459394466233575 ; % 1077 DNA_TGFB3_SNAIL_BCATENIN_TCF4_RNAP_NUCLEAR = DNA_TGFB3_NUCLEAR +
SNAIL_NUCLEAR + BCATENIN_TCF4_NUCLEAR + RNAP_NUCLEAR + MRNA_TGFB3_NUCLEAR DNA_TGFB3_SNAIL_BCATENIN_TCF4_RNAP_NUCLEAR =
DNA_TGFB3_NUCLEAR+SNAIL_NUCLEAR+BCATENIN_TCF4_NUCLEAR+RNAP_NUCLEAR+MRNA_TGFB3_NUCLEAR
0.9587793715687574 ; % 1078 DNA_TGFB3_NUCLEAR + SLUG_NUCLEAR = DNA_TGFB3_SLUG_NUCLEAR
DNA_TGFB3_NUCLEAR+SLUG_NUCLEAR = DNA_TGFB3_SLUG_NUCLEAR
0.05844908276465517 ; % 1079 DNA_TGFB3_SLUG_NUCLEAR = DNA_TGFB3_NUCLEAR + SLUG_NUCLEAR
DNA_TGFB3_SLUG_NUCLEAR = DNA_TGFB3_NUCLEAR+SLUG_NUCLEAR

2.95658850967513944 ; % 1080 DNA_TGFB3_SLUG_NUCLEAR + BCATENIN_TCF4_NUCLEAR = DNA_TGFB3_SLUG_BCATENIN_TCF4_NUCLEAR DNA_TGFB3_SLUG_NUCLEAR+BCATENIN_TCF4_NUCLEAR = DNA_TGFB3_SLUG_BCATENIN_TCF4_NUCLEAR
0.0005632819016923157 ; % 1081 DNA_TGFB3_SLUG_BCATENIN_TCF4_NUCLEAR = DNA_TGFB3_SLUG_NUCLEAR + BCATENIN_TCF4_NUCLEAR DNA_TGFB3_SLUG_BCATENIN_TCF4_NUCLEAR = DNA_TGFB3_SLUG_NUCLEAR+BCATENIN_TCF4_NUCLEAR
0.93358643566747774 ; % 1082 DNA_TGFB3_SLUG_BCATENIN_TCF4_NUCLEAR + RNAP_NUCLEAR = DNA_TGFB3_SLUG_BCATENIN_TCF4_RNAP_NUCLEAR DNA_TGFB3_SLUG_BCATENIN_TCF4_NUCLEAR+RNAP_NUCLEAR = DNA_TGFB3_SLUG_BCATENIN_TCF4_RNAP_NUCLEAR
0.006430467636958169 ; % 1083 DNA_TGFB3_SLUG_BCATENIN_TCF4_RNAP_NUCLEAR = DNA_TGFB3_SLUG_BCATENIN_TCF4_NUCLEAR + RNAP_NUCLEAR DNA_TGFB3_SLUG_BCATENIN_TCF4_RNAP_NUCLEAR = DNA_TGFB3_SLUG_BCATENIN_TCF4_NUCLEAR+RNAP_NUCLEAR
0.90383640685612883 ; % 1084 DNA_TGFB3_SLUG_BCATENIN_TCF4_RNAP_NUCLEAR = DNA_TGFB3_NUCLEAR + SLUG_NUCLEAR + BCATENIN_TCF4_NUCLEAR + RNAP_NUCLEAR + MRNA_TGFB3_NUCLEAR DNA_TGFB3_SLUG_BCATENIN_TCF4_RNAP_NUCLEAR = DNA_TGFB3_NUCLEAR+SLUG_NUCLEAR+BCATENIN_TCF4_NUCLEAR+RNAP_NUCLEAR+MRNA_TGFB3_NUCLEAR
0.4850069321453715 ; % 1085 MRNA_TGFB2_NUCLEAR + NEXPORT_NUCLEAR = MRNA_TGFB2_NEXPORT_NUCLEAR MRNA_TGFB2_NUCLEAR+NEXPORT_NUCLEAR = MRNA_TGFB2_NEXPORT_NUCLEAR
0.08170558704635998 ; % 1086 MRNA_TGFB2_NEXPORT_NUCLEAR = MRNA_TGFB2_NUCLEAR + NEXPORT_NUCLEAR MRNA_TGFB2_NEXPORT_NUCLEAR = MRNA_TGFB2_NUCLEAR+NEXPORT_NUCLEAR
0.5781424117965585 ; % 1087 MRNA_TGFB2_NEXPORT_NUCLEAR = MRNA_TGFB2_CYTOSOL + NEXPORT_NUCLEAR MRNA_TGFB2_NEXPORT_NUCLEAR = MRNA_TGFB2_CYTOSOL+NEXPORT_NUCLEAR
0.9990814845683813 ; % 1088 MRNA_TGFB2_CYTOSOL + RIBOSOME_CYTOSOL = MRNA_TGFB2_RIBOSOME_CYTOSOL MRNA_TGFB2_CYTOSOL+RIBOSOME_CYTOSOL = MRNA_TGFB2_RIBOSOME_CYTOSOL
0.0064580080776362354 ; % 1089 MRNA_TGFB2_RIBOSOME_CYTOSOL = MRNA_TGFB2_CYTOSOL + RIBOSOME_CYTOSOL MRNA_TGFB2_RIBOSOME_CYTOSOL = MRNA_TGFB2_CYTOSOL+RIBOSOME_CYTOSOL
0.6949779528069032 ; % 1090 MRNA_TGFB2_RIBOSOME_CYTOSOL = MRNA_TGFB2_START_RIBOSOME_CYTOSOL MRNA_TGFB2_RIBOSOME_CYTOSOL = MRNA_TGFB2_START_RIBOSOME_CYTOSOL
0.6785773412130911 ; % 1091 MRNA_TGFB2_START_RIBOSOME_CYTOSOL = RIBOSOME_CYTOSOL + TGFB2_CYTOSOL + MRNA_TGFB2_CYTOSOL MRNA_TGFB2_START_RIBOSOME_CYTOSOL = RIBOSOME_CYTOSOL+TGFB2_CYTOSOL+MRNA_TGFB2_CYTOSOL
0.43054744497003544 ; % 1092 MRNA_TGFB2_CYTOSOL = [] MRNA_TGFB2_CYTOSOL = []
0.3506301009784325 ; % 1093 TGFB2_CYTOSOL = [] TGFB2_CYTOSOL = []
0.6622835370213042 ; % 1094 DNA_TGFB2_NUCLEAR + PAX3_NUCLEAR = DNA_TGFB2_PAX3_NUCLEAR DNA_TGFB2_NUCLEAR+PAX3_NUCLEAR = DNA_TGFB2_PAX3_NUCLEAR
0.06348150010650078 ; % 1095 DNA_TGFB2_PAX3_NUCLEAR = DNA_TGFB2_NUCLEAR + PAX3_NUCLEAR DNA_TGFB2_PAX3_NUCLEAR = DNA_TGFB2_NUCLEAR+PAX3_NUCLEAR
0.3315168400872974 ; % 1096 DNA_TGFB2_PAX3_NUCLEAR + PSMAD1_SMAD4_NUCLEAR = DNA_TGFB2_PAX3_PSMAD1_SMAD4_NUCLEAR DNA_TGFB2_PAX3_NUCLEAR+PSMAD1_SMAD4_NUCLEAR = DNA_TGFB2_PAX3_PSMAD1_SMAD4_NUCLEAR
0.06507976572532394 ; % 1097 DNA_TGFB2_PAX3_PSMAD1_SMAD4_NUCLEAR = DNA_TGFB2_PAX3_NUCLEAR + PSMAD1_SMAD4_NUCLEAR DNA_TGFB2_PAX3_PSMAD1_SMAD4_NUCLEAR = DNA_TGFB2_PAX3_NUCLEAR+PSMAD1_SMAD4_NUCLEAR
0.7711975728734458 ; % 1098 DNA_TGFB2_PAX3_PSMAD1_SMAD4_NUCLEAR + RNAP_NUCLEAR = DNA_TGFB2_PAX3_PSMAD1_SMAD4_RNAP_NUCLEAR DNA_TGFB2_PAX3_PSMAD1_SMAD4_NUCLEAR+RNAP_NUCLEAR = DNA_TGFB2_PAX3_PSMAD1_SMAD4_RNAP_NUCLEAR
0.010531070462283743 ; % 1099 DNA_TGFB2_PAX3_PSMAD1_SMAD4_RNAP_NUCLEAR = DNA_TGFB2_PAX3_PSMAD1_SMAD4_NUCLEAR + RNAP_NUCLEAR DNA_TGFB2_PAX3_PSMAD1_SMAD4_RNAP_NUCLEAR = DNA_TGFB2_PAX3_PSMAD1_SMAD4_NUCLEAR+RNAP_NUCLEAR
0.5764951821425189 ; % 1100 DNA_TGFB2_PAX3_PSMAD1_SMAD4_RNAP_NUCLEAR = DNA_TGFB2_NUCLEAR + PAX3_NUCLEAR + PSMAD1_SMAD4_NUCLEAR + RNAP_NUCLEAR + MRNA_TGFB2_NUCLEAR DNA_TGFB2_PAX3_PSMAD1_SMAD4_RNAP_NUCLEAR = DNA_TGFB2_NUCLEAR+PAX3_NUCLEAR+PSMAD1_SMAD4_NUCLEAR+RNAP_NUCLEAR+MRNA_TGFB2_NUCLEAR
0.7298277826495015 ; % 1101 PAX3_CYTOSOL + NIMPORT_NUCLEAR = PAX3_NIMPORT_NUCLEAR PAX3_CYTOSOL+NIMPORT_NUCLEAR = PAX3_NIMPORT_NUCLEAR
0.037725802977387195 ; % 1102 PAX3_NIMPORT_NUCLEAR = PAX3_CYTOSOL + NIMPORT_NUCLEAR PAX3_NIMPORT_NUCLEAR = PAX3_CYTOSOL+NIMPORT_NUCLEAR
0.2943601757351937 ; % 1103 PAX3_NIMPORT_NUCLEAR = NIMPORT_NUCLEAR + PAX3_NUCLEAR PAX3_NIMPORT_NUCLEAR = NIMPORT_NUCLEAR+PAX3_NUCLEAR
0.19066027008711983 ; % 1104 PAX3_NUCLEAR + NEXPORT_NUCLEAR = PAX3_NEXPORT_NUCLEAR PAX3_NUCLEAR+NEXPORT_NUCLEAR = PAX3_NEXPORT_NUCLEAR
0.08465340058514474 ; % 1105 PAX3_NEXPORT_NUCLEAR = PAX3_NUCLEAR + NEXPORT_NUCLEAR PAX3_NEXPORT_NUCLEAR = PAX3_NUCLEAR+NEXPORT_NUCLEAR
0.2941437227259286 ; % 1106 PAX3_NEXPORT_NUCLEAR = NEXPORT_NUCLEAR + PAX3_CYTOSOL PAX3_NEXPORT_NUCLEAR = NEXPORT_NUCLEAR+PAX3_CYTOSOL
0.00617221557970149 ; % 1107 PSMAD1_CYTOSOL + SMAD4_CYTOSOL = PSMAD1_SMAD4_CYTOSOL PSMAD1_CYTOSOL+SMAD4_CYTOSOL = PSMAD1_SMAD4_CYTOSOL
0.023791508158311526 ; % 1108 PSMAD1_SMAD4_CYTOSOL = PSMAD1_CYTOSOL + SMAD4_CYTOSOL PSMAD1_SMAD4_CYTOSOL = PSMAD1_CYTOSOL+SMAD4_CYTOSOL
0.14347556112494964 ; % 1109 PSMAD1_SMAD4_CYTOSOL + NIMPORT_NUCLEAR = PSMAD1_SMAD4_NIMPORT_NUCLEAR PSMAD1_SMAD4_CYTOSOL+NIMPORT_NUCLEAR = PSMAD1_SMAD4_NIMPORT_NUCLEAR
0.036688798507741927 ; % 1110 PSMAD1_SMAD4_NIMPORT_NUCLEAR = PSMAD1_SMAD4_CYTOSOL + NIMPORT_NUCLEAR PSMAD1_SMAD4_NIMPORT_NUCLEAR = PSMAD1_SMAD4_CYTOSOL+NIMPORT_NUCLEAR
0.6963136653286528 ; % 1111 PSMAD1_SMAD4_NIMPORT_NUCLEAR = NIMPORT_NUCLEAR + PSMAD1_SMAD4_NUCLEAR PSMAD1_SMAD4_NIMPORT_NUCLEAR = NIMPORT_NUCLEAR+PSMAD1_SMAD4_NUCLEAR
0.29027669234818865 ; % 1112 PSMAD1_SMAD4_NUCLEAR + NEXPORT_NUCLEAR = PSMAD1_SMAD4_NEXPORT_NUCLEAR PSMAD1_SMAD4_NUCLEAR+NEXPORT_NUCLEAR = PSMAD1_SMAD4_NEXPORT_NUCLEAR
0.09480446405616899 ; % 1113 PSMAD1_SMAD4_NEXPORT_NUCLEAR = PSMAD1_SMAD4_NUCLEAR + NEXPORT_NUCLEAR PSMAD1_SMAD4_NEXPORT_NUCLEAR = PSMAD1_SMAD4_NUCLEAR+NEXPORT_NUCLEAR
0.37793673166475517 ; % 1114 PSMAD1_SMAD4_NEXPORT_NUCLEAR = NEXPORT_NUCLEAR + PSMAD1_SMAD4_CYTOSOL PSMAD1_SMAD4_NEXPORT_NUCLEAR = NEXPORT_NUCLEAR+PSMAD1_SMAD4_CYTOSOL
0.5543713655333042 ; % 1115 MRNA_VIMENTIN_NUCLEAR + NEXPORT_NUCLEAR = MRNA_VIMENTIN_NEXPORT_NUCLEAR MRNA_VIMENTIN_NUCLEAR+NEXPORT_NUCLEAR = MRNA_VIMENTIN_NEXPORT_NUCLEAR
0.06590140632861317 ; % 1116 MRNA_VIMENTIN_NEXPORT_NUCLEAR = MRNA_VIMENTIN_NUCLEAR + NEXPORT_NUCLEAR MRNA_VIMENTIN_NEXPORT_NUCLEAR = MRNA_VIMENTIN_NUCLEAR+NEXPORT_NUCLEAR
0.19183873330111634 ; % 1117 MRNA_VIMENTIN_NEXPORT_NUCLEAR = MRNA_VIMENTIN_CYTOSOL + NEXPORT_NUCLEAR MRNA_VIMENTIN_NEXPORT_NUCLEAR = MRNA_VIMENTIN_CYTOSOL+NEXPORT_NUCLEAR
0.6116435695122195 ; % 1118 MRNA_VIMENTIN_CYTOSOL + RIBOSOME_CYTOSOL = MRNA_VIMENTIN_RIBOSOME_CYTOSOL MRNA_VIMENTIN_CYTOSOL+RIBOSOME_CYTOSOL = MRNA_VIMENTIN_RIBOSOME_CYTOSOL
0.03206197161049751 ; % 1119 MRNA_VIMENTIN_RIBOSOME_CYTOSOL = MRNA_VIMENTIN_CYTOSOL + RIBOSOME_CYTOSOL MRNA_VIMENTIN_RIBOSOME_CYTOSOL = MRNA_VIMENTIN_CYTOSOL+RIBOSOME_CYTOSOL
0.751583895984501 ; % 1120 MRNA_VIMENTIN_RIBOSOME_CYTOSOL = MRNA_VIMENTIN_START_RIBOSOME_CYTOSOL MRNA_VIMENTIN_RIBOSOME_CYTOSOL = MRNA_VIMENTIN_START_RIBOSOME_CYTOSOL
0.08230348368469531 ; % 1121 MRNA_VIMENTIN_START_RIBOSOME_CYTOSOL = RIBOSOME_CYTOSOL + VIMENTIN_CYTOSOL + MRNA_VIMENTIN_CYTOSOL MRNA_VIMENTIN_START_RIBOSOME_CYTOSOL = RIBOSOME_CYTOSOL+VIMENTIN_CYTOSOL+MRNA_VIMENTIN_CYTOSOL
0.3600881994900167 ; % 1122 MRNA_VIMENTIN_CYTOSOL = [] MRNA_VIMENTIN_CYTOSOL = []
0.18233949835885782 ; % 1123 VIMENTIN_CYTOSOL = [] VIMENTIN_CYTOSOL = []

0.933746963050898 ; % 1124 DNA_VIMENTIN_NUCLEAR + BCATENIN_LEF1_NUCLEAR = DNA_VIMENTIN_BCATENIN_LEF1_NUCLEAR DNA_VIMENTIN_NUCLEAR+BCATENIN_LEF1_NUCLEAR = DNA_VIMENTIN_BCATENIN_LEF1_NUCLEAR
0.00529883223873911822; % 1125 DNA_VIMENTIN_BCATENIN_LEF1_NUCLEAR = DNA_VIMENTIN_NUCLEAR + BCATENIN_LEF1_NUCLEAR DNA_VIMENTIN_BCATENIN_LEF1_NUCLEAR = DNA_VIMENTIN_NUCLEAR+BCATENIN_LEF1_NUCLEAR
0.94574432804475578 ; % 1126 DNA_VIMENTIN_BCATENIN_LEF1_NUCLEAR + RNAP_NUCLEAR = DNA_VIMENTIN_BCATENIN_LEF1_RNAP_NUCLEAR DNA_VIMENTIN_BCATENIN_LEF1_NUCLEAR+RNAP_NUCLEAR = DNA_VIMENTIN_BCATENIN_LEF1_RNAP_NUCLEAR
0.025355941671139741 ; % 1127 DNA_VIMENTIN_BCATENIN_LEF1_RNAP_NUCLEAR = DNA_VIMENTIN_BCATENIN_LEF1_NUCLEAR + RNAP_NUCLEAR DNA_VIMENTIN_BCATENIN_LEF1_RNAP_NUCLEAR = DNA_VIMENTIN_BCATENIN_LEF1_NUCLEAR+RNAP_NUCLEAR
0.42502705255690143 ; % 1128 DNA_VIMENTIN_BCATENIN_LEF1_RNAP_NUCLEAR = DNA_VIMENTIN_NUCLEAR + BCATENIN_LEF1_NUCLEAR + RNAP_NUCLEAR + MRNA_VIMENTIN_NUCLEAR DNA_VIMENTIN_BCATENIN_LEF1_RNAP_NUCLEAR = DNA_VIMENTIN_NUCLEAR+BCATENIN_LEF1_NUCLEAR+RNAP_NUCLEAR+MRNA_VIMENTIN_NUCLEAR
0.7359994633988156 ; % 1129 DNA_VIMENTIN_NUCLEAR + LEF1_NUCLEAR = DNA_VIMENTIN_LEF1_NUCLEAR DNA_VIMENTIN_NUCLEAR+LEF1_NUCLEAR = DNA_VIMENTIN_LEF1_NUCLEAR
0.037752819371371586 ; % 1130 DNA_VIMENTIN_LEF1_NUCLEAR = DNA_VIMENTIN_NUCLEAR + LEF1_NUCLEAR DNA_VIMENTIN_LEF1_NUCLEAR = DNA_VIMENTIN_NUCLEAR+LEF1_NUCLEAR
0.4304591719750822 ; % 1131 DNA_VIMENTIN_LEF1_NUCLEAR + PSMAD2_SMAD4_NUCLEAR = DNA_VIMENTIN_LEF1_PSMAD2_SMAD4_NUCLEAR DNA_VIMENTIN_LEF1_NUCLEAR+PSMAD2_SMAD4_NUCLEAR = DNA_VIMENTIN_LEF1_PSMAD2_SMAD4_NUCLEAR
0.012410542455107067 ; % 1132 DNA_VIMENTIN_LEF1_PSMAD2_SMAD4_NUCLEAR = DNA_VIMENTIN_LEF1_NUCLEAR + PSMAD2_SMAD4_NUCLEAR DNA_VIMENTIN_LEF1_PSMAD2_SMAD4_NUCLEAR = DNA_VIMENTIN_LEF1_NUCLEAR+PSMAD2_SMAD4_NUCLEAR
0.8017017007987758 ; % 1133 DNA_VIMENTIN_LEF1_PSMAD2_SMAD4_NUCLEAR + RNAP_NUCLEAR = DNA_VIMENTIN_LEF1_PSMAD2_SMAD4_RNAP_NUCLEAR DNA_VIMENTIN_LEF1_PSMAD2_SMAD4_NUCLEAR+RNAP_NUCLEAR = DNA_VIMENTIN_LEF1_PSMAD2_SMAD4_RNAP_NUCLEAR
0.023025974890033676 ; % 1134 DNA_VIMENTIN_LEF1_PSMAD2_SMAD4_RNAP_NUCLEAR = DNA_VIMENTIN_LEF1_PSMAD2_SMAD4_NUCLEAR + RNAP_NUCLEAR DNA_VIMENTIN_LEF1_PSMAD2_SMAD4_RNAP_NUCLEAR = DNA_VIMENTIN_LEF1_PSMAD2_SMAD4_NUCLEAR+RNAP_NUCLEAR
0.022657810821324564 ; % 1135 DNA_VIMENTIN_LEF1_PSMAD2_SMAD4_RNAP_NUCLEAR = DNA_VIMENTIN_NUCLEAR + LEF1_NUCLEAR + PSMAD2_SMAD4_NUCLEAR + RNAP_NUCLEAR + MRNA_VIMENTIN_NUCLEAR DNA_VIMENTIN_LEF1_PSMAD2_SMAD4_RNAP_NUCLEAR = DNA_VIMENTIN_NUCLEAR+LEF1_NUCLEAR+PSMAD2_SMAD4_NUCLEAR+RNAP_NUCLEAR+MRNA_VIMENTIN_NUCLEAR
0.8041552408319446 ; % 1136 LEF1_CYTOSOL + NIMPORT_NUCLEAR = LEF1_NIMPORT_NUCLEAR LEF1_CYTOSOL+NIMPORT_NUCLEAR = LEF1_NIMPORT_NUCLEAR
0.02364981823348049 ; % 1137 LEF1_NIMPORT_NUCLEAR = LEF1_CYTOSOL + NIMPORT_NUCLEAR LEF1_NIMPORT_NUCLEAR = LEF1_CYTOSOL+NIMPORT_NUCLEAR
0.528919155551982 ; % 1138 LEF1_NIMPORT_NUCLEAR = NIMPORT_NUCLEAR + LEF1_NUCLEAR LEF1_NIMPORT_NUCLEAR = NIMPORT_NUCLEAR+LEF1_NUCLEAR
0.04098648153561901 ; % 1139 LEF1_NUCLEAR + NEXPORT_NUCLEAR = LEF1_NEXPORT_NUCLEAR LEF1_NUCLEAR+NEXPORT_NUCLEAR = LEF1_NEXPORT_NUCLEAR
0.09146862207562576 ; % 1140 LEF1_NEXPORT_NUCLEAR = LEF1_NUCLEAR + NEXPORT_NUCLEAR LEF1_NEXPORT_NUCLEAR = LEF1_NUCLEAR+NEXPORT_NUCLEAR
0.5594531208281086 ; % 1141 LEF1_NEXPORT_NUCLEAR = NEXPORT_NUCLEAR + LEF1_CYTOSOL LEF1_NEXPORT_NUCLEAR = NEXPORT_NUCLEAR+LEF1_CYTOSOL
0.6137261668090083 ; % 1142 DNA_VIMENTIN_LEF1_NUCLEAR + PSMAD3_SMAD4_NUCLEAR = DNA_VIMENTIN_LEF1_PSMAD3_SMAD4_NUCLEAR DNA_VIMENTIN_LEF1_NUCLEAR+PSMAD3_SMAD4_NUCLEAR = DNA_VIMENTIN_LEF1_PSMAD3_SMAD4_NUCLEAR
0.009737057497278313 ; % 1143 DNA_VIMENTIN_LEF1_PSMAD3_SMAD4_NUCLEAR = DNA_VIMENTIN_LEF1_NUCLEAR + PSMAD3_SMAD4_NUCLEAR DNA_VIMENTIN_LEF1_PSMAD3_SMAD4_NUCLEAR = DNA_VIMENTIN_LEF1_NUCLEAR+PSMAD3_SMAD4_NUCLEAR
0.5823813176666843 ; % 1144 DNA_VIMENTIN_LEF1_PSMAD3_SMAD4_NUCLEAR + RNAP_NUCLEAR = DNA_VIMENTIN_LEF1_PSMAD3_SMAD4_RNAP_NUCLEAR DNA_VIMENTIN_LEF1_PSMAD3_SMAD4_NUCLEAR+RNAP_NUCLEAR = DNA_VIMENTIN_LEF1_PSMAD3_SMAD4_RNAP_NUCLEAR
0.051680041664943346 ; % 1145 DNA_VIMENTIN_LEF1_PSMAD3_SMAD4_RNAP_NUCLEAR = DNA_VIMENTIN_LEF1_PSMAD3_SMAD4_NUCLEAR + RNAP_NUCLEAR DNA_VIMENTIN_LEF1_PSMAD3_SMAD4_RNAP_NUCLEAR = DNA_VIMENTIN_LEF1_PSMAD3_SMAD4_NUCLEAR+RNAP_NUCLEAR
0.08962497182038665 ; % 1146 DNA_VIMENTIN_LEF1_PSMAD3_SMAD4_RNAP_NUCLEAR = DNA_VIMENTIN_NUCLEAR + LEF1_NUCLEAR + PSMAD3_SMAD4_NUCLEAR + RNAP_NUCLEAR + MRNA_VIMENTIN_NUCLEAR DNA_VIMENTIN_LEF1_PSMAD3_SMAD4_RNAP_NUCLEAR = DNA_VIMENTIN_NUCLEAR+LEF1_NUCLEAR+PSMAD3_SMAD4_NUCLEAR+RNAP_NUCLEAR+MRNA_VIMENTIN_NUCLEAR
0.62358035346184966 ; % 1147 DNA_ECADHERIN_NUCLEAR + NFATC1_NUCLEAR = DNA_ECADHERIN_NFATC1_NUCLEAR DNA_ECADHERIN_NUCLEAR+NFATC1_NUCLEAR = DNA_ECADHERIN_NFATC1_NUCLEAR
0.003968379412761332 ; % 1148 DNA_ECADHERIN_NFATC1_NUCLEAR = DNA_ECADHERIN_NUCLEAR + NFATC1_NUCLEAR DNA_ECADHERIN_NFATC1_NUCLEAR = DNA_ECADHERIN_NUCLEAR+NFATC1_NUCLEAR
0.6198477541215658 ; % 1149 DNA_ECADHERIN_NFATC1_NUCLEAR + RNAP_NUCLEAR = DNA_ECADHERIN_NFATC1_RNAP_NUCLEAR DNA_ECADHERIN_NFATC1_NUCLEAR+RNAP_NUCLEAR = DNA_ECADHERIN_NFATC1_RNAP_NUCLEAR
0.07780243834244122 ; % 1150 DNA_ECADHERIN_NFATC1_RNAP_NUCLEAR = DNA_ECADHERIN_NFATC1_NUCLEAR + RNAP_NUCLEAR DNA_ECADHERIN_NFATC1_RNAP_NUCLEAR = DNA_ECADHERIN_NFATC1_NUCLEAR+RNAP_NUCLEAR
0.629866051164546 ; % 1151 DNA_ECADHERIN_NFATC1_RNAP_NUCLEAR = DNA_ECADHERIN_NUCLEAR + NFATC1_NUCLEAR + RNAP_NUCLEAR + MRNA_ECADHERIN_NUCLEAR DNA_ECADHERIN_NFATC1_RNAP_NUCLEAR = DNA_ECADHERIN_NUCLEAR+NFATC1_NUCLEAR+RNAP_NUCLEAR+MRNA_ECADHERIN_NUCLEAR
0.00045340623280635812; % 1152 DNA_ECADHERIN_NUCLEAR + SNAIL_NUCLEAR = DNA_ECADHERIN_SNAIL_NUCLEAR DNA_ECADHERIN_NUCLEAR+SNAIL_NUCLEAR = DNA_ECADHERIN_SNAIL_NUCLEAR
0.746528240239407 ; % 1153 DNA_ECADHERIN_SNAIL_NUCLEAR = DNA_ECADHERIN_NUCLEAR + SNAIL_NUCLEAR DNA_ECADHERIN_SNAIL_NUCLEAR = DNA_ECADHERIN_NUCLEAR+SNAIL_NUCLEAR
0.00028952961987271664; % 1154 DNA_ECADHERIN_NUCLEAR + SLUG_NUCLEAR = DNA_ECADHERIN_SLUG_NUCLEAR DNA_ECADHERIN_NUCLEAR+SLUG_NUCLEAR = DNA_ECADHERIN_SLUG_NUCLEAR
0.30508744645194832 ; % 1155 DNA_ECADHERIN_SLUG_NUCLEAR = DNA_ECADHERIN_NUCLEAR + SLUG_NUCLEAR DNA_ECADHERIN_SLUG_NUCLEAR = DNA_ECADHERIN_NUCLEAR+SLUG_NUCLEAR
0.0004211969880194234 ; % 1156 DNA_ECADHERIN_NUCLEAR + TWIST_NUCLEAR = DNA_ECADHERIN_TWIST_NUCLEAR DNA_ECADHERIN_NUCLEAR+TWIST_NUCLEAR = DNA_ECADHERIN_TWIST_NUCLEAR
0.598382828695121 ; % 1157 DNA_ECADHERIN_TWIST_NUCLEAR = DNA_ECADHERIN_NUCLEAR + TWIST_NUCLEAR DNA_ECADHERIN_TWIST_NUCLEAR = DNA_ECADHERIN_NUCLEAR+TWIST_NUCLEAR
10.9833610667458117 ; % 1158 DNA_ECADHERIN_NUCLEAR + PSMAD2_SMAD4_LEF1_NUCLEAR = DNA_ECADHERIN_PSMAD2_SMAD4_LEF1_NUCLEAR DNA_ECADHERIN_NUCLEAR+PSMAD2_SMAD4_LEF1_NUCLEAR = DNA_ECADHERIN_PSMAD2_SMAD4_LEF1_NUCLEAR
0.001924519456629695 ; % 1159 DNA_ECADHERIN_PSMAD2_SMAD4_LEF1_NUCLEAR = DNA_ECADHERIN_NUCLEAR + PSMAD2_SMAD4_LEF1_NUCLEAR DNA_ECADHERIN_PSMAD2_SMAD4_LEF1_NUCLEAR = DNA_ECADHERIN_NUCLEAR+PSMAD2_SMAD4_LEF1_NUCLEAR
0.9160893063397343 ; % 1160 PSMAD2_SMAD4_CYTOSOL + LEF1_CYTOSOL = PSMAD2_SMAD4_LEF1_CYTOSOL PSMAD2_SMAD4_CYTOSOL+LEF1_CYTOSOL = PSMAD2_SMAD4_LEF1_CYTOSOL
0.006609704069273768 ; % 1161 PSMAD2_SMAD4_LEF1_CYTOSOL = PSMAD2_SMAD4_CYTOSOL + LEF1_CYTOSOL PSMAD2_SMAD4_LEF1_CYTOSOL = PSMAD2_SMAD4_CYTOSOL+LEF1_CYTOSOL
0.988381930294002 ; % 1162 PSMAD2_SMAD4_LEF1_CYTOSOL + NIMPORT_NUCLEAR = PSMAD2_SMAD4_LEF1_NIMPORT_NUCLEAR PSMAD2_SMAD4_LEF1_CYTOSOL+NIMPORT_NUCLEAR = PSMAD2_SMAD4_LEF1_NIMPORT_NUCLEAR
0.006372435799513568 ; % 1163 PSMAD2_SMAD4_LEF1_NIMPORT_NUCLEAR = PSMAD2_SMAD4_LEF1_CYTOSOL + NIMPORT_NUCLEAR PSMAD2_SMAD4_LEF1_NIMPORT_NUCLEAR = PSMAD2_SMAD4_LEF1_CYTOSOL+NIMPORT_NUCLEAR

0.9865763957818503 ; % 1164 PSMAD2_SMAD4_LEF1_NIMPORT_NUCLEAR = NIMPORT_NUCLEAR + PSMAD2_SMAD4_LEF1_NUCLEAR PSMAD2_SMAD4_LEF1_NIMPORT_NUCLEAR = NIMPORT_NUCLEAR+PSMAD2_SMAD4_LEF1_NUCLEAR
0.0045577040173680894 ; % 1165 PSMAD2_SMAD4_LEF1_NUCLEAR + NEXPORT_NUCLEAR = PSMAD2_SMAD4_LEF1_NEXPORT_NUCLEAR PSMAD2_SMAD4_LEF1_NUCLEAR+NEXPORT_NUCLEAR = PSMAD2_SMAD4_LEF1_NEXPORT_NUCLEAR
0.05511382169521936 ; % 1166 PSMAD2_SMAD4_LEF1_NEXPORT_NUCLEAR = PSMAD2_SMAD4_LEF1_NUCLEAR + NEXPORT_NUCLEAR PSMAD2_SMAD4_LEF1_NEXPORT_NUCLEAR = PSMAD2_SMAD4_LEF1_NUCLEAR+NEXPORT_NUCLEAR
0.030637592982548334 ; % 1167 PSMAD2_SMAD4_LEF1_NEXPORT_NUCLEAR = NEXPORT_NUCLEAR + PSMAD2_SMAD4_LEF1_CYTOSOL PSMAD2_SMAD4_LEF1_NEXPORT_NUCLEAR = NEXPORT_NUCLEAR+PSMAD2_SMAD4_LEF1_CYTOSOL
0.014545335631093836 ; % 1168 DNA_VECADHERIN_NUCLEAR + NFATC1_NUCLEAR = DNA_VECADHERIN_NFATC1_NUCLEAR DNA_VECADHERIN_NUCLEAR+NFATC1_NUCLEAR = DNA_VECADHERIN_NFATC1_NUCLEAR
0.0670217867217895 ; % 1169 DNA_VECADHERIN_NFATC1_NUCLEAR = DNA_VECADHERIN_NUCLEAR + NFATC1_NUCLEAR DNA_VECADHERIN_NFATC1_NUCLEAR = DNA_VECADHERIN_NUCLEAR+NFATC1_NUCLEAR
0.4745250965685228 ; % 1170 DNA_VECADHERIN_NFATC1_NUCLEAR + RNAP_NUCLEAR = DNA_VECADHERIN_NFATC1_RNAP_NUCLEAR DNA_VECADHERIN_NFATC1_NUCLEAR+RNAP_NUCLEAR = DNA_VECADHERIN_NFATC1_RNAP_NUCLEAR
0.038044607910185546 ; % 1171 DNA_VECADHERIN_NFATC1_RNAP_NUCLEAR = DNA_VECADHERIN_NFATC1_NUCLEAR + RNAP_NUCLEAR DNA_VECADHERIN_NFATC1_RNAP_NUCLEAR = DNA_VECADHERIN_NFATC1_NUCLEAR+RNAP_NUCLEAR
0.9935944967873709 ; % 1172 DNA_VECADHERIN_NFATC1_RNAP_NUCLEAR = DNA_VECADHERIN_NUCLEAR + NFATC1_NUCLEAR + RNAP_NUCLEAR + MRNA_VECADHERIN_NUCLEAR DNA_VECADHERIN_NFATC1_RNAP_NUCLEAR = DNA_VECADHERIN_NUCLEAR+NFATC1_NUCLEAR+RNAP_NUCLEAR+MRNA_VECADHERIN_NUCLEAR
0.703950399024606 ; % 1173 DNA_VECADHERIN_NUCLEAR + SNAIL_NUCLEAR = DNA_VECADHERIN_SNAIL_NUCLEAR DNA_VECADHERIN_NUCLEAR+SNAIL_NUCLEAR = DNA_VECADHERIN_SNAIL_NUCLEAR
0.0526623517423019 ; % 1174 DNA_VECADHERIN_SNAIL_NUCLEAR = DNA_VECADHERIN_NUCLEAR + SNAIL_NUCLEAR DNA_VECADHERIN_SNAIL_NUCLEAR = DNA_VECADHERIN_NUCLEAR+SNAIL_NUCLEAR
0.6397713167279583 ; % 1175 DNA_VECADHERIN_NUCLEAR + SLUG_NUCLEAR = DNA_VECADHERIN_SLUG_NUCLEAR DNA_VECADHERIN_NUCLEAR+SLUG_NUCLEAR = DNA_VECADHERIN_SLUG_NUCLEAR
0.007425026654045075 ; % 1176 DNA_VECADHERIN_SLUG_NUCLEAR = DNA_VECADHERIN_NUCLEAR + SLUG_NUCLEAR DNA_VECADHERIN_SLUG_NUCLEAR = DNA_VECADHERIN_NUCLEAR+SLUG_NUCLEAR
0.08042107480684346 ; % 1177 DNA_VECADHERIN_NUCLEAR + TWIST_NUCLEAR = DNA_VECADHERIN_TWIST_NUCLEAR DNA_VECADHERIN_NUCLEAR+TWIST_NUCLEAR = DNA_VECADHERIN_TWIST_NUCLEAR
0.021079792645148643 ; % 1178 DNA_VECADHERIN_TWIST_NUCLEAR = DNA_VECADHERIN_NUCLEAR + TWIST_NUCLEAR DNA_VECADHERIN_TWIST_NUCLEAR = DNA_VECADHERIN_NUCLEAR+TWIST_NUCLEAR
0.49046822044526084 ; % 1179 DNA_VECADHERIN_NUCLEAR + LEF1_NUCLEAR = DNA_VECADHERIN_LEF1_NUCLEAR DNA_VECADHERIN_NUCLEAR+LEF1_NUCLEAR = DNA_VECADHERIN_LEF1_NUCLEAR
0.033845260108793074 ; % 1180 DNA_VECADHERIN_LEF1_NUCLEAR = DNA_VECADHERIN_NUCLEAR + LEF1_NUCLEAR DNA_VECADHERIN_LEF1_NUCLEAR = DNA_VECADHERIN_NUCLEAR+LEF1_NUCLEAR
0.03809992816596819 ; % 1181 MRNA_DSCR1_NUCLEAR + NEXPORT_NUCLEAR = MRNA_DSCR1_NEXPORT_NUCLEAR MRNA_DSCR1_NUCLEAR+NEXPORT_NUCLEAR = MRNA_DSCR1_NEXPORT_NUCLEAR
0.08455285168999081 ; % 1182 MRNA_DSCR1_NEXPORT_NUCLEAR = MRNA_DSCR1_NUCLEAR + NEXPORT_NUCLEAR MRNA_DSCR1_NEXPORT_NUCLEAR = MRNA_DSCR1_NUCLEAR+NEXPORT_NUCLEAR
0.5889360252987179 ; % 1183 MRNA_DSCR1_NEXPORT_NUCLEAR = MRNA_DSCR1_CYTOSOL + NEXPORT_NUCLEAR MRNA_DSCR1_NEXPORT_NUCLEAR = MRNA_DSCR1_CYTOSOL+NEXPORT_NUCLEAR
0.3849362137945965 ; % 1184 MRNA_DSCR1_CYTOSOL + RIBOSOME_CYTOSOL = MRNA_DSCR1_RIBOSOME_CYTOSOL MRNA_DSCR1_CYTOSOL+RIBOSOME_CYTOSOL = MRNA_DSCR1_RIBOSOME_CYTOSOL
9.199981793933444E-4 ; % 1185 MRNA_DSCR1_RIBOSOME_CYTOSOL = MRNA_DSCR1_CYTOSOL + RIBOSOME_CYTOSOL MRNA_DSCR1_RIBOSOME_CYTOSOL = MRNA_DSCR1_CYTOSOL+RIBOSOME_CYTOSOL
0.306859001219532 ; % 1186 MRNA_DSCR1_RIBOSOME_CYTOSOL = MRNA_DSCR1_START_RIBOSOME_CYTOSOL MRNA_DSCR1_RIBOSOME_CYTOSOL = MRNA_DSCR1_START_RIBOSOME_CYTOSOL
0.9026466931638294 ; % 1187 MRNA_DSCR1_START_RIBOSOME_CYTOSOL = RIBOSOME_CYTOSOL + DSCR1_CYTOSOL + MRNA_DSCR1_CYTOSOL MRNA_DSCR1_START_RIBOSOME_CYTOSOL = RIBOSOME_CYTOSOL+DSCR1_CYTOSOL+MRNA_DSCR1_CYTOSOL
0.13632144838973648 ; % 1188 MRNA_DSCR1_CYTOSOL = [] MRNA_DSCR1_CYTOSOL = []
0.12536452459075836 ; % 1189 DSCR1_CYTOSOL = [] DSCR1_CYTOSOL = []
0.7186488019708738 ; % 1190 DNA_DSCR1_NUCLEAR + NFATC1_NUCLEAR = DNA_DSCR1_NFATC1_NUCLEAR DNA_DSCR1_NUCLEAR+NFATC1_NUCLEAR = DNA_DSCR1_NFATC1_NUCLEAR
0.06697971909044166 ; % 1191 DNA_DSCR1_NFATC1_NUCLEAR = DNA_DSCR1_NUCLEAR + NFATC1_NUCLEAR DNA_DSCR1_NFATC1_NUCLEAR = DNA_DSCR1_NUCLEAR+NFATC1_NUCLEAR
0.9310573641548964 ; % 1192 DNA_DSCR1_NFATC1_NUCLEAR + RNAP_NUCLEAR = DNA_DSCR1_NFATC1_RNAP_NUCLEAR DNA_DSCR1_NFATC1_NUCLEAR+RNAP_NUCLEAR = DNA_DSCR1_NFATC1_RNAP_NUCLEAR
0.08272382064184494 ; % 1193 DNA_DSCR1_NFATC1_RNAP_NUCLEAR = DNA_DSCR1_NFATC1_NUCLEAR + RNAP_NUCLEAR DNA_DSCR1_NFATC1_RNAP_NUCLEAR = DNA_DSCR1_NFATC1_NUCLEAR+RNAP_NUCLEAR
0.4152452695250941 ; % 1194 DNA_DSCR1_NFATC1_RNAP_NUCLEAR = DNA_DSCR1_NUCLEAR + NFATC1_NUCLEAR + RNAP_NUCLEAR + MRNA_DSCR1_NUCLEAR DNA_DSCR1_NFATC1_RNAP_NUCLEAR = DNA_DSCR1_NUCLEAR+NFATC1_NUCLEAR+RNAP_NUCLEAR+MRNA_DSCR1_NUCLEAR
0.3580735457077039 ; % 1195 MRNA_SOX9_NUCLEAR + NEXPORT_NUCLEAR = MRNA_SOX9_NEXPORT_NUCLEAR MRNA_SOX9_NUCLEAR+NEXPORT_NUCLEAR = MRNA_SOX9_NEXPORT_NUCLEAR
0.02043676138044588 ; % 1196 MRNA_SOX9_NEXPORT_NUCLEAR = MRNA_SOX9_NUCLEAR + NEXPORT_NUCLEAR MRNA_SOX9_NEXPORT_NUCLEAR = MRNA_SOX9_NUCLEAR+NEXPORT_NUCLEAR
0.7354592492953207 ; % 1197 MRNA_SOX9_NEXPORT_NUCLEAR = MRNA_SOX9_CYTOSOL + NEXPORT_NUCLEAR MRNA_SOX9_NEXPORT_NUCLEAR = MRNA_SOX9_CYTOSOL+NEXPORT_NUCLEAR
0.03732395950425704 ; % 1198 MRNA_SOX9_CYTOSOL + RIBOSOME_CYTOSOL = MRNA_SOX9_RIBOSOME_CYTOSOL MRNA_SOX9_CYTOSOL+RIBOSOME_CYTOSOL = MRNA_SOX9_RIBOSOME_CYTOSOL
0.051672282583862195 ; % 1199 MRNA_SOX9_RIBOSOME_CYTOSOL = MRNA_SOX9_CYTOSOL + RIBOSOME_CYTOSOL MRNA_SOX9_RIBOSOME_CYTOSOL = MRNA_SOX9_CYTOSOL+RIBOSOME_CYTOSOL
0.5606078974217104 ; % 1200 MRNA_SOX9_RIBOSOME_CYTOSOL = MRNA_SOX9_START_RIBOSOME_CYTOSOL MRNA_SOX9_RIBOSOME_CYTOSOL = MRNA_SOX9_START_RIBOSOME_CYTOSOL
0.20809241382886512 ; % 1201 MRNA_SOX9_START_RIBOSOME_CYTOSOL = RIBOSOME_CYTOSOL + SOX9_CYTOSOL + MRNA_SOX9_CYTOSOL MRNA_SOX9_START_RIBOSOME_CYTOSOL = RIBOSOME_CYTOSOL+SOX9_CYTOSOL+MRNA_SOX9_CYTOSOL
0.03201419618542595 ; % 1202 MRNA_SOX9_CYTOSOL = [] MRNA_SOX9_CYTOSOL = []
0.18316182217509586 ; % 1203 SOX9_CYTOSOL = [] SOX9_CYTOSOL = []
0.767450975673607 ; % 1204 DNA_SOX9_NUCLEAR + GATA_FOG2_NUCLEAR = DNA_SOX9_GATA_FOG2_NUCLEAR DNA_SOX9_NUCLEAR+GATA_FOG2_NUCLEAR = DNA_SOX9_GATA_FOG2_NUCLEAR
0.013732718706108716 ; % 1205 DNA_SOX9_GATA_FOG2_NUCLEAR = DNA_SOX9_NUCLEAR + GATA_FOG2_NUCLEAR DNA_SOX9_GATA_FOG2_NUCLEAR = DNA_SOX9_NUCLEAR+GATA_FOG2_NUCLEAR
0.4331728669898506 ; % 1206 DNA_SOX9_GATA_FOG2_NUCLEAR + PSMAD5_SMAD4_NUCLEAR = DNA_SOX9_GATA_FOG2_PSMAD5_SMAD4_NUCLEAR DNA_SOX9_GATA_FOG2_NUCLEAR+PSMAD5_SMAD4_NUCLEAR = DNA_SOX9_GATA_FOG2_PSMAD5_SMAD4_NUCLEAR
0.007709130593105407 ; % 1207 DNA_SOX9_GATA_FOG2_PSMAD5_SMAD4_NUCLEAR = DNA_SOX9_GATA_FOG2_NUCLEAR + PSMAD5_SMAD4_NUCLEAR DNA_SOX9_GATA_FOG2_PSMAD5_SMAD4_NUCLEAR = DNA_SOX9_GATA_FOG2_NUCLEAR+PSMAD5_SMAD4_NUCLEAR
0.5130732726568538 ; % 1208 DNA_SOX9_GATA_FOG2_PSMAD5_SMAD4_NUCLEAR + RNAP_NUCLEAR = DNA_SOX9_GATA_FOG2_PSMAD5_SMAD4_RNAP_NUCLEAR DNA_SOX9_GATA_FOG2_PSMAD5_SMAD4_NUCLEAR+RNAP_NUCLEAR = DNA_SOX9_GATA_FOG2_PSMAD5_SMAD4_RNAP_NUCLEAR

0.01182484160582492 ; % 1209 DNA_SOX9_GATA_FOG2_PSMAD5_SMAD4_RNAP_NUCLEAR = DNA_SOX9_GATA_FOG2_PSMAD5_SMAD4_NUCLEAR + RNAP_NUCLEAR DNA_SOX9_GATA_FOG2_PSMAD5_SMAD4_RNAP_NUCLEAR = DNA_SOX9_GATA_FOG2_PSMAD5_SMAD4_NUCLEAR+RNAP_NUCLEAR

0.15615556605825476 ; % 1210 DNA_SOX9_GATA_FOG2_PSMAD5_SMAD4_RNAP_NUCLEAR = DNA_SOX9_NUCLEAR + GATA_FOG2_NUCLEAR + PSMAD5_SMAD4_NUCLEAR + RNAP_NUCLEAR + MRNA_SOX9_NUCLEAR DNA_SOX9_GATA_FOG2_PSMAD5_SMAD4_RNAP_NUCLEAR = DNA_SOX9_NUCLEAR+GATA_FOG2_NUCLEAR+PSMAD5_SMAD4_NUCLEAR+RNAP_NUCLEAR+MRNA_SOX9_NUCLEAR

0.9492492252799193 ; % 1211 GATA_FOG2_CYTOSOL + NIMPORT_NUCLEAR = GATA_FOG2_NIMPORT_NUCLEAR GATA_FOG2_CYTOSOL+NIMPORT_NUCLEAR = GATA_FOG2_NIMPORT_NUCLEAR

0.003352513933930124 ; % 1212 GATA_FOG2_NIMPORT_NUCLEAR = GATA_FOG2_CYTOSOL + NIMPORT_NUCLEAR GATA_FOG2_NIMPORT_NUCLEAR = GATA_FOG2_CYTOSOL+NIMPORT_NUCLEAR

0.8281008021436643 ; % 1213 GATA_FOG2_NIMPORT_NUCLEAR = NIMPORT_NUCLEAR + GATA_FOG2_NUCLEAR GATA_FOG2_NIMPORT_NUCLEAR = NIMPORT_NUCLEAR+GATA_FOG2_NUCLEAR

0.9953607083419445 ; % 1214 GATA_FOG2_NUCLEAR + NEXPORT_NUCLEAR = GATA_FOG2_NEXPORT_NUCLEAR GATA_FOG2_NUCLEAR+NEXPORT_NUCLEAR = GATA_FOG2_NEXPORT_NUCLEAR

0.012794353055366093 ; % 1215 GATA_FOG2_NEXPORT_NUCLEAR = GATA_FOG2_NUCLEAR + NEXPORT_NUCLEAR GATA_FOG2_NEXPORT_NUCLEAR = GATA_FOG2_NUCLEAR+NEXPORT_NUCLEAR

0.29729593270758115 ; % 1216 GATA_FOG2_NEXPORT_NUCLEAR = NEXPORT_NUCLEAR + GATA_FOG2_CYTOSOL GATA_FOG2_NEXPORT_NUCLEAR = NEXPORT_NUCLEAR+GATA_FOG2_CYTOSOL

0.32945502426550566 ; % 1217 PSMAD5_CYTOSOL + SMAD4_CYTOSOL = PSMAD5_SMAD4_CYTOSOL PSMAD5_CYTOSOL+SMAD4_CYTOSOL = PSMAD5_SMAD4_CYTOSOL

0.03392130413805796 ; % 1218 PSMAD5_SMAD4_CYTOSOL = PSMAD5_CYTOSOL + SMAD4_CYTOSOL PSMAD5_SMAD4_CYTOSOL = PSMAD5_CYTOSOL+SMAD4_CYTOSOL

0.06037245501194399 ; % 1219 PSMAD5_SMAD4_CYTOSOL + NIMPORT_NUCLEAR = PSMAD5_SMAD4_NIMPORT_NUCLEAR PSMAD5_SMAD4_CYTOSOL+NIMPORT_NUCLEAR = PSMAD5_SMAD4_NIMPORT_NUCLEAR

0.019327110366098812 ; % 1220 PSMAD5_SMAD4_NIMPORT_NUCLEAR = PSMAD5_SMAD4_CYTOSOL + NIMPORT_NUCLEAR PSMAD5_SMAD4_NIMPORT_NUCLEAR = PSMAD5_SMAD4_CYTOSOL+NIMPORT_NUCLEAR

0.413638780975064 ; % 1221 PSMAD5_SMAD4_NIMPORT_NUCLEAR = NIMPORT_NUCLEAR + PSMAD5_SMAD4_NUCLEAR PSMAD5_SMAD4_NIMPORT_NUCLEAR = NIMPORT_NUCLEAR+PSMAD5_SMAD4_NUCLEAR

0.38367898710858195 ; % 1222 PSMAD5_SMAD4_NUCLEAR + NEXPORT_NUCLEAR = PSMAD5_SMAD4_NEXPORT_NUCLEAR PSMAD5_SMAD4_NUCLEAR+NEXPORT_NUCLEAR = PSMAD5_SMAD4_NEXPORT_NUCLEAR

0.06342488067787042 ; % 1223 PSMAD5_SMAD4_NEXPORT_NUCLEAR = PSMAD5_SMAD4_NUCLEAR + NEXPORT_NUCLEAR PSMAD5_SMAD4_NEXPORT_NUCLEAR = PSMAD5_SMAD4_NUCLEAR+NEXPORT_NUCLEAR

0.47003700538150883 ; % 1224 PSMAD5_SMAD4_NEXPORT_NUCLEAR = NEXPORT_NUCLEAR + PSMAD5_SMAD4_CYTOSOL PSMAD5_SMAD4_NEXPORT_NUCLEAR = NEXPORT_NUCLEAR+PSMAD5_SMAD4_CYTOSOL

0.2853669880510131 ; % 1225 MRNA_PAX3_NUCLEAR + NEXPORT_NUCLEAR = MRNA_PAX3_NEXPORT_NUCLEAR MRNA_PAX3_NUCLEAR+NEXPORT_NUCLEAR = MRNA_PAX3_NEXPORT_NUCLEAR

0.0608893016821006 ; % 1226 MRNA_PAX3_NEXPORT_NUCLEAR = MRNA_PAX3_NUCLEAR + NEXPORT_NUCLEAR MRNA_PAX3_NEXPORT_NUCLEAR = MRNA_PAX3_NUCLEAR+NEXPORT_NUCLEAR

0.8244073199565453 ; % 1227 MRNA_PAX3_NEXPORT_NUCLEAR = MRNA_PAX3_CYTOSOL + NEXPORT_NUCLEAR MRNA_PAX3_NEXPORT_NUCLEAR = MRNA_PAX3_CYTOSOL+NEXPORT_NUCLEAR

0.8824962709827538 ; % 1228 MRNA_PAX3_CYTOSOL + RIBOSOME_CYTOSOL = MRNA_PAX3_RIBOSOME_CYTOSOL MRNA_PAX3_CYTOSOL+RIBOSOME_CYTOSOL = MRNA_PAX3_RIBOSOME_CYTOSOL

0.07303247894620196 ; % 1229 MRNA_PAX3_RIBOSOME_CYTOSOL = MRNA_PAX3_CYTOSOL + RIBOSOME_CYTOSOL MRNA_PAX3_RIBOSOME_CYTOSOL = MRNA_PAX3_CYTOSOL+RIBOSOME_CYTOSOL

0.3257197829542823 ; % 1230 MRNA_PAX3_RIBOSOME_CYTOSOL = MRNA_PAX3_START_RIBOSOME_CYTOSOL MRNA_PAX3_RIBOSOME_CYTOSOL = MRNA_PAX3_START_RIBOSOME_CYTOSOL

0.7183157058844206 ; % 1231 MRNA_PAX3_START_RIBOSOME_CYTOSOL = RIBOSOME_CYTOSOL + PAX3_CYTOSOL + MRNA_PAX3_CYTOSOL MRNA_PAX3_START_RIBOSOME_CYTOSOL = RIBOSOME_CYTOSOL+PAX3_CYTOSOL+MRNA_PAX3_CYTOSOL

0.058007441496302437 ; % 1232 MRNA_PAX3_CYTOSOL = [] MRNA_PAX3_CYTOSOL = []

0.20226415783851553 ; % 1233 PAX3_CYTOSOL = [] PAX3_CYTOSOL = []

0.7594455409157992 ; % 1234 DNA_PAX3_NUCLEAR + PSMAD1_SMAD4_NUCLEAR = DNA_PAX3_PSMAD1_SMAD4_NUCLEAR DNA_PAX3_NUCLEAR+PSMAD1_SMAD4_NUCLEAR = DNA_PAX3_PSMAD1_SMAD4_NUCLEAR

0.09914423485236457 ; % 1235 DNA_PAX3_PSMAD1_SMAD4_NUCLEAR = DNA_PAX3_NUCLEAR + PSMAD1_SMAD4_NUCLEAR DNA_PAX3_PSMAD1_SMAD4_NUCLEAR = DNA_PAX3_NUCLEAR+PSMAD1_SMAD4_NUCLEAR

0.5788295603070166 ; % 1236 DNA_PAX3_PSMAD1_SMAD4_NUCLEAR + RNAP_NUCLEAR = DNA_PAX3_PSMAD1_SMAD4_RNAP_NUCLEAR DNA_PAX3_PSMAD1_SMAD4_NUCLEAR+RNAP_NUCLEAR = DNA_PAX3_PSMAD1_SMAD4_RNAP_NUCLEAR

0.0037607619426477945 ; % 1237 DNA_PAX3_PSMAD1_SMAD4_RNAP_NUCLEAR = DNA_PAX3_PSMAD1_SMAD4_NUCLEAR + RNAP_NUCLEAR DNA_PAX3_PSMAD1_SMAD4_RNAP_NUCLEAR = DNA_PAX3_PSMAD1_SMAD4_NUCLEAR+RNAP_NUCLEAR

0.7364255606134201 ; % 1238 DNA_PAX3_PSMAD1_SMAD4_RNAP_NUCLEAR = DNA_PAX3_NUCLEAR + PSMAD1_SMAD4_NUCLEAR + RNAP_NUCLEAR + MRNA_PAX3_NUCLEAR DNA_PAX3_PSMAD1_SMAD4_RNAP_NUCLEAR = DNA_PAX3_NUCLEAR+PSMAD1_SMAD4_NUCLEAR+RNAP_NUCLEAR+MRNA_PAX3_NUCLEAR

0.2598793229430447 ; % 1239 MRNA_MMP9_NUCLEAR + NEXPORT_NUCLEAR = MRNA_MMP9_NEXPORT_NUCLEAR MRNA_MMP9_NUCLEAR+NEXPORT_NUCLEAR = MRNA_MMP9_NEXPORT_NUCLEAR

0.00802021766712764 ; % 1240 MRNA_MMP9_NEXPORT_NUCLEAR = MRNA_MMP9_NUCLEAR + NEXPORT_NUCLEAR MRNA_MMP9_NEXPORT_NUCLEAR = MRNA_MMP9_NUCLEAR+NEXPORT_NUCLEAR

0.15172707903343563 ; % 1241 MRNA_MMP9_NEXPORT_NUCLEAR = MRNA_MMP9_CYTOSOL + NEXPORT_NUCLEAR MRNA_MMP9_NEXPORT_NUCLEAR = MRNA_MMP9_CYTOSOL+NEXPORT_NUCLEAR

0.5443964368192185 ; % 1242 MRNA_MMP9_CYTOSOL + RIBOSOME_CYTOSOL = MRNA_MMP9_RIBOSOME_CYTOSOL MRNA_MMP9_CYTOSOL+RIBOSOME_CYTOSOL = MRNA_MMP9_RIBOSOME_CYTOSOL

0.025031512152313196 ; % 1243 MRNA_MMP9_RIBOSOME_CYTOSOL = MRNA_MMP9_CYTOSOL + RIBOSOME_CYTOSOL MRNA_MMP9_RIBOSOME_CYTOSOL = MRNA_MMP9_CYTOSOL+RIBOSOME_CYTOSOL

0.7448154362095564 ; % 1244 MRNA_MMP9_RIBOSOME_CYTOSOL = MRNA_MMP9_START_RIBOSOME_CYTOSOL MRNA_MMP9_RIBOSOME_CYTOSOL = MRNA_MMP9_START_RIBOSOME_CYTOSOL

0.36367857799965486 ; % 1245 MRNA_MMP9_START_RIBOSOME_CYTOSOL = RIBOSOME_CYTOSOL + MMP9_CYTOSOL + MRNA_MMP9_CYTOSOL MRNA_MMP9_START_RIBOSOME_CYTOSOL = RIBOSOME_CYTOSOL+MMP9_CYTOSOL+MRNA_MMP9_CYTOSOL

0.4741477954585023 ; % 1246 MRNA_MMP9_CYTOSOL = [] MRNA_MMP9_CYTOSOL = []

0.19819791130415254 ; % 1247 MMP9_CYTOSOL = [] MMP9_CYTOSOL = []

0.25316218792900247 ; % 1248 DNA_MMP9_NUCLEAR + P_AP1_NUCLEAR = DNA_MMP9_P_AP1_NUCLEAR DNA_MMP9_NUCLEAR+P_AP1_NUCLEAR = DNA_MMP9_P_AP1_NUCLEAR

0.04597531834436702 ; % 1249 DNA_MMP9_P_AP1_NUCLEAR = DNA_MMP9_NUCLEAR + P_AP1_NUCLEAR DNA_MMP9_P_AP1_NUCLEAR = DNA_MMP9_NUCLEAR+P_AP1_NUCLEAR

0.6608126681633986 ; % 1250 DNA_MMP9_P_AP1_NUCLEAR + RNAP_NUCLEAR = DNA_MMP9_P_AP1_RNAP_NUCLEAR DNA_MMP9_P_AP1_NUCLEAR+RNAP_NUCLEAR = DNA_MMP9_P_AP1_RNAP_NUCLEAR

0.029570987307335386 ; % 1251 DNA_MMP9_P_AP1_RNAP_NUCLEAR = DNA_MMP9_P_AP1_NUCLEAR + RNAP_NUCLEAR DNA_MMP9_P_AP1_RNAP_NUCLEAR = DNA_MMP9_P_AP1_NUCLEAR+RNAP_NUCLEAR

0.6431881766629125 ; % 1252 DNA_MMP9_P_AP1_RNAP_NUCLEAR = DNA_MMP9_NUCLEAR + P_AP1_NUCLEAR + RNAP_NUCLEAR + MRNA_MMP9_NUCLEAR DNA_MMP9_P_AP1_RNAP_NUCLEAR = DNA_MMP9_NUCLEAR+P_AP1_NUCLEAR+RNAP_NUCLEAR+MRNA_MMP9_NUCLEAR

0.21131734860744078 ; % 1253 DNA_MMP9_NUCLEAR + TBX20_NUCLEAR = DNA_MMP9_TBX20_NUCLEAR DNA_MMP9_NUCLEAR+TBX20_NUCLEAR = DNA_MMP9_TBX20_NUCLEAR

0.07905305091568852 ; % 1254 DNA_MMP9_TBX20_NUCLEAR = DNA_MMP9_NUCLEAR + TBX20_NUCLEAR
DNA_MMP9_TBX20_NUCLEAR = DNA_MMP9_NUCLEAR+TBX20_NUCLEAR
0.4430759626075055 ; % 1255 DNA_MMP9_TBX20_NUCLEAR + PSMAD5_SMAD4_NUCLEAR =
DNA_MMP9_TBX20_PSMAD5_SMAD4_NUCLEAR DNA_MMP9_TBX20_NUCLEAR+PSMAD5_SMAD4_NUCLEAR = DNA_MMP9_TBX20_PSMAD5_SMAD4_NUCLEAR
0.046020625230951254 ; % 1256 DNA_MMP9_TBX20_PSMAD5_SMAD4_NUCLEAR = DNA_MMP9_TBX20_NUCLEAR +
PSMAD5_SMAD4_NUCLEAR DNA_MMP9_TBX20_PSMAD5_SMAD4_NUCLEAR = DNA_MMP9_TBX20_NUCLEAR+PSMAD5_SMAD4_NUCLEAR
0.3335900943927633 ; % 1257 DNA_MMP9_TBX20_PSMAD5_SMAD4_NUCLEAR + RNAP_NUCLEAR =
DNA_MMP9_TBX20_PSMAD5_SMAD4_RNAP_NUCLEAR DNA_MMP9_TBX20_PSMAD5_SMAD4_NUCLEAR+RNAP_NUCLEAR =
DNA_MMP9_TBX20_PSMAD5_SMAD4_RNAP_NUCLEAR
0.09203962710085331 ; % 1258 DNA_MMP9_TBX20_PSMAD5_SMAD4_RNAP_NUCLEAR =
DNA_MMP9_TBX20_PSMAD5_SMAD4_NUCLEAR + RNAP_NUCLEAR DNA_MMP9_TBX20_PSMAD5_SMAD4_RNAP_NUCLEAR =
DNA_MMP9_TBX20_PSMAD5_SMAD4_NUCLEAR+RNAP_NUCLEAR
0.7935096071646445 ; % 1259 DNA_MMP9_TBX20_PSMAD5_SMAD4_RNAP_NUCLEAR = DNA_MMP9_NUCLEAR +
TBX20_NUCLEAR + PSMAD5_SMAD4_NUCLEAR + RNAP_NUCLEAR + MRNA_MMP9_NUCLEAR DNA_MMP9_TBX20_PSMAD5_SMAD4_RNAP_NUCLEAR =
DNA_MMP9_NUCLEAR+TBX20_NUCLEAR+PSMAD5_SMAD4_NUCLEAR+RNAP_NUCLEAR+MRNA_MMP9_NUCLEAR
1.07527846535449E-4 ; % 1260 MRNA_NFATC1_NUCLEAR + NEXPORT_NUCLEAR =
MRNA_NFATC1_NEXPORT_NUCLEAR MRNA_NFATC1_NUCLEAR+NEXPORT_NUCLEAR = MRNA_NFATC1_NEXPORT_NUCLEAR
0.008093749630559088 ; % 1261 MRNA_NFATC1_NEXPORT_NUCLEAR = MRNA_NFATC1_NUCLEAR +
NEXPORT_NUCLEAR MRNA_NFATC1_NEXPORT_NUCLEAR = MRNA_NFATC1_NUCLEAR+NEXPORT_NUCLEAR
0.5053959288290942 ; % 1262 MRNA_NFATC1_NEXPORT_NUCLEAR = MRNA_NFATC1_CYTOSOL +
NEXPORT_NUCLEAR MRNA_NFATC1_NEXPORT_NUCLEAR = MRNA_NFATC1_CYTOSOL+NEXPORT_NUCLEAR
0.002188634517492627 ; % 1263 MRNA_NFATC1_CYTOSOL + RIBOSOME_CYTOSOL =
MRNA_NFATC1_RIBOSOME_CYTOSOL MRNA_NFATC1_CYTOSOL+RIBOSOME_CYTOSOL = MRNA_NFATC1_RIBOSOME_CYTOSOL
0.07551530454628938 ; % 1264 MRNA_NFATC1_RIBOSOME_CYTOSOL = MRNA_NFATC1_CYTOSOL +
RIBOSOME_CYTOSOL MRNA_NFATC1_RIBOSOME_CYTOSOL = MRNA_NFATC1_CYTOSOL+RIBOSOME_CYTOSOL
0.7190719640193961 ; % 1265 MRNA_NFATC1_RIBOSOME_CYTOSOL =
MRNA_NFATC1_START_RIBOSOME_CYTOSOL MRNA_NFATC1_RIBOSOME_CYTOSOL = MRNA_NFATC1_START_RIBOSOME_CYTOSOL
0.22068814431673855 ; % 1266 MRNA_NFATC1_START_RIBOSOME_CYTOSOL = RIBOSOME_CYTOSOL +
NFATC1_CYTOSOL + MRNA_NFATC1_CYTOSOL MRNA_NFATC1_START_RIBOSOME_CYTOSOL =
RIBOSOME_CYTOSOL+NFATC1_CYTOSOL+MRNA_NFATC1_CYTOSOL
0.3194669005610719 ; % 1267 MRNA_NFATC1_CYTOSOL = [] MRNA_NFATC1_CYTOSOL = []
0.4710685457312312 ; % 1268 NFATC1_CYTOSOL = [] NFATC1_CYTOSOL = []
0.5178629578611977 ; % 1269 DNA_NFATC1_NUCLEAR + P_AP1_NUCLEAR = DNA_NFATC1_P_AP1_NUCLEAR
DNA_NFATC1_NUCLEAR+P_AP1_NUCLEAR = DNA_NFATC1_P_AP1_NUCLEAR
0.07400867179767422 ; % 1270 DNA_NFATC1_P_AP1_NUCLEAR = DNA_NFATC1_NUCLEAR + P_AP1_NUCLEAR
DNA_NFATC1_P_AP1_NUCLEAR = DNA_NFATC1_NUCLEAR+P_AP1_NUCLEAR
0.2811654800302711 ; % 1271 DNA_NFATC1_P_AP1_NUCLEAR + RNAP_NUCLEAR =
DNA_NFATC1_P_AP1_RNAP_NUCLEAR DNA_NFATC1_P_AP1_NUCLEAR+RNAP_NUCLEAR = DNA_NFATC1_P_AP1_RNAP_NUCLEAR
0.016947127352985227 ; % 1272 DNA_NFATC1_P_AP1_RNAP_NUCLEAR = DNA_NFATC1_P_AP1_NUCLEAR +
RNAP_NUCLEAR DNA_NFATC1_P_AP1_RNAP_NUCLEAR = DNA_NFATC1_P_AP1_NUCLEAR+RNAP_NUCLEAR
0.9680373357183878 ; % 1273 DNA_NFATC1_P_AP1_RNAP_NUCLEAR = DNA_NFATC1_NUCLEAR + P_AP1_NUCLEAR
+ RNAP_NUCLEAR + MRNA_NFATC1_NUCLEAR DNA_NFATC1_P_AP1_RNAP_NUCLEAR =
DNA_NFATC1_NUCLEAR+P_AP1_NUCLEAR+RNAP_NUCLEAR+MRNA_NFATC1_NUCLEAR
0.17966295040479507 ; % 1274 DNA_NFATC1_NUCLEAR + P_SP1_NUCLEAR = DNA_NFATC1_P_SP1_NUCLEAR
DNA_NFATC1_NUCLEAR+P_SP1_NUCLEAR = DNA_NFATC1_P_SP1_NUCLEAR
0.015195294975141676 ; % 1275 DNA_NFATC1_P_SP1_NUCLEAR = DNA_NFATC1_NUCLEAR + P_SP1_NUCLEAR
DNA_NFATC1_P_SP1_NUCLEAR = DNA_NFATC1_NUCLEAR+P_SP1_NUCLEAR
0.8827464659750346 ; % 1276 DNA_NFATC1_P_SP1_NUCLEAR + RNAP_NUCLEAR =
DNA_NFATC1_P_SP1_RNAP_NUCLEAR DNA_NFATC1_P_SP1_NUCLEAR+RNAP_NUCLEAR = DNA_NFATC1_P_SP1_RNAP_NUCLEAR
0.06408667563941049 ; % 1277 DNA_NFATC1_P_SP1_RNAP_NUCLEAR = DNA_NFATC1_P_SP1_NUCLEAR +
RNAP_NUCLEAR DNA_NFATC1_P_SP1_RNAP_NUCLEAR = DNA_NFATC1_P_SP1_NUCLEAR+RNAP_NUCLEAR
0.1023729232293995 ; % 1278 DNA_NFATC1_P_SP1_RNAP_NUCLEAR = DNA_NFATC1_NUCLEAR + P_SP1_NUCLEAR
+ RNAP_NUCLEAR + MRNA_NFATC1_NUCLEAR DNA_NFATC1_P_SP1_RNAP_NUCLEAR =
DNA_NFATC1_NUCLEAR+P_SP1_NUCLEAR+RNAP_NUCLEAR+MRNA_NFATC1_NUCLEAR
0.889038240685759 ; % 1279 DNA_NFATC1_NUCLEAR + PSMAD2_SMAD4_NUCLEAR =
DNA_NFATC1_PSMAD2_SMAD4_NUCLEAR DNA_NFATC1_NUCLEAR+PSMAD2_SMAD4_NUCLEAR = DNA_NFATC1_PSMAD2_SMAD4_NUCLEAR
0.0021758680091960993 ; % 1280 DNA_NFATC1_PSMAD2_SMAD4_NUCLEAR = DNA_NFATC1_NUCLEAR +
PSMAD2_SMAD4_NUCLEAR DNA_NFATC1_PSMAD2_SMAD4_NUCLEAR = DNA_NFATC1_NUCLEAR+PSMAD2_SMAD4_NUCLEAR
0.820106536287432 ; % 1281 DNA_NFATC1_PSMAD2_SMAD4_NUCLEAR + RNAP_NUCLEAR =
DNA_NFATC1_PSMAD2_SMAD4_RNAP_NUCLEAR DNA_NFATC1_PSMAD2_SMAD4_NUCLEAR+RNAP_NUCLEAR =
DNA_NFATC1_PSMAD2_SMAD4_RNAP_NUCLEAR
0.00546996469963920905 ; % 1282 DNA_NFATC1_PSMAD2_SMAD4_RNAP_NUCLEAR =
DNA_NFATC1_PSMAD2_SMAD4_NUCLEAR + RNAP_NUCLEAR DNA_NFATC1_PSMAD2_SMAD4_RNAP_NUCLEAR =
DNA_NFATC1_PSMAD2_SMAD4_NUCLEAR+RNAP_NUCLEAR
0.80479140139075349 ; % 1283 DNA_NFATC1_PSMAD2_SMAD4_RNAP_NUCLEAR = DNA_NFATC1_NUCLEAR +
PSMAD2_SMAD4_NUCLEAR + RNAP_NUCLEAR + MRNA_NFATC1_NUCLEAR DNA_NFATC1_PSMAD2_SMAD4_RNAP_NUCLEAR =
DNA_NFATC1_NUCLEAR+PSMAD2_SMAD4_NUCLEAR+RNAP_NUCLEAR+MRNA_NFATC1_NUCLEAR
0.8411885237187595 ; % 1284 DNA_NFATC1_NUCLEAR + PSMAD3_SMAD4_NUCLEAR =
DNA_NFATC1_PSMAD3_SMAD4_NUCLEAR DNA_NFATC1_NUCLEAR+PSMAD3_SMAD4_NUCLEAR = DNA_NFATC1_PSMAD3_SMAD4_NUCLEAR
0.0035900318411721165 ; % 1285 DNA_NFATC1_PSMAD3_SMAD4_NUCLEAR = DNA_NFATC1_NUCLEAR +
PSMAD3_SMAD4_NUCLEAR DNA_NFATC1_PSMAD3_SMAD4_NUCLEAR = DNA_NFATC1_NUCLEAR+PSMAD3_SMAD4_NUCLEAR
0.830870289022124 ; % 1286 DNA_NFATC1_PSMAD3_SMAD4_NUCLEAR + RNAP_NUCLEAR =
DNA_NFATC1_PSMAD3_SMAD4_RNAP_NUCLEAR DNA_NFATC1_PSMAD3_SMAD4_NUCLEAR+RNAP_NUCLEAR =
DNA_NFATC1_PSMAD3_SMAD4_RNAP_NUCLEAR
0.06307398024198943 ; % 1287 DNA_NFATC1_PSMAD3_SMAD4_RNAP_NUCLEAR =
DNA_NFATC1_PSMAD3_SMAD4_NUCLEAR + RNAP_NUCLEAR DNA_NFATC1_PSMAD3_SMAD4_RNAP_NUCLEAR =
DNA_NFATC1_PSMAD3_SMAD4_NUCLEAR+RNAP_NUCLEAR
0.7091357342262075 ; % 1288 DNA_NFATC1_PSMAD3_SMAD4_RNAP_NUCLEAR = DNA_NFATC1_NUCLEAR +
PSMAD3_SMAD4_NUCLEAR + RNAP_NUCLEAR + MRNA_NFATC1_NUCLEAR DNA_NFATC1_PSMAD3_SMAD4_RNAP_NUCLEAR =
DNA_NFATC1_NUCLEAR+PSMAD3_SMAD4_NUCLEAR+RNAP_NUCLEAR+MRNA_NFATC1_NUCLEAR
0.36644289691466203 ; % 1289 DNA_NFATC1_NUCLEAR + MSX1_NUCLEAR = DNA_NFATC1_MSX1_NUCLEAR
DNA_NFATC1_NUCLEAR+MSX1_NUCLEAR = DNA_NFATC1_MSX1_NUCLEAR
0.07552863874253106 ; % 1290 DNA_NFATC1_MSX1_NUCLEAR = DNA_NFATC1_NUCLEAR + MSX1_NUCLEAR
DNA_NFATC1_MSX1_NUCLEAR = DNA_NFATC1_NUCLEAR+MSX1_NUCLEAR
0.7252093298717156 ; % 1291 DNA_NFATC1_MSX1_NUCLEAR + PSMAD5_SMAD4_NUCLEAR =
DNA_NFATC1_MSX1_PSMAD5_SMAD4_NUCLEAR DNA_NFATC1_MSX1_NUCLEAR+PSMAD5_SMAD4_NUCLEAR =
DNA_NFATC1_MSX1_PSMAD5_SMAD4_NUCLEAR
0.047004479568735984 ; % 1292 DNA_NFATC1_MSX1_PSMAD5_SMAD4_NUCLEAR = DNA_NFATC1_MSX1_NUCLEAR +
PSMAD5_SMAD4_NUCLEAR DNA_NFATC1_MSX1_PSMAD5_SMAD4_NUCLEAR = DNA_NFATC1_MSX1_NUCLEAR+PSMAD5_SMAD4_NUCLEAR
0.7337646259341032 ; % 1293 DNA_NFATC1_MSX1_PSMAD5_SMAD4_NUCLEAR + RNAP_NUCLEAR =
DNA_NFATC1_MSX1_PSMAD5_SMAD4_RNAP_NUCLEAR DNA_NFATC1_MSX1_PSMAD5_SMAD4_NUCLEAR+RNAP_NUCLEAR =
DNA_NFATC1_MSX1_PSMAD5_SMAD4_RNAP_NUCLEAR

0.08802855000369092 ; % 1294 DNA_NFATC1_MSX1_PSMAD5_SMAD4_RNAP_NUCLEAR = DNA_NFATC1_MSX1_PSMAD5_SMAD4_NUCLEAR + RNAP_NUCLEAR DNA_NFATC1_MSX1_PSMAD5_SMAD4_RNAP_NUCLEAR = DNA_NFATC1_MSX1_PSMAD5_SMAD4_NUCLEAR+RNAP_NUCLEAR

0.06880015332133194 ; % 1295 DNA_NFATC1_MSX1_PSMAD5_SMAD4_RNAP_NUCLEAR = DNA_NFATC1_NUCLEAR + MSX1_NUCLEAR + PSMAD5_SMAD4_NUCLEAR + RNAP_NUCLEAR + MRNA_NFATC1_NUCLEAR DNA_NFATC1_MSX1_PSMAD5_SMAD4_RNAP_NUCLEAR = DNA_NFATC1_NUCLEAR+MSX1_NUCLEAR+PSMAD5_SMAD4_NUCLEAR+RNAP_NUCLEAR+MRNA_NFATC1_NUCLEAR

0.6689443738056666 ; % 1296 MSX1_CYTOSOL + NIMPORT_NUCLEAR = MSX1_NIMPORT_NUCLEAR MSX1_CYTOSOL+NIMPORT_NUCLEAR = MSX1_NIMPORT_NUCLEAR

0.017754249855942927 ; % 1297 MSX1_NIMPORT_NUCLEAR = MSX1_CYTOSOL + NIMPORT_NUCLEAR MSX1_NIMPORT_NUCLEAR = MSX1_CYTOSOL+NIMPORT_NUCLEAR

0.2245081567476357 ; % 1298 MSX1_NIMPORT_NUCLEAR = NIMPORT_NUCLEAR + MSX1_NUCLEAR MSX1_NIMPORT_NUCLEAR = NIMPORT_NUCLEAR+MSX1_NUCLEAR

0.07149574809722836 ; % 1299 MSX1_NUCLEAR + NEXPORT_NUCLEAR = MSX1_NEXPORT_NUCLEAR MSX1_NUCLEAR+NEXPORT_NUCLEAR = MSX1_NEXPORT_NUCLEAR

0.0915683765435206 ; % 1300 MSX1_NEXPORT_NUCLEAR = MSX1_NUCLEAR + NEXPORT_NUCLEAR MSX1_NEXPORT_NUCLEAR = MSX1_NUCLEAR+NEXPORT_NUCLEAR

0.19359445369746953 ; % 1301 MSX1_NEXPORT_NUCLEAR = NEXPORT_NUCLEAR + MSX1_CYTOSOL MSX1_NEXPORT_NUCLEAR = NEXPORT_NUCLEAR+MSX1_CYTOSOL

0.7237106754267346 ; % 1302 MRNA_CALCNCAM_NUCLEAR + NEXPORT_NUCLEAR = MRNA_CALCNCAM_NEXPORT_NUCLEAR MRNA_CALCNCAM_NUCLEAR+NEXPORT_NUCLEAR = MRNA_CALCNCAM_NEXPORT_NUCLEAR

0.08719688343431319 ; % 1303 MRNA_CALCNCAM_NEXPORT_NUCLEAR = MRNA_CALCNCAM_NUCLEAR + NEXPORT_NUCLEAR MRNA_CALCNCAM_NEXPORT_NUCLEAR = MRNA_CALCNCAM_NUCLEAR+NEXPORT_NUCLEAR

0.41551766351748876 ; % 1304 MRNA_CALCNCAM_NEXPORT_NUCLEAR = MRNA_CALCNCAM_CYTOSOL + NEXPORT_NUCLEAR MRNA_CALCNCAM_NEXPORT_NUCLEAR = MRNA_CALCNCAM_CYTOSOL+NEXPORT_NUCLEAR

0.09372786112900522 ; % 1305 MRNA_CALCNCAM_CYTOSOL + RIBOSOME_CYTOSOL = MRNA_CALCNCAM_RIBOSOME_CYTOSOL MRNA_CALCNCAM_CYTOSOL+RIBOSOME_CYTOSOL = MRNA_CALCNCAM_RIBOSOME_CYTOSOL

0.028298676692311498 ; % 1306 MRNA_CALCNCAM_RIBOSOME_CYTOSOL = MRNA_CALCNCAM_CYTOSOL + RIBOSOME_CYTOSOL MRNA_CALCNCAM_RIBOSOME_CYTOSOL = MRNA_CALCNCAM_CYTOSOL+RIBOSOME_CYTOSOL

0.42230298255569065 ; % 1307 MRNA_CALCNCAM_RIBOSOME_CYTOSOL = MRNA_CALCNCAM_START_RIBOSOME_CYTOSOL MRNA_CALCNCAM_RIBOSOME_CYTOSOL = MRNA_CALCNCAM_START_RIBOSOME_CYTOSOL

0.6899746708745279 ; % 1308 MRNA_CALCNCAM_START_RIBOSOME_CYTOSOL = RIBOSOME_CYTOSOL + CALCNCAM_CYTOSOL + MRNA_CALCNCAM_CYTOSOL MRNA_CALCNCAM_START_RIBOSOME_CYTOSOL = RIBOSOME_CYTOSOL+CALCNCAM_CYTOSOL+MRNA_CALCNCAM_CYTOSOL

0.2788934888111168 ; % 1309 MRNA_CALCNCAM_CYTOSOL = [] MRNA_CALCNCAM_CYTOSOL = []

0.4602964714652141 ; % 1310 CALCNCAM_CYTOSOL = [] CALCNCAM_CYTOSOL = []

0.2202946319760979 ; % 1311 DNA_CALCNCAM_NUCLEAR + ACTIVE_NCID_CSL_NUCLEAR = DNA_CALCNCAM_ACTIVE_NCID_CSL_NUCLEAR DNA_CALCNCAM_NUCLEAR+ACTIVE_NCID_CSL_NUCLEAR = DNA_CALCNCAM_ACTIVE_NCID_CSL_NUCLEAR

0.009881702780120218 ; % 1312 DNA_CALCNCAM_ACTIVE_NCID_CSL_NUCLEAR = DNA_CALCNCAM_NUCLEAR + ACTIVE_NCID_CSL_NUCLEAR DNA_CALCNCAM_ACTIVE_NCID_CSL_NUCLEAR = DNA_CALCNCAM_NUCLEAR+ACTIVE_NCID_CSL_NUCLEAR

0.09373274098394357 ; % 1313 DNA_CALCNCAM_ACTIVE_NCID_CSL_NUCLEAR + RNAP_NUCLEAR = DNA_CALCNCAM_ACTIVE_NCID_CSL_RNAP_NUCLEAR DNA_CALCNCAM_ACTIVE_NCID_CSL_NUCLEAR+RNAP_NUCLEAR = DNA_CALCNCAM_ACTIVE_NCID_CSL_RNAP_NUCLEAR

0.08181660647388961 ; % 1314 DNA_CALCNCAM_ACTIVE_NCID_CSL_RNAP_NUCLEAR = DNA_CALCNCAM_ACTIVE_NCID_CSL_NUCLEAR + RNAP_NUCLEAR DNA_CALCNCAM_ACTIVE_NCID_CSL_RNAP_NUCLEAR = DNA_CALCNCAM_ACTIVE_NCID_CSL_NUCLEAR+RNAP_NUCLEAR

0.5766945666344662 ; % 1315 DNA_CALCNCAM_ACTIVE_NCID_CSL_RNAP_NUCLEAR = DNA_CALCNCAM_NUCLEAR + ACTIVE_NCID_CSL_NUCLEAR + RNAP_NUCLEAR + MRNA_CALCNCAM_NUCLEAR DNA_CALCNCAM_ACTIVE_NCID_CSL_RNAP_NUCLEAR = DNA_CALCNCAM_NUCLEAR+ACTIVE_NCID_CSL_NUCLEAR+RNAP_NUCLEAR+MRNA_CALCNCAM_NUCLEAR

0.9764764256601042 ; % 1316 MRNA_TWIST_NUCLEAR + NEXPORT_NUCLEAR = MRNA_TWIST_NEXPORT_NUCLEAR MRNA_TWIST_NUCLEAR+NEXPORT_NUCLEAR = MRNA_TWIST_NEXPORT_NUCLEAR

0.007680599641556152 ; % 1317 MRNA_TWIST_NEXPORT_NUCLEAR = MRNA_TWIST_NUCLEAR + NEXPORT_NUCLEAR MRNA_TWIST_NEXPORT_NUCLEAR = MRNA_TWIST_NUCLEAR+NEXPORT_NUCLEAR

0.6283157155264475 ; % 1318 MRNA_TWIST_NEXPORT_NUCLEAR = MRNA_TWIST_CYTOSOL + NEXPORT_NUCLEAR MRNA_TWIST_NEXPORT_NUCLEAR = MRNA_TWIST_CYTOSOL+NEXPORT_NUCLEAR

0.7861943534004907 ; % 1319 MRNA_TWIST_CYTOSOL + RIBOSOME_CYTOSOL = MRNA_TWIST_RIBOSOME_CYTOSOL MRNA_TWIST_CYTOSOL+RIBOSOME_CYTOSOL = MRNA_TWIST_RIBOSOME_CYTOSOL

0.024810907012924367 ; % 1320 MRNA_TWIST_RIBOSOME_CYTOSOL = MRNA_TWIST_CYTOSOL + RIBOSOME_CYTOSOL MRNA_TWIST_RIBOSOME_CYTOSOL = MRNA_TWIST_CYTOSOL+RIBOSOME_CYTOSOL

0.9733956420331028 ; % 1321 MRNA_TWIST_RIBOSOME_CYTOSOL = MRNA_TWIST_START_RIBOSOME_CYTOSOL MRNA_TWIST_RIBOSOME_CYTOSOL = MRNA_TWIST_START_RIBOSOME_CYTOSOL

0.020456595661354937 ; % 1322 MRNA_TWIST_START_RIBOSOME_CYTOSOL = RIBOSOME_CYTOSOL + TWIST_CYTOSOL + MRNA_TWIST_CYTOSOL MRNA_TWIST_START_RIBOSOME_CYTOSOL = RIBOSOME_CYTOSOL+TWIST_CYTOSOL+MRNA_TWIST_CYTOSOL

0.10432874307064466 ; % 1323 MRNA_TWIST_CYTOSOL = [] MRNA_TWIST_CYTOSOL = []

0.4242100412421443 ; % 1324 TWIST_CYTOSOL = [] TWIST_CYTOSOL = []

0.9460529549694152 ; % 1325 DNA_TWIST_NUCLEAR + PSMAD1_SMAD4_NUCLEAR = DNA_TWIST_PSMAD1_SMAD4_NUCLEAR DNA_TWIST_NUCLEAR+PSMAD1_SMAD4_NUCLEAR = DNA_TWIST_PSMAD1_SMAD4_NUCLEAR

0.0981879741833334 ; % 1326 DNA_TWIST_PSMAD1_SMAD4_NUCLEAR = DNA_TWIST_NUCLEAR + PSMAD1_SMAD4_NUCLEAR DNA_TWIST_PSMAD1_SMAD4_NUCLEAR = DNA_TWIST_NUCLEAR+PSMAD1_SMAD4_NUCLEAR

0.0610413064629044 ; % 1327 DNA_TWIST_PSMAD1_SMAD4_NUCLEAR + RNAP_NUCLEAR = DNA_TWIST_PSMAD1_SMAD4_RNAP_NUCLEAR DNA_TWIST_PSMAD1_SMAD4_NUCLEAR+RNAP_NUCLEAR = DNA_TWIST_PSMAD1_SMAD4_RNAP_NUCLEAR

0.01306663572830108 ; % 1328 DNA_TWIST_PSMAD1_SMAD4_RNAP_NUCLEAR = DNA_TWIST_PSMAD1_SMAD4_NUCLEAR + RNAP_NUCLEAR DNA_TWIST_PSMAD1_SMAD4_RNAP_NUCLEAR = DNA_TWIST_PSMAD1_SMAD4_NUCLEAR+RNAP_NUCLEAR

0.28316461716764874 ; % 1329 DNA_TWIST_PSMAD1_SMAD4_RNAP_NUCLEAR = DNA_TWIST_NUCLEAR + PSMAD1_SMAD4_NUCLEAR + RNAP_NUCLEAR + MRNA_TWIST_NUCLEAR DNA_TWIST_PSMAD1_SMAD4_RNAP_NUCLEAR = DNA_TWIST_NUCLEAR+PSMAD1_SMAD4_NUCLEAR+RNAP_NUCLEAR+MRNA_TWIST_NUCLEAR

0.833443195677032 ; % 1330 DNA_TWIST_NUCLEAR + PSMAD5_SMAD4_NUCLEAR = DNA_TWIST_PSMAD5_SMAD4_NUCLEAR DNA_TWIST_NUCLEAR+PSMAD5_SMAD4_NUCLEAR = DNA_TWIST_PSMAD5_SMAD4_NUCLEAR

0.06706499972894701 ; % 1331 DNA_TWIST_PSMAD5_SMAD4_NUCLEAR = DNA_TWIST_NUCLEAR + PSMAD5_SMAD4_NUCLEAR DNA_TWIST_PSMAD5_SMAD4_NUCLEAR = DNA_TWIST_NUCLEAR+PSMAD5_SMAD4_NUCLEAR

0.7237535405026247 ; % 1332 DNA_TWIST_PSMAD5_SMAD4_NUCLEAR + RNAP_NUCLEAR = DNA_TWIST_PSMAD5_SMAD4_RNAP_NUCLEAR DNA_TWIST_PSMAD5_SMAD4_NUCLEAR+RNAP_NUCLEAR = DNA_TWIST_PSMAD5_SMAD4_RNAP_NUCLEAR

1.1612451795217638E-5 ; % 1333 DNA_TWIST_PSMAD5_SMAD4_RNAP_NUCLEAR = DNA_TWIST_PSMAD5_SMAD4_NUCLEAR + RNAP_NUCLEAR DNA_TWIST_PSMAD5_SMAD4_RNAP_NUCLEAR = DNA_TWIST_PSMAD5_SMAD4_NUCLEAR+RNAP_NUCLEAR

0.26789623806921803 ; % 1334 DNA_TWIST_PSMAD5_SMAD4_RNAP_NUCLEAR = DNA_TWIST_NUCLEAR + PSMAD5_SMAD4_NUCLEAR + RNAP_NUCLEAR + MRNA_TWIST_NUCLEAR DNA_TWIST_PSMAD5_SMAD4_RNAP_NUCLEAR = DNA_TWIST_NUCLEAR+PSMAD5_SMAD4_NUCLEAR+RNAP_NUCLEAR+MRNA_TWIST_NUCLEAR

0.43402666222804458 ; % 1335 RIBOSOME_CYTOSOL = [] RIBOSOME_CYTOSOL = []

0.5721014878218912 ; % 1336 [] = RIBOSOME_CYTOSOL [] = RIBOSOME_CYTOSOL

0.55917431295969734 ; % 1337 RNAP_NUCLEAR = [] RNAP_NUCLEAR = []

0.7737339878760369 ; % 1338 [] = RNAP_NUCLEAR [] = RNAP_NUCLEAR

0.4453581876192623 ; % 1339 NIMPORT_NUCLEAR = [] NIMPORT_NUCLEAR = []
0.6759602194907085 ; % 1340 [] = NIMPORT_NUCLEAR [] = NIMPORT_NUCLEAR
0.37226596293207034 ; % 1341 NEXPORT_NUCLEAR = [] NEXPORT_NUCLEAR = []
0.5686117240528282 ; % 1342 [] = NEXPORT_NUCLEAR [] = NEXPORT_NUCLEAR
0.29113754796576835 ; % 1343 EXIMPORT_CYTOSOL = [] EXIMPORT_CYTOSOL = []
0.53911564684036277 ; % 1344 [] = EXIMPORT_CYTOSOL [] = EXIMPORT_CYTOSOL
0.47207334500989193 ; % 1345 EXEXPORT_CYTOSOL = [] EXEXPORT_CYTOSOL = []
0.633731428010798 ; % 1346 [] = EXEXPORT_CYTOSOL [] = EXEXPORT_CYTOSOL
0.12884992534950973 ; % 1347 GDP_CYTOSOL = [] GDP_CYTOSOL = []
0.2643297919584675 ; % 1348 [] = GDP_CYTOSOL [] = GDP_CYTOSOL
0.4660448941130764 ; % 1349 GTP_CYTOSOL = [] GTP_CYTOSOL = []
0.6142457904868078 ; % 1350 [] = GTP_CYTOSOL [] = GTP_CYTOSOL
0.411697198887914 ; % 1351 PIP2_CYTOSOL = [] PIP2_CYTOSOL = []
0.63544301674632329 ; % 1352 [] = PIP2_CYTOSOL [] = PIP2_CYTOSOL
0.1437430833834576 ; % 1353 PIP3_CYTOSOL = [] PIP3_CYTOSOL = []
0.0 ; % 1354 [] = PIP3_CYTOSOL [] = PIP3_CYTOSOL
0.3195424457637901 ; % 1355 GATA_FOG2_CYTOSOL = [] GATA_FOG2_CYTOSOL = []
0.8941842829502842 ; % 1356 [] = GATA_FOG2_CYTOSOL [] = GATA_FOG2_CYTOSOL
0.27035584332982354 ; % 1357 DELTEX_NEDD4_CYTOSOL = [] DELTEX_NEDD4_CYTOSOL = []
0.8319233414138181 ; % 1358 [] = DELTEX_NEDD4_CYTOSOL [] = DELTEX_NEDD4_CYTOSOL
0.6472432825423382 ; % 1359 WNT9A_EXTRACELLULAR + FRIZZLED_CYTOSOL = WNT9A_FRIZZLED_CYTOSOL
WNT9A_EXTRACELLULAR+FRIZZLED_CYTOSOL = WNT9A_FRIZZLED_CYTOSOL
0.07117722685074866 ; % 1360 WNT9A_FRIZZLED_CYTOSOL = WNT9A_EXTRACELLULAR + FRIZZLED_CYTOSOL
WNT9A_FRIZZLED_CYTOSOL = WNT9A_EXTRACELLULAR+FRIZZLED_CYTOSOL
0.17770134462401355 ; % 1361 WNT9A_FRIZZLED_CYTOSOL + DISHEVELLED_CYTOSOL =
WNT9A_FRIZZLED_DISHEVELLED_CYTOSOL WNT9A_FRIZZLED_CYTOSOL+DISHEVELLED_CYTOSOL = WNT9A_FRIZZLED_DISHEVELLED_CYTOSOL
0.08147618866296401 ; % 1362 WNT9A_FRIZZLED_DISHEVELLED_CYTOSOL = WNT9A_FRIZZLED_CYTOSOL +
DISHEVELLED_CYTOSOL WNT9A_FRIZZLED_DISHEVELLED_CYTOSOL = WNT9A_FRIZZLED_CYTOSOL+DISHEVELLED_CYTOSOL
0.9260001091725943 ; % 1363 WNT9A_FRIZZLED_DISHEVELLED_CYTOSOL + LRP_CYTOSOL =
WNT9A_FRIZZLED_DISHEVELLED_LRP_CYTOSOL WNT9A_FRIZZLED_DISHEVELLED_CYTOSOL+LRP_CYTOSOL =
WNT9A_FRIZZLED_DISHEVELLED_LRP_CYTOSOL
0.06286742192856727 ; % 1364 WNT9A_FRIZZLED_DISHEVELLED_LRP_CYTOSOL =
WNT9A_FRIZZLED_DISHEVELLED_CYTOSOL + LRP_CYTOSOL WNT9A_FRIZZLED_DISHEVELLED_LRP_CYTOSOL =
WNT9A_FRIZZLED_DISHEVELLED_CYTOSOL+LRP_CYTOSOL
0.2599375494408255 ; % 1365 WNT9A_FRIZZLED_DISHEVELLED_LRP_CYTOSOL + AXIN_CYTOSOL =
WNT9A_FRIZZLED_DISHEVELLED_LRP_AXIN_CYTOSOL WNT9A_FRIZZLED_DISHEVELLED_LRP_CYTOSOL+AXIN_CYTOSOL =
WNT9A_FRIZZLED_DISHEVELLED_LRP_AXIN_CYTOSOL
0.08294819653915285 ; % 1366 WNT9A_FRIZZLED_DISHEVELLED_LRP_AXIN_CYTOSOL =
WNT9A_FRIZZLED_DISHEVELLED_LRP_CYTOSOL + AXIN_CYTOSOL WNT9A_FRIZZLED_DISHEVELLED_LRP_AXIN_CYTOSOL =
WNT9A_FRIZZLED_DISHEVELLED_LRP_CYTOSOL+AXIN_CYTOSOL
0.999195594657313 ; % 1367 VEGFA_EXTRACELLULAR + VEGFR2_CYTOSOL = VEGFA_VEGFR2_CYTOSOL
VEGFA_EXTRACELLULAR+VEGFR2_CYTOSOL = VEGFA_VEGFR2_CYTOSOL
0.0040426287032167335 ; % 1368 VEGFA_VEGFR2_CYTOSOL = VEGFA_EXTRACELLULAR + VEGFR2_CYTOSOL
VEGFA_VEGFR2_CYTOSOL = VEGFA_EXTRACELLULAR+VEGFR2_CYTOSOL
0.6680836437038423 ; % 1369 VEGFA_VEGFR2_CYTOSOL + SHC_CYTOSOL = VEGFA_VEGFR2_SHC_CYTOSOL
VEGFA_VEGFR2_CYTOSOL+SHC_CYTOSOL = VEGFA_VEGFR2_SHC_CYTOSOL
1.050561456712451E-4 ; % 1370 VEGFA_VEGFR2_SHC_CYTOSOL = VEGFA_VEGFR2_CYTOSOL + SHC_CYTOSOL
VEGFA_VEGFR2_SHC_CYTOSOL = VEGFA_VEGFR2_CYTOSOL+SHC_CYTOSOL
0.7499130884575897 ; % 1371 BMP2_EXTRACELLULAR + BMPRII_CYTOSOL = BMP2_BMPRII_CYTOSOL
BMP2_EXTRACELLULAR+BMPRII_CYTOSOL = BMP2_BMPRII_CYTOSOL
0.03015373284614914 ; % 1372 BMP2_BMPRII_CYTOSOL = BMP2_EXTRACELLULAR + BMPRII_CYTOSOL
BMP2_BMPRII_CYTOSOL = BMP2_EXTRACELLULAR+BMPRII_CYTOSOL
0.4430480136425038 ; % 1373 BMP2_BMPRII_CYTOSOL + ALK2_CYTOSOL = BMP2_BMPRII_ALK2_CYTOSOL
BMP2_BMPRII_CYTOSOL+ALK2_CYTOSOL = BMP2_BMPRII_ALK2_CYTOSOL
0.08024363741577445 ; % 1374 BMP2_BMPRII_ALK2_CYTOSOL = BMP2_BMPRII_CYTOSOL + ALK2_CYTOSOL
BMP2_BMPRII_ALK2_CYTOSOL = BMP2_BMPRII_CYTOSOL+ALK2_CYTOSOL
0.4527839260019898 ; % 1375 BMP2_BMPRII_CYTOSOL + ALK3_CYTOSOL = BMP2_BMPRII_ALK3_CYTOSOL
BMP2_BMPRII_CYTOSOL+ALK3_CYTOSOL = BMP2_BMPRII_ALK3_CYTOSOL
0.07555814966923205 ; % 1376 BMP2_BMPRII_ALK3_CYTOSOL = BMP2_BMPRII_CYTOSOL + ALK3_CYTOSOL
BMP2_BMPRII_ALK3_CYTOSOL = BMP2_BMPRII_CYTOSOL+ALK3_CYTOSOL
0.42033455850723433 ; % 1377 BMP2_BMPRII_CYTOSOL + ALK6_CYTOSOL = BMP2_BMPRII_ALK6_CYTOSOL
BMP2_BMPRII_CYTOSOL+ALK6_CYTOSOL = BMP2_BMPRII_ALK6_CYTOSOL
0.05360561500779816 ; % 1378 BMP2_BMPRII_ALK6_CYTOSOL = BMP2_BMPRII_CYTOSOL + ALK6_CYTOSOL
BMP2_BMPRII_ALK6_CYTOSOL = BMP2_BMPRII_CYTOSOL+ALK6_CYTOSOL
0.26554844291456015 ; % 1379 BMP2_BMPRII_ALK2_CYTOSOL + SHC_CYTOSOL =
BMP2_BMPRII_ALK2_SHC_CYTOSOL BMP2_BMPRII_ALK2_CYTOSOL+SHC_CYTOSOL = BMP2_BMPRII_ALK2_SHC_CYTOSOL
0.0682989735888384 ; % 1380 BMP2_BMPRII_ALK2_SHC_CYTOSOL = BMP2_BMPRII_ALK2_CYTOSOL +
SHC_CYTOSOL BMP2_BMPRII_ALK2_SHC_CYTOSOL = BMP2_BMPRII_ALK2_CYTOSOL+SHC_CYTOSOL
0.5318555191224043 ; % 1381 BMP2_BMPRII_ALK2_SHC_CYTOSOL + GRB2_CYTOSOL =
BMP2_BMPRII_ALK2_SHC_GRB2_CYTOSOL BMP2_BMPRII_ALK2_SHC_CYTOSOL+GRB2_CYTOSOL = BMP2_BMPRII_ALK2_SHC_GRB2_CYTOSOL
0.06023806442881577 ; % 1382 BMP2_BMPRII_ALK2_SHC_GRB2_CYTOSOL = BMP2_BMPRII_ALK2_SHC_CYTOSOL +
GRB2_CYTOSOL BMP2_BMPRII_ALK2_SHC_GRB2_CYTOSOL = BMP2_BMPRII_ALK2_SHC_CYTOSOL+GRB2_CYTOSOL
0.5018033633271693 ; % 1383 BMP2_BMPRII_ALK2_SHC_GRB2_CYTOSOL + SOS_CYTOSOL =
BMP2_BMPRII_ALK2_SHC_GRB2_SOS_CYTOSOL BMP2_BMPRII_ALK2_SHC_GRB2_CYTOSOL+SOS_CYTOSOL = BMP2_BMPRII_ALK2_SHC_GRB2_SOS_CYTOSOL
0.010980796300690055 ; % 1384 BMP2_BMPRII_ALK2_SHC_GRB2_SOS_CYTOSOL =
BMP2_BMPRII_ALK2_SHC_GRB2_CYTOSOL + SOS_CYTOSOL BMP2_BMPRII_ALK2_SHC_GRB2_SOS_CYTOSOL =
BMP2_BMPRII_ALK2_SHC_GRB2_CYTOSOL+SOS_CYTOSOL
0.583952871439399 ; % 1385 TGFB2_EXTRACELLULAR + BMPRII_CYTOSOL = TGFB2_BMPRII_CYTOSOL
TGFB2_EXTRACELLULAR+BMPRII_CYTOSOL = TGFB2_BMPRII_CYTOSOL
0.0864691167082994 ; % 1386 TGFB2_BMPRII_CYTOSOL = TGFB2_EXTRACELLULAR + BMPRII_CYTOSOL
TGFB2_BMPRII_CYTOSOL = TGFB2_EXTRACELLULAR+BMPRII_CYTOSOL
0.14456008868041614 ; % 1387 TGFB2_BMPRII_CYTOSOL + ALK2_CYTOSOL = TGFB2_BMPRII_ALK2_CYTOSOL
TGFB2_BMPRII_CYTOSOL+ALK2_CYTOSOL = TGFB2_BMPRII_ALK2_CYTOSOL
0.03786975170073778 ; % 1388 TGFB2_BMPRII_ALK2_CYTOSOL = TGFB2_BMPRII_CYTOSOL + ALK2_CYTOSOL
TGFB2_BMPRII_ALK2_CYTOSOL = TGFB2_BMPRII_CYTOSOL+ALK2_CYTOSOL
0.4111952266064901 ; % 1389 TGFB2_BMPRII_ALK2_CYTOSOL + ENDOGLIN_CYTOSOL =
TGFB2_BMPRII_ALK2_ENDOGLIN_CYTOSOL TGFB2_BMPRII_ALK2_CYTOSOL+ENDOGLIN_CYTOSOL = TGFB2_BMPRII_ALK2_ENDOGLIN_CYTOSOL
0.04551097163302329 ; % 1390 TGFB2_BMPRII_ALK2_ENDOGLIN_CYTOSOL = TGFB2_BMPRII_ALK2_CYTOSOL +
ENDOGLIN_CYTOSOL TGFB2_BMPRII_ALK2_ENDOGLIN_CYTOSOL = TGFB2_BMPRII_ALK2_CYTOSOL+ENDOGLIN_CYTOSOL
0.3541853581911274 ; % 1391 TGFB2_BMPRII_ALK2_ENDOGLIN_CYTOSOL + SHC_CYTOSOL =
TGFB2_BMPRII_ALK2_ENDOGLIN_SHC_CYTOSOL TGFB2_BMPRII_ALK2_ENDOGLIN_CYTOSOL+SHC_CYTOSOL =
TGFB2_BMPRII_ALK2_ENDOGLIN_SHC_CYTOSOL

0.07477115098335378 ; % 1392 TGFB2_BMPRII_ALK2_ENDOGLIN_SHC_CYTOSOL = TGFB2_BMPRII_ALK2_ENDOGLIN_CYTOSOL + SHC_CYTOSOL TGFB2_BMPRII_ALK2_ENDOGLIN_SHC_CYTOSOL = TGFB2_BMPRII_ALK2_ENDOGLIN_CYTOSOL+SHC_CYTOSOL
0.05258693919605484 ; % 1393 TGFB2_BMPRII_ALK2_ENDOGLIN_SHC_CYTOSOL + GRB2_CYTOSOL = TGFB2_BMPRII_ALK2_ENDOGLIN_SHC_GRB2_CYTOSOL TGFB2_BMPRII_ALK2_ENDOGLIN_SHC_CYTOSOL+GRB2_CYTOSOL = TGFB2_BMPRII_ALK2_ENDOGLIN_SHC_GRB2_CYTOSOL
0.03094091222662633 ; % 1394 TGFB2_BMPRII_ALK2_ENDOGLIN_SHC_GRB2_CYTOSOL = TGFB2_BMPRII_ALK2_ENDOGLIN_SHC_CYTOSOL + GRB2_CYTOSOL TGFB2_BMPRII_ALK2_ENDOGLIN_SHC_GRB2_CYTOSOL = TGFB2_BMPRII_ALK2_ENDOGLIN_SHC_CYTOSOL+GRB2_CYTOSOL
0.17448932974147513 ; % 1395 TGFB2_BMPRII_ALK2_ENDOGLIN_SHC_GRB2_CYTOSOL + SOS_CYTOSOL = TGFB2_BMPRII_ALK2_ENDOGLIN_SHC_GRB2_SOS_CYTOSOL TGFB2_BMPRII_ALK2_ENDOGLIN_SHC_GRB2_CYTOSOL+SOS_CYTOSOL = TGFB2_BMPRII_ALK2_ENDOGLIN_SHC_GRB2_SOS_CYTOSOL
0.005288796696930565 ; % 1396 TGFB2_BMPRII_ALK2_ENDOGLIN_SHC_GRB2_SOS_CYTOSOL = TGFB2_BMPRII_ALK2_ENDOGLIN_SHC_GRB2_CYTOSOL + SOS_CYTOSOL TGFB2_BMPRII_ALK2_ENDOGLIN_SHC_GRB2_SOS_CYTOSOL = TGFB2_BMPRII_ALK2_ENDOGLIN_SHC_GRB2_CYTOSOL+SOS_CYTOSOL
1.4675753713122575E-4 ; % 1397 TGFB3_EXTRACELLULAR + TGFBRII_CYTOSOL = TGFB3_TGFBRII_CYTOSOL TGFB3_EXTRACELLULAR+TGFBRII_CYTOSOL = TGFB3_TGFBRII_CYTOSOL
0.05667415053139039 ; % 1398 TGFB3_TGFBRII_CYTOSOL = TGFB3_EXTRACELLULAR + TGFBRII_CYTOSOL TGFB3_TGFBRII_CYTOSOL = TGFB3_EXTRACELLULAR+TGFBRII_CYTOSOL
0.24717274782430065 ; % 1399 TGFB3_TGFBRII_CYTOSOL + ALK1_CYTOSOL = TGFB3_TGFBRII_ALK1_CYTOSOL TGFB3_TGFBRII_CYTOSOL+ALK1_CYTOSOL = TGFB3_TGFBRII_ALK1_CYTOSOL
0.06474592888569149 ; % 1400 TGFB3_TGFBRII_ALK1_CYTOSOL = TGFB3_TGFBRII_CYTOSOL + ALK1_CYTOSOL TGFB3_TGFBRII_ALK1_CYTOSOL = TGFB3_TGFBRII_CYTOSOL+ALK1_CYTOSOL
0.62938378170872 ; % 1401 TGFB3_TGFBRII_ALK1_CYTOSOL + TGFBRIII_CYTOSOL = TGFB3_TGFBRII_ALK1_TGFBRIII_CYTOSOL TGFB3_TGFBRII_ALK1_CYTOSOL+TGFBRIII_CYTOSOL = TGFB3_TGFBRII_ALK1_TGFBRIII_CYTOSOL
0.07253075276596654 ; % 1402 TGFB3_TGFBRII_ALK1_TGFBRIII_CYTOSOL = TGFB3_TGFBRII_ALK1_CYTOSOL + TGFBRIII_CYTOSOL TGFB3_TGFBRII_ALK1_TGFBRIII_CYTOSOL = TGFB3_TGFBRII_ALK1_CYTOSOL+TGFBRIII_CYTOSOL
0.10753968048394291 ; % 1403 TGFB3_TGFBRII_CYTOSOL + ALK5_CYTOSOL = TGFB3_TGFBRII_ALK5_CYTOSOL TGFB3_TGFBRII_CYTOSOL+ALK5_CYTOSOL = TGFB3_TGFBRII_ALK5_CYTOSOL
0.04134845879166874 ; % 1404 TGFB3_TGFBRII_ALK5_CYTOSOL = TGFB3_TGFBRII_CYTOSOL + ALK5_CYTOSOL TGFB3_TGFBRII_ALK5_CYTOSOL = TGFB3_TGFBRII_CYTOSOL+ALK5_CYTOSOL
0.6370182786218236 ; % 1405 TGFB3_TGFBRII_ALK5_CYTOSOL + TGFBRIII_CYTOSOL = TGFB3_TGFBRII_ALK5_TGFBRIII_CYTOSOL TGFB3_TGFBRII_ALK5_CYTOSOL+TGFBRIII_CYTOSOL = TGFB3_TGFBRII_ALK5_TGFBRIII_CYTOSOL
0.010612050342788748 ; % 1406 TGFB3_TGFBRII_ALK5_TGFBRIII_CYTOSOL = TGFB3_TGFBRII_ALK5_CYTOSOL + TGFBRIII_CYTOSOL TGFB3_TGFBRII_ALK5_TGFBRIII_CYTOSOL = TGFB3_TGFBRII_ALK5_CYTOSOL+TGFBRIII_CYTOSOL
0.5533272719738573 ; % 1407 TGFB3_TGFBRII_ALK5_TGFBRIII_CYTOSOL + ENDOGLIN_CYTOSOL = TGFB3_TGFBRII_ALK5_TGFBRIII_ENDOGLIN_CYTOSOL TGFB3_TGFBRII_ALK5_TGFBRIII_CYTOSOL+ENDOGLIN_CYTOSOL = TGFB3_TGFBRII_ALK5_TGFBRIII_ENDOGLIN_CYTOSOL
0.06309696607422316 ; % 1408 TGFB3_TGFBRII_ALK5_TGFBRIII_ENDOGLIN_CYTOSOL = TGFB3_TGFBRII_ALK5_TGFBRIII_CYTOSOL + ENDOGLIN_CYTOSOL TGFB3_TGFBRII_ALK5_TGFBRIII_ENDOGLIN_CYTOSOL = TGFB3_TGFBRII_ALK5_TGFBRIII_CYTOSOL+ENDOGLIN_CYTOSOL
0.6833659471045659 ; % 1409 TGFB2_EXTRACELLULAR + TGFBRII_CYTOSOL = TGFB2_TGFBRII_CYTOSOL TGFB2_EXTRACELLULAR+TGFBRII_CYTOSOL = TGFB2_TGFBRII_CYTOSOL
0.07444027863677731 ; % 1410 TGFB2_TGFBRII_CYTOSOL = TGFB2_EXTRACELLULAR + TGFBRII_CYTOSOL TGFB2_TGFBRII_CYTOSOL = TGFB2_EXTRACELLULAR+TGFBRII_CYTOSOL
0.6537000555882052 ; % 1411 TGFB2_TGFBRII_CYTOSOL + ALK1_CYTOSOL = TGFB2_TGFBRII_ALK1_CYTOSOL TGFB2_TGFBRII_CYTOSOL+ALK1_CYTOSOL = TGFB2_TGFBRII_ALK1_CYTOSOL
0.08850473405525189 ; % 1412 TGFB2_TGFBRII_ALK1_CYTOSOL = TGFB2_TGFBRII_CYTOSOL + ALK1_CYTOSOL TGFB2_TGFBRII_ALK1_CYTOSOL = TGFB2_TGFBRII_CYTOSOL+ALK1_CYTOSOL
0.4651239213016717 ; % 1413 TGFB2_TGFBRII_ALK1_CYTOSOL + TGFBRIII_CYTOSOL = TGFB2_TGFBRII_ALK1_TGFBRIII_CYTOSOL TGFB2_TGFBRII_ALK1_CYTOSOL+TGFBRIII_CYTOSOL = TGFB2_TGFBRII_ALK1_TGFBRIII_CYTOSOL
0.030178469814886734 ; % 1414 TGFB2_TGFBRII_ALK1_TGFBRIII_CYTOSOL = TGFB2_TGFBRII_ALK1_CYTOSOL + TGFBRIII_CYTOSOL TGFB2_TGFBRII_ALK1_TGFBRIII_CYTOSOL = TGFB2_TGFBRII_ALK1_CYTOSOL+TGFBRIII_CYTOSOL
0.19690097921003713 ; % 1415 TGFB2_TGFBRII_CYTOSOL + ALK5_CYTOSOL = TGFB2_TGFBRII_ALK5_CYTOSOL TGFB2_TGFBRII_CYTOSOL+ALK5_CYTOSOL = TGFB2_TGFBRII_ALK5_CYTOSOL
0.09935480855124648 ; % 1416 TGFB2_TGFBRII_ALK5_CYTOSOL = TGFB2_TGFBRII_CYTOSOL + ALK5_CYTOSOL TGFB2_TGFBRII_ALK5_CYTOSOL = TGFB2_TGFBRII_CYTOSOL+ALK5_CYTOSOL
0.1288673533789424 ; % 1417 TGFB2_TGFBRII_ALK5_CYTOSOL + TGFBRIII_CYTOSOL = TGFB2_TGFBRII_ALK5_TGFBRIII_CYTOSOL TGFB2_TGFBRII_ALK5_CYTOSOL+TGFBRIII_CYTOSOL = TGFB2_TGFBRII_ALK5_TGFBRIII_CYTOSOL
0.09723589820711243 ; % 1418 TGFB2_TGFBRII_ALK5_TGFBRIII_CYTOSOL = TGFB2_TGFBRII_ALK5_CYTOSOL + TGFBRIII_CYTOSOL TGFB2_TGFBRII_ALK5_TGFBRIII_CYTOSOL = TGFB2_TGFBRII_ALK5_CYTOSOL+TGFBRIII_CYTOSOL
0.762747081861526 ; % 1419 TGFB2_TGFBRII_ALK5_TGFBRIII_CYTOSOL + ENDOGLIN_CYTOSOL = TGFB2_TGFBRII_ALK5_TGFBRIII_ENDOGLIN_CYTOSOL TGFB2_TGFBRII_ALK5_TGFBRIII_CYTOSOL+ENDOGLIN_CYTOSOL = TGFB2_TGFBRII_ALK5_TGFBRIII_ENDOGLIN_CYTOSOL
0.014529944218480619 ; % 1420 TGFB2_TGFBRII_ALK5_TGFBRIII_ENDOGLIN_CYTOSOL = TGFB2_TGFBRII_ALK5_TGFBRIII_CYTOSOL + ENDOGLIN_CYTOSOL TGFB2_TGFBRII_ALK5_TGFBRIII_ENDOGLIN_CYTOSOL = TGFB2_TGFBRII_ALK5_TGFBRIII_CYTOSOL+ENDOGLIN_CYTOSOL
0.2763859473166461 ; % 1421 JAG1_EXTRACELLULAR + NOTCH1_CYTOSOL = JAG1_NOTCH1_CYTOSOL JAG1_EXTRACELLULAR+NOTCH1_CYTOSOL = JAG1_NOTCH1_CYTOSOL
0.0641776440743194 ; % 1422 JAG1_NOTCH1_CYTOSOL = JAG1_EXTRACELLULAR + NOTCH1_CYTOSOL JAG1_NOTCH1_CYTOSOL = JAG1_EXTRACELLULAR+NOTCH1_CYTOSOL
0.15010262187820933 ; % 1423 JAG1_NOTCH1_CYTOSOL + TACE_CYTOSOL = JAG1_NOTCH1_TACE_CYTOSOL JAG1_NOTCH1_CYTOSOL+TACE_CYTOSOL = JAG1_NOTCH1_TACE_CYTOSOL
0.005374996347419292 ; % 1424 JAG1_NOTCH1_TACE_CYTOSOL = JAG1_NOTCH1_CYTOSOL + TACE_CYTOSOL JAG1_NOTCH1_TACE_CYTOSOL = JAG1_NOTCH1_CYTOSOL+TACE_CYTOSOL
0.8100595496225582 ; % 1425 DELTA4_EXTRACELLULAR + NOTCH1_CYTOSOL = DELTA4_NOTCH1_CYTOSOL DELTA4_EXTRACELLULAR+NOTCH1_CYTOSOL = DELTA4_NOTCH1_CYTOSOL
0.07509514443982951 ; % 1426 DELTA4_NOTCH1_CYTOSOL = DELTA4_EXTRACELLULAR + NOTCH1_CYTOSOL DELTA4_NOTCH1_CYTOSOL = DELTA4_EXTRACELLULAR+NOTCH1_CYTOSOL
0.5896583185091641 ; % 1427 DELTA4_NOTCH1_CYTOSOL + TACE_CYTOSOL = DELTA4_NOTCH1_TACE_CYTOSOL DELTA4_NOTCH1_CYTOSOL+TACE_CYTOSOL = DELTA4_NOTCH1_TACE_CYTOSOL
0.09510215650272963 ; % 1428 DELTA4_NOTCH1_TACE_CYTOSOL = DELTA4_NOTCH1_CYTOSOL + TACE_CYTOSOL DELTA4_NOTCH1_TACE_CYTOSOL = DELTA4_NOTCH1_CYTOSOL+TACE_CYTOSOL
0.5197929560606321 ; % 1429 ACTIVE_PI3K_CYTOSOL + PIP2_CYTOSOL = ACTIVE_PI3K_PIP2_CYTOSOL ACTIVE_PI3K_CYTOSOL+PIP2_CYTOSOL = ACTIVE_PI3K_PIP2_CYTOSOL
0.041457890216383866 ; % 1430 ACTIVE_PI3K_PIP2_CYTOSOL = ACTIVE_PI3K_CYTOSOL + PIP2_CYTOSOL ACTIVE_PI3K_PIP2_CYTOSOL = ACTIVE_PI3K_CYTOSOL+PIP2_CYTOSOL
0.028790172408215353 ; % 1431 ACTIVE_PI3K_PIP2_CYTOSOL = ACTIVE_PI3K_CYTOSOL + PIP3_CYTOSOL ACTIVE_PI3K_PIP2_CYTOSOL = ACTIVE_PI3K_CYTOSOL+PIP3_CYTOSOL
0.6742517740734068 ; % 1432 PTEN_CYTOSOL + PIP3_CYTOSOL = PTEN_PIP3_CYTOSOL PTEN_CYTOSOL+PIP3_CYTOSOL = PTEN_PIP3_CYTOSOL
0.06225996347543276 ; % 1433 PTEN_PIP3_CYTOSOL = PTEN_CYTOSOL + PIP3_CYTOSOL PTEN_PIP3_CYTOSOL = PTEN_CYTOSOL+PIP3_CYTOSOL

0.3495464459300982 ; % 1434 PTEN_PIP3_CYTOSOL = PTEN_CYTOSOL + PIP2_CYTOSOL PTEN_PIP3_CYTOSOL = PTEN_CYTOSOL+PIP2_CYTOSOL
0.78796705848212 ; % 1435 PDK1_CYTOSOL + PIP3_CYTOSOL = PDK1_PIP3_CYTOSOL
PDK1_CYTOSOL+PIP3_CYTOSOL = PDK1_PIP3_CYTOSOL
0.0929095245936462 ; % 1436 PDK1_PIP3_CYTOSOL = PDK1_CYTOSOL + PIP3_CYTOSOL PDK1_PIP3_CYTOSOL = PDK1_CYTOSOL+PIP3_CYTOSOL
0.4317451947259917 ; % 1437 PDK1_PIP3_CYTOSOL + AKT_CYTOSOL = PDK1_PIP3_AKT_CYTOSOL
PDK1_PIP3_CYTOSOL+AKT_CYTOSOL = PDK1_PIP3_AKT_CYTOSOL
0.00794593845616003 ; % 1438 PDK1_PIP3_AKT_CYTOSOL = PDK1_PIP3_CYTOSOL + AKT_CYTOSOL
PDK1_PIP3_AKT_CYTOSOL = PDK1_PIP3_CYTOSOL+AKT_CYTOSOL
0.05712111895848748 ; % 1439 PDK1_PIP3_AKT_CYTOSOL = PDK1_PIP3_CYTOSOL + ACTIVE_AKT_CYTOSOL
PDK1_PIP3_AKT_CYTOSOL = PDK1_PIP3_CYTOSOL+ACTIVE_AKT_CYTOSOL
0.05451183398568826 ; % 1440 ACTIVE_AKT_CYTOSOL + GSK3B_CYTOSOL = ACTIVE_AKT_GSK3B_CYTOSOL
ACTIVE_AKT_CYTOSOL+GSK3B_CYTOSOL = ACTIVE_AKT_GSK3B_CYTOSOL
0.09544308519187727 ; % 1441 ACTIVE_AKT_GSK3B_CYTOSOL = ACTIVE_AKT_CYTOSOL + GSK3B_CYTOSOL
ACTIVE_AKT_GSK3B_CYTOSOL = ACTIVE_AKT_CYTOSOL+GSK3B_CYTOSOL
0.6988781519059352 ; % 1442 ACTIVE_AKT_GSK3B_CYTOSOL = ACTIVE_AKT_CYTOSOL + P_GSK3B_CYTOSOL
ACTIVE_AKT_GSK3B_CYTOSOL = ACTIVE_AKT_CYTOSOL+P_GSK3B_CYTOSOL
0.02559074327068167 ; % 1443 AKT_PASE_CYTOSOL + ACTIVE_PI3K_CYTOSOL = AKT_PASE_ACTIVE_PI3K_CYTOSOL
AKT_PASE_CYTOSOL+ACTIVE_PI3K_CYTOSOL = AKT_PASE_ACTIVE_PI3K_CYTOSOL
0.0258476234705326 ; % 1444 AKT_PASE_ACTIVE_PI3K_CYTOSOL = AKT_PASE_CYTOSOL + ACTIVE_PI3K_CYTOSOL
AKT_PASE_ACTIVE_PI3K_CYTOSOL = AKT_PASE_CYTOSOL+ACTIVE_PI3K_CYTOSOL
0.4953183637882027 ; % 1445 AKT_PASE_ACTIVE_PI3K_CYTOSOL = AKT_PASE_CYTOSOL + PI3K_CYTOSOL
AKT_PASE_ACTIVE_PI3K_CYTOSOL = AKT_PASE_CYTOSOL+PI3K_CYTOSOL
0.20450046233162755 ; % 1446 AKT_PASE_CYTOSOL + ACTIVE_AKT_CYTOSOL = AKT_PASE_ACTIVE_AKT_CYTOSOL
AKT_PASE_CYTOSOL+ACTIVE_AKT_CYTOSOL = AKT_PASE_ACTIVE_AKT_CYTOSOL
0.09206912782257391 ; % 1447 AKT_PASE_ACTIVE_AKT_CYTOSOL = AKT_PASE_CYTOSOL + ACTIVE_AKT_CYTOSOL
AKT_PASE_ACTIVE_AKT_CYTOSOL = AKT_PASE_CYTOSOL+ACTIVE_AKT_CYTOSOL
0.3460017908541758 ; % 1448 AKT_PASE_ACTIVE_AKT_CYTOSOL = AKT_PASE_CYTOSOL + AKT_CYTOSOL
AKT_PASE_ACTIVE_AKT_CYTOSOL = AKT_PASE_CYTOSOL+AKT_CYTOSOL
0.27776734236815326 ; % 1449 AKT_PASE_CYTOSOL + P_GSK3B_CYTOSOL = AKT_PASE_P_GSK3B_CYTOSOL
AKT_PASE_CYTOSOL+P_GSK3B_CYTOSOL = AKT_PASE_P_GSK3B_CYTOSOL
0.00304044391659466 ; % 1450 AKT_PASE_P_GSK3B_CYTOSOL = AKT_PASE_CYTOSOL + P_GSK3B_CYTOSOL
AKT_PASE_P_GSK3B_CYTOSOL = AKT_PASE_CYTOSOL+P_GSK3B_CYTOSOL
0.8676631943954042 ; % 1451 AKT_PASE_P_GSK3B_CYTOSOL = AKT_PASE_CYTOSOL + GSK3B_CYTOSOL
AKT_PASE_P_GSK3B_CYTOSOL = AKT_PASE_CYTOSOL+GSK3B_CYTOSOL
0.4188794952366329 ; % 1452 AXIN_CYTOSOL + BCATENIN_CYTOSOL = AXIN_BCATENIN_CYTOSOL
AXIN_CYTOSOL+BCATENIN_CYTOSOL = AXIN_BCATENIN_CYTOSOL
0.0685477060786686 ; % 1453 AXIN_BCATENIN_CYTOSOL = AXIN_CYTOSOL + BCATENIN_CYTOSOL
AXIN_BCATENIN_CYTOSOL = AXIN_CYTOSOL+BCATENIN_CYTOSOL
0.9606003475741256 ; % 1454 AXIN_BCATENIN_CYTOSOL + APC_CYTOSOL = AXIN_BCATENIN_APC_CYTOSOL
AXIN_BCATENIN_CYTOSOL+APC_CYTOSOL = AXIN_BCATENIN_APC_CYTOSOL
0.02776938057494597 ; % 1455 AXIN_BCATENIN_APC_CYTOSOL = AXIN_BCATENIN_CYTOSOL + APC_CYTOSOL
AXIN_BCATENIN_APC_CYTOSOL = AXIN_BCATENIN_CYTOSOL+APC_CYTOSOL
0.8907901963314437 ; % 1456 AXIN_BCATENIN_APC_CYTOSOL + CK1_CYTOSOL = AXIN_BCATENIN_APC_CK1_CYTOSOL AXIN_BCATENIN_APC_CYTOSOL+CK1_CYTOSOL = AXIN_BCATENIN_APC_CK1_CYTOSOL
0.09742942185492434 ; % 1457 AXIN_BCATENIN_APC_CK1_CYTOSOL = AXIN_BCATENIN_APC_CYTOSOL + CK1_CYTOSOL AXIN_BCATENIN_APC_CK1_CYTOSOL = AXIN_BCATENIN_APC_CYTOSOL+CK1_CYTOSOL
0.03452231051821808 ; % 1458 AXIN_BCATENIN_APC_CYTOSOL + GSK3B_CYTOSOL = AXIN_BCATENIN_APC_GSK3B_CYTOSOL AXIN_BCATENIN_APC_CYTOSOL+GSK3B_CYTOSOL = AXIN_BCATENIN_APC_GSK3B_CYTOSOL
0.04209029696361758 ; % 1459 AXIN_BCATENIN_APC_GSK3B_CYTOSOL = AXIN_BCATENIN_APC_CYTOSOL + GSK3B_CYTOSOL AXIN_BCATENIN_APC_GSK3B_CYTOSOL = AXIN_BCATENIN_APC_CYTOSOL+GSK3B_CYTOSOL
0.4319566537711762 ; % 1460 AXIN_BCATENIN_APC_CK1_CYTOSOL = CK1_CYTOSOL + AXIN_CYTOSOL + APC_CYTOSOL + PP_BCATENIN_CYTOSOL AXIN_BCATENIN_APC_CK1_CYTOSOL = CK1_CYTOSOL+AXIN_CYTOSOL+APC_CYTOSOL+PP_BCATENIN_CYTOSOL
0.20726938161225128 ; % 1461 AXIN_BCATENIN_APC_GSK3B_CYTOSOL = GSK3B_CYTOSOL + AXIN_CYTOSOL + APC_CYTOSOL + PP_BCATENIN_CYTOSOL AXIN_BCATENIN_APC_GSK3B_CYTOSOL = GSK3B_CYTOSOL+AXIN_CYTOSOL+APC_CYTOSOL+PP_BCATENIN_CYTOSOL
0.40972393817805053 ; % 1462 PP_BCATENIN_CYTOSOL + BTRCP_CYTOSOL = PP_BCATENIN_BTRCP_CYTOSOL
PP_BCATENIN_CYTOSOL+BTRCP_CYTOSOL = PP_BCATENIN_BTRCP_CYTOSOL
0.09476293725100088 ; % 1463 PP_BCATENIN_BTRCP_CYTOSOL = PP_BCATENIN_CYTOSOL + BTRCP_CYTOSOL
PP_BCATENIN_BTRCP_CYTOSOL = PP_BCATENIN_CYTOSOL+BTRCP_CYTOSOL
0.13425931209161557 ; % 1464 PP_BCATENIN_BTRCP_CYTOSOL = BTRCP_CYTOSOL + UB_PP_BCATENIN_CYTOSOL
PP_BCATENIN_BTRCP_CYTOSOL = BTRCP_CYTOSOL+UB_PP_BCATENIN_CYTOSOL
0.7256142986538963 ; % 1465 GSK3B_CYTOSOL + NFATC1_CYTOSOL = GSK3B_NFATC1_CYTOSOL
GSK3B_CYTOSOL+NFATC1_CYTOSOL = GSK3B_NFATC1_CYTOSOL
0.04009245285152627 ; % 1466 GSK3B_NFATC1_CYTOSOL = GSK3B_CYTOSOL + NFATC1_CYTOSOL
GSK3B_NFATC1_CYTOSOL = GSK3B_CYTOSOL+NFATC1_CYTOSOL
0.38404841232945275 ; % 1467 GSK3B_NFATC1_CYTOSOL = GSK3B_CYTOSOL + P_NFATC1_CYTOSOL
GSK3B_NFATC1_CYTOSOL = GSK3B_CYTOSOL+P_NFATC1_CYTOSOL
0.13537378562044527 ; % 1468 UB_PP_BCATENIN_CYTOSOL = [] UB_PP_BCATENIN_CYTOSOL = []
0.6840334422776655 ; % 1469 JAG1_NOTCH1_TACE_CYTOSOL = JAG1_NCED_CYTOSOL + ACTIVE_NCID_CYTOSOL
JAG1_NOTCH1_TACE_CYTOSOL = JAG1_NCED_CYTOSOL+ACTIVE_NCID_CYTOSOL
0.07568538461311392 ; % 1470 DELTA4_NOTCH1_TACE_CYTOSOL = DELTA4_NCED_CYTOSOL + ACTIVE_NCID_CYTOSOLDELTA4_NOTCH1_TACE_CYTOSOL = DELTA4_NCED_CYTOSOL+ACTIVE_NCID_CYTOSOL
0.04709894228038258 ; % 1471 ACTIVE_NCID_CYTOSOL + SEL1_CYTOSOL = ACTIVE_NCID_SEL1_CYTOSOL
ACTIVE_NCID_CYTOSOL+SEL1_CYTOSOL = ACTIVE_NCID_SEL1_CYTOSOL
0.05127366042275477 ; % 1472 ACTIVE_NCID_SEL1_CYTOSOL = ACTIVE_NCID_CYTOSOL + SEL1_CYTOSOL
ACTIVE_NCID_SEL1_CYTOSOL = ACTIVE_NCID_CYTOSOL+SEL1_CYTOSOL
0.050972505891123676 ; % 1473 ACTIVE_NCID_SEL1_CYTOSOL = SEL1_CYTOSOL + UB_ACTIVE_NCID_CYTOSOL
ACTIVE_NCID_SEL1_CYTOSOL = SEL1_CYTOSOL+UB_ACTIVE_NCID_CYTOSOL
0.8543786642156181 ; % 1474 JAG1_NCED_CYTOSOL + DELTEX_NEDD4_CYTOSOL = JAG1_NCED_DELTEX_NEDD4_CYTOSOL JAG1_NCED_CYTOSOL+DELTEX_NEDD4_CYTOSOL = JAG1_NCED_DELTEX_NEDD4_CYTOSOL
0.03988907406494192 ; % 1475 JAG1_NCED_DELTEX_NEDD4_CYTOSOL = JAG1_NCED_CYTOSOL + DELTEX_NEDD4_CYTOSOL JAG1_NCED_DELTEX_NEDD4_CYTOSOL = JAG1_NCED_CYTOSOL+DELTEX_NEDD4_CYTOSOL
0.3631869009777403 ; % 1476 JAG1_NCED_DELTEX_NEDD4_CYTOSOL = DELTEX_NEDD4_CYTOSOL + UB_JAG1_NCED_CYTOSOL JAG1_NCED_DELTEX_NEDD4_CYTOSOL = DELTEX_NEDD4_CYTOSOL+UB_JAG1_NCED_CYTOSOL
0.00264766075673728 ; % 1477 DELTA4_NCED_CYTOSOL + DELTEX_NEDD4_CYTOSOL = DELTA4_NCED_DELTEX_NEDD4_CYTOSOL DELTA4_NCED_CYTOSOL+DELTEX_NEDD4_CYTOSOL = DELTA4_NCED_DELTEX_NEDD4_CYTOSOL
0.05357437901010942 ; % 1478 DELTA4_NCED_DELTEX_NEDD4_CYTOSOL = DELTA4_NCED_CYTOSOL + DELTEX_NEDD4_CYTOSOL DELTA4_NCED_DELTEX_NEDD4_CYTOSOL = DELTA4_NCED_CYTOSOL+DELTEX_NEDD4_CYTOSOL
0.5922101855856718 ; % 1479 DELTA4_NCED_DELTEX_NEDD4_CYTOSOL = DELTEX_NEDD4_CYTOSOL + UB_DELTA4_NCED_CYTOSOL DELTA4_NCED_DELTEX_NEDD4_CYTOSOL = DELTEX_NEDD4_CYTOSOL+UB_DELTA4_NCED_CYTOSOL

0.4334109839703474 ; % 1480 UB_JAG1_NECD_CYTOSOL = [] UB_JAG1_NECD_CYTOSOL = []
0.4121447454033347 ; % 1481 UB_DELTA4_NECD_CYTOSOL = [] UB_DELTA4_NECD_CYTOSOL = []
0.024604835412359582 ; % 1482 JAG1_NECD_EXTRACELLULAR = [] JAG1_NECD_EXTRACELLULAR = []
0.42321842021925066 ; % 1483 UB_ACTIVE_NCID_CYTOSOL = [] UB_ACTIVE_NCID_CYTOSOL = []
0.3654473162985936 ; % 1484 RAS_CYTOSOL + GDP_CYTOSOL = RAS_GDP_CYTOSOL
RAS_CYTOSOL+GDP_CYTOSOL = RAS_GDP_CYTOSOL
0.027285543520855195 ; % 1485 RAS_GDP_CYTOSOL = RAS_CYTOSOL + GDP_CYTOSOL RAS_GDP_CYTOSOL =
RAS_CYTOSOL+GDP_CYTOSOL
0.02129309631861409 ; % 1486 TGFB2_BMPRII_ALK2_ENDOGLIN_SHC_GRB2_SOS_CYTOSOL + RAS_GDP_CYTOSOL
= TGFB2_BMPRII_ALK2_ENDOGLIN_SHC_GRB2_SOS_RAS_GDP_CYTOSOL
TGFB2_BMPRII_ALK2_ENDOGLIN_SHC_GRB2_SOS_CYTOSOL+RAS_GDP_CYTOSOL =
TGFB2_BMPRII_ALK2_ENDOGLIN_SHC_GRB2_SOS_RAS_GDP_CYTOSOL
0.033712910629131655 ; % 1487 TGFB2_BMPRII_ALK2_ENDOGLIN_SHC_GRB2_SOS_RAS_GDP_CYTOSOL =
TGFB2_BMPRII_ALK2_ENDOGLIN_SHC_GRB2_SOS_CYTOSOL + RAS_GDP_CYTOSOL TGFB2_BMPRII_ALK2_ENDOGLIN_SHC_GRB2_SOS_RAS_GDP_CYTOSOL
= TGFB2_BMPRII_ALK2_ENDOGLIN_SHC_GRB2_SOS_CYTOSOL+RAS_GDP_CYTOSOL
0.1811918771681723 ; % 1488 TGFB2_BMPRII_ALK2_ENDOGLIN_SHC_GRB2_SOS_RAS_GDP_CYTOSOL +
GTP_CYTOSOL = TGFB2_BMPRII_ALK2_ENDOGLIN_SHC_GRB2_SOS_CYTOSOL + RAS_GTP_CYTOSOL + GDP_CYTOSOL
TGFB2_BMPRII_ALK2_ENDOGLIN_SHC_GRB2_SOS_RAS_GDP_CYTOSOL+GTP_CYTOSOL =
TGFB2_BMPRII_ALK2_ENDOGLIN_SHC_GRB2_SOS_CYTOSOL+RAS_GTP_CYTOSOL+GDP_CYTOSOL
0.8525355618641878 ; % 1489 BMP2_BMPRII_ALK2_SHC_GRB2_SOS_CYTOSOL + RAS_GDP_CYTOSOL =
BMP2_BMPRII_ALK2_SHC_GRB2_SOS_RAS_GDP_CYTOSOL BMP2_BMPRII_ALK2_SHC_GRB2_SOS_CYTOSOL+RAS_GDP_CYTOSOL =
BMP2_BMPRII_ALK2_SHC_GRB2_SOS_RAS_GDP_CYTOSOL
0.09357673938577171 ; % 1490 BMP2_BMPRII_ALK2_SHC_GRB2_SOS_RAS_GDP_CYTOSOL =
BMP2_BMPRII_ALK2_SHC_GRB2_SOS_CYTOSOL + RAS_GDP_CYTOSOL BMP2_BMPRII_ALK2_SHC_GRB2_SOS_RAS_GDP_CYTOSOL =
BMP2_BMPRII_ALK2_SHC_GRB2_SOS_CYTOSOL+RAS_GDP_CYTOSOL
0.4827323261920309 ; % 1491 BMP2_BMPRII_ALK2_SHC_GRB2_SOS_RAS_GDP_CYTOSOL + GTP_CYTOSOL =
BMP2_BMPRII_ALK2_SHC_GRB2_SOS_CYTOSOL + RAS_GTP_CYTOSOL + GDP_CYTOSOL
BMP2_BMPRII_ALK2_SHC_GRB2_SOS_RAS_GDP_CYTOSOL+GTP_CYTOSOL =
BMP2_BMPRII_ALK2_SHC_GRB2_SOS_CYTOSOL+RAS_GTP_CYTOSOL+GDP_CYTOSOL
0.6309001574384063 ; % 1492 RAS_GTP_CYTOSOL + RAF_CYTOSOL = RAS_GTP_RAF_CYTOSOL
RAS_GTP_CYTOSOL+RAF_CYTOSOL = RAS_GTP_RAF_CYTOSOL
0.06076960954251556 ; % 1493 RAS_GTP_RAF_CYTOSOL = RAS_GTP_CYTOSOL + RAF_CYTOSOL
RAS_GTP_RAF_CYTOSOL = RAS_GTP_CYTOSOL+RAF_CYTOSOL
0.2659273893227704 ; % 1494 RAS_GTP_RAF_CYTOSOL = ACTIVE_RAF_CYTOSOL + RAS_GTP_CYTOSOL
RAS_GTP_RAF_CYTOSOL = ACTIVE_RAF_CYTOSOL+RAS_GTP_CYTOSOL
0.8683077751131456 ; % 1495 ACTIVE_RAF_CYTOSOL + MEK_CYTOSOL = ACTIVE_RAF_MEK_CYTOSOL
ACTIVE_RAF_CYTOSOL+MEK_CYTOSOL = ACTIVE_RAF_MEK_CYTOSOL
0.07016621343539779 ; % 1496 ACTIVE_RAF_MEK_CYTOSOL = ACTIVE_RAF_CYTOSOL + MEK_CYTOSOL
ACTIVE_RAF_MEK_CYTOSOL = ACTIVE_RAF_CYTOSOL+MEK_CYTOSOL
0.8474761324367217 ; % 1497 ACTIVE_RAF_MEK_CYTOSOL = ACTIVE_RAF_CYTOSOL + P_MEK_CYTOSOL
ACTIVE_RAF_MEK_CYTOSOL = ACTIVE_RAF_CYTOSOL+P_MEK_CYTOSOL
0.4621601351689908 ; % 1498 ACTIVE_RAF_CYTOSOL + P_MEK_CYTOSOL = ACTIVE_RAF_P_MEK_CYTOSOL
ACTIVE_RAF_CYTOSOL+P_MEK_CYTOSOL = ACTIVE_RAF_P_MEK_CYTOSOL
0.05588768541374525 ; % 1499 ACTIVE_RAF_P_MEK_CYTOSOL = ACTIVE_RAF_CYTOSOL + P_MEK_CYTOSOL
ACTIVE_RAF_P_MEK_CYTOSOL = ACTIVE_RAF_CYTOSOL+P_MEK_CYTOSOL
0.05047513019783878 ; % 1500 ACTIVE_RAF_P_MEK_CYTOSOL = ACTIVE_RAF_CYTOSOL + PP_MEK_CYTOSOL
ACTIVE_RAF_P_MEK_CYTOSOL = ACTIVE_RAF_CYTOSOL+PP_MEK_CYTOSOL
0.6820727563687394 ; % 1501 PP_MEK_CYTOSOL + ERK_CYTOSOL = PP_MEK_ERK_CYTOSOL
PP_MEK_CYTOSOL+ERK_CYTOSOL = PP_MEK_ERK_CYTOSOL
0.008916316213951558 ; % 1502 PP_MEK_ERK_CYTOSOL = PP_MEK_CYTOSOL + ERK_CYTOSOL
PP_MEK_ERK_CYTOSOL = PP_MEK_CYTOSOL+ERK_CYTOSOL
0.22391960450927473 ; % 1503 PP_MEK_ERK_CYTOSOL = PP_MEK_CYTOSOL + P_ERK_CYTOSOL
PP_MEK_ERK_CYTOSOL = PP_MEK_CYTOSOL+P_ERK_CYTOSOL
0.7302897817095368 ; % 1504 PP_MEK_CYTOSOL + P_ERK_CYTOSOL = PP_MEK_P_ERK_CYTOSOL
PP_MEK_CYTOSOL+P_ERK_CYTOSOL = PP_MEK_P_ERK_CYTOSOL
0.037282008979755435 ; % 1505 PP_MEK_P_ERK_CYTOSOL = PP_MEK_CYTOSOL + P_ERK_CYTOSOL
PP_MEK_P_ERK_CYTOSOL = PP_MEK_CYTOSOL+P_ERK_CYTOSOL
0.7245356005346338 ; % 1506 PP_MEK_P_ERK_CYTOSOL = PP_MEK_CYTOSOL + PP_ERK_CYTOSOL
PP_MEK_P_ERK_CYTOSOL = PP_MEK_CYTOSOL+PP_ERK_CYTOSOL
0.3197622743646096 ; % 1507 ACTIVE_RAF_CYTOSOL + RAF_PASE_CYTOSOL = ACTIVE_RAF_RAF_PASE_CYTOSOL
ACTIVE_RAF_CYTOSOL+RAF_PASE_CYTOSOL = ACTIVE_RAF_RAF_PASE_CYTOSOL
0.019020023046072546 ; % 1508 ACTIVE_RAF_RAF_PASE_CYTOSOL = ACTIVE_RAF_CYTOSOL + RAF_PASE_CYTOSOL
ACTIVE_RAF_RAF_PASE_CYTOSOL = ACTIVE_RAF_CYTOSOL+RAF_PASE_CYTOSOL
0.27648886868023714 ; % 1509 ACTIVE_RAF_RAF_PASE_CYTOSOL = RAF_PASE_CYTOSOL + RAF_CYTOSOL
ACTIVE_RAF_RAF_PASE_CYTOSOL = RAF_PASE_CYTOSOL+RAF_CYTOSOL
0.45409923971495236 ; % 1510 PP_MEK_CYTOSOL + MEK_PASE_CYTOSOL = PP_MEK_MEK_PASE_CYTOSOL
PP_MEK_CYTOSOL+MEK_PASE_CYTOSOL = PP_MEK_MEK_PASE_CYTOSOL
0.05580335435345893 ; % 1511 PP_MEK_MEK_PASE_CYTOSOL = PP_MEK_CYTOSOL + MEK_PASE_CYTOSOL
PP_MEK_MEK_PASE_CYTOSOL = PP_MEK_CYTOSOL+MEK_PASE_CYTOSOL
0.6492962291501434 ; % 1512 PP_MEK_MEK_PASE_CYTOSOL = MEK_PASE_CYTOSOL + P_MEK_CYTOSOL
PP_MEK_MEK_PASE_CYTOSOL = MEK_PASE_CYTOSOL+P_MEK_CYTOSOL
0.5988021377969366 ; % 1513 P_MEK_CYTOSOL + MEK_PASE_CYTOSOL = P_MEK_MEK_PASE_CYTOSOL
P_MEK_CYTOSOL+MEK_PASE_CYTOSOL = P_MEK_MEK_PASE_CYTOSOL
0.09291905045948527 ; % 1514 P_MEK_MEK_PASE_CYTOSOL = P_MEK_CYTOSOL + MEK_PASE_CYTOSOL
P_MEK_MEK_PASE_CYTOSOL = P_MEK_CYTOSOL+MEK_PASE_CYTOSOL
0.026065374979508893 ; % 1515 P_MEK_MEK_PASE_CYTOSOL = MEK_PASE_CYTOSOL + MEK_CYTOSOL
P_MEK_MEK_PASE_CYTOSOL = MEK_PASE_CYTOSOL+MEK_CYTOSOL
0.9017029979562975 ; % 1516 PP_ERK_CYTOSOL + ERK_PASE_CYTOSOL = PP_ERK_ERK_PASE_CYTOSOL
PP_ERK_CYTOSOL+ERK_PASE_CYTOSOL = PP_ERK_ERK_PASE_CYTOSOL
0.02629843855980305 ; % 1517 PP_ERK_ERK_PASE_CYTOSOL = PP_ERK_CYTOSOL + ERK_PASE_CYTOSOL
PP_ERK_ERK_PASE_CYTOSOL = PP_ERK_CYTOSOL+ERK_PASE_CYTOSOL
0.9872962677478923 ; % 1518 PP_ERK_ERK_PASE_CYTOSOL = ERK_PASE_CYTOSOL + P_ERK_CYTOSOL
PP_ERK_ERK_PASE_CYTOSOL = ERK_PASE_CYTOSOL+P_ERK_CYTOSOL
0.6190580534231794 ; % 1519 P_ERK_CYTOSOL + ERK_PASE_CYTOSOL = P_ERK_ERK_PASE_CYTOSOL
P_ERK_CYTOSOL+ERK_PASE_CYTOSOL = P_ERK_ERK_PASE_CYTOSOL
0.09745920484937548 ; % 1520 P_ERK_ERK_PASE_CYTOSOL = P_ERK_CYTOSOL + ERK_PASE_CYTOSOL
P_ERK_ERK_PASE_CYTOSOL = P_ERK_CYTOSOL+ERK_PASE_CYTOSOL
0.9462306007701528 ; % 1521 P_ERK_ERK_PASE_CYTOSOL = ERK_PASE_CYTOSOL + ERK_CYTOSOL
P_ERK_ERK_PASE_CYTOSOL = ERK_PASE_CYTOSOL+ERK_CYTOSOL
0.7797899318745652 ; % 1522 TGFB2_BMPRII_ALK2_ENDOGLIN_SHC_GRB2_SOS_CYTOSOL + PP_ERK_CYTOSOL =
TGFB2_BMPRII_ALK2_ENDOGLIN_SHC_GRB2_SOS_PP_ERK_CYTOSOL TGFB2_BMPRII_ALK2_ENDOGLIN_SHC_GRB2_SOS_CYTOSOL+PP_ERK_CYTOSOL =
TGFB2_BMPRII_ALK2_ENDOGLIN_SHC_GRB2_SOS_PP_ERK_CYTOSOL

0.089402622992118 86 ; % 1523 TGFB2_BMPRII_ALK2_ENDOGLIN_SHC_GRB2_SOS_PP_ERK_CYTOSOL =
TGFB2_BMPRII_ALK2_ENDOGLIN_SHC_GRB2_SOS_CYTOSOL + PP_ERK_CYTOSOL TGFB2_BMPRII_ALK2_ENDOGLIN_SHC_GRB2_SOS_PP_ERK_CYTOSOL =
TGFB2_BMPRII_ALK2_ENDOGLIN_SHC_GRB2_SOS_CYTOSOL+PP_ERK_CYTOSOL
0.8314544596860927 ; % 1524 TGFB2_BMPRII_ALK2_ENDOGLIN_SHC_GRB2_SOS_PP_ERK_CYTOSOL =
PP_ERK_CYTOSOL + TGFB2_BMPRII_ALK2_ENDOGLIN_SHC_GRB2_CYTOSOL + SOS_CYTOSOL
TGFB2_BMPRII_ALK2_ENDOGLIN_SHC_GRB2_SOS_PP_ERK_CYTOSOL =
PP_ERK_CYTOSOL+TGFB2_BMPRII_ALK2_ENDOGLIN_SHC_GRB2_CYTOSOL+SOS_CYTOSOL
0.7403028419797757 ; % 1525 BMP2_BMPRII_ALK2_SHC_GRB2_SOS_CYTOSOL + PP_ERK_CYTOSOL =
BMP2_BMPRII_ALK2_SHC_GRB2_SOS_PP_ERK_CYTOSOL BMP2_BMPRII_ALK2_SHC_GRB2_SOS_CYTOSOL+PP_ERK_CYTOSOL =
BMP2_BMPRII_ALK2_SHC_GRB2_SOS_PP_ERK_CYTOSOL
0.019915641894977444 ; % 1526 BMP2_BMPRII_ALK2_SHC_GRB2_SOS_PP_ERK_CYTOSOL =
BMP2_BMPRII_ALK2_SHC_GRB2_SOS_CYTOSOL + PP_ERK_CYTOSOL BMP2_BMPRII_ALK2_SHC_GRB2_SOS_PP_ERK_CYTOSOL =
BMP2_BMPRII_ALK2_SHC_GRB2_SOS_CYTOSOL+PP_ERK_CYTOSOL
0.061986533052099335 ; % 1527 BMP2_BMPRII_ALK2_SHC_GRB2_SOS_PP_ERK_CYTOSOL = PP_ERK_CYTOSOL +
BMP2_BMPRII_ALK2_SHC_GRB2_CYTOSOL + SOS_CYTOSOL BMP2_BMPRII_ALK2_SHC_GRB2_SOS_PP_ERK_CYTOSOL =
PP_ERK_CYTOSOL+BMP2_BMPRII_ALK2_SHC_GRB2_CYTOSOL+SOS_CYTOSOL
0.4896853922511609 ; % 1528 PP_ERK_CYTOSOL + AP1_CYTOSOL = PP_ERK_AP1_CYTOSOL
PP_ERK_CYTOSOL+AP1_CYTOSOL = PP_ERK_AP1_CYTOSOL
0.09520316733081992 ; % 1529 PP_ERK_AP1_CYTOSOL = PP_ERK_CYTOSOL + AP1_CYTOSOL
PP_ERK_AP1_CYTOSOL = PP_ERK_CYTOSOL+AP1_CYTOSOL
0.15297795865713093 ; % 1530 PP_ERK_AP1_CYTOSOL = PP_ERK_CYTOSOL + P_AP1_CYTOSOL
PP_ERK_AP1_CYTOSOL = PP_ERK_CYTOSOL+P_AP1_CYTOSOL
0.5975433893240303 ; % 1531 PP_ERK_CYTOSOL + SP1_CYTOSOL = PP_ERK_SP1_CYTOSOL
PP_ERK_CYTOSOL+SP1_CYTOSOL = PP_ERK_SP1_CYTOSOL
0.050453708245729104 ; % 1532 PP_ERK_SP1_CYTOSOL = PP_ERK_CYTOSOL + SP1_CYTOSOL
PP_ERK_SP1_CYTOSOL = PP_ERK_CYTOSOL+SP1_CYTOSOL
0.2753206746479774 ; % 1533 PP_ERK_SP1_CYTOSOL = PP_ERK_CYTOSOL + P_SP1_CYTOSOL
PP_ERK_SP1_CYTOSOL = PP_ERK_CYTOSOL+P_SP1_CYTOSOL
0.8930851064915863 ; % 1534 PP_ERK_CYTOSOL + CJUN_CYTOSOL = PP_ERK_CJUN_CYTOSOL
PP_ERK_CYTOSOL+CJUN_CYTOSOL = PP_ERK_CJUN_CYTOSOL
0.08639752115140081 ; % 1535 PP_ERK_CJUN_CYTOSOL = PP_ERK_CYTOSOL + CJUN_CYTOSOL
PP_ERK_CJUN_CYTOSOL = PP_ERK_CYTOSOL+CJUN_CYTOSOL
0.7607547026608246 ; % 1536 PP_ERK_CJUN_CYTOSOL = PP_ERK_CYTOSOL + P_CJUN_CYTOSOL
PP_ERK_CJUN_CYTOSOL = PP_ERK_CYTOSOL+P_CJUN_CYTOSOL
0.9383216853929269 ; % 1537 PP_ERK_CYTOSOL + CPLA2_CYTOSOL = PP_ERK_CPLA2_CYTOSOL
PP_ERK_CYTOSOL+CPLA2_CYTOSOL = PP_ERK_CPLA2_CYTOSOL
0.017566049286847043 ; % 1538 PP_ERK_CPLA2_CYTOSOL = PP_ERK_CYTOSOL + CPLA2_CYTOSOL
PP_ERK_CPLA2_CYTOSOL = PP_ERK_CYTOSOL+CPLA2_CYTOSOL
0.22711727424242933 ; % 1539 PP_ERK_CPLA2_CYTOSOL = PP_ERK_CYTOSOL + P_CPLA2_CYTOSOL
PP_ERK_CPLA2_CYTOSOL = PP_ERK_CYTOSOL+P_CPLA2_CYTOSOL
0.00908717759666282 ; % 1540 PP_ERK_CYTOSOL + SMAD2_CYTOSOL = PP_ERK_SMAD2_CYTOSOL
PP_ERK_CYTOSOL+SMAD2_CYTOSOL = PP_ERK_SMAD2_CYTOSOL
0.04577700872029053 ; % 1541 PP_ERK_SMAD2_CYTOSOL = PP_ERK_CYTOSOL + SMAD2_CYTOSOL
PP_ERK_SMAD2_CYTOSOL = PP_ERK_CYTOSOL+SMAD2_CYTOSOL
0.5017153656344642 ; % 1542 PP_ERK_SMAD2_CYTOSOL = PP_ERK_CYTOSOL + P_SMAD2_CYTOSOL
PP_ERK_SMAD2_CYTOSOL = PP_ERK_CYTOSOL+P_SMAD2_CYTOSOL
0.0036278479697245325 ; % 1543 PP_ERK_CYTOSOL + SMAD3_CYTOSOL = PP_ERK_SMAD3_CYTOSOL
PP_ERK_CYTOSOL+SMAD3_CYTOSOL = PP_ERK_SMAD3_CYTOSOL
0.05836673638236113 ; % 1544 PP_ERK_SMAD3_CYTOSOL = PP_ERK_CYTOSOL + SMAD3_CYTOSOL
PP_ERK_SMAD3_CYTOSOL = PP_ERK_CYTOSOL+SMAD3_CYTOSOL
0.31703818126340566 ; % 1545 PP_ERK_SMAD3_CYTOSOL = PP_ERK_CYTOSOL + P_SMAD3_CYTOSOL
PP_ERK_SMAD3_CYTOSOL = PP_ERK_CYTOSOL+P_SMAD3_CYTOSOL
0.00272418441970879 ; % 1546 P_CPLA2_CYTOSOL + PKC_CYTOSOL = P_CPLA2_PKC_CYTOSOL
P_CPLA2_CYTOSOL+PKC_CYTOSOL = P_CPLA2_PKC_CYTOSOL
0.8501728879602906 ; % 1547 P_CPLA2_PKC_CYTOSOL = P_CPLA2_CYTOSOL + PKC_CYTOSOL
P_CPLA2_PKC_CYTOSOL = P_CPLA2_CYTOSOL+PKC_CYTOSOL
0.7546073529398805 ; % 1548 P_CPLA2_PKC_CYTOSOL = P_CPLA2_CYTOSOL + P_PKC_CYTOSOL
P_CPLA2_PKC_CYTOSOL = P_CPLA2_CYTOSOL+P_PKC_CYTOSOL
0.00022528645324735186; % 1549 P_PKC_CYTOSOL + SMAD2_CYTOSOL = P_PKC_SMAD2_CYTOSOL
P_PKC_CYTOSOL+SMAD2_CYTOSOL = P_PKC_SMAD2_CYTOSOL
0.03384768199634832 ; % 1550 P_PKC_SMAD2_CYTOSOL = P_PKC_CYTOSOL + SMAD2_CYTOSOL
P_PKC_SMAD2_CYTOSOL = P_PKC_CYTOSOL+SMAD2_CYTOSOL
0.687617189600002 ; % 1551 P_PKC_SMAD2_CYTOSOL = P_PKC_CYTOSOL + P_SMAD2_CYTOSOL
P_PKC_SMAD2_CYTOSOL = P_PKC_CYTOSOL+P_SMAD2_CYTOSOL
0.00016372544687844082; % 1552 P_PKC_CYTOSOL + SMAD3_CYTOSOL = P_PKC_SMAD3_CYTOSOL
P_PKC_CYTOSOL+SMAD3_CYTOSOL = P_PKC_SMAD3_CYTOSOL
0.06121615975821997 ; % 1553 P_PKC_SMAD3_CYTOSOL = P_PKC_CYTOSOL + SMAD3_CYTOSOL
P_PKC_SMAD3_CYTOSOL = P_PKC_CYTOSOL+SMAD3_CYTOSOL
0.36009604866247824 ; % 1554 P_PKC_SMAD3_CYTOSOL = P_PKC_CYTOSOL + P_SMAD3_CYTOSOL
P_PKC_SMAD3_CYTOSOL = P_PKC_CYTOSOL+P_SMAD3_CYTOSOL
0.06729324295516959 ; % 1555 P_PKC_CYTOSOL + IKB_NFKB_CYTOSOL = P_PKC_IKB_NFKB_CYTOSOL
P_PKC_CYTOSOL+IKB_NFKB_CYTOSOL = P_PKC_IKB_NFKB_CYTOSOL
0.08376878808332205 ; % 1556 P_PKC_IKB_NFKB_CYTOSOL = P_PKC_CYTOSOL + IKB_NFKB_CYTOSOL
P_PKC_IKB_NFKB_CYTOSOL = P_PKC_CYTOSOL+IKB_NFKB_CYTOSOL
0.6658117772336646 ; % 1557 P_PKC_IKB_NFKB_CYTOSOL = P_PKC_CYTOSOL + P_IKB_NFKB_CYTOSOL
P_PKC_IKB_NFKB_CYTOSOL = P_PKC_CYTOSOL+P_IKB_NFKB_CYTOSOL
0.0027897963637703027 ; % 1558 GPASE_CYTOSOL + P_AP1_CYTOSOL = GPASE_P_AP1_CYTOSOL
GPASE_CYTOSOL+P_AP1_CYTOSOL = GPASE_P_AP1_CYTOSOL
0.0601878316804977 ; % 1559 GPASE_P_AP1_CYTOSOL = GPASE_CYTOSOL + P_AP1_CYTOSOL
GPASE_P_AP1_CYTOSOL = GPASE_CYTOSOL+P_AP1_CYTOSOL
0.07891956777473075 ; % 1560 GPASE_P_AP1_CYTOSOL = GPASE_CYTOSOL + AP1_CYTOSOL
GPASE_P_AP1_CYTOSOL = GPASE_CYTOSOL+AP1_CYTOSOL
0.5315584063235371 ; % 1561 GPASE_CYTOSOL + P_SP1_CYTOSOL = GPASE_P_SP1_CYTOSOL
GPASE_CYTOSOL+P_SP1_CYTOSOL = GPASE_P_SP1_CYTOSOL
0.03615544077033689 ; % 1562 GPASE_P_SP1_CYTOSOL = GPASE_CYTOSOL + P_SP1_CYTOSOL
GPASE_P_SP1_CYTOSOL = GPASE_CYTOSOL+P_SP1_CYTOSOL
0.2088947125970736 ; % 1563 GPASE_P_SP1_CYTOSOL = GPASE_CYTOSOL + SP1_CYTOSOL
GPASE_P_SP1_CYTOSOL = GPASE_CYTOSOL+SP1_CYTOSOL
0.17798855481677767 ; % 1564 GPASE_CYTOSOL + P_CJUN_CYTOSOL = GPASE_P_CJUN_CYTOSOL
GPASE_CYTOSOL+P_CJUN_CYTOSOL = GPASE_P_CJUN_CYTOSOL
0.025438548254903215 ; % 1565 GPASE_P_CJUN_CYTOSOL = GPASE_CYTOSOL + P_CJUN_CYTOSOL
GPASE_P_CJUN_CYTOSOL = GPASE_CYTOSOL+P_CJUN_CYTOSOL

0.42716652751018835 ; % 1566 GPASE_P_CJUN_CYTOSOL = GPASE_CYTOSOL + CJUN_CYTOSOL
GPASE_P_CJUN_CYTOSOL = GPASE_CYTOSOL+CJUN_CYTOSOL
0.02739876362545446 ; % 1567 GPASE_CYTOSOL + P_CPLA2_CYTOSOL = GPASE_P_CPLA2_CYTOSOL
GPASE_CYTOSOL+P_CPLA2_CYTOSOL = GPASE_P_CPLA2_CYTOSOL
0.03274725365738842 ; % 1568 GPASE_P_CPLA2_CYTOSOL = GPASE_CYTOSOL + P_CPLA2_CYTOSOL
GPASE_P_CPLA2_CYTOSOL = GPASE_CYTOSOL+P_CPLA2_CYTOSOL
0.6704769938620023 ; % 1569 GPASE_P_CPLA2_CYTOSOL = GPASE_CYTOSOL + CPLA2_CYTOSOL
GPASE_P_CPLA2_CYTOSOL = GPASE_CYTOSOL+CPLA2_CYTOSOL
0.9706903628558254 ; % 1570 GPASE_CYTOSOL + P_SMAD2_CYTOSOL = GPASE_P_SMAD2_CYTOSOL
GPASE_CYTOSOL+P_SMAD2_CYTOSOL = GPASE_P_SMAD2_CYTOSOL
0.006687538627677514 ; % 1571 GPASE_P_SMAD2_CYTOSOL = GPASE_CYTOSOL + P_SMAD2_CYTOSOL
GPASE_P_SMAD2_CYTOSOL = GPASE_CYTOSOL+P_SMAD2_CYTOSOL
0.8631920751265187 ; % 1572 GPASE_P_SMAD2_CYTOSOL = GPASE_CYTOSOL + SMAD2_CYTOSOL
GPASE_P_SMAD2_CYTOSOL = GPASE_CYTOSOL+SMAD2_CYTOSOL
0.7313532786396573 ; % 1573 GPASE_CYTOSOL + P_SMAD3_CYTOSOL = GPASE_P_SMAD3_CYTOSOL
GPASE_CYTOSOL+P_SMAD3_CYTOSOL = GPASE_P_SMAD3_CYTOSOL
0.030450001346030698 ; % 1574 GPASE_P_SMAD3_CYTOSOL = GPASE_CYTOSOL + P_SMAD3_CYTOSOL
GPASE_P_SMAD3_CYTOSOL = GPASE_CYTOSOL+P_SMAD3_CYTOSOL
0.7696428467143489 ; % 1575 GPASE_P_SMAD3_CYTOSOL = GPASE_CYTOSOL + SMAD3_CYTOSOL
GPASE_P_SMAD3_CYTOSOL = GPASE_CYTOSOL+SMAD3_CYTOSOL
0.01045357196653407 ; % 1576 GPASE_CYTOSOL + P_NFATC1_CYTOSOL = GPASE_P_NFATC1_CYTOSOL
GPASE_CYTOSOL+P_NFATC1_CYTOSOL = GPASE_P_NFATC1_CYTOSOL
0.06787278643900517 ; % 1577 GPASE_P_NFATC1_CYTOSOL = GPASE_CYTOSOL + P_NFATC1_CYTOSOL
GPASE_P_NFATC1_CYTOSOL = GPASE_CYTOSOL+P_NFATC1_CYTOSOL
0.2131829053223503 ; % 1578 GPASE_P_NFATC1_CYTOSOL = GPASE_CYTOSOL + NFATC1_CYTOSOL
GPASE_P_NFATC1_CYTOSOL = GPASE_CYTOSOL+NFATC1_CYTOSOL
0.30576803192442614 ; % 1579 GPASE_CYTOSOL + P_PKC_CYTOSOL = GPASE_P_PKC_CYTOSOL
GPASE_CYTOSOL+P_PKC_CYTOSOL = GPASE_P_PKC_CYTOSOL
0.07709523643578828 ; % 1580 GPASE_P_PKC_CYTOSOL = GPASE_CYTOSOL + P_PKC_CYTOSOL
GPASE_P_PKC_CYTOSOL = GPASE_CYTOSOL+P_PKC_CYTOSOL
0.07902624850772588 ; % 1581 GPASE_P_PKC_CYTOSOL = GPASE_CYTOSOL + PKC_CYTOSOL
GPASE_P_PKC_CYTOSOL = GPASE_CYTOSOL+PKC_CYTOSOL
0.8838222948573942 ; % 1582 BMP2_BMPRII_ALK2_CYTOSOL + SMAD1_CYTOSOL =
BMP2_BMPRII_ALK2_SMAD1_CYTOSOL BMP2_BMPRII_ALK2_CYTOSOL+SMAD1_CYTOSOL = BMP2_BMPRII_ALK2_SMAD1_CYTOSOL
0.021343800595991558 ; % 1583 BMP2_BMPRII_ALK2_SMAD1_CYTOSOL = BMP2_BMPRII_ALK2_CYTOSOL +
SMAD1_CYTOSOL BMP2_BMPRII_ALK2_SMAD1_CYTOSOL = BMP2_BMPRII_ALK2_CYTOSOL+SMAD1_CYTOSOL
0.4502447524872155 ; % 1584 BMP2_BMPRII_ALK2_SMAD1_CYTOSOL = BMP2_BMPRII_ALK2_CYTOSOL +
PSMAD1_CYTOSOL BMP2_BMPRII_ALK2_SMAD1_CYTOSOL = BMP2_BMPRII_ALK2_CYTOSOL+PSMAD1_CYTOSOL
0.9735789101517578 ; % 1585 BMP2_BMPRII_ALK2_CYTOSOL + SMAD5_CYTOSOL =
BMP2_BMPRII_ALK2_SMAD5_CYTOSOL BMP2_BMPRII_ALK2_CYTOSOL+SMAD5_CYTOSOL = BMP2_BMPRII_ALK2_SMAD5_CYTOSOL
0.010753997677813088 ; % 1586 BMP2_BMPRII_ALK2_SMAD5_CYTOSOL = BMP2_BMPRII_ALK2_CYTOSOL +
SMAD5_CYTOSOL BMP2_BMPRII_ALK2_SMAD5_CYTOSOL = BMP2_BMPRII_ALK2_CYTOSOL+SMAD5_CYTOSOL
0.9479284391395204 ; % 1587 BMP2_BMPRII_ALK2_SMAD5_CYTOSOL = BMP2_BMPRII_ALK2_CYTOSOL +
PSMAD5_CYTOSOL BMP2_BMPRII_ALK2_SMAD5_CYTOSOL = BMP2_BMPRII_ALK2_CYTOSOL+PSMAD5_CYTOSOL
0.5962048608049514 ; % 1588 BMP2_BMPRII_ALK3_CYTOSOL + SMAD1_CYTOSOL =
BMP2_BMPRII_ALK3_SMAD1_CYTOSOL BMP2_BMPRII_ALK3_CYTOSOL+SMAD1_CYTOSOL = BMP2_BMPRII_ALK3_SMAD1_CYTOSOL
0.030382040919290365 ; % 1589 BMP2_BMPRII_ALK3_SMAD1_CYTOSOL = BMP2_BMPRII_ALK3_CYTOSOL +
SMAD1_CYTOSOL BMP2_BMPRII_ALK3_SMAD1_CYTOSOL = BMP2_BMPRII_ALK3_CYTOSOL+SMAD1_CYTOSOL
0.37281328302784855 ; % 1590 BMP2_BMPRII_ALK3_SMAD1_CYTOSOL = BMP2_BMPRII_ALK3_CYTOSOL +
PSMAD1_CYTOSOL BMP2_BMPRII_ALK3_SMAD1_CYTOSOL = BMP2_BMPRII_ALK3_CYTOSOL+PSMAD1_CYTOSOL
0.008755229220723026 ; % 1591 BMP2_BMPRII_ALK3_CYTOSOL + SMAD5_CYTOSOL =
BMP2_BMPRII_ALK3_SMAD5_CYTOSOL BMP2_BMPRII_ALK3_CYTOSOL+SMAD5_CYTOSOL = BMP2_BMPRII_ALK3_SMAD5_CYTOSOL
0.07956406494765314 ; % 1592 BMP2_BMPRII_ALK3_SMAD5_CYTOSOL = BMP2_BMPRII_ALK3_CYTOSOL +
SMAD5_CYTOSOL BMP2_BMPRII_ALK3_SMAD5_CYTOSOL = BMP2_BMPRII_ALK3_CYTOSOL+SMAD5_CYTOSOL
0.3303974781821156 ; % 1593 BMP2_BMPRII_ALK3_SMAD5_CYTOSOL = BMP2_BMPRII_ALK3_CYTOSOL +
PSMAD5_CYTOSOL BMP2_BMPRII_ALK3_SMAD5_CYTOSOL = BMP2_BMPRII_ALK3_CYTOSOL+PSMAD5_CYTOSOL
0.7259628744510505 ; % 1594 BMP2_BMPRII_ALK6_CYTOSOL + SMAD1_CYTOSOL =
BMP2_BMPRII_ALK6_SMAD1_CYTOSOL BMP2_BMPRII_ALK6_CYTOSOL+SMAD1_CYTOSOL = BMP2_BMPRII_ALK6_SMAD1_CYTOSOL
0.057729087355286146 ; % 1595 BMP2_BMPRII_ALK6_SMAD1_CYTOSOL = BMP2_BMPRII_ALK6_CYTOSOL +
SMAD1_CYTOSOL BMP2_BMPRII_ALK6_SMAD1_CYTOSOL = BMP2_BMPRII_ALK6_CYTOSOL+SMAD1_CYTOSOL
0.8592508847016416 ; % 1596 BMP2_BMPRII_ALK6_SMAD1_CYTOSOL = BMP2_BMPRII_ALK6_CYTOSOL +
PSMAD1_CYTOSOL BMP2_BMPRII_ALK6_SMAD1_CYTOSOL = BMP2_BMPRII_ALK6_CYTOSOL+PSMAD1_CYTOSOL
0.9809088642205303 ; % 1597 BMP2_BMPRII_ALK6_CYTOSOL + SMAD5_CYTOSOL =
BMP2_BMPRII_ALK6_SMAD5_CYTOSOL BMP2_BMPRII_ALK6_CYTOSOL+SMAD5_CYTOSOL = BMP2_BMPRII_ALK6_SMAD5_CYTOSOL
0.043534110226768286 ; % 1598 BMP2_BMPRII_ALK6_SMAD5_CYTOSOL = BMP2_BMPRII_ALK6_CYTOSOL +
SMAD5_CYTOSOL BMP2_BMPRII_ALK6_SMAD5_CYTOSOL = BMP2_BMPRII_ALK6_CYTOSOL+SMAD5_CYTOSOL
0.016072153251427523 ; % 1599 BMP2_BMPRII_ALK6_SMAD5_CYTOSOL = BMP2_BMPRII_ALK6_CYTOSOL +
PSMAD5_CYTOSOL BMP2_BMPRII_ALK6_SMAD5_CYTOSOL = BMP2_BMPRII_ALK6_CYTOSOL+PSMAD5_CYTOSOL
0.4143626270079682 ; % 1600 TGFB3_TGFBRII_ALK1_TGFBRIII_CYTOSOL + SMAD2_CYTOSOL =
TGFB3_TGFBRII_ALK1_TGFBRIII_SMAD2_CYTOSOL TGFB3_TGFBRII_ALK1_TGFBRIII_CYTOSOL+SMAD2_CYTOSOL =
TGFB3_TGFBRII_ALK1_TGFBRIII_SMAD2_CYTOSOL
0.093307014740267 ; % 1601 TGFB3_TGFBRII_ALK1_TGFBRIII_SMAD2_CYTOSOL =
TGFB3_TGFBRII_ALK1_TGFBRIII_CYTOSOL + SMAD2_CYTOSOL TGFB3_TGFBRII_ALK1_TGFBRIII_SMAD2_CYTOSOL =
TGFB3_TGFBRII_ALK1_TGFBRIII_CYTOSOL+SMAD2_CYTOSOL
0.5631330348652333 ; % 1602 TGFB3_TGFBRII_ALK1_TGFBRIII_SMAD2_CYTOSOL =
TGFB3_TGFBRII_ALK1_TGFBRIII_CYTOSOL + PSMAD2_CYTOSOL TGFB3_TGFBRII_ALK1_TGFBRIII_SMAD2_CYTOSOL =
TGFB3_TGFBRII_ALK1_TGFBRIII_CYTOSOL+PSMAD2_CYTOSOL
0.15622160190609957 ; % 1603 TGFB3_TGFBRII_ALK1_TGFBRIII_CYTOSOL + SMAD3_CYTOSOL =
TGFB3_TGFBRII_ALK1_TGFBRIII_SMAD3_CYTOSOL TGFB3_TGFBRII_ALK1_TGFBRIII_CYTOSOL+SMAD3_CYTOSOL =
TGFB3_TGFBRII_ALK1_TGFBRIII_SMAD3_CYTOSOL
0.0820397087607564 ; % 1604 TGFB3_TGFBRII_ALK1_TGFBRIII_SMAD3_CYTOSOL =
TGFB3_TGFBRII_ALK1_TGFBRIII_CYTOSOL + SMAD3_CYTOSOL TGFB3_TGFBRII_ALK1_TGFBRIII_SMAD3_CYTOSOL =
TGFB3_TGFBRII_ALK1_TGFBRIII_CYTOSOL+SMAD3_CYTOSOL
0.7684171061020444 ; % 1605 TGFB3_TGFBRII_ALK1_TGFBRIII_SMAD3_CYTOSOL =
TGFB3_TGFBRII_ALK1_TGFBRIII_CYTOSOL + PSMAD3_CYTOSOL TGFB3_TGFBRII_ALK1_TGFBRIII_SMAD3_CYTOSOL =
TGFB3_TGFBRII_ALK1_TGFBRIII_CYTOSOL+PSMAD3_CYTOSOL
0.5223156483960247 ; % 1606 TGFB3_TGFBRII_ALK5_TGFBRIII_ENDOGLIN_CYTOSOL + SMAD2_CYTOSOL =
TGFB3_TGFBRII_ALK5_TGFBRIII_ENDOGLIN_SMAD2_CYTOSOL TGFB3_TGFBRII_ALK5_TGFBRIII_ENDOGLIN_CYTOSOL+SMAD2_CYTOSOL =
TGFB3_TGFBRII_ALK5_TGFBRIII_ENDOGLIN_SMAD2_CYTOSOL
0.0030849846871043862 ; % 1607 TGFB3_TGFBRII_ALK5_TGFBRIII_ENDOGLIN_SMAD2_CYTOSOL =
TGFB3_TGFBRII_ALK5_TGFBRIII_ENDOGLIN_CYTOSOL + SMAD2_CYTOSOL TGFB3_TGFBRII_ALK5_TGFBRIII_ENDOGLIN_SMAD2_CYTOSOL =
TGFB3_TGFBRII_ALK5_TGFBRIII_ENDOGLIN_CYTOSOL+SMAD2_CYTOSOL

0.6237687761811694 ; % 1608 TGFB3_TGFBRII_ALK5_TGFBRIII_ENDOGLIN_SMAD2_CYTOSOL = TGFB3_TGFBRII_ALK5_TGFBRIII_ENDOGLIN_CYTOSOL + PSMAD2_CYTOSOL TGFB3_TGFBRII_ALK5_TGFBRIII_ENDOGLIN_SMAD2_CYTOSOL = TGFB3_TGFBRII_ALK5_TGFBRIII_ENDOGLIN_CYTOSOL+PSMAD2_CYTOSOL
0.7162315359808622 ; % 1609 TGFB3_TGFBRII_ALK5_TGFBRIII_ENDOGLIN_CYTOSOL + SMAD3_CYTOSOL = TGFB3_TGFBRII_ALK5_TGFBRIII_ENDOGLIN_SMAD3_CYTOSOL TGFB3_TGFBRII_ALK5_TGFBRIII_ENDOGLIN_CYTOSOL+SMAD3_CYTOSOL = TGFB3_TGFBRII_ALK5_TGFBRIII_ENDOGLIN_SMAD3_CYTOSOL
0.057620260416550675 ; % 1610 TGFB3_TGFBRII_ALK5_TGFBRIII_ENDOGLIN_SMAD3_CYTOSOL = TGFB3_TGFBRII_ALK5_TGFBRIII_ENDOGLIN_CYTOSOL + SMAD3_CYTOSOL TGFB3_TGFBRII_ALK5_TGFBRIII_ENDOGLIN_SMAD3_CYTOSOL = TGFB3_TGFBRII_ALK5_TGFBRIII_ENDOGLIN_CYTOSOL+SMAD3_CYTOSOL
0.6000018384898842 ; % 1611 TGFB3_TGFBRII_ALK5_TGFBRIII_ENDOGLIN_SMAD3_CYTOSOL = TGFB3_TGFBRII_ALK5_TGFBRIII_ENDOGLIN_CYTOSOL + PSMAD3_CYTOSOL TGFB3_TGFBRII_ALK5_TGFBRIII_ENDOGLIN_SMAD3_CYTOSOL = TGFB3_TGFBRII_ALK5_TGFBRIII_ENDOGLIN_CYTOSOL+PSMAD3_CYTOSOL
0.00014769313416331928 ; % 1612 TGFB2_TGFBRII_ALK1_TGFBRIII_CYTOSOL + SMAD2_CYTOSOL = TGFB2_TGFBRII_ALK1_TGFBRIII_SMAD2_CYTOSOL TGFB2_TGFBRII_ALK1_TGFBRIII_CYTOSOL+SMAD2_CYTOSOL = TGFB2_TGFBRII_ALK1_TGFBRIII_SMAD2_CYTOSOL
0.34819331219832904 ; % 1613 TGFB2_TGFBRII_ALK1_TGFBRIII_SMAD2_CYTOSOL = TGFB2_TGFBRII_ALK1_TGFBRIII_CYTOSOL + SMAD2_CYTOSOL TGFB2_TGFBRII_ALK1_TGFBRIII_SMAD2_CYTOSOL = TGFB2_TGFBRII_ALK1_TGFBRIII_CYTOSOL+SMAD2_CYTOSOL
0.0024136236913857134 ; % 1614 TGFB2_TGFBRII_ALK1_TGFBRIII_SMAD2_CYTOSOL = TGFB2_TGFBRII_ALK1_TGFBRIII_CYTOSOL + PSMAD2_CYTOSOL TGFB2_TGFBRII_ALK1_TGFBRIII_SMAD2_CYTOSOL = TGFB2_TGFBRII_ALK1_TGFBRIII_CYTOSOL+PSMAD2_CYTOSOL
0.0001665471828437052 ; % 1615 TGFB2_TGFBRII_ALK1_TGFBRIII_CYTOSOL + SMAD3_CYTOSOL = TGFB2_TGFBRII_ALK1_TGFBRIII_SMAD3_CYTOSOL TGFB2_TGFBRII_ALK1_TGFBRIII_CYTOSOL+SMAD3_CYTOSOL = TGFB2_TGFBRII_ALK1_TGFBRIII_SMAD3_CYTOSOL
0.5605410211528871 ; % 1616 TGFB2_TGFBRII_ALK1_TGFBRIII_SMAD3_CYTOSOL = TGFB2_TGFBRII_ALK1_TGFBRIII_CYTOSOL + SMAD3_CYTOSOL TGFB2_TGFBRII_ALK1_TGFBRIII_SMAD3_CYTOSOL = TGFB2_TGFBRII_ALK1_TGFBRIII_CYTOSOL+SMAD3_CYTOSOL
0.0008133368610320912 ; % 1617 TGFB2_TGFBRII_ALK1_TGFBRIII_SMAD3_CYTOSOL = TGFB2_TGFBRII_ALK1_TGFBRIII_CYTOSOL + PSMAD3_CYTOSOL TGFB2_TGFBRII_ALK1_TGFBRIII_SMAD3_CYTOSOL = TGFB2_TGFBRII_ALK1_TGFBRIII_CYTOSOL+PSMAD3_CYTOSOL
0.000109269506310881 ; % 1618 TGFB2_TGFBRII_ALK5_TGFBRIII_ENDOGLIN_CYTOSOL + SMAD2_CYTOSOL = TGFB2_TGFBRII_ALK5_TGFBRIII_ENDOGLIN_SMAD2_CYTOSOL TGFB2_TGFBRII_ALK5_TGFBRIII_ENDOGLIN_CYTOSOL+SMAD2_CYTOSOL = TGFB2_TGFBRII_ALK5_TGFBRIII_ENDOGLIN_SMAD2_CYTOSOL
0.5034711841849052 ; % 1619 TGFB2_TGFBRII_ALK5_TGFBRIII_ENDOGLIN_SMAD2_CYTOSOL = TGFB2_TGFBRII_ALK5_TGFBRIII_ENDOGLIN_CYTOSOL + SMAD2_CYTOSOL TGFB2_TGFBRII_ALK5_TGFBRIII_ENDOGLIN_SMAD2_CYTOSOL = TGFB2_TGFBRII_ALK5_TGFBRIII_ENDOGLIN_CYTOSOL+SMAD2_CYTOSOL
0.0006821629481382607 ; % 1620 TGFB2_TGFBRII_ALK5_TGFBRIII_ENDOGLIN_SMAD2_CYTOSOL = TGFB2_TGFBRII_ALK5_TGFBRIII_ENDOGLIN_CYTOSOL + PSMAD2_CYTOSOL TGFB2_TGFBRII_ALK5_TGFBRIII_ENDOGLIN_SMAD2_CYTOSOL = TGFB2_TGFBRII_ALK5_TGFBRIII_ENDOGLIN_CYTOSOL+PSMAD2_CYTOSOL
0.0001500184259086736 4; % 1621 TGFB2_TGFBRII_ALK5_TGFBRIII_ENDOGLIN_CYTOSOL + SMAD3_CYTOSOL = TGFB2_TGFBRII_ALK5_TGFBRIII_ENDOGLIN_SMAD3_CYTOSOL TGFB2_TGFBRII_ALK5_TGFBRIII_ENDOGLIN_CYTOSOL+SMAD3_CYTOSOL = TGFB2_TGFBRII_ALK5_TGFBRIII_ENDOGLIN_SMAD3_CYTOSOL
0.4830148585814499 ; % 1622 TGFB2_TGFBRII_ALK5_TGFBRIII_ENDOGLIN_SMAD3_CYTOSOL = TGFB2_TGFBRII_ALK5_TGFBRIII_ENDOGLIN_CYTOSOL + SMAD3_CYTOSOL TGFB2_TGFBRII_ALK5_TGFBRIII_ENDOGLIN_SMAD3_CYTOSOL = TGFB2_TGFBRII_ALK5_TGFBRIII_ENDOGLIN_CYTOSOL+SMAD3_CYTOSOL
0.0001464564557507135 3; % 1623 TGFB2_TGFBRII_ALK5_TGFBRIII_ENDOGLIN_SMAD3_CYTOSOL = TGFB2_TGFBRII_ALK5_TGFBRIII_ENDOGLIN_CYTOSOL + PSMAD3_CYTOSOL TGFB2_TGFBRII_ALK5_TGFBRIII_ENDOGLIN_SMAD3_CYTOSOL = TGFB2_TGFBRII_ALK5_TGFBRIII_ENDOGLIN_CYTOSOL+PSMAD3_CYTOSOL
0.00024013058037425594; % 1624 SMURF1_CYTOSOL + PSMAD1_CYTOSOL = SMURF1_PSMAD1_CYTOSOL SMURF1_CYTOSOL+PSMAD1_CYTOSOL = SMURF1_PSMAD1_CYTOSOL
0.3185867127703606 ; % 1625 SMURF1_PSMAD1_CYTOSOL = SMURF1_CYTOSOL + PSMAD1_CYTOSOL SMURF1_PSMAD1_CYTOSOL = SMURF1_CYTOSOL+PSMAD1_CYTOSOL
0.36561905035377806 ; % 1626 SMURF1_PSMAD1_CYTOSOL = SMURF1_CYTOSOL + UB_PSMAD1_CYTOSOL SMURF1_PSMAD1_CYTOSOL = SMURF1_CYTOSOL+UB_PSMAD1_CYTOSOL
0.00006643632440229951; % 1627 SMURF1_CYTOSOL + PSMAD5_CYTOSOL = SMURF1_PSMAD5_CYTOSOL SMURF1_CYTOSOL+PSMAD5_CYTOSOL = SMURF1_PSMAD5_CYTOSOL
0.0764681971678722 ; % 1628 SMURF1_PSMAD5_CYTOSOL = SMURF1_CYTOSOL + PSMAD5_CYTOSOL SMURF1_PSMAD5_CYTOSOL = SMURF1_CYTOSOL+PSMAD5_CYTOSOL
0.26744885520467143 ; % 1629 SMURF1_PSMAD5_CYTOSOL = SMURF1_CYTOSOL + UB_PSMAD5_CYTOSOL SMURF1_PSMAD5_CYTOSOL = SMURF1_CYTOSOL+UB_PSMAD5_CYTOSOL
0.0003534560126102534 ; % 1630 SMURF2_CYTOSOL + PSMAD2_CYTOSOL = SMURF2_PSMAD2_CYTOSOL SMURF2_CYTOSOL+PSMAD2_CYTOSOL = SMURF2_PSMAD2_CYTOSOL
0.8163385329250107 ; % 1631 SMURF2_PSMAD2_CYTOSOL = SMURF2_CYTOSOL + PSMAD2_CYTOSOL SMURF2_PSMAD2_CYTOSOL = SMURF2_CYTOSOL+PSMAD2_CYTOSOL
0.10674279141439047 ; % 1632 SMURF2_PSMAD2_CYTOSOL = SMURF2_CYTOSOL + UB_PSMAD2_CYTOSOL SMURF2_PSMAD2_CYTOSOL = SMURF2_CYTOSOL+UB_PSMAD2_CYTOSOL
0.0009168025543367888 3; % 1633 SMURF2_CYTOSOL + PSMAD3_CYTOSOL = SMURF2_PSMAD3_CYTOSOL SMURF2_CYTOSOL+PSMAD3_CYTOSOL = SMURF2_PSMAD3_CYTOSOL
0.1410125571251133 ; % 1634 SMURF2_PSMAD3_CYTOSOL = SMURF2_CYTOSOL + PSMAD3_CYTOSOL SMURF2_PSMAD3_CYTOSOL = SMURF2_CYTOSOL+PSMAD3_CYTOSOL
0.2978641294341158 ; % 1635 SMURF2_PSMAD3_CYTOSOL = SMURF2_CYTOSOL + UB_PSMAD3_CYTOSOL SMURF2_PSMAD3_CYTOSOL = SMURF2_CYTOSOL+UB_PSMAD3_CYTOSOL
0.23324915502438331 ; % 1636 UB_PSMAD1_CYTOSOL = [] UB_PSMAD1_CYTOSOL = []
0.20941986532299117 ; % 1637 UB_PSMAD2_CYTOSOL = [] UB_PSMAD2_CYTOSOL = []
0.02458733626780385 ; % 1638 UB_PSMAD3_CYTOSOL = [] UB_PSMAD3_CYTOSOL = []
0.20410953277974203 ; % 1639 UB_PSMAD5_CYTOSOL = [] UB_PSMAD5_CYTOSOL = []
0.031232146866218136 ; % 1640 BMP2_BMPRII_ALK2_CYTOSOL = [] BMP2_BMPRII_ALK2_CYTOSOL = []
0.019658629667977445 ; % 1641 BMP2_BMPRII_ALK3_CYTOSOL = [] BMP2_BMPRII_ALK3_CYTOSOL = []
0.09065239288582017 ; % 1642 BMP2_BMPRII_ALK6_CYTOSOL = [] BMP2_BMPRII_ALK6_CYTOSOL = []
0.04346272457000899 ; % 1643 TGFB3_TGFBRII_ALK1_TGFBRIII_CYTOSOL = [] TGFB3_TGFBRII_ALK1_TGFBRIII_CYTOSOL = []
0.04438546667420112 ; % 1644 TGFB3_TGFBRII_ALK5_TGFBRIII_ENDOGLIN_CYTOSOL = [] TGFB3_TGFBRII_ALK5_TGFBRIII_ENDOGLIN_CYTOSOL = []
0.033319241586448517 ; % 1645 TGFB2_TGFBRII_ALK5_TGFBRIII_ENDOGLIN_CYTOSOL = [] TGFB2_TGFBRII_ALK5_TGFBRIII_ENDOGLIN_CYTOSOL = []
0.013236671846121273 ; % 1646 TGFB2_TGFBRII_ALK1_TGFBRIII_CYTOSOL = [] TGFB2_TGFBRII_ALK1_TGFBRIII_CYTOSOL = []
10.5999120317824057 ; % 1647 BCATENIN_CYTOSOL + ECADHERIN_CYTOSOL = BCATENIN_ECADHERIN_CYTOSOL BCATENIN_CYTOSOL+ECADHERIN_CYTOSOL = BCATENIN_ECADHERIN_CYTOSOL
0.00001115639115582083; % 1648 BCATENIN_ECADHERIN_CYTOSOL = BCATENIN_CYTOSOL + ECADHERIN_CYTOSOL BCATENIN_ECADHERIN_CYTOSOL = BCATENIN_CYTOSOL+ECADHERIN_CYTOSOL
10.32501078431318176 ; % 1649 BCATENIN_CYTOSOL + VECADHERIN_CYTOSOL = BCATENIN_VECADHERIN_CYTOSOL BCATENIN_CYTOSOL+VECADHERIN_CYTOSOL = BCATENIN_VECADHERIN_CYTOSOL

0.00005776712141603666; % 1650 BCATENIN_VECADHERIN_CYTOSOL = BCATENIN_CYTOSOL + VECADHERIN_CYTOSOL BCATENIN_VECADHERIN_CYTOSOL = BCATENIN_CYTOSOL+VECADHERIN_CYTOSOL
2.46286302385161693 ; % 1651 BCATENIN_CYTOSOL + PECAM1_CYTOSOL = BCATENIN_PECAM1_CYTOSOL BCATENIN_CYTOSOL+PECAM1_CYTOSOL = BCATENIN_PECAM1_CYTOSOL
0.0008516099323708987 ; % 1652 BCATENIN_PECAM1_CYTOSOL = BCATENIN_CYTOSOL + PECAM1_CYTOSOL BCATENIN_PECAM1_CYTOSOL = BCATENIN_CYTOSOL+PECAM1_CYTOSOL
0.3443997944883932 ; % 1653 IKB_CYTOSOL + NFKB_CYTOSOL = IKB_NFKB_CYTOSOL IKB_CYTOSOL+NFKB_CYTOSOL = IKB_NFKB_CYTOSOL
0.8101801890022028 ; % 1654 P_IKB_NFKB_CYTOSOL = P_IKB_CYTOSOL + NFKB_CYTOSOL P_IKB_NFKB_CYTOSOL = P_IKB_CYTOSOL+NFKB_CYTOSOL
0.0367396231330024 ; % 1655 P_IKB_CYTOSOL + NFKB_CYTOSOL = P_IKB_NFKB_CYTOSOL P_IKB_CYTOSOL+NFKB_CYTOSOL = P_IKB_NFKB_CYTOSOL
0.06499744136140728 ; % 1656 ACTIVE_AKT_CYTOSOL + IKB_NFKB_CYTOSOL = ACTIVE_AKT_IKB_NFKB_CYTOSOL ACTIVE_AKT_CYTOSOL+IKB_NFKB_CYTOSOL = ACTIVE_AKT_IKB_NFKB_CYTOSOL
0.0915493242999715 ; % 1657 ACTIVE_AKT_IKB_NFKB_CYTOSOL = ACTIVE_AKT_CYTOSOL + IKB_NFKB_CYTOSOL ACTIVE_AKT_IKB_NFKB_CYTOSOL = ACTIVE_AKT_CYTOSOL+IKB_NFKB_CYTOSOL
0.8627263202971025 ; % 1658 ACTIVE_AKT_IKB_NFKB_CYTOSOL = ACTIVE_AKT_CYTOSOL + P_IKB_NFKB_CYTOSOL ACTIVE_AKT_IKB_NFKB_CYTOSOL = ACTIVE_AKT_CYTOSOL+P_IKB_NFKB_CYTOSOL
0.7607723103326829 ; % 1659 VEGFA_VEGFR2_SHC_CYTOSOL + PI3K_CYTOSOL = VEGFA_VEGFR2_SHC_PI3K_CYTOSOL VEGFA_VEGFR2_SHC_CYTOSOL+PI3K_CYTOSOL = VEGFA_VEGFR2_SHC_PI3K_CYTOSOL
0.09731465879918465 ; % 1660 VEGFA_VEGFR2_SHC_PI3K_CYTOSOL = VEGFA_VEGFR2_SHC_CYTOSOL + PI3K_CYTOSOL VEGFA_VEGFR2_SHC_PI3K_CYTOSOL = VEGFA_VEGFR2_SHC_CYTOSOL+PI3K_CYTOSOL
0.5073625455213779 ; % 1661 VEGFA_VEGFR2_SHC_PI3K_CYTOSOL = VEGFA_VEGFR2_SHC_CYTOSOL + ACTIVE_PI3K_CYTOSOL VEGFA_VEGFR2_SHC_PI3K_CYTOSOL = VEGFA_VEGFR2_SHC_CYTOSOL+ACTIVE_PI3K_CYTOSOL
0.44696745895454926 ; % 1662 BMP2_BMPRII_ALK2_SHC_GRB2_SOS_CYTOSOL + PI3K_CYTOSOL = BMP2_BMPRII_ALK2_SHC_GRB2_SOS_PI3K_CYTOSOL BMP2_BMPRII_ALK2_SHC_GRB2_SOS_CYTOSOL+PI3K_CYTOSOL = BMP2_BMPRII_ALK2_SHC_GRB2_SOS_PI3K_CYTOSOL
0.0383486817899375 ; % 1663 BMP2_BMPRII_ALK2_SHC_GRB2_SOS_PI3K_CYTOSOL = BMP2_BMPRII_ALK2_SHC_GRB2_SOS_CYTOSOL + PI3K_CYTOSOL BMP2_BMPRII_ALK2_SHC_GRB2_SOS_PI3K_CYTOSOL = BMP2_BMPRII_ALK2_SHC_GRB2_SOS_CYTOSOL+PI3K_CYTOSOL
0.6821496097859371 ; % 1664 BMP2_BMPRII_ALK2_SHC_GRB2_SOS_PI3K_CYTOSOL = BMP2_BMPRII_ALK2_SHC_GRB2_SOS_CYTOSOL + ACTIVE_PI3K_CYTOSOL BMP2_BMPRII_ALK2_SHC_GRB2_SOS_PI3K_CYTOSOL = BMP2_BMPRII_ALK2_SHC_GRB2_SOS_CYTOSOL+ACTIVE_PI3K_CYTOSOL
0.67542573304516 ; % 1665 AKT_PASE_CYTOSOL + P_PLCG_CYTOSOL = AKT_PASE_P_PLCG_CYTOSOL AKT_PASE_CYTOSOL+P_PLCG_CYTOSOL = AKT_PASE_P_PLCG_CYTOSOL
0.09208143434570443 ; % 1666 AKT_PASE_P_PLCG_CYTOSOL = AKT_PASE_CYTOSOL + P_PLCG_CYTOSOL AKT_PASE_P_PLCG_CYTOSOL = AKT_PASE_CYTOSOL+P_PLCG_CYTOSOL
0.14429222447230905 ; % 1667 AKT_PASE_P_PLCG_CYTOSOL = AKT_PASE_CYTOSOL + PLCG_CYTOSOL AKT_PASE_P_PLCG_CYTOSOL = AKT_PASE_CYTOSOL+PLCG_CYTOSOL
0.15412321373299387 ; % 1668 AKT_PASE_CYTOSOL + P_PKC_CYTOSOL = AKT_PASE_P_PKC_CYTOSOL AKT_PASE_CYTOSOL+P_PKC_CYTOSOL = AKT_PASE_P_PKC_CYTOSOL
0.06535815972436103 ; % 1669 AKT_PASE_P_PKC_CYTOSOL = AKT_PASE_CYTOSOL + P_PKC_CYTOSOL AKT_PASE_P_PKC_CYTOSOL = AKT_PASE_CYTOSOL+P_PKC_CYTOSOL
0.46343474587636324 ; % 1670 AKT_PASE_P_PKC_CYTOSOL = AKT_PASE_CYTOSOL + PKC_CYTOSOL AKT_PASE_P_PKC_CYTOSOL = AKT_PASE_CYTOSOL+PKC_CYTOSOL
0.9436425854258056 ; % 1671 AKT_PASE_CYTOSOL + P_SPK_CYTOSOL = AKT_PASE_P_SPK_CYTOSOL AKT_PASE_CYTOSOL+P_SPK_CYTOSOL = AKT_PASE_P_SPK_CYTOSOL
0.01243423887917633 ; % 1672 AKT_PASE_P_SPK_CYTOSOL = AKT_PASE_CYTOSOL + P_SPK_CYTOSOL AKT_PASE_P_SPK_CYTOSOL = AKT_PASE_CYTOSOL+P_SPK_CYTOSOL
0.4530701756748112 ; % 1673 AKT_PASE_P_SPK_CYTOSOL = AKT_PASE_CYTOSOL + SPK_CYTOSOL AKT_PASE_P_SPK_CYTOSOL = AKT_PASE_CYTOSOL+SPK_CYTOSOL
0.47575363492154865 ; % 1674 AKT_PASE_CYTOSOL + P_SP1_CYTOSOL = AKT_PASE_P_SP1_CYTOSOL AKT_PASE_CYTOSOL+P_SP1_CYTOSOL = AKT_PASE_P_SP1_CYTOSOL
0.044424808815843125 ; % 1675 AKT_PASE_P_SP1_CYTOSOL = AKT_PASE_CYTOSOL + P_SP1_CYTOSOL AKT_PASE_P_SP1_CYTOSOL = AKT_PASE_CYTOSOL+P_SP1_CYTOSOL
0.5669934105197201 ; % 1676 AKT_PASE_P_SP1_CYTOSOL = AKT_PASE_CYTOSOL + SP1_CYTOSOL AKT_PASE_P_SP1_CYTOSOL = AKT_PASE_CYTOSOL+SP1_CYTOSOL
0.5316885546631417 ; % 1677 VEGFA_VEGFR2_CYTOSOL + PLCG_CYTOSOL = VEGFA_VEGFR2_PLCG_CYTOSOL VEGFA_VEGFR2_CYTOSOL+PLCG_CYTOSOL = VEGFA_VEGFR2_PLCG_CYTOSOL
0.09781352390210057 ; % 1678 VEGFA_VEGFR2_PLCG_CYTOSOL = VEGFA_VEGFR2_CYTOSOL + PLCG_CYTOSOL VEGFA_VEGFR2_PLCG_CYTOSOL = VEGFA_VEGFR2_CYTOSOL+PLCG_CYTOSOL
0.3313730288094986 ; % 1679 VEGFA_VEGFR2_PLCG_CYTOSOL = VEGFA_VEGFR2_CYTOSOL + P_PLCG_CYTOSOL VEGFA_VEGFR2_PLCG_CYTOSOL = VEGFA_VEGFR2_CYTOSOL+P_PLCG_CYTOSOL
0.32664200555025447 ; % 1680 P_PLCG_CYTOSOL + PIP2_CYTOSOL = P_PLCG_PIP2_CYTOSOL P_PLCG_CYTOSOL+PIP2_CYTOSOL = P_PLCG_PIP2_CYTOSOL
0.009406156600468209 ; % 1681 P_PLCG_PIP2_CYTOSOL = P_PLCG_CYTOSOL + PIP2_CYTOSOL P_PLCG_PIP2_CYTOSOL = P_PLCG_CYTOSOL+PIP2_CYTOSOL
0.7693157566440377 ; % 1682 P_PLCG_PIP2_CYTOSOL = P_PLCG_CYTOSOL + ACTIVE_PIP2_CYTOSOL P_PLCG_PIP2_CYTOSOL = P_PLCG_CYTOSOL+ACTIVE_PIP2_CYTOSOL
0.3057053821442832 ; % 1683 ACTIVE_PI3K_CYTOSOL + PKC_CYTOSOL = ACTIVE_PI3K_PKC_CYTOSOL ACTIVE_PI3K_CYTOSOL+PKC_CYTOSOL = ACTIVE_PI3K_PKC_CYTOSOL
0.005302057140590732 ; % 1684 ACTIVE_PI3K_PKC_CYTOSOL = ACTIVE_PI3K_CYTOSOL + PKC_CYTOSOL ACTIVE_PI3K_PKC_CYTOSOL = ACTIVE_PI3K_CYTOSOL+PKC_CYTOSOL
0.7369871426437897 ; % 1685 ACTIVE_PI3K_PKC_CYTOSOL = ACTIVE_PI3K_CYTOSOL + ACTIVE_PKC_CYTOSOL ACTIVE_PI3K_PKC_CYTOSOL = ACTIVE_PI3K_CYTOSOL+ACTIVE_PKC_CYTOSOL
0.20928778556866567 ; % 1686 ACTIVE_PIP2_CYTOSOL + PKC_CYTOSOL = ACTIVE_PIP2_PKC_CYTOSOL ACTIVE_PIP2_CYTOSOL+PKC_CYTOSOL = ACTIVE_PIP2_PKC_CYTOSOL
0.09080715278619261 ; % 1687 ACTIVE_PIP2_PKC_CYTOSOL = ACTIVE_PIP2_CYTOSOL + PKC_CYTOSOL ACTIVE_PIP2_PKC_CYTOSOL = ACTIVE_PIP2_CYTOSOL+PKC_CYTOSOL
0.0034958618599655322 ; % 1688 ACTIVE_PIP2_PKC_CYTOSOL = ACTIVE_PIP2_CYTOSOL + P_PKC_CYTOSOL ACTIVE_PIP2_PKC_CYTOSOL = ACTIVE_PIP2_CYTOSOL+P_PKC_CYTOSOL
0.4634464145908038 ; % 1689 P_PKC_CYTOSOL + SPK_CYTOSOL = P_PKC_SPK_CYTOSOL P_PKC_CYTOSOL+SPK_CYTOSOL = P_PKC_SPK_CYTOSOL
0.049372093692808865 ; % 1690 P_PKC_SPK_CYTOSOL = P_PKC_CYTOSOL + SPK_CYTOSOL P_PKC_SPK_CYTOSOL = P_PKC_CYTOSOL+SPK_CYTOSOL
0.28796540967967277 ; % 1691 P_PKC_SPK_CYTOSOL = P_PKC_CYTOSOL + P_SPK_CYTOSOL P_PKC_SPK_CYTOSOL = P_PKC_CYTOSOL+P_SPK_CYTOSOL
0.11058669282261258 ; % 1692 P_PKC_CYTOSOL + SP1_CYTOSOL = P_PKC_SP1_CYTOSOL P_PKC_CYTOSOL+SP1_CYTOSOL = P_PKC_SP1_CYTOSOL
0.005468900999515258 ; % 1693 P_PKC_SP1_CYTOSOL = P_PKC_CYTOSOL + SP1_CYTOSOL P_PKC_SP1_CYTOSOL = P_PKC_CYTOSOL+SP1_CYTOSOL
0.1986357903794277 ; % 1694 P_PKC_SP1_CYTOSOL = P_PKC_CYTOSOL + P_SP1_CYTOSOL P_PKC_SP1_CYTOSOL = P_PKC_CYTOSOL+P_SP1_CYTOSOL

```
	0.19680616343811408	;	%	1695	P_SPK_CYTOSOL + RAF_CYTOSOL = P_SPK_RAF_CYTOSOL
	P_SPK_CYTOSOL+RAF_CYTOSOL = P_SPK_RAF_CYTOSOL
	0.0951158761735051	;	%	1696	P_SPK_RAF_CYTOSOL = P_SPK_CYTOSOL + RAF_CYTOSOL   P_SPK_RAF_CYTOSOL =
P_SPK_CYTOSOL+RAF_CYTOSOL
	0.4118740602208194	;	%	1697	P_SPK_RAF_CYTOSOL = P_SPK_CYTOSOL + ACTIVE_RAF_CYTOSOL
	P_SPK_RAF_CYTOSOL = P_SPK_CYTOSOL+ACTIVE_RAF_CYTOSOL
	0.3457153158293569	;	%	1698	ACTIVE_PIP2_CYTOSOL = []	ACTIVE_PIP2_CYTOSOL = []
	0.4060170046032885	;	%	1699	VEGFA_VEGFR2_SHC_CYTOSOL = []	VEGFA_VEGFR2_SHC_CYTOSOL = []
	0.4497157568382065	;	%	1700	BMP2_BMPRII_ALK2_SHC_GRB2_SOS_CYTOSOL = []
	BMP2_BMPRII_ALK2_SHC_GRB2_SOS_CYTOSOL = []
];

% Initial conditions --
IC=[
	0.0	;%	1	TGFB3_CYTOSOL	TGFB3_CYTOSOL
	0.0	;%	2	EXEXPORT_TGFB3_CYTOSOL	EXEXPORT_TGFB3_CYTOSOL
	0.0	;%	3	TGFB2_CYTOSOL	TGFB2_CYTOSOL
	0.0	;%	4	EXEXPORT_TGFB2_CYTOSOL	EXEXPORT_TGFB2_CYTOSOL
	0.0	;%	5	DNA_SMURF1_RNAP_NUCLEAR	DNA_SMURF1_RNAP_NUCLEAR
	0.0	;%	6	MRNA_SMURF1_NUCLEAR	MRNA_SMURF1_NUCLEAR
	0.0	;%	7	MRNA_SMURF1_NEXPORT_NUCLEAR	MRNA_SMURF1_NEXPORT_NUCLEAR
	0.0	;%	8	MRNA_SMURF1_CYTOSOL	MRNA_SMURF1_CYTOSOL
	0.0	;%	9	MRNA_SMURF1_RIBOSOME_CYTOSOL	MRNA_SMURF1_RIBOSOME_CYTOSOL
	0.0	;%	10	MRNA_SMURF1_START_RIBOSOME_CYTOSOL	MRNA_SMURF1_START_RIBOSOME_CYTOSOL
	0.0	;%	11	SMURF1_CYTOSOL	SMURF1_CYTOSOL
	0.0	;%	12	DNA_SMURF2_RNAP_NUCLEAR	DNA_SMURF2_RNAP_NUCLEAR
	0.0	;%	13	MRNA_SMURF2_NUCLEAR	MRNA_SMURF2_NUCLEAR
	0.0	;%	14	MRNA_SMURF2_NEXPORT_NUCLEAR	MRNA_SMURF2_NEXPORT_NUCLEAR
	0.0	;%	15	MRNA_SMURF2_CYTOSOL	MRNA_SMURF2_CYTOSOL
	0.0	;%	16	MRNA_SMURF2_RIBOSOME_CYTOSOL	MRNA_SMURF2_RIBOSOME_CYTOSOL
	0.0	;%	17	MRNA_SMURF2_START_RIBOSOME_CYTOSOL	MRNA_SMURF2_START_RIBOSOME_CYTOSOL
	0.0	;%	18	SMURF2_CYTOSOL	SMURF2_CYTOSOL
	0.0	;%	19	DNA_SMAD1_RNAP_NUCLEAR	DNA_SMAD1_RNAP_NUCLEAR
	0.0	;%	20	MRNA_SMAD1_NUCLEAR	MRNA_SMAD1_NUCLEAR
	0.0	;%	21	MRNA_SMAD1_NEXPORT_NUCLEAR	MRNA_SMAD1_NEXPORT_NUCLEAR
	0.0	;%	22	MRNA_SMAD1_CYTOSOL	MRNA_SMAD1_CYTOSOL
	0.0	;%	23	MRNA_SMAD1_RIBOSOME_CYTOSOL	MRNA_SMAD1_RIBOSOME_CYTOSOL
	0.0	;%	24	MRNA_SMAD1_START_RIBOSOME_CYTOSOL	MRNA_SMAD1_START_RIBOSOME_CYTOSOL
	0.0	;%	25	SMAD1_CYTOSOL	SMAD1_CYTOSOL
	0.0	;%	26	DNA_SMAD2_RNAP_NUCLEAR	DNA_SMAD2_RNAP_NUCLEAR
	0.0	;%	27	MRNA_SMAD2_NUCLEAR	MRNA_SMAD2_NUCLEAR
	0.0	;%	28	MRNA_SMAD2_NEXPORT_NUCLEAR	MRNA_SMAD2_NEXPORT_NUCLEAR
	0.0	;%	29	MRNA_SMAD2_CYTOSOL	MRNA_SMAD2_CYTOSOL
	0.0	;%	30	MRNA_SMAD2_RIBOSOME_CYTOSOL	MRNA_SMAD2_RIBOSOME_CYTOSOL
	0.0	;%	31	MRNA_SMAD2_START_RIBOSOME_CYTOSOL	MRNA_SMAD2_START_RIBOSOME_CYTOSOL
	0.0	;%	32	SMAD2_CYTOSOL	SMAD2_CYTOSOL
	0.0	;%	33	DNA_SMAD3_RNAP_NUCLEAR	DNA_SMAD3_RNAP_NUCLEAR
	0.0	;%	34	MRNA_SMAD3_NUCLEAR	MRNA_SMAD3_NUCLEAR
	0.0	;%	35	MRNA_SMAD3_NEXPORT_NUCLEAR	MRNA_SMAD3_NEXPORT_NUCLEAR
	0.0	;%	36	MRNA_SMAD3_CYTOSOL	MRNA_SMAD3_CYTOSOL
	0.0	;%	37	MRNA_SMAD3_RIBOSOME_CYTOSOL	MRNA_SMAD3_RIBOSOME_CYTOSOL
	0.0	;%	38	MRNA_SMAD3_START_RIBOSOME_CYTOSOL	MRNA_SMAD3_START_RIBOSOME_CYTOSOL
	0.0	;%	39	SMAD3_CYTOSOL	SMAD3_CYTOSOL
	0.0	;%	40	DNA_SMAD4_RNAP_NUCLEAR	DNA_SMAD4_RNAP_NUCLEAR
	0.0	;%	41	MRNA_SMAD4_NUCLEAR	MRNA_SMAD4_NUCLEAR
	0.0	;%	42	MRNA_SMAD4_NEXPORT_NUCLEAR	MRNA_SMAD4_NEXPORT_NUCLEAR
	0.0	;%	43	MRNA_SMAD4_CYTOSOL	MRNA_SMAD4_CYTOSOL
	0.0	;%	44	MRNA_SMAD4_RIBOSOME_CYTOSOL	MRNA_SMAD4_RIBOSOME_CYTOSOL
	0.0	;%	45	MRNA_SMAD4_START_RIBOSOME_CYTOSOL	MRNA_SMAD4_START_RIBOSOME_CYTOSOL
	0.0	;%	46	SMAD4_CYTOSOL	SMAD4_CYTOSOL
	0.0	;%	47	DNA_SMAD5_RNAP_NUCLEAR	DNA_SMAD5_RNAP_NUCLEAR
	0.0	;%	48	MRNA_SMAD5_NUCLEAR	MRNA_SMAD5_NUCLEAR
	0.0	;%	49	MRNA_SMAD5_NEXPORT_NUCLEAR	MRNA_SMAD5_NEXPORT_NUCLEAR
	0.0	;%	50	MRNA_SMAD5_CYTOSOL	MRNA_SMAD5_CYTOSOL
	0.0	;%	51	MRNA_SMAD5_RIBOSOME_CYTOSOL	MRNA_SMAD5_RIBOSOME_CYTOSOL
	0.0	;%	52	MRNA_SMAD5_START_RIBOSOME_CYTOSOL	MRNA_SMAD5_START_RIBOSOME_CYTOSOL
	0.0	;%	53	SMAD5_CYTOSOL	SMAD5_CYTOSOL
	0.0	;%	54	DNA_SMAD6_RNAP_NUCLEAR	DNA_SMAD6_RNAP_NUCLEAR
	0.0	;%	55	MRNA_SMAD6_NUCLEAR	MRNA_SMAD6_NUCLEAR
	0.0	;%	56	MRNA_SMAD6_NEXPORT_NUCLEAR	MRNA_SMAD6_NEXPORT_NUCLEAR
	0.0	;%	57	MRNA_SMAD6_CYTOSOL	MRNA_SMAD6_CYTOSOL
	0.0	;%	58	MRNA_SMAD6_RIBOSOME_CYTOSOL	MRNA_SMAD6_RIBOSOME_CYTOSOL
	0.0	;%	59	MRNA_SMAD6_START_RIBOSOME_CYTOSOL	MRNA_SMAD6_START_RIBOSOME_CYTOSOL
	0.0	;%	60	SMAD6_CYTOSOL	SMAD6_CYTOSOL
	0.0	;%	61	DNA_SMAD7_RNAP_NUCLEAR	DNA_SMAD7_RNAP_NUCLEAR
	0.0	;%	62	MRNA_SMAD7_NUCLEAR	MRNA_SMAD7_NUCLEAR
	0.0	;%	63	MRNA_SMAD7_NEXPORT_NUCLEAR	MRNA_SMAD7_NEXPORT_NUCLEAR
	0.0	;%	64	MRNA_SMAD7_CYTOSOL	MRNA_SMAD7_CYTOSOL
	0.0	;%	65	MRNA_SMAD7_RIBOSOME_CYTOSOL	MRNA_SMAD7_RIBOSOME_CYTOSOL
	0.0	;%	66	MRNA_SMAD7_START_RIBOSOME_CYTOSOL	MRNA_SMAD7_START_RIBOSOME_CYTOSOL
	0.0	;%	67	SMAD7_CYTOSOL	SMAD7_CYTOSOL
	0.0	;%	68	DNA_ENDOGLIN_RNAP_NUCLEAR	DNA_ENDOGLIN_RNAP_NUCLEAR
	0.0	;%	69	MRNA_ENDOGLIN_NUCLEAR	MRNA_ENDOGLIN_NUCLEAR
	0.0	;%	70	MRNA_ENDOGLIN_NEXPORT_NUCLEAR	MRNA_ENDOGLIN_NEXPORT_NUCLEAR
	0.0	;%	71	MRNA_ENDOGLIN_CYTOSOL	MRNA_ENDOGLIN_CYTOSOL
	0.0	;%	72	MRNA_ENDOGLIN_RIBOSOME_CYTOSOL	MRNA_ENDOGLIN_RIBOSOME_CYTOSOL
	0.0	;%	73	MRNA_ENDOGLIN_START_RIBOSOME_CYTOSOL	MRNA_ENDOGLIN_START_RIBOSOME_CYTOSOL
	0.0	;%	74	ENDOGLIN_CYTOSOL	ENDOGLIN_CYTOSOL
	0.0	;%	75	DNA_ALK1_RNAP_NUCLEAR	DNA_ALK1_RNAP_NUCLEAR
	0.0	;%	76	MRNA_ALK1_NUCLEAR	MRNA_ALK1_NUCLEAR
	0.0	;%	77	MRNA_ALK1_NEXPORT_NUCLEAR	MRNA_ALK1_NEXPORT_NUCLEAR
	0.0	;%	78	MRNA_ALK1_CYTOSOL	MRNA_ALK1_CYTOSOL
	0.0	;%	79	MRNA_ALK1_RIBOSOME_CYTOSOL	MRNA_ALK1_RIBOSOME_CYTOSOL
```

```
0.0     ;%      80      MRNA_ALK1_START_RIBOSOME_CYTOSOL        MRNA_ALK1_START_RIBOSOME_CYTOSOL
0.0     ;%      81      ALK1_CYTOSOL    ALK1_CYTOSOL
0.0     ;%      82      DNA_ALK2_RNAP_NUCLEAR   DNA_ALK2_RNAP_NUCLEAR
0.0     ;%      83      MRNA_ALK2_NUCLEAR       MRNA_ALK2_NUCLEAR
0.0     ;%      84      MRNA_ALK2_NEXPORT_NUCLEAR       MRNA_ALK2_NEXPORT_NUCLEAR
0.0     ;%      85      MRNA_ALK2_CYTOSOL       MRNA_ALK2_CYTOSOL
0.0     ;%      86      MRNA_ALK2_RIBOSOME_CYTOSOL      MRNA_ALK2_RIBOSOME_CYTOSOL
0.0     ;%      87      MRNA_ALK2_START_RIBOSOME_CYTOSOL        MRNA_ALK2_START_RIBOSOME_CYTOSOL
0.0     ;%      88      ALK2_CYTOSOL    ALK2_CYTOSOL
0.0     ;%      89      DNA_ALK3_RNAP_NUCLEAR   DNA_ALK3_RNAP_NUCLEAR
0.0     ;%      90      MRNA_ALK3_NUCLEAR       MRNA_ALK3_NUCLEAR
0.0     ;%      91      MRNA_ALK3_NEXPORT_NUCLEAR       MRNA_ALK3_NEXPORT_NUCLEAR
0.0     ;%      92      MRNA_ALK3_CYTOSOL       MRNA_ALK3_CYTOSOL
0.0     ;%      93      MRNA_ALK3_RIBOSOME_CYTOSOL      MRNA_ALK3_RIBOSOME_CYTOSOL
0.0     ;%      94      MRNA_ALK3_START_RIBOSOME_CYTOSOL        MRNA_ALK3_START_RIBOSOME_CYTOSOL
0.0     ;%      95      ALK3_CYTOSOL    ALK3_CYTOSOL
0.0     ;%      96      DNA_ALK5_RNAP_NUCLEAR   DNA_ALK5_RNAP_NUCLEAR
0.0     ;%      97      MRNA_ALK5_NUCLEAR       MRNA_ALK5_NUCLEAR
0.0     ;%      98      MRNA_ALK5_NEXPORT_NUCLEAR       MRNA_ALK5_NEXPORT_NUCLEAR
0.0     ;%      99      MRNA_ALK5_CYTOSOL       MRNA_ALK5_CYTOSOL
0.0     ;%      100     MRNA_ALK5_RIBOSOME_CYTOSOL      MRNA_ALK5_RIBOSOME_CYTOSOL
0.0     ;%      101     MRNA_ALK5_START_RIBOSOME_CYTOSOL        MRNA_ALK5_START_RIBOSOME_CYTOSOL
0.0     ;%      102     ALK5_CYTOSOL    ALK5_CYTOSOL
0.0     ;%      103     DNA_ALK6_RNAP_NUCLEAR   DNA_ALK6_RNAP_NUCLEAR
0.0     ;%      104     MRNA_ALK6_NUCLEAR       MRNA_ALK6_NUCLEAR
0.0     ;%      105     MRNA_ALK6_NEXPORT_NUCLEAR       MRNA_ALK6_NEXPORT_NUCLEAR
0.0     ;%      106     MRNA_ALK6_CYTOSOL       MRNA_ALK6_CYTOSOL
0.0     ;%      107     MRNA_ALK6_RIBOSOME_CYTOSOL      MRNA_ALK6_RIBOSOME_CYTOSOL
0.0     ;%      108     MRNA_ALK6_START_RIBOSOME_CYTOSOL        MRNA_ALK6_START_RIBOSOME_CYTOSOL
0.0     ;%      109     ALK6_CYTOSOL    ALK6_CYTOSOL
0.0     ;%      110     DNA_SHC_RNAP_NUCLEAR    DNA_SHC_RNAP_NUCLEAR
0.0     ;%      111     MRNA_SHC_NUCLEAR        MRNA_SHC_NUCLEAR
0.0     ;%      112     MRNA_SHC_NEXPORT_NUCLEAR        MRNA_SHC_NEXPORT_NUCLEAR
0.0     ;%      113     MRNA_SHC_CYTOSOL        MRNA_SHC_CYTOSOL
0.0     ;%      114     MRNA_SHC_RIBOSOME_CYTOSOL       MRNA_SHC_RIBOSOME_CYTOSOL
0.0     ;%      115     MRNA_SHC_START_RIBOSOME_CYTOSOL         MRNA_SHC_START_RIBOSOME_CYTOSOL
0.0     ;%      116     SHC_CYTOSOL     SHC_CYTOSOL
0.0     ;%      117     DNA_GRB2_RNAP_NUCLEAR   DNA_GRB2_RNAP_NUCLEAR
0.0     ;%      118     MRNA_GRB2_NUCLEAR       MRNA_GRB2_NUCLEAR
0.0     ;%      119     MRNA_GRB2_NEXPORT_NUCLEAR       MRNA_GRB2_NEXPORT_NUCLEAR
0.0     ;%      120     MRNA_GRB2_CYTOSOL       MRNA_GRB2_CYTOSOL
0.0     ;%      121     MRNA_GRB2_RIBOSOME_CYTOSOL      MRNA_GRB2_RIBOSOME_CYTOSOL
0.0     ;%      122     MRNA_GRB2_START_RIBOSOME_CYTOSOL        MRNA_GRB2_START_RIBOSOME_CYTOSOL
0.0     ;%      123     GRB2_CYTOSOL    GRB2_CYTOSOL
0.0     ;%      124     DNA_SOS_RNAP_NUCLEAR    DNA_SOS_RNAP_NUCLEAR
0.0     ;%      125     MRNA_SOS_NUCLEAR        MRNA_SOS_NUCLEAR
0.0     ;%      126     MRNA_SOS_NEXPORT_NUCLEAR        MRNA_SOS_NEXPORT_NUCLEAR
0.0     ;%      127     MRNA_SOS_CYTOSOL        MRNA_SOS_CYTOSOL
0.0     ;%      128     MRNA_SOS_RIBOSOME_CYTOSOL       MRNA_SOS_RIBOSOME_CYTOSOL
0.0     ;%      129     MRNA_SOS_START_RIBOSOME_CYTOSOL         MRNA_SOS_START_RIBOSOME_CYTOSOL
0.0     ;%      130     SOS_CYTOSOL     SOS_CYTOSOL
0.0     ;%      131     DNA_BMPRII_RNAP_NUCLEAR         DNA_BMPRII_RNAP_NUCLEAR
0.0     ;%      132     MRNA_BMPRII_NUCLEAR             MRNA_BMPRII_NUCLEAR
0.0     ;%      133     MRNA_BMPRII_NEXPORT_NUCLEAR     MRNA_BMPRII_NEXPORT_NUCLEAR
0.0     ;%      134     MRNA_BMPRII_CYTOSOL             MRNA_BMPRII_CYTOSOL
0.0     ;%      135     MRNA_BMPRII_RIBOSOME_CYTOSOL            MRNA_BMPRII_RIBOSOME_CYTOSOL
0.0     ;%      136     MRNA_BMPRII_START_RIBOSOME_CYTOSOL      MRNA_BMPRII_START_RIBOSOME_CYTOSOL
0.0     ;%      137     BMPRII_CYTOSOL  BMPRII_CYTOSOL
0.0     ;%      138     DNA_TGFBRII_RNAP_NUCLEAR        DNA_TGFBRII_RNAP_NUCLEAR
0.0     ;%      139     MRNA_TGFBRII_NUCLEAR            MRNA_TGFBRII_NUCLEAR
0.0     ;%      140     MRNA_TGFBRII_NEXPORT_NUCLEAR            MRNA_TGFBRII_NEXPORT_NUCLEAR
0.0     ;%      141     MRNA_TGFBRII_CYTOSOL            MRNA_TGFBRII_CYTOSOL
0.0     ;%      142     MRNA_TGFBRII_RIBOSOME_CYTOSOL           MRNA_TGFBRII_RIBOSOME_CYTOSOL
0.0     ;%      143     MRNA_TGFBRII_START_RIBOSOME_CYTOSOL     MRNA_TGFBRII_START_RIBOSOME_CYTOSOL
0.0     ;%      144     TGFBRII_CYTOSOL         TGFBRII_CYTOSOL
0.0     ;%      145     DNA_TGFBRIII_RNAP_NUCLEAR       DNA_TGFBRIII_RNAP_NUCLEAR
0.0     ;%      146     MRNA_TGFBRIII_NUCLEAR           MRNA_TGFBRIII_NUCLEAR
0.0     ;%      147     MRNA_TGFBRIII_NEXPORT_NUCLEAR           MRNA_TGFBRIII_NEXPORT_NUCLEAR
0.0     ;%      148     MRNA_TGFBRIII_CYTOSOL           MRNA_TGFBRIII_CYTOSOL
0.0     ;%      149     MRNA_TGFBRIII_RIBOSOME_CYTOSOL          MRNA_TGFBRIII_RIBOSOME_CYTOSOL
0.0     ;%      150     MRNA_TGFBRIII_START_RIBOSOME_CYTOSOL    MRNA_TGFBRIII_START_RIBOSOME_CYTOSOL
0.0     ;%      151     TGFBRIII_CYTOSOL        TGFBRIII_CYTOSOL
0.0     ;%      152     DNA_MSX1_RNAP_NUCLEAR   DNA_MSX1_RNAP_NUCLEAR
0.0     ;%      153     MRNA_MSX1_NUCLEAR       MRNA_MSX1_NUCLEAR
0.0     ;%      154     MRNA_MSX1_NEXPORT_NUCLEAR       MRNA_MSX1_NEXPORT_NUCLEAR
0.0     ;%      155     MRNA_MSX1_CYTOSOL       MRNA_MSX1_CYTOSOL
0.0     ;%      156     MRNA_MSX1_RIBOSOME_CYTOSOL      MRNA_MSX1_RIBOSOME_CYTOSOL
0.0     ;%      157     MRNA_MSX1_START_RIBOSOME_CYTOSOL        MRNA_MSX1_START_RIBOSOME_CYTOSOL
0.0     ;%      158     MSX1_CYTOSOL    MSX1_CYTOSOL
0.0     ;%      159     DNA_AP1_RNAP_NUCLEAR    DNA_AP1_RNAP_NUCLEAR
0.0     ;%      160     MRNA_AP1_NUCLEAR        MRNA_AP1_NUCLEAR
0.0     ;%      161     MRNA_AP1_NEXPORT_NUCLEAR        MRNA_AP1_NEXPORT_NUCLEAR
0.0     ;%      162     MRNA_AP1_CYTOSOL        MRNA_AP1_CYTOSOL
0.0     ;%      163     MRNA_AP1_RIBOSOME_CYTOSOL       MRNA_AP1_RIBOSOME_CYTOSOL
0.0     ;%      164     MRNA_AP1_START_RIBOSOME_CYTOSOL         MRNA_AP1_START_RIBOSOME_CYTOSOL
0.0     ;%      165     AP1_CYTOSOL     AP1_CYTOSOL
0.0     ;%      166     DNA_GPASE_RNAP_NUCLEAR  DNA_GPASE_RNAP_NUCLEAR
0.0     ;%      167     MRNA_GPASE_NUCLEAR      MRNA_GPASE_NUCLEAR
0.0     ;%      168     MRNA_GPASE_NEXPORT_NUCLEAR      MRNA_GPASE_NEXPORT_NUCLEAR
0.0     ;%      169     MRNA_GPASE_CYTOSOL      MRNA_GPASE_CYTOSOL
0.0     ;%      170     MRNA_GPASE_RIBOSOME_CYTOSOL             MRNA_GPASE_RIBOSOME_CYTOSOL
0.0     ;%      171     MRNA_GPASE_START_RIBOSOME_CYTOSOL       MRNA_GPASE_START_RIBOSOME_CYTOSOL
0.0     ;%      172     GPASE_CYTOSOL   GPASE_CYTOSOL
```

0.0 ;% 173 DNA_TCF4_RNAP_NUCLEAR DNA_TCF4_RNAP_NUCLEAR
0.0 ;% 174 MRNA_TCF4_NUCLEAR MRNA_TCF4_NUCLEAR
0.0 ;% 175 MRNA_TCF4_NEXPORT_NUCLEAR MRNA_TCF4_NEXPORT_NUCLEAR
0.0 ;% 176 MRNA_TCF4_CYTOSOL MRNA_TCF4_CYTOSOL
0.0 ;% 177 MRNA_TCF4_RIBOSOME_CYTOSOL MRNA_TCF4_RIBOSOME_CYTOSOL
0.0 ;% 178 MRNA_TCF4_START_RIBOSOME_CYTOSOL MRNA_TCF4_START_RIBOSOME_CYTOSOL
0.0 ;% 179 TCF4_CYTOSOL TCF4_CYTOSOL
0.0 ;% 180 DNA_NOTCH1_RNAP_NUCLEAR DNA_NOTCH1_RNAP_NUCLEAR
0.0 ;% 181 MRNA_NOTCH1_NUCLEAR MRNA_NOTCH1_NUCLEAR
0.0 ;% 182 MRNA_NOTCH1_NEXPORT_NUCLEAR MRNA_NOTCH1_NEXPORT_NUCLEAR
0.0 ;% 183 MRNA_NOTCH1_CYTOSOL MRNA_NOTCH1_CYTOSOL
0.0 ;% 184 MRNA_NOTCH1_RIBOSOME_CYTOSOL MRNA_NOTCH1_RIBOSOME_CYTOSOL
0.0 ;% 185 MRNA_NOTCH1_START_RIBOSOME_CYTOSOL MRNA_NOTCH1_START_RIBOSOME_CYTOSOL
0.0 ;% 186 NOTCH1_CYTOSOL NOTCH1_CYTOSOL
0.0 ;% 187 DNA_SEL1_RNAP_NUCLEAR DNA_SEL1_RNAP_NUCLEAR
0.0 ;% 188 MRNA_SEL1_NUCLEAR MRNA_SEL1_NUCLEAR
0.0 ;% 189 MRNA_SEL1_NEXPORT_NUCLEAR MRNA_SEL1_NEXPORT_NUCLEAR
0.0 ;% 190 MRNA_SEL1_CYTOSOL MRNA_SEL1_CYTOSOL
0.0 ;% 191 MRNA_SEL1_RIBOSOME_CYTOSOL MRNA_SEL1_RIBOSOME_CYTOSOL
0.0 ;% 192 MRNA_SEL1_START_RIBOSOME_CYTOSOL MRNA_SEL1_START_RIBOSOME_CYTOSOL
0.0 ;% 193 SEL1_CYTOSOL SEL1_CYTOSOL
0.0 ;% 194 DNA_CSL_RNAP_NUCLEAR DNA_CSL_RNAP_NUCLEAR
0.0 ;% 195 MRNA_CSL_NUCLEAR MRNA_CSL_NUCLEAR
0.0 ;% 196 MRNA_CSL_NEXPORT_NUCLEAR MRNA_CSL_NEXPORT_NUCLEAR
0.0 ;% 197 MRNA_CSL_CYTOSOL MRNA_CSL_CYTOSOL
0.0 ;% 198 MRNA_CSL_RIBOSOME_CYTOSOL MRNA_CSL_RIBOSOME_CYTOSOL
0.0 ;% 199 MRNA_CSL_START_RIBOSOME_CYTOSOL MRNA_CSL_START_RIBOSOME_CYTOSOL
0.0 ;% 200 CSL_CYTOSOL CSL_CYTOSOL
0.0 ;% 201 DNA_RAS_RNAP_NUCLEAR DNA_RAS_RNAP_NUCLEAR
0.0 ;% 202 MRNA_RAS_NUCLEAR MRNA_RAS_NUCLEAR
0.0 ;% 203 MRNA_RAS_NEXPORT_NUCLEAR MRNA_RAS_NEXPORT_NUCLEAR
0.0 ;% 204 MRNA_RAS_CYTOSOL MRNA_RAS_CYTOSOL
0.0 ;% 205 MRNA_RAS_RIBOSOME_CYTOSOL MRNA_RAS_RIBOSOME_CYTOSOL
0.0 ;% 206 MRNA_RAS_START_RIBOSOME_CYTOSOL MRNA_RAS_START_RIBOSOME_CYTOSOL
0.0 ;% 207 RAS_CYTOSOL RAS_CYTOSOL
0.0 ;% 208 DNA_RAF_RNAP_NUCLEAR DNA_RAF_RNAP_NUCLEAR
0.0 ;% 209 MRNA_RAF_NUCLEAR MRNA_RAF_NUCLEAR
0.0 ;% 210 MRNA_RAF_NEXPORT_NUCLEAR MRNA_RAF_NEXPORT_NUCLEAR
0.0 ;% 211 MRNA_RAF_CYTOSOL MRNA_RAF_CYTOSOL
0.0 ;% 212 MRNA_RAF_RIBOSOME_CYTOSOL MRNA_RAF_RIBOSOME_CYTOSOL
0.0 ;% 213 MRNA_RAF_START_RIBOSOME_CYTOSOL MRNA_RAF_START_RIBOSOME_CYTOSOL
0.0 ;% 214 RAF_CYTOSOL RAF_CYTOSOL
0.0 ;% 215 DNA_MEK_RNAP_NUCLEAR DNA_MEK_RNAP_NUCLEAR
0.0 ;% 216 MRNA_MEK_NUCLEAR MRNA_MEK_NUCLEAR
0.0 ;% 217 MRNA_MEK_NEXPORT_NUCLEAR MRNA_MEK_NEXPORT_NUCLEAR
0.0 ;% 218 MRNA_MEK_CYTOSOL MRNA_MEK_CYTOSOL
0.0 ;% 219 MRNA_MEK_RIBOSOME_CYTOSOL MRNA_MEK_RIBOSOME_CYTOSOL
0.0 ;% 220 MRNA_MEK_START_RIBOSOME_CYTOSOL MRNA_MEK_START_RIBOSOME_CYTOSOL
0.0 ;% 221 MEK_CYTOSOL MEK_CYTOSOL
0.0 ;% 222 DNA_ERK_RNAP_NUCLEAR DNA_ERK_RNAP_NUCLEAR
0.0 ;% 223 MRNA_ERK_NUCLEAR MRNA_ERK_NUCLEAR
0.0 ;% 224 MRNA_ERK_NEXPORT_NUCLEAR MRNA_ERK_NEXPORT_NUCLEAR
0.0 ;% 225 MRNA_ERK_CYTOSOL MRNA_ERK_CYTOSOL
0.0 ;% 226 MRNA_ERK_RIBOSOME_CYTOSOL MRNA_ERK_RIBOSOME_CYTOSOL
0.0 ;% 227 MRNA_ERK_START_RIBOSOME_CYTOSOL MRNA_ERK_START_RIBOSOME_CYTOSOL
0.0 ;% 228 ERK_CYTOSOL ERK_CYTOSOL
0.0 ;% 229 DNA_SPK_RNAP_NUCLEAR DNA_SPK_RNAP_NUCLEAR
0.0 ;% 230 MRNA_SPK_NUCLEAR MRNA_SPK_NUCLEAR
0.0 ;% 231 MRNA_SPK_NEXPORT_NUCLEAR MRNA_SPK_NEXPORT_NUCLEAR
0.0 ;% 232 MRNA_SPK_CYTOSOL MRNA_SPK_CYTOSOL
0.0 ;% 233 MRNA_SPK_RIBOSOME_CYTOSOL MRNA_SPK_RIBOSOME_CYTOSOL
0.0 ;% 234 MRNA_SPK_START_RIBOSOME_CYTOSOL MRNA_SPK_START_RIBOSOME_CYTOSOL
0.0 ;% 235 SPK_CYTOSOL SPK_CYTOSOL
0.0 ;% 236 DNA_PLCG_RNAP_NUCLEAR DNA_PLCG_RNAP_NUCLEAR
0.0 ;% 237 MRNA_PLCG_NUCLEAR MRNA_PLCG_NUCLEAR
0.0 ;% 238 MRNA_PLCG_NEXPORT_NUCLEAR MRNA_PLCG_NEXPORT_NUCLEAR
0.0 ;% 239 MRNA_PLCG_CYTOSOL MRNA_PLCG_CYTOSOL
0.0 ;% 240 MRNA_PLCG_RIBOSOME_CYTOSOL MRNA_PLCG_RIBOSOME_CYTOSOL
0.0 ;% 241 MRNA_PLCG_START_RIBOSOME_CYTOSOL MRNA_PLCG_START_RIBOSOME_CYTOSOL
0.0 ;% 242 PLCG_CYTOSOL PLCG_CYTOSOL
0.0 ;% 243 DNA_RAF_PASE_RNAP_NUCLEAR DNA_RAF_PASE_RNAP_NUCLEAR
0.0 ;% 244 MRNA_RAF_PASE_NUCLEAR MRNA_RAF_PASE_NUCLEAR
0.0 ;% 245 MRNA_RAF_PASE_NEXPORT_NUCLEAR MRNA_RAF_PASE_NEXPORT_NUCLEAR
0.0 ;% 246 MRNA_RAF_PASE_CYTOSOL MRNA_RAF_PASE_CYTOSOL
0.0 ;% 247 MRNA_RAF_PASE_RIBOSOME_CYTOSOL MRNA_RAF_PASE_RIBOSOME_CYTOSOL
0.0 ;% 248 MRNA_RAF_PASE_START_RIBOSOME_CYTOSOL MRNA_RAF_PASE_START_RIBOSOME_CYTOSOL
0.0 ;% 249 RAF_PASE_CYTOSOL RAF_PASE_CYTOSOL
0.0 ;% 250 DNA_MEK_PASE_RNAP_NUCLEAR DNA_MEK_PASE_RNAP_NUCLEAR
0.0 ;% 251 MRNA_MEK_PASE_NUCLEAR MRNA_MEK_PASE_NUCLEAR
0.0 ;% 252 MRNA_MEK_PASE_NEXPORT_NUCLEAR MRNA_MEK_PASE_NEXPORT_NUCLEAR
0.0 ;% 253 MRNA_MEK_PASE_CYTOSOL MRNA_MEK_PASE_CYTOSOL
0.0 ;% 254 MRNA_MEK_PASE_RIBOSOME_CYTOSOL MRNA_MEK_PASE_RIBOSOME_CYTOSOL
0.0 ;% 255 MRNA_MEK_PASE_START_RIBOSOME_CYTOSOL
MRNA_MEK_PASE_START_RIBOSOME_CYTOSOL
0.0 ;% 256 MEK_PASE_CYTOSOL MEK_PASE_CYTOSOL
0.0 ;% 257 DNA_ERK_PASE_RNAP_NUCLEAR DNA_ERK_PASE_RNAP_NUCLEAR
0.0 ;% 258 MRNA_ERK_PASE_NUCLEAR MRNA_ERK_PASE_NUCLEAR
0.0 ;% 259 MRNA_ERK_PASE_NEXPORT_NUCLEAR MRNA_ERK_PASE_NEXPORT_NUCLEAR
0.0 ;% 260 MRNA_ERK_PASE_CYTOSOL MRNA_ERK_PASE_CYTOSOL
0.0 ;% 261 MRNA_ERK_PASE_RIBOSOME_CYTOSOL MRNA_ERK_PASE_RIBOSOME_CYTOSOL
0.0 ;% 262 MRNA_ERK_PASE_START_RIBOSOME_CYTOSOL MRNA_ERK_PASE_START_RIBOSOME_CYTOSOL
0.0 ;% 263 ERK_PASE_CYTOSOL ERK_PASE_CYTOSOL
0.0 ;% 264 DNA_SP1_RNAP_NUCLEAR DNA_SP1_RNAP_NUCLEAR

0.0 ;% 265 MRNA_SP1_NUCLEAR MRNA_SP1_NUCLEAR
0.0 ;% 266 MRNA_SP1_NEXPORT_NUCLEAR MRNA_SP1_NEXPORT_NUCLEAR
0.0 ;% 267 MRNA_SP1_CYTOSOL MRNA_SP1_CYTOSOL
0.0 ;% 268 MRNA_SP1_RIBOSOME_CYTOSOL MRNA_SP1_RIBOSOME_CYTOSOL
0.0 ;% 269 MRNA_SP1_START_RIBOSOME_CYTOSOL MRNA_SP1_START_RIBOSOME_CYTOSOL
0.0 ;% 270 SP1_CYTOSOL SP1_CYTOSOL
0.0 ;% 271 DNA_CJUN_RNAP_NUCLEAR DNA_CJUN_RNAP_NUCLEAR
0.0 ;% 272 MRNA_CJUN_NUCLEAR MRNA_CJUN_NUCLEAR
0.0 ;% 273 MRNA_CJUN_NEXPORT_NUCLEAR MRNA_CJUN_NEXPORT_NUCLEAR
0.0 ;% 274 MRNA_CJUN_CYTOSOL MRNA_CJUN_CYTOSOL
0.0 ;% 275 MRNA_CJUN_RIBOSOME_CYTOSOL MRNA_CJUN_RIBOSOME_CYTOSOL
0.0 ;% 276 MRNA_CJUN_START_RIBOSOME_CYTOSOL MRNA_CJUN_START_RIBOSOME_CYTOSOL
0.0 ;% 277 CJUN_CYTOSOL CJUN_CYTOSOL
0.0 ;% 278 DNA_CPLA2_RNAP_NUCLEAR DNA_CPLA2_RNAP_NUCLEAR
0.0 ;% 279 MRNA_CPLA2_NUCLEAR MRNA_CPLA2_NUCLEAR
0.0 ;% 280 MRNA_CPLA2_NEXPORT_NUCLEAR MRNA_CPLA2_NEXPORT_NUCLEAR
0.0 ;% 281 MRNA_CPLA2_CYTOSOL MRNA_CPLA2_CYTOSOL
0.0 ;% 282 MRNA_CPLA2_RIBOSOME_CYTOSOL MRNA_CPLA2_RIBOSOME_CYTOSOL
0.0 ;% 283 MRNA_CPLA2_START_RIBOSOME_CYTOSOL MRNA_CPLA2_START_RIBOSOME_CYTOSOL
0.0 ;% 284 CPLA2_CYTOSOL CPLA2_CYTOSOL
0.0 ;% 285 DNA_GSK3B_RNAP_NUCLEAR DNA_GSK3B_RNAP_NUCLEAR
0.0 ;% 286 MRNA_GSK3B_NUCLEAR MRNA_GSK3B_NUCLEAR
0.0 ;% 287 MRNA_GSK3B_NEXPORT_NUCLEAR MRNA_GSK3B_NEXPORT_NUCLEAR
0.0 ;% 288 MRNA_GSK3B_CYTOSOL MRNA_GSK3B_CYTOSOL
0.0 ;% 289 MRNA_GSK3B_RIBOSOME_CYTOSOL MRNA_GSK3B_RIBOSOME_CYTOSOL
0.0 ;% 290 MRNA_GSK3B_START_RIBOSOME_CYTOSOL MRNA_GSK3B_START_RIBOSOME_CYTOSOL
0.0 ;% 291 GSK3B_CYTOSOL GSK3B_CYTOSOL
0.0 ;% 292 DNA_CK1_RNAP_NUCLEAR DNA_CK1_RNAP_NUCLEAR
0.0 ;% 293 MRNA_CK1_NUCLEAR MRNA_CK1_NUCLEAR
0.0 ;% 294 MRNA_CK1_NEXPORT_NUCLEAR MRNA_CK1_NEXPORT_NUCLEAR
0.0 ;% 295 MRNA_CK1_CYTOSOL MRNA_CK1_CYTOSOL
0.0 ;% 296 MRNA_CK1_RIBOSOME_CYTOSOL MRNA_CK1_RIBOSOME_CYTOSOL
0.0 ;% 297 MRNA_CK1_START_RIBOSOME_CYTOSOL MRNA_CK1_START_RIBOSOME_CYTOSOL
0.0 ;% 298 CK1_CYTOSOL CK1_CYTOSOL
0.0 ;% 299 DNA_APC_RNAP_NUCLEAR DNA_APC_RNAP_NUCLEAR
0.0 ;% 300 MRNA_APC_NUCLEAR MRNA_APC_NUCLEAR
0.0 ;% 301 MRNA_APC_NEXPORT_NUCLEAR MRNA_APC_NEXPORT_NUCLEAR
0.0 ;% 302 MRNA_APC_CYTOSOL MRNA_APC_CYTOSOL
0.0 ;% 303 MRNA_APC_RIBOSOME_CYTOSOL MRNA_APC_RIBOSOME_CYTOSOL
0.0 ;% 304 MRNA_APC_START_RIBOSOME_CYTOSOL MRNA_APC_START_RIBOSOME_CYTOSOL
0.0 ;% 305 APC_CYTOSOL APC_CYTOSOL
0.0 ;% 306 DNA_LRP_RNAP_NUCLEAR DNA_LRP_RNAP_NUCLEAR
0.0 ;% 307 MRNA_LRP_NUCLEAR MRNA_LRP_NUCLEAR
0.0 ;% 308 MRNA_LRP_NEXPORT_NUCLEAR MRNA_LRP_NEXPORT_NUCLEAR
0.0 ;% 309 MRNA_LRP_CYTOSOL MRNA_LRP_CYTOSOL
0.0 ;% 310 MRNA_LRP_RIBOSOME_CYTOSOL MRNA_LRP_RIBOSOME_CYTOSOL
0.0 ;% 311 MRNA_LRP_START_RIBOSOME_CYTOSOL MRNA_LRP_START_RIBOSOME_CYTOSOL
0.0 ;% 312 LRP_CYTOSOL LRP_CYTOSOL
0.0 ;% 313 DNA_AXIN_RNAP_NUCLEAR DNA_AXIN_RNAP_NUCLEAR
0.0 ;% 314 MRNA_AXIN_NUCLEAR MRNA_AXIN_NUCLEAR
0.0 ;% 315 MRNA_AXIN_NEXPORT_NUCLEAR MRNA_AXIN_NEXPORT_NUCLEAR
0.0 ;% 316 MRNA_AXIN_CYTOSOL MRNA_AXIN_CYTOSOL
0.0 ;% 317 MRNA_AXIN_RIBOSOME_CYTOSOL MRNA_AXIN_RIBOSOME_CYTOSOL
0.0 ;% 318 MRNA_AXIN_START_RIBOSOME_CYTOSOL MRNA_AXIN_START_RIBOSOME_CYTOSOL
0.0 ;% 319 AXIN_CYTOSOL AXIN_CYTOSOL
0.0 ;% 320 DNA_PKC_RNAP_NUCLEAR DNA_PKC_RNAP_NUCLEAR
0.0 ;% 321 MRNA_PKC_NUCLEAR MRNA_PKC_NUCLEAR
0.0 ;% 322 MRNA_PKC_NEXPORT_NUCLEAR MRNA_PKC_NEXPORT_NUCLEAR
0.0 ;% 323 MRNA_PKC_CYTOSOL MRNA_PKC_CYTOSOL
0.0 ;% 324 MRNA_PKC_RIBOSOME_CYTOSOL MRNA_PKC_RIBOSOME_CYTOSOL
0.0 ;% 325 MRNA_PKC_START_RIBOSOME_CYTOSOL MRNA_PKC_START_RIBOSOME_CYTOSOL
0.0 ;% 326 PKC_CYTOSOL PKC_CYTOSOL
0.0 ;% 327 DNA_BTRCP_RNAP_NUCLEAR DNA_BTRCP_RNAP_NUCLEAR
0.0 ;% 328 MRNA_BTRCP_NUCLEAR MRNA_BTRCP_NUCLEAR
0.0 ;% 329 MRNA_BTRCP_NEXPORT_NUCLEAR MRNA_BTRCP_NEXPORT_NUCLEAR
0.0 ;% 330 MRNA_BTRCP_CYTOSOL MRNA_BTRCP_CYTOSOL
0.0 ;% 331 MRNA_BTRCP_RIBOSOME_CYTOSOL MRNA_BTRCP_RIBOSOME_CYTOSOL
0.0 ;% 332 MRNA_BTRCP_START_RIBOSOME_CYTOSOL MRNA_BTRCP_START_RIBOSOME_CYTOSOL
0.0 ;% 333 BTRCP_CYTOSOL BTRCP_CYTOSOL
0.0 ;% 334 DNA_FRIZZLED_RNAP_NUCLEAR DNA_FRIZZLED_RNAP_NUCLEAR
0.0 ;% 335 MRNA_FRIZZLED_NUCLEAR MRNA_FRIZZLED_NUCLEAR
0.0 ;% 336 MRNA_FRIZZLED_NEXPORT_NUCLEAR MRNA_FRIZZLED_NEXPORT_NUCLEAR
0.0 ;% 337 MRNA_FRIZZLED_CYTOSOL MRNA_FRIZZLED_CYTOSOL
0.0 ;% 338 MRNA_FRIZZLED_RIBOSOME_CYTOSOL MRNA_FRIZZLED_RIBOSOME_CYTOSOL
0.0 ;% 339 MRNA_FRIZZLED_START_RIBOSOME_CYTOSOL MRNA_FRIZZLED_START_RIBOSOME_CYTOSOL
0.0 ;% 340 FRIZZLED_CYTOSOL FRIZZLED_CYTOSOL
0.0 ;% 341 DNA_BCATENIN_RNAP_NUCLEAR DNA_BCATENIN_RNAP_NUCLEAR
0.0 ;% 342 MRNA_BCATENIN_NUCLEAR MRNA_BCATENIN_NUCLEAR
0.0 ;% 343 MRNA_BCATENIN_NEXPORT_NUCLEAR MRNA_BCATENIN_NEXPORT_NUCLEAR
0.0 ;% 344 MRNA_BCATENIN_CYTOSOL MRNA_BCATENIN_CYTOSOL
0.0 ;% 345 MRNA_BCATENIN_RIBOSOME_CYTOSOL MRNA_BCATENIN_RIBOSOME_CYTOSOL
0.0 ;% 346 MRNA_BCATENIN_START_RIBOSOME_CYTOSOL MRNA_BCATENIN_START_RIBOSOME_CYTOSOL
0.0 ;% 347 BCATENIN_CYTOSOL BCATENIN_CYTOSOL
0.0 ;% 348 DNA_DISHEVELLED_RNAP_NUCLEAR DNA_DISHEVELLED_RNAP_NUCLEAR
0.0 ;% 349 MRNA_DISHEVELLED_NUCLEAR MRNA_DISHEVELLED_NUCLEAR
0.0 ;% 350 MRNA_DISHEVELLED_NEXPORT_NUCLEAR MRNA_DISHEVELLED_NEXPORT_NUCLEAR
0.0 ;% 351 MRNA_DISHEVELLED_CYTOSOL MRNA_DISHEVELLED_CYTOSOL
0.0 ;% 352 MRNA_DISHEVELLED_RIBOSOME_CYTOSOL MRNA_DISHEVELLED_RIBOSOME_CYTOSOL
0.0 ;% 353 MRNA_DISHEVELLED_START_RIBOSOME_CYTOSOL
MRNA_DISHEVELLED_START_RIBOSOME_CYTOSOL
0.0 ;% 354 DISHEVELLED_CYTOSOL DISHEVELLED_CYTOSOL
0.0 ;% 355 DNA_ECADHERIN_RNAP_NUCLEAR DNA_ECADHERIN_RNAP_NUCLEAR
0.0 ;% 356 MRNA_ECADHERIN_NUCLEAR MRNA_ECADHERIN_NUCLEAR

0.0 ;% 357 MRNA_ECADHERIN_NEXPORT_NUCLEAR MRNA_ECADHERIN_NEXPORT_NUCLEAR
0.0 ;% 358 MRNA_ECADHERIN_CYTOSOL MRNA_ECADHERIN_CYTOSOL
0.0 ;% 359 MRNA_ECADHERIN_RIBOSOME_CYTOSOL MRNA_ECADHERIN_RIBOSOME_CYTOSOL
0.0 ;% 360 MRNA_ECADHERIN_START_RIBOSOME_CYTOSOL
MRNA_ECADHERIN_START_RIBOSOME_CYTOSOL
0.0 ;% 361 ECADHERIN_CYTOSOL ECADHERIN_CYTOSOL
0.0 ;% 362 DNA_VECADHERIN_RNAP_NUCLEAR DNA_VECADHERIN_RNAP_NUCLEAR
0.0 ;% 363 MRNA_VECADHERIN_NUCLEAR MRNA_VECADHERIN_NUCLEAR
0.0 ;% 364 MRNA_VECADHERIN_NEXPORT_NUCLEAR MRNA_VECADHERIN_NEXPORT_NUCLEAR
0.0 ;% 365 MRNA_VECADHERIN_CYTOSOL MRNA_VECADHERIN_CYTOSOL
0.0 ;% 366 MRNA_VECADHERIN_RIBOSOME_CYTOSOL MRNA_VECADHERIN_RIBOSOME_CYTOSOL
0.0 ;% 367 MRNA_VECADHERIN_START_RIBOSOME_CYTOSOL
MRNA_VECADHERIN_START_RIBOSOME_CYTOSOL
0.0 ;% 368 VECADHERIN_CYTOSOL VECADHERIN_CYTOSOL
0.0 ;% 369 DNA_PECAM1_RNAP_NUCLEAR DNA_PECAM1_RNAP_NUCLEAR
0.0 ;% 370 MRNA_PECAM1_NUCLEAR MRNA_PECAM1_NUCLEAR
0.0 ;% 371 MRNA_PECAM1_NEXPORT_NUCLEAR MRNA_PECAM1_NEXPORT_NUCLEAR
0.0 ;% 372 MRNA_PECAM1_CYTOSOL MRNA_PECAM1_CYTOSOL
0.0 ;% 373 MRNA_PECAM1_RIBOSOME_CYTOSOL MRNA_PECAM1_RIBOSOME_CYTOSOL
0.0 ;% 374 MRNA_PECAM1_START_RIBOSOME_CYTOSOL MRNA_PECAM1_START_RIBOSOME_CYTOSOL
0.0 ;% 375 PECAM1_CYTOSOL PECAM1_CYTOSOL
0.0 ;% 376 DNA_AKT_RNAP_NUCLEAR DNA_AKT_RNAP_NUCLEAR
0.0 ;% 377 MRNA_AKT_NUCLEAR MRNA_AKT_NUCLEAR
0.0 ;% 378 MRNA_AKT_NEXPORT_NUCLEAR MRNA_AKT_NEXPORT_NUCLEAR
0.0 ;% 379 MRNA_AKT_CYTOSOL MRNA_AKT_CYTOSOL
0.0 ;% 380 MRNA_AKT_RIBOSOME_CYTOSOL MRNA_AKT_RIBOSOME_CYTOSOL
0.0 ;% 381 MRNA_AKT_START_RIBOSOME_CYTOSOL MRNA_AKT_START_RIBOSOME_CYTOSOL
0.0 ;% 382 AKT_CYTOSOL AKT_CYTOSOL
0.0 ;% 383 DNA_PI3K_RNAP_NUCLEAR DNA_PI3K_RNAP_NUCLEAR
0.0 ;% 384 MRNA_PI3K_NUCLEAR MRNA_PI3K_NUCLEAR
0.0 ;% 385 MRNA_PI3K_NEXPORT_NUCLEAR MRNA_PI3K_NEXPORT_NUCLEAR
0.0 ;% 386 MRNA_PI3K_CYTOSOL MRNA_PI3K_CYTOSOL
0.0 ;% 387 MRNA_PI3K_RIBOSOME_CYTOSOL MRNA_PI3K_RIBOSOME_CYTOSOL
0.0 ;% 388 MRNA_PI3K_START_RIBOSOME_CYTOSOL MRNA_PI3K_START_RIBOSOME_CYTOSOL
0.0 ;% 389 PI3K_CYTOSOL PI3K_CYTOSOL
0.0 ;% 390 DNA_PTEN_RNAP_NUCLEAR DNA_PTEN_RNAP_NUCLEAR
0.0 ;% 391 MRNA_PTEN_NUCLEAR MRNA_PTEN_NUCLEAR
0.0 ;% 392 MRNA_PTEN_NEXPORT_NUCLEAR MRNA_PTEN_NEXPORT_NUCLEAR
0.0 ;% 393 MRNA_PTEN_CYTOSOL MRNA_PTEN_CYTOSOL
0.0 ;% 394 MRNA_PTEN_RIBOSOME_CYTOSOL MRNA_PTEN_RIBOSOME_CYTOSOL
0.0 ;% 395 MRNA_PTEN_START_RIBOSOME_CYTOSOL MRNA_PTEN_START_RIBOSOME_CYTOSOL
0.0 ;% 396 PTEN_CYTOSOL PTEN_CYTOSOL
0.0 ;% 397 DNA_PDK1_RNAP_NUCLEAR DNA_PDK1_RNAP_NUCLEAR
0.0 ;% 398 MRNA_PDK1_NUCLEAR MRNA_PDK1_NUCLEAR
0.0 ;% 399 MRNA_PDK1_NEXPORT_NUCLEAR MRNA_PDK1_NEXPORT_NUCLEAR
0.0 ;% 400 MRNA_PDK1_CYTOSOL MRNA_PDK1_CYTOSOL
0.0 ;% 401 MRNA_PDK1_RIBOSOME_CYTOSOL MRNA_PDK1_RIBOSOME_CYTOSOL
0.0 ;% 402 MRNA_PDK1_START_RIBOSOME_CYTOSOL MRNA_PDK1_START_RIBOSOME_CYTOSOL
0.0 ;% 403 PDK1_CYTOSOL PDK1_CYTOSOL
0.0 ;% 404 DNA_AKT_PASE_RNAP_NUCLEAR DNA_AKT_PASE_RNAP_NUCLEAR
0.0 ;% 405 MRNA_AKT_PASE_NUCLEAR MRNA_AKT_PASE_NUCLEAR
0.0 ;% 406 MRNA_AKT_PASE_NEXPORT_NUCLEAR MRNA_AKT_PASE_NEXPORT_NUCLEAR
0.0 ;% 407 MRNA_AKT_PASE_CYTOSOL MRNA_AKT_PASE_CYTOSOL
0.0 ;% 408 MRNA_AKT_PASE_RIBOSOME_CYTOSOL MRNA_AKT_PASE_RIBOSOME_CYTOSOL
0.0 ;% 409 MRNA_AKT_PASE_START_RIBOSOME_CYTOSOL MRNA_AKT_PASE_START_RIBOSOME_CYTOSOL
0.0 ;% 410 AKT_PASE_CYTOSOL AKT_PASE_CYTOSOL
0.0 ;% 411 DNA_IKB_RNAP_NUCLEAR DNA_IKB_RNAP_NUCLEAR
0.0 ;% 412 MRNA_IKB_NUCLEAR MRNA_IKB_NUCLEAR
0.0 ;% 413 MRNA_IKB_NEXPORT_NUCLEAR MRNA_IKB_NEXPORT_NUCLEAR
0.0 ;% 414 MRNA_IKB_CYTOSOL MRNA_IKB_CYTOSOL
0.0 ;% 415 MRNA_IKB_RIBOSOME_CYTOSOL MRNA_IKB_RIBOSOME_CYTOSOL
0.0 ;% 416 MRNA_IKB_START_RIBOSOME_CYTOSOL MRNA_IKB_START_RIBOSOME_CYTOSOL
0.0 ;% 417 IKB_CYTOSOL IKB_CYTOSOL
0.0 ;% 418 DNA_NFKB_RNAP_NUCLEAR DNA_NFKB_RNAP_NUCLEAR
0.0 ;% 419 MRNA_NFKB_NUCLEAR MRNA_NFKB_NUCLEAR
0.0 ;% 420 MRNA_NFKB_NEXPORT_NUCLEAR MRNA_NFKB_NEXPORT_NUCLEAR
0.0 ;% 421 MRNA_NFKB_CYTOSOL MRNA_NFKB_CYTOSOL
0.0 ;% 422 MRNA_NFKB_RIBOSOME_CYTOSOL MRNA_NFKB_RIBOSOME_CYTOSOL
0.0 ;% 423 MRNA_NFKB_START_RIBOSOME_CYTOSOL MRNA_NFKB_START_RIBOSOME_CYTOSOL
0.0 ;% 424 NFKB_CYTOSOL NFKB_CYTOSOL
0.0 ;% 425 DNA_VEGFR2_RNAP_NUCLEAR DNA_VEGFR2_RNAP_NUCLEAR
0.0 ;% 426 MRNA_VEGFR2_NUCLEAR MRNA_VEGFR2_NUCLEAR
0.0 ;% 427 MRNA_VEGFR2_NEXPORT_NUCLEAR MRNA_VEGFR2_NEXPORT_NUCLEAR
0.0 ;% 428 MRNA_VEGFR2_CYTOSOL MRNA_VEGFR2_CYTOSOL
0.0 ;% 429 MRNA_VEGFR2_RIBOSOME_CYTOSOL MRNA_VEGFR2_RIBOSOME_CYTOSOL
0.0 ;% 430 MRNA_VEGFR2_START_RIBOSOME_CYTOSOL MRNA_VEGFR2_START_RIBOSOME_CYTOSOL
0.0 ;% 431 VEGFR2_CYTOSOL VEGFR2_CYTOSOL
0.0 ;% 432 DNA_SNAIL_RNAP_NUCLEAR DNA_SNAIL_RNAP_NUCLEAR
0.0 ;% 433 MRNA_SNAIL_NUCLEAR MRNA_SNAIL_NUCLEAR
0.0 ;% 434 MRNA_SNAIL_NEXPORT_NUCLEAR MRNA_SNAIL_NEXPORT_NUCLEAR
0.0 ;% 435 MRNA_SNAIL_CYTOSOL MRNA_SNAIL_CYTOSOL
0.0 ;% 436 MRNA_SNAIL_RIBOSOME_CYTOSOL MRNA_SNAIL_RIBOSOME_CYTOSOL
0.0 ;% 437 MRNA_SNAIL_START_RIBOSOME_CYTOSOL MRNA_SNAIL_START_RIBOSOME_CYTOSOL
0.0 ;% 438 SNAIL_CYTOSOL SNAIL_CYTOSOL
0.0 ;% 439 DNA_SLUG_RNAP_NUCLEAR DNA_SLUG_RNAP_NUCLEAR
0.0 ;% 440 MRNA_SLUG_NUCLEAR MRNA_SLUG_NUCLEAR
0.0 ;% 441 MRNA_SLUG_NEXPORT_NUCLEAR MRNA_SLUG_NEXPORT_NUCLEAR
0.0 ;% 442 MRNA_SLUG_CYTOSOL MRNA_SLUG_CYTOSOL
0.0 ;% 443 MRNA_SLUG_RIBOSOME_CYTOSOL MRNA_SLUG_RIBOSOME_CYTOSOL
0.0 ;% 444 MRNA_SLUG_START_RIBOSOME_CYTOSOL MRNA_SLUG_START_RIBOSOME_CYTOSOL
0.0 ;% 445 SLUG_CYTOSOL SLUG_CYTOSOL
0.0 ;% 446 DNA_YREG1_RNAP_NUCLEAR DNA_YREG1_RNAP_NUCLEAR
0.0 ;% 447 MRNA_YREG1_NUCLEAR MRNA_YREG1_NUCLEAR

0.0 ;% 448 MRNA_YREG1_NEXPORT_NUCLEAR MRNA_YREG1_NEXPORT_NUCLEAR
0.0 ;% 449 MRNA_YREG1_CYTOSOL MRNA_YREG1_CYTOSOL
0.0 ;% 450 MRNA_YREG1_RIBOSOME_CYTOSOL MRNA_YREG1_RIBOSOME_CYTOSOL
0.0 ;% 451 MRNA_YREG1_START_RIBOSOME_CYTOSOL MRNA_YREG1_START_RIBOSOME_CYTOSOL
0.0 ;% 452 YREG1_CYTOSOL YREG1_CYTOSOL
0.0 ;% 453 DNA_LOADING_RNAP_NUCLEAR DNA_LOADING_RNAP_NUCLEAR
0.0 ;% 454 MRNA_LOADING_NUCLEAR MRNA_LOADING_NUCLEAR
0.0 ;% 455 MRNA_LOADING_NEXPORT_NUCLEAR MRNA_LOADING_NEXPORT_NUCLEAR
0.0 ;% 456 MRNA_LOADING_CYTOSOL MRNA_LOADING_CYTOSOL
0.0 ;% 457 MRNA_LOADING_RIBOSOME_CYTOSOL MRNA_LOADING_RIBOSOME_CYTOSOL
0.0 ;% 458 MRNA_LOADING_START_RIBOSOME_CYTOSOL MRNA_LOADING_START_RIBOSOME_CYTOSOL
0.0 ;% 459 LOADING_CYTOSOL LOADING_CYTOSOL
0.0 ;% 460 MRNA_TBX20_NUCLEAR MRNA_TBX20_NUCLEAR
0.0 ;% 461 MRNA_TBX20_NEXPORT_NUCLEAR MRNA_TBX20_NEXPORT_NUCLEAR
0.0 ;% 462 MRNA_TBX20_CYTOSOL MRNA_TBX20_CYTOSOL
0.0 ;% 463 MRNA_TBX20_RIBOSOME_CYTOSOL MRNA_TBX20_RIBOSOME_CYTOSOL
0.0 ;% 464 MRNA_TBX20_START_RIBOSOME_CYTOSOL MRNA_TBX20_START_RIBOSOME_CYTOSOL
0.0 ;% 465 TBX20_CYTOSOL TBX20_CYTOSOL
0.0 ;% 466 TWIST_NUCLEAR TWIST_NUCLEAR
0.0 ;% 467 DNA_TBX20_TWIST_NUCLEAR DNA_TBX20_TWIST_NUCLEAR
0.0 ;% 468 DNA_TBX20_TWIST_RNAP_NUCLEAR DNA_TBX20_TWIST_RNAP_NUCLEAR
0.0 ;% 469 TWIST_CYTOSOL TWIST_CYTOSOL
0.0 ;% 470 TWIST_NIMPORT_NUCLEAR TWIST_NIMPORT_NUCLEAR
0.0 ;% 471 TWIST_NEXPORT_NUCLEAR TWIST_NEXPORT_NUCLEAR
0.0 ;% 472 ACTIVE_NCID_CSL_NUCLEAR ACTIVE_NCID_CSL_NUCLEAR
0.0 ;% 473 DNA_PTEN_ACTIVE_NCID_CSL_NUCLEAR DNA_PTEN_ACTIVE_NCID_CSL_NUCLEAR
0.0 ;% 474 DNA_PTEN_ACTIVE_NCID_CSL_RNAP_NUCLEAR DNA_PTEN_ACTIVE_NCID_CSL_RNAP_NUCLEAR
0.0 ;% 475 ACTIVE_NCID_CSL_CYTOSOL ACTIVE_NCID_CSL_CYTOSOL
0.0 ;% 476 ACTIVE_NCID_CSL_NIMPORT_NUCLEAR ACTIVE_NCID_CSL_NIMPORT_NUCLEAR
0.0 ;% 477 ACTIVE_NCID_CSL_NEXPORT_NUCLEAR ACTIVE_NCID_CSL_NEXPORT_NUCLEAR
0.0 ;% 478 MRNA_ALPHASMA_NUCLEAR MRNA_ALPHASMA_NUCLEAR
0.0 ;% 479 MRNA_ALPHASMA_NEXPORT_NUCLEAR MRNA_ALPHASMA_NEXPORT_NUCLEAR
0.0 ;% 480 MRNA_ALPHASMA_CYTOSOL MRNA_ALPHASMA_CYTOSOL
0.0 ;% 481 MRNA_ALPHASMA_RIBOSOME_CYTOSOL MRNA_ALPHASMA_RIBOSOME_CYTOSOL
0.0 ;% 482 MRNA_ALPHASMA_START_RIBOSOME_CYTOSOL
MRNA_ALPHASMA_START_RIBOSOME_CYTOSOL
0.0 ;% 483 ALPHASMA_CYTOSOL ALPHASMA_CYTOSOL
0.0 ;% 484 BCATENIN_LEF1_NUCLEAR BCATENIN_LEF1_NUCLEAR
0.0 ;% 485 DNA_ALPHASMA_BCATENIN_LEF1_NUCLEAR DNA_ALPHASMA_BCATENIN_LEF1_NUCLEAR
0.0 ;% 486 DNA_ALPHASMA_BCATENIN_LEF1_RNAP_NUCLEAR
DNA_ALPHASMA_BCATENIN_LEF1_RNAP_NUCLEAR
0.0 ;% 487 LEF1_CYTOSOL LEF1_CYTOSOL
0.0 ;% 488 BCATENIN_LEF1_CYTOSOL BCATENIN_LEF1_CYTOSOL
0.0 ;% 489 BCATENIN_LEF1_NIMPORT_NUCLEAR BCATENIN_LEF1_NIMPORT_NUCLEAR
0.0 ;% 490 BCATENIN_LEF1_NEXPORT_NUCLEAR BCATENIN_LEF1_NEXPORT_NUCLEAR
0.0 ;% 491 DNA_ALPHASMA_ACTIVE_NCID_CSL_NUCLEAR DNA_ALPHASMA_ACTIVE_NCID_CSL_NUCLEAR
0.0 ;% 492 DNA_ALPHASMA_ACTIVE_NCID_CSL_RNAP_NUCLEAR
DNA_ALPHASMA_ACTIVE_NCID_CSL_RNAP_NUCLEAR
0.0 ;% 493 NFACT1_NUCLEAR NFACT1_NUCLEAR
0.0 ;% 494 DNA_VEGFR2_NFACT1_NUCLEAR DNA_VEGFR2_NFACT1_NUCLEAR
0.0 ;% 495 DNA_VEGFR2_NFACT1_RNAP_NUCLEAR DNA_VEGFR2_NFACT1_RNAP_NUCLEAR
0.0 ;% 496 NFACT1_CYTOSOL NFACT1_CYTOSOL
0.0 ;% 497 NFACT1_NIMPORT_NUCLEAR NFACT1_NIMPORT_NUCLEAR
0.0 ;% 498 NFACT1_NEXPORT_NUCLEAR NFACT1_NEXPORT_NUCLEAR
0.0 ;% 499 DNA_VEGFR2_ACTIVE_NCID_CSL_NUCLEAR DNA_VEGFR2_ACTIVE_NCID_CSL_NUCLEAR
0.0 ;% 500 DNA_VEGFR2_ACTIVE_NCID_CSL_RNAP_NUCLEAR
DNA_VEGFR2_ACTIVE_NCID_CSL_RNAP_NUCLEAR
0.0 ;% 501 MRNA_CYCLINB2_NUCLEAR MRNA_CYCLINB2_NUCLEAR
0.0 ;% 502 MRNA_CYCLINB2_NEXPORT_NUCLEAR MRNA_CYCLINB2_NEXPORT_NUCLEAR
0.0 ;% 503 MRNA_CYCLINB2_CYTOSOL MRNA_CYCLINB2_CYTOSOL
0.0 ;% 504 MRNA_CYCLINB2_RIBOSOME_CYTOSOL MRNA_CYCLINB2_RIBOSOME_CYTOSOL
0.0 ;% 505 MRNA_CYCLINB2_START_RIBOSOME_CYTOSOL MRNA_CYCLINB2_START_RIBOSOME_CYTOSOL
0.0 ;% 506 CYCLINB2_CYTOSOL CYCLINB2_CYTOSOL
0.0 ;% 507 TBX20_NUCLEAR TBX20_NUCLEAR
0.0 ;% 508 DNA_CYCLINB2_TBX20_NUCLEAR DNA_CYCLINB2_TBX20_NUCLEAR
0.0 ;% 509 DNA_CYCLINB2_TBX20_RNAP_NUCLEAR DNA_CYCLINB2_TBX20_RNAP_NUCLEAR
0.0 ;% 510 TBX20_NIMPORT_NUCLEAR TBX20_NIMPORT_NUCLEAR
0.0 ;% 511 TBX20_NEXPORT_NUCLEAR TBX20_NEXPORT_NUCLEAR
0.0 ;% 512 DNA_CYCLINB2_TWIST_NUCLEAR DNA_CYCLINB2_TWIST_NUCLEAR
0.0 ;% 513 DNA_CYCLINB2_TWIST_RNAP_NUCLEAR DNA_CYCLINB2_TWIST_RNAP_NUCLEAR
0.0 ;% 514 DNA_CYCLINB2_BCATENIN_LEF1_NUCLEAR DNA_CYCLINB2_BCATENIN_LEF1_NUCLEAR
0.0 ;% 515 DNA_CYCLINB2_BCATENIN_LEF1_RNAP_NUCLEAR
DNA_CYCLINB2_BCATENIN_LEF1_RNAP_NUCLEAR
0.0 ;% 516 NFATC1_NUCLEAR NFATC1_NUCLEAR
0.0 ;% 517 DNA_PECAM1_NFATC1_NUCLEAR DNA_PECAM1_NFATC1_NUCLEAR
0.0 ;% 518 DNA_PECAM1_NFATC1_RNAP_NUCLEAR DNA_PECAM1_NFATC1_RNAP_NUCLEAR
0.0 ;% 519 NFATC1_CYTOSOL NFATC1_CYTOSOL
0.0 ;% 520 NFATC1_NIMPORT_NUCLEAR NFATC1_NIMPORT_NUCLEAR
0.0 ;% 521 NFATC1_NEXPORT_NUCLEAR NFATC1_NEXPORT_NUCLEAR
0.0 ;% 522 P_AP1_NUCLEAR P_AP1_NUCLEAR
0.0 ;% 523 DNA_SLUG_P_AP1_NUCLEAR DNA_SLUG_P_AP1_NUCLEAR
0.0 ;% 524 DNA_SLUG_P_AP1_RNAP_NUCLEAR DNA_SLUG_P_AP1_RNAP_NUCLEAR
0.0 ;% 525 P_AP1_CYTOSOL P_AP1_CYTOSOL
0.0 ;% 526 P_AP1_NIMPORT_NUCLEAR P_AP1_NIMPORT_NUCLEAR
0.0 ;% 527 P_AP1_NEXPORT_NUCLEAR P_AP1_NEXPORT_NUCLEAR
0.0 ;% 528 P_SP1_NUCLEAR P_SP1_NUCLEAR
0.0 ;% 529 DNA_SLUG_P_SP1_NUCLEAR DNA_SLUG_P_SP1_NUCLEAR
0.0 ;% 530 DNA_SLUG_P_SP1_RNAP_NUCLEAR DNA_SLUG_P_SP1_RNAP_NUCLEAR
0.0 ;% 531 P_SP1_CYTOSOL P_SP1_CYTOSOL
0.0 ;% 532 P_SP1_NIMPORT_NUCLEAR P_SP1_NIMPORT_NUCLEAR
0.0 ;% 533 P_SP1_NEXPORT_NUCLEAR P_SP1_NEXPORT_NUCLEAR
0.0 ;% 534 BCATENIN_TCF4_NUCLEAR BCATENIN_TCF4_NUCLEAR
0.0 ;% 535 DNA_SLUG_BCATENIN_TCF4_NUCLEAR DNA_SLUG_BCATENIN_TCF4_NUCLEAR

0.0 ;% 536 DNA_SLUG_BCATENIN_TCF4_RNAP_NUCLEAR DNA_SLUG_BCATENIN_TCF4_RNAP_NUCLEAR
0.0 ;% 537 BCATENIN_TCF4_CYTOSOL BCATENIN_TCF4_CYTOSOL
0.0 ;% 538 BCATENIN_TCF4_NIMPORT_NUCLEAR BCATENIN_TCF4_NIMPORT_NUCLEAR
0.0 ;% 539 BCATENIN_TCF4_NEXPORT_NUCLEAR BCATENIN_TCF4_NEXPORT_NUCLEAR
0.0 ;% 540 DNA_SLUG_ACTIVE_NCID_CSL_NUCLEAR DNA_SLUG_ACTIVE_NCID_CSL_NUCLEAR
0.0 ;% 541 DNA_SLUG_ACTIVE_NCID_CSL_RNAP_NUCLEAR DNA_SLUG_ACTIVE_NCID_CSL_RNAP_NUCLEAR
0.0 ;% 542 DNA_SNAIL_P_AP1_NUCLEAR DNA_SNAIL_P_AP1_NUCLEAR
0.0 ;% 543 DNA_SNAIL_P_AP1_RNAP_NUCLEAR DNA_SNAIL_P_AP1_RNAP_NUCLEAR
0.0 ;% 544 DNA_SNAIL_P_SP1_NUCLEAR DNA_SNAIL_P_SP1_NUCLEAR
0.0 ;% 545 DNA_SNAIL_P_SP1_RNAP_NUCLEAR DNA_SNAIL_P_SP1_RNAP_NUCLEAR
0.0 ;% 546 DNA_SNAIL_BCATENIN_TCF4_NUCLEAR DNA_SNAIL_BCATENIN_TCF4_NUCLEAR
0.0 ;% 547 DNA_SNAIL_BCATENIN_TCF4_RNAP_NUCLEAR DNA_SNAIL_BCATENIN_TCF4_RNAP_NUCLEAR
0.0 ;% 548 DNA_SNAIL_ACTIVE_NCID_CSL_NUCLEAR DNA_SNAIL_ACTIVE_NCID_CSL_NUCLEAR
0.0 ;% 549 DNA_SNAIL_ACTIVE_NCID_CSL_RNAP_NUCLEAR DNA_SNAIL_ACTIVE_NCID_CSL_RNAP_NUCLEAR
0.0 ;% 550 MRNA_LEF1_NUCLEAR MRNA_LEF1_NUCLEAR
0.0 ;% 551 MRNA_LEF1_NEXPORT_NUCLEAR MRNA_LEF1_NEXPORT_NUCLEAR
0.0 ;% 552 MRNA_LEF1_CYTOSOL MRNA_LEF1_CYTOSOL
0.0 ;% 553 MRNA_LEF1_RIBOSOME_CYTOSOL MRNA_LEF1_RIBOSOME_CYTOSOL
0.0 ;% 554 MRNA_LEF1_START_RIBOSOME_CYTOSOL MRNA_LEF1_START_RIBOSOME_CYTOSOL
0.0 ;% 555 DNA_LEF1_P_SP1_NUCLEAR DNA_LEF1_P_SP1_NUCLEAR
0.0 ;% 556 DNA_LEF1_P_SP1_RNAP_NUCLEAR DNA_LEF1_P_SP1_RNAP_NUCLEAR
0.0 ;% 557 DNA_LEF1_P_AP1_NUCLEAR DNA_LEF1_P_AP1_NUCLEAR
0.0 ;% 558 DNA_LEF1_P_AP1_RNAP_NUCLEAR DNA_LEF1_P_AP1_RNAP_NUCLEAR
0.0 ;% 559 YREG1_NUCLEAR YREG1_NUCLEAR
0.0 ;% 560 DNA_LEF1_YREG1_NUCLEAR DNA_LEF1_YREG1_NUCLEAR
0.0 ;% 561 YREG1_NIMPORT_NUCLEAR YREG1_NIMPORT_NUCLEAR
0.0 ;% 562 YREG1_NEXPORT_NUCLEAR YREG1_NEXPORT_NUCLEAR
0.0 ;% 563 DNA_LEF1_BCATENIN_TCF4_NUCLEAR DNA_LEF1_BCATENIN_TCF4_NUCLEAR
0.0 ;% 564 DNA_LEF1_BCATENIN_TCF4_RNAP_NUCLEAR DNA_LEF1_BCATENIN_TCF4_RNAP_NUCLEAR
0.0 ;% 565 PSMAD2_SMAD4_NUCLEAR PSMAD2_SMAD4_NUCLEAR
0.0 ;% 566 DNA_LEF1_PSMAD2_SMAD4_NUCLEAR DNA_LEF1_PSMAD2_SMAD4_NUCLEAR
0.0 ;% 567 DNA_LEF1_PSMAD2_SMAD4_RNAP_NUCLEAR DNA_LEF1_PSMAD2_SMAD4_RNAP_NUCLEAR
0.0 ;% 568 PSMAD2_CYTOSOL PSMAD2_CYTOSOL
0.0 ;% 569 PSMAD2_SMAD4_CYTOSOL PSMAD2_SMAD4_CYTOSOL
0.0 ;% 570 PSMAD2_SMAD4_NIMPORT_NUCLEAR PSMAD2_SMAD4_NIMPORT_NUCLEAR
0.0 ;% 571 PSMAD2_SMAD4_NEXPORT_NUCLEAR PSMAD2_SMAD4_NEXPORT_NUCLEAR
0.0 ;% 572 PSMAD3_SMAD4_NUCLEAR PSMAD3_SMAD4_NUCLEAR
0.0 ;% 573 DNA_LEF1_PSMAD3_SMAD4_NUCLEAR DNA_LEF1_PSMAD3_SMAD4_NUCLEAR
0.0 ;% 574 DNA_LEF1_PSMAD3_SMAD4_RNAP_NUCLEAR DNA_LEF1_PSMAD3_SMAD4_RNAP_NUCLEAR
0.0 ;% 575 PSMAD3_CYTOSOL PSMAD3_CYTOSOL
0.0 ;% 576 PSMAD3_SMAD4_CYTOSOL PSMAD3_SMAD4_CYTOSOL
0.0 ;% 577 PSMAD3_SMAD4_NIMPORT_NUCLEAR PSMAD3_SMAD4_NIMPORT_NUCLEAR
0.0 ;% 578 PSMAD3_SMAD4_NEXPORT_NUCLEAR PSMAD3_SMAD4_NEXPORT_NUCLEAR
0.0 ;% 579 SNAIL_NUCLEAR SNAIL_NUCLEAR
0.0 ;% 580 DNA_YREG1_SNAIL_NUCLEAR DNA_YREG1_SNAIL_NUCLEAR
0.0 ;% 581 SNAIL_NIMPORT_NUCLEAR SNAIL_NIMPORT_NUCLEAR
0.0 ;% 582 SNAIL_NEXPORT_NUCLEAR SNAIL_NEXPORT_NUCLEAR
0.0 ;% 583 SLUG_NUCLEAR SLUG_NUCLEAR
0.0 ;% 584 DNA_YREG1_SLUG_NUCLEAR DNA_YREG1_SLUG_NUCLEAR
0.0 ;% 585 SLUG_NIMPORT_NUCLEAR SLUG_NIMPORT_NUCLEAR
0.0 ;% 586 SLUG_NEXPORT_NUCLEAR SLUG_NEXPORT_NUCLEAR
0.0 ;% 587 DNA_YREG1_TWIST_NUCLEAR DNA_YREG1_TWIST_NUCLEAR
0.0 ;% 588 DNA_TGFBRIII_P_SP1_NUCLEAR DNA_TGFBRIII_P_SP1_NUCLEAR
0.0 ;% 589 DNA_TGFBRIII_P_SP1_PSMAD3_SMAD4_NUCLEAR
DNA_TGFBRIII_P_SP1_PSMAD3_SMAD4_NUCLEAR
0.0 ;% 590 DNA_TGFBRIII_P_SP1_PSMAD3_SMAD4_RNAP_NUCLEAR
DNA_TGFBRIII_P_SP1_PSMAD3_SMAD4_RNAP_NUCLEAR
0.0 ;% 591 MRNA_CREB_NUCLEAR MRNA_CREB_NUCLEAR
0.0 ;% 592 MRNA_CREB_NEXPORT_NUCLEAR MRNA_CREB_NEXPORT_NUCLEAR
0.0 ;% 593 MRNA_CREB_CYTOSOL MRNA_CREB_CYTOSOL
0.0 ;% 594 MRNA_CREB_RIBOSOME_CYTOSOL MRNA_CREB_RIBOSOME_CYTOSOL
0.0 ;% 595 MRNA_CREB_START_RIBOSOME_CYTOSOL MRNA_CREB_START_RIBOSOME_CYTOSOL
0.0 ;% 596 CREB_CYTOSOL CREB_CYTOSOL
0.0 ;% 597 DNA_CREB_SNAIL_NUCLEAR DNA_CREB_SNAIL_NUCLEAR
0.0 ;% 598 DNA_CREB_SLUG_NUCLEAR DNA_CREB_SLUG_NUCLEAR
0.0 ;% 599 MRNA_TGFB3_NUCLEAR MRNA_TGFB3_NUCLEAR
0.0 ;% 600 MRNA_TGFB3_NEXPORT_NUCLEAR MRNA_TGFB3_NEXPORT_NUCLEAR
0.0 ;% 601 MRNA_TGFB3_CYTOSOL MRNA_TGFB3_CYTOSOL
0.0 ;% 602 MRNA_TGFB3_RIBOSOME_CYTOSOL MRNA_TGFB3_RIBOSOME_CYTOSOL
0.0 ;% 603 MRNA_TGFB3_START_RIBOSOME_CYTOSOL MRNA_TGFB3_START_RIBOSOME_CYTOSOL
0.0 ;% 604 DNA_TGFB3_YREG1_NUCLEAR DNA_TGFB3_YREG1_NUCLEAR
0.0 ;% 605 DNA_TGFB3_SNAIL_NUCLEAR DNA_TGFB3_SNAIL_NUCLEAR
0.0 ;% 606 DNA_TGFB3_SNAIL_BCATENIN_TCF4_NUCLEAR DNA_TGFB3_SNAIL_BCATENIN_TCF4_NUCLEAR
0.0 ;% 607 DNA_TGFB3_SNAIL_BCATENIN_TCF4_RNAP_NUCLEAR
DNA_TGFB3_SNAIL_BCATENIN_TCF4_RNAP_NUCLEAR
0.0 ;% 608 DNA_TGFB3_SLUG_NUCLEAR DNA_TGFB3_SLUG_NUCLEAR
0.0 ;% 609 DNA_TGFB3_SLUG_BCATENIN_TCF4_NUCLEAR DNA_TGFB3_SLUG_BCATENIN_TCF4_NUCLEAR
0.0 ;% 610 DNA_TGFB3_SLUG_BCATENIN_TCF4_RNAP_NUCLEAR
DNA_TGFB3_SLUG_BCATENIN_TCF4_RNAP_NUCLEAR
0.0 ;% 611 MRNA_TGFB2_NUCLEAR MRNA_TGFB2_NUCLEAR
0.0 ;% 612 MRNA_TGFB2_NEXPORT_NUCLEAR MRNA_TGFB2_NEXPORT_NUCLEAR
0.0 ;% 613 MRNA_TGFB2_CYTOSOL MRNA_TGFB2_CYTOSOL
0.0 ;% 614 MRNA_TGFB2_RIBOSOME_CYTOSOL MRNA_TGFB2_RIBOSOME_CYTOSOL
0.0 ;% 615 MRNA_TGFB2_START_RIBOSOME_CYTOSOL MRNA_TGFB2_START_RIBOSOME_CYTOSOL
0.0 ;% 616 PAX3_NUCLEAR PAX3_NUCLEAR
0.0 ;% 617 DNA_TGFB2_PAX3_NUCLEAR DNA_TGFB2_PAX3_NUCLEAR
0.0 ;% 618 PSMAD1_SMAD4_NUCLEAR PSMAD1_SMAD4_NUCLEAR
0.0 ;% 619 DNA_TGFB2_PAX3_PSMAD1_SMAD4_NUCLEAR DNA_TGFB2_PAX3_PSMAD1_SMAD4_NUCLEAR
0.0 ;% 620 DNA_TGFB2_PAX3_PSMAD1_SMAD4_RNAP_NUCLEAR
DNA_TGFB2_PAX3_PSMAD1_SMAD4_RNAP_NUCLEAR
0.0 ;% 621 PAX3_CYTOSOL PAX3_CYTOSOL
0.0 ;% 622 PAX3_NIMPORT_NUCLEAR PAX3_NIMPORT_NUCLEAR
0.0 ;% 623 PAX3_NEXPORT_NUCLEAR PAX3_NEXPORT_NUCLEAR

0.0 ;% 624 PSMAD1_CYTOSOL PSMAD1_CYTOSOL
0.0 ;% 625 PSMAD1_SMAD4_CYTOSOL PSMAD1_SMAD4_CYTOSOL
0.0 ;% 626 PSMAD1_SMAD4_NIMPORT_NUCLEAR PSMAD1_SMAD4_NIMPORT_NUCLEAR
0.0 ;% 627 PSMAD1_SMAD4_NEXPORT_NUCLEAR PSMAD1_SMAD4_NEXPORT_NUCLEAR
0.0 ;% 628 MRNA_VIMENTIN_NUCLEAR MRNA_VIMENTIN_NUCLEAR
0.0 ;% 629 MRNA_VIMENTIN_NEXPORT_NUCLEAR MRNA_VIMENTIN_NEXPORT_NUCLEAR
0.0 ;% 630 MRNA_VIMENTIN_CYTOSOL MRNA_VIMENTIN_CYTOSOL
0.0 ;% 631 MRNA_VIMENTIN_RIBOSOME_CYTOSOL MRNA_VIMENTIN_RIBOSOME_CYTOSOL
0.0 ;% 632 MRNA_VIMENTIN_START_RIBOSOME_CYTOSOL MRNA_VIMENTIN_START_RIBOSOME_CYTOSOL
0.0 ;% 633 VIMENTIN_CYTOSOL VIMENTIN_CYTOSOL
0.0 ;% 634 DNA_VIMENTIN_BCATENIN_LEF1_NUCLEAR DNA_VIMENTIN_BCATENIN_LEF1_NUCLEAR
0.0 ;% 635 DNA_VIMENTIN_BCATENIN_LEF1_RNAP_NUCLEAR
DNA_VIMENTIN_BCATENIN_LEF1_RNAP_NUCLEAR
0.0 ;% 636 LEF1_NUCLEAR LEF1_NUCLEAR
0.0 ;% 637 DNA_VIMENTIN_LEF1_NUCLEAR DNA_VIMENTIN_LEF1_NUCLEAR
0.0 ;% 638 DNA_VIMENTIN_LEF1_PSMAD2_SMAD4_NUCLEAR
DNA_VIMENTIN_LEF1_PSMAD2_SMAD4_NUCLEAR
0.0 ;% 639 DNA_VIMENTIN_LEF1_PSMAD2_SMAD4_RNAP_NUCLEAR
DNA_VIMENTIN_LEF1_PSMAD2_SMAD4_RNAP_NUCLEAR
0.0 ;% 640 LEF1_NIMPORT_NUCLEAR LEF1_NIMPORT_NUCLEAR
0.0 ;% 641 LEF1_NEXPORT_NUCLEAR LEF1_NEXPORT_NUCLEAR
0.0 ;% 642 DNA_VIMENTIN_LEF1_PSMAD3_SMAD4_NUCLEAR
DNA_VIMENTIN_LEF1_PSMAD3_SMAD4_NUCLEAR
0.0 ;% 643 DNA_VIMENTIN_LEF1_PSMAD3_SMAD4_RNAP_NUCLEAR
DNA_VIMENTIN_LEF1_PSMAD3_SMAD4_RNAP_NUCLEAR
0.0 ;% 644 DNA_ECADHERIN_NFATC1_NUCLEAR DNA_ECADHERIN_NFATC1_NUCLEAR
0.0 ;% 645 DNA_ECADHERIN_NFATC1_RNAP_NUCLEAR DNA_ECADHERIN_NFATC1_RNAP_NUCLEAR
0.0 ;% 646 DNA_ECADHERIN_SNAIL_NUCLEAR DNA_ECADHERIN_SNAIL_NUCLEAR
0.0 ;% 647 DNA_ECADHERIN_SLUG_NUCLEAR DNA_ECADHERIN_SLUG_NUCLEAR
0.0 ;% 648 DNA_ECADHERIN_TWIST_NUCLEAR DNA_ECADHERIN_TWIST_NUCLEAR
0.0 ;% 649 PSMAD2_SMAD4_LEF1_NUCLEAR PSMAD2_SMAD4_LEF1_NUCLEAR
0.0 ;% 650 DNA_ECADHERIN_PSMAD2_SMAD4_LEF1_NUCLEAR
DNA_ECADHERIN_PSMAD2_SMAD4_LEF1_NUCLEAR
0.0 ;% 651 PSMAD2_SMAD4_LEF1_CYTOSOL PSMAD2_SMAD4_LEF1_CYTOSOL
0.0 ;% 652 PSMAD2_SMAD4_LEF1_NIMPORT_NUCLEAR PSMAD2_SMAD4_LEF1_NIMPORT_NUCLEAR
0.0 ;% 653 PSMAD2_SMAD4_LEF1_NEXPORT_NUCLEAR PSMAD2_SMAD4_LEF1_NEXPORT_NUCLEAR
0.0 ;% 654 DNA_VECADHERIN_NFATC1_NUCLEAR DNA_VECADHERIN_NFATC1_NUCLEAR
0.0 ;% 655 DNA_VECADHERIN_NFATC1_RNAP_NUCLEAR DNA_VECADHERIN_NFATC1_RNAP_NUCLEAR
0.0 ;% 656 DNA_VECADHERIN_SNAIL_NUCLEAR DNA_VECADHERIN_SNAIL_NUCLEAR
0.0 ;% 657 DNA_VECADHERIN_SLUG_NUCLEAR DNA_VECADHERIN_SLUG_NUCLEAR
0.0 ;% 658 DNA_VECADHERIN_TWIST_NUCLEAR DNA_VECADHERIN_TWIST_NUCLEAR
0.0 ;% 659 DNA_VECADHERIN_LEF1_NUCLEAR DNA_VECADHERIN_LEF1_NUCLEAR
0.0 ;% 660 MRNA_DSCR1_NUCLEAR MRNA_DSCR1_NUCLEAR
0.0 ;% 661 MRNA_DSCR1_NEXPORT_NUCLEAR MRNA_DSCR1_NEXPORT_NUCLEAR
0.0 ;% 662 MRNA_DSCR1_CYTOSOL MRNA_DSCR1_CYTOSOL
0.0 ;% 663 MRNA_DSCR1_RIBOSOME_CYTOSOL MRNA_DSCR1_RIBOSOME_CYTOSOL
0.0 ;% 664 MRNA_DSCR1_START_RIBOSOME_CYTOSOL MRNA_DSCR1_START_RIBOSOME_CYTOSOL
0.0 ;% 665 _CYTOSOL DSCR1_CYTOSOL
0.0 ;% 666 DNA_DSCR1_NFATC1_NUCLEAR DNA_DSCR1_NFATC1_NUCLEAR
0.0 ;% 667 DNA_DSCR1_NFATC1_RNAP_NUCLEAR DNA_DSCR1_NFATC1_RNAP_NUCLEAR
0.0 ;% 668 MRNA_SOX9_NUCLEAR MRNA_SOX9_NUCLEAR
0.0 ;% 669 MRNA_SOX9_NEXPORT_NUCLEAR MRNA_SOX9_NEXPORT_NUCLEAR
0.0 ;% 670 MRNA_SOX9_CYTOSOL MRNA_SOX9_CYTOSOL
0.0 ;% 671 MRNA_SOX9_RIBOSOME_CYTOSOL MRNA_SOX9_RIBOSOME_CYTOSOL
0.0 ;% 672 MRNA_SOX9_START_RIBOSOME_CYTOSOL MRNA_SOX9_START_RIBOSOME_CYTOSOL
0.0 ;% 673 SOX9_CYTOSOL SOX9_CYTOSOL
0.0 ;% 674 GATA_FOG2_NUCLEAR GATA_FOG2_NUCLEAR
0.0 ;% 675 DNA_SOX9_GATA_FOG2_NUCLEAR DNA_SOX9_GATA_FOG2_NUCLEAR
0.0 ;% 676 PSMAD5_SMAD4_NUCLEAR PSMAD5_SMAD4_NUCLEAR
0.0 ;% 677 DNA_SOX9_GATA_FOG2_PSMAD5_SMAD4_NUCLEAR
DNA_SOX9_GATA_FOG2_PSMAD5_SMAD4_NUCLEAR
0.0 ;% 678 DNA_SOX9_GATA_FOG2_PSMAD5_SMAD4_RNAP_NUCLEAR
DNA_SOX9_GATA_FOG2_PSMAD5_SMAD4_RNAP_NUCLEAR
0.0 ;% 679 GATA_FOG2_NIMPORT_NUCLEAR GATA_FOG2_NIMPORT_NUCLEAR
0.0 ;% 680 GATA_FOG2_NEXPORT_NUCLEAR GATA_FOG2_NEXPORT_NUCLEAR
0.0 ;% 681 PSMAD5_CYTOSOL PSMAD5_CYTOSOL
0.0 ;% 682 PSMAD5_SMAD4_CYTOSOL PSMAD5_SMAD4_CYTOSOL
0.0 ;% 683 PSMAD5_SMAD4_NIMPORT_NUCLEAR PSMAD5_SMAD4_NIMPORT_NUCLEAR
0.0 ;% 684 PSMAD5_SMAD4_NEXPORT_NUCLEAR PSMAD5_SMAD4_NEXPORT_NUCLEAR
0.0 ;% 685 MRNA_PAX3_NUCLEAR MRNA_PAX3_NUCLEAR
0.0 ;% 686 MRNA_PAX3_NEXPORT_NUCLEAR MRNA_PAX3_NEXPORT_NUCLEAR
0.0 ;% 687 MRNA_PAX3_CYTOSOL MRNA_PAX3_CYTOSOL
0.0 ;% 688 MRNA_PAX3_RIBOSOME_CYTOSOL MRNA_PAX3_RIBOSOME_CYTOSOL
0.0 ;% 689 MRNA_PAX3_START_RIBOSOME_CYTOSOL MRNA_PAX3_START_RIBOSOME_CYTOSOL
0.0 ;% 690 DNA_PAX3_PSMAD1_SMAD4_NUCLEAR DNA_PAX3_PSMAD1_SMAD4_NUCLEAR
0.0 ;% 691 DNA_PAX3_PSMAD1_SMAD4_RNAP_NUCLEAR DNA_PAX3_PSMAD1_SMAD4_RNAP_NUCLEAR
0.0 ;% 692 MRNA_MMP9_NUCLEAR MRNA_MMP9_NUCLEAR
0.0 ;% 693 MRNA_MMP9_NEXPORT_NUCLEAR MRNA_MMP9_NEXPORT_NUCLEAR
0.0 ;% 694 MRNA_MMP9_CYTOSOL MRNA_MMP9_CYTOSOL
0.0 ;% 695 MRNA_MMP9_RIBOSOME_CYTOSOL MRNA_MMP9_RIBOSOME_CYTOSOL
0.0 ;% 696 MRNA_MMP9_START_RIBOSOME_CYTOSOL MRNA_MMP9_START_RIBOSOME_CYTOSOL
0.0 ;% 697 MMP9_CYTOSOL MMP9_CYTOSOL
0.0 ;% 698 DNA_MMP9_P_AP1_NUCLEAR DNA_MMP9_P_AP1_NUCLEAR
0.0 ;% 699 DNA_MMP9_P_AP1_RNAP_NUCLEAR DNA_MMP9_P_AP1_RNAP_NUCLEAR
0.0 ;% 700 DNA_MMP9_TBX20_NUCLEAR DNA_MMP9_TBX20_NUCLEAR
0.0 ;% 701 DNA_MMP9_TBX20_PSMAD5_SMAD4_NUCLEAR DNA_MMP9_TBX20_PSMAD5_SMAD4_NUCLEAR
0.0 ;% 702 DNA_MMP9_TBX20_PSMAD5_SMAD4_RNAP_NUCLEAR
DNA_MMP9_TBX20_PSMAD5_SMAD4_RNAP_NUCLEAR
0.0 ;% 703 MRNA_NFATC1_NUCLEAR MRNA_NFATC1_NUCLEAR
0.0 ;% 704 MRNA_NFATC1_NEXPORT_NUCLEAR MRNA_NFATC1_NEXPORT_NUCLEAR
0.0 ;% 705 MRNA_NFATC1_CYTOSOL MRNA_NFATC1_CYTOSOL
0.0 ;% 706 MRNA_NFATC1_RIBOSOME_CYTOSOL MRNA_NFATC1_RIBOSOME_CYTOSOL
0.0 ;% 707 MRNA_NFATC1_START_RIBOSOME_CYTOSOL MRNA_NFATC1_START_RIBOSOME_CYTOSOL

0.0 ;% 708 DNA_NFATC1_P_AP1_NUCLEAR DNA_NFATC1_P_AP1_NUCLEAR
0.0 ;% 709 DNA_NFATC1_P_AP1_RNAP_NUCLEAR DNA_NFATC1_P_AP1_RNAP_NUCLEAR
0.0 ;% 710 DNA_NFATC1_P_SP1_NUCLEAR DNA_NFATC1_P_SP1_NUCLEAR
0.0 ;% 711 DNA_NFATC1_P_SP1_RNAP_NUCLEAR DNA_NFATC1_P_SP1_RNAP_NUCLEAR
0.0 ;% 712 DNA_NFATC1_PSMAD2_SMAD4_NUCLEAR DNA_NFATC1_PSMAD2_SMAD4_NUCLEAR
0.0 ;% 713 DNA_NFATC1_PSMAD2_SMAD4_RNAP_NUCLEAR DNA_NFATC1_PSMAD2_SMAD4_RNAP_NUCLEAR
0.0 ;% 714 DNA_NFATC1_PSMAD3_SMAD4_NUCLEAR DNA_NFATC1_PSMAD3_SMAD4_NUCLEAR
0.0 ;% 715 DNA_NFATC1_PSMAD3_SMAD4_RNAP_NUCLEAR DNA_NFATC1_PSMAD3_SMAD4_RNAP_NUCLEAR
0.0 ;% 716 MSX1_NUCLEAR MSX1_NUCLEAR
0.0 ;% 717 DNA_NFATC1_MSX1_NUCLEAR DNA_NFATC1_MSX1_NUCLEAR
0.0 ;% 718 DNA_NFATC1_MSX1_PSMAD5_SMAD4_NUCLEAR DNA_NFATC1_MSX1_PSMAD5_SMAD4_NUCLEAR
0.0 ;% 719 DNA_NFATC1_MSX1_PSMAD5_SMAD4_RNAP_NUCLEAR
DNA_NFATC1_MSX1_PSMAD5_SMAD4_RNAP_NUCLEAR
0.0 ;% 720 MSX1_NIMPORT_NUCLEAR MSX1_NIMPORT_NUCLEAR
0.0 ;% 721 MSX1_NEXPORT_NUCLEAR MSX1_NEXPORT_NUCLEAR
0.0 ;% 722 MRNA_CALCNCAM_NUCLEAR MRNA_CALCNCAM_NUCLEAR
0.0 ;% 723 MRNA_CALCNCAM_NEXPORT_NUCLEAR MRNA_CALCNCAM_NEXPORT_NUCLEAR
0.0 ;% 724 MRNA_CALCNCAM_CYTOSOL MRNA_CALCNCAM_CYTOSOL
0.0 ;% 725 MRNA_CALCNCAM_RIBOSOME_CYTOSOL MRNA_CALCNCAM_RIBOSOME_CYTOSOL
0.0 ;% 726 MRNA_CALCNCAM_START_RIBOSOME_CYTOSOL
MRNA_CALCNCAM_START_RIBOSOME_CYTOSOL
0.0 ;% 727 CALCNCAM_CYTOSOL CALCNCAM_CYTOSOL
0.0 ;% 728 DNA_CALCNCAM_ACTIVE_NCID_CSL_NUCLEAR DNA_CALCNCAM_ACTIVE_NCID_CSL_NUCLEAR
0.0 ;% 729 DNA_CALCNCAM_ACTIVE_NCID_CSL_RNAP_NUCLEAR
DNA_CALCNCAM_ACTIVE_NCID_CSL_RNAP_NUCLEAR
0.0 ;% 730 MRNA_TWIST_NUCLEAR MRNA_TWIST_NUCLEAR
0.0 ;% 731 MRNA_TWIST_NEXPORT_NUCLEAR MRNA_TWIST_NEXPORT_NUCLEAR
0.0 ;% 732 MRNA_TWIST_CYTOSOL MRNA_TWIST_CYTOSOL
0.0 ;% 733 MRNA_TWIST_RIBOSOME_CYTOSOL MRNA_TWIST_RIBOSOME_CYTOSOL
0.0 ;% 734 MRNA_TWIST_START_RIBOSOME_CYTOSOL MRNA_TWIST_START_RIBOSOME_CYTOSOL
0.0 ;% 735 DNA_TWIST_PSMAD1_SMAD4_NUCLEAR DNA_TWIST_PSMAD1_SMAD4_NUCLEAR
0.0 ;% 736 DNA_TWIST_PSMAD1_SMAD4_RNAP_NUCLEAR DNA_TWIST_PSMAD1_SMAD4_RNAP_NUCLEAR
0.0 ;% 737 DNA_TWIST_PSMAD5_SMAD4_NUCLEAR DNA_TWIST_PSMAD5_SMAD4_NUCLEAR
0.0 ;% 738 DNA_TWIST_PSMAD5_SMAD4_RNAP_NUCLEAR DNA_TWIST_PSMAD5_SMAD4_RNAP_NUCLEAR
0.0 ;% 739 WNT9A_FRIZZLED_CYTOSOL WNT9A_FRIZZLED_CYTOSOL
0.0 ;% 740 WNT9A_FRIZZLED_DISHEVELLED_CYTOSOL WNT9A_FRIZZLED_DISHEVELLED_CYTOSOL
0.0 ;% 741 WNT9A_FRIZZLED_DISHEVELLED_LRP_CYTOSOL
WNT9A_FRIZZLED_DISHEVELLED_LRP_CYTOSOL
0.0 ;% 742 WNT9A_FRIZZLED_DISHEVELLED_LRP_AXIN_CYTOSOL
WNT9A_FRIZZLED_DISHEVELLED_LRP_AXIN_CYTOSOL
0.0 ;% 743 VEGFA_VEGFR2_CYTOSOL VEGFA_VEGFR2_CYTOSOL
0.0 ;% 744 VEGFA_VEGFR2_SHC_CYTOSOL VEGFA_VEGFR2_SHC_CYTOSOL
0.0 ;% 745 BMP2_BMPRII_CYTOSOL BMP2_BMPRII_CYTOSOL
0.0 ;% 746 BMP2_BMPRII_ALK2_CYTOSOL BMP2_BMPRII_ALK2_CYTOSOL
0.0 ;% 747 BMP2_BMPRII_ALK3_CYTOSOL BMP2_BMPRII_ALK3_CYTOSOL
0.0 ;% 748 BMP2_BMPRII_ALK6_CYTOSOL BMP2_BMPRII_ALK6_CYTOSOL
0.0 ;% 749 BMP2_BMPRII_ALK2_SHC_CYTOSOL BMP2_BMPRII_ALK2_SHC_CYTOSOL
0.0 ;% 750 BMP2_BMPRII_ALK2_SHC_GRB2_CYTOSOL BMP2_BMPRII_ALK2_SHC_GRB2_CYTOSOL
0.0 ;% 751 BMP2_BMPRII_ALK2_SHC_GRB2_SOS_CYTOSOL BMP2_BMPRII_ALK2_SHC_GRB2_SOS_CYTOSOL
0.0 ;% 752 TGFB2_BMPRII_CYTOSOL TGFB2_BMPRII_CYTOSOL
0.0 ;% 753 TGFB2_BMPRII_ALK2_CYTOSOL TGFB2_BMPRII_ALK2_CYTOSOL
0.0 ;% 754 TGFB2_BMPRII_ALK2_ENDOGLIN_CYTOSOL TGFB2_BMPRII_ALK2_ENDOGLIN_CYTOSOL
0.0 ;% 755 TGFB2_BMPRII_ALK2_ENDOGLIN_SHC_CYTOSOL
TGFB2_BMPRII_ALK2_ENDOGLIN_SHC_CYTOSOL
0.0 ;% 756 TGFB2_BMPRII_ALK2_ENDOGLIN_SHC_GRB2_CYTOSOL
TGFB2_BMPRII_ALK2_ENDOGLIN_SHC_GRB2_CYTOSOL
0.0 ;% 757 TGFB2_BMPRII_ALK2_ENDOGLIN_SHC_GRB2_SOS_CYTOSOL
TGFB2_BMPRII_ALK2_ENDOGLIN_SHC_GRB2_SOS_CYTOSOL
0.0 ;% 758 TGFB3_TGFBRII_CYTOSOL TGFB3_TGFBRII_CYTOSOL
0.0 ;% 759 TGFB3_TGFBRII_ALK1_CYTOSOL TGFB3_TGFBRII_ALK1_CYTOSOL
0.0 ;% 760 TGFB3_TGFBRII_ALK1_TGFBRIII_CYTOSOL TGFB3_TGFBRII_ALK1_TGFBRIII_CYTOSOL
0.0 ;% 761 TGFB3_TGFBRII_ALK5_CYTOSOL TGFB3_TGFBRII_ALK5_CYTOSOL
0.0 ;% 762 TGFB3_TGFBRII_ALK5_TGFBRIII_CYTOSOL TGFB3_TGFBRII_ALK5_TGFBRIII_CYTOSOL
0.0 ;% 763 TGFB3_TGFBRII_ALK5_TGFBRIII_ENDOGLIN_CYTOSOL
TGFB3_TGFBRII_ALK5_TGFBRIII_ENDOGLIN_CYTOSOL
0.0 ;% 764 TGFB2_TGFBRII_CYTOSOL TGFB2_TGFBRII_CYTOSOL
0.0 ;% 765 TGFB2_TGFBRII_ALK1_CYTOSOL TGFB2_TGFBRII_ALK1_CYTOSOL
0.0 ;% 766 TGFB2_TGFBRII_ALK1_TGFBRIII_CYTOSOL TGFB2_TGFBRII_ALK1_TGFBRIII_CYTOSOL
0.0 ;% 767 TGFB2_TGFBRII_ALK5_CYTOSOL TGFB2_TGFBRII_ALK5_CYTOSOL
0.0 ;% 768 TGFB2_TGFBRII_ALK5_TGFBRIII_CYTOSOL TGFB2_TGFBRII_ALK5_TGFBRIII_CYTOSOL
0.0 ;% 769 TGFB2_TGFBRII_ALK5_TGFBRIII_ENDOGLIN_CYTOSOL
TGFB2_TGFBRII_ALK5_TGFBRIII_ENDOGLIN_CYTOSOL
0.0 ;% 770 JAG1_NOTCH1_CYTOSOL JAG1_NOTCH1_CYTOSOL
0.0 ;% 771 TACE_CYTOSOL TACE_CYTOSOL
0.0 ;% 772 JAG1_NOTCH1_TACE_CYTOSOL JAG1_NOTCH1_TACE_CYTOSOL
0.0 ;% 773 DELTA4_NOTCH1_CYTOSOL DELTA4_NOTCH1_CYTOSOL
0.0 ;% 774 DELTA4_NOTCH1_TACE_CYTOSOL DELTA4_NOTCH1_TACE_CYTOSOL
0.0 ;% 775 ACTIVE_PI3K_CYTOSOL ACTIVE_PI3K_CYTOSOL
0.0 ;% 776 ACTIVE_PI3K_PIP2_CYTOSOL ACTIVE_PI3K_PIP2_CYTOSOL
0.0 ;% 777 PTEN_PIP3_CYTOSOL PTEN_PIP3_CYTOSOL
0.0 ;% 778 PDK1_PIP3_CYTOSOL PDK1_PIP3_CYTOSOL
0.0 ;% 779 PDK1_PIP3_AKT_CYTOSOL PDK1_PIP3_AKT_CYTOSOL
0.0 ;% 780 ACTIVE_AKT_CYTOSOL ACTIVE_AKT_CYTOSOL
0.0 ;% 781 ACTIVE_AKT_GSK3B_CYTOSOL ACTIVE_AKT_GSK3B_CYTOSOL
0.0 ;% 782 P_GSK3B_CYTOSOL P_GSK3B_CYTOSOL
0.0 ;% 783 AKT_PASE_ACTIVE_PI3K_CYTOSOL AKT_PASE_ACTIVE_PI3K_CYTOSOL
0.0 ;% 784 AKT_PASE_ACTIVE_AKT_CYTOSOL AKT_PASE_ACTIVE_AKT_CYTOSOL
0.0 ;% 785 AKT_PASE_P_GSK3B_CYTOSOL AKT_PASE_P_GSK3B_CYTOSOL
0.0 ;% 786 AXIN_BCATENIN_CYTOSOL AXIN_BCATENIN_CYTOSOL
0.0 ;% 787 AXIN_BCATENIN_APC_CYTOSOL AXIN_BCATENIN_APC_CYTOSOL
0.0 ;% 788 AXIN_BCATENIN_APC_CK1_CYTOSOL AXIN_BCATENIN_APC_CK1_CYTOSOL
0.0 ;% 789 AXIN_BCATENIN_APC_GSK3B_CYTOSOL AXIN_BCATENIN_APC_GSK3B_CYTOSOL
0.0 ;% 790 PP_BCATENIN_CYTOSOL PP_BCATENIN_CYTOSOL

0.0 ;% 791 PP_BCATENIN_BTRCP_CYTOSOL PP_BCATENIN_BTRCP_CYTOSOL
0.0 ;% 792 UB_PP_BCATENIN_CYTOSOL UB_PP_BCATENIN_CYTOSOL
0.0 ;% 793 GSK3B_NFATC1_CYTOSOL GSK3B_NFATC1_CYTOSOL
0.0 ;% 794 P_NFATC1_CYTOSOL P_NFATC1_CYTOSOL
0.0 ;% 795 JAG1_NCED_CYTOSOL JAG1_NCED_CYTOSOL
0.0 ;% 796 DELTA4_NCED_CYTOSOL DELTA4_NCED_CYTOSOL
0.0 ;% 797 ACTIVE_NCID_SEL1_CYTOSOL ACTIVE_NCID_SEL1_CYTOSOL
0.0 ;% 798 UB_ACTIVE_NCID_CYTOSOL UB_ACTIVE_NCID_CYTOSOL
0.0 ;% 799 JAG1_NCED_DELTEX_NEDD4_CYTOSOL JAG1_NCED_DELTEX_NEDD4_CYTOSOL
0.0 ;% 800 UB_JAG1_NCED_CYTOSOL UB_JAG1_NCED_CYTOSOL
0.0 ;% 801 DELTA4_NCED_DELTEX_NEDD4_CYTOSOL DELTA4_NCED_DELTEX_NEDD4_CYTOSOL
0.0 ;% 802 UB_DELTA4_NCED_CYTOSOL UB_DELTA4_NCED_CYTOSOL
0.0 ;% 803 UB_JAG1_NECD_CYTOSOL UB_JAG1_NECD_CYTOSOL
0.0 ;% 804 UB_DELTA4_NECD_CYTOSOL UB_DELTA4_NECD_CYTOSOL
0.0 ;% 805 JAG1_NECD_EXTRACELLULAR JAG1_NECD_EXTRACELLULAR
0.0 ;% 806 RAS_GDP_CYTOSOL RAS_GDP_CYTOSOL
0.0 ;% 807 TGFB2_BMPRII_ALK2_ENDOGLIN_SHC_GRB2_SOS_RAS_GDP_CYTOSOL
TGFB2_BMPRII_ALK2_ENDOGLIN_SHC_GRB2_SOS_RAS_GDP_CYTOSOL
0.0 ;% 808 RAS_GTP_CYTOSOL RAS_GTP_CYTOSOL
0.0 ;% 809 BMP2_BMPRII_ALK2_SHC_GRB2_SOS_RAS_GDP_CYTOSOL
BMP2_BMPRII_ALK2_SHC_GRB2_SOS_RAS_GDP_CYTOSOL
0.0 ;% 810 RAS_GTP_RAF_CYTOSOL RAS_GTP_RAF_CYTOSOL
0.0 ;% 811 ACTIVE_RAF_CYTOSOL ACTIVE_RAF_CYTOSOL
0.0 ;% 812 ACTIVE_RAF_MEK_CYTOSOL ACTIVE_RAF_MEK_CYTOSOL
0.0 ;% 813 P_MEK_CYTOSOL P_MEK_CYTOSOL
0.0 ;% 814 ACTIVE_RAF_P_MEK_CYTOSOL ACTIVE_RAF_P_MEK_CYTOSOL
0.0 ;% 815 PP_MEK_CYTOSOL PP_MEK_CYTOSOL
0.0 ;% 816 PP_MEK_ERK_CYTOSOL PP_MEK_ERK_CYTOSOL
0.0 ;% 817 P_ERK_CYTOSOL P_ERK_CYTOSOL
0.0 ;% 818 PP_MEK_P_ERK_CYTOSOL PP_MEK_P_ERK_CYTOSOL
0.0 ;% 819 PP_ERK_CYTOSOL PP_ERK_CYTOSOL
0.0 ;% 820 ACTIVE_RAF_RAF_PASE_CYTOSOL ACTIVE_RAF_RAF_PASE_CYTOSOL
0.0 ;% 821 PP_MEK_MEK_PASE_CYTOSOL PP_MEK_MEK_PASE_CYTOSOL
0.0 ;% 822 P_MEK_MEK_PASE_CYTOSOL P_MEK_MEK_PASE_CYTOSOL
0.0 ;% 823 PP_ERK_ERK_PASE_CYTOSOL PP_ERK_ERK_PASE_CYTOSOL
0.0 ;% 824 P_ERK_ERK_PASE_CYTOSOL P_ERK_ERK_PASE_CYTOSOL
0.0 ;% 825 TGFB2_BMPRII_ALK2_ENDOGLIN_SHC_GRB2_SOS_PP_ERK_CYTOSOL
TGFB2_BMPRII_ALK2_ENDOGLIN_SHC_GRB2_SOS_PP_ERK_CYTOSOL
0.0 ;% 826 BMP2_BMPRII_ALK2_SHC_GRB2_SOS_PP_ERK_CYTOSOL
BMP2_BMPRII_ALK2_SHC_GRB2_SOS_PP_ERK_CYTOSOL
0.0 ;% 827 PP_ERK_AP1_CYTOSOL PP_ERK_AP1_CYTOSOL
0.0 ;% 828 PP_ERK_SP1_CYTOSOL PP_ERK_SP1_CYTOSOL
0.0 ;% 829 PP_ERK_CJUN_CYTOSOL PP_ERK_CJUN_CYTOSOL
0.0 ;% 830 P_CJUN_CYTOSOL P_CJUN_CYTOSOL
0.0 ;% 831 PP_ERK_CPLA2_CYTOSOL PP_ERK_CPLA2_CYTOSOL
0.0 ;% 832 P_CPLA2_CYTOSOL P_CPLA2_CYTOSOL
0.0 ;% 833 PP_ERK_SMAD2_CYTOSOL PP_ERK_SMAD2_CYTOSOL
0.0 ;% 834 P_SMAD2_CYTOSOL P_SMAD2_CYTOSOL
0.0 ;% 835 PP_ERK_SMAD3_CYTOSOL PP_ERK_SMAD3_CYTOSOL
0.0 ;% 836 P_SMAD3_CYTOSOL P_SMAD3_CYTOSOL
0.0 ;% 837 P_CPLA2_PKC_CYTOSOL P_CPLA2_PKC_CYTOSOL
0.0 ;% 838 P_PKC_CYTOSOL P_PKC_CYTOSOL
0.0 ;% 839 P_PKC_SMAD2_CYTOSOL P_PKC_SMAD2_CYTOSOL
0.0 ;% 840 P_PKC_SMAD3_CYTOSOL P_PKC_SMAD3_CYTOSOL
0.0 ;% 841 IKB_NFKB_CYTOSOL IKB_NFKB_CYTOSOL
0.0 ;% 842 P_PKC_IKB_NFKB_CYTOSOL P_PKC_IKB_NFKB_CYTOSOL
0.0 ;% 843 P_IKB_NFKB_CYTOSOL P_IKB_NFKB_CYTOSOL
0.0 ;% 844 GPASE_P_AP1_CYTOSOL GPASE_P_AP1_CYTOSOL
0.0 ;% 845 GPASE_P_SP1_CYTOSOL GPASE_P_SP1_CYTOSOL
0.0 ;% 846 GPASE_P_CJUN_CYTOSOL GPASE_P_CJUN_CYTOSOL
0.0 ;% 847 GPASE_P_CPLA2_CYTOSOL GPASE_P_CPLA2_CYTOSOL
0.0 ;% 848 GPASE_P_SMAD2_CYTOSOL GPASE_P_SMAD2_CYTOSOL
0.0 ;% 849 GPASE_P_SMAD3_CYTOSOL GPASE_P_SMAD3_CYTOSOL
0.0 ;% 850 GPASE_P_NFATC1_CYTOSOL GPASE_P_NFATC1_CYTOSOL
0.0 ;% 851 GPASE_P_PKC_CYTOSOL GPASE_P_PKC_CYTOSOL
0.0 ;% 852 BMP2_BMPRII_ALK2_SMAD1_CYTOSOL BMP2_BMPRII_ALK2_SMAD1_CYTOSOL
0.0 ;% 853 BMP2_BMPRII_ALK2_SMAD5_CYTOSOL BMP2_BMPRII_ALK2_SMAD5_CYTOSOL
0.0 ;% 854 BMP2_BMPRII_ALK3_SMAD1_CYTOSOL BMP2_BMPRII_ALK3_SMAD1_CYTOSOL
0.0 ;% 855 BMP2_BMPRII_ALK3_SMAD5_CYTOSOL BMP2_BMPRII_ALK3_SMAD5_CYTOSOL
0.0 ;% 856 BMP2_BMPRII_ALK6_SMAD1_CYTOSOL BMP2_BMPRII_ALK6_SMAD1_CYTOSOL
0.0 ;% 857 BMP2_BMPRII_ALK6_SMAD5_CYTOSOL BMP2_BMPRII_ALK6_SMAD5_CYTOSOL
0.0 ;% 858 TGFB3_TGFBRII_ALK1_TGFBRIII_SMAD2_CYTOSOL
TGFB3_TGFBRII_ALK1_TGFBRIII_SMAD2_CYTOSOL
0.0 ;% 859 TGFB3_TGFBRII_ALK1_TGFBRIII_SMAD3_CYTOSOL
TGFB3_TGFBRII_ALK1_TGFBRIII_SMAD3_CYTOSOL
0.0 ;% 860 TGFB3_TGFBRII_ALK5_TGFBRIII_ENDOGLIN_SMAD2_CYTOSOL
TGFB3_TGFBRII_ALK5_TGFBRIII_ENDOGLIN_SMAD2_CYTOSOL
0.0 ;% 861 TGFB3_TGFBRII_ALK5_TGFBRIII_ENDOGLIN_SMAD3_CYTOSOL
TGFB3_TGFBRII_ALK5_TGFBRIII_ENDOGLIN_SMAD3_CYTOSOL
0.0 ;% 862 TGFB2_TGFBRII_ALK1_TGFBRIII_SMAD2_CYTOSOL
TGFB2_TGFBRII_ALK1_TGFBRIII_SMAD2_CYTOSOL
0.0 ;% 863 TGFB2_TGFBRII_ALK1_TGFBRIII_SMAD3_CYTOSOL
TGFB2_TGFBRII_ALK1_TGFBRIII_SMAD3_CYTOSOL
0.0 ;% 864 TGFB2_TGFBRII_ALK5_TGFBRIII_ENDOGLIN_SMAD2_CYTOSOL
TGFB2_TGFBRII_ALK5_TGFBRIII_ENDOGLIN_SMAD2_CYTOSOL
0.0 ;% 865 TGFB2_TGFBRII_ALK5_TGFBRIII_ENDOGLIN_SMAD3_CYTOSOL
TGFB2_TGFBRII_ALK5_TGFBRIII_ENDOGLIN_SMAD3_CYTOSOL
0.0 ;% 866 SMURF1_PSMAD1_CYTOSOL SMURF1_PSMAD1_CYTOSOL
0.0 ;% 867 UB_PSMAD1_CYTOSOL UB_PSMAD1_CYTOSOL
0.0 ;% 868 SMURF1_PSMAD5_CYTOSOL SMURF1_PSMAD5_CYTOSOL
0.0 ;% 869 UB_PSMAD5_CYTOSOL UB_PSMAD5_CYTOSOL
0.0 ;% 870 SMURF2_PSMAD2_CYTOSOL SMURF2_PSMAD2_CYTOSOL
0.0 ;% 871 UB_PSMAD2_CYTOSOL UB_PSMAD2_CYTOSOL

0.0 ;% 872 SMURF2_PSMAD3_CYTOSOL SMURF2_PSMAD3_CYTOSOL
0.0 ;% 873 UB_PSMAD3_CYTOSOL UB_PSMAD3_CYTOSOL
0.0 ;% 874 BCATENIN_ECADHERIN_CYTOSOL BCATENIN_ECADHERIN_CYTOSOL
0.0 ;% 875 BCATENIN_VECADHERIN_CYTOSOL BCATENIN_VECADHERIN_CYTOSOL
0.0 ;% 876 BCATENIN_PECAM1_CYTOSOL BCATENIN_PECAM1_CYTOSOL
0.0 ;% 877 P_IKB_CYTOSOL P_IKB_CYTOSOL
0.0 ;% 878 ACTIVE_AKT_IKB_NFKB_CYTOSOL ACTIVE_AKT_IKB_NFKB_CYTOSOL
0.0 ;% 879 VEGFA_VEGFR2_SHC_PI3K_CYTOSOL VEGFA_VEGFR2_SHC_PI3K_CYTOSOL
0.0 ;% 880 BMP2_BMPRII_ALK2_SHC_GRB2_SOS_PI3K_CYTOSOL
BMP2_BMPRII_ALK2_SHC_GRB2_SOS_PI3K_CYTOSOL
0.0 ;% 881 P_PLCG_CYTOSOL P_PLCG_CYTOSOL
0.0 ;% 882 AKT_PASE_P_PLCG_CYTOSOL AKT_PASE_P_PLCG_CYTOSOL
0.0 ;% 883 AKT_PASE_P_PKC_CYTOSOL AKT_PASE_P_PKC_CYTOSOL
0.0 ;% 884 P_SPK_CYTOSOL P_SPK_CYTOSOL
0.0 ;% 885 AKT_PASE_P_SPK_CYTOSOL AKT_PASE_P_SPK_CYTOSOL
0.0 ;% 886 AKT_PASE_P_SP1_CYTOSOL AKT_PASE_P_SP1_CYTOSOL
0.0 ;% 887 VEGFA_VEGFR2_PLCG_CYTOSOL VEGFA_VEGFR2_PLCG_CYTOSOL
0.0 ;% 888 P_PLCG_PIP2_CYTOSOL P_PLCG_PIP2_CYTOSOL
0.0 ;% 889 ACTIVE_PIP2_CYTOSOL ACTIVE_PIP2_CYTOSOL
0.0 ;% 890 ACTIVE_PI3K_PKC_CYTOSOL ACTIVE_PI3K_PKC_CYTOSOL
0.0 ;% 891 ACTIVE_PKC_CYTOSOL ACTIVE_PKC_CYTOSOL
0.0 ;% 892 ACTIVE_PIP2_PKC_CYTOSOL ACTIVE_PIP2_PKC_CYTOSOL
0.0 ;% 893 P_PKC_SPK_CYTOSOL P_PKC_SPK_CYTOSOL
0.0 ;% 894 P_PKC_SP1_CYTOSOL P_PKC_SP1_CYTOSOL
0.0 ;% 895 P_SPK_RAF_CYTOSOL P_SPK_RAF_CYTOSOL
100.0 ;% 896 RNAP_NUCLEAR RNAP_NUCLEAR
100.0 ;% 897 RIBOSOME_CYTOSOL RIBOSOME_CYTOSOL
100.0 ;% 898 NIMPORT_NUCLEAR NIMPORT_NUCLEAR
100.0 ;% 899 NEXPORT_NUCLEAR NEXPORT_NUCLEAR
100.0 ;% 900 EXIMPORT_CYTOSOL EXIMPORT_CYTOSOL
100.0 ;% 901 EXEXPORT_CYTOSOL EXEXPORT_CYTOSOL
100.0 ;% 902 GDP_CYTOSOL GDP_CYTOSOL
100.0 ;% 903 GTP_CYTOSOL GTP_CYTOSOL
100.0 ;% 904 PIP2_CYTOSOL PIP2_CYTOSOL
0.0 ;% 905 PIP3_CYTOSOL PIP3_CYTOSOL
0.0 ;% 906 GATA_FOG2_CYTOSOL GATA_FOG2_CYTOSOL
0.0 ;% 907 DELTEX_NEDD4_CYTOSOL DELTEX_NEDD4_CYTOSOL
1.0 ;% 908 DNA_SMURF1_NUCLEAR DNA_SMURF1_NUCLEAR
1.0 ;% 909 DNA_SMURF2_NUCLEAR DNA_SMURF2_NUCLEAR
5.0 ;% 910 DNA_SMAD1_NUCLEAR DNA_SMAD1_NUCLEAR
10.0 ;% 911 DNA_SMAD2_NUCLEAR DNA_SMAD2_NUCLEAR
10.0 ;% 912 DNA_SMAD3_NUCLEAR DNA_SMAD3_NUCLEAR
20.0 ;% 913 DNA_SMAD4_NUCLEAR DNA_SMAD4_NUCLEAR
5.0 ;% 914 DNA_SMAD5_NUCLEAR DNA_SMAD5_NUCLEAR
1.0 ;% 915 DNA_SMAD6_NUCLEAR DNA_SMAD6_NUCLEAR
1.0 ;% 916 DNA_SMAD7_NUCLEAR DNA_SMAD7_NUCLEAR
1.0 ;% 917 DNA_ENDOGLIN_NUCLEAR DNA_ENDOGLIN_NUCLEAR
1.0 ;% 918 DNA_ALK1_NUCLEAR DNA_ALK1_NUCLEAR
1.0 ;% 919 DNA_ALK2_NUCLEAR DNA_ALK2_NUCLEAR
1.0 ;% 920 DNA_ALK3_NUCLEAR DNA_ALK3_NUCLEAR
1.0 ;% 921 DNA_ALK5_NUCLEAR DNA_ALK5_NUCLEAR
1.0 ;% 922 DNA_ALK6_NUCLEAR DNA_ALK6_NUCLEAR
1.0 ;% 923 DNA_SHC_NUCLEAR DNA_SHC_NUCLEAR
1.0 ;% 924 DNA_GRB2_NUCLEAR DNA_GRB2_NUCLEAR
1.0 ;% 925 DNA_SOS_NUCLEAR DNA_SOS_NUCLEAR
1.0 ;% 926 DNA_BMPRII_NUCLEAR DNA_BMPRII_NUCLEAR
1.0 ;% 927 DNA_MSX1_NUCLEAR DNA_MSX1_NUCLEAR
1.0 ;% 928 DNA_AP1_NUCLEAR DNA_AP1_NUCLEAR
2.0 ;% 929 DNA_GPASE_NUCLEAR DNA_GPASE_NUCLEAR
1.0 ;% 930 DNA_TCF4_NUCLEAR DNA_TCF4_NUCLEAR
0.0 ;% 931 DNA_NOTCH1_NUCLEAR DNA_NOTCH1_NUCLEAR
0.0 ;% 932 DNA_SEL1_NUCLEAR DNA_SEL1_NUCLEAR
0.0 ;% 933 DNA_CSL_NUCLEAR DNA_CSL_NUCLEAR
1.0 ;% 934 DNA_RAS_NUCLEAR DNA_RAS_NUCLEAR
1.0 ;% 935 DNA_RAF_NUCLEAR DNA_RAF_NUCLEAR
1.0 ;% 936 DNA_MEK_NUCLEAR DNA_MEK_NUCLEAR
1.0 ;% 937 DNA_ERK_NUCLEAR DNA_ERK_NUCLEAR
1.0 ;% 938 DNA_RAF_PASE_NUCLEAR DNA_RAF_PASE_NUCLEAR
1.0 ;% 939 DNA_MEK_PASE_NUCLEAR DNA_MEK_PASE_NUCLEAR
1.0 ;% 940 DNA_ERK_PASE_NUCLEAR DNA_ERK_PASE_NUCLEAR
1.0 ;% 941 DNA_SP1_NUCLEAR DNA_SP1_NUCLEAR
0.0 ;% 942 DNA_CJUN_NUCLEAR DNA_CJUN_NUCLEAR
0.0 ;% 943 DNA_CPLA2_NUCLEAR DNA_CPLA2_NUCLEAR
0.0 ;% 944 DNA_GSK3B_NUCLEAR DNA_GSK3B_NUCLEAR
0.0 ;% 945 DNA_CK1_NUCLEAR DNA_CK1_NUCLEAR
0.0 ;% 946 DNA_APC_NUCLEAR DNA_APC_NUCLEAR
0.0 ;% 947 DNA_LRP_NUCLEAR DNA_LRP_NUCLEAR
0.0 ;% 948 DNA_AXIN_NUCLEAR DNA_AXIN_NUCLEAR
1.0 ;% 949 DNA_PKC_NUCLEAR DNA_PKC_NUCLEAR
0.0 ;% 950 DNA_BTRCP_NUCLEAR DNA_BTRCP_NUCLEAR
0.0 ;% 951 DNA_FRIZZLED_NUCLEAR DNA_FRIZZLED_NUCLEAR
1.0 ;% 952 DNA_BCATENIN_NUCLEAR DNA_BCATENIN_NUCLEAR
0.0 ;% 953 DNA_DISHEVELLED_NUCLEAR DNA_DISHEVELLED_NUCLEAR
1.0 ;% 954 DNA_AKT_NUCLEAR DNA_AKT_NUCLEAR
1.0 ;% 955 DNA_PI3K_NUCLEAR DNA_PI3K_NUCLEAR
1.0 ;% 956 DNA_PTEN_NUCLEAR DNA_PTEN_NUCLEAR
1.0 ;% 957 DNA_PDK1_NUCLEAR DNA_PDK1_NUCLEAR
1.0 ;% 958 DNA_AKT_PASE_NUCLEAR DNA_AKT_PASE_NUCLEAR
0.0 ;% 959 DNA_IKB_NUCLEAR DNA_IKB_NUCLEAR
0.0 ;% 960 DNA_NFKB_NUCLEAR DNA_NFKB_NUCLEAR
1.0 ;% 961 DNA_VEGFR2_NUCLEAR DNA_VEGFR2_NUCLEAR
0.0 ;% 962 DNA_TBX20_NUCLEAR DNA_TBX20_NUCLEAR
0.0 ;% 963 DNA_ALPHASMA_NUCLEAR DNA_ALPHASMA_NUCLEAR

```
		0.0		;%		964		DNA_CYCLINB2_NUCLEAR		DNA_CYCLINB2_NUCLEAR
		0.0		;%		965		DNA_PECAM1_NUCLEAR		DNA_PECAM1_NUCLEAR
		0.0		;%		966		DNA_SLUG_NUCLEAR	DNA_SLUG_NUCLEAR
		0.0		;%		967		DNA_SNAIL_NUCLEAR	DNA_SNAIL_NUCLEAR
		0.0		;%		968		DNA_LEF1_NUCLEAR	DNA_LEF1_NUCLEAR
		1.0		;%		969		DNA_TGFBRII_NUCLEAR	DNA_TGFBRII_NUCLEAR
		1.0		;%		970		DNA_TGFBRIII_NUCLEAR		DNA_TGFBRIII_NUCLEAR
		0.0		;%		971		DNA_TGFB3_NUCLEAR	DNA_TGFB3_NUCLEAR
		0.0		;%		972		DNA_TGFB2_NUCLEAR	DNA_TGFB2_NUCLEAR
		1.0		;%		973		DNA_VIMENTIN_NUCLEAR		DNA_VIMENTIN_NUCLEAR
		1.0		;%		974		DNA_ECADHERIN_NUCLEAR		DNA_ECADHERIN_NUCLEAR
		1.0		;%		975		DNA_VECADHERIN_NUCLEAR		DNA_VECADHERIN_NUCLEAR
		0.0		;%		976		DNA_DSCR1_NUCLEAR	DNA_DSCR1_NUCLEAR
		0.0		;%		977		DNA_SOX9_NUCLEAR	DNA_SOX9_NUCLEAR
		0.0		;%		978		DNA_PAX3_NUCLEAR	DNA_PAX3_NUCLEAR
		0.0		;%		979		DNA_MMP9_NUCLEAR	DNA_MMP9_NUCLEAR
		1.0		;%		980		DNA_NFATC1_NUCLEAR	DNA_NFATC1_NUCLEAR
		0.0		;%		981		DNA_CALCNCAM_NUCLEAR		DNA_CALCNCAM_NUCLEAR
		0.0		;%		982		DNA_TWIST_NUCLEAR	DNA_TWIST_NUCLEAR
		0.0		;%		983		DNA_SPK_NUCLEAR		DNA_SPK_NUCLEAR
		0.0		;%		984		DNA_PLCG_NUCLEAR	DNA_PLCG_NUCLEAR
		0.0		;%		985		DNA_CREB_NUCLEAR	DNA_CREB_NUCLEAR
		1.0		;%		986		DNA_YREG1_NUCLEAR	DNA_YREG1_NUCLEAR
		1.0		;%		987		DNA_LOADING_NUCLEAR		DNA_LOADING_NUCLEAR
		0.0		;%		988		WNT9A_EXTRACELLULAR		WNT9A_EXTRACELLULAR
		0.0		;%		989		VEGFA_EXTRACELLULAR		VEGFA_EXTRACELLULAR
		0.0		;%		990		BMP2_EXTRACELLULAR	BMP2_EXTRACELLULAR
		0.0		;%		991		TGFB2_EXTRACELLULAR		TGFB2_EXTRACELLULAR
		0.0		;%		992		TGFB3_EXTRACELLULAR		TGFB3_EXTRACELLULAR
		0.0		;%		993		JAG1_EXTRACELLULAR	JAG1_EXTRACELLULAR
		0.0		;%		994		DELTA4_EXTRACELLULAR		DELTA4_EXTRACELLULAR
		0.0		;%		995		ACTIVE_NCID_CYTOSOL	ACTIVE_NCID_CYTOSOL
];

% Load parameter sets from disk -
NPARAMETERS=length(k);
NSTATES=length(IC);
kV = [k ; IC];
% Ok, override the choice of parameters above, load from disk -
if (~isempty(INDEX))
	cmd=['load PSET_',num2str(INDEX),'.mat'];
	eval(cmd);
	kV = kP;
	% get k and IC -
	k=kV(1:NPARAMETERS);
	IC=kV((NPARAMETERS+1):end);
end;

% ========== DO NOT EDIT BELOW THIS LINE ==============
DF.STOICHIOMETRIC_MATRIX=S;
DF.RATE_CONSTANT_VECTOR=k;
DF.INITIAL_CONDITIONS=IC;
DF.NUMBER_PARAMETERS=NPARAMETERS;
DF.NUMBER_OF_STATES=NSTATES;
DF.PARAMETER_VECTOR=kV;
% ====================================================
return;
```

Appendix - D

Supplementary Methods and Figures

Formulation and Solution of the Model Equations. The EMT model was formulated as a set of coupled non-linear ordinary differential equations (ODEs):

$$\frac{d\mathbf{x}}{dt} = \mathbf{S} \cdot \mathbf{r}\left(\mathbf{x}, \mathbf{p}\right) \qquad \mathbf{x}\left(t_o\right) = \mathbf{x}_o \tag{S1}$$

The symbol $\mathbf{S}$ denotes the stoichiometric matrix (995×1700). The quantity $\mathbf{x}$ denotes the concentration vector of proteins or protein complexes (995×1). The term $\mathbf{r}\left(\mathbf{x}, \mathbf{p}\right)$ denotes the vector of reaction rates (1700×1), where $\mathbf{p}$ denotes the vector of kinetic parameters. The (i, j) element of the matrix $\mathbf{S}$, denoted by σ_{ij}, described how protein i was involved in rate j. If $\sigma_{ij} < 0$, protein i was consumed by r_j. Conversely, if $\sigma_{ij} > 0$, protein i was produced by r_j. Lastly, if $\sigma_{ij} = 0$, protein i was not involved in rate j. We assumed mass-action kinetics for each interaction in the network. All reversible interactions were split into two irreversible steps, and complex processes such as transcription or translations were broken into elementary mass-action steps. Thus, the rate expression for interaction q was given by:

$$r_q\left(\mathbf{x}, k_q\right) = k_q \prod_{j \in \{\mathbf{R}_q\}} x_j^{-\sigma_{jq}} \tag{S2}$$

The set $\{\mathbf{R}_q\}$ denotes reactants for reaction q, while σ_{jq} denotes the stoichiometric coefficient (element of the matrix $\mathbf{S}$) governing species j in reaction q. The quantity k_q denotes the rate constant (unknown) governing reaction q.

Model equations were generated using UNIVERSAL from an SBML input file (available in the supplemental materials). UNIVERSAL is an open source Objective-C/Java code generator, available at Google Code (http://code.google.com/p/universal-code-generator/). The model equations were solved using the LSODE routine in OCTAVE (v 3.0.5; www.octave.org) on an Apple workstation (Apple, Cupertino, CA; OS X v10.6.4).

Estimation and Cross-Validation of a Population of EMT models. We used the Pareto Optimal Ensemble Technique (POETs) multiobjective optimization framework in combination with leave-one-out cross-validation to estimate an ensemble of TGFβ/EMT models. Cross-validation was used to calculate both training and prediction error during the parameter estimation procedure (35). The 41 intracellular protein and mRNA data-sets used for identification were organized into 11 objective functions. These 11 objective functions were then partitioned, where each partition contained ten training objectives and one validation objective. POETs integrates standard search strategies e.g., Simulated Annealing (SA) or Pattern Search (PS) with a Pareto-rank fitness assignment (9). Denote a candidate parameter set at iteration $i+1$ as $\mathbf{k}_{i+1}$. The squared error for $\mathbf{k}_{i+1}$ for training set j was defined as:

$$E_j(\mathbf{k}) = \sum_{i=1}^{\mathcal{T}_j} \left(\hat{\mathcal{M}}_{ij} - \hat{y}_{ij}(\mathbf{k}) \right)^2 \tag{S3}$$

The symbol $\hat{\mathcal{M}}_{ij}$ denotes scaled experimental observations (from training set j) while $\hat{y}_{ij}$ denotes the scaled simulation output (from training set j). The quantity i denotes the sampled time-index and $\mathcal{T}_j$ denotes the number of time points for experiment j. In this study, the experimental data used for model training was typically the band intensity from Western or Northern blots. Band intensity was estimated using the ImageJ software package (36). The scaled measurement for species x at time $i = \{t_1, t_2, .., t_n\}$ in condition j is given by:

$$\hat{\mathcal{M}}_{ij} = \frac{\mathcal{M}_{ij} - \min_i \mathcal{M}_{ij}}{\max_i \mathcal{M}_{ij} - \min_i \mathcal{M}_{ij}} \tag{S4}$$

Under this scaling, the lowest intensity band equaled zero while the highest intensity band equaled one. A similar scaling was defined for the simulation output. By doing this scaling, we trained the model on the relative change in blot intensity, over conditions or time (depending upon the experiment). Thus, when using multiple data sets (possibly from different sources) that were qualitatively similar but quantitatively different e.g., slightly different blot intensities over time or condition, we captured the underlying trends in the scaled data.

We computed the Pareto rank of $\mathbf{k}_{i+1}$ by comparing the simulation error at iteration $i+1$ against

an archive of accepted parameter sets $\mathbf{K}_i$. We used the Fonseca and Fleming ranking scheme (37) to estimate the number of parameter sets in the archive that dominate $\mathbf{k}_{i+1}$. Parameter sets with increasing rank were progressively further away from the optimal trade-off surface. The parameter set $\mathbf{k}_{i+1}$ was accepted or rejected by POETs with probability $\mathcal{P}(\mathbf{k}_{i+1})$:

$$\mathcal{P}(\mathbf{k}_{i+1}) \equiv \exp\left\{-rank\left(\mathbf{k}_{i+1} \mid \mathbf{K}_i\right)/T\right\} \tag{S5}$$

where T is the annealing temperature and $rank\left(\mathbf{k}_{i+1} \mid \mathbf{K}_i\right)$ denotes the Pareto rank for $\mathbf{k}_{i+1}$. The annealing temperature was discretized into 10 quanta between T_o and T_f and adjusted according to the schedule $T_k = \beta^k T_0$ where β was defined as $(T_f/T_o)^{1/10}$. The initial temperature was $T_o = n/log(2)$, where $n = 4$ in this study and the final temperature was $T_f = 0.1$. The epoch-counter k was incremented after the addition of 100 members to the ensemble. Thus, as the ensemble grew, the likelihood of accepting parameter sets with a large Pareto rank decreased. To generate parameter diversity, we randomly perturbed each parameter by $\leq \pm 25\%$ at iteration of the search. In addition, we performed a local pattern search every q-iterations to minimize the residual for a single random or the worst performing objective function. The local pattern-search algorithm has been described previously (38). From the 15,000 probable EMT models, we selected N = 1093 models with Pareto rank ≤ 1 for subsequent analysis.

Robustness Analysis of the EMT Model Population. Robustness coefficients were calculated for 55 models selected from the ensemble (rank-zero, low-correlation, minimum error selection). We surveyed only this subset of models (instead of the entire population of low rank models) because of the computational cost of the robustness analysis. The selected models were all rank ≤ 1 and were largely uncorrelated; 67% of the selected models had a correlation less that 0.28, where the mean correlation was 0.28 $\pm$ 0.04. For each of the 55 models, coefficients were calculated as shown previously (13). Briefly, Robustness coefficients (denoted by $\alpha(i, j, t_o, t_f)$) are the ratio of the integrated concentration of a network marker in the presence (numerator) and absence (denominator) of a structural or operational perturbation. The quantities t_0 and t_f denote the initial and final simulation time, respectively, while i and j denote the indices for the marker and the perturbation respectively. If $\alpha(i, j, t_o, t_f) > 1$, then the perturbation *increased* the marker con-

centration. Conversely, if $\alpha\left(i,j,t_o,t_f\right) < 1$ the perturbation *decreased* the marker concentration. Lastly, if $\alpha\left(i,j,t_o,t_f\right) \sim 1$ the perturbation did not influence the marker concentration.

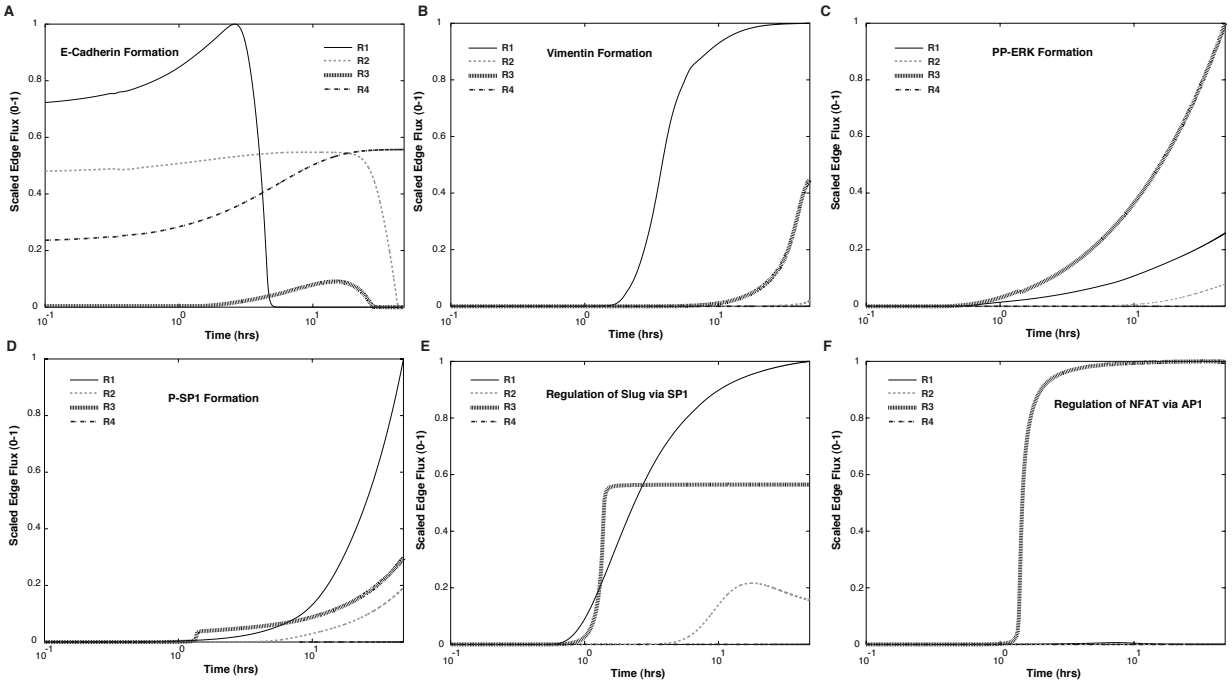

Figure 7. S1: Flux-analysis describing flow through the four distinct regions.

O#	**Species (cystolic protein)**	**Cell Type**	**Training**	**Prediction**	**Random**	**Source**
O1	LEF1	DLD1 CC, MDCKII, A375 MC	0.73 ± 0.22	0.66 ± 0.18	0.87 ± 0.02	Medici et al., 2008
O2	Vimenin	DLD1 CC, MDCKII, A375 MC	0.96 ± 0.11	1.00 ± 0.15	0.23 ± 0.04	"
O3	TGFbeta3	DLD1 CC, MDCKII, A375 MC	1 00 ± 0.13	0.77 ± 0.22	0.61 ± 0.04	"
O4	E-Caderin	DLD1 CC, MDCKII, A375 MC	0 54 ± 0.16	0.00 ± 0.00	0.15 ± 0.03	"
O5	beta-catenin	DLD1 CC, MDCKII, A375 MC	0.99 ± 0.25	0.00 ± 0.00	0.00 ± 0.00	"
O6	TGFbeta3	DLD1 CC, MDCKII, A375 MC	0.89 ± 0.14	0.71 ± 0.12	0.58 ± 0.04	"
O7	Snail	DLD1 CC, MDCKII, A375 MC	0.00 ± 0.00	0.00 ± 0.00	0.00 ± 0.00	"
O8	LEF1	DLD1 CC, MDCKII, A375 MC	1.00 ± 0.14	1.00 ± 0.25	0.61 ± 0.05	"
O9	E-Caderin	DLD1 CC, MDCKII, A375 MC	0.96 ± 0.20	0.86 ± 0.19	0.00 ± 0.00	"
O10	Slug	DLD1 CC, MDCKII, A375 MC	1.00 ± 0.20	1.00 ± 0.12	0.00 ± 0.00	"
O11	LEF1	DLD1 CC, MDCKII, A375 MC	1.00 ± 0.15	1.00 ± 0.25	0.86 ± 0.03	"
P#	**Species**		**Simulated**	**Experimental**	**Random**	**Source**
P1	E-caderin (mRNA)	MDCKII	0.10 ± 0.01	0.13 ± 0.02	0.27 ± 0.03	Medici et al., 2006
P2	pSmad2	MDCKII	0.58 ± 0.12	0.80 ± 0.04	0.13 ± 0.03	"
P3	LEF1 (mRNA)	MDCKII	0.76 ± 0.05	0.65 ± 0.04	0.18 ± 0.03	"

Table T1: Our model was able to effectively predict the simulated experiments 78 percent of the time. The high predictability can be contributed to the leave-one-out cross validation scheme, objective functions with overlapping data, and multi-objective optimization (POETs). The residuals between the EMT model, intracellular protein, and mRNA data sets (organized into 11 objective functions) were simultaneously minimized using the POETs multi-objective optimization algorithm (9). Because the parameter identification problem was under-determined, we used an iterative leave-one-out cross-validation strategy to independently estimate both the prediction and training error during the parameter estimation process. At each iteration of the cross-validation, a single objective was reserved for validation while the remaining ten were used for training. Thus, eleven different model families consisting of more than 15,000 probable models, were generated by the optimization procedure. Of the 15,000 probable models, we selected N$\sim$1100 models with Pareto rank one or less for further study. These models were largely uncorrelated; the mean model correlation was 0.23$\pm$0.03, as 71% of the models had a correlation less than 0.23. Approximately 78% of the training objectives were statistically significantly better (at a 95% confidence interval) than randomized parameter sets generated from the best-fit nominal set (starting point for the optimization). The most tightly constrained parameters governed LEF1 expression, Snail transcription, and TGFβ3 regulation, while the least constrained parameters involved crosstalk between MAPK and ERK mediated AP1 activation.

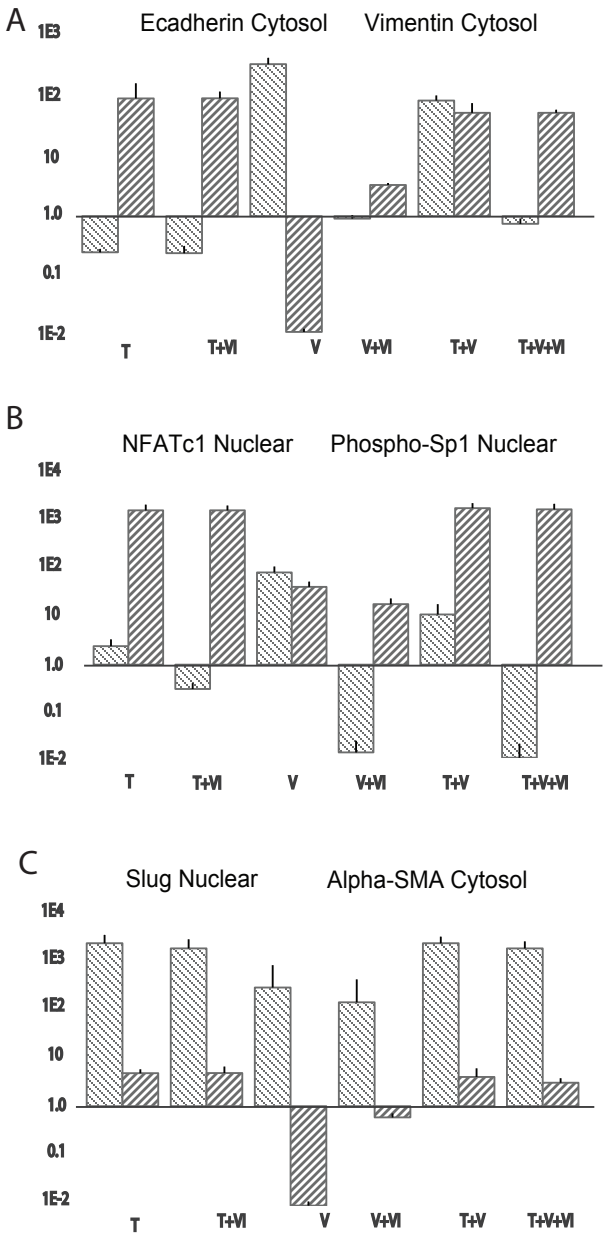

Figure 7. S2: Simulated TGFβ2 and VEGFA (known inducer of NFAT) combination re-creates phenotype heterogeneity through NFAT and phospho-Sp1. Bar graphs represent the raw simulated values at 48 hr. (A-C) These simulations were further quantified by plotting concentrations at 48 hrs for downstream targets (ecadherin, vimentin, phospho-Sp1, nuclear NFAT, alpha-SMA, and Slug). In whole, high levels of phospho-Sp1 correlated with vimentin expression, while NFAT was found largely responsible for maintaining ecadherin expression, although neither mutually exclusive.

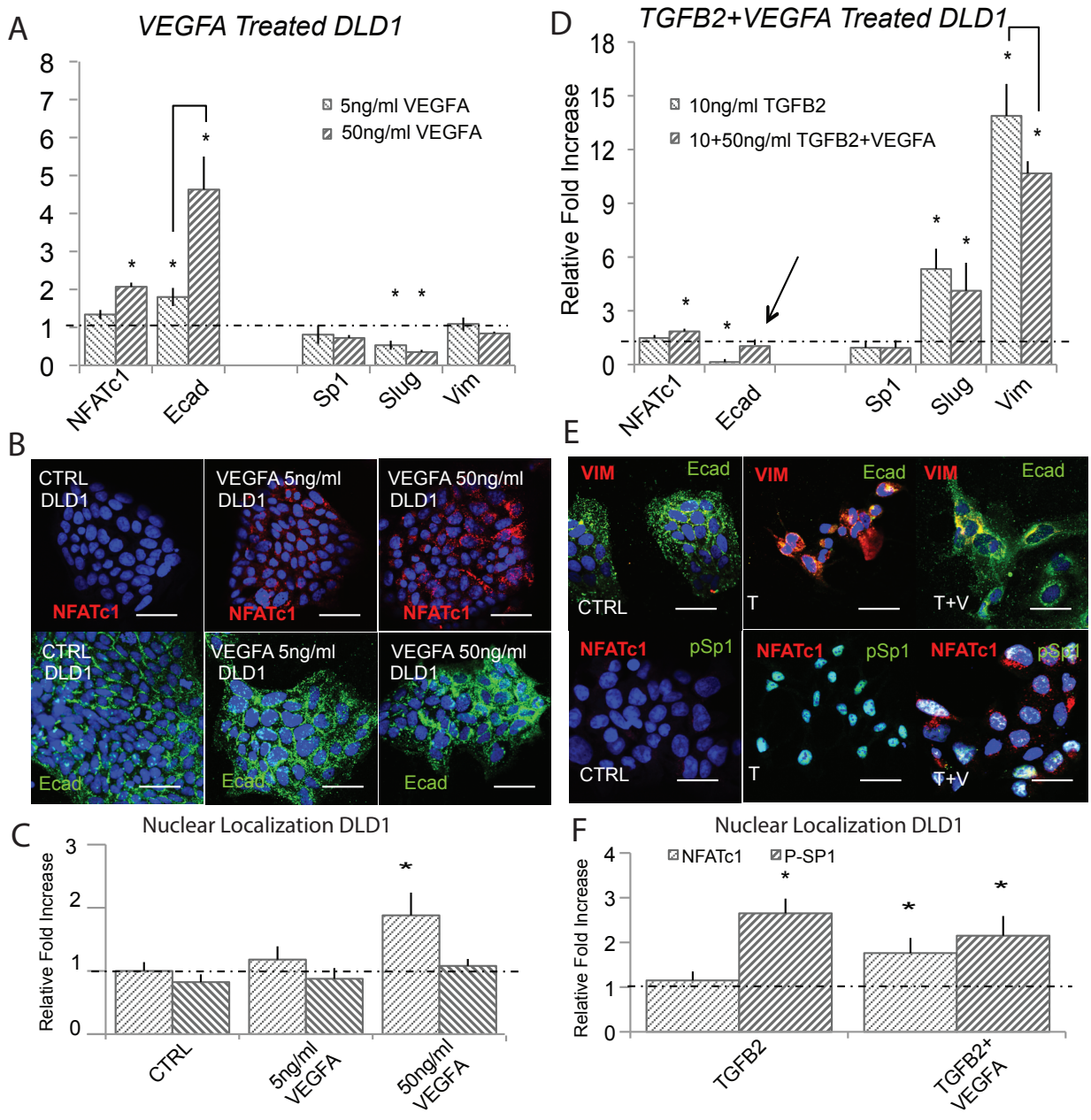

Figure 7. S3: VEGFA attentuates TGFβ2 to induce phenotype heterogeneity in DLD1. (A) In DLD1, we found that 5ng/ml of VEGFA increased NFATc1 and ecadherin gene expression via qPCR and 50ng/ml potentiated this effect at 48 hrs. (B-C) These findings were confirmed at the protein level via immunofluorescence, as ecadherin levels and nuclear localization of NFATc1 increased. (D) Treatment with (10ng/ml) TGFβ2 resulted in mesenchymal transformation as measured via qPCR against target genes Slug, ecadherin, vimentin, Sp1, and NFATc1. (E-F) Immunofluorescence and nuclear localization revealed a strong presence of phospho-Sp1. (D) Combination of VEGFA (50ng/ml) and TGFβ2 (10ng/ml) treatment resulted in increased Slug, NFATc1, and vimentin expression, while also increaseing ecadherin levels compared to control. (E) Immunofluorescence confirmed these results, as both ecadherin and vimentin levels were elevated. (F) A signficant increase in nuclear localization of both NFATc1 and phospho-Sp1 were also found. Magnification, 40x. Scale bars: 50μm. C=Control, T=TGFβ2 , V=VEGFA, VI=NFAT inhibitor (VIVIT). Asterisks signify statistical differences from each other according to a one-way ANOVA with Tukey's post hoc ($p \prec 0.05$).

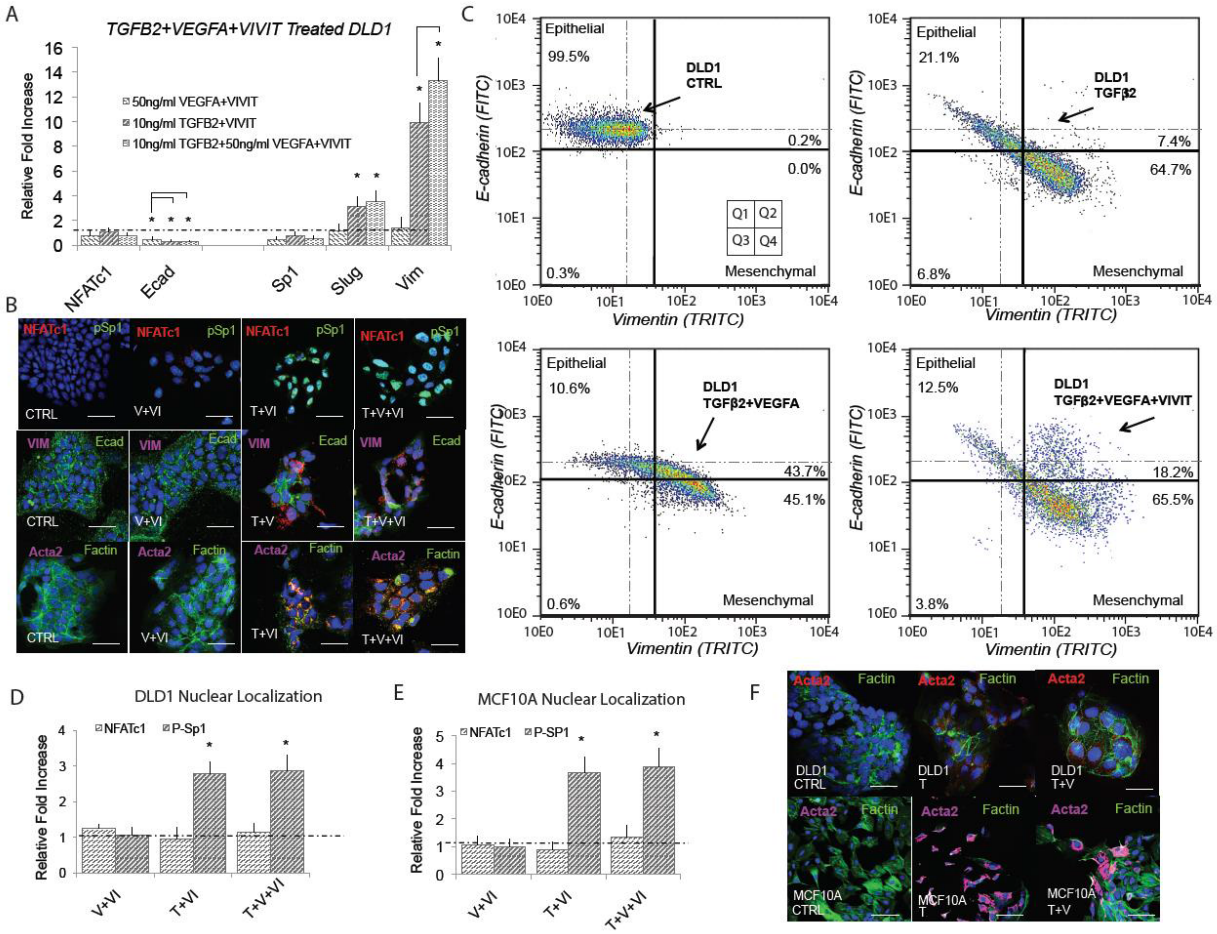

Figure 7. S4: Ecadherin expression is dependent upon NFAT activity in DLD1. (A) Treatment with VEGFA (50ng/ml) and NFAT inhibitory peptide VIVIT (10μM) resulted in significantly reduced ecadherin expression via qPCR at 48hrs. Addition of TGFβ2 (10ng/ml) and VIVIT resulted in increased Slug and vimentin expression, while inhibiting ecadherin levels. Combined TGFβ2, VEGFA, and VIVIT treatment resulted in target genes Slug and vimentin expression increased, while inhibiting ecadherin levels. No change in Sp1 or NFATc1 expression was found. (B) These findings were confirmed via immunofluorescence as the VIVIT inhibitors was shown to inhibit ecadherin levels in all three cases. We also found no change in gene or nuclear localization of NFATc1 in all three cases, while phospho-Sp1 was found to increase in both TGFβ conditions. (C) Quantitative flow cytometry also confirmed this trend. (D,E) TGFβ2, VEGFA and VIVIT treatment in DLD1 and MCF10A resulted in no change of Sp1 expression or NFATc1 expression. (G) Likewise, no change in nuclear localization of NFAT in all three cases, however phospho-Sp1 was found to increase in both TGFβ conditions. Magnification, 40x. Scale bars: 50μm. C=Control, T=TGFβ2 , V=VEGFA, VI= NFAT inhibitor (VIVIT). Asterisks signify statistical differences from each other according to a one-way ANOVA with Tukey's post hoc ($p \prec 0.05$).

VITA

Russell was born February 15, 1985 in Trenton, New Jersey, the son of Drew Allen Gould and Margaret Ann Gould. Russell attended public schools all his life, and entertained a career in the Navy before opting to go to the Rensselaer Polytechnic Institute to study mechanical and bioengineering. He graduated in 2006 with a Bachelor's degree in Biomedical Engineering, and his research there was focused on understanding the role of shear role and inflammatory factors on the progression of atherosclerosis. Cornell University provided a completely new area of research for him where he could focus on regenerative and biological medicine for applications in cardiovascular disease. While at Cornell, Russell met his future wife Katrina Shum. The next chapter of their life will be in Baltimore, MD, where Russell has a postdoctoral position in a cardiovascular cell biology lab with Dr. Hal Dietz.